

THIS WEEK

EDITORIALS

WORLD VIEW Yvo de Boer on the lessons of the climate talks in Copenhagen **p.477**

CHILDHOOD LOST Did Neanderthals simply grow up too fast? **p.478**



HOOKED Antarctic toothfish is sustainable — official **p.480**

The party's over

Caffeinated alcoholic drinks, popular with students, are now being targeted by US regulators. But if government is serious about addressing alcohol abuse, it must confront more powerful foes.

Do alcohol and caffeine mix? The US Food and Drug Administration (FDA) has ruled they do not. Last week, FDA officials stamped on the makers of pre-mixed caffeinated alcoholic drinks, saying the products are “adulterated” by the addition of caffeine, which it said in this context was an “unsafe food additive”.

The FDA's target was drinks such as Four Loko, a can of which packs the punch of a bottle of wine and two or three cups of coffee and may sell for less than US\$3. The food regulator, prompted by a wave of publicity for incidents in which young people were made seriously ill after over-indulging in the drinks, says manufacturers of Four Loko and six other caffeinated alcoholic drinks must remove the caffeine from their products, or their products from store shelves — or risk having them seized. Even before the decision was announced, Four Loko's maker, a small company called Phusion Projects in Chicago, Illinois, had agreed to remove the caffeine from its popular flagship product.

The drinks are said by the FDA to be of special concern because the caffeine counters the alcohol's soporific effects, leading largely young and inexperienced drinkers to drink more, and to perceive themselves as more capable, and less drunk, than they actually are. The science in this area is in its early days and incomplete, but several studies do show cause for concern. One measured the breath-alcohol levels of 623 drinkers — almost all of them students — leaving bars in a Florida university district in 2008. It found those who had consumed alcohol mixed with caffeinated energy drinks were three times more likely to leave the bar highly intoxicated, and four times more likely to intend to drive, compared with drinkers who consumed alcohol alone (D. L. Thombs *et al.* *Add. Behav.* **35**, 325–330; 2010).

The FDA's move is a sensible precaution as far as it goes, but it can hardly be seen as serious government action to curb the death, disease and destruction caused by alcohol. The National Institute on Alcohol Abuse and Alcoholism, in Bethesda, Maryland, puts the US annual bill for the medical, social and economic cost of alcohol abuse at \$235 billion — almost 80% more than the costs related to all other addictive drugs combined. Alcohol, which damages virtually every organ system, claims more than 80,000 lives each year in the United States alone, and is responsible for about one-third of all fatal car crashes, half of all homicides, one-third of all suicides and one-third of all hospital admissions.

Nor are trends encouraging. In a 2007 survey of more than 100,000 15- and 16-year-olds in 35 European countries by the European Monitoring Centre for Drugs and Drug Addiction in Lisbon, Portugal, almost half said they had drunk heavily in the previous month.

The US makers of the caffeinated alcohol drinks, who made no secret of courting young people with their products, were an easy target for the FDA: small and obscure and without political muscle. The big global players, Anheuser-Busch InBev and MillerCoors, under pressure from state attorneys-general pulled their own caffeinated alcoholic drinks from the market in 2008, and agreed not to make them in future.

That they were willing to walk away without a fight speaks to the tiny sliver of US alcohol sales that such caffeinated drinks represent. Sales of alcoholic drinks are estimated to be worth about \$100 billion a year; by contrast, sales of Four Loko, the most popular of the FDA-targeted drinks, were just \$144 million over the past 12 months.

Government must look far more seriously at curbing alcohol consumption.

If the move against these small companies is truly driven by evidence-based policy-making for public health, and not by the scoring of easy political points, the government must now look far more seriously at curbing alcohol consumption more generally, whether through higher taxes, stricter penalties for sales to underage drinkers, or — taking a leaf from the FDA's proposed script for cigarette packaging — requiring bottles to be emblazoned with graphic photos of cirrhotic livers, oesophageal varices and smashed vehicles under prominent messages such as ‘Alcohol Kills’.

The industry will, of course, fight tooth and nail against any such moves. And in the beginning at least, it may triumph, as strong-armed soft-drinks manufacturers have in forestalling ‘soda taxes’ aimed at combating obesity. But if policy-makers are serious about limiting the damage caused by problem drinking, they must work towards a day when alcohol abuse has the same pariah status as tobacco. Not only would this move save untold lives, it would make a great deal of scientific sense. ■

Treated fairly?

Moves to price new pharmaceuticals sensibly shouldn't damage the industry's health.

Europe has long had a love-hate relationship with the pharmaceutical industry. When politicians wish to boast of the high-tech and knowledge-based economies they have fostered, they wheel out the profitable returns from drug companies. Yet when the public mood suits, those same politicians criticize the profits, and use them to justify calls for price cuts.

The price of medicines, especially costly new drugs, is again a hot topic in cash-strapped Europe. Several countries are weighing up new ways to determine both the cost and the value of such medicines. The move would have pleased Oscar Wilde, who famously remarked that a cynic knew the price of everything and the value of nothing; but the pharmaceutical giants are nervous.

Done well, novel pricing mechanisms could foster innovative

research and spread the benefits of new medicines more widely. Done poorly, they could drive a wedge between governments and the industry, one of the most important parts of Europe's research base.

Whether an individual believes that drugs are overpriced is often determined by their politics, their health and whether they have ever worked in the pharmaceutical sector. What is not in doubt is that uncontrolled drug pricing is not a sustainable policy and that governments are taking action to drive prices down. Price cuts forced on the industry by politicians can be divisive. More innovative approaches, already under discussion in a number of countries, seem a better bet. Science can and should inform this reform.

Earlier this month, Germany pushed a law through its lower house to restructure its pharmaceutical market. These rules will allow companies to set prices for a year, after which they will have to prove that new medicines deserve to be priced higher than the going market rate for similar products. This is a sensible strategy. A healthy market needs significantly better drugs, not more of the same.

Britain, too, is seeking to pay for drugs only what it thinks they are worth. At the moment, the National Institute for Health and Clinical Excellence (NICE) helps in the task by producing solid research on the cost-effectiveness of new drugs. At present, the deliberations of NICE are merely used to accept or reject a drug for widespread use as priced by its manufacturers. Recently, it rejected Roche's Avastin (bevacizumab) treatment for patients with colorectal cancer, which costs £20,800 (US\$33,000) per patient but was judged to bring only modest benefit.

Next month the UK government will consult on plans to shift from this approach to a value-based pricing model, under which drug

companies and health officials would effectively haggle over price. Such a move is fraught with difficulty and must be very carefully managed. NICE may be the enemy of patient groups desperate for expensive treatments, but it is internationally respected for its robust use of scientific evidence. Under the coming changes, some experts fear that decisions on whether to introduce high-priced drugs will be fobbed off onto regions or even individual physicians — a move that could bring widespread variation in the availability of new drugs.

Poorly cast drug pricing mechanisms could drive a wedge between government and big pharma.

There are also legitimate concerns about the impact of such variable pricing systems on the pharmaceutical sector. With the approximate cost of bringing a drug to market now \$1 billion, and an expensive new wave of medicines such as the protein-derived biologics on the horizon, governments must be prepared to pay a high price for innovative drugs, or risk seeing science stall.

If industry is to cooperate with the changes, which it should, politicians must proceed on the basis that a new regime must be designed to value and distribute drugs in a better way, not simply to reduce national deficits by shrinking their health-care bills.

Some dire warnings are unlikely to be realized — such as those from industry groups that a system that hits profits could see their members abandon an ungrateful Europe. But governments must remember that big pharma is a crucial component of the continent's research ecology. It should not be exploited for short-term political and economic gain. ■

Citizen scientists

Scientists should speak out on the environmental effects of ventures such as tar-sands mining.

Canada's international reputation as a green and gentle nation has long been a matter of national pride. But is that reputation deserved? Canada's actions on environmental issues — from ignoring Kyoto Protocol targets to obstructing progress at United Nations climate-change talks — are increasingly raising eyebrows, both at home and abroad. Perhaps nothing is more emblematic of this reality gap than Canada's determination to mine its tar sands at a frantic rate. The sands are a dirty source of oil. They require more energy for oil extraction than do conventional reserves, producing extra greenhouse-gas emissions. The industry has torn up vast swathes of landscape, created toxic ponds of waste and released pollutants into waterways. Where such issues justify pressure for action, it is crucial that scientists such as David Schindler (see page 499) highlight them.

It would be unrealistic to expect that we could harvest fossil fuels or minerals without an effect on the environment. No form of mining is clean. But the fast development of the tar sands, combined with weak regulation and a lack of effective watchdogs, have made them an environmentalist's nightmare. Both independent scientists and mining companies are already taking steps to mitigate the sands' environmental impact. The industry reduced extraction emissions per barrel by an average of about 30% in the 1990s. And, at the University of Alberta in Edmonton, work is under way to find a way to extract oil from tar sands without using vast quantities of water, effectively replacing the current method with a chemical 'dry cleaning' process. Such a technique, if feasible, would reduce pressure on the local rivers as a water supply and would dampen the continual expansion of toxic tailings ponds.

Companies are unlikely to invest in expensive remedial solutions

unless they are forced to do so by environmental regulations, some of which are already in place. The provincial Albertan government is seemingly more progressive than the federal Canadian government in its climate-change plan. Large companies have had to meet a one-time 12% reduction in their emissions per barrel from 2007 onwards, with those that have been unable to comply paying Can\$15 (US\$14.7) per tonne on their extra emissions, making the province one of only a few places in the world with a mandated price on carbon. There are rules insisting that companies have plans to reclaim lands used and to deal with tailings ponds. And there are fines for non-compliance. The oil company Syncrude was last month fined Can\$3.2 million for the deaths of 1,600 birds that landed in its tailings ponds — the biggest environmental fine in Alberta's history. From this, Can\$1.3 million will go to the University of Alberta for research into better bird deterrents, which the company will be obliged to enact.

But many of these rules are weaker than they seem. A boom in production will still see overall emissions go through the roof. Only a single 1 km² plot has been certified as reclaimed so far in more than 600 km² of mining area. A long-promised Alberta land-use framework, which would set limits on development, has yet to be completed. And of five mining operations that have had their plans for dealing with tailings ponds evaluated, just two met directives. The other three were granted grace periods extending to 2018 to sort out their mess.

Canada's tar sands, like the Deepwater Horizon oil spill, are a warning sign of things to come. Future sources of fossil fuels will only get dirtier and riskier. Many have predicted that the next big boom will be in shale gas, which suffers from methane gas leaks that could make it as 'dirty' a resource as coal. It is more important than ever for scientists to monitor environmental impacts and to speak up to raise legitimate concerns. The University of Maryland's Margaret Palmer helped to bring international attention to the environmental problems associated with mountain-top mining, for example, leading to more stringent enforcement of regulations in the United States. Scientists can make a difference, not, as some critics allege, by playing politics, but by applying their expertise as concerned citizens. ■

➔ **NATURE.COM**
To comment online,
click on Editorials at:
go.nature.com/xhunq



Copenhagen shows we need caution in Cancún

Next week's climate meeting in Mexico should avoid talk of more ambitious targets, says Yvo de Boer. First, we need people to believe in green growth.

What can we expect from the next round of international climate negotiations, which begin next week in Cancún, Mexico? A lead negotiator from a major developing country recently told me that the probable outcome was “anybody’s guess”. That gives me an uncomfortable feeling that Cancún will be Copenhagen revisited. There are many good reasons why that climate conference last year proved so difficult, and delivered what it did (or did not). Two should be borne in mind.

First, there was no shared understanding of what the conference was supposed to deliver. The 2008 Bali Action Plan, the document that underpinned the process intended to culminate in Copenhagen, spoke of decisions being taken. But what decisions? Some countries argued that the world needed to adopt a new legal treaty under the United Nations Framework Convention on Climate Change, which would set a series of binding targets for industrialized countries and herald the demise of the Kyoto Protocol. Others expected agreement on a second period under the Kyoto Protocol and a new legal arrangement largely directed at the United States. Still more nations sought only an operational step towards a legal instrument or instruments. In the weeks before the Copenhagen meeting, a growing number of world leaders expressed the need for a political declaration as the best outcome. In the end, that is what the conference delivered.

The second reason is the widespread fear that ambitious climate-change policy will damage economic growth. Concerns over energy prices, energy security and material scarcity in the face of a ballooning world population have done much to drive global desire for a greener, leaner and meaner economic model. Although many nations pay lip service to this green growth model, most of them, deep in their hearts, are still unsure. In fact, many developing nations fear that the intent of the West is to use climate as an excuse to keep developing nations poor and maintain the current economic status quo.

The lessons for Cancún therefore seem obvious: keep it practical, keep it simple and don’t overreach. The negotiations must explore ways for all nations, especially those in the developing world, to consider the merits of green growth. No sensible country will accept a new legal agreement if the economic consequences remain unclear.

I believe that this requires a practical framework in each of the following six areas. Only then will countries responsibly be able to decide whether a new legal instrument is the proper route to take global climate action forward.

First, we need a mechanism that helps developing countries to assess their green growth potential, develop a clear strategy and access international financial support to implement it.

The ‘prompt start’ finance that was promised in Copenhagen offers a foundation to develop that strategy. Long-term financial commitments and a widened range of market-based mechanisms will be crucial to its implementation. Second — and essential — is an increased capacity to assess and plan the probable national responses to a changing climate, especially in the smaller and poorer developing nations. We need a capacity-building programme driven by institutions that can deliver the required hard economic analysis.

A third critical element for success in Cancún is to strike a better balance when considering climate adaptation and mitigation. The lack of attention to adaptation is one of the main shortcomings of the Kyoto Protocol. A fourth point would be to ensure that the delivery mechanism helps to push key technologies into developing economies. Private-sector investment must be mobilized to drive innovation and to lower the cost of generic but essential technologies, such as renewable-energy equipment.

Fifth, an agreement to reward action to combat deforestation and forest degradation would offer a real premium for countries with no other significant mitigation potential, and would help to limit the cost of future action on emissions. Sixth, a robust framework to monitor, report and verify both action and support will ensure that nations pull their weight.

You will notice that more ambitious targets are not on my list. The realist in me suggests that we need to work with what we have, in the same way as President Mohamed Nasheed of the Maldives accepted the Copenhagen Accord — not because he liked it, but because he realized

that it was the best he could get. Am I selling the climate short? Yes. The approach I outline here will not be enough to limit temperature increase to a maximum 2°C rise, and I would happily trade any of my six points for a stronger outcome.

Experience with sulphur dioxide trading in the United States and carbon trading in the European Union suggests that a modest start can be an effective way to get the ball rolling and to ‘learn by doing’. The Copenhagen Accord’s promise to review action in 2015 at least offers the chance to reconsider our ambition once we have a clearer picture of the tools that will be available. Above all, I hope that the lack of a shared sense of direction will not bedevil the talks in Cancún as it did last year. Those familiar with the rules of football will know that many people issued the UN climate process in Copenhagen the equivalent of a cautionary yellow card. It should tread carefully to avoid the unfortunate consequences of a second. ■ **SEE NEWS P.488**

Yvo de Boer is special global adviser for climate change and sustainability at KPMG. From 2006 to 2010 he was executive secretary of the UN Framework Convention on Climate Change.

I HOPE THAT THE
LACK
OF A SHARED SENSE OF
DIRECTION WILL NOT
BEDEVIL
THE TALKS IN CANCÚN.

➔ **NATURE.COM**
Discuss this article
online at:
go.nature.com/ixwub9

RESEARCH HIGHLIGHTS

Selections from the
scientific literature

CANCER

Metabolic link to breast cancer

A protein that senses a cell's metabolic state may serve as a 'switch' to allow breast cancer to develop. This could be a molecular reason for why a high intake of calories and weight gain are strong risk factors for breast cancer.

Kevin Gardner of the National Cancer Institute in Bethesda, Maryland, and his colleagues looked at the protein CtBP, which acts as a metabolic sensor. The protein is activated when it binds to NADH, an important indicator of a cell's metabolic activity. The researchers found that silencing CtBP expression increased expression of *BRCA1*, a tumour-suppressor gene associated with breast cancer. This suggests that greater activation of CtBP lowers the protective effects of *BRCA1*. *Nature Struct. Mol. Biol.* doi:10.1038/nsmb.1941 (2010)

EVOLUTION

Neanderthals matured fast

Analysis of fossil teeth from ancient humans and Neanderthals suggests that Neanderthals grew and matured more rapidly than *Homo sapiens*. This finding helps to pin down an evolutionary origin for humans' prolonged childhood and adolescence, which may have provided an evolutionary advantage.

Tanya Smith at Harvard University in Cambridge, Massachusetts, with Paul Tafforeau at the European Synchrotron Radiation Facility in Grenoble, France, and their colleagues used X-ray imaging to reveal microscopic growth

tracks inside fossil teeth from juvenile *H. sapiens* and Neanderthals (pictured). The tracks indicate developmental features such as daily growth rate.

Dental maturation was faster in the Neanderthals than in both ancient and modern-day humans. *Proc. Natl Acad. Sci. USA* doi:10.1073/pnas.1010906107 (2010)



P. TAFFOREAU & T. SMITH



SCIENCE/AAAS

GENOMICS

Similar bodies, different genomes

A species of marine zooplankton looks like some of its relatives but has a drastically different genomic structure. This suggests, contrary to conventional thinking, that conserved genomic architecture is not needed to maintain morphological features between species.

Daniel Chourrout at the University of Bergen in Norway and Patrick Wincker at Genoscope in Evry, France, and their co-workers analysed the genome of the tunicate *Oikopleura dioica*

(pictured), a rapidly evolving organism that is one of the closest relatives to the vertebrates. They found several unusual features, including an order of genes on the chromosomes that was very different from that of related species.

The authors conclude that some genome features are not necessarily adaptive even if they are shared by many animals, and such features can disappear when evolution accelerates.

Science doi:10.1126/science.1194167 (2010)

STRUCTURAL BIOLOGY

Dopamine receptor revealed

The neurotransmitter dopamine, which is involved in drug addiction and certain psychiatric disorders, binds to five subtypes of receptor in the brain. Some psychiatric drugs block two of these receptors, the similar D2R and D3R, but often have side

effects. Researchers have now elucidated the crystal structure of D3R, which is a potential target for new drugs to treat substance abuse. The structure may help drug developers to tailor their compounds to this and related receptors.

Raymond Stevens at the Scripps Research Institute in La Jolla, California, and his colleagues crystallized D3R in complex with a drug, eticlopride, that binds both

D3R and D2R. On comparing the structure with that of a molecule that blocks only D3R, they found that D3R has a second binding site not present on D2R.

Science 330, 1091–1095 (2010)

DEVELOPMENTAL BIOLOGY

Blood-vessel cells turn to bone

In the rare disease fibrodysplasia ossificans progressiva (FOP), a mutation in the *Alk2* gene results in the formation of bone in soft tissues. Now researchers show that the bone cells derive from others that form the inner lining of blood vessels, called endothelial cells. These become stem-like cells before re-differentiating into bone. This process could be important in normal tissue repair, suggest Damian Medici at Harvard Medical School and Bjorn Olsen at the Harvard School of Dental Medicine, both in Boston, Massachusetts, and their colleagues.

The team found that cells from bony lesions in patients with FOP expressed marker proteins specific for endothelium. And when mutant *Alk2* was introduced into normal human endothelial cells, it conferred characteristics of mesenchymal stem cells. When cultured in appropriate conditions, the endothelial-derived 'stem cells' transformed into bone, cartilage and fat cells.

Nature Med. doi:10.1038/nm.2252 (2010)

GENE THERAPY

Small RNAs aid cell transplants

With the help of small RNA molecules called microRNAs, a metabolic and neurodegenerative disorder might be treated using gene therapy.

Patients with Krabbe's disease lack a functioning version of an enzyme called GALC. Transplants of

genetically engineered blood stem cells that later develop into white blood cells could potentially deliver a corrected version of GALC. But expressing the protein in the stem cells kills them.

Alessandra Biffi and Luigi Naldini of the San Raffaele Scientific Institute in Milan, Italy, and their colleagues identified gene-silencing microRNAs that are expressed in the stem cells, but not in the mature white blood cells. The researchers then modified the stem cells so that GALC expression was suppressed by a microRNA in the stem cells but not in the white blood cells. As the cells developed, they were able to deliver GALC to diseased tissues in a mouse model of Krabbe's disease.

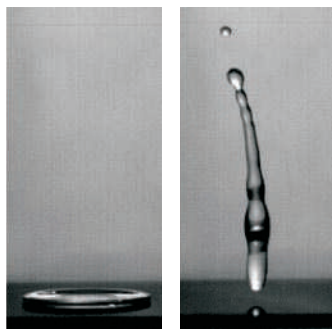
Science Transl. Med. doi:10.1126/scitranslmed.3001522 (2010)

MATERIALS SCIENCE

Stopping ice before it forms

Ice accumulation on aircraft and other structures can be dangerous, but de-icing procedures are expensive or environmentally unfriendly. Joanna Aizenberg at Harvard University in Cambridge, Massachusetts, and her collaborators show how ice could be prevented from forming on cold surfaces.

Combining theoretical predictions with experiments, the authors fabricated a silicon surface with honeycomb-like microstructures and coated it with a water-repellent polymer film. There was minimal contact time and heat transfer between the surface and a falling water droplet,



COMMUNITY CHOICE

The most viewed papers in science

GEOLOGY

Hills emerge as glaciers retreat

HIGHLY READ
on geology.
gsapubs.org
in October

Most drumlins — small, rounded hills — were formed under melting Pleistocene ice sheets. But the recent retreat of the Múlajökull glacier in Hofsjökull, Iceland, has uncovered the only known active drumlin field created during modern times.

Mark Johnson of the University of Gothenburg, Sweden and his colleagues identified more than 50 drumlins in this field and studied their sediment layers. Some theories posit that drumlins are carved out from the sediment by a rush of glacial meltwater. By contrast, the new observations suggest that drumlins form by sediment being repeatedly deposited and then eroded underneath the glacier over successive rounds of glacier growth and retreat.

Geology doi:10.1130/G31371.1 (2010)

such that after it made contact (pictured, left), the droplet fully retracted (right) before it could freeze. This prevented ice formation in temperatures down to about -25°C .

ACS Nano doi:10.1021/nn102557p (2010)

ZOOLOGY

Fish cocoons block biting bugs

The mucus cocoons in which some fish sleep seem to protect them from attacks by parasitic invertebrates.

Alexandra Grutter at the University of Queensland in Brisbane, Australia, and her colleagues placed coral-reef parrotfish (*Chlorurus sordidus*) in bins of water with parasitic gnathiid isopods overnight. They found that only 10% of fish in cocoons were attacked by the parasites, compared with 94.4% of fish that had been teased out of their shelters.

Secreting the mucus to prevent parasite attacks — a mechanism thought to be unique to these fish — costs around 2.5% of a fish's daily energy budget, the researchers calculate.

Biol. Lett. doi:10.1098/rsbl.2010.0916 (2010)

CHEMISTRY

Molecular matchmaking

Structures up to centimetres long have been created by the self-assembly of gel particles that 'recognize' each other at the molecular level. Such molecular recognition has previously been used to self-assemble molecules at the microscopic scale.

Akira Harada of Osaka University in Japan and his colleagues prepared acrylamide-based 'host' gels bearing cyclodextrin rings, and other gels with smaller 'guest' hydrocarbons. The rings and the guest molecules bound to each other, allowing small pieces of gel to self-assemble in specific ways (pictured).

Nature Chem. doi:10.1038/nchem.893 (2010)

NATURE.COM

For the latest research published by Nature visit:

www.nature.com/latestresearch

SEVEN DAYS

The news in brief

POLICY

Addictions institute

An addictions research institute merging two currently separate bodies of the US National Institutes of Health (NIH) “makes scientific sense”, NIH director Francis Collins declared on 18 November. Collins has asked a task force to produce a restructuring plan for the National Institute on Drug Abuse (budget: US\$1 billion) and the National Institute on Alcohol Abuse and Alcoholism (budget: \$462 million) sometime in the summer of 2011. Scientists funded by the alcohol-research institute have opposed the move. See go.nature.com/col7bt for more.

Organ harvesting

An inquiry published on 16 November details how organs were illegally removed for testing from the dead bodies of nuclear workers in the United Kingdom between 1955 and 1992, without obtaining relatives’ consent in many cases. Medical officers who analysed the organs — in part for research on allowable radiation exposures — apparently did not consider the ethical implications of their work, although they did not conceal it, and did not fully appreciate the law, the Redfern Inquiry found. Regulations on the use of human tissues have been made more stringent in the past few years. See go.nature.com/ynaivp for more.

Oil-spill blame

An interim report by the US National Academy of Engineering and the National Research Council, part of the National Academies, lists a number of engineering and regulatory flaws that led to the explosion at BP’s Deepwater Horizon oil rig in the Gulf of



Seafood stewardship

A long-running debate about whether to classify an Antarctic fishery as ‘sustainable’ has concluded. The Antarctic toothfish (*Dissostichus mawsoni*, pictured) caught in the Ross Sea can now be sold with a Marine Stewardship Council (MSC) sustainability badge, after Moody Marine — the company based in Derby, UK, examining the status of the toothfish — addressed objections to its sustainability assessment. Some scientists have said that not enough is known about the toothfish to certify it as sustainable, and also argued that the MSC certification process failed to protect the environment and needed reform (see *Nature* 467, 28–29; 2010). Others have defended the MSC (see *Nature* 467, 531; 2010).

Mexico in April. The report, released on 16 November, noted that pivotal choices made during the drilling were intended to reduce costs and time — despite earlier findings by the White House oil-spill commission that firms did not cut corners to save money.

Biosecurity labs

Two planned US biosecurity labs have not yet been adequately vetted for safety, says the National Research Council (NRC). A report released on 15 November concludes that the US government’s latest safety assessment underestimates the

chances, as well as the impact, of an accidental pathogen release by the National Bio and Agro-Defense Facility to be built in Manhattan, Kansas. On 18 November, a separate NRC committee criticized the methods used to gauge the risk to public safety posed by the National Emerging Infectious Diseases Laboratory, built in central Boston, Massachusetts, but not yet in operation.

Synthetic biology

An office within the White House should develop a clear and coordinated approach to US research in synthetic biology, and an

authoritative, independent body should challenge and correct sensational media claims about the topic. These were two of 19 provisional recommendations debated at a 17 November public meeting by a 13-member presidential commission studying ethical issues and the risks and benefits of synthetic biology. The commission expects to complete its report for President Barack Obama in mid-December. See go.nature.com/jp8bhk for more.

Climate bill killed

Canada’s Senate defeated the nation’s climate-change bill on 16 November, quashing legislation to cut greenhouse-gas emissions. The bill called for cuts in emissions of 25% below the 1990 level by 2020, and a long-term target of 80% by 2050. See go.nature.com/1qrprc for more.

Nuclear Korea

Three US scientists have reported being shown round a modern uranium-enrichment plant in Yongbyon, North Korea, earlier this month — a surprising display of the country’s expertise in nuclear technology. North Korea’s current weapons programme is based on plutonium. Siegfried Hecker, a former director of Los Alamos National Laboratory and now at Stanford University, California, said the facility seemed to be designed primarily for nuclear power generation — although it could be converted to produce highly enriched weapons-grade uranium.

BUSINESS

Pharma cuts

A number of big pharmaceutical companies announced restructuring plans last week. German chemicals giant Bayer,

CHENG/HOEFLING

headquartered in Leverkusen, said it would spend €1 billion (US\$1.4 billion) cutting 4,500 jobs — but also creating 2,500 positions in emerging markets — by the end of 2012. Novartis, based in Basel, Switzerland, headlined cost-cutting measures but gave no overall figures on costs or job cuts. And Basel-based rival Roche said it would cut 4,800 jobs (6% of its workforce) over two years and drop research into RNA interference (see page 487 for more).

Stem-cell trial

The second-ever clinical trial of a therapy involving human embryonic stem cells (ES cells) has received the green light from the US Food and Drug Administration. In phase I/II trials, Advanced Cell Technology in Marlborough, Massachusetts, will inject retinal cells derived from human ES cells into the eyes of 12 patients, to examine the safety of a therapy for Stargardt's macular degeneration, an inherited form of progressive juvenile blindness. See go.nature.com/v5sohq for more.

Lupus drug

A potential blockbuster drug to treat the autoimmune disease lupus looks likely to be approved in the United States. An advisory panel to the US Food and Drug

Administration (FDA) gave Benlysta (belimumab) the green light on 17 November despite concerns over side effects. The drug inhibits a protein that, in lupus, causes the body to produce antibodies attacking its own tissues. It was developed by Human Genome Sciences in Rockville, Maryland, in partnership with GlaxoSmithKline in London. Benlysta would be the first drug to be approved specifically to treat systemic lupus erythematosus for half a century. An FDA decision is expected in the next two weeks.

PEOPLE

Researcher resigns



Anil Potti (pictured), a researcher on cancer genetics at Duke University in Durham, North

Carolina, has resigned amid investigations into his alleged research misconduct. A letter from Huntington Willard, director of Duke's Institute for Genome Sciences and Policy, on 19 November said that Potti had accepted full responsibility for anomalies in data handling, analysis and management. Three clinical trials based on Potti's research were suspended and have been closed, and one

of his papers (D. Hsu *et al.* *J. Clin. Oncol.* 25, 4350–4357; 2007) was retracted last week.

FUNDING

ITER cost-cutting

Plans for savings to ITER, a roughly €15-billion (US\$20-billion) fusion reactor being built near Cadarache, France, have won political backing from the project's seven international partners. On 18 November, members of ITER's council endorsed plans to consolidate contracts and reduce staffing costs. The council also supported a plan to forgo full testing of some of the machine's massive superconducting magnets. All told, the plans will save more than €100 million, but Osamu Motojima, ITER's director-general, says that still more savings must be found.

Physics rescue

The world-renowned Erwin Schrödinger International Institute for Mathematical Physics in Vienna has been rescued from imminent closure after more than 200 international researchers wrote letters of support to the Austrian government. National cost-cutting threatened the institute's budget, but on 16 November, research minister Beatrix Karl promised to find extra cash for universities that

COMING UP

29 NOV–10 DEC

Delegates at this year's United Nations climate summit in Cancún, Mexico, hope to reinvigorate the negotiations that effectively stalled last year in Copenhagen. See page 489 for more. <http://cc2010.mx/en>

29 NOV–3 DEC

The Materials Research Society meets in Boston, Massachusetts. go.nature.com/zkg5rq

1 DECEMBER

Nominations are expected for the next head of the California Institute for Regenerative Medicine in San Francisco; Bob Klein, chairman of the state stem-cell agency, steps down this month.

integrate institutes. The University of Vienna snapped up Schrödinger — although the fate of dozens of other such non-university academic institutes in Austria remains uncertain. See go.nature.com/bb8esd for more.

European funding

The process of applying for research grants from Europe's Framework programme should be simplified, say leading researchers evaluating the current programme, which runs until 2013. Their report, published on 18 November, asks the European Commission to trust researchers more and to cut overly bureaucratic accounting regimes. It also says the Framework programme should fund more grants based on ideas from researchers, rather than those directed by the commission and politicians.

► **NATURE.COM**

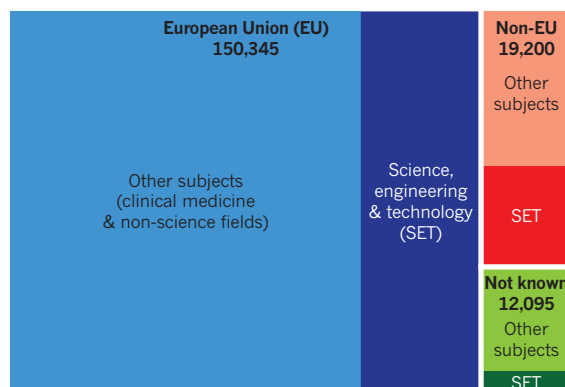
For daily news updates see: www.nature.com/news

TREND WATCH

The scale of restrictions facing researchers who want UK visas has become slightly clearer. A temporary cap on visas is already in place; as *Nature* went to press, the government was reported to have decided to allow 43,000 highly skilled non-European Union migrants — who make up about a tenth of university staff (see chart) — to enter the country each year. This would be 13% fewer than in 2009, which is the lower limit of an advisory committee's recommendations last week of 13–25% cuts.

IMMIGRATION AT UK UNIVERSITIES

Around 16% of UK universities' science, engineering and technology staff are not from the European Union (2008–09).



NEWS IN FOCUS

NOBELS Did the physics prize committee do its homework properly? **p.486**

PHARMA RNA interference stumbles on the way to the clinic **p.487**

CLIMATE Modest hopes for next week's Cancún meeting **p.488**

MICROBIOME Probing the human body's inner ecosystems **p.492**



J. RAEDLE/GETTY

Cholera is a disease of poverty, and spreads rapidly in communities lacking clean water supplies and sanitation.

PUBLIC HEALTH

Cholera tightens grip on Haiti

Those tackling the epidemic are struggling to keep pace with an escalating crisis.

BY DECLAN BUTLER

As cholera rages through Haiti, some epidemiologists are warning that the country could face more than half a million cases over the coming year. Yet tracking and treating the disease is proving increasingly difficult as civil unrest grips the country.

Roughly 20,000 clinical cases, and 1,100 deaths, have officially been reported since the outbreak was first detected on 21 October in the Artibonite region of Haiti — figures likely to be underestimates, say epidemiologists,

given the many additional cases in the wider community. “It’s spreading like wildfire,” says Andrew Camilli, a cholera researcher at Tufts University School of Medicine in Boston, Massachusetts (see ‘Epidemic proportions’).

As the current Haitian population has never been exposed to cholera, they lack any immunity to the disease, which makes the toll even greater. Vaccination might have helped, but it has never been tested during a large cholera

outbreak and was not an option in Haiti because of the vaccine’s scarcity and the logistical difficulties in getting it to people in time (see ‘Would cholera vaccines have helped in Haiti?’).

Cholera is caused by the bacterium *Vibrio cholerae*, transmitted through contaminated water supplies or by direct contact with infective faecal material. Haiti already lacked clean water and basic sanitation, and conditions have deteriorated further following January’s huge earthquake (see *Nature* **467**, 1018–1019; 2010) and Hurricane Tomas in early November.

Some 80% of symptomatic cholera cases ▶

► **NATURE.COM**
Cholera receives relatively little R&D funding see:
go.nature.com/jb9iuh

STOPPING AN EPIDEMIC

Would cholera vaccines have helped in Haiti?

When the cholera outbreak started in Haiti, health agencies briefly contemplated using vaccines to try to curb it. But they abandoned the idea once it became clear that the available global production was completely insufficient for an effective vaccination campaign — only a few hundred thousand doses would have been available, and even these would have taken weeks to manufacture, whereas millions of doses were needed.

Only one cholera vaccine — Dukoral — is approved by the World Health Organization (WHO). Made by the small Dutch company Crucell, based in Leiden, it is aimed at people travelling to cholera-endemic areas, and as such is too expensive to be widely deployed in the developing world. A second vaccine called Shanchol, already licensed in India, is currently going through the WHO's approval process. Developed by the International Vaccine Institute in Seoul, with support from the Bill & Melinda Gates Foundation, the vaccine is produced by Shantha in Hyderabad, India, and should cost less than US\$1 a dose.

Even if sufficient Dukoral or Shanchol had been available at the start of the Haitian outbreak, it might have had little impact. Two doses of the vaccines have to be given a fortnight apart, with protective immunity taking another week to form. Mounting a large vaccination campaign also causes inevitable delays. So it is by no means clear that vaccination would have made any major dent in the spread of the disease.

The logistics would have been daunting, says Claire-Lise Chaignat, coordinator of the WHO's Global Task Force on Cholera Control. Just vaccinating the 2 million people in the Haitian capital Port-au-Prince would have required rapid deployment of some 4 million vaccine doses. That's a huge logistical challenge in any situation, but in the dire conditions Haiti now finds itself in it would be "almost impossible", she says.

Had sufficient vaccine been available, Jon Andrus, deputy director of the Pan American Health Organization, says that he would have considered trying vaccination in case it had a positive impact. Pre-emptive vaccination

of people in the neighbouring Dominican Republic could also have made sense, he says.

In the longer term, vaccination for cholera deserves further study, says Robert Quick, an epidemiologist at the Enteric Diseases Epidemiology Branch of the Centers for Disease Control and Prevention in Atlanta, Georgia. If a longer-lasting and highly efficient single-dose vaccine could be developed it might make a significant impact on outbreaks such as Haiti's. A single-dose vaccine called Orochol has been developed, but its manufacturer, the Swiss company Berna Biotech (acquired by Crucell, based in Berne, in 2006), stopped making it in 2004 after switching its limited production facilities to make another vaccine.

But Quick emphasizes that a single-dose vaccine would not be a panacea, and stark choices would remain. Mounting a vaccine campaign during an outbreak takes away scarce resources and staff, he argues. "Do you want staff treating people, or vaccinating?" he asks. "The first priority is saving lives." **D.B.**

► are mild or moderate, but 20% cause severe dehydration from watery diarrhoea that can kill within hours if untreated. Until the 1970s, when oral rehydration therapy was widely introduced, death rates during outbreaks often exceeded 50%. But cholera is eminently treatable if patients are promptly rehydrated, and public-health responses to cholera epidemics typically reduce mortality rates to below 1%.

Experts think that conditions in Haiti are resulting in far higher death rates than this. At the beginning of the outbreak, mortality was estimated at around 9%, falling to an estimated 4–6% over the past few weeks as patients began to be treated.

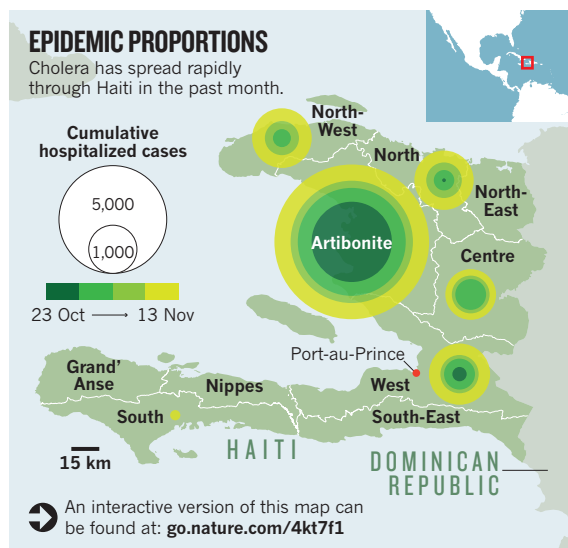
That gain, however, has been wiped out by riots that were fanned by rumours that Nepalese UN peacekeepers were the source of the outbreak. The row over the source has been self-defeating, says Jon Andrus, deputy director of the Pan American Health Organization (PAHO), the regional office of the World Health Organization. With many of the sick unable to get past roadblocks to reach treatment centres, and deliveries of supplies held up, death rates have again soared past 9%, he says. The precise death toll is uncertain, like everything else about the outbreak. PAHO relies partly on a vast network of humanitarian groups and non-governmental organizations, such as Doctors

Without Borders and the UN Children's Fund, to collect and report data from the field. Many of these groups aren't coordinated well with each other, and Andrus says that it's a huge challenge to ensure data quality, adherence

to be several undetected asymptomatic carriers shedding bacteria and spreading disease, complicating predictions of how the epidemic will spread. But the data are often good enough for their key functions: pinpointing trends such as a rapid increase of cases in an area, or the appearance of geographical clusters. These hotspots can then be targeted for rapid intervention.

Last week, PAHO announced that the epidemiology suggested that 200,000 more cases could be expected in Haiti over the next year, but Andrus says that more recent estimates are likely to raise that figure to more than 500,000. Having these numbers is crucial to making sure that enough lifesaving supplies and staff are on hand when and where they are needed. "We are doing everything possible to keep ahead of the game, to be weeks in advance, so that we don't get into a situation where we run out of supplies," he says.

Health officials are also alert to the risk that the Haiti outbreak could spread further into the neighbouring Dominican Republic, where cases have been reported, and far beyond. Experts are mindful of how a 1991 outbreak in Peru — the first in the Americas in a century — led to a suite of entrenched large cholera outbreaks across the Americas in the ensuing decade (except the Caribbean). "We've put the whole hemisphere on alert," says Andrus. ■



to a standardized cholera case definition, and timely reporting. "Coordinating these groups on a normal day in Haiti would be difficult enough, but in post-earthquake Haiti in the middle of a cholera outbreak, it becomes a huge challenge," he says.

For every clinical case of cholera there will

STEM CELLS

Korean deaths spark inquiry

Cases highlight the challenge of policing multinational trade in stem-cell treatments.

BY DAVID CYRANOSKI IN LOS ANGELES

The controversy over stem-cell tourism, in which patients travel to other countries for unapproved stem-cell treatments, continues to grow. In June, researchers in Thailand reported finding “strange lesions” in a patient who had died following stem-cell therapy for kidney disease (see *Nature* **465**, 997; 2010). And in August, an 18-month-old Romanian boy died after receiving a brain injection of stem cells.

Now South Korea is trying to crack down on the practice. Following the recent deaths of two Koreans who had received injections of stem cells, the Korea Food and Drug Administration and the health ministry last week launched an investigation into companies offering the treatments. But the latest cases highlight the difficulty of policing these therapies or determining their safety, because some companies are setting up operations around the globe, taking advantage of loopholes in other countries’ regulations.

One of the companies under scrutiny is Seoul-based RNL Bio, which formulated the cells used to treat the two Korean patients. The firm prepares stem cells at its processing centre in Seoul and sends them to affiliated clinics in China, Japan or elsewhere. Patients travel to these clinics to have the injections, which are illegal in South Korea.

DRUG OR BODY PART?

In a statement, RNL Bio’s chief executive, Ra Jeong-chan, has denied that his company’s treatments had anything to do with the deaths. The Korean media are reporting that one patient, a 73-year-old man, died in Japan following a pulmonary embolism; the other failed to wake after receiving an anaesthetic while in China.

Jin Han Hong, president of RNL Life Science, the company’s subsidiary in Los Angeles, California, says that the government’s investigation will try to determine whether their stem-cell processing in Korea should be banned. “The government wants to define it as a drug and make it illegal,” says Hong, who defends the practice: “From our viewpoint it is just part of the patient’s body.”

Nobuyoshi Tani, head of the regenerative medicine office of the Japanese health

ministry’s Research and Development Division, says that companies must gain government approval before they can sell stem-cell therapies in Japan. But Japanese doctors don’t need approval to import stem cells for use in their practice.

Last year, China passed regulations that would require stem-cell therapies to pass clinical trials, but there has been much debate about how those rules should be implemented. While the government puts together guidelines, companies such as RNL Bio face an uncertain regulatory situation (see *Nature* **467**, 633; 2010).



RNL Life Science offers patient testimony at its California offices.

RNL Bio hopes to attract more US customers with the opening of RNL Life Science in 2009. Last week *Nature* visited the office, situated in a shopping mall called Koreatown Galleria, to learn more about the company’s products. Jane Shin, whose business card describes her as a “stem-cell consultant”, explained that patients visit an affiliated Los Angeles clinic where a plastic surgeon removes about 5 grams of fatty tissue. The sample is sent to the company’s Maryland processing centre, where mesenchymal stem cells — which normally regenerate fat, bone or cartilage in the body — are isolated and sent to Seoul to be cultured. Even the simplest stem-cell treatments, such as those for arthritis, require 100 million cells, says Hong. Preparing and banking these cells for three years costs US\$7,500; every subsequent 100 million cells cost an additional \$5,000. Standard courses are 600 million cells, says Shin. “The more cells you use, the better you get.”

Shin says that 10,000 patients worldwide, including 130 from the United States, have

received injections of the firm’s stem cells. About half have had facial injections, hoping to rejuvenate their appearance, but the company claims that the cells have been used to treat ailments including Parkinson’s disease, kidney failure and diabetes.

STEM-CELL BANKING

Hong admits that there is not yet conclusive clinical-trial evidence that the treatment can help these various conditions, although the company is running trials in South Korea. Asked why RNL would start offering a therapy

before it was proven effective, he says that the company offers only stem-cell isolation and banking services, not stem-cell therapy. “We don’t offer therapy,” he says. “It’s true that we note the potential but we don’t make promises.”

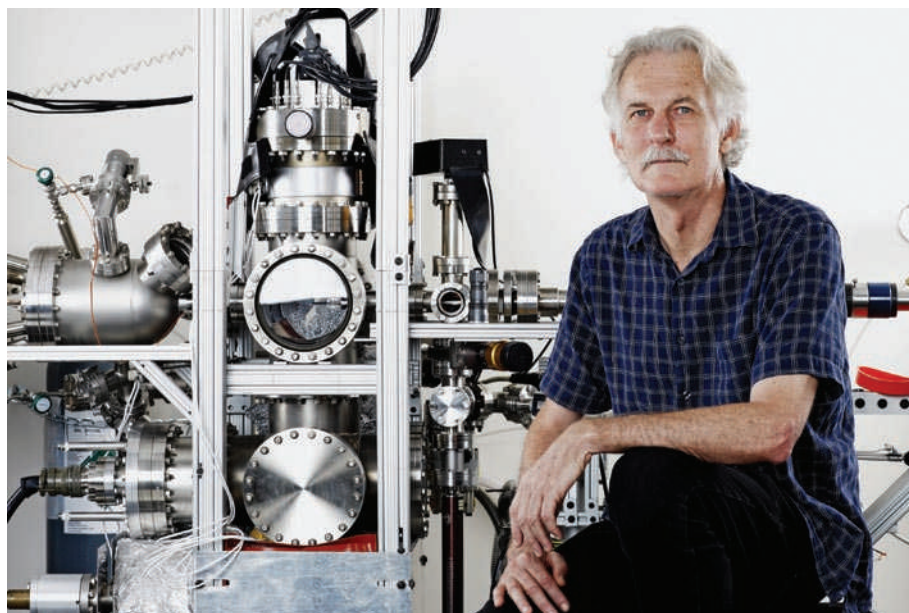
But Hong and Shin do talk openly about treatments. Shin, for example, provided details about injection sites and the diseases that could be treated. RNL’s patients are recommended to go to affiliated clinics such as the RNL Sunrise Regenerative Medical Center in Yangji, China. And Shin also provided a brochure that describes how a patient recovered from rheumatoid arthritis following treatment. According to the brochure, the patient was “escorted by RNL staff” to the Yangji centre.

And looking out from the front window of the Los Angeles office, a wide-screen TV broadcasts testimony of patients happy with the results of the company’s services.

Stem-cell scientists contacted by *Nature* are sceptical about the efficacy of RNL’s preparations. “Spontaneous differentiation of adipose-derived stem cells into therapeutic cell types for Parkinson’s disease is biologically unrealistic,” says Oliver Cooper, director of the Stem Cell Facility at Harvard University’s Center for Neuroregeneration Research in Belmont, Massachusetts. Other scientists echoed his sentiments.

Cooper’s team hopes to treat Parkinson’s with stem cells. But the researchers will implant the cells only after they have differentiated into neurons. Injecting immature stem cells, he says, “does not provide a long-term treatment for Parkinson’s disease, and the risk associated with uncontrolled growth of transplanted stem cells is unacceptable.” ■

D. CYRANOSKI



Walter de Heer says that background information supporting the physics award contains inaccuracies.

PHYSICS

Nobel document triggers debate

Critics say that explanation of the 2010 award in physics slights other contributions to graphene research.

BY EUGENIE SAMUEL REICH

Controversy surfaced last week over a document issued by the Nobel Committee for Physics to explain its awarding of the 2010 prize, leaving the committee on the defensive. It is scrambling to correct errors while standing by the process underlying its decision.

Last month, the committee awarded the prize to Andre Geim and Konstantin Novoselov at the University of Manchester, UK, “for groundbreaking experiments regarding the two-dimensional material graphene”. The novel material — composed of a single crystalline layer of carbon atoms — could have a host of applications, from touch screens to transistors.

The deliberations of the Nobel committee are notoriously secretive, but for a sense of its thinking researchers turn to the ‘Scientific Background’ document prepared by members of the Royal Swedish Academy of Sciences and placed online at the time of the prize announcement.

That document came under fire last week as researchers questioned several alleged

misstatements. “The Nobel prize committee did not do its homework,” says physicist Walter de Heer of the Georgia Institute of Technology in Atlanta, who sent a letter to the committee on 17 November listing his objections.

According to the background document, Geim and Novoselov galvanized the field with a widely cited 2004 paper¹. In a caption, the Nobel document describes a figure from the paper as showing data on graphene’s electronic properties — but the data were actually collected from a few layers of graphene stacked together, a material better known as graphite. The distinction is significant because the two have different electronic properties.

De Heer says in his letter that Novoselov and Geim did not report measurements on single-layer graphene until 2005 (ref. 2). He also says that a 2004 paper by his own group³ included measurements made on a single layer of graphene, although he did not realize it at the time.

Other alleged errors in the document downplay the work of Philip Kim of Columbia University in New York, who many think should have shared the prize. When the Manchester group published crucial electronic measurements on graphene⁴ in *Nature* in 2005, the

paper appeared back-to-back with one from Kim’s group⁵. “He made an important contribution and I would gladly have shared the prize with him,” says Geim.

Geim and other experts contacted by *Nature* agree that the document does not seem to have been carefully assembled. “It could have been written better,” says Geim, who only read it after controversy erupted over its contents.

De Heer also accuses the committee of falling for a straw-man argument when it says that Geim and Novoselov’s work came as a complete surprise to the physics community because graphene was presumed to be unstable. “That statement is inaccurate,” agrees Paul McEuen of Cornell University in Ithaca, New York. Prior observations of graphene⁶ date back to at least 1962.

The committee seems to be responding to some of the criticisms. “We will make a correction to the web version,” says Ingemar Lundström, chairman of the committee. “Some of the things we also think are mistakes.”

Since de Heer’s letter became public, other graphene researchers have contacted *Nature* to take issue with the Nobel committee’s document. Bor Jang, co-founder of graphene producer Angstrom Materials in Dayton, Ohio, says that Geim and Novoselov have often wrongly been credited with discovering graphene — an implication also made by the subheading “the discovery of graphene”, which appears in the document shortly before their work is discussed. “I totally disagree with this assessment,” says Jang.

De Heer says he thinks that the award of the prize for graphene this year is premature, saying more time is needed to see the material’s potential fulfilled. But he strongly denies being motivated by sour grapes. His concern with the document, he says, is that its errors mis-

represent contributions made by several researchers.

Per Delsing at Chalmers University of Technology in Gothenburg, Sweden,

an adjunct member of the Nobel committee, acknowledges that there is some dispute about whether graphene was believed to be stable and whether the 2004 work came as a surprise to the community or not. But he defends the committee’s work. “Different people can of course have different opinions. Let me assure you that the Nobel committee has done a lot of research into this issue,” he says. ■

“The Nobel prize committee did not do its homework.”

1. Novoselov, K. S. *et al. Science* **306**, 666–669 (2004).
2. Novoselov, K. S. *et al. Proc. Natl Acad. Sci. USA* **102**, 10451–10453 (2005).
3. Berger, C. *et al. J. Phys. Chem. B* **108**, 19912–19916 (2004).
4. Novoselov, K. S. *et al. Nature* **438**, 197–200 (2005).
5. Zhang, Y. *et al. Nature* **438**, 201–204 (2005).
6. Boehm, H. P. *et al. Zeitschrift für Naturforschung B* **17**, 150 (1962).

PHARMACEUTICALS

Drug giants turn their backs on RNA interference

A once much-touted technique faces a difficult transition to the clinic.

BY HEIDI LEDFORD

Not long ago, a technique called RNA interference (RNAi) seemed to be on the fast track to commercial success. Its discovery in 1998 revealed a new way to halt the production of specific proteins using specially designed RNA molecules, and it quickly became a favourite tool of basic research. In 2006, the scientists who made the discovery were awarded the Nobel prize for medicine, and the New Jersey-based pharmaceutical giant Merck paid more than US\$1 billion to snatch up Sirna Therapeutics in San Francisco, California — one of the first biotechnology companies aiming to harness RNAi to create new drugs.

Yet all that seemed like ancient history last week when drugs and diagnostics corporation Roche in Basel, Switzerland — a major investor in RNAi-based drug research — announced it was killing its programme after spending three years and more than \$500 million on the technique. Although part of a larger restructuring to cut costs, the move is the latest indication that big pharma may be losing faith in RNAi.

“The momentum now seems to be heading a bit against RNAi,” says Alan Carr, an analyst at Needham & Company, an investment-banking firm in New York. Roche’s 17 November announcement, which sent stock prices at RNAi companies plunging, came just two months after another Swiss-based multinational, Novartis, declined to spend \$100 million to extend a partnership with Alnylam, a prominent RNAi company based in Cambridge, Massachusetts.

The development of RNAi-based drugs has stalled as companies confront the challenge of delivering RNA molecules, which are notoriously fragile, to target cells in the human body, and then coaxing those cells to take up the RNA. “Getting these molecules exactly where we want them to go is a little more difficult

A SAMPLING OF RNAI THERAPIES IN CLINICAL TRIALS

| Indication | Company | Clinical phase | Delivery method |
|----------------------------------|---|----------------|--------------------|
| Age-related macular degeneration | Quark Pharmaceuticals/ Pfizer/Silence Therapeutics | Phase II | Naked RNA |
| Diabetic macular oedema | Quark Pharmaceuticals/Pfizer | Phase II | Naked RNA |
| HIV | Benitec | Phase I | Lentivirus vector |
| Liver cancer | Alnylam/Tekmira | Phase I | Lipid nanoparticle |
| TTR amyloidosis | Alnylam/Tekmira | Phase I | Lipid nanoparticle |
| Respiratory syncytial virus | Alnylam/Cubist Pharmaceuticals/ Kyowa Hakko Kirin | Phase II | Inhaled naked RNA |

than originally thought,” says Michael French, chief executive of Marina Biotech, an RNAi company based in Bothell, Washington.

Of the dozen RNAi-based therapeutics in early clinical testing, most apply the RNA molecules directly to the target tissues, or aim to shut down the production of a protein in the liver, which takes up the RNA as it filters the blood (see table). Several candidates also package the RNA within a lipid nanoparticle, a delivery vehicle that both protects the RNA and allows it to be shuttled across cell membranes. Investors expect Alnylam to emerge in the next few years with the first commercially viable RNAi-based therapeutic, which would treat a rare disease called transthyretin amyloidosis — in which an abnormal form of a blood protein is deposited in the nerves and organs — by shutting down the production of the protein in the liver.

Although Alnylam shed about 50 of its 225 employees when its partnership with Novartis ended, chief executive John Maraganore is optimistic. “There’s going to be a steady drumbeat of increasing frequency that really validates RNAi as a whole new drug class,” he says. “We’re feeling pretty damn good about where things are right now.”

Until that validation arrives, investors may be

wary of the RNAi platform, says Josh Schimmer, an analyst at the investment bank Leerink Swann & Company in New York. “Alnylam has a very interesting drug at this point,” says Schimmer. “It’s premature to say they have a very promising platform.”

Companies such as Alnylam have built their business by enticing big pharmaceutical companies in as partners. That strategy has paid off: Alnylam has \$372 million in cash, an unheard-of sum for a young biotechnology company with no drugs yet on the market. But the number of deals with major pharmaceutical firms has slowed, says Carr. “There was a wave of interest earlier on and it’s just not there now.”

Some holdouts remain. Merck spokeswoman Carolyn Lappetito says her company has not pulled back from RNAi. “It’s a long haul,” she says. “We have not decided to make any big changes.” And although Novartis ended its relationship with Alnylam, the company can now develop the 31 RNAi-based candidate drugs generated during the five-year partnership. In comparison, the three years Roche spent in the field hardly seems enough time to fully evaluate the technique, says Maraganore. “Three years is nothing,” he adds. “It’s like kicking your three-year-old out of the house and telling him to get a job.” ■



DAILY NEWS

- Age markers in blood go.nature.com/8emsfx
- Coral bleaching goes from bad to worse go.nature.com/uxg2ih
- Funding woes afflict African herbal-therapy institute go.nature.com/wuaujd
- Tumours grow their own blood vessels go.nature.com/w82jlp

VIDEO



Zebrafish that stop swimming when left without company could be suffering from depression go.nature.com/hwzsrj

ON THE BLOG

- Scientists respond to ocean acidification doubts go.nature.com/evzraf
- Drugs hit teen brains harder go.nature.com/ta4hhj
- Views of Hartley 2 go.nature.com/n2rlha
- Animal genomes contain ‘skeletons’ of ancient viruses go.nature.com/6bkarg

I. SPENCE/ALAMY



E. RUÍZ/EPA/CORBIS

The United Nations hopes that talks in Cancún will succeed where last year's Copenhagen summit failed.

ENVIRONMENT

Climate talks focus on lesser goals

With nations in gridlock over emissions, UN negotiators are concentrating on side deals to revive an ailing process.

BY JEFF TOLLEFSON

The ivory-coloured beaches of Cancún promise tourists a chance to forget their worries. But there is no such assurance for the international negotiators who will flock to the Mexican resort next week to attend the sixteenth gathering of the United Nations Framework Convention on Climate Change.

One year after the near-collapse of climate talks in Copenhagen, participants will be hard-pressed to map a viable path forward. Global climate negotiations began in 1992 at the United Nations Earth Summit in Rio de Janeiro, Brazil, and led to the 1997 Kyoto Protocol, in which industrialized countries agreed to curb their emissions. But the protocol was intended as a first step, and countries have been struggling to agree on a follow-up treaty ever since. Jairam Ramesh, India's environment minister, says that Cancún is the "last chance" for such talks.

Given China's continued opposition to a hard target for cuts in greenhouse-gas emissions, and the failure of the United States to pass climate legislation, there is virtually no hope of a

binding global emissions treaty at the Cancún meeting, which will run from 29 November to 10 December. But the door remains open for progress on forestry, adaptation and technology transfer, agreements on which were close to fruition in Copenhagen but were ultimately held back by the principal dispute over emissions. This time, negotiators hope to take a bottom-up approach by settling on a package of smaller agreements that could serve as a starting point for real — albeit limited — action, even as broader treaty negotiations continue. Christiana Figueres, who took office as United Nations climate chief in May, says that Cancún can be successful if parties are willing to compromise and "balance their expectations" about the outcome.

"It's a question of trying to get some incremental gains," says Saleemul Huq, a senior fellow at the International Institute for Environment and Development (IIED) in London. "The approach of all-or-nothing that we took in Copenhagen blew up in our faces, and we can't just sit back and do nothing at all."

World leaders descended on Denmark in December 2009 to extend the Kyoto agreement, which is set to go dormant after the current commitment period expires in 2012.

NATURE.COM
For ongoing coverage
of the Cancún
meeting, visit:
www.nature.com/news

The goal was a new deal that included the United States — which has never signed the Kyoto Protocol — and the largest emerging economies, where emissions are growing at an alarming rate. After days of fruitless wrangling, a last-minute agreement brokered between the United States, China, India, Brazil and South Africa offered a way forward, but the effort buckled when a handful of developing countries who had no say in the crafting of the deal objected that commitments from industrialized nations to reduce carbon emissions did not go far enough. The accord failed to gain unanimous support, and negotiators returned home with no clarity on how to proceed.

Countries have spent the past year arguing over the details of the Copenhagen Accord, but the world's largest greenhouse-gas emitters, China and the United States, are at odds. The United States wants to see 'measurable' and 'verifiable' commitments from developing countries — as stated in the accord — whereas China and others question how the United

States will meet its own commitment without legislative support from Congress.

"The reality is that until there is some kind of movement from the largest economy in the world, it is unrealistic for others to show their hand," says Shyam Saran, who stepped down this year as India's chief climate negotiator. Negotiators are currently marking time on the big issue and focusing on a more piecemeal approach, in the hope that these smaller initiatives will eventually "add up to something significant," he says.

There has been considerable progress on initiatives that would funnel money from industrialized nations to developing countries, and help them to reduce emissions from deforestation (see 'Hope in the Amazon') and adapt to the changing climate. Negotiators also seem to be converging on the creation of a network of innovation centres to help developing countries to cope with climate and reduce emissions, although disputes over intellectual property could hamper technology transfer. But these

agreements ultimately depend on financing.

In the Copenhagen Accord, which has now been endorsed by most nations, rich countries agreed to provide money for programmes to help the developing world: a total of US\$30 billion by 2012, increasing to \$100 billion a year

"The approach of all-or-nothing blew up in our faces, and we can't just do nothing."

by 2020. An analysis by the IIED has identified roughly \$28.5 billion that has been pledged for short-term financing so far, but it is not always clear whether these pledges represent new money or existing aid repackaged as climate finance.

Nor is it clear how countries will live up to the longer-term commitment. Nations are discussing a multitude of financing mechanisms, from direct appropriations to levies and carbon taxes on international transport.

At the Cancún talks, Mexico will have a strategic role in pulling these agreements together, both as the host nation and as an emerging economy that has been willing to engage with developed countries and talk about climate commitments from developing countries. The Mexican delegation will convene key parties in an effort to guide the process and keep everybody on track. They will also have a hand in guiding parallel — but separate — talks over extending the Kyoto Protocol, although little progress is expected on that front.

Meanwhile, thousands of professional negotiators assigned to specific aspects of a collective climate deal will be working to remove bracketed language — representing areas of disagreement — and assemble a single text that can be unanimously approved by the conference. The parties will also try to establish a new deadline for further decisions, either next year at talks in Cape Town, South Africa, or in 2012, when countries will mark the twentieth anniversary of the start of the climate talks.

But there are no guarantees that old ghosts won't come back to haunt Cancún, making it hard to reach any significant agreement. US negotiators have warned that the Copenhagen Accord is a package deal, meaning that the financing it has already promised is contingent on developing countries living up to their part of the deal. And that means that disputes about emissions commitments could once again hold up progress in other areas.

"I don't think you make progress on any of these issues without some progress on all of them," says Eileen Claussen, president of the Pew Center on Global Climate Change in Arlington, Virginia. She anticipates two possible climate outcomes: in the positive scenario, countries will make incremental progress in negotiations and continue to implement climate policies at home, opening the way to a more comprehensive treaty a few years down the road. "The negative scenario," she says, "is that it all blows up." ■ SEE WORLD VIEW, P.477

SUCCESS STORY

Hope in the Amazon

Amid gloomy assessments of the scant progress made in curbing carbon emissions worldwide, there is encouraging news: deforestation in the Brazilian Amazon has slowed. Last year, it dropped to 7,464 square kilometres, down 73% from a 2003/2004 peak of 27,423 square kilometres (see chart).

Brazil was initially opposed to developed nations buying rainforest credits to offset their emissions instead of reducing them, so it crafted its own forest-carbon policy. Enforcement of logging rules and land titles was stepped up, and in 2008 it created the Amazon Fund, a donor system that encourages wealthy nations to contribute to antideforestation schemes but doesn't confer carbon credits. Norway made a US\$1-billion pledge — equating to about 200 million tonnes of emission reductions at current carbon conversion prices.

At the 2009 climate talks in Copenhagen, Brazil pledged to cut deforestation by 80% by 2020. Depending on the final deforestation total for 2010, which Paulo Moutinho, executive director of the Amazon

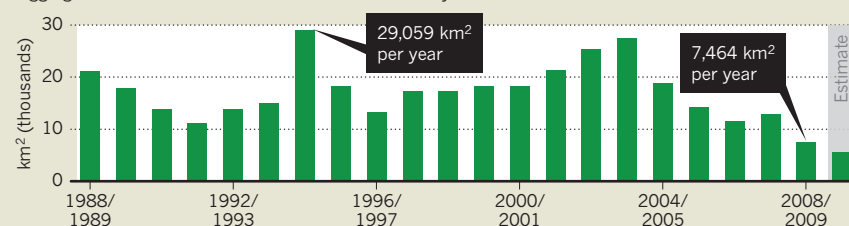
Environmental Research Institute in Brasília, says is expected to be 5,000–6,000 square kilometres, it might be able to meet that target a decade early. According to calculations by the Union of Concerned Scientists in Cambridge, Massachusetts, the resulting reduction in emissions could total 1 gigatonne (10⁹ tonnes) of carbon dioxide a year, equivalent to reductions promised by the United States over the next decade.

The goal of the forestry talks in Cancún is to create a broader framework that will encourage similar efforts elsewhere. But it could be difficult for Brazil to maintain such progress in the coming years, says Moutinho, citing rising demand for agricultural commodities, ongoing development and road construction in the Amazon and growing pressure to weaken the country's forest-protection laws.

"This context represents a big challenge" for incoming president Dilma Rousseff, who will take office in January 2011, says Moutinho. "Let's pray that she will be able to deal with it." **J.T.**

The deforestation decline

Logging in the Brazilian Amazon is at its lowest for 20 years.



SOURCE: INPE

CANCER

The roots of resistance

Learning how melanoma fights back may yield new therapies.

BY HEIDI LEDFORD

A promising new cancer drug called PLX4032 made waves earlier this year for its success against the deadly cancer melanoma. The results of a clinical trial were dramatic, with some patients emerging nearly cancer-free. But for most, the drug stopped working about seven months after therapy began, and the tumours returned¹. This week, two follow-up studies reveal why PLX4032 fails and how tumours' resistance to it might be overcome.

About half of patients with melanoma have a mutated version of the B-RAF protein, which is thought to help trigger the growth of tumour cells. PLX4032 was designed by Plexxikon, a pharmaceutical company in Berkeley, California, to selectively inhibit it. In one study², PLX4032 shrank tumours in 24 of 32 patients with B-RAF mutations. But tumours often evolve ways to evade treatment, and this was no exception. Levi Garraway, an oncologist at the Dana-Farber

Cancer Institute in Boston, Massachusetts, and his colleagues have now found that excessive production of a cancer-promoting protein called COT can shield cultured cells from PLX4032. High levels of COT were also found in two of three PLX4032-resistant tumours taken from patients who had received the drug³.

A group led by Roger Lo, a dermatologist at the University of California, Los Angeles, found two other ways for tumour cells to short-circuit PLX4032: by reactivating the B-RAF signalling pathway damped down by the drug, or by stimulating tumour-cell growth mediated by a different protein⁴. Larger studies will be needed to assess the importance of both groups' results for clinical applications.

Still, the findings are a crucial step towards determining how to overcome PLX4032 resistance, says Alexis Borisy, chief executive of Foundation Medicine in Cambridge, Massachusetts, which is developing diagnostic tests for tumours. Pharmaceutical firms have already started clinical trials to test PLX4032 in combination with

experimental drugs that inhibit MEK, a protein involved in cell growth. When Garraway's team tested this combination in their cultured tumour cells, they found that it overcame the effects of high levels of COT expression.

Clinicians may need to combine four or more drugs to create a potent cancer-fighting cocktail, says Borisy. PLX4032 is a good place to start, he notes: its highly selective targeting of B-RAF means it could have fewer unwanted side effects. "It's an exciting opportunity," he says. ■

1. Ledford, H. *Nature* **467**, 140–141 (2010).
2. Flaherty, K. T. *et al. N. Engl. J. Med.* **363**, 809–819 (2010).
3. Johannessen, C. M. *et al. Nature* advance online publication doi:10.1038/nature09627 (2010).
4. Nazarian, R. *et al. Nature* advance online publication doi:10.1038/nature09626 (2010).

CORRECTION

The News story 'China tackles surge in mental illness' (*Nature* **468**, 145; 2010) incorrectly implied that Wanjun Guo leads a 20-million-yuan project to survey mental disorders in the 'post Wenchuan earthquake' region. Guo is merely a participant in the project, which is itself only part of a 20-million-yuan effort to study the psychological impact of the quake and identify potential interventions.

COMMENT

WOMEN A call for more female leaders round the climate-policy table **p.502**



PANDAS Torn between conservation and economics **p.503**

SCULPTURE Insects made magnificent at monstrous size **p.506**

ASTROPHYSICS In praise of the James Webb Space Telescope **p.508**

J. REZAC/GREENPEACE/EYEVINE



Tar sands need solid science

As Canada exploits its oil sands ever faster, **David Schindler** calls for industry-independent environmental monitoring to back up better water-quality regulation.

When Canadian-born movie director James Cameron visited his home country's tar-sands mining operation this September, he concluded: "The oil sands can be either a blessing or a curse to Alberta, depending on how they are developed." He called for better monitoring, independent research, more consideration of the needs of aboriginal groups and a slowdown of development until better technologies are developed. It seems the creator of *Avatar* and *Titanic* — movies that showcase disasters following hubris — is better able than local politicians and industrialists to see that megadevelopments often don't have rosy outcomes.

The debate about oil-sands extraction has become polarized, with players cast as either totally against, or for developing the sands rapidly without regard for environmental consequences. Both positions are based on very little evidence. A more moderate approach, with the pace of development based on solid environmental science, would be better in the long run.

The current environmental monitoring programmes for Alberta's waterways are in my view sporadic and poorly designed. Water quality — in which I have expertise and have done research in the tar-sands area — is not the only, or even the main, problem. There are serious concerns about issues

including possible disastrous ruptures of tailings ponds that could spread toxic chemicals as far as the Beaufort Sea, the low rate at which land is being reclaimed after the end of mining, and greenhouse-gas emissions. Regulation is a problem in these areas too, but basic improvements in monitoring science would not help to sort these things out easily. By contrast, better information could make a big difference to water quality.

MINING BOOM

Industrial development of Alberta's oil sands began in 1967. The cost of producing usable oil from the bituminous sands was high, and companies struggled for ►

the next 30 years. As the price of conventional oil edged upwards at the turn of the millennium, development in the oil sands increased at a frantic pace. Production rocketed from 760,000 barrels of oil a day in 2005 to 1.3 million barrels a day in 2006, and is projected to reach 3.3 million barrels or more a day by 2020. The proven reserve is listed as the planet's second largest after Saudi Arabia, with around 170 billion barrels recoverable at 2006 prices.

The extraction of oil from the sands is energy intensive: the energy cost per barrel is higher than for conventional crude oil, although it is difficult to quantify the life-cycle emission differences. Emissions of carbon dioxide from the Canadian oil sands are expected to reach 108 megatonnes by 2020 — a fifth of Canada's current national emissions. The extraction also requires a huge amount of water — 2–5 barrels of water per barrel of oil. Much of the used water ends up in toxic tailings ponds, which can kill birds that land in them and are suspected of seeping chemicals into groundwater.

By 2008, the industrial footprint of the oil-sands operation was 650 km² — about one-hundredth the size of Alberta (or Texas). The area of mine pits and tailings ponds is about four times larger than it was in 1992. Environmental groups and the handful of aboriginal communities living in towns near the oil sands (see map) have repeatedly warned that the rapid development has come at too high a cost to the environment.

The Canadian Association of Petroleum Producers, based in Calgary, Alberta, oil-sands companies and the Alberta provincial government have responded to criticism with their own publicity campaign. Websites, large newspaper ads, TV commercials and even electronic billboards in New York's Times Square and Piccadilly Circus in London portray oil-sands development as environmentally responsible. One ad aimed at US audiences reads "A good neighbor lends you a cup of sugar. A great neighbor

provides you with 1.4 million barrels of oil per day. And does it responsibly." Other ads tout the province's commitment to carbon capture and storage — in 2008, it committed to invest US\$2 billion in the technology — and to protecting land and water. But, so far, carbon capture and storage is only at the developmental stage, and there seems little prospect of it reducing emissions substantially. Nor do I think that water is being sufficiently protected.

OIL IN WATER

Bitumen contains a potent brew of toxic organic and inorganic chemicals. Lab studies show that fish eggs laid on sediments contaminated with bitumen often die, and survivors have high rates of malformations including spinal deformities, lesions, haematomas and eye defects^{1,2}. Similar malformations are observed in adult fish caught downstream of the oil sands by aboriginal people who rely on fish as a major source of protein. Researchers have seen slightly increased incidences of cancer in people downstream of the tar sands, which could be due to chance or industrial pollution³. More work is needed to investigate this question.

So far, no government agency seems to have taken full responsibility for ensuring adequate monitoring of the Athabasca River and its tributaries, which run through the area. The hazy Canadian constitution gives jurisdiction over fish and water that flows across provincial boundaries to the federal government and jurisdiction over land (including watersheds) to the provinces. Responsibilities and monitoring tasks are split between federal bodies including Environment Canada and Fisheries and Oceans Canada, and the provincial body Alberta Environment. Much of the water monitoring has ended up with the Regional Aquatics Monitoring Program (RAMP) — a body with some serious shortcomings.

"The fox has been left in charge of the henhouse."

RAMP is an industry-funded group designed to involve stakeholders from a wide range of groups including local and aboriginal communities, environmental non-governmental organizations (NGOs), government agencies at all levels, oil-sands developers and other industries. However, some aboriginal communities and environmental NGOs have left RAMP, expressing concerns about their opportunity to participate meaningfully or about the group's links with industry. According to a RAMP spokesperson, the group currently counts only 1 aboriginal community and no NGOs among its members, along with 8 government bodies, 12 energy companies and a gravel-mining company. The fox has been left in charge of the henhouse.

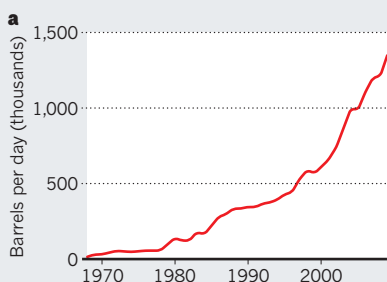
In 2004, a review of RAMP by three federal senior scientists highlighted "a serious problem related to scientific leadership", inconsistent sampling and methodology, and lack of accessibility to data⁴. It concluded that RAMP's data collection made it impossible to determine, for example, the extent to which mining has increased the concentrations of contaminants in the river over natural background levels. RAMP responded to this review by making some changes, including promising to open up its database to public view online — which hasn't happened yet. A new independent review of RAMP is due in December; I expect it will continue to find problems with the organization and its data.

Thanks in part to the past inaccessibility of RAMP data, there have been few independent analyses of its results. Kevin Timoney, a consultant for the Mikisew Cree First Nation band of aboriginal people, was able to obtain access before that group resigned from RAMP in November 2009. He and a colleague concluded that RAMP's data show increases in the concentrations of mercury in fish, and of polycyclic aromatic hydrocarbons in river water and sediments⁵. RAMP did not comment, but an Alberta Environment representative publicly attacked the study, accusing the authors of, among other things, lying and removing data from the study. Faced with a threat of legal action, he sent the authors a letter of retraction and apology this summer.

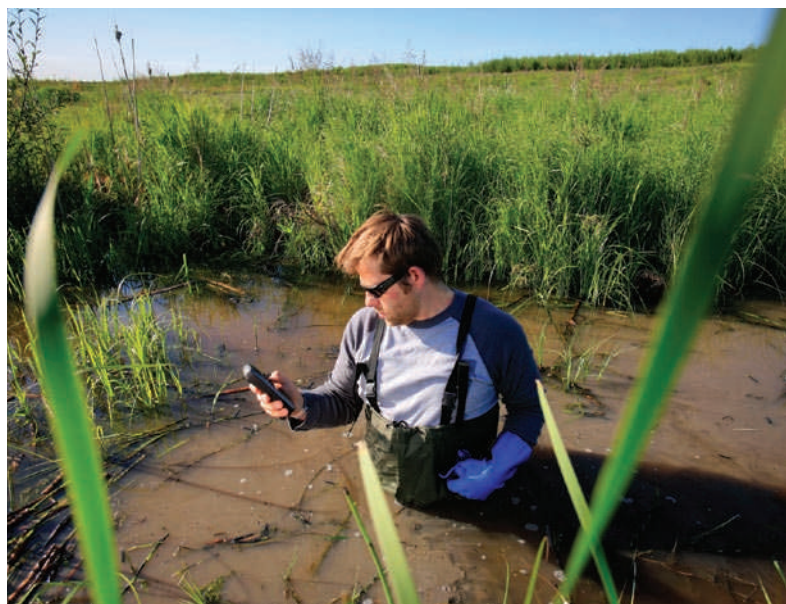
The Canadian House of Commons Standing Committee on Environment and Sustainable Development held 18 months of hearings in 2009 and 2010 on water issues in the oil sands. More than 60 witnesses testified. But the committee never issued a public report. According to news stories in July 2010, the committee destroyed the draft copies after failing to reach a consensus. The minority Liberal and New Democratic parties issued their own reports on the hearings^{6,7}, condemning the state of the science and the monitoring programme, and identifying many topics on which federal responsibilities

TAR-SANDS MINING IN CANADA

Oil production from the tar sands has rocketed (a), and the potential for mining expansion (b) could lead to more pollution.



SOURCE: IHS CERA, CAPP



Author David Schindler (left) holding a deformed whitefish from the Athabasca River. Scientists and activists (right) are trying to assess pollution in the area.

were being ignored, including protection of the Mackenzie River watershed (of which the Athabasca River is a part), aboriginal peoples, lands and species at risk. The oil industry and Alberta politicians largely dismissed these concerns.

EVIDENCE BASE

To redress the scarcity of peer-reviewed science, in 2007 I formed a small group of experts to test a frequent claim of the oil-sands industry and Alberta government that toxins in the Athabasca River and its tributaries are from natural seepage from bitumen deposits. This seemed unlikely, given the probable erosion of areas cleared of soil and vegetation for industrial use, seepage from 130 km² of tailings ponds, and airborne emissions from coke-fired upgraders that convert raw bitumen to synthetic crude oil. We mounted two field expeditions in 2008 — one during winter when the river was ice-covered and four months of snow had accumulated, and another during midsummer. As expected, we found a wide variety of toxic contaminants deposited in the snowpack, some detectable as far as 50 km from the main pollutant sources. In the river system, we found that industry added substantially to the natural contaminant loading^{8,9}. Alberta Environment continues to counter that environmental contaminants are largely natural in origin — even though, as far as I can tell, they have published no studies of atmospheric deposition of trace contaminants.

Two panels of experts, one federal and one provincial, have been appointed to resolve the disagreement between our conclusions and those of RAMP and provincial monitoring programmes. The federal panel is expected to report to the minister of the environment by mid-December 2010, the

provincial panel two months later. The panels contain recognized experts in the fields of water pollution, watershed monitoring and petroleum science; some are members of the Royal Society of Canada.

Ideally, Environment Canada should assume responsibility for monitoring the Athabasca River and its tributaries. They are the only agency with the necessary expertise in both contaminant chemistry and watershed monitoring. The sampling programme must be strategically designed to monitor airborne and waterborne pathways of contaminants, and to separate industrial from natural sources. Seasonal changes, such as the influx of pollutants from contaminated snow during spring snow melt, must be accounted for. Special attention must be paid to assessing the cumulative effects of so many megaprojects in one watershed¹⁰.

Overall, the effort needed is several times that currently invested by all groups in monitoring this important river. In addition, to restore public trust, a panel of independent scientists and community leaders should be formed to provide oversight of this monitoring programme. Results should be published in peer-reviewed scientific papers, and reported to the public at large. A good model is the US Geological Survey's National Water-Quality Assessment Program.

Meanwhile, the rush for expansion in the oil sands is resuming, after a months-long lull caused by the global recession. French energy giant Total is proposing another huge surface mine, and a decision by the provincial Energy Resources Conservation Board (ERCB) is expected by the end of 2010. The hearings for such applications follow a script as predictable as an opera: 'experts' sing their arias in praise of, or in opposition to, development of the oil sands,

generating hundreds of pages of testimony. The cast may vary, but the audience can guess the outcome: although the ERCB has added conditions and amendments to oil-sands proposals, it has never yet rejected a project.

In the face of such rampant expansion, it is ever-more vital that we have good, visible data against which the public can hold regulators to account. With better science in place to monitor water quality and protect the environment, moderation in oil-sands development should follow. ■

David Schindler is an ecologist at the University of Alberta, Edmonton, Alberta T6G 2E9, Canada.
e-mail: d.schindler@ualberta.ca

- Colavecchia, M. V. et al. *J. Toxicol. Environ. Health Part A* **69**, 967–994 (2006).
- Colavecchia, M. V. et al. *J. Toxicol. Environ. Health Part A* **70**, 1542–1555 (2007).
- Chen, Y. *Cancer Incidence in Fort Chipewyan, Alberta 1995–2000* (Alberta Cancer Board, Edmonton, 2009).
- Ayles, G. B. et al. *Oil Sands Regional Aquatic Monitoring Program (RAMP) Scientific Peer Review of the Five Year Report (1997–2001)* (Fisheries and Oceans Canada, Winnipeg, 2004); available at go.nature.com/tdsuag
- Timoney, K. P. & Lee, P. *Open Conserv. Biol. J.* **3**, 65–81 (2009).
- New Democrat Party of Canada. *Missing in Action: The Federal Government and Protection of Water in the Oil Sands* (2010); available at go.nature.com/pzuypx
- Liberal Party of Canada. *The Hidden Dimension: Water and the Oil Sands* (2010); available at go.nature.com/63vltb
- Kelly, E. N. et al. *Proc. Natl Acad. Sci. USA* **106**, 22346–22351 (2009).
- Kelly, E. N. et al. *Proc. Natl Acad. Sci. USA* **107**, 16178–16183 (2010).
- Squires, A. J., Westbrook, C. J. & Dubé, M. G. *Integr. Environ. Assess. Monit.* **6**, 119–134 (2009).

Further reading accompanies this article online at go.nature.com/qz5tki

Call in the women

A critical mass of female voices changes the tenor of political and corporate decisions — and should be used to galvanize climate policy, says **Susan Buckingham**.

In 1992, the United Nations called for women to be engaged in environmental decision-making at all levels. This was on the grounds of human rights and justice, and because of their distinctive experiences of childbirth, caring for vulnerable family members, unpaid or undervalued work and subsistence food production. These experiences often expose women to environmental problems in ways that are more direct and harsher than for men — for example, women suffer disproportionately from indoor air pollution in countries that use biofuels for cooking and heating.

Even in the developed world, women are still more likely to be involved with household tasks, from cleaning and grocery shopping to bill paying, in which environmental issues can be a direct concern. Such different experiences may lie behind different attitudes that men and women, on average, have to environmental issues. A 2009 Eurobarometer survey on behalf of the European Commission and European Parliament showed that men were more likely to think that carbon dioxide emissions have only a marginal effect on climate change (33% versus 29% for women), and that the seriousness of climate change has been exaggerated (31% versus 25% for women)¹.

The current landscape of industries, governments and other bodies with a say in climate-change issues — including transport, energy, waste management, architecture and city planning — is predominantly male. In the Intergovernmental Panel on Climate Change (IPCC), only 5 of the 31 chairs, co-chairs and vice-chairs are women. Perhaps surprisingly, this dearth of female faces extends to non-governmental organizations and campaign groups. In my eight years as chair of the UK-based Women's Environmental Network, I was struck by the machismo of much of the environmental campaigning sector.

Almost two decades on from that UN call, women's views are still not being heard where they count. This is more than unjust: it is a missed opportunity, given the political deadlock over addressing global warming. Although it is difficult to prove a connection between gender balance and decision-making, or to pinpoint causation, there are signs that a critical mass of women is linked to more progressive and positive outcomes. A recent study published in *Science*, for example, showed that collective intelligence rises with the number of women in a group — probably



Christiana Figueres, executive secretary of the UN Framework Convention on Climate Change.

because of their increased social sensitivity².

In 2007, in a survey of gender balance at senior management level in companies, McKinsey & Company, a management consultancy in New York, found a positive and significant relationship between the employment of three or more women in every ten or so appointments and factors such as company performance in leadership, innovation, return on equity and stock price³. It is generally thought that at least 30% women is needed in a group's leadership to alter decision-making. Less than this, and the women may be drowned out, feel too intimidated to comment or have been selected because their views tend to conform to those of their male colleagues.

BETTER TOGETHER

Gender balance has also been linked with environmental decision-making. In 2003, my colleagues and I made a study of waste-management systems for the European Commission⁴. We found that the local authorities with the highest recycling rates had a higher percentage of women managers than average. They also tended to include fewer engineers and more decision-makers from diverse backgrounds, including education.

Similar trends can be seen in national carbon emissions. Out of the 70 most developed countries in the world, only 18 reduced or stabilized their overall carbon emissions between 1990 and 2004 (ref. 5). Fourteen of

these had a greater-than-average percentage of female elected representatives. Again, that doesn't prove causation, but it hints that gender balance and more sustainable decision-making may go hand in hand.

A challenge to the male dominance of the climate-change community was launched in 2007 at the Conference of the Parties to the IPCC in Bali, through the creation of the Global Gender and Climate Alliance. It aims to ensure that gender concerns are integrated into the process for negotiating climate change. In March 2010, a coalition of women's environmental groups challenged the all-male nominations to the UN's High Level Advisory Group on Climate Change Financing. One woman, Christine Lagarde, the French minister of economic affairs, industry and employment, replaced a man in the advisory group, although alone she is unlikely to be able to make significant changes. Similarly, the May 2010 appointment of Christiana Figueres, a former government minister and environmental negotiator from Costa Rica, as the new executive secretary of the UN Framework Convention on Climate Change is encouraging, but alone it might not be enough.

Environmental consultant Candice Stevens, a former sustainable-development adviser to the Organisation for Economic Co-operation and Development, recently suggested that the "abysmally slow" progress on sustainable development might be linked to "sluggish" advances in achieving gender equality, and called for research to investigate this question⁶. More research is a good idea. But in my view, there is enough evidence now to justify increasing women's involvement in decision-making on climate change. We should do so without delay. ■

Susan Buckingham is a professor at the Centre for Human Geography, and is an associate of the Institute for the Environment at Brunel University, Uxbridge UB8 3PH, UK. e-mail: susan.buckingham@brunel.ac.uk

1. go.nature.com/xpi6ev
2. Woolley, A. W. et al. *Science* **330**, 686–688 (2010).
3. *Women Matter* (McKinsey, 2007); available at go.nature.com/aabhsn
4. Buckingham, S., Reeves, D. & Batchelor, A. *Local Environ.* **10**, 427–444.
5. United Nations Development Programme. *Fighting Climate Change*. Human Development Report 2007/2008 (UNDP, 2007).
6. Stevens, C. *Are Women the Key to Sustainable Development?* (Boston Univ./UN, 2010); available at go.nature.com/qexuub

O. BERG/EPA/CORBIS



Popularity has led to pandas being both hunted and conserved in the wild.

CONSERVATION

China's national treasure

The panda's plight shows how protection often vies with economic necessity, finds **Jane Qiu**.

Since the West first 'discovered' the giant panda (*Ailuropoda melanoleuca*) in 1869, the beast has emerged as China's biggest icon and as the face of global conservation. Pandas have been sent on diplomatic journeys and their image has adorned everything from chocolate to electronic goods.

In *The Way of the Panda*, science journalist Henry Nicholls charts the rich and curious history of the animal. He skillfully interweaves the species' rise to global fame with China's development as a nation since the late nineteenth century. And he explains how the panda's popularity has led to it being

both hunted and conserved in the wild.

At the centre of the tale is a female panda called Chi Chi. Intended to be sold to Brookfield Zoo near Chicago, Illinois, in 1958, she fell foul of politics when a US trade ban with Communist China blocked the deal. She was eventually obtained by London Zoo, where she became the focus of panda fervour. Greeted by millions of zoo visitors and appearing on television, Chi Chi became a household name. Her failed breeding attempts with An An, a male panda in Moscow Zoo, inspired cartoonists and journalists worldwide, who exploited

the parallels with the cold-war chill between the United Kingdom and Russia. In 1961, Chi Chi was immortalized by the World Wildlife Fund (WWF), when she was used as the basis for its panda logo.

Eighteen years later, WWF became the first international conservation agency to hold talks with China after the Cultural Revolution. This led to the start of the groundbreaking China-WWF research project on wild pandas in 1985. Traps and radio collars revealed the secret world of these elusive creatures: their foraging behaviour, their sex life, mother and cub relationships, and their communications, mostly through odour and vocalization. The WWF recorded the distribution of bamboo species across China, and intervened to protect the animals during periods when the bamboo forests flowered

and died. Today, there are thought to be about 1,600 pandas in the wild, mainly in the Sichuan, Shaanxi and Gansu provinces.



The Way of the Panda: The Curious History of China's Political Animal

HENRY NICHOLLS
Profile Books: 2010.
224 pp. £15.99

As Nicholls astutely explains, the panda's popular appeal has been both a blessing and a curse for the animals' survival in the wild. After the panda's existence became known in the West, specimens were sought, dead or alive,

by explorers, trophy hunters, taxonomists and animal collectors. In Sichuan, the provincial government banned the capture of pandas in 1938 amid the turmoil of the Sino-Japanese war. But they continued to be taken from the wild to satisfy the demand of zoos and diplomatic missions. Symbolizing friendship and goodwill, pairs of pandas were presented to US President Richard Nixon after his state visit to China in 1972, and to Hong Kong when it rejoined China in 1997.

The level of adulation given to pandas in zoos has distorted our view of them. Because they have had difficulty breeding in captivity and have highly limited, specific diets, pandas are often assumed to be inept, a species at an evolutionary dead end that might become extinct without human help. Yet scientists who study pandas in the wild have a very different picture. Wild pandas breed readily, have sophisticated foraging and communication skills, and are ferociously territorial. Nicholls argues that unless this distinction is acknowledged, we will "conserve the virtual rather than the real giant panda".

Indeed, as the number of pandas in captivity grows — and it is now around 300, thanks to artificial insemination and research into their reproductive behaviour — their wild counterparts are coming under increasing

► pressure. Human population growth, farming and the construction of dams and highways threaten panda reserves across China. Programmes to return captive pandas to the wild are a distraction from what really matters: protecting wild pandas, which are endangered not by their biology but by the loss and fragmentation of their habitat.

Nicholls acknowledges the enormous challenge China faces to balance economic development and conservation. He is right to point out that the country has made extraordinary leaps: it has added another 60 panda reserves covering more than 70% of suitable habitat; introduced tougher enforcement of blanket logging bans within nature reserves; and invested tens of billions of dollars in a series of policies, such as the Natural Forest Protection Programme and the Sloping Land Conversion Programme, to encourage forest protection and restoration.

Yet Nicholls does not sufficiently explore the substantial gap between these well-intentioned conservation plans and their incomplete implementation in practice, a problem that plagues many areas of development in the country. Despite China's pledge to protect the environment, economic development frequently takes precedence at the provincial level. Consequently, panda habitats are often destroyed or fragmented to make way for major infrastructure projects such as dams and highways.

Tourism is also a threat. For example, Jiuzhaigou, part of the pristine Sichuan Giant Panda Sanctuary — a World Heritage Site — is visited by millions of tourists each year. Nicholls notes that even when ecotourism is deliberately introduced to provide local people with a livelihood that is not damaging to nature reserves, economic benefits often go to investors based outside the community. Hotel and restaurant owners tend to import skilled workers rather than train locals. Hence, he points out, local people often continue to chop down trees or convert forests into farmland.

Through this engaging tale of the panda's plight, Nicholls highlights how conservation pressures are often pitched against economic ones. At the recent United Nations Convention on Biological Diversity summit in Nagoya, Japan, there was broad acknowledgement that radical steps to reform economic and social development are necessary to protect natural resources. Such a strategy could be the best hope for the giant panda and other species that face extinction. ■

Jane Qiu writes for *Nature* from Beijing.

HISTORY

Catching up with the Sun

Douglas Gough enjoys a wide-ranging tour of the many influences of our nearest star.

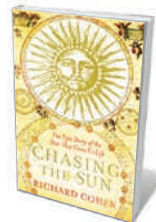


Louis XIV of France named himself the Sun King to bolster his authority.

To humankind, the Sun is the most important body in the Universe.

It has been deified and associated with fecundity and eroticism; it pervades literature, art and film, and it influences our daily moods. Studies of the Sun motivated revolutionary changes in scientific thought in the twentieth century — including quantum mechanics and general relativity — and today its workings still constitute a most important branch of astronomy and astrophysics. To write yet another work about our nearest star is a

formidable challenge that author Richard Cohen takes up with aplomb. *Chasing the Sun* paints a fascinating and far-reaching scene that incorporates nearly all aspects of solar phenomena.



Chasing the Sun: The Epic Story of the Star That Gives Us Life

RICHARD COHEN
Simon & Schuster/
Random House: 2010.
704 pp./608 pp.
£30/\$35

Cohen touches on a range of histories of Sun-related myths, religions, superstitions and traditions.

From Babylon, Egypt and Greece to China, Persia, India, Peru, Arabia and Japan, ancient cultures established observatories to chart the motions of the Sun, the Moon, planets and stars. Because the annual shift of the Sun's path across the sky is pertinent to the survival of agrarian societies, these cultures developed calendars to determine when crops should be sown.

The Sun was a god to many civilizations, and rulers often derived their authority by asserting that they were descended from it. Cohen describes the influence of the Sun on architecture, art, music, literature, poetry and even politics. He discusses how our understanding of the physical nature of the Sun has developed, and, to a lesser degree, how that knowledge has advanced our understanding of physics.

The narrative is liberally sprinkled with personal anecdotes, which is largely what makes the book so enjoyable. Cohen describes how, early in the morning of the summer solstice of 2005, he ascended Mount Fuji in Japan

to see the sunrise with the words "You run and you run to catch up with the Sun" from Pink Floyd's song *Time* running through his ears. At the summit, he bathed in the colours of the rapidly changing skyline — indigo, purple, ochre — and, when the full glare of the Sun struck home, he ►

"Many dates owe their origins to the Sun's movements — even the start of the UK tax year."

Books in brief



Blowout in the Gulf: The BP Oil Spill Disaster and the Future of Energy in America

William Freudenburg and Robert Gramling THE MIT PRESS
240 pp. \$18.95 (2010)

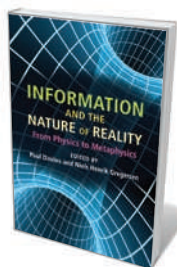
Environmental scientist William Freudenburg and sociologist Robert Gramling set the recent Gulf of Mexico oil spill in the broader context of energy policy. After examining decisions made during attempts to stifle the gushing well, they point the finger at the oil industry for cutting regulatory corners and pocketing the proceeds. In future, greater emphasis should be put on prevention, and risk assessments should include human as well as hardware foibles, they argue.



The Evolutionary World: How Adaptation Explains Everything from Seashells to Civilization

Geerat J. Vermeij THOMAS DUNNE BOOKS 336 pp. \$27.99 (2010)

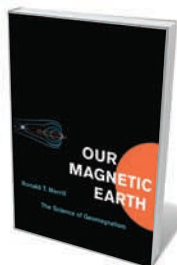
In his far-ranging book, geologist Geerat Vermeij stretches the implications of evolution to all aspects of society, from religion to morality. With a focus on adaptation and using examples from ecosystems around the world, he explains how natural selection has influenced human civilization and underpins our economic system, the development of communities and our attitudes to risk. Only by understanding these forces, he argues, can we prepare for the challenges that lie ahead.



Information and the Nature of Reality: From Physics to Metaphysics

Edited by Paul Davies and Niels Henrik Gregersen
CAMBRIDGE UNIVERSITY PRESS 398 pp. \$30 (2010)

Information, rather than mass and energy, is coming to be seen as the fundamental currency of the Universe. Eminent scientists, philosophers and theologians come together in this anthology to chart this shift in thinking. After describing the historical development of theories of quantum, biological and digital information, they contrast biological and physical approaches to information and examine the philosophical and ethical implications of the concept.



Our Magnetic Earth: The Science of Geomagnetism

Ronald T. Merrill UNIVERSITY OF CHICAGO PRESS 272 pp. \$25 (2010)

Earth's magnetic field is a valuable tool, influencing everything from compass settings to the migration of geese. It lays down in rocks a forensic record of the spreading of ocean floors, plate tectonics and past climate. It also protects our planet by deflecting damaging cosmic rays, and is sensed by organisms from bacteria to mammals. In his primer that is peppered with anecdotes, geophysicist Ronald Merrill explains why geomagnetism is central to Earth science and discusses how it could offer solutions to some of the biggest questions about our planet's future.



How Many Friends Does One Person Need? Dunbar's Number and Other Evolutionary Quirks

Robin Dunbar HARVARD UNIVERSITY PRESS 312 pp. \$27.95 (2010)

From our love of jokes to our degree of belief in religion, anthropologist Robin Dunbar seeks to explain why people behave as they do. Describing groundbreaking experiments that reveal how evolutionary biology underpins our behaviour, he asks why we laugh, why we should be suspicious of someone who has more than 150 friends on Facebook and why Barack Obama's 2008 US election victory was a foregone conclusion.

► understood why we say something ‘dawns’ on us. The book is also peppered with gems of information, such as the origins of the expressions high noon, high seas and plain sailing.

Much is said about time-keeping, and how many dates owe their origins to the Sun’s movements: pagan festivals, Christian festivals, even the start of the UK tax year on 6 April. Cohen also goes into the dangers of sunlight; for example, he relates how, after the 1999 solar eclipse in England, doctors in a London hospital reported that they could pinpoint the precise phase at which a patient had stared at the Sun from the shape of the ‘sickle’ damage to his or her retina.

This book is no stolid scholarly treatise. Cohen is mainly a storyteller, who, after more than seven years of research, has amassed a prodigious amount of information and organized it into an entertaining narrative. However, in not wanting to detract from the main point of his tale, he occasionally oversimplifies matters — especially those scientific ones for which veracity is sometimes left behind. For example, at the start of the book the casual reader might be led falsely to believe that the Sun is now contracting, later to fade into a red giant. This is contradicted

“The Sun did contract from the gas and dust of the interstellar medium, but that took just 10 million years.”

nearly 600 pages later by a paragraph offering a more accurate view. The Sun did initially contract from the gas and dust of the interstellar medium, but that took just 10 million years.

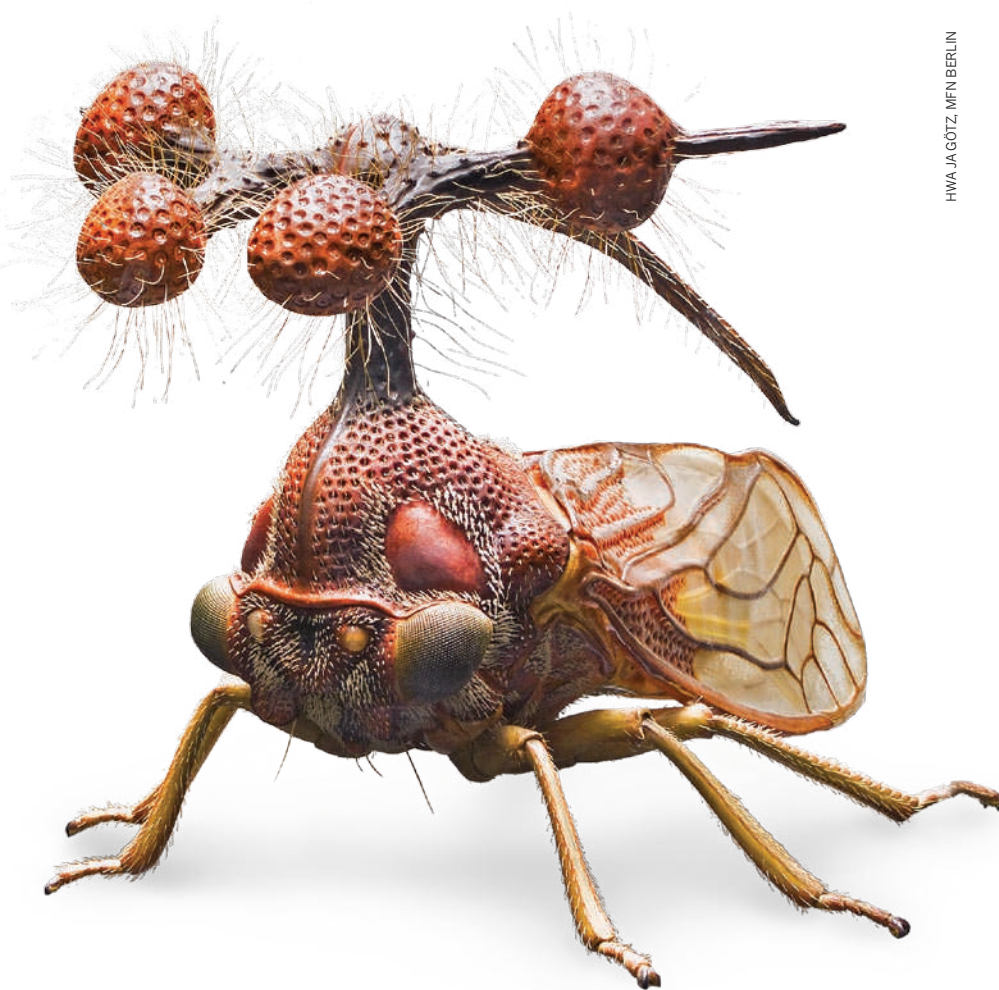
Since then and for almost all of its existence — some 4.6 billion years so far — it has been expanding, and will continue to do so at a steadily accelerating pace for nearly 6 billion years more. It will then expand rapidly into a highly luminous red giant, albeit with a lower surface temperature, before finally condensing to a white dwarf.

Despite shortcomings such as these, *Chasing the Sun* is a marvellous read. ■

Douglas Gough is a Leverhulme Emeritus Fellow at the Institute of Astronomy, and professor emeritus of theoretical astrophysics in the University of Cambridge, Madingley Road, Cambridge CB3 0HA, UK. e-mail: douglas@ast.cam.ac.uk

► NATURE.COM

For a review of discoveries from solar eclipses, see: go.nature.com/ezzc5b



HWA JA GÖTZ, MfN BERLIN

SCULPTURE

Terrible wonder

Alfred Keller’s fastidious models of insects highlight his skill as an observer and a sculptor, finds **Martin Kemp**.

Venturing upstairs in Berlin’s Museum für Gegenwart (Museum for Contemporary Art), we enter a darkened space inhabited by alien creatures, eerily spotlighted in glass cases.

The specimens in the exhibition, *Die Sammlungen* (The Collections), exude an air of menace. As we look more carefully, we begin to recognize some of the monsters as familiar insects, most obviously *Musca domestica*, the common housefly, and *Pulex irritans*, the flea, immortalized in Robert Hooke’s *Micrographia* of 1665. The models, enlarged by a factor of 100, recall Hooke’s comment about the terrible wonder of such magnified insects. He described the flea he viewed down his microscope as “adorn’d with a curiously polish’d suit of sable Armour, neatly jointed, and beset with multitudes

Die Sammlungen (The Collections)
Hamburger Bahnhof
Museum für
Gegenwart, Berlin.
Until 6 February 2011.

of sharp pinns, shap’d almost like Porcupine’s Quills, or bright conical Steel-bodkins”.

One of the large models on display is as bizarre a creature as we might ever see. It looks like a cartoon beetle with some ultra-sensitive receiving device of spheres and tendrils mounted on a short mast protruding from its back. It is in fact *Bocydium globulare*, the most extravagant of the leaf hoppers (pictured). The hollow globes, like the remarkable excrescences exhibited by other leaf hoppers, probably deter predators.

This model is by the brilliant sculptor, Alfred Keller (1902–55). Keller was trained as a kunstschnied, an ‘art blacksmith’. From 1930 until his early death he was employed

by the Berlin Museum für Naturkunde (Museum of Natural History), painstakingly labouring over his recreations of insects and their larvae. Each took a year to complete.

Keller worked first in plasticine, from which he cast a model in plaster. This plaster reference model he then recast in papier maché. Some details he added, cast in wax, with wings and bristles in celluloid and galalith (an early plastic material used in jewellery). Finally he coloured the surfaces, sometimes with additional gilding. The levels of patience and manual control Keller exercised were incredible. His fly, for example, boasts 2,653 bristles.

It may surprise some to find that papier maché — a material now associated with messy child's play — was used in such a refined manner for scientific modelling. It was developed as a serious medium by the anatomist Louis Auzoux of Paris. He was looking for a cheap and portable alternative to the wax models that graced only the best funded schools of medicine. During the 1820s Auzoux perfected his technique, mixing powdered stone and flax fibres into his paper pulp. The resulting models of bodies, with removable parts, were light, strong and flexible, and could be coloured and labelled.

Auzoux set up a factory and shop to manufacture and distribute his models worldwide, progressively extending his production to zoological and botanical examples. His large-scale insects proved especially popular. His shop in the Rue du Medecine in Paris survived into the 1990s; its remaining specimens were auctioned in 1998.

Although they used similar media and sometimes the same insect subjects, Keller and Auzoux stood at different ends of the modelling business. Auzoux produced on a commercial scale; Keller was a sculptor of monumental one-off portraits. Each model is a masterpiece, with no effort spared. It is difficult to see how such a skilled artisan could survive in today's museums, with their emphasis on cost analysis. Keller's exacting models may be things of the past, yet they are far from obsolete. Like the great habitat dioramas, they exercise a magnetic attraction.

Are Keller's models art or science? They are truly both. In the Museum für Gegenwart we tend to see their artistry; in the Museum für Naturkunde their scientific dimension. But Keller's artistry is always apparent in his observations of nature — and his scientific observations are central to his art. ■

Martin Kemp is emeritus professor of art history at the University of Oxford, UK.

INNOVATION

The ideas lab

Jascha Hoffman reads about some creative research environments that led to unexpected discoveries.

Biomedical engineer David Edwards is regarded as an innovation guru. His various achievements include bringing to the market new ways to deliver drugs to the lungs, as well as setting up Le Laboratoire, a forward-looking institution in Paris that seeks to harness the creativity of science and art (see *Nature* 449, 789; 2007). His growing empire of labs, galleries and non-profit organizations stretches from Paris to Cape Town to Cambridge, Massachusetts, where he lectures at Harvard University.

His latest book, *The Lab*, calls for a new breed of small, flexible institutions to support interdisciplinary researchers whom Edwards calls “artscientists”. Motivated by curiosity and passion, such researchers make unexpected discoveries that blur the conventional lines between science, business and art. Rather than prescribing the details of how such a lab should function, Edwards offers examples from his own experience: ingenious humanitarian projects, culinary novelties and science-based art installations.

Edwards's ideal laboratory requires large doses of supervision from experienced innovators. At Harvard, he has mentored undergraduates during their pursuit of ambitious humanitarian projects, including the development of soil-powered lighting for African villages using microbial fuel cells; the invention of a sleek water vessel whose collapsible skin was inspired by the design of living cells; and the creation of a soccer ball that generates electricity when you kick it. He is also on the board of Medicine in Need, an international non-profit organization that is pursuing an inhalable vaccine for tuberculosis.

One can sense the creative zeal when Edwards turns to his work on culinary technology. He describes a series of inventive soirées in Paris where guests were treated to caviar-like ‘flavour beads’ encapsulated in calcium alginate, or martinis that were turned to mist by ultrasound waves from piezoelectric crystals. The most popular of his foodstuff experiments is Le Whif, a form of breathable chocolate developed

with French chef Thierry Marx, inspired by Edwards's earlier research on inhalable drugs. Delayed by faulty inhalers that spewed cough-inducing clouds of cocoa powder, a working version of Le Whif went on sale this year.

As the curator of Le Laboratoire, Edwards also pairs conceptual artists with open-minded scientists. The results, displayed at his galleries in Paris and Cambridge, Massachusetts, are well intentioned but

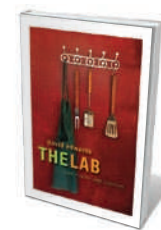
often incoherent. He describes in the book how he led Indian artist Shilpa Gupta to collaborate with Harvard psychologist and neuroscientist Mahzarin Banaji on an investigation of the biology of fear, resulting in an installation that required thousands of microphones to be strung from the ceiling. The puzzling opacity of such works brings to

mind the comment of Swiss art curator Hans Ulrich Obrist: “Bringing art to science gives you a good chance of having neither.”

Edwards's prose can be heavy with jargon and self-promotion. Whereas his previous book *Artscience* (Harvard University Press, 2008; see *Nature* 451, 246; 2008) presented a series of vignettes of researchers working at the edges of their disciplines, the focus on Edwards's own endeavours in *The Lab* can feel narrow. Yet his enthusiasm is infectious. He comes across as a free-spirited inventor and educator. He is also a pragmatist, conceding that an emphasis on the creative process, and a high tolerance for failure, may make it harder for inventive researchers to achieve financial autonomy.

In these austere times, Edwards takes a firm stance on the importance of the imagination: “If the lab sacrifices the playful, contemplative, daring, irreverent atmosphere of the creative band in order to gain sustainability,” he writes, “the organization may survive, but the lab will cease to exist.” ■

Jascha Hoffman is a writer based in San Francisco, California.
e-mail: jascha@jaschahoffman.com



The Lab: Creativity and Culture
DAVID EDWARDS
Harvard University
Press: 2010. 224 pp.
\$22.95

“In these austere times, Edwards takes a firm stance on the importance of the imagination.”

CORRESPONDENCE

IPCC yet to assess geoengineering

As co-chair of Working Group III of the Intergovernmental Panel on Climate Change (IPCC), I would like to clarify your misleading implication that I recommend geoengineering as an option for attaining ambitious climate targets (*Nature* 468, 13–14; 2010).

The IPCC does not have a mandate to recommend or dismiss specific policies or technologies. It aims to assess all relevant climate-change mitigation options on the basis of peer-reviewed scientific literature. This assessment must be unbiased, factual and policy-relevant, without being prescriptive.

There is ongoing public and scientific debate about using geoengineering as one of several options to mitigate climate change. Some decision-makers consider it a last resort in case technologies that are more conventional prove insufficient (for example, usage of renewable energy, carbon dioxide capture and storage, or nuclear power). Others are against a geoengineering option because of gaps in our knowledge, unwanted side effects and unmanageable risks. Notably, delegates at the United Nations Convention on Biological Diversity summit last month in Nagoya, Japan, agreed to call for a moratorium on geoengineering schemes (see go.nature.com/kc1b9c). Also, the governance structure of this option needs further consideration. Several fundamental questions must be answered before the deliberate alteration of Earth's radiation balance can be considered as a reliable option.

The IPCC will therefore assess the risks, feasibility, mitigation potential, costs and governance requirements of geoengineering for the first time in its Fifth

Assessment Report, due to be released in 2013–14.

Meanwhile, the three IPCC working groups are coordinating a meeting of expert scientists from different disciplines as a platform for exchange and discussion. The aim is to encourage research into the implications of different geoengineering technologies, as well as to study their potential impact on biodiversity, human society and the climate system.

Ottmar Edenhofer Potsdam Institute for Climate Impact Research, Germany.
ottmar.edenhofer@ipcc-wg3.de

An intellectual black hole

News items on climate change are now regularly flooded with negative online comments (see, for example, go.nature.com/Lfigec). These tend to have certain features in common.

The comment writers struggle to find words that are emphatic enough to express their contempt for anthropogenic global warming and for the 97% or so of active climate scientists who accept its reality. They feel attacked, lied to and conspired against: they are intensely angry. Their comments are often pervaded by heavy sarcasm. In their view, climate scientists are not merely mistaken, but foes of truth and liberty. They see themselves as fighting a powerful enemy — a posture that can be additive.

These comment authors rarely engage with the original science (in the above example, an article in *Geophysical Research Letters*). They have unplugged from the scientific discourse because they believe it to be driven by crypto-environmentalist (or crypto-communist) ideology. This conviction characterizes fundamentalisms: a true believer does not need to engage, they

already know. The denialists charge that it is the scientists who refuse to consider the evidence; alternatively, scientists know all about it and are lying. The parallels with some creationist rhetoric are striking.

Certain standard fallacies and counterfactuals are held by these commenters as irresistible 'gotchas' — any one of which makes the idea of human-induced global warming absurd (and further thought unnecessary). For example, a popular line of argument is that because climate has changed in the past without human input, humans cannot be changing it now. Mistaken beliefs are held that scientists on the Intergovernmental Panel on Climate Change, climate modellers and other researchers ignore factors such as water vapour, urban heat islands and the Sun.

The peculiar danger of any full-blown conspiracy theory is that it can become an intellectual black hole, a one-way trip. Hope lies mostly in keeping people out of the hole, rather than trying to rescue those who have fallen in.

Larry Gilman Sharon, Vermont, USA. lgilman@myfairpoint.net

Space telescope is worth the effort

Your sensationalist headline 'The telescope that ate astronomy' could more appropriately have highlighted the promise of NASA's James Webb Space Telescope (JWST) for astronomy's future (*Nature* 467, 1028–1030; 2010).

No facilities exist on or off this planet — or are called for in the recent US decadal survey of astronomy and astrophysics — for finding the first galaxies or for detecting liquid water on habitable planets around other stars. These capabilities have

been part of the JWST science plan since its inception.

Such transformative science is why NASA, the European Space Agency and the Canadian Space Agency took on the challenge of building a telescope of comparable scale to the ground-based W. M. Keck telescopes or one of Europe's Very Large Telescopes. This meant reducing the JWST's mass by almost two orders of magnitude compared with a Keck telescope, cooling it to -313°C and folding it to fit inside an Ariane 5 spacecraft for deployment 1.5 million kilometres from Earth.

Building the JWST has required the manufacture of 18 1.3-metre beryllium mirrors able to hold their shapes to better than 20 nanometres at cryogenic temperatures, and of a deployable gossamer sunshield the size of a tennis court.

It was equally challenging to build the Hubble Space Telescope. But it was worth it: Hubble has revolutionized our understanding of the Universe, inspired generations of school children with its breathtaking images and supported a community of 8,000 astronomers worldwide. Likewise, the efforts of today's space scientists are creating a revolutionary telescope for the next generation of scientists and engineers.

Matt Mountain, John Grunsfeld Space Telescope Science Institute, USA. mmountain@stsci.edu
Heidi Hammel Space Science Institute, USA.

CONTRIBUTIONS

Readers are welcome to comment online on anything published in *Nature*: www.nature.com/nature. Submissions to Correspondence may be sent to correspondence@nature.com.

Raiding the sweet shop

A type of sugar transporter has been discovered that exports glucose from cells. In plants, these transporters are targeted by disease-causing microbes that divert sugar production for their own use. [SEE ARTICLE P.527](#)

NICHOLAS J. TALBOT

Sweetening nectar, maintaining blood sugar levels and producing milk — these are just some of the many processes that require living cells to export sugar. It comes as a surprise, therefore, that until now the identity of the proteins responsible for sugar export has been unclear. On page 527 of this issue, Chen *et al.*¹ describe a family of sugar transporters, called SWEETs, that are essential for moving glucose between cells in both plants and animals. The importance of these transporters is highlighted by the fact that they are selectively targeted by pathogenic fungi and bacteria that plunder sugar from living plants.

Chen and colleagues' discovery¹ of SWEET transporters was aided by their use of a novel glucose nanosensor capable of measuring small changes in glucose concentration in living cells². The authors first scanned a database of candidate membrane proteins from the model plant *Arabidopsis* to identify genes encoding potential sugar transporters. These genes were then expressed in cultured human embryonic kidney cells together with the nanosensor. Protein nanosensors work by a mechanism known as fluorescence resonance energy transfer (FRET), in which binding of a ligand — in this case, glucose — causes a conformational change in the protein that results in emission of fluorescence proportional to the amount of glucose present^{2–4}.

Using this approach, as well as two independent methods, Chen *et al.* identified a candidate protein, AtSWEET1, that can transport sugar across plasma membranes, or between internal cellular compartments of living cells, and that defines a new type of glucose-efflux transporter. SWEET proteins contain seven helices that potentially span the cell or internal cellular membrane and that are predicted from the authors' modelling studies to form a single pore for transporting sugar across membranes. The authors find that the SWEET family is extensive in plants, with 17 members in *Arabidopsis* and 21 predicted in rice. But they also find that it occurs in animals — seven members in nematode worms and one in humans. All of the SWEETs have similar glucose-transport characteristics, implying that they have widespread roles in

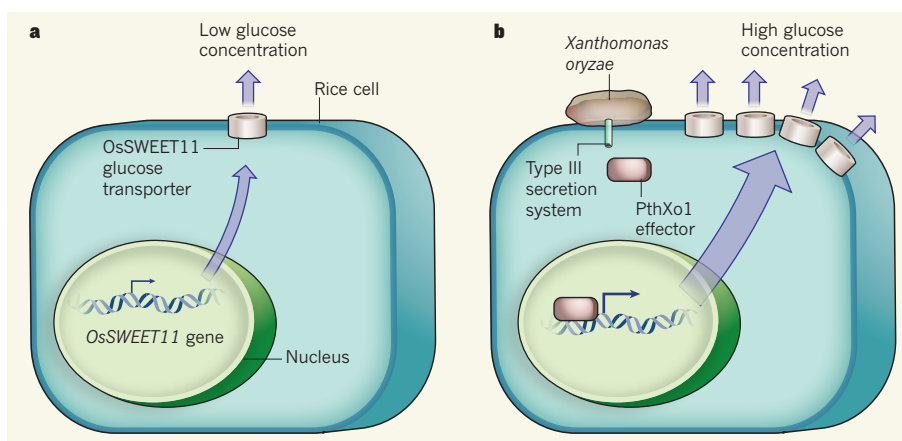


Figure 1 | Pathogen exploitation of plant SWEET genes. These genes, identified by Chen *et al.*¹, are targeted by bacteria to divert glucose into the intercellular spaces where the microorganisms grow. **a**, A rice cell in an uninfected plant has a set of SWEET-encoding genes, including *OsSWEET11*, and steady-state SWEET protein activity results in a low concentration of glucose outside the cell. **b**, The invading bacterium *Xanthomonas oryzae* uses a TAL effector protein, PthXo1, delivered by the type III secretion system, to increase *OsSWEET11* activity. Distinct SWEET-encoding genes are targeted by further TAL effectors, leading to increased extracellular glucose that fuels bacterial growth.

sugar export in both animals and plants.

What can we learn about intercellular sugar transport from the identification of the SWEET exporters? Several clues come from Chen and colleagues' investigations of the expression patterns of SWEET-encoding genes in diverse organisms, and also from their study of a range of previously reported mutant organisms whose characteristics turn out to be associated with genes now known to encode SWEET transporters. AtSWEET1, for instance, is highly expressed in *Arabidopsis* flowers, particularly in petals and stamens, suggesting that it is involved in supplying sugar to nectaries. AtSWEET8 is expressed in the tapetum — the nutritive layer of cells within the pollen sac that functions in pollen nutrition — and AtSWEET8 mutants cause male sterility, consistent with a function in pollen-tube development.

In animals, gene silencing of *CeSWEET1* in the nematode worm *Caenorhabditis elegans* causes fat accumulation, which may be a consequence of the loss of glucose efflux from cells. In mice, the *MmSWEET1* gene is highly expressed in the mammary gland during lactation, suggesting a function in glucose export to the cell's Golgi apparatus for synthesis and secretion of lactose for milk production. And

in humans, the HsSWEET1 transporter occurs predominantly within the Golgi, and is most abundantly found in the oviduct, epididymis and intestine — so raising the intriguing possibility of a hitherto unknown glucose-efflux pathway in which glucose is exported to the Golgi by a SWEET transporter to facilitate its secretion from epithelial cells to neighbouring tissue.

Accessing sugar from a host organism is, of course, also key to the survival and reproduction of microorganisms that need to invade and grow within living tissue⁵. Indeed, altering the expression and activity of SWEET efflux transporters would provide an elegant way of diverting glucose towards an invading pathogen. Remarkably, this ability seems to have evolved not only in bacterial plant pathogens but also in fungi. For example, Chen *et al.*¹ find that two plant-pathogenic fungi — the powdery mildew *Golovinomyces cichoracearum* and the grey mould *Botrytis cinerea* — induce the expression of distinct sets of SWEET genes during infection. How this is accomplished is unknown, but it may involve delivery of fungal effector proteins⁶ into plant cells to bring about changes in host gene expression.

There is increasing evidence that fungi and other microbial pathogens can dispatch

effector proteins into plant cells to cause changes in the cells' behaviour^{6,7}. Bacterial pathogens use the specialized type III secretion system that sends proteins directly into plant-host cells^{5,8}, providing evidence for effector-protein-driven modulation of SWEET activity (Fig. 1). In rice, the recessive gene *xa13* has been reported to confer resistance to the bacterium *Xanthomonas oryzae*⁹. It is now clear that *xa13* originates from a mutation in the promoter sequence of the *OsSWEET11* transporter gene. *Xanthomonas oryzae* delivers a transcriptional-activator-like (TAL) effector protein, PthXo1, into rice cells, where it is taken up by the nucleus and targets the *OsSWEET11* promoter¹. Mutation of the promoter therefore prevents the pathogen-induced increase in *OsSWEET11* expression. Thus, resistance to a bacterium develops because its ability to acquire sugar from the host plant is blocked.

Interestingly, a second glucose-efflux transporter gene, *OsSWEET14*, is activated by another *X. oryzae* TAL effector, AvrXa7, indicating that SWEETs are perhaps common

targets of bacterial effectors. This possibility is supported by Chen and colleagues' finding¹ that the bacterium *Pseudomonas syringae* pv. *tomato* induces expression of seven SWEET genes during infection of *Arabidopsis*. Pathogenic microorganisms are therefore able to manipulate the expression of sugar transporters and to divert the flow of glucose into the spaces between plant cells where the microorganisms can rapidly grow and reproduce. This ability may be pivotal to disease induction by microbes that proliferate in living host tissue.

The discovery of SWEETs opens up possibilities for studying the diverse roles of sugar transport in multicellular organisms, including the way in which glucose is moved from absorptive tissue to neighbouring cells in animals and its role in physiological processes such as lactation and control of blood glucose levels. In plants, the identification of SWEETs is likely to result in a far deeper knowledge of sink-source relationships in plant tissues, as well as providing insight into the biology of floral function and sexual reproduction.

Finally, understanding how pathogen effector proteins manipulate SWEET activity, and perhaps drive other forms of metabolic reprogramming in their hosts, may provide an exciting avenue for developing disease-control strategies. ■

Nicholas J. Talbot is at the School of Biosciences, University of Exeter, Exeter EX4 4QD, UK.
e-mail: n.j.talbot@exeter.ac.uk

1. Chen, L.-Q. *et al.* *Nature* **468**, 527–532 (2010).
2. Lalonde, S., Ehrhardt, D. W. & Frommer, W. B. *Curr. Opin. Plant Biol.* **8**, 574–581 (2005).
3. Takanaga, H. & Frommer, W. B. *FASEB J.* **24**, 2849–2858 (2010).
4. Takanaga, H., Chaudhuri, B. & Frommer, W. B. *Biochim. Biophys. Acta* **1778**, 1091–1099 (2008).
5. Jones, J. D. G. & Dangl, J. L. *Nature* **444**, 323–329 (2006).
6. Stergiopoulos, I. & de Wit, P. J. G. M. *Annu. Rev. Phytopathol.* **47**, 233–263 (2009).
7. Panstruga, R. & Dodds, P. N. *Science* **324**, 748–750 (2009).
8. Grant, S. R. *et al.* *Annu. Rev. Microbiol.* **60**, 425–449 (2006).
9. Yang, B., Sugio, A. & White, F. F. *Proc. Natl Acad. Sci. USA* **103**, 10503–10508 (2006).

COSMOLOGY

Geometry of the Universe

A neat way of measuring the geometry of the Universe offers a new test of the standard cosmological model. It probes, among other things, the elusive dark energy thought to be driving the Universe's expansion. SEE LETTER P.539

ALAN HEAVENS

Twenty years ago, most cosmologists thought the Universe was dominated by a large amount of dark matter, and the idea of dark energy was no more than a curiosity. Now, as a result of exquisite observations of the radiation left over from the Big Bang, the large-scale structure of galaxies and distant supernovae, all that has changed: we have a generally accepted 'standard cosmological model', in which 23% of the energy density of the Universe is in the form of dark matter, 73% in dark energy, and only 4% in the form of the ordinary matter that we know on Earth. On page 539 of this issue, Marinoni and Buzzi¹ describe a new technique for testing the cosmological model that is completely independent of previous methods.

To say the finding that dark energy contributes about three-quarters of the total energy density of the Universe was unexpected would be an understatement. Gravity slows the expansion of the Universe, and yet the Universe isn't playing ball — its expansion rate is actually accelerating, and this

requires a component of the Universe with a repulsive gravity, a role thought to be played by dark energy. Not surprisingly, many cosmologists regard determining the nature of dark energy and dark matter as the most

important scientific question of the decade.

Our picture of the Universe involves putting together a number of pieces of evidence, so it is appealing to hear of Marinoni and Buzzi's novel technique¹ for testing the cosmological model, not least because it provides a very direct and simple measurement of the geometry of the Universe. One of Einstein's most remarkable insights was that the geometry of the Universe depends on its contents. So we can use geometrical measurements to determine the amounts of dark matter and dark energy, and the nature of the latter.

The general idea of Marinoni and Buzzi's technique goes back to Alcock and Paczyński² and, curiously, exploits the fact that we cannot directly measure distances in cosmology — there is no prospect of placing rulers between us and a distant galaxy. Instead, we rely on

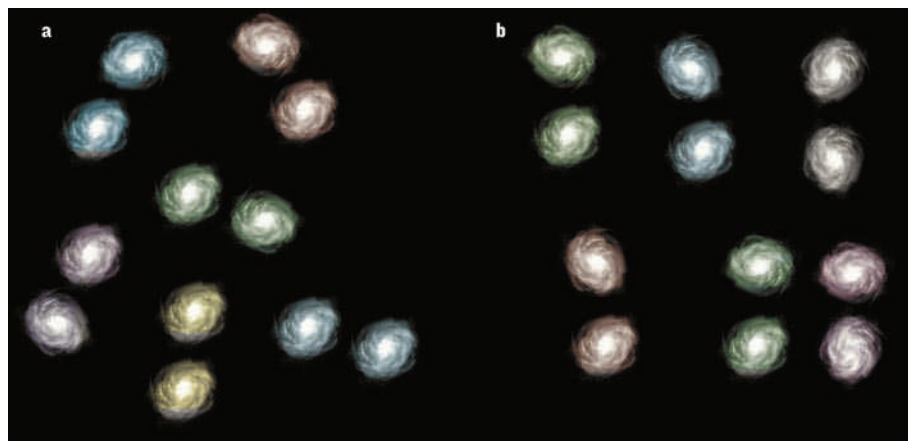


Figure 1 | The principle of Marinoni and Buzzi's cosmological technique¹. **a**, If the correct geometry and contents of the Universe are assumed, then the orientation of galaxy pairs should appear to be random. **b**, If not, then the pair orientations will show a preference for certain directions. (For clarity, the complications arising from the orbital speeds of the galaxies are not shown.)

Hubble's law, which states that the speed of recession of galaxies is proportional to distance. The speed can be measured using the Doppler effect, which shifts the galaxy light to the red end of the electromagnetic spectrum, hence the use of the term redshift in astronomy to describe how far away a galaxy is. For large distances, the argument is modified, but higher redshift still indicates greater distance. The bottom line is that the way that redshifts and angles on the sky (both of which are directly observable) translate to positions (which are not) depends on the geometry of the Universe.

So imagine we have a distant object that is completely spherical and expanding along with the rest of the Universe. By measuring the redshifts of different points on the surface of the sphere, one can map out the shape of the object, using the formula for changing redshifts and angles to positions. If we assume the correct contents and geometry of the Universe in the formula, the object will indeed appear to be spherical, but if we do not, the sphere will appear to be distorted. This is the essence of Alcock and Paczyński's idea. The key, of course, is to find spherical expanding objects, which unfortunately do not exist. However, one can be more subtle, and use something less tangible.

Marinoni and Buzzi¹ use the distribution of orientations of galaxy pairs in orbit around each other in binary systems. We expect the orientations to be completely random, with all orientations being equally likely — that is, the distribution of pairs is spherically symmetric. Only if we choose the correct contents and geometry (that is, the cosmological model that truly represents the Universe) in the calculation of the pairs' orientation, will the orientations appear to be evenly distributed (Fig. 1). So the authors¹ vary parameters that quantify the contents and the geometry until they find the values that best fit a random distribution.

This exercise needs to be done for very distant galaxies, several billion light years away, because the effects of different geometries are only substantial on very large scales. The main complication is that a galaxy's redshift, which enters the calculation of the orientations, has two components: a cosmological component arising from the expansion of the Universe and an additional Doppler component from the speed of the galaxy in orbit. This additional component distorts the distribution of angles, but in a known way that depends on the distribution of orbital speeds. Marinoni and Buzzi measure this distribution from nearby galaxies, and use it to analyse pairs of galaxies at high redshift in the DEEP2 galaxy redshift survey³.

The authors¹ find consistency with the standard cosmological model, with its flat geometry, and show that the dark energy is consistent with being a vacuum energy, which

can be represented by Einstein's famous cosmological constant. How might their technique fail? Clearly, we have to be certain that different pair orientations are detected with equal probability and that the orbital speeds are independent of orientation, as the authors' method assumes. The distribution of orbital velocities of the pairs also needs to be known, and this is perhaps the point one might worry about most. This distribution can be investigated in the local Universe, but the distribution is then assumed to be the same at high redshift. Because of the finite light travel time, the distant galaxies of the DEEP2 survey

are being seen as they were when the Universe was about half its present age, and galaxy-pair properties could have changed over that period. Nevertheless, Marinoni and Buzzi's study offers a novel and imaginative idea. ■

Alan Heavens is at the Institute for Astronomy, University of Edinburgh, Royal Observatory, Edinburgh EH9 3HJ, UK. e-mail: afh@roe.ac.uk

1. Marinoni, C. & Buzzi, A. *Nature* **468**, 539–541 (2010).
2. Alcock, C. & Paczyński, B. *Nature* **281**, 358–359 (1979).
3. Davis, M. et al. *Astrophys. J.* **660**, L1–L4 (2007).

PALAEOANTHROPOLOGY

Early *Homo sapiens* in China

The timing of the dispersal of our species from Africa is a continuing and lively topic of debate. Evidence that modern humans existed in China more than 100,000 years ago is both equivocal and thought-provoking.

ROBIN DENNELL

A report by Liu *et al.*, just published in *Proceedings of the National Academy of Sciences*¹, describes modern-human remains from south China that are dated to more than 100,000 years ago. Most researchers would agree that *Homo sapiens* originated in East Africa between about 190,000 and 160,000 years ago²; that members of the species briefly entered the Levant some 100,000–60,000 years ago³ (when they were displaced by

Neanderthals); but that they did not disperse across southern Asia and to Australia until 50,000–60,000 years ago^{4,5}. The new Chinese find implies that they could have left Africa up to 50,000 years earlier — how likely is this?

First, the discovery itself. The remains come from Zhirendong ('*Homo sapiens* cave'), which is a small cave in Guizhou Province. It was first filled with sediments, the bottom parts of which were eroded by water and replaced by younger deposits, leaving the older sediments as a remnant hanging from the cave

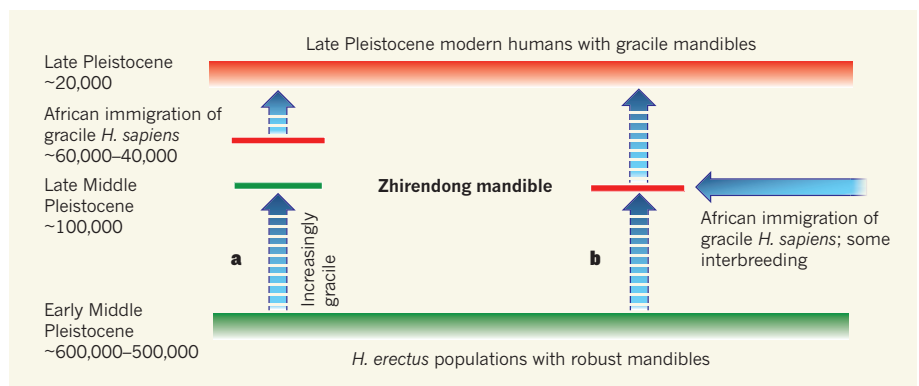


Figure 1 | Two interpretations of the Zhirendong mandible described by Liu and colleagues¹. a, The mandibles and face of *Homo erectus* became increasingly gracile by the time of the Zhirendong specimen, around 100,000 years ago, and acquired 'modern' features. Modern humans of African origin arrived later, perhaps 60,000–40,000 years ago. b, The view favoured by Liu *et al.* — modern humans, of African origin and with gracile features, arrived in south China about 100,000 years ago, and interbred with the indigenous population. Distinguishing between these options is difficult because of the lack of late Middle Pleistocene mandibular specimens from China, and the absence of skeletal evidence for the *Homo* lineage between south China and East Africa between 40,000 and 100,000 years ago. Numbers are indications of timing as years ago.

roof. The younger sediments are capped by several flowstones — calcite deposits produced inside caves by the action of water — that occur immediately below this remnant and have been dated by the uranium-series (^{230}Th) method to between about 28,000 and 108,000 years ago. The flowstones are in stratigraphic order, with the oldest at the bottom. Because they are continuous across the floor of the cave, they also prevented younger material from being introduced into the underlying deposits.

The human fossils were found below the oldest flowstone, and so they are about 100,000–113,000 years old, and possibly older. The associated faunal remains (of 21 large mammal species and 34 small ones) include some species now extinct in the region, such as the orang-utan (*Pongo*) and giant tapir (*Megatapirus*). Overall, 25% of the large mammals are extinct, and a late Middle Pleistocene age of the fauna is therefore consistent with the stratigraphic dating. The age and context of the human remains therefore seem sound.

Those remains consist of the front part of a mandible (lower jaw) and two molar teeth. The latter are small, and would be considered as modern in a Late Pleistocene west Eurasian (post-Neanderthal) sample, but there are insufficient east Asian specimens to show that they are unequivocally modern. Here, the mandible is the key piece of evidence. As described by Liu *et al.*¹, this possesses characteristics seen in both early modern humans and late archaic ones; in China, these are referred to as either 'archaic *Homo sapiens*' or 'late *Homo erectus*'. Modern aspects of the mandible include a feature called the anterior symphysis; archaic aspects are the lingual symphysis, and the mandible's overall robustness compared with the gracile (lighter) build of younger, modern-human ones.

The authors¹ interpret these characteristics as indicating that modern humans arrived in south China more than 100,000 years ago, and then interbred with the indigenous population. As they point out, this is incompatible with a scenario whereby an immigrant African population of modern humans totally replaced the local population, with no interbreeding.

Is it likely that modern humans entered China as early as 100,000 years ago? Most researchers would disagree: the earliest unequivocal evidence for modern humans from southeast Asia is a cranium from Niah Cave, Borneo, dated to around 40,000 years ago⁶, and the colonization of Australia by *H. sapiens* probably occurred no earlier than 50,000–60,000 years ago^{4,5}. Various estimates based on genetic analyses of modern populations suggest that *H. sapiens* first entered south Asia some 50,000–60,000 years ago⁷.

However, an earlier exit is not impossible. We need to remember that there is no skeletal evidence for the *Homo* lineage between Borneo and East Africa over the time span

40,000–100,000 years ago, and so it is a major assumption that modern humans were absent from southern Asia at this time. On palaeoclimatic grounds (as well as proximity to East Africa), it seems unlikely that modern humans entered the Levant in the last interglacial, some 125,000–110,000 years ago, but not the Arabian Peninsula. Once in eastern Arabia, there would have been few barriers to their dispersal eastwards into India.

Recent evidence⁸ from India indicates that, before 74,000 years ago (the age of the Toba eruption in Sumatra, Indonesia, ash from which forms a major marker horizon across India), stone-core-flaking techniques were similar to those from East Africa, and this implies that modern humans may already have been in India then. Some genetic analyses also suggest that modern humans were in south Asia before the Toba eruption⁹. Modern humans may therefore have entered southeast Asia earlier than currently thought.

All this is speculation until the requisite fossil evidence is found. However, one note of caution is necessary about the Zhirendong remains. Although there are several Chinese mandible specimens from the early part of the Middle Pleistocene, particularly from the Zhoukoudian locality, there are none from the later Middle Pleistocene. Because of this gap, we do not know how gracile the mandibles of *H. erectus* became in China between 300,000 and 150,000 years ago.

CELL BIOLOGY

Import and nuclear size

The size of a cell's nucleus is usually proportional to the size of the cell itself. How are the two linked? The answer lies, at least in part, in the import of one or more cytoplasmic cargoes into the nucleus.

ORNA COHEN-FIX

It is rare to come across a basic question in cell biology that is almost entirely unresolved, but what determines the size of a cell or of an organelle is one such question¹. Does the cell use a 'molecular ruler' to directly assess the size of its compartments, or does it use a surrogate, such as protein concentration, to determine how big its structures are? Reporting in *Cell*, Levy and Heald² provide evidence that at least partly answers these questions in regard to the size of the cell nucleus.

Regulation of nuclear size is perhaps one of the most striking, and enigmatic, examples of organelle-size control, because it is tightly linked to cell size³. Indeed, there is a constant ratio between nuclear and cell volumes (the N/C volume ratio), and deviations from it are

Does the Zhirendong specimen indicate an early immigrant population of *H. sapiens* that became more robust by interbreeding with the local population; or (more parsimoniously) does it simply indicate a late *H. erectus* population that became more gracile over time (Fig. 1)? If Liu *et al.*¹ are correct, we would expect to discover specimens of *H. sapiens* from south Asia and Arabia that are at least as old as the Zhirendong fossil. But if that fossil represents a late and increasingly gracile example of *H. erectus*, we would not.

Clearly, more fossils are needed. Meanwhile, this discovery allows tests of the hypothesis that our species left Africa much earlier than currently thought. ■

Robin Dennell is in the Department of Archaeology, University of Sheffield, Sheffield S1 4ET, UK.
e-mail: r.dennell@sheffield.ac.uk

1. Liu, W. *et al.* *Proc. Natl. Acad. Sci. USA* **107**, 19201–19206 (2010).
2. White, T. D. *et al.* *Nature* **423**, 742–747 (2003).
3. Shea, J. J. *Quat. Sci. Rev.* **27**, 2253–2270 (2008).
4. Klein, R. G. *Evol. Anthropol.* **17**, 267–281 (2008).
5. Mellars, P. *Science* **313**, 796–800 (2006).
6. Barker, G. W. W. *et al.* *J. Hum. Evol.* **52**, 243–261 (2007).
7. Macaulay, V. *et al.* *Science* **308**, 1034–1036 (2005).
8. Petraglia, M. *et al.* *Science* **317**, 114–116 (2007).
9. Cabrera, V. M., Abu-Amero, K. K., Larruga, J. M. & González, A. M. in *The Evolution of Human Populations in Arabia* (eds Petraglia, M. D. & Rose, J. I.) 79–87 (Springer, 2009).

associated with disease⁴. But how is this ratio regulated? To address this question, researchers have attempted^{5,6} to perturb the N/C volume ratio in yeast, but to no avail: neither nuclear-DNA content, nor varied growth conditions, nor drug treatments, could alter the ratio.

Another question is what aspect of cell volume affects nuclear size: is it the cell's entire volume; the volume of only the cytoplasm; or perhaps that of another organelle? In multi-nucleated fission yeast, the size of each nucleus is proportional to its surrounding cytoplasm⁶, but how the cytoplasm affects nuclear size, if at all, has remained unknown.

Levy and Heald² study regulation of nuclear size in two related frog species — *Xenopus laevis* and *Xenopus tropicalis* — that differ in both body size and the number of chromosome copies per cell (ploidy). *Xenopus laevis* is larger and its cells are tetraploid, whereas

X. tropicalis is smaller and its cells are diploid. The two species also differ in another aspect: the cells and nuclei of *X. laevis* are larger.

An advantage of *Xenopus* as an experimental model is that its nuclei can be assembled in a test tube using the chromatin (DNA–protein complexes) and extracts of its egg cytoplasm. This allowed Levy and Heald² to ask, what is the main determinant of nuclear size in *Xenopus*: the DNA or a cytoplasmic factor?

The authors added sperm chromatin from either *X. laevis* or *X. tropicalis* to egg extracts from either *X. laevis* or *X. tropicalis* (Fig. 1a). They found that, although both extracts can trigger assembly of the nuclear envelope around the chromatin, the *X. laevis* extract forms larger nuclei than the *X. tropicalis* extract, regardless of the DNA used. This indicates that one or more cytoplasmic factors determine nuclear size.

A hint of the underlying difference between the extracts from the two frog species came from the authors' analyses of nuclear import — the process by which proteins are transported into the nucleus⁷. Both the rate of nuclear import and the maximum size of the imported cargo were greater in the nuclei reconstituted with *X. laevis* extracts. The capacity for nuclear import therefore might be a regulator of nuclear size.

The two extracts differed in two proteins that mediate nuclear import — importin- α and Ntf2. In *X. laevis* extracts, the levels of importin- α were higher and those of Ntf2 lower than in *X. tropicalis* extracts. Indeed, when Levy and Heald added active (phosphorylated) importin- α to *X. tropicalis* extracts they observed an increase in nuclear size. The role of Ntf2 in regulating nuclear size is less straightforward. Nonetheless, *X. tropicalis* extracts supplemented with both active importin- α and an inhibitor of Ntf2 activity form nuclei that are similar in size to those formed in *X. laevis* extracts² (Fig. 1b).

That nuclear import affects nuclear size is perhaps not surprising, as a previous paper⁸ showed that, in the absence of import, the nuclear envelope — which forms around the chromosomes at the end of mitotic cell division — fails to expand. But in showing that, at least *in vitro*, import is a limiting factor for nuclear growth, Levy and Heald's report provides a specific step that could be targeted for regulating nuclear size *in vivo*.

Which of the cargoes carried by importin- α are crucial for controlling nuclear size? From an engineering standpoint, enlarging a structure could require an extension of its underlying framework. Whether the nucleus has an internal framework — the 'nuclear matrix' — is debatable, but there is no doubt that the nuclear lamina serves as a framework supporting the nuclear envelope. Indeed, Levy and Heald found that the addition of lamin B3, a component of the nuclear lamina, to *X. tropicalis* extracts resulted in increased

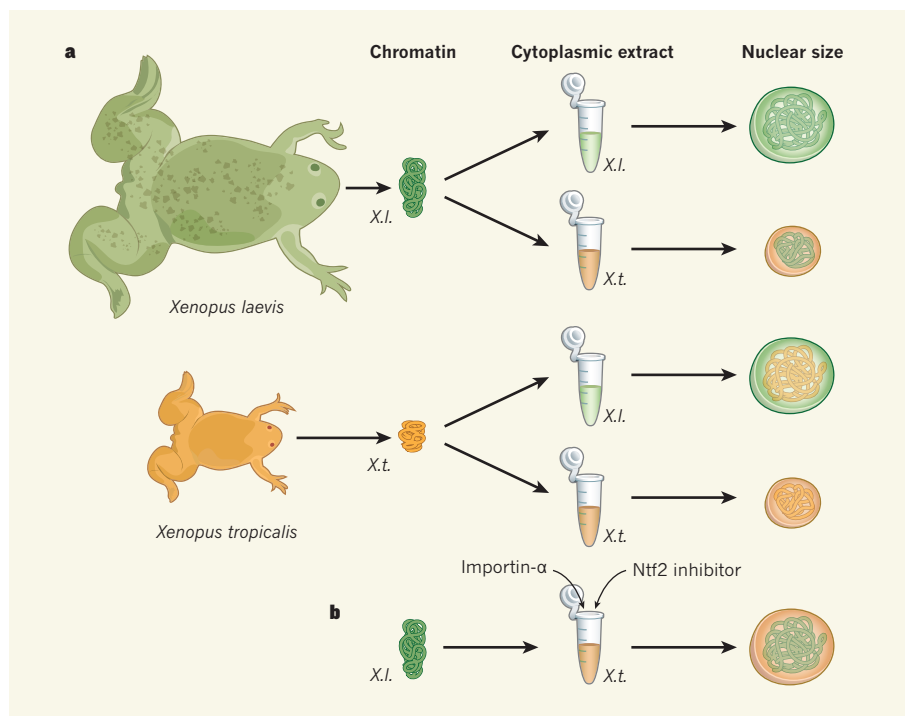


Figure 1 | The cytoplasm regulates nuclear size. **a**, To examine factors affecting nuclear size, Levy and Heald² mixed sperm chromatin from either *Xenopus laevis* (*X.l.*) or *X. tropicalis* (*X.t.*) with cytoplasmic extracts from the eggs of either *X. laevis* or *X. tropicalis*. They find that, regardless of the chromatin used, *X. laevis* extracts promote formation of large nuclei, whereas *X. tropicalis* extracts promote formation of smaller nuclei. (The drawings of *X. laevis* and *X. tropicalis* are to scale). **b**, Two proteins, importin- α and Ntf2, account for the differences between the *X. laevis* and *X. tropicalis* extracts: addition of importin- α and inhibition of Ntf2 activity in *X. tropicalis* extracts lead to formation of larger nuclei.

nuclear size. Thus, nuclear import may regulate nuclear size through controlling the availability of nuclear-lamina components.

Neither yeast nor plants have lamins, which raises the question of how general is regulation of nuclear size by lamin import. Whether nuclear import itself affects nuclear size in yeast is unresolved^{5,6}, although at least one study⁶ found that a prolonged inhibition of nuclear export increases nuclear volume by 50%. It could be, therefore, that nuclear size in yeast and plants also depends on nuclear import, not of lamin but of some other cargo.

The cell-free system Levy and Heald describe is remarkably useful for identifying proteins and processes that affect nuclear size. The next step will be to determine how such processes affect nuclear size within the cell, and whether they contribute to the N/C volume ratio. Levy and Heald did address this question by injecting importin- α into developing *X. laevis* embryos. They observed a transient increase in nuclear size in early stages of development, but whether cell volume is affected in any way remains unknown.

When considering the scaling of nuclear size with cell size, one must take into account the increase not only in volume, but also in surface area⁴. An influx of material through nuclear import could lead to physical stress that signals for an increase in the surface area of the nuclear envelope. Alternatively, because the nuclear

membrane is continuous with that of another organelle, the endoplasmic reticulum, the cell might regulate nuclear size by controlling the amount of endoplasmic-reticulum membrane that is allocated to the nucleus.

Nevertheless, geometry tells us that surface area increases at a slower rate than volume (surface area is a function of the radius squared, whereas volume is a function of the radius cubed). Intriguingly, a recent study⁹ on the scaling of transcription with cell size in yeast revealed that, whereas expression of most genes increases in proportion to the increase in cell size, the expression of genes encoding cell-surface proteins lags behind. How this size-sensing mechanism works isn't clear, but it would be interesting to examine whether the abundance of proteins associated with nuclear-envelope expansion is also 'size-sensitive'.

Levy and Heald's results² uncover a process that affects nuclear size, providing a glimpse into a mechanism that may couple nuclear volume to cell volume. To fully understand the N/C volume ratio, researchers need biological tools — mutants and/or RNAi knockdowns — that perturb this ratio. So to anyone who thinks that all the interesting basic cell-biological questions have been answered, here is one that is still wide open. ■

Orna Cohen-Fix is in the Laboratory of Molecular and Cellular Biology,

NIDDK, National Institutes of Health,
Bethesda, Maryland 20892, USA.
e-mail: ornac@helix.nih.gov

1. Chan, Y.-H. M. & Marshall, W. F. *Organogenesis* **6**, 88–96 (2010).
2. Levy, D. L. & Heald, R. *Cell* **143**, 288–298 (2010).
3. Wilson, E. B. *The Cell in Development and Heredity* (Macmillan, 1925).
4. Webster, M., Witkin, K. L. & Cohen-Fix, O.

- J. Cell Sci.* **122**, 1477–1486 (2009).
5. Jorgensen, P. et al. *Mol. Biol. Cell* **18**, 3523–3532 (2007).
6. Neumann, F. R. & Nurse, P. *J. Cell Biol.* **179**, 593–600 (2007).
7. Terry, L. J., Shows, E. B. & Wente, S. R. *Science* **318**, 1412–1416 (2007).
8. Newport, J. W., Wilson, K. L. & Dunphy, W. G. *J. Cell Biol.* **111**, 2247–2259 (1990).
9. Wu, C.-Y., Rolfe, P. A., Gifford, D. K. & Fink, G. R. *PLoS Biol.* **8**, e1000523 (2010).

quantum dots is known as quantum confinement. A key feature of quantum confinement is that it occurs when the diameter of a particle is about the same size as the wavelength of the particle's electronic wavefunction. For objects made of materials that have highly ordered structures, this occurs at the nanoscale, independently of the material used. In other words, as long as there is quantum confinement, there is no reason that materials other than semiconductors — including peptides — cannot form quantum dots.

Enter Gazit, Rosenman and colleagues¹. They observed that when a solution of diphenylalanine peptide in methanol is concentrated, the peptide molecules self-assemble into nanocrystalline structures (Fig. 1). These assemblies have an average diameter of 2.1 nanometres and consist of two diphenylalanine peptides, corresponding to a total of just four phenylalanine residues per assembly. The authors found that the peptide assemblies have the characteristic optical properties of quantum dots: on exciton formation, they emit light across a very narrow frequency range (that is, they have a narrow photoexcitation peak). But when the authors studied low-concentration solutions of the dipeptide, which contain discrete dipeptide molecules rather than nanocrystalline assemblies, they observed a broad excitation peak. This suggests that individual dipeptide molecules are not quantum dots.

The peptide quantum dots have an intriguing property not found in inorganic quantum dots: when Gazit, Rosenman and colleagues changed the solvent in which the dipeptide nanostructures were dispersed from methanol to water, the structures underwent further self-assembly to form peptide nanotubes. The nanotube dispersion had near-identical optical properties and X-ray diffraction patterns to those of the quantum-dot dispersion, thus proving that the quantum dots are the elementary, quantum-confined building blocks of the nanotubes.

Diphenylalanine-peptide nanotubes have been reported before. Their observed rigidity seems to be very high³, they are piezoelectric⁴ (they generate charge under mechanical strain) and they have been used as scaffolds to fabricate silver nanowires⁵. Gazit and Rosenman's groups have also previously observed quantum confinement in peptide nanostructures⁶, and have demonstrated that diphenylalanine peptides can assemble to form quantum wells (structures in which excitons are confined within two dimensions) that exhibit strong blue luminescence⁷. But the present paper¹ is the first to describe the elementary quantum-confined structures that underpin the earlier findings.

What makes this result even more interesting is that the self-assembly of the peptide quantum dots into nanotubes is completely reversible — the nanotubes disassembled back to individual quantum dots when the authors changed the dispersion solvent from water to

NANOTECHNOLOGY

Peptides as biological semiconductors

A simple peptide that assembles into desirable nanoscale structures is a striking example of how the whole can be greater than the sum of its parts. What's more, the assembly process is controllably reversible.

CHARLOTTE A. E. HAUSER
& SHUGUANG ZHANG

Could a simple, short peptide made of naturally occurring amino acids form structures that have the optical and electronic properties of semiconductor nanocrystals? Reporting in the *Journal of the American Chemical Society*, Gazit, Rosenman and colleagues¹ describe a peptide formed from just two phenylalanine amino acids that does exactly that. This is a remarkable discovery, because although conductive organic polymers are well known (their discoverers won the 2000 Nobel chemistry prize²), no one had envisaged that biological peptides could act as semiconductors. The reported dipeptide assemblies¹ represent an intriguing, bioorganic class of 'quantum dot' nanomaterial.

A quantum dot is a nanoscale, ordered structure whose excitons — energy-carrying

quasiparticles associated with semiconductors and insulators — are confined in three spatial dimensions. This means that quantum dots have electronic properties intermediate between those of bulk materials and discrete molecules. They are being used in solar cells, light-emitting devices and as fluorescent labelling agents in the biomedical industry.

Most quantum dots are made of inorganic semiconductors, often a single material such as silicon or germanium. Others are 'core-shell' structures, in which a semiconductor such as cadmium selenide (CdSe) or zinc sulphide (ZnS) is surrounded by another material. Such CdSe quantum dots have been particularly successful for a variety of applications, but the toxicity associated with cadmium is increasingly a concern. The search for cadmium-free quantum dots has therefore become a major area of research.

The phenomenon that constrains excitons in

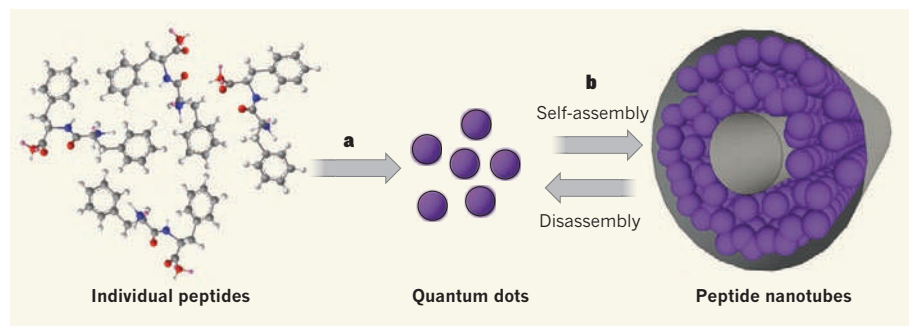


Figure 1 | Simple dipeptides are building blocks for quantum dots and nanotubes. **a**, Gazit, Rosenman and colleagues¹ report that when they concentrated a solution of diphenylalanine peptides in methanol, the molecules self-assembled into quantum dots. Each quantum dot was composed of two diphenylalanines. **b**, When the authors changed the solvent from methanol to water, the peptides further self-assembled to form nanotubes, each containing millions of quantum dots. The nanotube assembly process was completely reversible — when the solvent was changed back to methanol, the nanotubes disassembled into individual quantum dots.

methanol¹ (Fig. 1). One can thus modify the peptide architecture at will to fabricate either quantum dots or nanotubes. The synergistic effect of millions of quantum dots in a single nanotube might make them a promising material for new types of optical devices, such as light-emitting diodes and lasers.

The optical and electronic properties of inorganic quantum dots can be fine-tuned by varying the size of the nanostructures. Could the properties of peptide quantum dots also be fine-tuned? The answer is probably yes. Because the size of peptide quantum dots is governed by the specific amino acids in the peptide, a large number and variety of naturally occurring and/or synthetically customized amino acids could be used in countless combinations. In this way, it might one day be possible to tweak the size and properties of peptide quantum dots. Indeed, the authors¹ have already shown that a dipeptide made from a phenylalanine and a tryptophan amino acid forms a quantum dot that has different optical and electronic properties from that of the diphenylalanine analogues.

Peptide quantum dots represent arguably one of the simplest forms of quantum dot, but they also offer distinct advantages over other types. First, they are made of natural amino acids that are synthesized by plants and animals, so they shouldn't be too harmful to the environment. Their degradation products will also be harmless natural amino acids. This is unlike most inorganic quantum dots, especially those made of heavy metals. Second, the preparation of dipeptide quantum dots requires the formation of a single peptide bond, which makes them cheap and easy to produce at very high purity. Finally, given the availability of a wide range of amino acids that have diverse properties, perhaps peptide quantum dots will be discovered that have properties not yet observed in other such materials. Nevertheless, much theoretical work is needed to guide further development of peptide quantum dots. Let us hope that Gazit, Rosenman and colleagues' findings will attract people from other disciplines to further advance this nascent field.

Although nature has produced numerous wonderful peptides and proteins, if peptides had been proposed as potentially useful synthetic materials two decades ago, few people would have taken the idea seriously. But today, the use of peptide and protein materials is thriving in diverse areas that could never have been imagined. If quantum dots can be made from peptides, what other surprises might be in store? As Louis Pasteur best put it: "Chance favours the prepared mind." Gazit, Rosenman and colleagues' work¹ should help us to open our minds to be ready for more remarkable discoveries. ■

Charlotte A. E. Hauser is at the Institute of Bioengineering and Nanotechnology, 31 Biopolis Way, The Nanos, Singapore 138669.

Shuguang Zhang is at the Center for Biomedical Engineering, and the Center for Bits and Atoms, Massachusetts Institute of Technology, Cambridge, Massachusetts 02139, USA.

e-mails: chauser@ibn.a-star.edu.sg; shuguang@mit.edu

1. Amdursky, N., Molotskii, M., Gazit, E. & Rosenman, G.

QUANTUM OPTICS

Particles of light

Bose–Einstein condensation, which demonstrates the wave nature of material particles, now offers further illumination of wave–particle duality: it has been observed in light itself. SEE LETTER P.545

JAMES ANGLIN

“Art is the Tree of Life. Science is the Tree of Death.” So wrote the visionary English poet and artist William Blake¹ in 1826, contrasting the limitless creativity of art with the limiting rigidity of science. Blake understood the science of his day — well enough, for instance, to lump together “The Atoms of Democritus And Newton’s Particles of Light”, and compare them both to sand². In Blake’s time, both were conceived of as indivisible and indestructible, their motion governed by Newtonian mechanics. Nothing represented his harsh view of science better than the implication that, if light corpuscles could be neither created nor destroyed, then the Universe contained a fixed amount of light, which could never be increased (Fig. 1). On page 545 of this issue, Weitz and colleagues³ demonstrate that, even if that were true, the wave nature of light would still persist, through the Bose–Einstein condensation of photons. They also demonstrate the creativity that thrives within scientific rigour.

Modern physics teaches that light has wave as well as particle properties. But one of the most basic differences between the wave and particle theories is rarely emphasized in textbooks. Classical light waves are not conserved like the atoms of Democritus, but can easily be excited and absorbed. So, a lamp may run out of battery power, but it does not run out of light. In this respect, Newton’s particle theory of light was as false as the caloric theory of heat, according to which heat was a conserved substance held in matter like water in a sponge. In fact, both heat and light are simply convertible forms of energy. And it was the thermodynamics of light that led Planck and Einstein to the quantum unification of wave and particle theories.

Unlike classical particles, quantum particles such as electrons and photons can in

1. *J. Am. Chem. Soc.* **132**, 15632–15636 (2010).
2. http://nobelprize.org/nobel_prizes/chemistry/laureates/2000
3. Kol, N. et al. *Nano Lett.* **5**, 1343–1346 (2005).
4. Kholkin, A., Amdursky, N., Bdiqin, I., Gazit, E. & Rosenman, G. *ACS Nano* **4**, 610–614 (2009).
5. Reches, M. & Gazit, E. *Science* **300**, 625–627 (2003).
6. Amdursky, N., Gazit, E. & Rosenman, G. *Adv. Mater.* **22**, 2311–2315 (2010).
7. Amdursky, N. et al. *Nano Lett.* **9**, 3111–3115 (2009).



Figure 1 | The Ancient of Days painted by William Blake. “Nothing represented his harsh view of science better than the implication that, if light corpuscles could be neither created nor destroyed, then the Universe contained a fixed amount of light, which could never be increased.”

general be created and destroyed, and so the issue of whether the amount of light is fixed is now separate from the discussion of wave and particle behaviour. A basic question therefore seems natural: what would light be like if photons were, like atoms, wave-like but conserved? Weitz and colleagues³ have answered this question experimentally. By confining light within the narrow slice of space between two barely separated mirrors, and filling this slab-like cavity with a dye material, they have achieved thermal equilibration of light as a gas of conserved particles, rather than ordinary black-body radiation. The critical step in

WHITWORTH ART GALLERY, UNIV. MANCHESTER, UK/BRIDGEMAN ART LIBRARY

realizing such unusual thermalization is confining the light in one direction, so that every photon is forced to have a frequency at least as high as that of a standing wave. Because the separation between the mirrors is only a few micrometres, this minimum photon frequency is high — crucially, much higher than the frequency corresponding to the temperature of the dye.

This large frequency difference makes the energy budget of the system resemble the finances of a peculiar commercial firm that sells both skateboards and satellites. In the firm's ledgers, the billions column and the millions column must always be balanced separately, because the total volume of the skateboard business never amounts to a single satellite. In the Weitz group's system of dye and light, the thermal energy and the energy of excitations at the standing-wave frequency are similarly each conserved separately, because their scale discrepancy prevents one from balancing the other. And this means that the number of photons between the mirrors changes as photons are absorbed and re-emitted by the dye, but only in the same way that the number of atoms in a gas changes, locally, as the atoms drift around. In technical terms, the light in the Weitz group's experiment reaches thermal equilibrium with a chemical potential as well as a temperature, just like gases cooled to nanokelvin temperatures in magnetic traps. The textbook example of what this can allow is Bose–Einstein condensation, which confers the properties of classical wave physics on a gas of conserved quantum particles below a critical temperature, and is intimately related to the phenomena of superfluidity and superconductivity. The Weitz group has observed Bose–Einstein condensation of light, in remarkably close analogy to that of atoms.

As well as being a landmark achievement in itself, making photons behave thermodynamically as atoms, even to the point of Bose–Einstein condensation, illustrates a broader theme in current physics. Atomic gases have been made to behave as laser light⁴, and even as black holes⁵. The 'holes' left when electrons in graphene sheets are energetically displaced reproduce the behaviour of relativistic positrons⁶. Quantized spin-wave excitations in magnetic films have been made to behave as quantum gases⁷, and atomic gases have been made to behave as ferromagnets⁸. The discernible trend is that everything is becoming everything else. Physics is the art of the interchangeable.

The purely scientific merit in this trend is that demonstrating the interchangeability of physical details clarifies the few universal patterns and principles that really are conserved — the atoms, as it were, not of matter or of light, but of reality. In this sense, the reductionist progress of science proceeds at full tilt. But in the proliferation of startling masquerades, physical science is also taking

on more than ever the aspect of a creative art, in a medium that, with the advances of modern technology, is proving far less constraining than it once seemed. Light is unlimited — or not, as we choose. Blake spoke too soon. ■

James Anglin is in the OPTIMAS State Research Center and the Physics Department, Technical University Kaiserslautern, Kaiserslautern 67663, Germany.
e-mail: jangling@physik.uni-kl.de

MECHANOREGULATION

Cellular seat belts

Accurate cell division depends on proper attachment of chromosomes to the microtubule-based division apparatus. An impressive *in vitro* study shows how applied force plays a pivotal part in regulating such attachment. [SEE LETTER P.576](#)

YUTA SHIMAMOTO & TARUN M. KAPOOR

The main safety feature of seat belts is that if the vehicle jolts, an abrupt pull locks the belt, keeping the passenger in place. Cells also seem to carry a nanoscale version of seat belts: the kinetochores — macromolecular machines that consist of more than 50 different proteins and connect chromosomes to dynamic microtubules of the cell-division apparatus — keep the chromosomes from accidentally ending up in the wrong daughter cell (Akiyoshi *et al.*¹, page 576 of this issue).

Stable propagation of genomes through mitotic cell division depends on the equal partitioning of replicated DNA, which is packaged into sister chromatids. Equal division depends on chromosome bi-orientation — that is, attachment of sister chromatids to microtubules that extend from opposite ends of the bipolar spindle (Fig. 1a). Failure of bi-orientation is common, but the improper

attachments that emerge somehow get corrected². Classic studies in grasshopper cells indicated³ that differences in physical forces acting on a chromosome could be crucial for distinguishing between correct and incorrect attachments. But how force-based regulation may work has remained largely mysterious. A major barrier to progress has been the biochemical complexity of the kinetochores⁴ and, therefore, the tremendous difficulty in isolating them in a functional form.

Enter Akiyoshi and co-workers¹. The authors tagged different kinetochore proteins and developed conditions to isolate functional kinetochores from dividing yeast cells. Budding yeast is an ideal model system for such studies: not only can it be easily manipulated genetically, but also its kinetochore binds only one microtubule — unlike a human kinetochore, which can bind more than 20 microtubules. Nonetheless, the kinetochore architecture is essentially conserved across

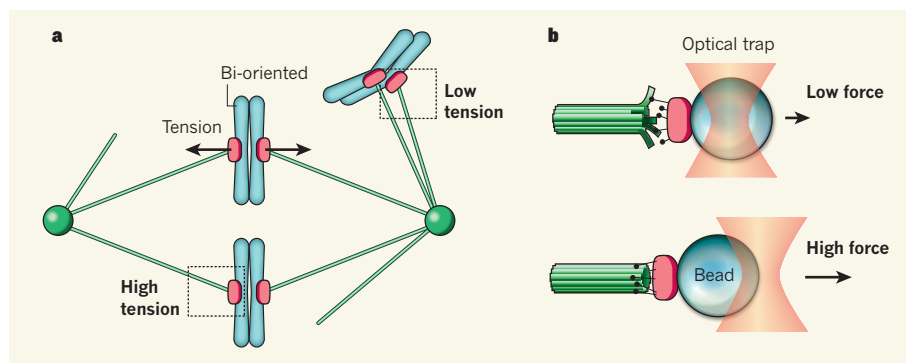


Figure 1 | Tension and chromosome-attachment state. **a**, Spindle microtubules (green) capture sister chromatids (blue) through kinetochores (pink). Tension across bi-oriented chromosomes is higher than across improperly attached chromosomes (dashed boxes). **b**, To investigate how force affects chromosome–microtubule attachment, Akiyoshi *et al.*¹ isolate minimal kinetochores, attach them to a bead and pull the bead with optical tweezers. They find that the reconstituted kinetochores attach to microtubules *in vitro* and that high tensile force enhances the lifetime of the attachment.

eukaryotes (organisms with nucleated cells), with microtubule-binding capacity increasing largely as a result of juxtaposing multiple copies of the core unit of the yeast kinetochore⁵.

A key feature of kinetochores *in vivo* is that they can remain attached to the ends of disassembling microtubules. The kinetochores Akiyoshi and colleagues isolate can also do this. What's more, although many of the typical structural proteins are present in the isolated kinetochores, key proteins — such as the enzyme Aurora kinase⁶ — that regulate chromosome attachment to the mitotic spindle are absent. These 'minimal' kinetochores therefore allow tests of how forces might regulate microtubule binding, independently of any potential regulation through protein phosphorylation.

Akiyoshi *et al.* attach the minimal kinetochores to a bead that they can manipulate with optical tweezers⁷ (Fig. 1b). A bead 'trapped' by optical tweezers behaves as if it is attached to a mechanical spring, such that a force restoring its position is proportional to the change in displacement. The authors examine interactions of the kinetochores with polymerizing and depolymerizing microtubules under different forces. This *in vitro* experiment recapitulates the pulling force that a kinetochore of a bi-oriented chromosome experiences within a cell.

It is reasonable to expect that the lifetime of the attachment between any two interacting partners, such as a ligand and its receptor, decreases as an applied force increases; this is because the mechanical work helps to overcome the detachment energy barrier⁸. Remarkably, however, Akiyoshi *et al.* reveal that force — in the range relevant to physiological forces that act on chromosomes — increases the lifetime of kinetochore–microtubule attachment twofold. The authors' further analysis reveals that the kinetochore–microtubule attachment behaves like a 'catch bond' — similar to a seat belt that locks in place when pulled abruptly⁹.

A catch bond can be modelled as a system with both a strongly bound state and a weakly bound state; force favours the strongly bound state. The minimal kinetochores are weakly bound to microtubules that are disassembling, and strongly bound to growing microtubules. Notably, applied force suppresses microtubule disassembly and can therefore favour the strongly bound state. On the basis of direct measurements and simple assumptions, Akiyoshi *et al.* develop a quantitative catch-bond model that accounts for the observed kinetochore–microtubule attachment behaviour.

The catch-bond mechanism may be considered as a mechanical extension of biochemical allosteric regulation. Force can be considered to be the equivalent of a molecule binding a protein's regulatory site and inducing a conformational change that modulates activity. Evidence from other cellular components

with catch-bond behaviour, such as the bacterial adhesion protein FimH, is consistent with this idea¹⁰. In the case of the kinetochore–microtubule interaction, it is possible that force directly induces a conformational change in microtubule tips¹¹. The strongly bound state could involve kinetochore interactions with microtubule protofilaments that are relatively straight, as seen in growing microtubules *in vitro*¹². The weakly bound state could have protofilaments splaying outwards, as seen in disassembling filaments¹².

Examining the structure of the minimal kinetochores and how they bind different microtubule-tip structures are essential next steps. Combining these structural studies with mutagenesis analysis should allow the design of experiments to test the catch-bond mechanism in dividing cells. Aurora kinases, or other proteins that correct errors in chromosome–spindle attachments, could have a role in fine-tuning the catch-bond mechanism. Experiments with purified kinetochores will also no doubt be useful in dissecting the interplay between these chemical and mechanical regulatory mechanisms.

In vitro studies of isolated kinetochores might help to settle another outstanding question regarding the regulation of chromosome segregation. If chromosomes are improperly attached to the spindle, a signalling network called the spindle-assembly checkpoint blocks

mitotic cell division before its anaphase step. It is unclear whether the spindle-assembly checkpoint directly responds to force (or tension)¹³. As the purified kinetochores contain proteins required for the spindle-assembly checkpoint, these kinetochores can be used to investigate whether the recruitment of checkpoint proteins — an early step in the signalling — is sensitive to force. Keep your seat belts fastened for the next phase of this exciting journey. ■

Yuta Shimamoto and Tarun M. Kapoor
are in the Laboratory of Chemistry and Cell Biology, Rockefeller University, New York, New York 10065, USA.
e-mail: kapoor@mail.rockefeller.edu

1. Akiyoshi, B. *et al.* *Nature* **468**, 576–579 (2010).
2. Nicklas, R. B. *Science* **275**, 632–637 (1997).
3. Nicklas, R. B. & Koch, C. A. *J. Cell Biol.* **43**, 40–50 (1969).
4. Santaguida, S. & Musacchio, A. *EMBO J.* **28**, 2511–2531 (2009).
5. Joglekar, A. P. *et al.* *J. Cell Biol.* **181**, 587–594 (2008).
6. Ruchaud, S., Carmena, M. & Earnshaw, W. C. *Nature Rev. Mol. Cell Biol.* **8**, 798–812 (2007).
7. Grier, D. G. *Nature* **424**, 810–816 (2003).
8. Bell, G. I. *Science* **200**, 618–627 (1978).
9. Thomas, W. E. *Curr. Opin. Struct. Biol.* **19**, 50–55 (2009).
10. Le Trong, I. *et al.* *Cell* **141**, 645–655 (2010).
11. McIntosh, J. R. *et al.* *Cell* **135**, 322–333 (2008).
12. Mandelkow, E. M., Mandelkow, E. & Milligan, R. A. *J. Cell Biol.* **114**, 977–991 (1991).
13. McIntosh, J. R. *Cold Spring Harb. Symp. Quant. Biol.* **56**, 613–619 (1991).

CANCER

The blind spot of p53

It is hoped that reactivating the tumour-suppressor protein p53 will help to combat cancer. However, fresh evidence suggests it is unlikely that all cells in a tumour will respond to such treatment. SEE LETTERS P.567 & P.572

ANTON BERNIS

The tumour suppressor that is most frequently mutated in human cancers is p53. Reactivation of this protein in tumours, which induces programmed cell death or cell-cycle arrest, is therefore an appealing therapeutic strategy. In this issue, however, Feldser *et al.*¹ and Junttila *et al.*² report work in mouse models of cancer showing that restoring p53 activity affects only advanced tumours, leaving untouched early lesions that are likely to one day become cancerous.

Earlier work^{3–5} suggested that restoring p53 function in several independent oncogene-driven mouse tumours elicits a potent anti-tumour response. The outcome was either programmed tumour-cell death by the process of apoptosis, or tumour-cell senescence. In fact, in two of the three animal models^{3–5}, even temporary p53 reactivation led to

prolonged survival. These data enhanced the appeal of p53 reactivation as a means of treating cancer.

Feldser *et al.* (page 572) and Junttila *et al.* (page 567) add a new twist to these observations. Both groups used variants of a mouse model of non-small-cell lung cancer (NSCLC) characterized by sporadic expression of a mutant *Kras* oncogene; this model closely resembles human NSCLC. Sporadic expression of physiological levels of mutant *Kras* in mice causes lung tumours that progress through different stages — from hyperplasia to adenoma to carcinoma. The advanced stages of the disease are marked by increased signalling flux through the RAS–MAPK pathway (the pathway in which *Kras* functions), probably due to additional alterations in this pathway. If sporadic tumour lesions associated with *Kras* mutations are also p53 deficient, they progress faster and become more malignant.

The authors^{1,2} set out to determine what would happen if p53 function were restored in these tumours.

Junttila and colleagues² used a variant of the mouse model in which the mutant *Kras* can be switched on by inhalation of an agent called AdenoCre. The p53 gene in these animals was replaced with a version that is inactive but can regain functionality on administration of the drug tamoxifen. The authors thus initiated tumorigenesis by AdenoCre exposure and then activated p53 functionality with tamoxifen. Feldser *et al.*¹ used a mouse model that randomly activates *Kras* at low frequency by the process of spontaneous recombination. Their animals could also be treated with tamoxifen to restore p53 functionality. The differences in the mouse models resulted in small differences in some of the measurements between the two studies, but the overall conclusions are fully congruent.

In contrast to the earlier studies^{3–5}, both teams found that, after induction of NSCLC by physiological levels of mutant *Kras*, tumour regression in response to p53 activation was hardly detectable or, at best, very modest. In both systems, in fact, only the more advanced adenocarcinoma lesions responded to induced p53 activity — by either cell-cycle arrest or a combination of cell-cycle arrest and apoptosis — whereas the less advanced lesions remained unaffected (Fig. 1).

At a molecular level, cells in the more malignant lesions showed enhanced signalling flux through the RAS–MAPK pathway, owing to amplification of the mutant *Kras*, loss of the normal *Kras* allele (gene copy) or other alterations affecting this pathway. Intriguingly, the high signalling flux was associated with high levels of another tumour-suppressor protein, p19^{Arf}, which acts upstream of p53. The less advanced lesions did not have increased p19^{Arf} levels, suggesting that enhanced activity of this protein is required to trigger the tumour-suppressive function of p53. Neither paper reports evidence of DNA damage in either the early or the advanced lesions: in this NSCLC model, therefore, DNA-damage response does not seem to play a significant part in activating p53.

These observations have important implications for understanding not just the ‘surveillance’ function of p53, but also the usefulness of restoring this tumour suppressor’s function as a therapeutic strategy. p53 does not affect early cancerous lesions that have a low oncogenic flux and retain low levels of p19^{Arf}; indeed, only after p19^{Arf} levels increase does p53 spring into action. This could be because organisms do not distinguish between normal pathway activation and moderate oncogenic signals: reacting to the latter would also compromise normal cell proliferation, which is essential for tissue maintenance, as well as tissue restoration after injury.

What do these findings^{1,2} mean for human

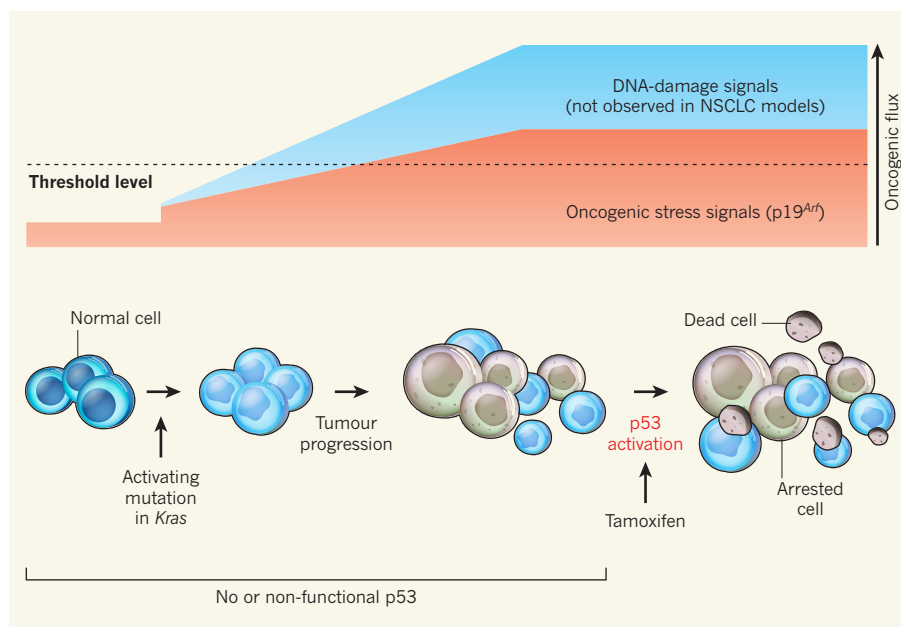


Figure 1 | Prerequisites for p53 activation. It is thought that a minimal level (threshold level) of oncogenic stress and/or DNA damage activates p53. Feldser *et al.*¹ and Junttila *et al.*² studied mouse models of non-small-cell lung cancer (NSCLC) characterized by oncogenic mutation of *Kras* to investigate what happens in the absence of p53. They find that, without p53, tumours could progress even if the oncogenic stress level increased above threshold level and the tumour-suppressor protein p19^{Arf} was activated. When the authors restored p53 function with tamoxifen, tumour cells with an increased oncogenic flux were either arrested or killed. Less advanced lesions were unaffected, however, probably because their oncogenic flux remained below the threshold level. The authors did not detect DNA-damage response, indicating that, at least in their models, it does not contribute to p53 activation.

cancers and their treatment? There is no reason to be discouraged by them. By the time they are diagnosed, human tumours are usually much more advanced and so will more resemble the tumours described in the earlier papers^{3–5} — those with a high oncogenic flux. Although advanced tumours might still contain cells with a low oncogenic flux from the earlier lesions, such cells probably constitute only a small fraction. Restoring p53 activity should, therefore, have a considerable effect on human tumours.

Nevertheless, Feldser and colleagues and Junttila and co-workers observe that cells with ‘early-lesion’ features are still present in the animals, even after p53 reactivation. Lesions containing such cells are obviously prone to progress to more advanced stages of cancer. Moreover, the two teams show that, at least in their NSCLC models, the DNA-damage-response pathway does not have a sizeable role in inducing p53’s anti-tumour activity — an observation that was also highlighted in a previous investigation of another cancer model⁶. The idea that the DNA-damage-response pathway does not contribute to p53’s tumour surveillance function is counterintuitive and warrants further research.

The studies^{1,2} do demonstrate that oncogenic flux is the main trigger for effective p53 action. In view of the crucial role of p19^{Arf} in this response — which might be more prominent than the role of its related human protein

p14^{ARF} — the NSCLC models seem particularly suitable for addressing the question of whether p53 responds to signals other than those from either the oncogene stress pathway, as governed by p19^{Arf}, or DNA damage.

Previous studies^{7–9} have pointed to p53 and p19^{Arf} having independent functions in tumour surveillance. A careful comparison of the loss of function of either p19^{Arf} or both p19^{Arf} and p53, with subsequent reactivation of p53, in these NSCLC models might help to further clarify the p19^{Arf}-independent tumour-suppressor roles of p53. This might also provide clues about how to selectively trigger p53 activity in the many human tumours in which the *INK4AB/p14^{ARF}* tumour-suppressor genes are either deleted or silenced. ■

Anton Berns is at the Netherlands Cancer Institute, 1066 CX Amsterdam, the Netherlands.
e-mail: a.berns@nki.nl

1. Feldser, D. M. *et al.* *Nature* **468**, 572–575 (2010).
2. Junttila, M. R. *et al.* *Nature* **468**, 567–571 (2010).
3. Martins, C. P., Brown-Swigart, L. & Evan, G. I. *Cell* **127**, 1323–1334 (2006).
4. Ventura, A. *et al.* *Nature* **445**, 661–665 (2007).
5. Xue, W. *et al.* *Nature* **445**, 656–660 (2007).
6. Christophorou, M. A., Ringshausen, I., Finch, A. J., Brown Swigart, L. & Evan, G. I. *Nature* **443**, 214–217 (2006).
7. Moore, L. *et al.* *Oncogene* **22**, 7831–7837 (2003).
8. Sherr, C. J. *Nature Rev. Cancer* **6**, 663–673 (2006).
9. Meek, D. W. *Nature Rev. Cancer* **9**, 714–723 (2009).

Direct conversion of human fibroblasts to multilineage blood progenitors

Eva Szabo¹, Shravanti Rampalli¹, Ruth M. Risueño¹, Angelique Schnerch^{1,2}, Ryan Mitchell^{1,2}, Aline Fiebig-Comyn¹, Marilyne Levadoux-Martin¹ & Mickie Bhatia^{1,2}

As is the case for embryo-derived stem cells, application of reprogrammed human induced pluripotent stem cells is limited by our understanding of lineage specification. Here we demonstrate the ability to generate progenitors and mature cells of the haematopoietic fate directly from human dermal fibroblasts without establishing pluripotency. Ectopic expression of OCT4 (also called POU5F1)-activated haematopoietic transcription factors, together with specific cytokine treatment, allowed generation of cells expressing the pan-leukocyte marker CD45. These unique fibroblast-derived cells gave rise to granulocytic, monocytic, megakaryocytic and erythroid lineages, and demonstrated *in vivo* engraftment capacity. We note that adult haematopoietic programs are activated, consistent with bypassing the pluripotent state to generate blood fate: this is distinct from haematopoiesis involving pluripotent stem cells, where embryonic programs are activated. These findings demonstrate restoration of multipotency from human fibroblasts, and suggest an alternative approach to cellular reprogramming for autologous cell-replacement therapies that avoids complications associated with the use of human pluripotent stem cells.

Mechanisms that govern induced pluripotent stem cell (iPSC) reprogramming from human fibroblasts remain poorly understood¹. The process is further complicated by cellular intermediates that fail to establish a stable pluripotent state, potentially due to the inability to establish the ideal expression context of reprogramming factors to complete pluripotency induction^{2–5}. These intermediates co-express genes associated with several differentiated lineages (neurons, epidermis and mesoderm)^{4,5}, raising the possibility that under unique conditions, fibroblasts could be induced to differentiate towards specified lineages. This maybe akin to recent demonstrations where fibroblasts were converted into single cell types, such as neurons, cardiomyocytes and macrophage-like cells^{6–8}. While these studies have examined fibroblast conversion in the murine model, a similar process remains to be extrapolated towards human applications.

Our preliminary observations indicated that human dermal fibroblasts (Fibs) predominantly expressing OCT4 during the pluripotent reprogramming process express lineage differentiation markers that include the human pan-haematopoietic marker CD45. While both OCT2 (also called POU2F2) and OCT1 (also called POU2F1) bind similar DNA target motifs to OCT4 (ref. 9), and play a role in lymphoid development^{10–12}, OCT4 is yet to be implicated in haematopoiesis. Here, by ectopic expression of the POU protein OCT4, we demonstrate and characterize direct haematopoietic fate conversion to multipotent blood progenitors from fibroblasts in the human.

Emergence of CD45⁺ cells from Fibs

Reprogramming towards pluripotency requires a cascade of events that encompasses generation of various intermediate cells among a rare subset of stable iPSCs capable of teratoma formation^{13,14} (Supplementary Fig. 1a–c). A portion of these intermediates form colonies that possess round cellular morphology resembling haematopoietic cells (Supplementary Fig. 2a), and express the human pan-haematopoietic marker CD45 (CD45⁺), but lack pluripotency marker Tra-1-60 (ref. 2) that is indicative of iPSCs (Supplementary Fig. 2b, c). These Fib-derived

CD45⁺ cells preferentially express OCT4 while demonstrating low levels of SOX2 and NANOG (Supplementary Fig. 2d, e). This suggested that Fib-derived intermediates could acquire a distinct lineage phenotype.

On the basis of these results, we compared the role of OCT4 during colony emergence from two sources of Fibs (adult dermal and neonatal foreskin) with that of NANOG or SOX2 alone (Fig. 1a). Transduced versus untransduced Fibs were examined between 14 and 21 days post-transduction (D14–D21; Supplementary Fig. 3). Unlike untransduced Fibs, or Fibs transduced with SOX2 (Fibs^{SOX2}) or NANOG (Fibs^{NANOG}), Fibs expressing OCT4 (Fibs^{OCT4}) gave rise to colonies (Fig. 1a, Supplementary Fig. 3b) and exhibited OCT4 expression at levels similar to those detected in established iPSCs (Fig. 1b). Fibs^{OCT4} exclusively gave rise to haematopoietic-like CD45⁺ cells (Fig. 1c). Furthermore, CD45⁺ cells (CD45⁺Fibs^{OCT4}) showed an increase in OCT4 expression (Supplementary Fig. 3c) with a concomitant decrease in the fibroblast specific gene expression¹⁵ (Fig. 1d). Approximately 1,000 genes were downregulated and an equal number upregulated at D4, resulting in a shift towards the FibCD45⁺ phenotype (Supplementary Table 1). To characterize and enhance emergence of CD45⁺ Fibs, we used Flt3 (FMS-like tyrosine kinase 3) ligand and SCF (stem cell factor), representing inductive growth factors essential for early haematopoiesis^{16,17}. Treatment with FLT3LG and SCF increased the frequency of CD45⁺ colony emergence from Fibs^{OCT4} by 4 to 6-fold, compared with untreated Fibs^{OCT4} (Fig. 1e, f), while no effect was detected from control Fibs (Fig. 1e, f, Supplementary Fig. 4). These data indicate that OCT4 is sufficient to initiate emergence of CD45⁺ cells from multiple sources of Fibs that are responsive to stimulation by early haematopoietic growth factors.

Conversion to CD45⁺ does not require iPSCs

Ectopic expression of OCT4 alone has been shown to result in pluripotent reprogramming of neural progenitors¹⁸. Accordingly, we examined the expression of a panel of genes known to be essential

¹Stem Cell and Cancer Research Institute, McMaster University, Hamilton, Ontario, Canada L8N 3Z5. ²Department of Biochemistry and Biomedical Sciences, McMaster University, Hamilton, Ontario, Canada L8N 3Z5.

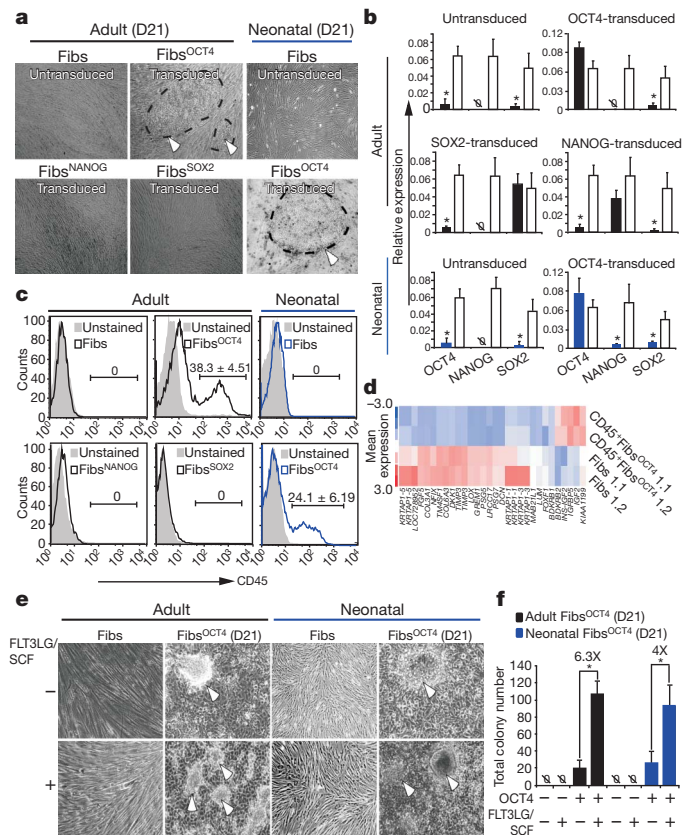


Figure 1 | OCT4 transduced human fibroblasts give rise to CD45⁺ colonies. **a**, Bright field images of adult and neonatal untransduced (Fibs) and OCT4- (Fibs^{OCT4}), SOX2- (Fibs^{SOX2}) or NANOG- (Fibs^{NANOG}) transduced Fibs at D21 (colonies, dashed lines and arrows) ($n = 6$). **b**, Relative gene expression at D21 of SOX2, NANOG and OCT4 in untransduced and transduced Fibs (shaded bars) in comparison with iPSCs (open bars; $n = 3$, $*P < 0.001$). **c**, FACS analysis of CD45 (pan-haematopoietic marker) levels at D21 in transduced and untransduced adult and neonatal Fibs ($n = 6$). **d**, Global gene analysis of fibroblast marker expression of Fibs at D0 versus D21. **e**, **f**, Bright field images (**e**) and enumeration of colonies (**f**) in adult and neonatal Fibs and Fibs^{OCT4} with and without Flt3 and SCF (six biological replicates; colonies, white arrows; error bars, s.e.m.; $*P < 0.001$).

for induction and maintenance of pluripotency¹⁴ during emergence of CD45⁺ Fibs. Apart from upregulation of OCT4 (Supplementary Fig. 5a), OCT4 transduction did not alter the pluripotency gene expression profile (Fig. 2a, b). Furthermore, related POU family members OCT2 and OCT1 remained unaffected (Supplementary Fig. 5b). On ectopic expression of OCT4 alone, pluripotency markers SSEA3 or Tra-1-60 were not detectable from Fibs^{OCT4}, whereas both gradually increased during establishment of iPSCs (Fig. 2c, d, Supplementary Fig. 5c–e). Unlike the fully reprogrammed hiPSCs ($n = 8$), injection of an equal number of OCT4-transduced or untransduced Fibs ($n = 6$) into immunodeficient mice failed to give rise to teratomas containing all three germ layers (Fig. 2e). Moreover, neither Fibs nor CD45⁺ Fibs^{OCT4} were immortalized, but could be maintained for approximately seven passages (Supplementary Fig. 6a), without elevation of MYC oncogene¹⁹ (Supplementary Fig. 6b). Accordingly, our results indicate that the Fibs^{OCT4} cells manifest a haematopoietic cell fate without the detectable phenotype or functional properties of transformed or pluripotent cells.

Haematopoietic progenitor of CD45⁺ Fibs^{OCT4}

Global gene expression analysis indicated that the CD45⁺ Fibs^{OCT4} cluster with mononuclear cells derived from mobilized peripheral blood (MPB)- and umbilical cord blood (UCB)-derived haematopoietic progenitors (CD34⁺ cells) (Supplementary Fig. 7a, b), suggesting that

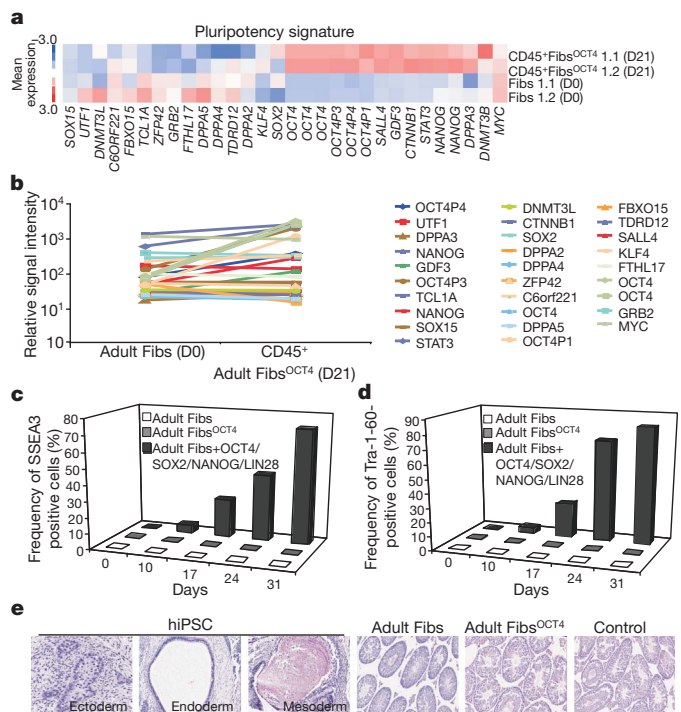


Figure 2 | OCT4 transduced dermal fibroblasts bypass the pluripotent state.

a, Pluripotency gene signature at D0 versus D21. **b**, Pluripotency marker levels over D0 to D21. **c**, **d**, Quantitative analysis of SSEA3 (**c**) and Tra-1-60 (**d**) in Fibs, Fibs^{OCT4} with and without SCF and FLT3LG, and Fibs transduced with OCT4, SOX2, NANOG, LIN28, over the human iPSC derivation timeline ($n = 3$). **e**, Teratomas derived from human iPSCs and testicular sections from mice injected with Fibs and Fibs^{OCT4} (Control, saline injected).

CD45⁺ Fibs^{OCT4} may possess functional haematopoietic potential of multiple blood cell types. To functionally characterize haematopoietic capacity, both adult and neonatal CD45⁺ Fibs^{OCT4} were physically isolated and cultured with a cytokine cocktail known to support human haematopoietic progenitor development (Fig. 3a) and expansion (Supplementary Fig. 7c, d). The resulting progeny retained CD45 expression and acquired myeloid-specific markers CD33 and CD13 (Fig. 3b and Supplementary Fig. 8). A subfraction of CD45⁺ Fibs^{OCT4} progeny included monocytes expressing CD14 (Fig. 3c, d, Supplementary Fig. 9a) that could be further stimulated by M-CSF and IL-4 to mature into macrophages capable of phagocytosis²⁰. CD45⁺ Fibs^{OCT4}-derived monocytes engulfed FITC-labelled latex beads (Fig. 3e, f, Supplementary Fig. 9b), unlike untransduced cytokine treated Fibs (Fig. 3e). Haematopoietic cytokine-treated CD45⁺ Fibs^{OCT4} derived from multiple sources of Fibs (adult and neonatal) also gave rise to granulocytic cell types distinct from monocytes (Supplementary Fig. 10a), as indicated by expression of CD15 (Fig. 3g, Supplementary Fig. 10b) and by characteristic cellular and polynuclear morphologies associated with neutrophils, eosinophils and basophils (Fig. 3h, Supplementary Fig. 10c). Without cytokines, CD45⁺ Fibs^{OCT4} cells retained CD45 expression, however, myeloid-specific markers were reduced and monocytic and granulocytic lineages were absent (Supplementary Fig. 11a, b). These results indicate that cytokine stimulation is necessary for haematopoietic expansion and maturation from CD45⁺ Fibs^{OCT4}.

Approximately one-quarter of cytokine-stimulated CD45⁺ Fibs^{OCT4} co-expressed CD34 (Fig. 3i, Supplementary Fig. 12). In a fashion similar to somatic UCB-derived progenitors, CD45⁺ Fibs^{OCT4} gave rise to colony forming units (CFUs), indicative of the clonal proliferative developmental potential of unipotent and bipotent progenitors of the granulocytic and macrophage lineages (Fig. 3j–l). On the basis of this *in vitro* myeloid capacity, CD45⁺ Fibs^{OCT4} progeny were transplanted into immunodeficient NOD/SCID IL2R γ -null (NSG) mice to characterize

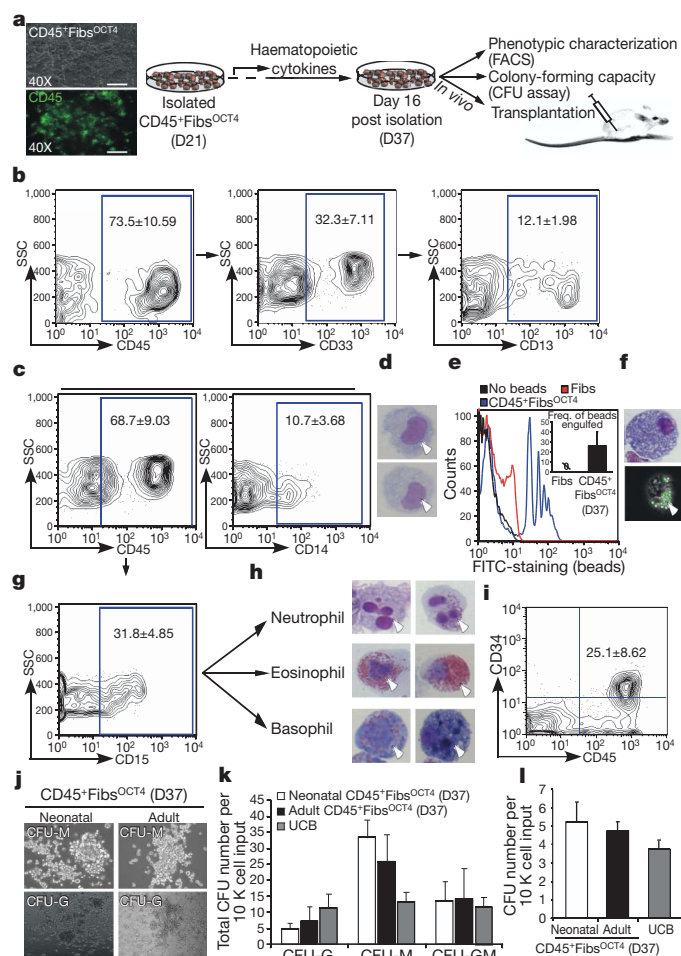


Figure 3 | *In vitro* generation of myeloid lineages from CD45⁺ Fibs **a**, Schema presenting myeloid lineage derivation from CD45⁺ Fibs^{OCT4}. **b**, FACS analysis of myeloid cells derived from CD45⁺ Fibs^{OCT4} ($n = 6$). **c**, FACS analysis of monocytes and **d**, Giemsa-Wright images of monocytes (white arrow) derived from CD45⁺ Fibs^{OCT4} ($n = 6$). **e**, FACS analysis of macrophages, using FITC-labelled latex-bead uptake; inset shows quantitative analysis ($n = 3$). **f**, Giemsa-Wright stained image and immunofluorescence image of FITC-beads engulfed by macrophages (white arrow). **g**, FACS analysis of granulocytes derived from CD45⁺ Fibs^{OCT4} ($n = 6$). **h**, Giemsa-Wright stained granulocytes containing neutrophils, eosinophils and basophils (white arrows) ($n = 6$). **i**, CD45⁺ Fibs^{OCT4} derived haematopoietic progenitors ($n = 9$). **j**, Images of granulocytic (CFU-G), monocytic (CFU-M) CFUs (20 \times). **k**, Quantification of granulocytic, monocytic and mixed granulocytic and monocytic (CFU-GM) CFU formation from CD45⁺CD34⁺ cells derived from adult and neonatal Fibs and UCB ($n = 3$). **l**, CFU frequency of adult and neonatal CD45⁺ Fibs^{OCT4} and UCB derived haematopoietic progenitors ($n = 3$; * $P < 0.001$). Error bars, s.e.m.

their *in vivo* potential (Fig. 4a). CD45⁺ Fibs^{OCT4}-derived cells engrafted all transplanted NSG recipients up to levels of 20%, as indicated by HLA-A/B/C⁺ cells (Fig. 4b), while Fibs and saline showed no engraftment (Fig. 4c). Engraftment levels of CD45⁺ Fibs^{OCT4} were comparable to UCB-derived progenitors and MPB-derived progenitors (Fig. 4d). Primary reconstituted NSG recipients exhibited a predominantly myeloid phenotype ($\sim 41\%$ CD45⁺CD14⁺) (Fig. 4c), compared with UCB and MPB cells (Fig. 4e). A proportion of the engrafted cells retained CFU initiation potential similar to cells from human UCB (Fig. 4f, Supplementary Fig. 13a–d). The ability to generate haematopoietic progenitors and the presence of engraftment, albeit at low levels, in the contralateral bones of the primary NSG recipients at 10 weeks post transplant (Supplementary Fig. 14a) supports the *in vivo* functional capacity of CD45⁺ Fibs^{OCT4}-derived cells. Engrafted CD45⁺ cells were only capable

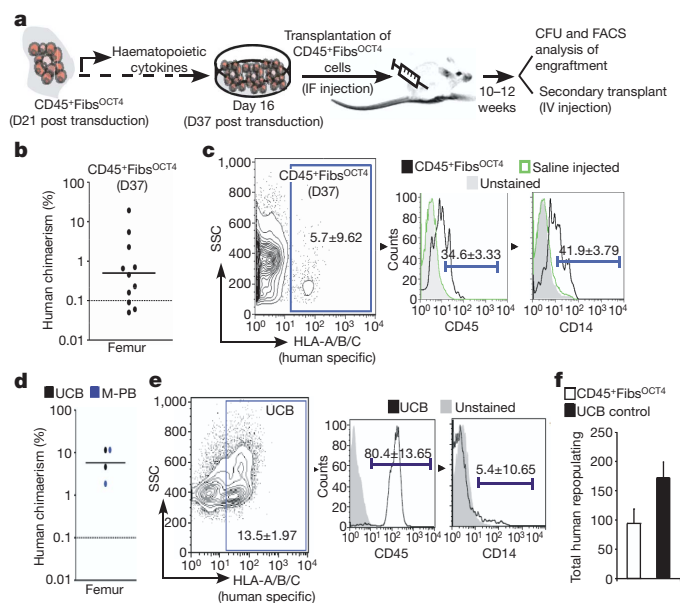


Figure 4 | *In vivo* capacity of CD45⁺ Fibs^{OCT4} **a**, Schematic of NOD/SCID IL2R γ c-null mice xenograft model for injection of CD45⁺ Fibs^{OCT4}. **b**, Graph representing human chimaerism of CD45⁺ Fibs^{OCT4} treated with cytokines ($n = 12$). **c**, FACS histograms of engrafted CD45⁺ and CD14⁺ population ($n = 12$). **d**, Graph representing human chimaerism of UCB derived progenitors and MPB cells ($n = 4$). **e**, Representative FACS histograms of engrafted UCB and MPB cells, showing the presence of CD45⁺ and CD14⁺ population ($n = 4$). **f**, CFU capacity of engrafted CD45⁺ Fibs^{OCT4} versus UCB ($n = 3$).

of limited engraftment ability in secondary recipient NSG mice (Supplementary Fig. 14b), indicating that they do not possess transformed leukaemic stem cell properties²¹, and thus represent safer haematopoietic transplantation product alternatives, as compared to hPSC-derived cells that retain tumour potential^{22,23}. Collectively, our data indicate that CD45⁺ Fibs^{OCT4} can give rise to functional haematopoietic progenitor-like cells that are able to mature into myeloid lineages *in vitro* and *in vivo*.

Erythroid and megakaryocytic potential of CD45⁺ Fibs

Despite the ability to derive all myeloid lineages from CD45⁺ Fibs^{OCT4}, erythroid cells were not detected. On OCT4 transduction, Fibs expressed the erythroblast marker CD71 at a frequency of nearly 40% (Fig. 5a). As Erythropoietin (EPO) induces early erythroid differentiation²⁴, we added EPO to Fibs^{OCT4} cultures, and observed a twofold increase in the number of Fibs expressing CD71, along with an increase in expression of Glycophorin-A (Fig. 5b) and adult β -globin protein (Fig. 5c). In contrast, Fibs (Fig. 5c) and hPSC-derived haematopoietic cells (Fig. 5c inset) lacked β -globin protein. In the absence of EPO, only β -globin transcript was expressed in the CD45⁺ Fibs^{OCT4} (Fig. 5d), while β -globin protein was undetectable (Fig. 5c). In contrast, and unlike haematopoietic cells derived from hPSCs²⁵, haematopoietic cells derived from CD45⁺ Fibs^{OCT4} lacked embryonic globin expression and expressed modest levels of fetal globin (Fig. 5d). EPO-treated CD45⁺ Fibs^{OCT4} exhibited both primitive and mature erythrocyte (enucleated) morphologies (Fig. 5e) and allowed for erythroid progenitor emergence, detected by colony formation (BFU-E) and CFU-Mixed colonies (CFU-Mix; dual myeloid and erythroid capacity), similar to that for UCB, without reduction in monocytic or granulocytic progenitor capacity (Fig. 5f, g, Supplementary Fig. 15a, b).

Studies have indicated that erythroid and megakaryocytic lineage commitment occur together and potentially arise from a common precursor population^{26,27}. EPO stimulation of CD45⁺ Fibs^{OCT4} induced emergence of megakaryocytic lineage, as detected by Megakaryocytic (Mk)-CFU assay²⁸, indicated by the presence of Mk-specific antigen GPIIb/IIIa (CD41; red/pink colonies) (Fig. 5h right panel, Fig. 5i), while

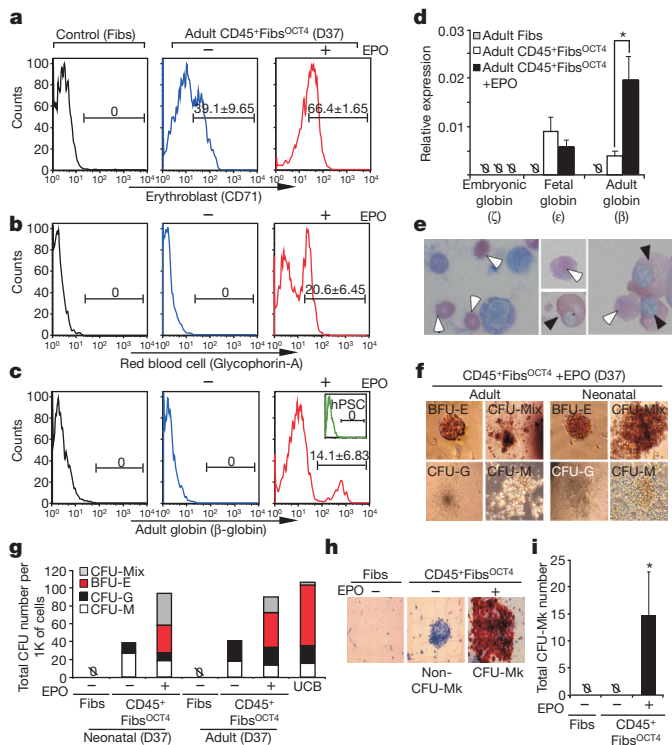


Figure 5 | EPO treated CD45⁺Fibs^{OCT4} generate erythroid and megakaryocytic progenitors. **a–c**, Representative FACS histograms of erythroblast marker, CD71 (**a**), Glycophorin-A (**b**) and adult-globin (**c**; upper panel, differentiated hPSCs) in Fibs and CD45⁺Fibs^{OCT4} with and without EPO ($n = 3$). **d**, Relative mRNA expression of embryonic, fetal and adult-globins ($n = 3$; $P < 0.001$). **e**, Giemsa-Wright stained EPO treated CD45⁺Fibs^{OCT4} showing primitive (black arrow) and mature (white arrow) erythrocyte morphologies. **f**, CFU images, and **g**, quantitative analysis of CFU formation of EPO treated adult and neonatal CD45⁺Fibs^{OCT4} (20 \times ; $n = 3$). (Erythroid blast forming units, BFU-E; all lineages, CFU-Mix). **h**, Megakaryocytic CFU (CFU-Mk) images (CD41⁺ cells; 20 \times), and **i**, quantification ($n = 3$; $P < 0.001$). \emptyset , not detected.

this haematopoietic progenitor type was absent in CD45⁺Fibs^{OCT4} without EPO (Fig. 5h middle panel, Fig. 5i) or control Fibs (Fig. 5h left panel, Fig. 5i). Taken together, EPO treatment induces definitive and not primitive (embryonic) haematopoietic programs²⁹, and reveals megakaryocytic lineage during conversion of Fibs to haematopoietic fate.

OCT4 haematopoietic program from Fibs

To develop a broader understanding of the role of OCT4 during haematopoietic conversion of Fibs (Fig. 6a), we examined gene expression and OCT4 occupancy over the time course of CD45⁺ cell emergence and maturation. As early as day (D) 4 post transduction, significant changes occur in molecular pathways, including metabolic and developmental processes (Supplementary Fig. 16a). Furthermore, global gene expression of the Fibs over the course of CD45⁺ cell emergence (D0, D4 and D21) indicated a decrease in fibroblast-specific gene expression¹⁵ (Fig. 6b), without pluripotency gene induction (Fig. 6c), excluding OCT4. Fibs^{OCT4} immediately upregulated haematopoietic cytokine receptors, including FLT3 and KIT, receptors of FLT3LG and SCF, respectively (Fig. 6d), along with transcription factors associated with early haematopoietic development (Fig. 6e, Supplementary Fig. 16b, c). In addition, Fibs possess low to undetectable levels of genes associated with pluripotency, such as NANOG and SOX2, or haematopoietic specification, such as SCL/TAL1, RUNX1, C/EBP α , GATA1 or PU.1/SPI1 (refs 6, 30–32) (Fig. 6f, Supplementary Fig. 17a). However, transduction with OCT4 was accompanied by a substantial increase of SCL, C/EBP α , GATA1 and RUNX1 (Fig. 6f). Interestingly, PU.1 and MIXL1, which were previously shown to regulate primitive blood development^{6,33,34},

were not differentially regulated (Fig. 6e, f, Supplementary Fig. 16b, c). Expression of genes associated with mesodermal transition from the pluripotent state, such as Brachyury and GATA2, were absent in both Fibs and CD45⁺Fibs^{OCT4} (Fig. 6f), indicating that haematopoietic specification from Fibs does not involve embryonic-mesodermal transitions^{35,36}. Molecular analysis of cytokine treated CD45⁺Fibs^{OCT4} (D37) revealed reduced OCT4 levels, while maintaining RUNX1, SCL and C/EBP α levels (Supplementary Fig. 17b), and expression of all adult globins, including haemoglobin- α , β and δ (Supplementary Fig. 17c, Fig. 5d).

Like OCT4, OCT1 and OCT2 are also able to regulate haematopoietic-specific genes (Supplementary Fig. 18)^{37–41}. While expression of OCT4 increased during CD45⁺ cell emergence, followed by a significant reduction on cytokine treatment, the levels of OCT2 and OCT1 remained unchanged (Fig. 6g), suggesting that OCT4 does not target other Oct family members. Nevertheless, OCT1, OCT2 and OCT4 have the potential to bind the same octamer (POU) binding sequences in a cell context specific manner, thereby raising the possibility that OCT4 has the capacity to bind and potentially regulate gene targets of OCT1 and OCT2 (refs 37–40) (Fig. 6h, Supplementary Fig. 18). Thus, we examined OCT4 occupancy of haematopoietic, non-haematopoietic and pluripotency genes that contain shared OCT1, OCT2 or OCT4 binding sequences in their putative promoters/enhancers (Fig. 6h, Supplementary Fig. 18). Consistent with changes in gene expression (Fig. 6f), RUNX1, SCL, CD45 and GATA1 displayed substantial OCT4 occupancy (Fig. 6i). To assess the specificity of OCT4 occupancy of haematopoietic targets during CD45⁺ cell emergence, we examined non-haematopoietic associated promoters previously shown to bind OCT1 or OCT2. Consistent with global gene expression (Supplementary Fig. 7a), housekeeping genes GADD45A and POLR2A exhibited an increase in OCT4 occupancy at their respective promoters, while non-haematopoietic genes MYF5 and NKX2.5, associated with mesodermal development, did not (Fig. 6j). In contrast to hPSCs, OCT4 did not occupy NANOG, MYC and TBX3 promoters (Fig. 6k) in CD45⁺Fibs^{OCT4}. While OCT4 binds its own promoter (Fig. 6k), it does not bind the OCT2 promoter (Fig. 6i), consistent with OCT2 expression (Supplementary Fig. 5a, b). Collectively, these temporal gene expression analyses along with OCT4 occupancy studies demonstrate that ectopic OCT4 expression orchestrates haematopoietic program potential in Fibs towards blood fate conversion.

Discussion

Our current study demonstrates the ability of human fibroblasts to be directly converted to multipotent haematopoietic progenitors of the myeloid, erythroid and megakaryocytic lineages via OCT4-dependent cellular programming without traversing the pluripotent state or activation of mesodermal pathways^{35,36}. Given that transition from primitive to definitive haematopoiesis is delineated by the shift from embryonic to adult haemoglobin expression²⁹, our study demonstrates that unlike hPSC-derived haematopoietic cells⁴², CD45⁺Fibs exclusively acquire adult-globin protein indicative of definitive haematopoietic program activation. Acquisition of the haematopoietic phenotype is linked to the direct binding of OCT4 to the regulatory loci of haematopoietic-specific genes^{37,40,41,43}. While OCT1 and OCT2 have been shown to play a role in adult lymphopoiesis^{10–12}, OCT4 has not been implicated in blood fate. Given the conservation between the native or predicted octamer binding sequences among OCT1, OCT2 and OCT4, it is highly possible that POU domains shared among OCT proteins have a redundant role in haematopoietic fate conversion. Although OCT4 converts fibroblasts to myeloid and erythroid progenitors, lymphoid fate was not detected. Accordingly, it is plausible that ectopic expression of OCT4, OCT1 and OCT2, coupled with lymphoid specific culture conditions, may support lymphoid conversion from Fibs, and is currently being pursued.

Although recent reports demonstrate conversion of mouse fibroblasts to neural, cardiac and macrophage-like cells^{6–8}, the present

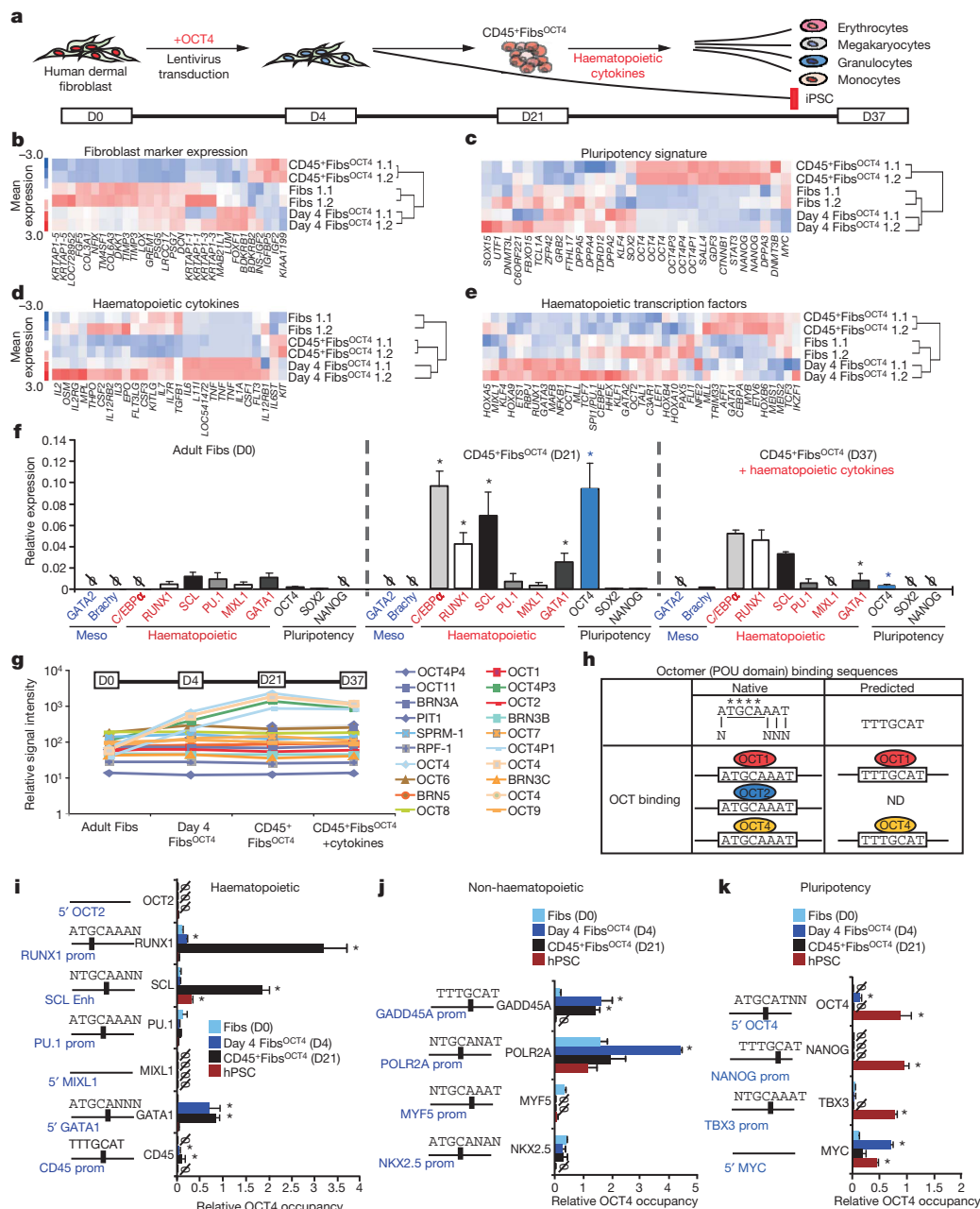


Figure 6 | OCT4 causes haematopoietic program activation in Fibs. **a**, Proposed model for haematopoietic fate conversion from CD45⁺ Fibs^{OCT4} (D0 to D37). **b–e**, Global gene expression based on fibroblast marker expression (**b**), pluripotency signature (**c**), haematopoietic cytokines (**d**) and haematopoietic transcription factors (**e**). **f**, Relative mRNA expression of mesodermal, haematopoietic specific and pluripotency genes at D0 versus D21 and D37 ($n = 4$, $*P < 0.001$). **g**, Gene expression profile of OCT (POU) genes.

study uniquely demonstrates the ability to generate multipotent, rather than unipotent (single lineage), cell types from fibroblasts in the human, hence establishing future clinical utility of these multipotent cells of the haematopoietic lineage. Taking into account the yield, expansion capacity and clinical feasibility⁴⁴ of using this direct conversion approach to haematopoietic fate (Supplementary Table 2), our technique could provide a reasonable basis for autologous cell replacement therapies.

METHODS SUMMARY

Cultures. Adult and neonatal dermal fibroblasts were cultured in F12-DMEM media supplemented with (1) IGFII and bFGF, or (2) IGFII, bFGF, Flt3 and SCF, on Matrigel-coated plates. Lentiviral vectors (pSIN) containing cDNAs of OCT4,

h, Schematic of native and predicted octamer binding sequences for OCT4, OCT1 and OCT2, (N, any nucleotide; starred/underlined, conserved octamer-binding region). **i–k**, Right panels: relative OCT4 occupancy of haematopoietic specific (**i**), non-haematopoietic (**j**) and pluripotency (**k**) gene enhancer/promoter regions ($n = 3$; $*P < 0.001$). **i–k**, Left panels: proximity maps of primers (arrows) relative to native or predicted octamer-binding region (black box).

NANOG, SOX2 and LIN28 were obtained from Addgene and were transfected into 293-FT cells using the virapower packaging kit (Invitrogen). Fibroblast transductions were performed at 24 h post 10^4 seeding on Matrigel. For derivation of CD45⁺ cells, fibroblasts were transduced with OCT4 expressing lentivirus and cultured in media (1) or (2), and iPSCs were derived as previously described¹⁵. Further haematopoietic differentiation was carried out using EB media supplemented with haematopoietic cytokines.

Functional/phenotype analysis. Flow cytometry analysis of haematopoietic and pluripotency markers was performed using FACSCalibur (Beckman Coulter), and analysis was performed using the FlowJo 8.8.6 software. Cell sorting was performed using FACSaria II (Becton-Dickinson); Histological profiling of haematopoietic cells was performed using Cytospin and Giemsa-Wright staining and confirmed by the McMaster Pathology and Hematology Group; CFU formation was assayed using Methocult and Megacult kits from Stem Cell Technologies;

Macrophage phagocytosis assay was performed using Fluorescein conjugated-latex beads (Sigma) as particle tracers to analyse uptake by monocytes derived from CD45⁺ FcγR^{OCT4} cells; *in vivo* engraftment capacity was evaluated by intrafemoral injection of CD45⁺ cells into NSG mice. Ten weeks later bone marrow from injected femur, contralateral bones and spleen was analysed for the presence of human cells by flow cytometry; teratoma formation was evaluated by intratesticular injection into NOD/SCID mice. Resulting teratomas were evaluated for the presence of mesoderm, endoderm and ectoderm through histological examination.

Molecular analysis. For qPCR and microarray analysis, RNA was extracted using a total RNA purification kit (Norgen). Microarray analysis was done using Human Gene 1.0 ST arrays (Affymetrix) and dChip software. OCT4 DNA occupancy (OCT4 ChIP) was done as previously described⁴⁵. See Supplementary Methods for additional details.

Full Methods and any associated references are available in the online version of the paper at www.nature.com/nature.

Received 17 August; accepted 20 October 2010.

Published online 7 November 2010.

- Jaenisch, R. & Young, R. Stem cells, the molecular circuitry of pluripotency and nuclear reprogramming. *Cell* **132**, 567–582 (2008).
- Chan, E. M. *et al.* Live cell imaging distinguishes bona fide human iPS cells from partially reprogrammed cells. *Nature Biotechnol.* **27**, 1033–1037 (2009).
- Lin, T. *et al.* A chemical platform for improved induction of human iPSCs. *Nature Methods* **6**, 805–808 (2009).
- Mikkelsen, T. S. *et al.* Dissecting direct reprogramming through integrative genomic analysis. *Nature* **454**, 49–55 (2008).
- Kanawaty, A. & Henderson, J. Genomic analysis of induced pluripotent stem (iPS) cells: routes to reprogramming. *Bioessays* **31**, 134–138 (2009).
- Feng, R. *et al.* PU.1 and C/EBP α / β convert fibroblasts into macrophage-like cells. *Proc. Natl Acad. Sci. USA* **105**, 6057–6062 (2008).
- Vierbuch, T. *et al.* Direct conversion of fibroblasts to functional neurons by defined factors. *Nature* **463**, 1035–1041 (2010).
- Ieda, M. *et al.* Direct reprogramming of fibroblasts into functional cardiomyocytes by defined factors. *Cell* **142**, 375–386 (2010).
- Kang, J., Shukla, A. & Tanti, D. Stem cells, stress, metabolism and cancer: a drama in two acts. *Trends Biochem. Sci.* **34**, 491–499 (2009).
- Brunner, C. *et al.* B cell-specific transgenic expression of Bcl2 rescues early B lymphopoiesis but not B cell responses in BOB.1/OBF.1-deficient mice. *J. Exp. Med.* **197**, 1205–1211 (2003).
- Emslie, D. *et al.* Oct2 enhances antibody-secreting cell differentiation through regulation of IL-5 receptor α chain expression on activated B cells. *J. Exp. Med.* **205**, 409–421 (2008).
- Pfisterer, P. *et al.* CRISP-3, a protein with homology to plant defense proteins, is expressed in mouse B cells under the control of Oct2. *Mol. Cell. Biol.* **16**, 6160–6168 (1996).
- Takahashi, K. *et al.* Induction of pluripotent stem cells from adult human fibroblasts by defined factors. *Cell* **131**, 861–872 (2007).
- Takahashi, K. & Yamanaka, S. Induction of pluripotent stem cells from mouse embryonic and adult fibroblast cultures by defined factors. *Cell* **126**, 663–676 (2006).
- Yu, J. *et al.* Induced pluripotent stem cell lines derived from human somatic cells. *Science* **318**, 1917–1920 (2007).
- Hassan, H. T. & Zander, A. Stem cell factor as a survival and growth factor in human normal and malignant hematopoiesis. *Acta Haematol.* **95**, 257–262 (1996).
- Lyman, S. D. *et al.* Molecular cloning of a ligand for the flt3/flk-2 tyrosine kinase receptor: a proliferative factor for primitive hematopoietic cells. *Cell* **75**, 1157–1167 (1993).
- Kim, J. B. *et al.* Direct reprogramming of human neural stem cells by OCT4. *Nature* **461**, 649–653 (2009).
- Lebofsky, R. & Walter, J. C. New Myc-anisms for DNA replication and tumorigenesis? *Cancer Cell* **12**, 102–103 (2007).
- Silverstein, S. C., Steinman, R. M. & Cohn, Z. A. Endocytosis. *Annu. Rev. Biochem.* **46**, 669–722 (1977).
- Hope, K. J., Jin, L. & Dick, J. E. Acute myeloid leukemia originates from a hierarchy of leukemic stem cell classes that differ in self-renewal capacity. *Nature Immunol.* **5**, 738–743 (2004).
- Roy, N. S. *et al.* Functional engraftment of human ES cell-derived dopaminergic neurons enriched by coculture with telomerase-immortalized midbrain astrocytes. *Nature Med.* **12**, 1259–1268 (2006).
- Amariglio, N. *et al.* Donor-derived brain tumor following neural stem cell transplantation in an ataxia telangiectasia patient. *PLoS Med.* **6**, e1000029 (2009).
- Fried, W. Erythropoietin and erythropoiesis. *Exp. Hematol.* **37**, 1007–1015 (2009).
- Perlingeiro, R. C., Kyba, M. & Daley, G. Q. Clonal analysis of differentiating embryonic stem cells reveals a hematopoietic progenitor with primitive erythroid and adult lymphoid-myeloid potential. *Development* **128**, 4597–4604 (2001).
- Debili, N. *et al.* Characterization of a bipotent erythro-megakaryocytic progenitor in human bone marrow. *Blood* **88**, 1284–1296 (1996).
- Klimchenko, O. *et al.* A common bipotent progenitor generates the erythroid and megakaryocyte lineages in embryonic stem cell-derived primitive hematopoiesis. *Blood* **114**, 1506–1517 (2009).
- Strodtbeck, D. *et al.* Graft clonogenicity and intensity of pre-treatment: factors affecting outcome of autologous peripheral hematopoietic cell transplantation in patients with acute myeloid leukemia in first remission. *Bone Marrow Transplant.* **36**, 1083–1088 (2005).
- Orkin, S. H. & Zon, L. I. Hematopoiesis and stem cells: plasticity versus developmental heterogeneity. *Nature Immunol.* **3**, 323–328 (2002).
- Shivdasani, R. A., Mayer, E. L. & Orkin, S. H. Absence of blood formation in mice lacking the T-cell leukaemia oncogene tal-1/SCL. *Nature* **373**, 432–434 (1995).
- Ichikawa, M., Asai, T., Chiba, S., Kurokawa, M. & Ogawa, S. Runx1/AML-1 ranks as a master regulator of adult hematopoiesis. *Cell Cycle* **3**, 722–724 (2004).
- Friedman, A. D. Transcriptional control of granulocyte and monocyte development. *Oncogene* **26**, 6816–6828 (2007).
- Koschmieder, S., Rosenbauer, F., Steidl, U., Owens, B. M. & Tenen, D. G. Role of transcription factors C/EBP α and PU.1 in normal hematopoiesis and leukemia. *Int. J. Hematol.* **81**, 368–377 (2005).
- Ng, E. S. *et al.* The primitive streak gene Mixl1 is required for efficient haematopoiesis and BMP4-induced ventral mesoderm patterning in differentiating ES cells. *Development* **132**, 873–884 (2005).
- Tsai, F. Y. *et al.* An early haematopoietic defect in mice lacking the transcription factor GATA-2. *Nature* **371**, 221–226 (1994).
- Vijayaragavan, K. *et al.* Noncanonical Wnt signaling orchestrates early developmental events toward hematopoietic cell fate from human embryonic stem cells. *Cell Stem Cell* **4**, 248–262 (2009).
- Boyer, L. A. *et al.* Core transcriptional regulatory circuitry in human embryonic stem cells. *Cell* **122**, 947–956 (2005).
- Kistler, B., Pfisterer, P. & Wirth, T. Lymphoid- and myeloid-specific activity of the PU.1 promoter is determined by the combinatorial action of octamer and ets transcription factors. *Oncogene* **11**, 1095–1106 (1995).
- Rodda, D. J. *et al.* Transcriptional regulation of nanog by OCT4 and SOX2. *J. Biol. Chem.* **280**, 24731–24737 (2005).
- Sridharan, R. *et al.* Role of the murine reprogramming factors in the induction of pluripotency. *Cell* **136**, 364–377 (2009).
- Ghozi, M. C., Bernstein, Y., Negreanu, V., Levanon, D. & Groner, Y. Expression of the human acute myeloid leukemia gene AML1 is regulated by two promoter regions. *Proc. Natl Acad. Sci. USA* **93**, 1935–1940 (1996).
- Chang, K. H. *et al.* Definitive-like erythroid cells derived from human embryonic stem cells coexpress high levels of embryonic and fetal globins with little or no adult globin. *Blood* **108**, 1515–1523 (2006).
- Kwon, U. K., Yen, P. H., Collins, T. & Wells, R. A. Differential lineage-specific regulation of murine CD45 transcription by Oct-1 and PU.1. *Biochem. Biophys. Res. Commun.* **344**, 146–154 (2006).
- Feugier, P. *et al.* Hematologic recovery after autologous PBPC transplantation: importance of the number of postthaw CD34⁺ cells. *Transfusion* **43**, 878–884 (2003).
- Rampalli, S. *et al.* p38 MAPK signaling regulates recruitment of Ash2L-containing methyltransferase complexes to specific genes during differentiation. *Nature Struct. Mol. Biol.* **14**, 1150–1156 (2007).

Supplementary Information is linked to the online version of the paper at www.nature.com/nature.

Acknowledgements This work was supported by grants to M.B. from the Canadian Institute of Health Research (CIHR), the Canadian Cancer Society Research Institute (CCS-RI), the StemCell Network and the Ontario Ministry of Research Innovation (MRI). M.B. is supported by the Canadian Chair Program and holds the Canada Research Chair in human stem cell biology. E.S. is supported by Ministry of Research and Innovation (MRI) and MITACS fellowships. R.M.R. is supported by a CCS-RI fellowship and R.M. is supported by an Ontario Graduate Scholarship (OGS). We thank T. Werbowetski-Ogilvie for her help.

Author Contributions All authors contributed to the acquisition, analysis and interpretation of the data; E.S., S.R., R.M.R. and M.B. initiated and designed the study; A.S. performed Affymetrix analyses; R.M.R. performed *in vivo* analyses; E.S., S.R., R.M.R. and M.B. wrote the paper.

Author Information Data are available on the NCBI Gene Expression Omnibus (GEO) and are accessible through GEO Series accession number GSE24621. Reprints and permissions information is available at www.nature.com/reprints. The authors declare no competing financial interests. Readers are welcome to comment on the online version of this article at www.nature.com/nature. Correspondence and requests for materials should be addressed to M.B. (mbhatia@mcmaster.ca).

METHODS

Cell culture. Primary human dermal adult fibroblasts derived from breast dermal tissue, and neonatal fibroblasts derived from foreskin tissue, were initially maintained in fibroblast medium (DMEM (Gibco)) supplemented with 10% v/v FBS (Neonatal Bovine Serum, HyClone), 1 mM L-glutamine (Gibco), and 1% v/v non-essential amino acids (NEAA; Gibco) before transduction with OCT4 lentivirus vector. Human dermal fibroblasts transduced with OCT4 were maintained on matrigel-coated dishes in complete F12 medium (F12 DMEM; Gibco) supplemented with 10% knockout serum replacement (Gibco), 1% NEAA (Gibco), 1 mM L-glutamine (Gibco), and 0.1 mM β -mercaptoethanol containing 16 ng ml⁻¹ bFGF (BD Biosciences) and 30 ng ml⁻¹ IGFII (Millipore), or in complete F12 medium containing 16 ng ml⁻¹ bFGF and 30 ng ml⁻¹ IGFII and supplemented with 300 ng ml⁻¹ Flt-3 (R&D Systems) and 300 ng ml⁻¹ stem cell factor (SCF; R&D Systems), for 21 days. The arising CD45⁺ OCT-transduced cells were transferred onto low attachment 24-well plates in haematopoietic medium, consisting of 80% knockout DMEM (KO-DMEM) (Gibco), 20% v/v non-heat inactivated fetal calf serum (FCS) (HyClone), 1% v/v NEAA, 1 mM L-glutamine and 0.1 mM β -mercaptoethanol (Sigma), for 16 days. Cultures were replaced with haematopoietic differentiation medium with cytokines (SCF, G-CSF, FLT3LG, IL-3, IL-6 and BMP-4; R&D Systems), or for erythroid/megakaryocytic differentiation the medium was supplemented with haematopoietic cytokines plus 3 U ml⁻¹ EPO and changed every 4 days. This was followed by collection for molecular and functional analysis.

Lentivirus production. Lentiviral vectors (pSIN) containing cDNAs of OCT4, NANOG, SOX2 and Lin-28 were obtained from Addgene. These vectors were transfected with virapower packaging kit from Invitrogen in a 293-FT packaging cells line. Viral supernatants were harvested 48 h after transfection and ultracentrifuged to concentrate the virus. An equal amount of each virus was used for fibroblast transduction in the presence of 8 μ g ml⁻¹ polybrene.

Lentivirus transduction. For generation of cells containing single transcription factors, human adult dermal fibroblasts (Fibs) (derived from breast skin; age 30–40 yr) or neonatal foreskin Fibs were seeded at a density of 10,000 cells per well on matrigel coated 12-well plates. Twenty-four hours after seeding, Fibs were infected with lentivirus expressing either OCT4 or NANOG or SOX2 (NANOG and SOX2 transduction was only performed for adult dermal Fibs). Transduced fibroblasts were then grown in complete F12 medium containing 16 ng ml⁻¹ bFGF and 30 ng ml⁻¹ IGFII supplemented with 300 ng ml⁻¹ Flt-3 and 300 ng ml⁻¹ SCF, or complete F12 medium containing 16 ng ml⁻¹ bFGF and 30 ng ml⁻¹ IGFII alone, for up to 21 days. Emerging CD45⁺ colonies were counted 14–21 days after infection. Colonies were picked manually and maintained on matrigel-coated wells. Molecular analysis was done on purified untransduced Fibs (D0), OCT4 transduced Fibs at day 4 (D4), CD45⁺ Fibs at day 21 (D21) and haematopoietic cytokine treated or untreated CD45⁺ Fibs at day 37 (D37). Day 4 post OCT4 transduction was chosen as the early event time point, based on a number of criteria: optimal time for recovery following transduction; visible morphological changes within the culture; and resumption of normal cell cycle kinetics. The day 4 OCT4 transduced Fibs (D4) were isolated by puromycin selection overnight (OCT4 vector contains a puromycin resistance cassette), and the purity of the sample was validated by staining for OCT4 followed by OCT4 expression analysis using flow cytometry; samples used for molecular analysis exhibited 99% OCT4 levels. The D21 and D37 CD45⁺ Fibs^{OCT4} were isolated on the basis of their CD45 expression. D21 and D37 cells were stained with CD45-APC antibody (BD Biosciences) and sorted using a FACSaria II (Becton Dickinson); samples used for molecular analysis exhibited 99% CD45 levels.

Induction of reprogramming. For generation of reprogrammed cells from fibroblasts, cells were seeded at the density of 10,000 cells per well on matrigel coated 12-well plates. Twenty-four hours after seeding, fibroblasts were transduced with lentivirus expressing OCT4/NANOG/SOX2/LIN28 (ref. 15). Transduced fibroblasts were then grown in F12 medium supplemented with 30 ng ml⁻¹ IGFII and 16 ng ml⁻¹ bFGF. Reprogrammed iPSC colonies were counted four weeks post infections. Colonies were picked manually and maintained on matrigel-coated wells.

Live staining. For live staining, sterile Tra-1-60 antibody (Millipore) was pre-conjugated with sterile Alexa Fluor-647 at room temperature. Reprogrammed colonies were washed once with F12 medium and incubated with Tra-1-60-Alexa 647 antibodies for 30 min at room temperature. Cultures were then washed twice to remove unbound antibody. Cells were visualized by an Olympus IX81 fluorescence microscope.

Flow cytometry. For pluripotency marker expression, cells were treated with collagenase IV, and then placed in cell dissociation buffer for 10 min at 37 °C (Gibco). Cell suspensions were stained with SSEA3 antibody (1:100) (Developmental Studies Hybridoma Bank, mAb clone MC-631, Univ. Iowa) or Tra-1-60-PE (1:100) antibody (BD Biosciences). For SSEA3 staining, Alexa Fluor-647 goat anti-rat IgM (1:1,000) (Molecular Probes, Invitrogen) was used as the secondary antibody.

Live cells were identified by 7-amino actinomycin (7AAD) exclusion and then analysed for cell surface marker expression using a FACSCalibur (Becton Dickinson). Collected events were analysed using FlowJo 8.8.6 Software (Tree Star).

Cells from the haematopoietic differentiation medium were disassociated with TrypLE (Gibco) at D16 and analysed for expression of haematopoietic progenitor and mature haematopoietic markers. Haematopoietic cells were identified by staining single cells with fluorochrome-conjugated monoclonal antibodies (mAb): CD34-FITC and APC- or FITC-labelled anti-human CD45 (BD Biosciences), FITC-anti-CD33 (BD Pharmingen), PE-anti-CD13 (BD Pharmingen), PE- or FITC-anti-CD71 (BD Pharmingen), FITC-anti-HLA-A/B/C (BD Pharmingen), PE-anti-CD15 (BD Pharmingen), PE-anti-CD15 (BD Pharmingen); PE anti-CD14 (BD Pharmingen), FITC- or PE-anti-GlyA (BD Pharmingen), and APC- or PE-anti- β -globin (SantaCruz Biotech). The mAb and their corresponding isotypes were used at 1–2 mg ml⁻¹; optimal working dilutions were determined for individual antibodies. Frequencies of cells possessing the haemogenic and haematopoietic phenotypes were determined on live cells by 7AAD (Immunotech) exclusion, using FACSCalibur (Beckman Coulter), and analysis was performed using FlowJo 8.8.6 Software.

RT-PCR and qPCR. Total RNA was isolated using the Norgen RNA isolation kit. RNA was then subjected to cDNA synthesis using superscript III (Invitrogen). Quantitative PCR (qPCR) was performed using Platinum SYBR Green-UDP mix (Invitrogen). For the analysis of the sample, the threshold was set to the detection of Gus-B (β -glucuronidase)⁴⁶ and then normalized to internal control GAPDH. The base line for the experiment was set to the gene expression levels observed in fibroblasts. Given the expression of some of the genes within this starting population of fibroblasts, we felt that we should include the gene expression pattern for these cells. Hence, the data are represented as delta cycle threshold ($\Delta C(t)$) versus delta $\Delta C(t)$ ($\Delta\Delta C(t)$). (qPCR primer sequences are provided in Supplementary Table 3.)

Genomic DNA was isolated using the All In One isolation kit (Norgen). For integration studies, 150 ng genomic DNA was used per PCR reaction. PCR reactions were performed using 2X PCR Master Mix (Fermentas).

Affymetrix analysis. Total RNA was extracted from human dermal fibroblasts (2 replicates), puromycin selected day 4 OCT4 transduced fibroblasts (2 replicates) and sorted CD45⁺ cells (2 replicates) using the Total RNA Purification Kit (Norgen). RNA integrity was assessed using Bioanalyser (Agilent Technologies). Sample labelling and hybridization to Human Gene 1.0 ST arrays (Affymetrix) were performed by the Ottawa Health Research Institute Microarray Core Facility (OHRI). Affymetrix data were extracted, normalized, and summarized with the robust multi-average (RMA) method implemented in the Affymetrix Expression Console. CEL files were imported into dChip software⁴⁷ for data normalization, extraction of signal intensities and probe-level analysis. All the data from each individual sample are available on the NCBI Gene Expression Omnibus (GEO), <http://www.ncbi.nlm.nih.gov/geo/> and are accessible through GEO Series accession number GSE24621.

Chromatin immunoprecipitation. ChIP was performed as described previously⁴⁵. Briefly, human pluripotent cells (H9 and iPSC1.2), human dermal fibroblast cells, puromycin selected day 4 OCT4 transduced cells, and sorted day 21 CD45⁺ cells were cross-linked using 1% formaldehyde. Chromatin was digested in buffer containing 0.1% SDS to obtain fragments of approximately of 1,000 bp length. Sonicated DNA was subjected to immunoprecipitation using anti-OCT4 (ChIP quality antibody; Cell Signaling Technology) and anti rabbit IgG antibodies (SantaCruz Biotechnology). Immunoprecipitated DNA was further reverse cross-linked, purified and subjected to qPCR analysis using UDG-Platinum SYBR Green mix (Invitrogen). The promoter specific ChIP primers are listed in Supplementary Table 4. To calculate the relative enrichment, signals observed in control antibody were subtracted from signals detected from the specific antibody; the resulting differences were divided by signals observed from one-fiftieth of the ChIP input material.

Megakaryocyte assay. To detect human megakaryocytes, the MegaCult-C Complete Kit with Cytokines (Stem Cell Technologies) was used. The derivation of megakaryocytes was done according to instructions included with the kit. The kit includes pre-screened components for optimal growth of megakaryocyte CFUs, such as thrombopoietin (TPO), Interleukin-3 (IL-3), IL-6, IL-11 and SCF, chamber slides for growth and antibodies for subsequent immunocytochemical staining. In short, 10,000 CD45⁺ EPO treated cells were plated in the MegaCult medium containing the cocktail of growth factors mentioned above. The human CFU-Mks were detectable by day 10 to 15 and were subsequently fixed and stained according to protocol. Mk-specific antigen GPIIb/IIIa (CD41) linked to a secondary biotinylated antibody-alkaline phosphatase avidin conjugated detection system was used, where Mk-CFUs were red/pink in colour.

Cytospin. 1,000 CD45⁺ OCT4 transduced cells were washed twice in cold 2% FBS in PBS and diluted in 500 µl of cold 1% FBS in PBS. The samples were loaded into the appropriate wells of the Cytospin centrifuge equipment. The samples were spun at 500 r.p.m. for 5 min to allow adherence to the slides. The slides were fixed with methanol for 1 min and allowed to dry for 30 min. Then slides were stained with Giemsa-Wright stain for 3 min, followed by 10 min in PBS and a quick wash in distilled water. The slides were allowed to dry overnight and mounted with mounting medium (Dako). Slides were viewed by an Olympus IX81 microscope. Blood cell typing/morphological criteria were confirmed by McMaster Pathology and Hematology.

Macrophage phagocytosis assay. Fluorescein (FITC) conjugated latex beads (Sigma) were used as particle tracers to analyse phagocytosis by monocytes derived from CD45⁺ Fibs^{OCT4} cells treated with IL-4 and M-CSF. To measure phagocytosis, 10 µl of packed beads suspended in 3% FBS in PBS was added to 10⁶ cells in Teflon tubes. After incubation for 90 min at 37 °C, cells were washed three times with cold PBS containing 3% FBS and 0.1% EDTA to remove free beads. The cells were then labelled to detect expression of CD45 (APC-conjugated) CD45 mAb together with FITC-bead uptake, and analysed by flow cytometry using FACSCalibur (BD) or visualized on tissue culture quality slides (VWR) and viewed by an Olympus IX81 fluorescence microscope.

Xenotransplant assays. NOD/SCID IL2R γ c null adult mice (NSG) were sublethally irradiated with 325 rads 24 h before transplantation. 5.0 × 10⁵ CD45⁺ OCT-transduced (D37) or human dermal fibroblasts or human mobilized peripheral blood or human umbilical cord blood lineage depleted cells were transplanted by intrafemoral injection. After 10 weeks, animals were culled, and bone marrow (BM) from injected femur, contralateral bones and spleen was analysed for the presence of human cells by flow cytometry (FACSCalibur, Becton Dickinson), followed by data analysis using FlowJo 8.8.6 Software (Tree Star). Cells positive for HLA-A/B/C and CD45 were analysed for the expression of haematopoietic lineage specific markers, such as CD14. For secondary transplants, total engrafted bone marrow cells were transplanted intravenously (IV injection) in adult irradiated NSG mice, as described for primary transplants. Genomic DNA from engrafted cells was then analysed using conventional PCR by primers specific for the α -satellite of human chromosome 17: forward, 5'-GGGATAATTTTCAGCTGACTAAACAG-3'; reverse, 5'-TTCCGTTTAGTTAGGTGCAGTTATC-3'.

Methylcellulose colony-forming assay. Cells were plated at 1,000 FACSAria II sorted (Becton Dickinson) CD45⁺ CD34⁺ cells or 5,000 total cells for EPO treatments were seeded in 1 ml of Methocult GF H4434 (Stem Cell Technologies). Colonies were scored after 14 days of culture using standard morphological criteria and analysed using the FACSCalibur (Becton Dickinson) for haematopoietic surface markers. Collected events were analysed using FlowJo 8.8.6 Software (Tree

Star). For colony derivation from xenotransplant derived engrafted cells, the cells were first sorted based on HLA-A/B/C (BD Biosciences) followed by CD45 expression using a human specific anti-CD45 (BD Biosciences). The HLA-A/B/C and CD45 double positive cells were then plated at a density of 1,000 cell ml⁻¹ in Methocult GF H4434. The colonies derived from engrafted cells were further analysed for haematopoietic surface markers using FACSAria II (Becton Dickinson). Collected events were analysed using FlowJo 8.8.6 Software (Tree Star).

Teratoma assay. The McMaster University Animal Care Council approved all procedures and protocols. Adult dermal fibroblasts, neonatal dermal (foreskin) fibroblasts, CD45⁺ OCT4 transduced adult dermal fibroblasts, CD45⁺ OCT4 transduced neonatal fibroblasts and iPSC 1.1 to 1.4 were treated with collagenase IV for 5–10 min, followed by collection and washing twice with saline and resuspended in saline. 500,000 cells per sample were injected intratesticularly into male NOD-SCID mice. Mice were killed 10–12 weeks after initial injection. Teratomas were extracted, embedded in paraffin and sectioned in 5-µm intervals followed by deparaffinization in xylene and processing through a graded series of alcohol concentrations. Samples were stained with haematoxylin and eosin or OCT4 followed by dehydration and xylene treatment. Slides were mounted using Permount and imaged by scanning slides using Aperio Scan Scope; images were captured using Image Scope v9.0.19.1516 software. Tissue was also collected from a variety of organs including lung, spleen, liver, brain and kidney to investigate the presence of metastatic cells. Tissue typing was performed based on stringent histological and morphological criteria specific for each germ layer subtype. Mesoderm lineages, such as bone, were identified using presence of osteocytes and bone spicules (dark pink); cartilage was identified by the presence of chondrocytes and specific staining (light blue) of the extra cellular matrix. Endoderm lineages, such as intestinal lumens, were identified by the presence of goblet cells in the lumen epithelium. Ectoderm lineages, such as skin, were identified based on distinguishing cell layer morphologies (that is, stratified); brain or neural tube was identified based on specific histological criteria. The presence of the germ layers and tissue typing was confirmed by McMaster Pathology.

Statistical analysis. All tests were performed using InStat Version 3.0a statistical software (GraphPad Software). Descriptive statistics including mean and s.e.m. along with one-way ANOVAs, and two-tailed *t*-tests were used to determine significant differences. *P* < 0.01 was considered significant.

46. Oshima, A. *et al.* Cloning, sequencing, and expression of cDNA for human β -glucuronidase. *Proc. Natl Acad. Sci. USA* **84**, 685–689 (1987).
47. Li, C. & Wong, W. H. Model-based analysis of oligonucleotide arrays: expression index computation and outlier detection. *Proc. Natl Acad. Sci. USA* **98**, 31–36 (2001).

Sugar transporters for intercellular exchange and nutrition of pathogens

Li-Qing Chen¹, Bi-Huei Hou¹, Sylvie Lalonde¹, Hitomi Takanaga¹, Mara L. Hartung¹, Xiao-Qing Qu¹, Woei-Jiun Guo¹, Jung-Gun Kim², William Underwood⁴, Bhavna Chaudhuri¹, Diane Chermak¹, Ginny Antony³, Frank F. White³, Shauna C. Somerville⁴, Mary Beth Mudgett² & Wolf B. Frommer¹

Sugar efflux transporters are essential for the maintenance of animal blood glucose levels, plant nectar production, and plant seed and pollen development. Despite broad biological importance, the identity of sugar efflux transporters has remained elusive. Using optical glucose sensors, we identified a new class of sugar transporters, named SWEETs, and show that at least six out of seventeen *Arabidopsis*, two out of over twenty rice and two out of seven homologues in *Caenorhabditis elegans*, and the single copy human protein, mediate glucose transport. *Arabidopsis* SWEET8 is essential for pollen viability, and the rice homologues SWEET11 and SWEET14 are specifically exploited by bacterial pathogens for virulence by means of direct binding of a bacterial effector to the SWEET promoter. Bacterial symbionts and fungal and bacterial pathogens induce the expression of different SWEET genes, indicating that the sugar efflux function of SWEET transporters is probably targeted by pathogens and symbionts for nutritional gain. The metazoan homologues may be involved in sugar efflux from intestinal, liver, epididymis and mammary cells.

The molecular nature of cellular sugar efflux in both plants and animals is unknown despite the fact that sugar efflux is an essential component for cellular exchange of carbon and energy in multicellular organisms^{1–4}. Sugar efflux from the tapetum or transmitting tract of the style, for example, fuels pollen development and pollen tube growth⁵. Flowers secrete sugars for nectar production to attract pollinators, and plants secrete carbohydrates into the rhizosphere, potentially to feed beneficial microorganisms⁶. Sugar efflux carriers are required at other sites, including mesophyll in leaves and the seed coat⁷. In mammals, glucose efflux from liver is crucial for the maintenance of blood glucose levels².

The primary goal of pathogens is to access nutrients from their hosts for reproduction. Phytopathogenic bacteria in the genera *Pseudomonas* and *Xanthomonas* can live in the intercellular space (apoplast) of plants, where they acquire carbohydrates for energy and carbon⁸. Successful pathogens probably co-opt nutrient efflux mechanisms of the host to redirect nutrient flux⁹. Plants and pathogens engage in an evolutionary tug-of-war, in which the plant limits pathogen access to nutrients and initiates immune responses, whereas the pathogen evolves adaptive strategies to gain access to nutrients and suppress host immunity. Insight into mechanisms used by pathogens to alter plant immunity is emerging. However, the mechanisms that pathogens use to alter host physiology, notably efflux of sugars to support growth, are poorly understood. We hypothesize that sugar efflux transporters are co-opted by pathogens to supply nutrients⁹. This hypothesis is supported by studies of sugar transfer from wheat leaves to powdery mildew^{10–12}. Pathogen glucose/H⁺ uptake transporters have been identified¹³; by contrast, plant sugar efflux mechanisms have remained elusive.

Identification of AtSWEET1 as a glucose uniporter

To identify new transporters potentially involved in glucose efflux, we screened genes encoding uncharacterized polytopic membrane proteins from the *Arabidopsis* membrane protein database Aramemnon¹⁴ using

a new mammalian expression system¹⁵. Candidate genes were co-expressed with the high-sensitivity fluorescence resonance energy transfer (FRET) glucose sensor, FLIPglu600μΔ13V, in human HEK293T cells, which have low endogenous glucose uptake activity^{15,16}. Among the genes tested, AtSWEET1 (AT1G21460) expression enabled HEK293T cells to accumulate glucose as detected by a glucose-induced negative FRET ratio change (Fig. 1a). To determine whether AtSWEET1 also mediates efflux from the cytosol, the FRET glucose sensor FLIPglu600μΔ13V^{ER} was expressed in the lumen of the endoplasmic reticulum (ER; Fig. 1b). Topologically, efflux across the plasma membrane from the cytoplasmic side is equivalent to efflux into the ER that is also initiated from the cytoplasmic side (Fig. 1c). The glucose-dependent response of the ER sensor demonstrates that AtSWEET1 can mediate both uptake across the plasma membrane and efflux into the ER. SWEET1 thus seems to function as a bidirectional uniporter/facilitator. The observed sugar uptake and efflux were not due to subcellular re-localization of the FRET sensors (Supplementary Fig. 1). A carboxy-terminal green fluorescent protein (GFP) fusion of AtSWEET1 was functional in cellular uptake and localized to the plasma membrane of HEK293T cells (Supplementary Fig. 2). AtSWEET1 carrying a premature stop codon at position 198 was non-functional (Supplementary Fig. 3). Induction of endogenous GLUT glucose transporters in AtSWEET1-expressing HEK293T cells was excluded based on insensitivity of uptake to the GLUT inhibitor cytochalasin B (Supplementary Fig. 4a, b) and lack of detectable changes of messenger RNA levels of known human GLUT and SGLT glucose transporters (Supplementary Fig. 4c). The transport function of AtSWEET1 was independently demonstrated by expression in a yeast mutant lacking all 18 hexose transporters¹⁷. AtSWEET1 enabled the yeast mutant to grow on glucose (Fig. 1d) and to accumulate intracellular glucose as determined with the FRET glucose sensor FLII¹²Pglu700μΔ6 (ref. 18) (Fig. 1e). AtSWEET1 functions as a low-affinity glucose transporter (Michaelis constant (K_m) ~9 mM; Fig. 1f). Consistent with a uniport transport mechanism, uptake

¹Department of Plant Biology, Carnegie Institution for Science, 260 Panama St, Stanford, California 94305, USA. ²Department of Biology, Stanford University, 228A Gilbert Bioscience Building, 371 Serra Mall, Stanford, California 94305, USA. ³Department of Plant Pathology, Kansas State University, Manhattan, Kansas 66506, USA. ⁴Energy Bioscience Institute, 130 Calvin Hall, MC 5230, Berkeley, California 94720, USA.

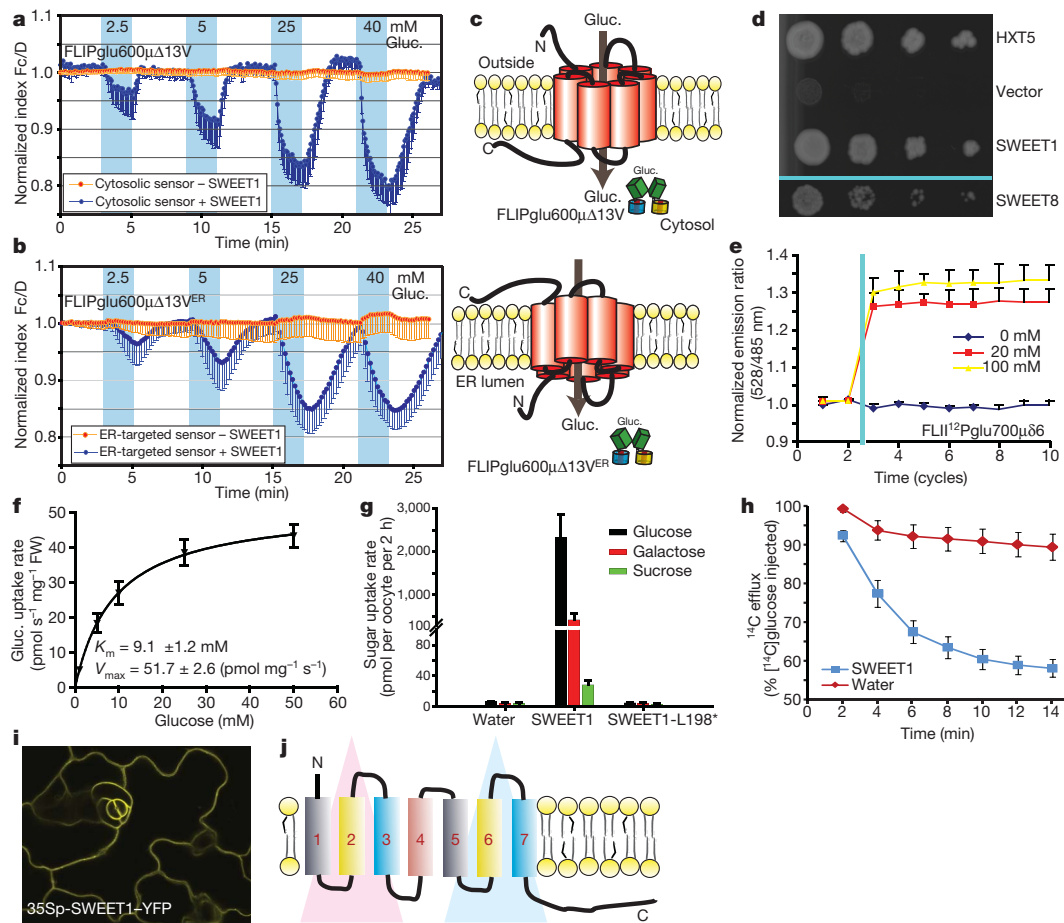


Figure 1 | Characterization of SWEET transporters. **a**, Identification of glucose transport activity for AtSWEET1 by co-expression with cytosolic FRET glucose sensor FLIPglu600 $\mu\Delta$ 13V in HEK293T cells¹⁵. Individual cells were analysed by quantitative ratio imaging of CFP and Venus emission (acquisition interval 5 s; F_c/D corresponds to normalized emission intensity ratio¹⁵). HEK293T/FLIPglu600 $\mu\Delta$ 13V cells were perfused with medium, followed by square pulses of increasing glucose (Gluc.) concentrations. Orange line indicates cells expressing sensor alone; blue line indicates cells co-expressing sensor and AtSWEET1; accumulation of glucose is shown by a negative FRET ratio change (blue line; mean \pm s.d.; $n > 10$). **b**, FRET imaging of glucose efflux from cytosol into ER. FLIPglu600 $\mu\Delta$ 13V^{ER} was targeted to the ER lumen¹⁵ (compare with panel **a**; acquisition interval 10 s; mean \pm s.d.; $n > 10$). **c**, Cartoon for SWEET influx across plasma membrane and efflux from cytosol to ER. Cytosolic FLIPglu600 $\mu\Delta$ 13V identifies glucose import from the

was largely pH-independent (Supplementary Fig. 5). AtSWEET1 did not efficiently complement mannose, fructose and galactose uptake deficiencies of the mutant (Supplementary Fig. 6). Radiotracer experiments in *Xenopus* oocytes were used as another measure for AtSWEET1 sugar uptake activity (Fig. 1g). Direct proof for efflux activity was obtained by monitoring time-dependent release of [¹⁴C]glucose from oocytes after injection of radiotracer (Fig. 1h). In support of the function in cellular uptake and efflux, a constitutively expressed AtSWEET1–yellow fluorescent protein (YFP) fusion localized to the plasma membrane in *Arabidopsis* leaves (Fig. 1i). On the basis of expression studies, AtSWEET1 is highly expressed in *Arabidopsis* flowers, where the protein may supply nutrients to the gametophyte or nectaries (Supplementary Fig. 7). The biochemical properties of AtSWEET1 are markedly similar to an unidentified transport activity characterized in roots using FRET sensors¹⁹. However, AtSWEET1 expression in roots was low, implicating other AtSWEET paralogues for this function.

SWEET1 belongs to a novel transporter family (PFAM PF03083) with 17 members in *Arabidopsis* and ~21 in rice (Supplementary Fig. 8).

extracellular face (extracellular N terminus). FLIPglu600 $\mu\Delta$ 13V^{ER} measures transport from the intracellular side (cytosolic C terminus). **d**, Complementation of yeast EBY4000 (ref. 17) lacking 18 hexose transporter genes with AtSWEET1, AtSWEET8, or yeast HXT5; control, empty vector. **e**, Glucose accumulation in EBY4000 co-expressing AtSWEET1 and FLIP¹²Pglu700 $\mu\Delta$ 6 before and after glucose addition (two cycles before glucose addition; mean \pm s.d.; $n = 3$). **f**, Kinetics of [¹⁴C]glucose accumulation by AtSWEET1 in EBY4000 (mean \pm s.d.; $n = 3$). **g**, AtSWEET1-mediated uptake of 1 mM [¹⁴C]glucose, [¹⁴C]galactose or [¹⁴C]sucrose into oocytes (mean \pm s.d.; $n = 8$ cells). **h**, [¹⁴C]glucose efflux from oocytes expressing AtSWEET1 (mean \pm s.e.; $n \geq 10$ cells; $P < 0.0005$). **i**, Confocal imaging of AtSWEET1–YFP in leaves of stably transformed *Arabidopsis* (panel width = 176 μ m). **j**, Structural model of SWEETs based on hydrophobicity plots (duplication of three transmembrane helices; red/blue triangles).

SWEETs fall into four subclades (Supplementary Fig. 8a) with 27–80% identity (Supplementary Fig. 8b). SWEETs are small proteins predicted to form a pore from seven transmembrane helices (Supplementary Fig. 9). Modelling indicates that the structure results from an ancient duplication of a 3-transmembrane-helix-domain polypeptide (1–3 and 5–7) fused via transmembrane helix 4 in a 3+1+3 configuration (Fig. 1j).

Diverse roles for SWEET paralogues

The phenotypes of several *sweet* mutants have been described. AtSWEET1 (clade 1) is 42% identical to its paralogue AtSWEET8 (clade 2) (Supplementary Fig. 8b). AtSWEET8 (also called *RPG1*) is expressed in the tapetum²⁰, and mutation of AtSWEET8 causes male sterility, compatible with a role in glucose efflux for pollen nutrition²⁰.

AtSWEET1 and AtSWEET8 share 31% and 34% amino acid sequence identity with rice OsSWEET11 (also called Os8N3 or Xa13; here named OsSWEET11 based on phylogeny)²¹. Similar to AtSWEET8, OsSWEET11 contributes to pollen viability, as RNA interference to OsSWEET11 reduced starch content in pollen and

caused male sterility in rice²¹ (Supplementary Fig. 8b). Expression studies indicate that the import function of SWEETs may also contribute to the nutrition of growing pollen tubes. Specifically, *AtSWEET1* is expressed in hydrated pollen and both *AtSWEET1* and *AtSWEET8* are expressed highly in pollen tubes²². *AtSWEET5* (also called *VEX1*) is expressed in mature, hydrated and germinating pollen and is found specifically in the vegetative cell of pollen grains, which may supply the generative cell with sugars²³. Silencing of the clade 3 SWEET homologue *NEC1* from petunia also triggered male sterility²⁴. *NEC1* is expressed in nectaries, and developmental regulation of *NEC1* correlates inversely with nectarial starch content, indicating a second function for *NEC1* in sugar secretion in nectaries²⁵. Hexoses, in particular galactose, fructose and glucose, accumulate in senescent leaves, and SWEET members may also function in mobilization of carbohydrate during senescence²⁶. The *AtSWEET15* (also called *SAG29*) gene is induced ~22-fold in leaves during senescence²⁷. Taken together, the SWEET sugar transporters probably supply carbohydrates to a variety of tissues in both monocotyledonous and dicotyledonous plants. Other SWEET members also function in glucose transport. For example, co-expression of *AtSWEET8* with FRET sensors FLIPglu600 μ Δ 13V or FLIPglu600 μ Δ 13V^{ER} in HEK293T cells leads to glucose transport across both plasma and ER membranes (Supplementary Fig. 10), and *AtSWEET8* complements the yeast glucose transport mutant (Fig. 1d and Supplementary Figs 5 and 11). At least four additional *Arabidopsis* SWEET genes (*AtSWEET4*, *AtSWEET5*, *AtSWEET7*, *AtSWEET13*) also function in glucose transport when expressed in yeast or HEK293T cells (Supplementary Figs 5, 11 and 12).

Potential role of SWEETs in pathogen nutrition

Many pathogens acquire glucose from their hosts^{9,11,13}, thus pathogens may hijack host sugar efflux systems dedicated for plant development. We tested whether mRNA levels of *Arabidopsis* SWEET family members were altered by challenge with bacterial and fungal pathogens. *Pseudomonas syringae* pv. *tomato* strain DC3000 infection highly induced mRNA levels of *AtSWEET4*, *AtSWEET5*, *AtSWEET7*, *AtSWEET8*, *AtSWEET10*, *AtSWEET12* and *AtSWEET15* in *Arabidopsis* leaves (Fig. 2). In contrast, the DC3000 type III secretion mutant (*ΔhrcU*), which cannot inject type III effector proteins into the host and is compromised in pathogenicity, did not induce three of the seven *AtSWEET* genes, demonstrating that SWEET mRNA abundance is modulated in a type-III-dependent manner (Fig. 2b). The fungal powdery mildew pathogen *Golovinomyces cichoracearum* induced a different set of *AtSWEET* mRNAs, most prominently *AtSWEET12* (Fig. 2a, c), and previous expression data have shown that infection with the fungal pathogen *Botrytis cinerea* induces expression of *AtSWEET4*, *AtSWEET15* and *AtSWEET17* (ref. 28). Pathogen-specific modulation of SWEET mRNA levels, therefore, probably alters sugar efflux at the site of infection, having an impact on pathogen growth and plant immunity.

OsSWEET11 underlies the dominant allele (*Xa13*) of the recessive resistance gene *xa13* (refs 21, 29, 30). Susceptibility alleles of *xa13* confer disease resistance against bacterial blight and have been isolated from geographically diverse rice accessions³⁰. All alleles tested carry mutations in the promoter region of the *OsSWEET11* gene and interfere with pathogen-specific induction of the gene^{21,31}. RNA interference of rice *OsSWEET11* confers resistance to the *Xanthomonas oryzae* pathovar *oryzae* (Xoo) strain PXO99^A, which otherwise grows in the apoplast and xylem of the host. *OsSWEET11* may, therefore, supply sugars to the pathogen by a uniport mechanism as demonstrated for the *Arabidopsis* homologues (Fig. 1a–h and Supplementary Figs 10–12). Consistent with cellular import/efflux functions, *OsSWEET11* localizes to the plasma membrane in rice callus²⁹. *OsSWEET11* is less efficiently targeted to the plasma membrane of HEK293T cells compared to *AtSWEET1* (Fig. 3a). Nevertheless, weak uptake activity was observed in HEK293T cells and oocytes (Fig. 3b, c).

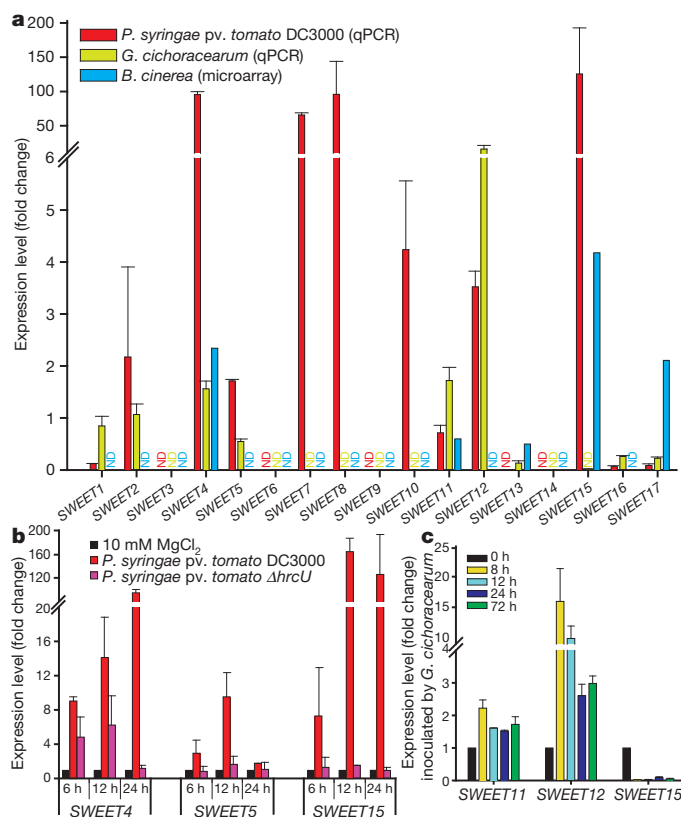


Figure 2 | Biotrophic bacteria or fungi induce mRNA levels of different SWEET genes. **a**, Induction of *AtSWEET* mRNAs by either the bacterium *Pseudomonas syringae* pv. *tomato* DC3000 (2×10^8 c.f.u. ml⁻¹, 8 h after inoculation, measured by qPCR, normalized by MgCl₂ buffer treatment), powdery mildew fungus *G. cichoracearum* (~25–35 conidiospores per mm², 48 h after inoculation, measured by qPCR; normalized to 0 h values), or by *Botrytis cinerea* (from microarray study²⁸) in *Arabidopsis* leaves. ND, not detectable. **b**, Induction of *AtSWEET4*, *AtSWEET5* and *AtSWEET15* by *P. syringae* DC3000 depends on a functional type III secretion system (T3S). Samples were collected at 6, 12 and 24 h after infiltration with 2×10^8 c.f.u. ml⁻¹ of DC3000 or DC3000 *ΔhrcU*, a T3S mutant. **c**, Infection by *G. cichoracearum* leads to induction of *AtSWEET11* and *AtSWEET12* but downregulation of *AtSWEET15*.

Infection of rice by Xoo PXO99^A requires the bacterial type III effector gene *pthXo1* (ref. 21). *PthXo1* is a TAL (transcriptional activator-like) effector, which directly interacts with the *OsSWEET11* promoter as shown by chromatin immune precipitation (Fig. 3d), as well as transient co-expression in *Nicotiana benthamiana* leaves (Supplementary Fig. 13)^{32,33}. *PthXo1* secreted by Xoo PXO99^A specifically activates transcription of *OsSWEET11* (ref. 21), presumably to induce sugar efflux to feed bacteria in the xylem and/or apoplast (Fig. 4a). When *pthXo1* is mutated (as in strain PXO99^AME2), transcription of *OsSWEET11* and pathogenicity are reduced²¹, consistent with a model of sugar supply limiting growth of the pathogen (Fig. 4b). If *OsSWEET11* becomes unavailable owing to mutations in the TAL effector binding element of the *OsSWEET11* promoter, or through RNA interference^{21,31}, the sugar supply becomes limiting and the pathogen cannot grow efficiently (Fig. 4c). Indeed, *ossweet11* (*xa13*) mutants are resistant to PXO99^A (ref. 21). *xa13*-mediated resistance can be defeated by PXO99^A expressing the alternative TAL effector gene *avrXa7* (Fig. 4d), compatible with the most parsimonious hypothesis that another *OsSWEET* gene is co-opted by the pathogen to support bacterial growth²¹. Indeed, *AvrXa7* activates the paralogue *OsSWEET14* (ref. 33). *OsSWEET14* is targeted more efficiently to the plasma membrane in HEK293T cells (Fig. 3e) and mediates glucose import in HEK293T cells and oocytes (Fig. 3c, f, h and Supplementary Fig. 14). *OsSWEET14* also functions as a low-affinity transporter

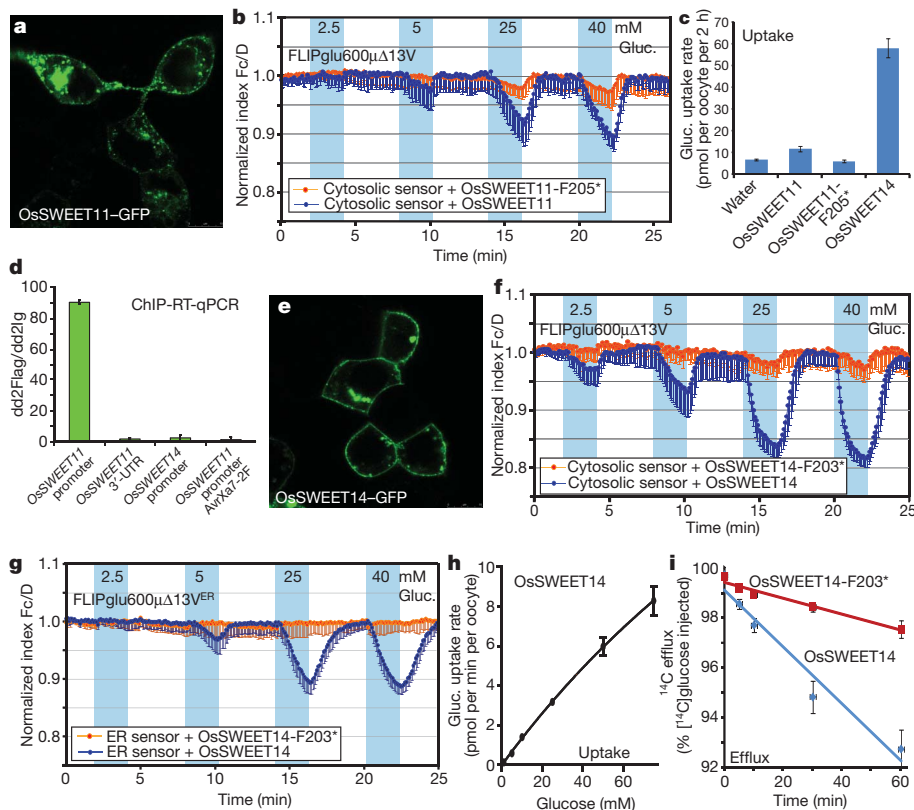
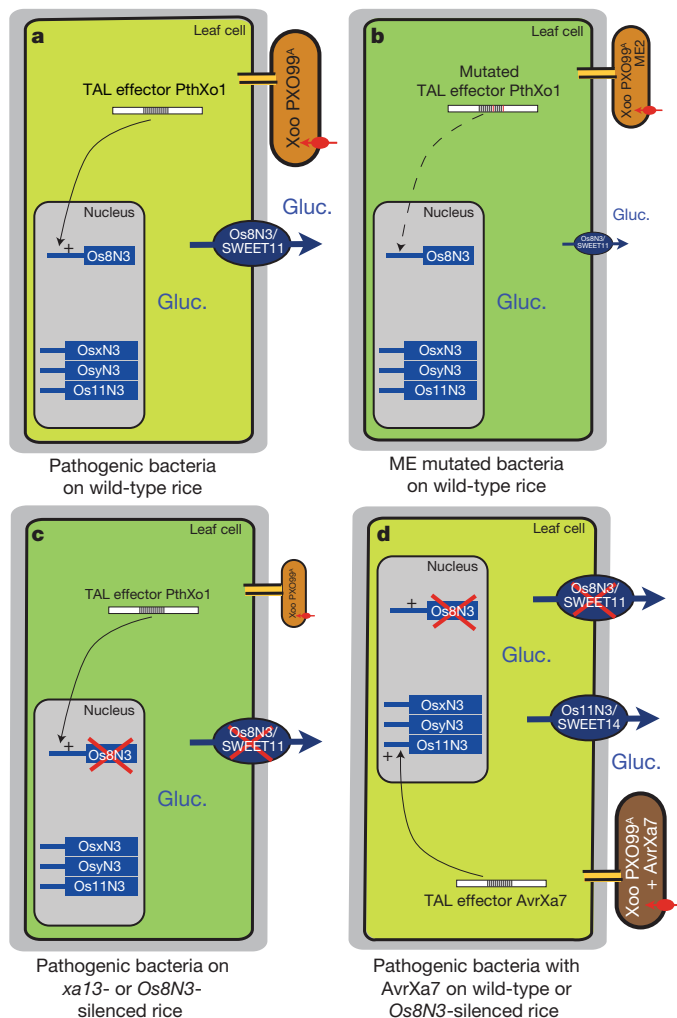


Figure 3 | Type-III-effector-specific induction of *OsSWEET11* to the plasma membrane of HEK293T cells (panel width = 61 μ m). **a**, Targeting of *OsSWEET11* to the plasma membrane of HEK293T cells (compare to Fig. 1a; significant above control in 4 of 6 experiments). Truncated *OsSWEET11* with premature stop codon at phenylalanine 205 (F205*) served as negative control (mean \pm s.d., $n > 10$). **b**, Co-expression of *OsSWEET11* with cytosolic FRET glucose sensor FLIPglu600 μ Δ 13V in HEK293T cells (compare to Fig. 1a). **c**, Glucose uptake (1 mM) mediated by *OsSWEET11* and *OsSWEET14* in oocytes (mean \pm s.d., $n \geq 7$). **d**, Enrichment of 5'-upstream *OsSWEET11* promoter DNA upon infection of rice with PXO99^A containing Flag-tagged PthXo1-2F. **e**, Efficient targeting of *OsSWEET11* to the plasma membrane of HEK293T cells (panel width = 61 μ m; mean \pm s.d.; $n = 2$). **f**, Co-expression of *OsSWEET14* with the cytosolic FRET glucose sensor FLIPglu600 μ Δ 13V in HEK293T cells (compare to Fig. 1a). Truncated *OsSWEET14* with a premature stop codon at phenylalanine 203 (F203*) served as negative control (mean \pm s.d., $n > 10$). **g**, Co-expression of *OsSWEET14* with ER-targeted FRET glucose sensor FLIPglu600 μ Δ 13V^{ER} in HEK293T cells (compare with Fig. 1b) (mean \pm s.d., $n > 10$). **h**, Concentration-dependent glucose uptake by *OsSWEET14* in oocytes (mean \pm s.d., $n \geq 7$). **i**, [¹⁴C]-efflux from glucose-injected oocytes mediated by *OsSWEET14* (50 nl of 50 mM glucose injected; mean \pm s.e., $n \geq 7$).



(Fig. 3h), mediating efflux in both HEK293T cells and oocytes (Fig. 3g, i). Our findings support a model that, besides inhibition of plant immunity, type III effectors and some TAL effectors can function specifically in diverting nutritional resources from the host^{34,35}.

Metazoan SWEETs as glucose transporters

SWEET homologues (SLC50) are also widespread in metazoan genomes and predicted to consist of seven transmembrane helices in a 3+1+3 configuration (Fig. 1j and Supplementary Figs 8 and 9). The *C. elegans* genome contains seven *SWEET* genes (*CeSWEET*), whereas the human genome contains a single homologue, which we name *HsSWEET1* (also called *RAG1API*). *CeSWEET1* mediated glucose accumulation in HEK293T cells when co-expressed with the sensor FLI1²Pglu700 μ Δ 6 (ref. 16), as well as efflux from the cytosol to the ER (Fig. 5a, b). Both N- and C-terminal GFP fusions of *CeSWEET1* were functional in cellular glucose uptake (Supplementary Fig. 15) and localized primarily to the Golgi, with lower levels at the plasma membrane of HEK293T cells (Fig. 5c, d). *CeSWEET1* mediated [¹⁴C]glucose and [¹⁴C]galactose uptake when expressed in oocytes (Fig. 5e, f). Similar to *OsSWEET14*, *CeSWEET1* glucose uptake did not saturate up to 50 mM, indicating that it is a low-affinity transporter (Fig. 5g). *CeSWEET1* expression in oocytes can also increase glucose efflux (Fig. 5h). RNAi inhibition of *CeSWEET1* affected fat accumulation in worms, compatible with a defect in cellular glucose efflux leading

Figure 4 | Model for the function of SWEET transporters in plant pathogenesis. **a**, The pathogenic Xoo strain PXO99^A injects TAL effector PthXo1 via the type III secretion system into rice cells. PthXo1 directly induces *OsSWEET11* leading to sugar efflux. Bacteria take up glucose and multiply. **b**, PXO99^A *pthXo1* mutant (PXO99^AME2) leads to loss of *OsSWEET11* induction and reduced bacterial growth (indicated as reduced size of bacterium). **c**, Mutation of the *OsSWEET11* effector binding element (EBE) leads to loss of PthXo1-mediated induction and reduced bacterial growth. **d**, Bacteria expressing effector AvrXa7 can circumvent loss of *OsSWEET11* induction by inducing *OsSWEET14*.

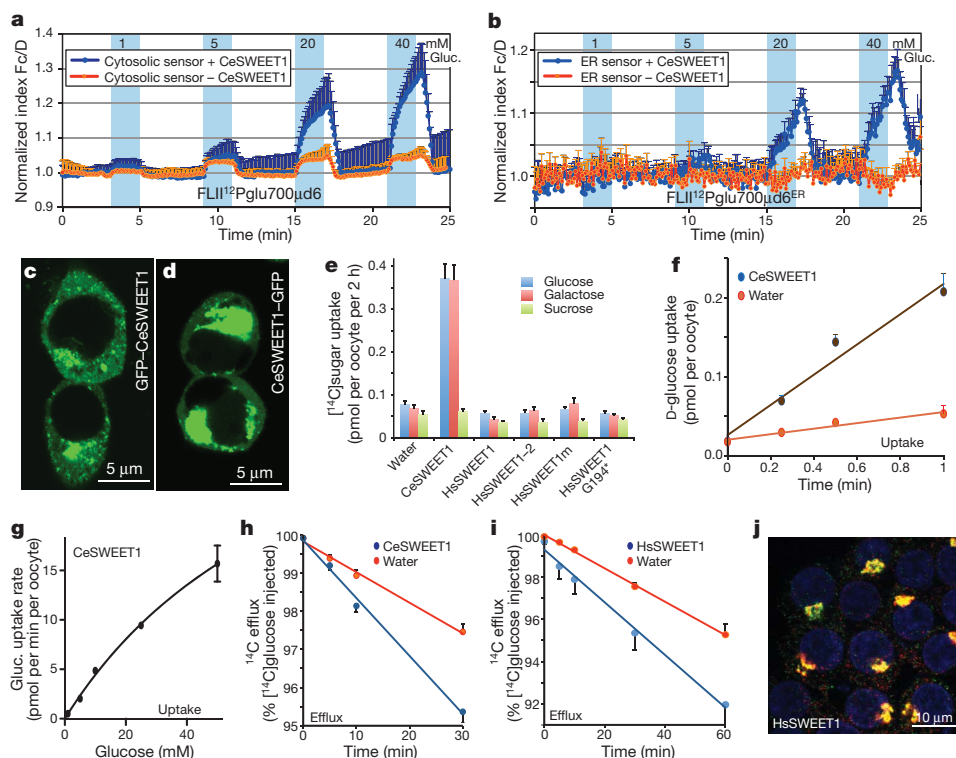


Figure 5 | Metazoan SWEET transporters. **a**, Detection of CeSWEET1 glucose uptake in HEK293T cells by co-expressing FLII¹²Pglu700μd6 (see legend under Fig. 1a) (mean + s.d., $n \geq 10$). **b**, Detection of CeSWEET1 glucose efflux into the ER of HEK293T cells by co-expressing FLII¹²Pglu700μd6 (see legend under Fig. 1b) (mean + s.d., $n \geq 10$). **c**, **d**, Localization of GFP-CeSWEET1 (**c**) and CeSWEET1-GFP (**d**) fusions in HEK293T cells. **e**, [¹⁴C]sugar uptake (5 mM) in *Xenopus* oocytes by CeSWEET1, HsSWEET1 (full length HsSWEET1; splice variant HsSWEET1-2; mean + s.d., $n \geq 8$), di-leucine motif mutant (HsSWEET1m) and deletion mutant G194*.

to lipid accumulation³⁶. Mutations in the homologue CiSWEET1/Ci-RGA from the sea squirt *Ciona* leads to early developmental defects, underlining the importance of SWEETs in metazoa³⁷.

The human homologue HsSWEET1 did not show significant glucose uptake in yeast and oocytes (Fig. 5e and Supplementary Figs 6 and 11). However, HsSWEET1 mediated weak efflux activity in oocytes (Fig. 5i). The efflux activity was not caused by unspecific leakiness of oocytes as efflux of other sugars was not increased in cells expressing HsSWEET1 or CeSWEET1 (Supplementary Fig. 16). Thus, HsSWEET1 either rectifies or, alternatively, might be involved in exocytosis. In contrast to the plant homologues, and compatible with vesicular efflux, HsSWEET1 localized to the Golgi of HEK293T cells with minimal presence at the plasma membrane (Fig. 5j and Supplementary Figs 17–19). Mutation of the potential di-leucine internalization motif at the C terminus³⁸ did not lead to increased plasma membrane localization or increased transporter activity (Fig. 5e and Supplementary Fig. 18). Expression data indicate ubiquitous expression throughout human tissues and cell lines, with highest expression in oviduct, epididymis and intestine (Supplementary Fig. 20). Immunolocalization data from the Human Protein Atlas are consistent with a localization in absorptive enterocytes^{39,40}. Moreover, mouse *MmSWEET1* expression was induced in the mammary gland during lactation (Supplementary Fig. 21). Localization is compatible with a function in supplying glucose to the Golgi for lactose synthesis and secretion⁴¹.

Our findings provide new insights into processes that involve sugar efflux from human cells. The human genome contains two additional classes of glucose transporters⁴². GLUTs are uniporters, whereas SGLTs are Na⁺-coupled co-transporters. GLUTs and SGLTs probably handle most of the uptake activities found in human cells. GLUT2 had

f, Time-dependent [¹⁴C]glucose uptake by CeSWEET1 in oocytes (mean + s.d., $n \geq 8$). **g**, Concentration-dependent [¹⁴C]glucose uptake by CeSWEET1 in oocytes (mean ± s.d., $n \geq 8$). **h**, Efflux measurements from oocytes expressing CeSWEET1 (mean ± s.e.; $n \geq 8$ cells; $P < 0.01$ after 5 min; 50 nM of 50 mM sugar injected). **i**, Efflux measurements from oocytes expressing HsSWEET1 (mean ± s.e.; $n \geq 8$ cells; $P < 0.05$). **j**, Immunolocalization of HsSWEET1 in HEK293T cells (merged channels: immuno-labelled HsSWEET1, red; Golgi marker, green; nuclei, blue).

originally been thought to be responsible for both import and efflux of glucose in liver and intestine. However, glucose efflux from GLUT2-null hepatocytes and GLUT2 knockout mice appeared unaffected^{2–4}. Oral glucose load of GLUT2 knockout mice resulted in normal rates of glucose appearance in the blood². Similarly, people affected with Fanconi-Bickel syndrome, caused by GLUT2 mutations⁴³, do not show abnormal carbohydrate ingestion, a process that requires efflux from intestinal cells⁴⁴. These findings led to the hypothesis for alternative efflux routes^{3,4}. HsSWEET1 is thus a candidate for the postulated alternative vesicular glucose efflux from the intestine and liver cells (Supplementary Fig. 22).

A new class of sugar transporters is described, members of which have been shown to function as uniporters and are thus able to support import and efflux of sugars from cells. SWEETs undoubtedly have many important native functions, including the supply of carbon skeletons and energy to the gametophyte in plants and cellular glucose efflux in animals. Our findings also support the model that in addition to the inhibition of plant immunity, type III effectors are involved in accessing nutritional resources of host plants^{34,35}. Notably, the founding member of the SWEET family, MtN3, was identified as a nodulin-specific EST in the legume *Medicago truncatula* and may have a role in symbiotic *Rhizobia*⁴⁵ nutrition. Knowledge of the full spectrum of pathogen effector molecules, and how they manipulate plant transport and metabolism to favour pathogen growth, will improve our understanding of host–pathogen interactions and may lead to new strategies for combating pathogen infections, which at the global scale lead to crop losses of over 10% annually⁴⁶. Moreover, analysis of the complete SWEET family may help to solve some of the mysteries of pollen nutrition, nectar production and carbon sequestration.

METHODS SUMMARY

Cell culture, transfection, image acquisition and FRET analysis were performed as described previously¹⁵. Yeast complementation and uptake assays were performed in EBV4000 (ref. 17). Tracer uptake and efflux assays were performed in *Xenopus* oocytes⁴⁷. *Arabidopsis* Col-0 plants were grown in growth chambers under 8 h light/16 h dark at 22 °C. qPCR was performed with gene-specific primers (Supplementary Table 1). See Methods for details.

Full Methods and any associated references are available in the online version of the paper at www.nature.com/nature.

Received 4 June; accepted 19 October 2010.

- Lalonde, S., Wipf, D. & Frommer, W. B. Transport mechanisms for organic forms of carbon and nitrogen between source and sink. *Annu. Rev. Plant Biol.* **55**, 341–372 (2004).
- Thorens, B., Guillaum, M. T., Beermann, F., Burcelin, R. & Jaquet, M. Transgenic reexpression of GLUT1 or GLUT2 in pancreatic β cells rescues GLUT2-null mice from early death and restores normal glucose-stimulated insulin secretion. *J. Biol. Chem.* **275**, 23751–23758 (2000).
- Stümpel, F., Burcelin, R., Jungermann, K. & Thorens, B. Normal kinetics of intestinal glucose absorption in the absence of GLUT2: evidence for a transport pathway requiring glucose phosphorylation and transfer into the endoplasmic reticulum. *Proc. Natl Acad. Sci. USA* **98**, 11330–11335 (2001).
- Hosokawa, M. & Thorens, B. Glucose release from GLUT2-null hepatocytes: characterization of a major and a minor pathway. *Am. J. Physiol. Endocrinol. Metab.* **E794–E801** (2002).
- Hesse, M., Pacini, E. & Willemsse, M. *The Tapetum: Cytology, Function, Biochemistry and Evolution* 1–152 (Springer, 2004).
- Bisseling, T., Dangl, J. L. & Schulze-Lefert, P. Next-generation communication. *Science* **324**, 691 (2009).
- Zhou, Y., Qu, H., Dibley, K. E., Offler, C. E. & Patrick, J. W. A suite of sucrose transporters expressed in coats of developing legume seeds includes novel pH-independent facilitators. *Plant J.* **49**, 750–764 (2007).
- Tang, D. J. et al. *Xanthomonas campestris* pv. *campestris* possesses a single gluconeogenic pathway that is required for virulence. *J. Bacteriol.* **187**, 6231–6237 (2005).
- Patrick, J. W. Solute efflux from the host at plant microorganism interfaces. *Aust. J. Plant Physiol.* **16**, 53–67 (1989).
- Aked, J. & Hall, J. L. The uptake of glucose, fructose and sucrose into the lower epidermis of leaf discs of pea (*Pisum sativum* L. cv. *Argenteum*). *New Phytol.* **123**, 271–276 (1993).
- Sutton, P. N., Henry, M. J. & Hall, J. L. Glucose, and not sucrose, is transported from wheat to wheat powdery mildew. *Planta* **208**, 426–430 (1999).
- Sutton, P. N., Gilbert, M. J., Williams, L. E. & Hall, J. L. Powdery mildew infection of wheat leaves changes host solute transport and invertase activity. *Physiol. Plant.* **129**, 787–795 (2007).
- Voegelé, R. T., Struck, C., Hahn, M. & Mendgen, K. The role of haustoria in sugar supply during infection of broad bean by the rust fungus *Uromyces fabae*. *Proc. Natl Acad. Sci. USA* **98**, 8133–8138 (2001).
- Aramemnon. Plant membrane protein database (<http://aramemnon.botanik.uni-koeln.de>) (2010).
- Takanaga, H. & Frommer, W. B. Facilitative plasma membrane transporters function during ER transit. *FASEB J.* **24**, 2849–2858 (2010).
- Takanaga, H., Chaudhuri, B. & Frommer, W. B. GLUT1 and GLUT9 as major contributors to glucose influx in HepG2 cells identified by a high sensitivity intramolecular FRET glucose sensor. *Biochim. Biophys. Acta* **1778**, 1091–1099 (2008).
- Wieczorke, R. et al. Concurrent knock-out of at least 20 transporter genes is required to block uptake of hexoses in *Saccharomyces cerevisiae*. *FEBS Lett.* **464**, 123–128 (1999).
- Bermejo, C., Haerizadeh, F., Takanaga, H., Chermak, D. & Frommer, W. B. Dynamic analysis of cytosolic glucose and ATP levels in yeast with optical sensors. *Biochem. J.* doi:10.1042/BJ20100946 (20 September 2010).
- Chaudhuri, B. et al. Protonophore- and pH-insensitive glucose and sucrose accumulation detected by FRET nanosensors in *Arabidopsis* root tips. *Plant J.* **56**, 948–962 (2008).
- Guan, Y. F. et al. RUPTURED POLLEN GRAIN1, a member of the MtN3/saliva gene family, is crucial for exine pattern formation and cell integrity of microspores in *Arabidopsis*. *Plant Physiol.* **147**, 852–863 (2008).
- Yang, B., Sugio, A. & White, F. F. Os8N3 is a host disease-susceptibility gene for bacterial blight of rice. *Proc. Natl Acad. Sci. USA* **103**, 10503–10508 (2006).
- Song, L. F., Zou, J. J., Zhang, W. Z., Wu, W. H. & Wang, Y. Ion transporters involved in pollen germination and pollen tube tip-growth. *Plant Signal. Behav.* **4**, 1193–1195 (2009).
- Engel, M. L., Holmes-Davis, R. & McCormick, S. Green sperm. Identification of male gamete promoters in *Arabidopsis*. *Plant Physiol.* **138**, 2124–2133 (2005).
- Ge, Y. X. et al. Partial silencing of the *NEC1* gene results in early opening of anthers in *Petunia hybrida*. *Mol. Genet. Genomics* **265**, 414–423 (2001).
- Ge, Y. X. et al. *NEC1*, a novel gene, highly expressed in nectary tissue of *Petunia hybrida*. *Plant J.* **24**, 725–734 (2000).
- Quirino, B. F., Reiter, W. D. & Amasino, R. D. One of two tandem *Arabidopsis* genes homologous to monosaccharide transporters is senescence-associated. *Plant Mol. Biol.* **46**, 447–457 (2001).
- Quirino, B. F., Normandy, J. & Amasino, R. M. Diverse range of gene activity during *Arabidopsis thaliana* leaf senescence includes pathogen-independent induction of defense-related genes. *Plant Mol. Biol.* **40**, 267–278 (1999).
- Ferrari, S. et al. Resistance to *Botrytis cinerea* induced in *Arabidopsis* by elicitors is independent of salicylic acid, ethylene, or jasmonate signaling but requires PHYTOALEXIN DEFICIENT3. *Plant Physiol.* **144**, 367–379 (2007).
- Yuan, M., Chu, Z., Li, X., Xu, C. & Wang, S. Pathogen-induced expression loss of function is the key factor in race-specific bacterial resistance conferred by a recessive R gene *xa13* in rice. *Plant Cell Physiol.* **50**, 947–955 (2009).
- Chu, Z. et al. Promoter mutations of an essential gene for pollen development result in disease resistance in rice. *Genes Dev.* **20**, 1250–1255 (2006).
- Chu, Z. et al. Targeting *xa13*, a recessive gene for bacterial blight resistance in rice. *Theor. Appl. Genet.* **112**, 455–461 (2006).
- Boch, J. et al. Breaking the code of DNA binding specificity of TAL-type III effectors. *Science* **326**, 1509–1512 (2009).
- Antony, G. et al. *xa13* recessive resistance to bacterial blight is defeated by the induction of disease susceptibility gene *Os11N3*. *Plant Cell* (in the press).
- Grant, S. R., Fisher, E. J., Chang, J. H., Mole, B. M. & Dangl, J. L. Subterfuge and manipulation: type III effector proteins of phytopathogenic bacteria. *Annu. Rev. Microbiol.* **60**, 425–449 (2006).
- Mansfield, J. W. From bacterial avirulence genes to effector functions via the hrp delivery system: an overview of 25 years of progress in our understanding of plant innate immunity. *Mol. Plant Pathol.* **10**, 721–734 (2009).
- Ashrafi, K. et al. Genome-wide RNAi analysis of *Caenorhabditis elegans* fat regulatory genes. *Nature* **421**, 268–272 (2003).
- Hamada, M., Wada, S., Kobayashi, K. & Satoh, N. *Ci-Rga*, a gene encoding an MtN3/saliva family transmembrane protein, is essential for tissue differentiation during embryogenesis of the ascidian *Ciona intestinalis*. *Differentiation* **73**, 364–376 (2005).
- Ibberson, M., Uldry, M. & Thorens, B. GLUTX1, a novel mammalian glucose transporter expressed in the central nervous system and insulin-sensitive tissues. *J. Biol. Chem.* **275**, 4607–4612 (2000).
- Berglund, L. et al. A gene-centric Human Protein Atlas for expression profiles based on antibodies. *Mol. Cell. Proteomics* **7**, 2019–2027 (2008).
- Human Protein Atlas. Small intestine [RAG1AP1] (http://www.proteinatlas.org/normal_unit.php?antibody_id=18095&mainannotation_id=1747049) (2010).
- Anderson, S. M., Rudolph, M. C., McManaman, J. L. & Neville, M. C. Key stages in mammary gland development. Secretory activation in the mammary gland: it's not just about milk protein synthesis! *Breast Cancer Res.* **9**, 204 (2007).
- Bioparadigms. SLC Tables (<http://www.bioparadigms.org/slc/intro.htm>) (2010).
- Santer, R. et al. Mutations in *GLUT2*, the gene for the liver-type glucose transporter, in patients with Fanconi-Bickel syndrome. *Nature Genet.* **17**, 324–326 (1997).
- Manz, F. et al. Fanconi-Bickel syndrome. *Pediatr. Nephrol.* **1**, 509–518 (1987).
- Udvardi, M. K., Yang, L.-J. O., Young, S. & Day, D. A. Sugar and amino acid transport across symbiotic membranes from soybean nodules. *Mol. Plant Microb. Int.* **3**, 334–340 (1990).
- Oerke, E. C. Crop losses to pests. *J. Agric. Sci.* **144**, 31–43 (2006).
- Hediger, M. A., Coady, M. J., Ikeda, T. S. & Wright, E. M. Expression cloning and cDNA sequencing of the Na⁺/glucose co-transporter. *Nature* **330**, 379–381 (1987).

Supplementary Information is linked to the online version of the paper at www.nature.com/nature.

Acknowledgements This work was made possible by grants from the Department of Energy (DE-FG02-04ER15542) and NIH (NIIDK; 1R01DK079109) to W.B.F., X.-Q.Q. was supported by The Carnegie Institution and the National Natural Science Foundation of China (NSFC; 30771288). NSF (IOS-0821801) and NIH (ZRO1GM06886-06A1) to M.B.M. and J.-G.K. was supported 50% by NIH and 50% by NSF. W.U. was supported in part by a NIH postdoctoral fellowship (F32GM083439-02). G.A. and F.F.W. were supported by grants from USDA NIFA (2007-35319-18103) and NSF Plant Genome (DBI-0820831).

Author Contributions W.B.F., S.L., M.B.M. and S.C.S. conceived and designed the experiments. L.-Q.C., B.-H.H., H.T., M.L.H., J.-G.K., X.-Q.Q., W.-J.G., W.U., B.C., G.A. and D.C. performed the experiments. W.B.F., S.L., M.B.M., G.A., F.F.W. and S.S. analysed the data. L.-Q.C. and W.B.F. wrote the manuscript.

Author Information Reprints and permissions information is available at www.nature.com/reprints. The authors declare no competing financial interests. Readers are welcome to comment on the online version of this article at www.nature.com/nature. Correspondence and requests for materials should be addressed to W.B.F. (wfrommer@carnegiescience.edu).

METHODS

qPCR and RT-PCR analysis. Total RNA was extracted from HepG2 or HEK293T cells using an RNeasy MINI kit (Qiagen), first strand cDNA was produced (New England Biolabs) and fragments of the predicted length were obtained by RT-PCR using a set of GLUT and SGLT primers published previously⁴⁸. Samples were separated on a 2% agarose gel. For samples inoculated by *Pseudomonas syringae* pv. *tomato* DC3000, total RNA was extracted from the leaves using Trizol reagent (Invitrogen). Real-time quantitative PCR (qPCR) was performed using HotStart-IT SYBR Green qPCR Master Mix (USB) according to the manufacturer's instructions on a 7300 PCR system (Applied Biosystems). Actin (*ACT8*) expression was used to normalize expression values in each sample; expression values were determined relative to the value of the sample infiltrated with 1 mM MgCl₂ buffer at each time point using the comparative 2^{-ΔΔCt} method⁴⁹. For samples infected by *G. cichoracearum* or *X. oryzae* pv. *oryzae*, qPCR assays were performed using a LightCycler 480 (Roche). For quantification, relative transcript levels for each gene were normalized to *ACT8* following the 2^{-ΔΔCt} method⁴⁹. Fold change was calculated relative to the untreated sample. Analysis was repeated twice independently. The observed induction is confirmed by microarray data (Genevestigator)⁵⁰.

Constructs. *AtSWEET1*, *AtSWEET8*, *OsSWEET11* and *OsSWEET14* ORFs were amplified by RT-PCR using specific primers from *Arabidopsis* and rice, respectively. First-strand cDNA from rice was provided by P. Ronald. SWEET ORFs were cloned into pDONR221 (Invitrogen) or pDONR221-f1 (ref. 51). Truncated versions of *AtSWEET1*-L198*, *OsSWEET11*-F205* and *OsSWEET14*-F203* were generated by introducing stop codons in transmembrane helix 7 by site-directed mutagenesis. All entry constructs were transferred to pDRf1-GW (ref. 52) and pOO2-GW (D. Loqué, unpublished results) by Gateway LR recombination reactions (a recombination reaction between an entry clone (containing attL) and a destination vector (containing attR), mediated by a host of recombination proteins to generate an expression clone (Entry Clone + Destination Vector Expression Clone)) (Invitrogen). *AtSWEET1* was cloned into p112-A1NE-GW for yeast co-transformation with FLN12-Pglu700μ86 in pDRf1-GW (ref. 18). Plasmid p112-A1NE-GW was generated by inserting a Gateway cassette into the SmaI restriction site of p112-A1NE⁵³. For radiotracer experiments, ORFs with stop codons for *AtSWEET1*, *OsSWEET11* and *OsSWEET14* were cloned into the pOO2-GW by Gateway LR recombination reactions.

The full-length splice variant *HsSWEET1-1* in pDNR-LIB was obtained from Open Biosystems (Clone ID 4076256). The truncated form *HsSWEET1*-G194* was generated by introducing a stop codon at leucine 194 by site-directed mutagenesis⁵⁴. Site-directed mutagenesis was used to mutate the putative internalization motif (*HsSWEET1*m Y216A, L218A, L219A). Products were cloned by *in vitro* BP recombination (Invitrogen) into pDONR221-f1, then mobilized into pOO2-GW by LR reactions. The shorter splice variant *HsSWEET1*-2 from Open Biosystems (Clone ID 3896154) in pCMV-SPORT6 was transferred into pOO2-GW by *in vitro* LR recombination. *CeSWEET1* (K02D7.5, Open Biosystems) was cloned into pOO2-GW using an LR reaction. The ORF of *AtSWEET1* without stop codon was cloned into the binary vector pX-YFP-GW by an LR reaction. *AtSWEET1*, *OsSWEET11*, *OsSWEET14*, *CeSWEET1* and *HsSWEET1* without stop codons were cloned into C-terminal GFP fusion vector pcDNA-DEST47 (Invitrogen) for localization studies. *AtSWEET1*, *CeSWEET1* and *HsSWEET1* with stop codons were cloned into the N-terminal GFP fusion vector pcDNA-DEST53 (Invitrogen) for localization studies. For yeast growth assays, ORFs were expressed from pDRf1-GW. For GFP localization in yeast, *AtSWEET1* and the truncated *AtSWEET1*Δ198 were cloned in vector pDR-GW-eGFP⁵².

FRET analysis. Mammalian cell culture, transfection, image acquisition and FRET analysis were performed as described^{15,55}.

Yeast expression. The strain EBY4000 (*hxt1* through -17Δ::loxP *gal2*Δ::loxP *stl1*Δ::loxP *agt1*Δ::loxP *ydl247w*Δ::loxP *yjr160c*Δ::loxP)¹⁷ was transformed with *AtSWEET1*, *AtSWEET8* and *HXT5* and grown on SD (synthetic deficient) medium supplemented with 2% maltose and auxotrophic requirements. For complementation growth assays, cells were grown overnight in liquid minimum medium to an optical density at 600 nm (OD₆₀₀) of ~0.6, then OD₆₀₀ was adjusted to ~0.2 with water. Serial dilutions (×1, ×5, ×25 and ×125) were plated on SD media containing either 2% maltose (as control) or 2% glucose plus respective auxotrophic requirements. Growth was documented by scanning (CanoScan, Canon) after 2–5 days at 30 °C.

Yeast uptake. Yeast cells were grown in SD medium supplemented with 2% maltose and auxotrophic markers. Cells were harvested at OD₆₀₀ 0.5–0.7 by centrifugation, and washed twice in ice-cold distilled water. Cell pellets were weighed after supernatant had been removed. Cells were re-suspended 5–10% (w/v) in 40 mM potassium phosphate buffer, pH 6.0. Cells were pre-incubated in potassium phosphate buffer for 5 min at 30 °C. For each reaction, 330 μl pre-warmed buffer containing 20 mM glucose (0.55 μCi D-[U-¹⁴C] glucose;

590 kBq μmol⁻¹, Amersham) was added to an equal volume of cells. 120 μl aliquot were withdrawn and transferred to ice-cold water. Cells were harvested by vacuum filtration onto a glassfibre filters (GF/C, Whatman), and washed twice in 10 ml ice-cold water. Filters were transferred to scintillation vials containing 5 ml Ultima Gold XR Scintillation liquid (Perkin Elmer). Radioactivity taken up by the cells was measured by liquid scintillation spectrometry. To determine the pH-dependence of *AtSWEET1* activity, 40 mM potassium phosphate uptake buffer at specified pH was used. Three independent transformants were used for each uptake experiment.

Xenopus oocytes isolation and RNA injection. After linearization of the pOO2 plasmids with MluI, capped cRNAs were synthesized *in vitro* by SP6 RNA polymerase using mMESSAGE mMACHINE kit (Ambion, Inc.). *Xenopus laevis* oocytes were provided by M. Goodman. Microinjection was carried out as described^{47,56}. 25–50 ng cRNA was injected into healthy looking oocytes (RNase-free water was used as control). Oocytes expressing *AtSWEET1* were maintained at 18 °C in modified Barth's saline (MBS, in mM: 88 NaCl, 1 KCl, 2.4 NaHCO₃, 0.82 MgSO₄, 0.33 Ca(NO₃)₂, 0.41 CaCl₂, 20 HEPES-Tris, pH 7.5) with 100 μM gentamycin, 100 U ml⁻¹ penicillin and 100 μM streptomycin solution for 2–3 d. Incubation buffer was changed every 24 h. For all other SWEETs, injected oocytes were maintained in L-15 oocyte medium (7.4 g l⁻¹ Leibovitz's L-15 medium (Sigma), 3.57 g l⁻¹ HEPES pH 7.5) with 100 mg l⁻¹ gentamycin.

Tracer uptake in Xenopus oocytes. The assay was performed with modification as described previously⁵⁷. Two days after injection, groups of 7–16 oocytes were transferred into tubes containing 200 μl Na-Ringer (in mM: 115 NaCl, 2 KCl, 1 MgCl₂, 1.8 CaCl₂, 10 HEPES-Tris, pH 7.5) 100 mg l⁻¹ gentamycin and D-glucose (4 μCi ml⁻¹ D-[¹⁴C(U)]-glucose; PerkinElmer), galactose (4 μCi ml⁻¹ D-[¹⁴C]-galactose; American Radiolabelled Chemicals) or sucrose (4 μCi ml⁻¹ D-[¹⁴C(U)]-sucrose; PerkinElmer). After incubation at 20 °C, cells were transferred to ice-cold Na-Ringer, washed three times, solubilized with 100 μl 1% (w/v) SDS, and measured individually.

Tracer efflux assay in Xenopus oocytes. Efflux was measured as described⁵⁸. Two days after cRNA injection, oocytes were injected with 50 nl solution containing 5, 10 or 50 mM D-glucose or sucrose with 0.18 μCi μl⁻¹ D-[¹⁴C(U)]glucose. Cells were immediately washed once in Na-Ringer (except *AtSWEET1* in MBS). At defined time points, reaction buffer (450 μl; except *AtSWEET1* in 950 μl) was removed for scintillation counting. Oocytes were solubilized with 1% SDS and analysed for retained radioactivity.

Analysis of glucose accumulation in yeast cells by FRET sensors. FRET measurements in yeast cells were performed as described¹⁸.

Plant growth and pathogen infection. *Arabidopsis* Col-0 plants were grown in growth chambers under 8 h light/14 h dark at 22 °C. Five-week-old leaves were infiltrated with a 1 mM MgCl₂ buffer, 2 × 10⁸ c.f.u. ml⁻¹ *Pseudomonas syringae* pv. *tomato* DC3000 or *Pseudomonas syringae* pv. *tomato* DC3000 *ΔhrpC* suspensions in 1 mM MgCl₂ using needleless syringes. Leaf samples were collected after 6, 12 and 24-h incubation in the light. *G. cichoracearum* inoculation was performed as described⁵⁹. Plants were placed in a 'settling tower' (cardboard box) and inoculated with *G. cichoracearum* spores by holding infected squash leaves over the settling tower and using compressed air (duster cans) to blow spores off of the squash leaves for settling onto *Arabidopsis* plants. Inoculum density was ~25–35 conidiospores per mm². After inoculation, plants were incubated for 1 h in a dark dew chamber, then transferred to a growth chamber at 16 h day length, 70% relative humidity.

Chromosome immune precipitation (ChIP) assay. Two-week-old rice seedlings (cultivar IR24) were infected with Flag-tagged effector *X. oryzae* pv. *oryzae* strains ME2(*avrXa7*-2F) or ME2(*pthXo1*-2F) at OD₆₀₀ 0.5. At 20 h after inoculation, ChIP complexes were prepared from 3.0 g of inoculated leaf tissue for each treatment. Immune complexes were prepared as described⁶⁰ with minor modifications. Effector-associated DNA complexes were immunoprecipitated using monoclonal Flag antibody (Sigma, 12 μg ml⁻¹). The same amount of mouse nonspecific IgG antibody was added in the control. Enriched DNA obtained was analysed by real-time qPCR using promoter and 3' UTR specific primers (provided Supplementary Table 3). Two microlitres of eluted DNA was used in each reaction. qPCR and analysis was performed as described above. Values are expressed as a ratio of the 2^{-ΔΔCt} value from Flag-tagged antibody precipitate complexes over the 2^{-ΔΔCt} value of the nonspecific IgG complexes. PXO99^ΔME2 (*avrXa7*-F2) served as control for effector specificity.

Alignment and phylogenetic analysis. Multiple alignment of SWEET amino acid sequences was performed with CLUSTALW⁶¹ using default parameters, and a phylogenetic analysis was performed using the software Mega V3.1. Bootstrapping was performed 1,000 times to obtain support values for each branch. For pair-wise comparison, multiple alignments of complete amino acid sequences were conducted using the Vector NTI advance 11.0.

Confocal microscopy. Fluorescence imaging of plants and mammalian cells expressing AtSWEET1-YFP, AtSWEET8-YFP, CeSWEET1-GFP, GFP-CeSWEET1, OsSWEET11-GFP and OsSWEET14-GFP was performed on a Leica TCS SP5 microscope. YFP was visualized by excitation with an argon laser at 514 nm and spectral detector set between 525 and 560 nm for the emission. GFP was visualized by excitation with an argon laser at 488 nm and spectral detector set between 500 and 545 nm for the emission. Specimens were observed with 40/0.75-1.25NA HCX PL APO CS objective.

48. Fehr, M., Takanaga, H., Ehrhardt, D. W. & Frommer, W. B. Evidence for high-capacity bidirectional glucose transport across the endoplasmic reticulum membrane by genetically encoded fluorescence resonance energy transfer nanosensors. *Mol. Cell. Biol.* **25**, 11102–11112 (2005).
49. Livak, K. J. & Schmittgen, T. D. Analysis of relative gene expression data using real-time quantitative PCR and the $2^{-\Delta\Delta CT}$ method. *Methods* **25**, 402–408 (2001).
50. Hruz, T. *et al.* Genevestigator v3: a reference expression database for the meta-analysis of transcriptomes. *Adv. Bioinformatics* **2008**, 420747 (2008).
51. Lalonde, S. *et al.* A membrane protein/signaling protein interaction network for Arabidopsis version AMPv2. *Front. Physiol.* doi:10.3389/fphys.2010.00024 (22 September 2010).
52. Loqué, D., Lalonde, S., Looger, L. L., von Wiren, N. & Frommer, W. B. A cytosolic trans-activation domain essential for ammonium uptake. *Nature* **446**, 195–198 (2007).
53. Riesmeier, J. W., Willmitzer, L. & Frommer, W. B. Isolation and characterization of a sucrose carrier cDNA from spinach by functional expression in yeast. *EMBO J.* **11**, 4705–4713 (1992).
54. Kunkel, T. A., Bebenek, K. & McClary, J. Efficient site-directed mutagenesis using uracil-containing DNA. *Methods Enzymol.* **204**, 125–139 (1991).
55. Hou, B. H., Takanaga, H., Griesbeck, O. & Frommer, W. B. Osmotic induction of calcium accumulation in human embryonic kidney cells detected with a high sensitivity FRET calcium sensor. *Cell Calcium* **46**, 130–135 (2009).
56. Ballatori, N., Wang, W., Li, L. & Truong, A. T. An endogenous ATP-sensitive glutathione S-conjugate efflux mechanism in *Xenopus laevis* oocytes. *Am. J. Physiol.* **270**, R1156–R1162 (1996).
57. Dettelle, D., Wiernsperger, N. & Devos, P. Metformin interaction with insulin-regulated glucose uptake, using the *Xenopus laevis* oocyte model expressing the mammalian transporter GLUT4. *Eur. J. Pharmacol.* **377**, 127–136 (1999).
58. Chernova, M. N. *et al.* Electrogenic sulfate/chloride exchange in *Xenopus* oocytes mediated by murine AE1 E699Q. *J. Gen. Physiol.* **109**, 345–360 (1997).
59. Vogel, J. & Somerville, S. Isolation and characterization of powdery mildew-resistant Arabidopsis mutants. *Proc. Natl Acad. Sci. USA* **97**, 1897–1902 (2000).
60. Haring, M. *et al.* Chromatin immunoprecipitation: optimization, quantitative analysis and data normalization. *Plant Methods* **3**, 11 (2007).
61. Thompson, J. D., Higgins, D. G. & Gibson, T. J. CLUSTAL W: improving the sensitivity of progressive multiple sequence alignment through sequence weighting, position-specific gap penalties and weight matrix choice. *Nucleic Acids Res.* **22**, 4673–4680 (1994).

Structure and control of the actin regulatory WAVE complex

Zhucheng Chen^{1,2}, Dominika Borek^{1*}, Shae B. Padrick^{1,2*}, Timothy S. Gomez³, Zoltan Metlagel^{1,2}, Ayman M. Ismail^{1,2}, Junko Umetani^{1,2}, Daniel D. Billadeau³, Zbyszek Otwinowski¹ & Michael K. Rosen^{1,2}

Members of the Wiskott–Aldrich syndrome protein (WASP) family control cytoskeletal dynamics by promoting actin filament nucleation with the Arp2/3 complex. The WASP relative WAVE regulates lamellipodia formation within a 400-kilodalton, hetero-pentameric WAVE regulatory complex (WRC). The WRC is inactive towards the Arp2/3 complex, but can be stimulated by the Rac GTPase, kinases and phosphatidylinositols. Here we report the 2.3-ångström crystal structure of the WRC and complementary mechanistic analyses. The structure shows that the activity-bearing VCA motif of WAVE is sequestered by a combination of intramolecular and intermolecular contacts within the WRC. Rac and kinases appear to destabilize a WRC element that is necessary for VCA sequestration, suggesting the way in which these signals stimulate WRC activity towards the Arp2/3 complex. The spatial proximity of the Rac binding site and the large basic surface of the WRC suggests how the GTPase and phospholipids could cooperatively recruit the complex to membranes.

Members of the WASP family are central to the control of cellular actin dynamics^{1–3}. These proteins receive information from multiple signalling pathways and respond by promoting the actin nucleating activity of the ubiquitous Arp2/3 complex. In this way, WASP proteins control actin assembly spatially and temporally in processes including cell migration, polarization, adhesion and vesicle trafficking.

The WASP family is defined by a conserved C-terminal VCA motif (for the verprolin-homology, central and acidic regions), which binds and activates the Arp2/3 complex^{1,3}. This element must be tightly regulated to ensure proper spatial and temporal control over actin assembly. In the best-understood family members, WASP and N-WASP, the VCA is autoinhibited by intramolecular interactions with a regulatory element termed the GTPase binding domain (GBD)⁴. Various ligands can bind to WASP/N-WASP simultaneously, and destabilize GBD–VCA contacts, leading to activation^{1,3}. Activation of all family members appears to be restricted to membranes. Superimposed on allosteric control and coupled with membrane recruitment, the activity of WASP proteins can be substantially increased by dimerization, or more generally oligomerization/clustering at membranes⁵.

Although WASP and N-WASP can exist independently in cells, WAVE proteins are constitutively associated with four additional proteins inside cells: Sra1/Cyfp1, Nap1/Hem-2, Abi and HSPC300 (refs 6 and 7). The components of this ~400-kDa pentamer, termed the WRC, have all been implicated in control of Arp2/3-complex-mediated actin assembly in a wide range of systems^{1,8}. Sra1/Cyfp1 also has a distinct role in translational control^{9,10}. WAVE proteins lack an inhibitory GBD, and the mechanism of VCA regulation within the WRC is not known. The WRC can be activated by a wide range of stimuli, including the Rac GTPase and acidic phospholipids^{6,11–14}, which appear to act cooperatively at the plasma membrane^{12,14}. Furthermore, components of the WRC can be phosphorylated at numerous positions (<http://www.phosphosite.org/proteinAction.do?id=7256&showAllSites=true>), with some modifications enhancing signalling activity^{14–19}. The

mechanisms by which ligands act individually and cooperatively to recruit and activate the WRC are not known.

Here we report the 2.3-Å crystal structure of the WRC and complementary biochemical and cell biological analyses. The combined data reveal how the WAVE VCA is inhibited within the complex and provide plausible mechanisms for WRC activation by Rac and phosphorylation, and for cooperative membrane recruitment by Rac and phospholipids. Our analyses provide an integrated picture of how the WRC orchestrates multiple signalling pathways to control actin polymerization at the plasma membrane.

Overall structure of the WRC

To facilitate crystallization of the WRC we genetically deleted the C-terminal proline-rich region and SH3 domain of Abi2, and replaced the proline-rich region of WAVE1 with an 18-residue linker. Sra1, Nap1 and HSPC300 were full-length. The resulting miniWRC is inactive towards the Arp2/3 complex but can be stimulated by Rac1-GMPPNP¹³.

Crystals of miniWRC contained one complex in the asymmetric unit and diffracted to 2.3 Å at a synchrotron light source. Phases were obtained by multiple isomorphous replacement with anomalous scattering (MIRAS) using preparations containing selenomethionine-labelled Sra1 and Nap1 (Supplementary Table 1). The final structure was refined to $R_{\text{work}}/R_{\text{free}} = 18.8\%/23.7\%$. MiniWRC has an elongated shape with approximate dimensions of 200 Å × 110 Å × 80 Å (Fig. 1). Two-dimensional class averages from electron micrographs of negatively stained miniWRC and full-length WRC are indistinguishable, and have dimensions similar to the crystal structure (Supplementary Fig. 1). The structure of miniWRC is thus probably a faithful representation of the structured elements of the WRC.

MiniWRC can be delineated into two subcomplexes: an Sra1:Nap1 dimer and a WAVE1:Abi2:HSPC300 trimer (Fig. 1). Sra1 and Nap1 have homologous structures (see below) and interact extensively to create an elongated pseudo-symmetric dimer, which forms a platform

¹Department of Biochemistry, University of Texas Southwestern Medical Center at Dallas, 5323 Harry Hines Boulevard, Dallas, Texas 75390, USA. ²Howard Hughes Medical Institute, UT Southwestern Medical Center, Dallas, Texas 75390, USA. ³Division of Oncology Research, Schulze Center for Novel Therapeutics, College of Medicine, Mayo Clinic, 200 First Street SW, Rochester, Minnesota 55905, USA. *These authors contributed equally to this work.

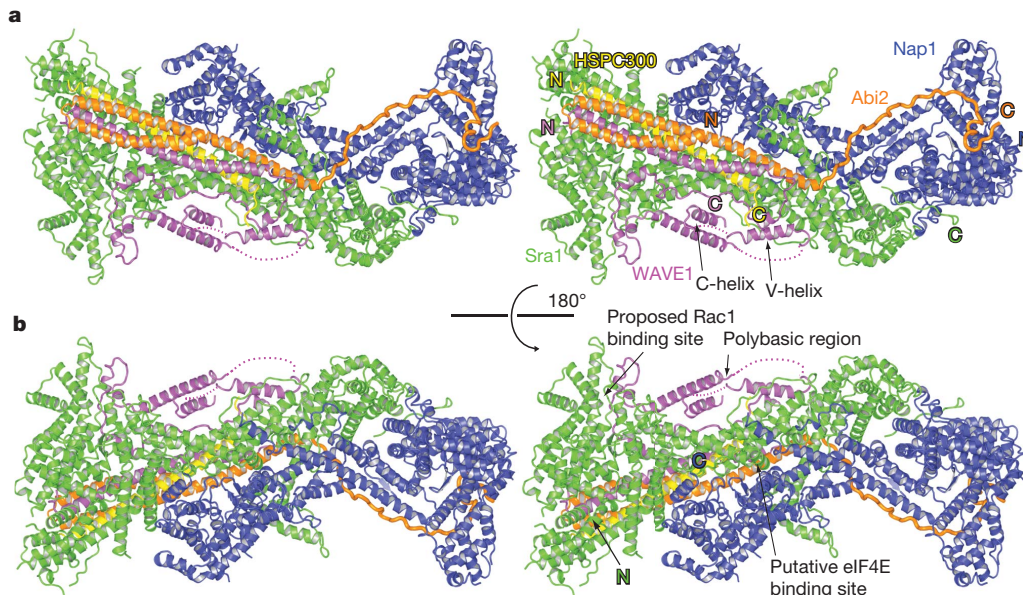


Figure 1 | MiniWRC structure. **a**, Stereo view of miniWRC. Sra1, Nap1, WAVE1, Abi2 and HSPC300 are green, blue, magenta, orange and yellow, respectively. The A-region (residues 545–559), α 6–V region linker (residues 185–485) and the sequence connecting V- and C-helices (residues 519–528) are

for the trimer (Supplementary Fig. 2). The amino (N)-terminal helix of Sra1 links to the rest of the complex through a flexible sequence that lacks electron density (residues 23–56), and contacts an adjacent molecule in the crystal lattice (Supplementary Fig. 3). The trimer contacts the Sra1:Nap1 dimer in a tripartite manner. A long four-helix bundle created by a helix from HSPC300 (residues 14–68), two helices from Abi2 (residues 1–39 and 43–112) and a helix from WAVE1 (residues 26–81) contacts Sra1 extensively and is aligned roughly parallel to the long axis of the dimer (Supplementary Figs 4 and 5). The most extensive contacts are made by HSPC300, which is sandwiched between Sra1 and Abi2:WAVE1 across the entire length of its helix. The ‘homeo-domain homologous region’ of Abi2 (residues 112–155)²⁰ adopts an extended conformation running around the rim of a large cavity on Nap1 (Supplementary Fig. 6). The carboxy (C) terminus of WAVE1, including the V- and the C-regions, forms an irregular, loosely packed chain that lies against a concave surface of Sra1 adjacent to the long side of the four-helix bundle. As detailed below, interactions of elements in the C terminus of WAVE1 with Sra1 and each other are central to the regulation of WRC activity.

The structure reveals that Sra1 and Nap1 have the same domain organization; their coordinates can be superimposed with a root mean square deviation (r.m.s.d.) of 6.9 Å for 681 C α atoms with Dali Z-score 17.9 (Supplementary Fig. 7)²¹. Thus, they belong to the same protein family despite their low sequence identity (13%). Homology between Sra1 and Nap1 is also supported by HHpred²², which showed additional human members of this family that are similar in size: KIAA1033/SWIP and Strumpellin, with similarity extending over their entire lengths. When analysed pairwise, SWIP is more similar to Sra1 and Strumpellin is more similar to Nap1. We and others recently reported that SWIP and Strumpellin form a pentameric complex (SHRC, for WASH Regulatory Complex) containing the proteins CCDC53 and Fam21, and another WASP family member, WASH^{23–25}. Within the SHRC the WASH VCA is inactive²³. HHpred and biochemical analyses suggest that CCDC53, and the N termini of WASH and Fam21 are structurally and/or functionally similar to HSPC300 and the N termini of WAVE and Abi, respectively²³. These many similarities, coupled with the similar overall shape of the WRC and SHRC²³, suggest that the SHRC is analogously organized as a large SWIP:Strumpellin platform bound to a helical bundle of

not observed in the electron density. The latter two are shown as dashed lines. **b**, 180° rotation about a horizontal axis from **a**. The polybasic region and the proposed Rac1 and eIF4E binding sites are indicated.

WASH:CCDC53:Fam21, with the WASH VCA sequestered by a similar mechanism.

We validated the structural organization observed in the crystal by replacing wild-type WAVE2 in HeLa cells with mutants targeting the trimer interface. Mutating the WAVE-HSPC300 interface (I50D/L54D_{WAVE2}) or the WAVE-HSPC300/Abi interface (L40D/F51D_{WAVE2}) appreciably decreased co-immunoprecipitation of WAVE2 with the four other components of the WRC (Supplementary Fig. 4), consistent with structural predictions.

Mechanism of WRC inhibition

The structure explains the inhibited nature of the WRC. In the complex, the WAVE1 VCA is bound by a conserved surface of Sra1 and residues 82–184 of WAVE1, which form five helices (α 2– α 6) and a series of intervening loops. This element of WAVE1 traces a meandering path across a concave surface of Sra1, and we refer to it as the ‘meander region’ (Fig. 2a and Supplementary Fig. 8). Contacts between the meander region and Sra1 bury over 2,100 Å² (about 56% of the total WAVE1–Sra1 interface; Supplementary Fig. 9). The meander sequence is highly conserved among the different WAVE proteins (Supplementary Fig. 8), as is its contact surface on Sra1, suggesting that its interactions and irregular structure are conserved.

The V- and C-regions of the VCA lie on the surface of Sra1 and form two amphipathic helices (residues 500–514 and 531–543, respectively) that also pack against α 2 and α 6 of WAVE1, respectively (Supplementary Fig. 10). The A-region of the VCA (residues 545–559) is probably disordered, given that it is not observed in the electron density. During actin filament nucleation, the V-region recruits an initial actin monomer to the nascent filament, while the C- and A-regions contribute binding energy and induce activating conformational changes in the Arp2/3 complex^{26,27}. The structure and complementary experimental data below indicate that sequestration of both the V- and the C-regions by Sra1 and the meander region of WAVE1 underlies VCA inhibition within the WRC.

Inhibition of the V-region involves a combination of contacts to actin-binding residues and induction of structure that is incompatible with actin binding (Fig. 2b). In the complex of the V-region of WAVE2 with actin²⁸, residues equivalent to 497–507 of WAVE1 form a helix that inserts into the cleft between actin subdomains 1 and 3.

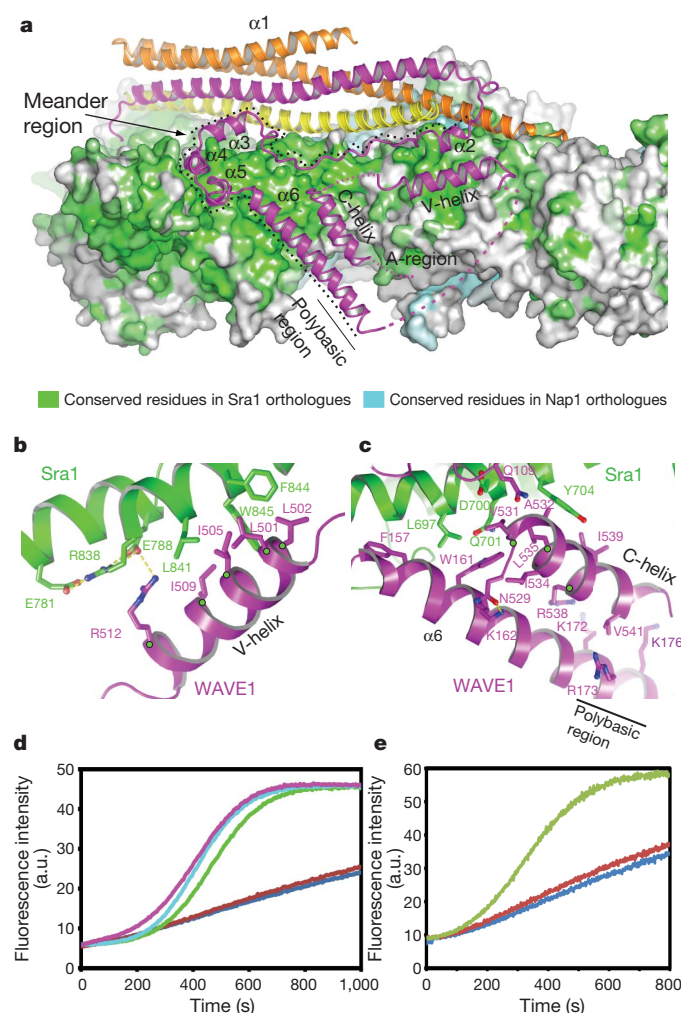


Figure 2 | Mechanism of WRC inhibition. **a**, MiniWRC (rotated 90° about a horizontal axis from Fig. 1a). Sra1 and Nap1 are grey surfaces with conserved residues shown in green and cyan, respectively. Ribbons coloured as in Fig. 1. The meander region is indicated with a dashed line. **b**, V-helix–Sra1 interactions. Hydrogen bonds are dashed. Green dots indicate actin-binding residues. **c**, C-helix binding interface. Green dots indicate residues important for Arp2/3 activation. **d**, **e**, Arp2/3-mediated pyrene–actin assembly assays of miniWRC mutants. a.u., arbitrary units. **d**, L697D/Y704D_{Sra1}-miniWRC (light blue), L841A/F844A/W845A_{Sra1}-miniWRC (green), with Sra1 mutated at C- and V-helix binding site, respectively; miniWRC (brown); control (dark blue); VCA (magenta). **e**, W161E/K162D_{WAVE1}-miniWRC (green), with WAVE1 mutated at the C-helix contact site; miniWRC (brown); control (dark blue).

Residues equivalent to 508–516 are extended, and the Ile 509 and Arg 512 equivalents contact actin. In the structure of miniWRC, the entire V-region is helical, and the side chains of Leu 501, Leu 502, Ile 505, Ile 509 and Arg 512 are buried in the Sra1 interface, making the V-region inaccessible to actin. Sequestration of the V-region is an important contributor to WRC inhibition, because mutating V-helix contact residues Leu 841, Phe 844 and Trp 845 of Sra1 constitutively activates miniWRC towards the Arp2/3 complex (L841A/F844A/W845A_{Sra1}-miniWRC, Fig. 2d), producing branched filaments (Supplementary Fig. 11).

The C-helix is also critical for activation of the Arp2/3 complex²⁹, because mutations of Val 531, Leu 535 or Arg 538 in the WAVE1 VCA reduce activity towards the Arp2/3 complex by at least half. In the miniWRC, the C-helix buries its hydrophobic face in the Sra1– $\alpha 6$ interface (Fig. 2c, Supplementary Figs 8 and 9). Intermolecularly, Val 531, Ala 532, Leu 535 and Ile 539 of WAVE1 make van der Waals contacts with Sra1. Intramolecularly, Val 531, Ile 534, Leu 535, Arg 538 and Val 541 of the C-helix pack against $\alpha 6$. Hence,

the structure shows that the WRC sequesters C-helix residues that are important for activation of the Arp2/3 complex, resulting in inhibition. This mechanism is also supported by mutagenesis: perturbing contacts of the C-helix with either Sra1 (L697D/Y704D_{Sra1}-miniWRC, Fig. 2d) or the $\alpha 6$ helix (W161E/K162D_{WAVE1}-miniWRC, Fig. 2e) leads to constitutive activation of the miniWRC *in vitro*. Additionally, replacement of wild-type WAVE2 with equivalent levels of the analogous $\alpha 6$ mutant (W160E/K161D_{WAVE2}) in HeLa cells does not alter the integrity of the complex (Supplementary Fig. 4), but causes a dramatic redistribution of actin, with loss of stress fibres and assembly of filaments at the cell periphery, again consistent with constitutive activation of the WRC (Fig. 3a).

Interactions of the VCA, and perhaps the structure of the entire meander–VCA element, appear to be highly cooperative, as perturbation of either the V- or C-region contacts produces WRC activity near that of the isolated VCA (Figs 2d and e).

Activation by Rac

Rac plays an important role in controlling actin polymerization and lamellipodia formation through activation of the WRC *in vivo*^{8,30,31}. Rac1 binds to recombinant WRC and activates it *in vitro* at micromolar concentrations under optimized assay conditions without disrupting the integrity of the complex^{13,14} (Supplementary Fig. 12). By analogy to the activation of WASP by Cdc42 (ref. 4), we reasoned that removing the VCA from the WRC would increase its affinity for Rac1. Indeed, in pull-down assays immobilized GST–Rac1:GMPPNP (a GTP analogue) bound a VCA-deleted WRC (Δ WRC) to a greater extent than miniWRC (Supplementary Fig. 13). Using equilibrium dialysis we measured a dissociation constant $K_D = 1–2 \mu\text{M}$ for Δ WRC. MiniWRC bound Rac with lower affinity, having $K_D = 7–10 \mu\text{M}$ (Fig. 3b). The constitutively active L697D/Y704D_{Sra1}-miniWRC (Fig. 3b) had affinity similar to that of Δ WRC, consistent with the idea that sequestration of the VCA motif competes with Rac1 binding. These results imply that Rac1 binds to the body of the WRC competitively with the VCA (either directly or indirectly), leading to activation of the complex.

To define the Rac1 interaction surface better, we searched for Δ WRC mutants with defects in Rac1 binding. Examination of the structure of WRC identified several conserved surface patches. Mutations L697D/Y704D, L841A/F844A/W845A or E250K/Q399A of Sra1 did not perturb the binding of Δ WRC to Rac1 (data not shown). However, Sra1 mutations C179R, R190D, M632D and E434K/F626A severely impaired binding of Δ WRC to Rac1 without altering the integrity of the recombinant complex (Fig. 3b and Supplementary Fig. 13). These highly conserved Sra1 residues are located in a patch adjacent to $\alpha 4–\alpha 6$ of the WAVE1 meander region (Fig. 3c and Supplementary Fig. 14). Furthermore, truncation of $\alpha 6$ ($\Delta 154_{\text{WAVE1}}$ -WRC) also decreases Rac1 binding (Fig. 3c and Supplementary Fig. 13), suggesting that the helix or adjacent parts of the meander may contact the bound GTPase directly or stabilize its interaction sites on Sra1. These data implicate a Rac1 binding site on the WRC involving an Sra1 surface and perhaps part of the meander region of WAVE1. Interactions of Rac1 could then trigger conformational changes in the meander region and/or its contact site on Sra1. Because the meander appears to cooperatively stabilize the V- and C-regions of WAVE1 (see above), these perturbations could drive WRC activation by causing release of the VCA.

Activation by phosphorylation

In cells, phosphorylation of the meander region modulates WRC activity. Several groups report that phosphorylation of the strictly conserved Tyr 150 of WAVE2 (Tyr 151 in WAVE1 and WAVE3) by the Abl kinase is important for WRC-mediated actin assembly and lamellipodia formation^{15–17}. Additionally, phosphorylation of WAVE Tyr 125 by Src or Thr 138 by Cdk5 alters cellular actin dynamics^{18,19}.

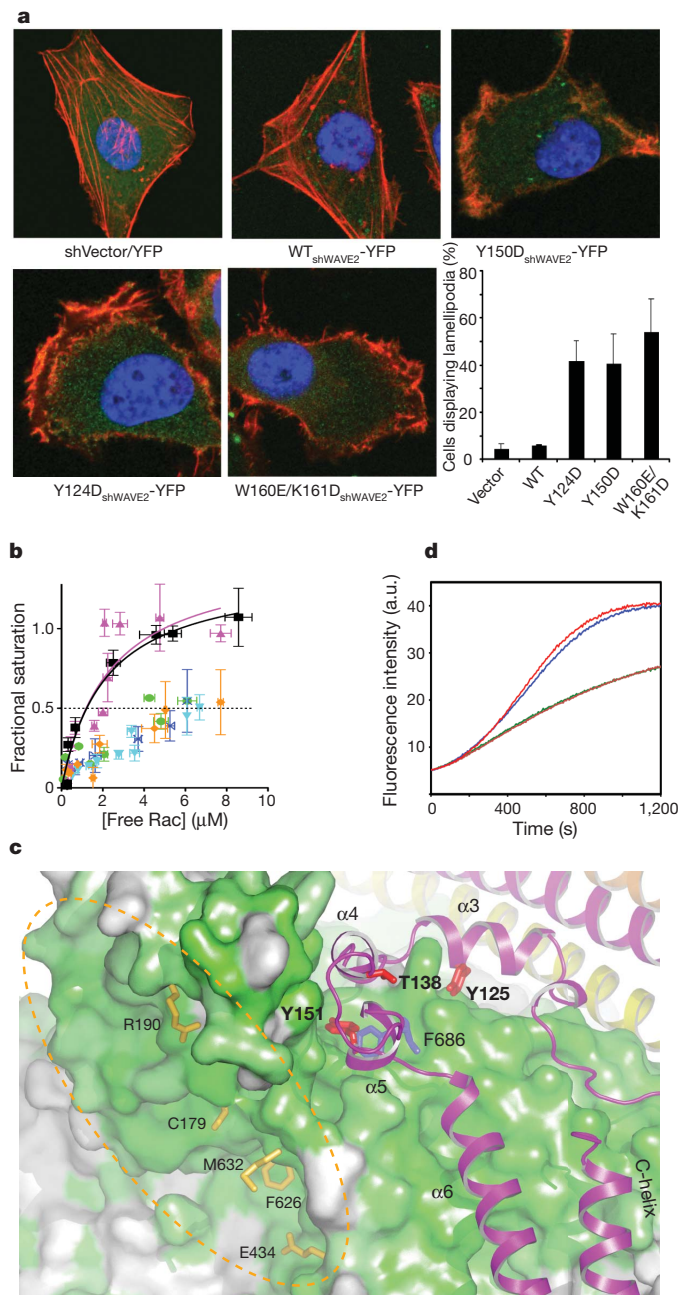


Figure 3 | Mechanisms of WRC activation by Rac1 and phosphorylation. **a**, HeLa cells were transfected with shVector-yellow fluorescent protein (YFP) control, or vectors simultaneously suppressing WAVE2 and expressing shRNA-resistant YFP-tagged WAVE2 proteins (green) and scored blindly for lamellipodial phenotype. F-actin is visualized with phalloidin (red). Error bars in lower right panel show the standard deviation for at least three independent measurements. **b**, Fractional saturation of WRC versus free Rac1-GMPPNP measured by equilibrium dialysis. Error bars indicate the standard deviation in at least two independent measurements. K_D is estimated from Rac concentration at 50% saturation; curves are binding isotherms to guide the eye. Pink uptriangle, ΔWRC (containing WAVE1(1–186)); black square, L697D/Y704D_{Sra1}-miniWRC; gold diamond, miniWRC; green circle, E434K/F626A_{Sra1}-ΔWRC; blue cross, R190D_{Sra1}-ΔWRC; cyan downtriangle, Δ154_{WAVE1}-WRC (containing WAVE1(1–154)). **c**, WAVE1 meander region. Sra1 residues involved in binding Rac1 and WAVE1 Y151 are gold and blue sticks, respectively. The dashed oval indicates the proposed Rac1-binding surface. Phosphorylated WAVE1 residues Tyr 125, Thr 138 and Tyr 151 are red sticks. **d**, Arp2/3-mediated pyrene-actin assembly assays with miniWRC (green) or miniWRC containing Y151E_{WAVE1} (blue) or F686E_{Sra1} (red). The control assay (orange) lacked WRC.

Tyr 151 of WAVE1 is located in the $\alpha 5$ – $\alpha 6$ loop of the meander region, and is buried in a hydrophobic pocket formed by Sra1 and WAVE1 (Fig. 3c and Supplementary Fig. 9). Phosphorylation of Tyr 151 would thus disrupt the contacts between the meander region and Sra1, leading to destabilization of the C-helix of the VCA motif and WRC activation. To test this idea, we reconstituted a miniWRC containing a phospho-mimicking Y151E mutation *in vitro*, and generated the analogous full-length WRC in HeLa cells using a knock-down/re-expression strategy. Consistent with the structural predictions, the mutant complexes displayed high actin assembly activity both *in vivo* and *in vitro* (Fig. 3a and d). Mutation of the Y151-binding pocket in Sra1 (F686E_{Sra1}-miniWRC) equivalently activates the WRC (Fig. 3d).

Tyr 125 of WAVE1 is also strictly conserved from animals to plants (Supplementary Fig. 8). This residue is located in $\alpha 3$ and its side chain packs against Gln 685 and makes a hydrogen bond to Asp 689 of Sra1 (Fig. 3c and Supplementary Fig. 9). Phosphorylation of Tyr 125 should disrupt the contact with Asp 689, and could destabilize the meander region of WAVE1, leading to release of the VCA. Consistent with this, replacement of WAVE2 with a Y124D mutant in cells increased lamellipodia formation (Fig. 3a). Thr 138 of WAVE1 makes intramolecular contacts with $\alpha 4$ and $\alpha 5$; its hydroxyl group is part of a network of hydrogen bonds that span these secondary elements (Fig. 3c and Supplementary Fig. 9). Phosphorylation of Thr 138 may thus also perturb the structure of the meander region, again contributing to activation of the WRC^{18,19}.

Together, the data suggest that, analogous to Rac1 activation, phosphorylation could destabilize the meander region and/or its interactions with Sra1, leading to release of the VCA and activation of the WRC.

Discussion

The WRC is typically densely clustered at its sites of action in cells. This is believed to be necessary for spatially restricted actin assembly during, for example, polarized cell movement¹. Clustering is mediated by the combined actions of phosphoinositide lipids and Rac, as well as various SH3-containing proteins^{1,3}. The polybasic region of WAVE2 (equivalent to residues 172–184 of WAVE1) can bind phosphoinositide lipids *in vitro*, and is essential for membrane recruitment of the WRC and formation of lamellipodia in cells¹². Surface electrostatic calculations show that the face containing the WAVE1:Abi2:HSPC300 four-helix bundle is negatively charged (Fig. 4a), whereas much of the face of the complex adjacent to the polybasic region is positively charged (Fig. 4b). This polar distribution suggests that when the WRC is recruited to the plasma membrane, the side covered by the four-helix bundle is exposed to the cytoplasm, and the opposite side contacts the membrane. In this orientation, Rac would bind approximately to the side of the WRC (Fig. 4c), and then its C-terminal isoprene group, the polybasic region of WAVE and the basic surface of the Sra1/Nap1 dimer could all be directed towards the plasma membrane. The meander region and the VCA motif of WAVE would face the cytoplasm, making them accessible to other regulators (for example, kinases), and to the Arp2/3 complex and actin. This organization would allow simultaneous phosphoinositide and Rac binding, cooperatively recruiting the WRC to membranes and enhancing allosteric activation. Self-association of the WRC at membranes¹⁴, and consequent enhanced activity⁵, could be mediated by intercomplex binding of the N-terminal helix of Sra1 with the WAVE/Abi/HSPC300 trimer, as observed in the crystal lattice (Supplementary Fig. 3).

Sra1 was recently reported to support translation inhibition through simultaneous binding to the translational regulator FMRP and the translation initiation factor eIF4E^{9,10}. However, the putative mode of eIF4E binding is incompatible with the WRC structure (Fig. 1b, Supplementary Fig. 15). Thus, eIF4E may bind to isolated Sra1, but not the WRC, consistent with the finding that eIF4E co-immunoprecipitates with Sra1 but not WAVE⁹. These observations

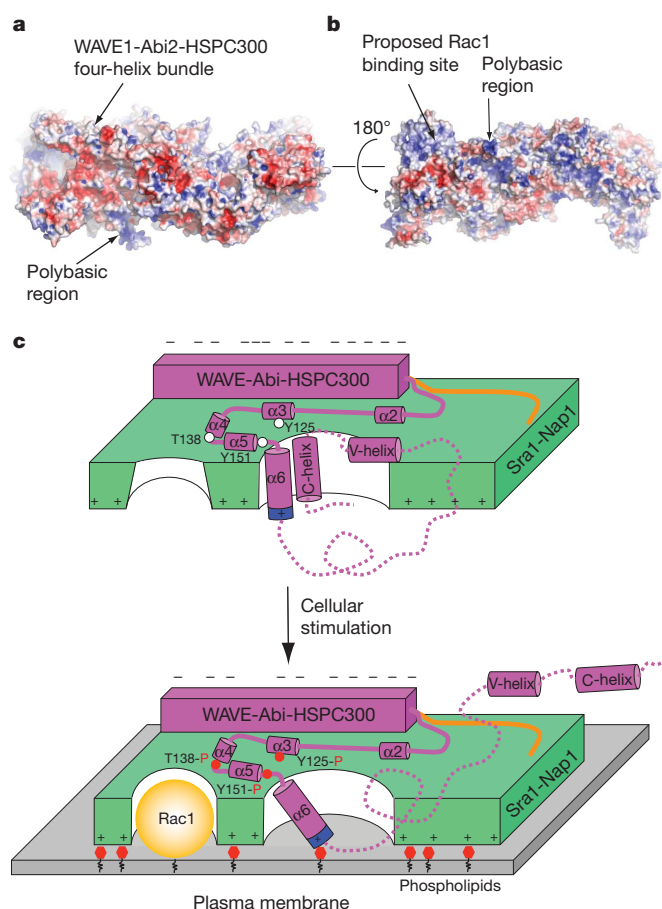


Figure 4 | Model for cooperative membrane recruitment and activation of the WRC. **a, b**, Electrostatic surface of miniWRC (-5 kT per electron (red) to $+5$ kT per electron (blue)), oriented as in Fig. 1a and b, respectively. **c**, Schematic illustrating proposed WRC orientation at the plasma membrane and cooperative recruitment and activation by Rac and phospholipids. Plus and minus signs indicate regions of positive and negative surface charge. Phosphorylation sites in WAVE1 meander are indicated in red. Disordered elements of WAVE1 are indicated with dotted purple lines. It remains unclear what portions of the meander are disrupted by different stimuli.

suggest that Sra1 may partition between the WRC, which regulates actin dynamics, and a free (or alternatively complexed) state that regulates translation. Similar arguments have also been made regarding different pools of Nap1 (ref. 32) and Abi (ref. 33). Interestingly, defects in Sra1 or its ligands in both pathways—protocadherin-10, which binds the WRC³⁴, and FMRP—are implicated in autism and other mental disorders^{35,36}, suggesting that an appropriate balance of these pathways or their joint action may be needed for proper neuronal development and function. Future studies of the intact WRC and its separate components will reveal how this system coordinates multiple processes in normal and abnormal cellular function.

METHODS SUMMARY

Sra1, Nap1, WAVE1, Abi2 and HSPC300 were overexpressed separately, partially purified, assembled into an Sra1:Nap1 dimer and a WAVE1/Abi2/HSPC300 trimer, respectively, and then assembled into the miniWRC pentamer. Further purification produced homogeneous samples. Crystals of miniWRC were obtained by hanging-drop vapour diffusion at 4°C . All the data sets were collected at the ID-19 beamline (Advanced Photon Source) and processed with the HKL3000 suite³⁷ and CCP4 suites³⁸. Experimental phases were determined from selenium-MIRAS data collected on samples containing either SeMet-Sra1 or SeMet-Nap1, and analysed using ShelXD³⁹. Phases were improved using MLPHARE⁴⁰ and Parrot⁴¹. The atomic model of the complex was built using Buccaneer⁴² and Coot⁴³, and refined using Refmac 5 (ref. 44). Equilibrium dialysis was done at room temperature and protein concentrations were determined using Deep Purple gel staining (GE Healthcare). Actin polymerization and

GST-Rac1 pull-down assays were performed as described previously¹³. HeLa cells were grown directly on coverslips, fixed in 4% paraformaldehyde, and prepared for immunofluorescence as described²⁵.

Full Methods and any associated references are available in the online version of the paper at www.nature.com/nature.

Received 18 April; accepted 25 October 2010.

1. Takenawa, T. & Suetsugu, S. The WASP-WAVE protein network: connecting the membrane to the cytoskeleton. *Nature Rev. Mol. Cell Biol.* **8**, 37–48 (2007).
2. Pollitt, A. Y. & Insall, R. H. WASP and SCAR/WAVE proteins: the drivers of actin assembly. *J. Cell Sci.* **122**, 2575–2578 (2009).
3. Padrick, S. B. & Rosen, M. K. Physical mechanisms of signal integration by WASP family proteins. *Annu. Rev. Biochem.* **79**, 707–735 (2010).
4. Kim, A. S., Kakalis, L. T., Abdul-Manan, N., Liu, G. A. & Rosen, M. K. Autoinhibition and activation mechanisms of the Wiskott-Aldrich syndrome protein. *Nature* **404**, 151–158 (2000).
5. Padrick, S. B. *et al.* Hierarchical regulation of WASP/WAVE proteins. *Mol. Cell* **32**, 426–438 (2008).
6. Eden, S., Rohatgi, R., Podtelejnikov, A. V., Mann, M. & Kirschner, M. W. Mechanism of regulation of WAVE1-induced actin nucleation by Rac1 and Nck. *Nature* **418**, 790–793 (2002).
7. Stovold, C. F., Millard, T. H. & Machesky, L. M. Inclusion of Scar/WAVE3 in a similar complex to Scar/WAVE1 and 2. *BMC Cell Biol.* **6**, 11 (2005).
8. Vartiainen, M. K. & Machesky, L. M. The WASP-Arp2/3 pathway: genetic insights. *Curr. Opin. Cell Biol.* **16**, 174–181 (2004).
9. Napoli, I. *et al.* The fragile X syndrome protein represses activity-dependent translation through CYFIP1, a new 4E-BP. *Cell* **134**, 1042–1054 (2008).
10. Schenck, A. *et al.* CYFIP/Sra-1 controls neuronal connectivity in *Drosophila* and links the Rac1 GTPase pathway to the fragile X protein. *Neuron* **38**, 887–898 (2003).
11. Kobayashi, K. *et al.* p140Sra-1 (specifically Rac1-associated protein) is a novel specific target for Rac1 small GTPase. *J. Biol. Chem.* **273**, 291–295 (1998).
12. Oikawa, T. *et al.* PtdIns(3,4,5)P3 binding is necessary for WAVE2-induced formation of lamellipodia. *Nature Cell Biol.* **6**, 420–426 (2004).
13. Ismail, A. M., Padrick, S. B., Chen, B., Umetani, J. & Rosen, M. K. The WAVE regulatory complex is inhibited. *Nature Struct. Mol. Biol.* **16**, 561–563 (2009).
14. Lebensohn, A. M. & Kirschner, M. W. Activation of the WAVE complex by coincident signals controls actin assembly. *Mol. Cell* **36**, 512–524 (2009).
15. Sossey-Alaoui, K., Li, X. & Cowell, J. K. c-Abl-mediated phosphorylation of WAVE3 is required for lamellipodia formation and cell migration. *J. Biol. Chem.* **282**, 26257–26265 (2007).
16. Stuart, J. R., Gonzalez, F. H., Kawai, H. & Yuan, Z. M. c-Abl interacts with the WAVE2 signaling complex to induce membrane ruffling and cell spreading. *J. Biol. Chem.* **281**, 31290–31297 (2006).
17. Leng, Y. *et al.* Abelson-interactor-1 promotes WAVE2 membrane translocation and Abelson-mediated tyrosine phosphorylation required for WAVE2 activation. *Proc. Natl Acad. Sci. USA* **102**, 1098–1103 (2005).
18. Miyamoto, Y., Yamauchi, J. & Tanoue, A. Cdk5 phosphorylation of WAVE2 regulates oligodendrocyte precursor cell migration through nonreceptor tyrosine kinase Fyn. *J. Neurosci.* **28**, 8326–8337 (2008).
19. Ardern, H. *et al.* Src-dependent phosphorylation of Scar1 promotes its association with the Arp2/3 complex. *Cell Motil. Cytoskeleton* **63**, 6–13 (2006).
20. Dai, Z. & Pendergast, A. M. Abi-2, a novel SH3-containing protein interacts with the c-Abl tyrosine kinase and modulates c-Abl transforming activity. *Genes Dev.* **9**, 2569–2582 (1995).
21. Holm, L., Kaariainen, S., Rosenstrom, P. & Schenkel, A. Searching protein structure databases with DALI Lite v.3. *Bioinformatics* **24**, 2780–2781 (2008).
22. Soding, J., Biegert, A. & Lupas, A. N. The HHpred interactive server for protein homology detection and structure prediction. *Nucleic Acids Res.* **33**, 244–248 (2005).
23. Jia, D. *et al.* WASH and WAVE actin regulators of the Wiskott-Aldrich syndrome protein (WASP) family are controlled by analogous structurally related complexes. *Proc. Natl Acad. Sci. USA* **107**, 10442–10447 (2010).
24. Derivery, E. *et al.* The Arp2/3 activator WASH controls the fission of endosomes through a large multiprotein complex. *Dev. Cell* **17**, 712–723 (2009).
25. Gomez, T. S. & Billadeau, D. D. A. FAM21-containing WASH complex regulates retromer-dependent sorting. *Dev. Cell* **17**, 699–711 (2009).
26. Goley, E. D., Rodenbusch, S. E., Martin, A. C. & Welch, M. D. Critical conformational changes in the Arp2/3 complex are induced by nucleotide and nucleation promoting factor. *Mol. Cell* **16**, 269–279 (2004).
27. Marchand, J. B., Kaiser, D. A., Pollard, T. D. & Higgs, H. N. Interaction of WASP/Scar proteins with actin and vertebrate Arp2/3 complex. *Nature Cell Biol.* **3**, 76–82 (2001).
28. Chereau, D. *et al.* Actin-bound structures of Wiskott-Aldrich syndrome protein (WASP)-homology domain 2 and the implications for filament assembly. *Proc. Natl Acad. Sci. USA* **102**, 16644–16649 (2005).
29. Panchal, S. C., Kaiser, D. A., Torres, E., Pollard, T. D. & Rosen, M. K. A conserved amphipathic helix in WASP/Scar proteins is essential for activation of Arp2/3 complex. *Nature Struct. Biol.* **10**, 591–598 (2003).
30. Stradal, T. E. *et al.* Regulation of actin dynamics by WASP and WAVE family proteins. *Trends Cell Biol.* **14**, 303–311 (2004).
31. Steffen, A. *et al.* Sra-1 and Nap1 link Rac to actin assembly driving lamellipodia formation. *EMBO J.* **23**, 749–759 (2004).
32. Weiner, O. D. *et al.* Hem-1 complexes are essential for Rac activation, actin polymerization, and myosin regulation during neutrophil chemotaxis. *PLoS Biol.* **4**, e38 (2006).

33. Ryu, J. R., Echarrri, A., Li, R. & Pendergast, A. M. Regulation of cell-cell adhesion by Abi/Diaphanous complexes. *Mol. Cell. Biol.* **29**, 1735–1748 (2009).
34. Nakao, S., Platek, A., Hirano, S. & Takeichi, M. Contact-dependent promotion of cell migration by the OL-protocadherin-Nap1 interaction. *J. Cell Biol.* **182**, 395–410 (2008).
35. Nowicki, S. T. *et al.* The Prader-Willi phenotype of fragile X syndrome. *J. Dev. Behav. Pediatr.* **28**, 133–138 (2007).
36. Stefansson, H. *et al.* Large recurrent microdeletions associated with schizophrenia. *Nature* **455**, 232–236 (2008).
37. Minor, W., Cymborowski, M., Otwinowski, Z. & Chruszcz, M. HKL-3000: the integration of data reduction and structure solution—from diffraction images to an initial model in minutes. *Acta Crystallogr. D* **62**, 859–866 (2006).
38. Dodson, E. J., Winn, M. & Ralph, A. Collaborative Computational Project number 4: providing programs for protein crystallography. *Methods Enzymol.* **277**, 620–633 (1997).
39. Sheldrick, G. M. A short history of SHELX. *Acta Crystallogr. A* **64**, 112–122 (2008).
40. Otwinowski, Z. M. W. Processing of X-ray diffraction data collected in oscillation mode. *Methods Enzymol.* **276**, 307–326 (1997).
41. Zhang, K. Y., Cowtan, K. & Main, P. Combining constraints for electron-density modification. *Methods Enzymol.* **277**, 53–64 (1997).
42. Cowtan, K. The Buccaneer software for automated model building. 1. Tracing protein chains. *Acta Crystallogr. D Biol. Crystallogr.* **62**, 1002–1011 (2006).
43. Emsley, P. & Cowtan, K. Coot: model-building tools for molecular graphics. *Acta Crystallogr. D* **60**, 2126–2132 (2004).
44. Murshudov, G. N., Vagin, A. A. & Dodson, E. J. Refinement of macromolecular structures by the maximum-likelihood method. *Acta Crystallogr. D* **53**, 240–255 (1997).

Supplementary Information is linked to the online version of the paper at www.nature.com/nature.

Acknowledgements We thank B. Chen for providing samples of full-length WRC and VCA polypeptide for electron microscopy and some biochemical analyses, C. Pak for helping with the total internal reflection fluorescence experiment, D. Tomchick and C. Brautigam for technical assistance and N. Grishin for assistance with sequence analysis and discussion. Research was supported by fellowships from the Cancer Research Institute and the NIH (1F32-GM06917902) to Z.C. and S.B.P., respectively, an Allergic Diseases Training grant (AI07047) to T.S.G., grants from the NIH to D.D.B. (R01-AI065474), Z.O. (R01-GM053163) and M.K.R. (R01-GM056322), a grant from the Welch Foundation to M.K.R. (I-1544) and the Howard Hughes Medical Institute. D.D.B. is a Leukemia and Lymphoma Society Scholar. Use of the Argonne National Laboratory Structural Biology Center beamlines at the Advanced Photon Source was supported by the US DOE under contract DE-AC02-06CH11357.

Author Contributions M.K.R. oversaw the project. Z.C., A.I., S.B.P. and J.U. developed the WRC reconstitution. D.B., Z.C. and Z.O. determined the structure of the WRC. Z.C. performed the biochemical experiments. D.D.B. and T.S.G. performed the cellular experiments. Z.M. performed the electron microscopy experiments. Z.C., Z.O. and M.K.R. analysed the WRC structure. D.B., Z.C., Z.O., S.B.P. and M.K.R. wrote the manuscript.

Author Information The atomic coordinates of the WRC have been deposited in the Protein Data Bank under accession code 3P8C. Reprints and permissions information is available at www.nature.com/reprints. The authors declare no competing financial interests. Readers are welcome to comment on the online version of this article at www.nature.com/nature. Correspondence and requests for materials should be addressed to M.K.R. (michael.rosen@utsouthwestern.edu).

METHODS

Protein expression and purification. The proteins were handled with a modified version of the earlier protocol¹³. Mutants were generated using QuikChange (Stratagene). To achieve maximal expression, His-tagged Sra1 (1–1253) and Nap1 (1–1128) were separately overexpressed in sf9 cells and Hi5 cells, respectively. Cells were lysed together and the Sra1:Nap1 complex was partially purified by a Ni-affinity column. For miniWRC, WAVE1–186VCA (WAVE1(1–186)-(GlyGlySer)₆-VCA(485–559)), Abi2 (1–158) and full-length HSPC300 (1–75) were expressed separately in *Escherichia coli* as MBP-fusion proteins, purified with amylose-affinity chromatography and assembled into the trimer sub-complex by incubation in the presence of 1% NP-40 (Sigma) for 48 h. The trimer was isolated using Source 15Q chromatography, and then mixed with the Sra1:Nap1 dimer at a 1:1.5 molar ratio overnight on ice to form the pentameric complex. Excess Sra1:Nap1 dimer was removed by an amylose-affinity column. The eluted complex was further purified using Mono Q chromatography. The fusion tags were removed by treatment with TEV protease at room temperature for 4–6 h. The sample was brought to homogeneity by a Superdex200 column equilibrated with protein buffer (200 mM NaCl, 12% glycerol (w/v), 10 mM Tris-HCl, 5 mM DTT, pH 8.0), concentrated to about 10 mg ml⁻¹ and stored at -80 °C. Selenomethionine-labelled Sra1 and Nap1 were obtained by culturing insect cells in methionine-free medium according to standard protocols (Expression Systems). ΔWRC and Δ154_{WAVE1}-WRC were produced in the same way as miniWRC, but contained WAVE1(1–186) and WAVE1(1–154), respectively.

Crystallization. Crystals were grown at 4 °C by hanging-drop vapour diffusion methods. The native miniWRC crystals grew from 10% (w/v) glycerol, 4% PEG 10,000, 12–20% PEG 300, 100 mM Tris-HCl, 2 mM TCEP, 2 mM EDTA, pH 8.5 with protein to reservoir volume ratio 1:1.8. Crystals form in space group *P*₂₁₂₁₂, with *a* = 103.5 Å, *b* = 113.8 Å, *c* = 323.0 Å and diffracted only to 4.2 Å. Extensive optimization failed to improve crystal quality. The crystals with selenomethionine-labelled Sra1 and Nap1 grew from similar conditions in the same space group, with *a* = 97.0 Å, *b* = 114.0 Å, *c* = 327.2 Å, and diffracted to 2.3 Å.

Data processing and structure solution. The structure of miniWRC was solved by experimental phasing using data processed with the HKL3000 suite^{37,40} (Supplementary Table 1). The initial phases were obtained by combining data from three crystals: the first two contained Se-labelled Sra1 and the third contained Se-labelled Nap1. There was a significant level of non-isomorphism between crystals. In the case of the structure with Se-labelled Sra1, there was an additional component of non-isomorphism due to the breaking of crystal symmetry (*P*₂₁ versus *P*₂₁₂₁₂). The symmetry violation was larger than experimental uncertainty, but still small enough to use the higher-symmetry space group (*P*₂₁₂₁₂) in structure solution. So the two data sets for the Sra1-labelled crystals scaled together were used for structure refinement in the *P*₂₁₂₁₂ space group. Radiation-induced non-isomorphism present in the collected data sets was corrected with the use of novel procedures⁴⁵. The data were anisotropic, with the best direction diffracting to 2.29 Å. To use the data fully, structure factors were anisotropically sharpened to make the resolution fall-off isotropic. In consequence, the shell-based *R*_{merge} values did not have statistical meaning in this case. To define the resolution properly we used an *I*/σ(*I*) criterion, where *I* represents averaged intensity after correcting for anisotropy, and σ(*I*) is defined for each reflection separately. The very small change of *R*_{free} at higher resolutions is an indicator that the procedure worked correctly.

After all these corrections, the heavy atom substructure for the averaged Sra1-*P*₂₁₂₁₂ was determined by ShelxD³⁹ called within the HKL3000 suite^{37,40}. Using initial phases, the positions of heavy atoms for the other data set (Se-labelled Nap1) were determined by searching for peaks in the anomalous difference map. The complete set of heavy atom positions was refined using MLPHARE⁴⁰ with anomalous differences only. Density modification was performed with Parrot⁴¹, and initial model building with Buccaneer⁴² (Supplementary Table 1). The rest of the model was built manually, using Coot⁴³ and Refmac⁴⁴, where experimental phases were used as an additional restraint.

Refinement was performed with Refmac, using the TLSMD server to generate TLS bodies for refinement⁴⁶, and the Molprobit server⁴⁷ to check the validity of the structure. The final refinement is summarized in Supplementary Table 1, which shows that 98.26%, 99.96% and 0.04% of the amino acid residues are in the favoured, additional allowed and disallowed region of the Ramachandran plots, respectively.

Equilibrium dialysis. Equilibrium dialysis was performed at room temperature using a fast micro-equilibrium dialyser (Harvard Apparatus). Rac1 (Q61L) was charged with GMP-PNP in pH 7.5 buffer containing 20 mM Tris-HCl, 150 mM NaCl, 14% (w/v) glycerol and 2 mM MgCl₂. WRC constructs were used at 4 μM. After reaching equilibrium (about 40 h), the concentrations of free Rac1 in one chamber and total Rac1 in the other chamber of the dialyser were analysed by SDS-PAGE gels, stained with Deep Purple (GE Healthcare) and quantified with ImageGauge (Fujifilm) by comparison to a standard curve generated from gels

containing known concentrations of Rac1. Nonlinear curve fitting to extract *K*_D was performed using Prism 5. At Rac1 concentrations above about 10 μM, technical limitations—such as bubble formation, protein instability over an extended dialysis time (required by high solution viscosity) and loss—prevented us from obtaining reproducible data in this regime. Thus, *K*_D was estimated from the approximate 50% saturation point in the assay.

Actin polymerization and GST pulldown assays. Arp2/3-complex-mediated actin polymerization assays were performed as described¹³ using 4 μM actin (5% pyrene labelled) and 10 nM Arp2/3 complex in KMEI-20G buffer (20% (w/v) glycerol, 50 mM KCl, 1 mM MgCl₂, 1 mM EGTA and 10 mM imidazole pH 7.0). The data in Supplementary Fig. 12 used 1 μM actin (5% pyrene labelled) and 30 nM Arp2/3 complex in buffer lacking glycerol. 5 nM WAVE1-Abi2-HSPC300 trimer was used as the aggregated VCA. Different concentrations of WAVE1 VCA (residues 485–559) were also used.

GST pulldown experiments were performed using 40 μM GST-Rac1 (20 μM for ΔWRC and Δ154-WRC comparison), 1.5 μM WRC constructs and 60 μl glutathione sepharose 4B resin in 0.2 ml pulldown buffer (10 mM Na-Hepes pH 7.0, 100 mM NaCl, 2 mM MgCl₂, 10% glycerol (w/v) and 2 mM DTT). After gentle mixing at room temperature for 30 min, the resin was spun down, washed three times with 0.4 ml pulldown buffer, and eluted with 30 mM reduced glutathione. The eluted proteins were resolved by SDS-PAGE and visualized with Coomassie blue.

Cell biology studies. HeLa cells were transfected with shVector-YFP control and various short hairpin (sh)WAVE2/HA-YFP-WAVE2 reconstitution vectors based on established protocols^{25,48}. We used shWAVE2 (GAGAAGAGAAAGC ACAGGA), and made shRNA-resistant WAVE2 complementary DNA (GAAAAAGGAAACACAGGA) to generate HA-YFP suppression/reconstitution vectors as described²⁵. Transfectants were analysed 72 h post transfection by immunoprecipitation or immunofluorescence. Anti-HA affinity matrix and anti-HA-HRP were from Roche. Rabbit anti-Nap1 was generated using a synthetic peptide corresponding to amino acids 1117–1128 of human Nap1. Anti-Sra1/PIR121 was previously described⁴⁷. Anti-WAVE1 was obtained from Upstate Biotechnology. Alexa Fluor-647 phalloidin was used (Invitrogen) to stain the actin filament. Images were obtained with an LSM-710 laser scanning confocal microscope (Carl Zeiss) and analysed for the presence of lamellipodia formation. For quantification, more than 200 cells for each transfected cell population, in at least three independent experiments, were blindly scored.

Electron microscopy. For negative staining electron microscopy, 4 μl of protein solution (10 μg ml⁻¹) was applied to glow-discharged carbon-coated 300-mesh Cu/Rh grids (Emsdium) and incubated for 30–60 s. Excess solution was blotted off with filter paper (Whatman #1), the grid was washed with 4 μl of protein buffer and stained with 2% uranyl acetate. Grids were imaged under low-dose conditions (10–25 electrons per Å²) on an FEI Tecnai G2 Spirit BioTwin electron microscope (FEI) with a LaB6 filament operated at 120 kV at a nominal magnification of 30,000×. Images were recorded with a Gatan 2,048 × 2,048-pixel charge-coupled device (CCD) camera (Gatan) using 0.8–2.5 μm underfocus, with a final resolution of 3.63 Å per pixel on the object. Particles were picked manually using the *boxer* application in EMAN⁴⁹, normalized, and filtered to 22 Å. Ten class averages were generated using nine iterations of reference-free classification (*refine2d.py*), using a common reference to orient the classes to show the 'upright' view. Classes with fewer than eight particles were discarded automatically after each iteration.

Calculation of surface conservation. The conservation scores were calculated using the ConSurf Server⁵⁰. Increasing conservation (scored from 1 to 9) was colour-coded in the figures by the spectra of white-to-green and white-to-cyan for Sra1 and Nap1, respectively. Residues that were scored 7–9 (green in Sra1 and cyan in Nap1) are considered to be conserved, which typically have a single amino acid in about 80% of the sequences we examined. The sequences of Sra1 orthologues used in the calculation are: NP_055423.1(Hs_Sra1), AAH72814.1, AAU05773.1, NP_974801.2, XP_001790637.1, EEN67132.1, NP_499949.2, Q6UK63.1, NP_650447.1, NP_997924.1, CAQ17050.1, NP_035500.2, XP_001379666.1, XP_001745727.1, EDO41734.1, NP_001048941.1, XP_001753041.1, XP_002468523.1, XP_002198076.1, EDV20545.1 and XP_002268225.1. The sequences of Nap1 orthologues used are: NP_038464.1(Hs_Nap1), NP_181056.2, ABN04850.1, NP_001062406.1, EDQ74364.1, XP_001369085.1, NP_001232275.1, NP_058661.1, NP_001087969.1, XP_690388.2, CAA56333.1, NP_001137348.1, XP_002221623.1, NP_524214.1, XP_971119.1, EEC12517.1, XP_001184421.1, EDO45022.1, NP_502368.1, CAZ27842.1, XP_644083.1 and EAY21283.1.

Total internal reflection fluorescence microscopy. Actin (1 μM) was polymerized in the presence of Arp2/3 complex (10 nM), N-WASP VCA (0.1 μM) or active L841A/F844A/W845A_{Sra1}-miniWRC (0.1 μM) in KMEI buffer for 20 min, before adding Alexa-488-phalloidin (1:50 dilution). As a negative control, actin (1 μM) alone was polymerized for 1 h. Alexa 488-phalloidin-bound filaments were diluted 1,000-fold before adsorbing onto poly-D-lysine-coated glass-bottom dishes (Ted

Pella) for 10 min. Filaments were imaged using a laser-based total internal reflection fluorescence microscope (Olympus IX-71 base microscope), Micro-Manager 1.3 (Vale lab), and a Photometrics Cascade II 512 EMCCD camera.

45. Borek, D., Ginell, S. L., Cymborowski, M., Minor, W. & Otwinowski, Z. The many faces of radiation-induced changes. *J. Synchrotron Radiat.* **14**, 24–33 (2007).
46. Painter, J. & Merritt, E. A. Optimal description of a protein structure in terms of multiple groups undergoing TLS motion. *Acta Crystallogr. D* **62**, 439–450 (2006).
47. Davis, I. W. *et al.* MolProbity: all-atom contacts and structure validation for proteins and nucleic acids. *Nucleic Acids Res.* **35**, 375–383 (2007).
48. Nolz, J. C. *et al.* The WAVE2 complex regulates actin cytoskeletal reorganization and CRAC-mediated calcium entry during T cell activation. *Curr. Biol.* **16**, 24–34 (2006).
49. Ludtke, S. J., Baldwin, P. R. & Chiu, W. EMAN: semiautomated software for high-resolution single-particle reconstructions. *J. Struct. Biol.* **128**, 82–97 (1999).
50. Landau, M. *et al.* ConSurf 2005: the projection of evolutionary conservation scores of residues on protein structures. *Nucleic Acids Res.* **33**, 299–302 (2005).

A geometric measure of dark energy with pairs of galaxies

Christian Marinoni^{1,2} & Adeline Buzzi¹

Observations^{1,2} indicate that the expansion of the Universe is accelerating, which is attributed to a ‘dark energy’ component that opposes gravity^{3,4}. There is a purely geometric test of the expansion of the Universe (the Alcock–Paczynski test), which would provide an independent way of investigating the abundance (Ω_X) and equation of state (w_X) of dark energy⁵. It is based on an analysis of the geometrical distortions expected from comparing the real-space and redshift-space shape of distant cosmic structures, but it has proved difficult to implement^{6–18}. Here we report an analysis of the symmetry properties of distant pairs of galaxies from archival data^{19,20}. This allows us to determine that the Universe is flat. By alternately fixing its spatial geometry at $\Omega_k \equiv 0$ and the dark energy equation-of-state parameter at $w_X \equiv -1$, and using the results of baryon acoustic oscillations, we can establish at the 68.3% confidence level that $-0.85 > w_X > -1.12$ and $0.60 < \Omega_X < 0.80$.

Previous attempts to implement the Alcock–Paczynski test with clusters of galaxies^{5,6}, cosmic voids^{7,8} or the large-scale galaxy distribution^{9–18} failed to unveil the expected geometrical deformations because the peculiar, non-Hubble, motions^{21,22} of test objects induce

additional distortions that are difficult to model and subtract. Galaxy pairs offer a viable way to overcome this limitation.

Consider a binary system, for example, a gravitationally bound pair of galaxies A and B at cosmological redshift z (see Fig. 1). A terrestrial observer can directly measure the angular separation θ subtended by A and B. The amplitude of the tilting angle t of the pair with respect to the observer’s line of sight can be indirectly inferred only if the radial comoving distances χ to the pairs’ members are known. In a uniform Universe with constant-curvature spatial geometries (labelled by the indices $k = 0, \pm 1$), we obtain²³:

$$\sin^2 t = \left\{ 1 + \left[C_k(\chi_A) \cot \theta - \frac{S_k(\chi_A) C_k(\chi_B)}{S_k(\chi_B) \sin \theta} \right]^2 \right\}^{-1} \quad (1)$$

where $C_k^2(\chi) = 1 - kS_k^2(\chi)$ and where, using the Kronecker delta symbol, $S_k(\chi) = \delta_{k,-1} \sinh(\chi) + \delta_{k,0} \chi + \delta_{k,1} \sin(\chi)$. We note that the angle t is not an observable for the terrestrial observer because distances depend not only on the redshift $z = \frac{\lambda_{\text{meas}}}{\lambda_{\text{emis}}} - 1$ of the radiation emitted by a

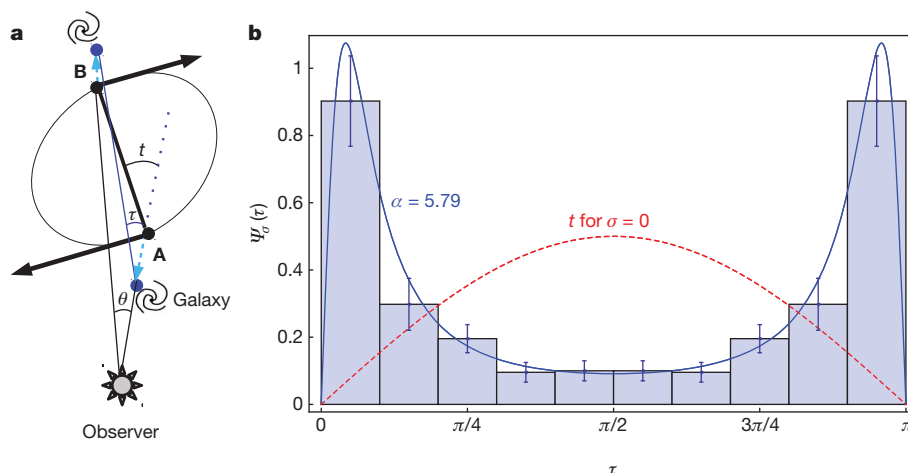


Figure 1 | Geometry and statistics of binary galactic systems. **a**, The two galaxies are labelled A and B (black dots) and subtend an angle θ at the observer position. The tilting angle t measures the inclination of the geodesic separation between A and B with respect to the observer’s line of sight (dotted line). This angle is expected to be uniformly distributed in the interval $[0, \pi]$. Pair members have peculiar velocities, generated by the gravitational action of the dark matter halo in which galaxies are embedded, the line-of-sight component of which alters the apparent geometry of the system (but not the angle θ). (The black line represents the real-space separation vector between pairs’ members. The blue line is the apparent separation vector measured by the observer because of the geometric distortions induced by peculiar velocities of the pair’s members.) As a consequence, a terrestrial observer will spuriously conclude that the tilting angle is τ . We note that peculiar velocities are typically larger than the radial separation (in velocity units) of the members. Their net average effect is to stretch the system along the observer’s line of sight. As a consequence, the

apparent tilt τ is not uniformly distributed. Instead, its distribution function is bimodal and, depending on the value of the adimensional velocity perturbation function $\sigma(z)$, peaks around 0 and π . This is shown in **b**, where the predictions of equation (2) are compared with data from the local Universe ($z \approx 0$). The histogram shows the observed distribution obtained by applying equation (1) to 721 pairs of the SDSS. Error bars represent 1σ Poisson uncertainties. The superimposed red dashed line corresponds to the uniform distribution of the angle t expected in the ideal case $\sigma = 0$. The blue solid line corresponds to the choice $\alpha = 5.79$, that is, the normalization inferred from the fact that, for this sample, $\langle \sin^2 \tau \rangle = 0.211 \pm 0.01$. The actual measurement is performed in the interval $[0, \pi/2]$ and replicated symmetrically in the interval $[\pi/2, \pi]$. Despite the fine tuning of the parameter α , it is remarkable that this simple, approximate model is able to reproduce both the overall shape and particular features of the observed distribution.

¹Centre de Physique Théorique, UMR 6207 CNRS—Université de Provence, Campus de Luminy, Case 907, 13288 Marseille cedex 9, France. ²Institut Universitaire de France, 103 boulevard Saint-Michel, 75005 Paris, France.

distant galaxy, but also on the *a priori* unknown values of cosmological parameters, in particular the abundance of dark energy Ω_X and its equation of state w_X . However, because the separation vector between A and B is randomly oriented, the probability distribution function of t can be predicted: $\phi(t) = \sin(t)/2$. As a result, the expectation value $\mu = \langle \sin^2 t \rangle$ is a cosmology-independent quantity equal to $2/3$ (ref. 9).

Adoption of the correct cosmological metric is a necessary but not sufficient condition for the sample mean m_N —which a terrestrial observer estimates by averaging equation (1) over N binaries—to be an unbiased estimator of μ . In fact, not only will a wrong choice of the background metric contribute to breaking the expected geometrical symmetry, but so will galaxy dynamics: the peculiar motion of the pair's members modifies the distribution of t . Consequently, m_N will significantly differ from μ even when the correct set of cosmological parameters is adopted in the analysis. However, the simplicity of the two-body dynamics makes the removal of the peculiar velocity effects in binaries straightforward.

Orbital motions cause a Doppler remap of t into an apparent angle τ (see Fig. 1a), making binaries appear on average more stretched along the observer's line of sight. This preferential orientation in a direction that is statistically improbable can be quantified. We find that the probability distribution function of τ is (see Fig. 1b and Supplementary Information):

$$\psi_\sigma(\tau) d\tau = \frac{1}{2} \frac{(1+\sigma^2)(1+\tan^2 \tau)}{[1+(1+\sigma^2)\tan^2 \tau]^{3/2}} |\tan \tau| d\tau \quad (2)$$

and that, therefore, the isotropic expectation $\mu = 2/3$ is replaced by the average anisotropy of pairs (AAP) function:

$$\mu_\sigma = \frac{(1+\sigma^2) \arctan(\sigma) - \sigma}{\sigma^3} \quad (3)$$

The adimensional velocity perturbation $\sigma^2 = \left(\frac{1+z}{c} \right)^2 \left\langle \left(\frac{dv_{\parallel}}{dz} \right)^2 \right\rangle$

encapsulates corrections for peculiar motions of the pair members (v_{\parallel}). Its amplitude can be fully specified: theory constrains its dependence on redshift, space geometry and mass-energy content of the Universe in terms of the cosmic expansion rate E —that is, $\sigma(z) = \alpha E(z)^{-1} (1+z)$ —and a calibrating sample of galaxy pairs identified in the local Universe allows us to fix its overall normalization α (see Supplementary Information). We note that in the idealized limit of no peculiar motions ($\sigma \rightarrow 0$), one recovers the unperturbed, cosmology-independent result $\mu_\sigma \rightarrow \mu = 2/3$.

We identify binary systems in the seventh data release of the Sloan Digital Sky Survey¹⁹ (at $z \approx 0$) and in the third data release of the DEEP2 survey²⁰ (up to $z \approx 1.45$). Spectroscopic redshift accuracy for both the high- and low-redshift samples is of the order of 30 km s^{-1} (ref. 24). To define a local calibrating sample, we have limited the SDSS sample depth to $z < 0.05$. In this way, distances inferred from redshift do not depend on the chosen background cosmological model. To be selected as physical pairs, galaxies must satisfy the following three criteria. (1) the comoving transverse separation $r_\perp = S_k(\chi) d\theta$ must be less than $r_{\perp, \text{max}} = 0.7 h^{-1}$ megaparsecs (Mpc), roughly the distance between Andromeda and the Milky Way (to ensure close pair selection), and it must be greater than $r_{\perp, \text{min}} = 20 h^{-1}$ kiloparsecs (kpc) (to exclude mergers or non-unique entries in the original catalogues). (2) to avoid projection effects, the recession velocity difference $dV = cdz/(1+z)$ (see Supplementary Information) has an upper limit $dV_{\text{max}} = 700 \text{ km s}^{-1}$ (the threshold above which the relative increase $\Delta N/N$ in the sample size when the velocity bin is augmented by 100 km s^{-1} is smaller than 1%). (3) there should be no other additional galaxy in the catalogue within a projected separation of $r_3 = 4 h^{-1} \text{ Mpc}$ and a velocity difference dV_{max} (to ensure the isolation of the pair). We have found that 721 galaxy pairs from the SDSS sample meet the selection requirements, while at high redshift the number of identified

systems depends on cosmological parameters. For instance, we recover 509 (330) binaries in a standard Λ CDM (Einstein–de Sitter) model.

Figure 2 shows that the estimated average anisotropy of pairs $m_N(z)$ matches the theoretically predicted value $\mu_\sigma(z)$ only if the analysis is carried out in the true metric background. Given the size of current deep-redshift surveys, we cannot yet explore all the parameters that are necessary to characterize the cosmological model fully. We will thus focus our analysis on only two lower-dimensional parameter subspaces. For the ‘cosmological constant’ (Λ) scenario, we consider only dark energy models with $w_X \equiv -1$, but we allow for non-zero spatial curvature Ω_k . In the ‘dark energy’ scenario, we assume that the Universe is flat ($\Omega_k = 0$) and that the equation-of-state parameter is constant ($w_X \equiv w_0$), but allow its value to differ from -1 .

The likelihood of both the scenarios is shown in Fig. 3. The precision of the amplitude of the cosmological constant, as measured by the effective surface of the 68.3% confidence contours in the $\Omega_m - \Omega_\Lambda$ plane (where Ω_m is the abundance of matter in the Universe), improves on current supernovae (of type Ia) estimates²⁵ by a factor of about 3. Our results alone imply that the curvature of the Universe is negligible, namely $\Omega_k = 0.10^{+0.20}_{-0.35}$ at the 68.3% confidence level. This figure should be compared with the supernovae type Ia result $\Omega_k = -0.1 \pm 0.4$ (ref. 26) and acquires even more significance if contrasted with the fact that the analysis of the cosmic microwave background itself cannot put strong limits on the geometry of the Universe unless an external prior on the present-day value of the Hubble parameter H_0 is assumed²⁷. Figure 3 also shows how constraints on cosmological parameters, particularly on w_0 , are significantly improved when we combine our results with constraints from the Sloan Digital Sky Survey (SDSS) measurement of baryon acoustic oscillations²⁸. For the Λ scenario, the joint likelihood contours imply that $0.60 < \Omega_X < 0.80$ at the 68.3% confidence level. The best value found for the matter density parameters, $\Omega_m = 0.27^{+0.03}_{-0.02}$,

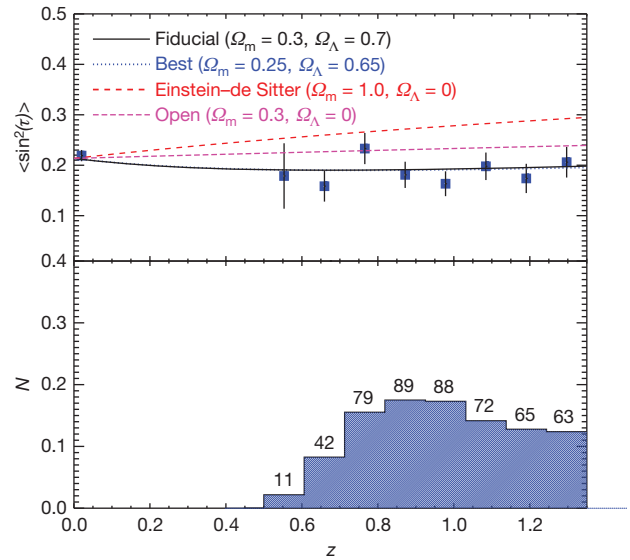


Figure 2 | Diagram of the average anisotropy of pairs from the SDSS (Data Release 7)¹⁹ and DEEP2²⁰ data. Blue squares represent the observed average anisotropy of pairs. The observable is measured by averaging equation (1) over a sample of distant binary systems in the fiducial cosmology. The 1σ error bars are the standard deviation of the mean $\langle \sin^2 t \rangle$ in each redshift bin. Data points reconstructed in different backgrounds randomly scatter by at most 1σ around the fiducial value. Curves represent the theoretical redshift scaling of the AAP as predicted by equation (3) in different cosmological models (specified by the matter density Ω_m and the dark energy density Ω_Λ). These different models describe a universe with negative curvature (open), a flat decelerating universe (Einstein–de Sitter) and two different accelerating universes (fiducial and best models). A goodness-of-fit test for the best model gives $\chi^2_{\text{d.o.f.}} \approx 5.5$ for 7 degrees of freedom (d.o.f.). A total of 509 binary systems were used. We show their redshift distribution in the bottom panel.

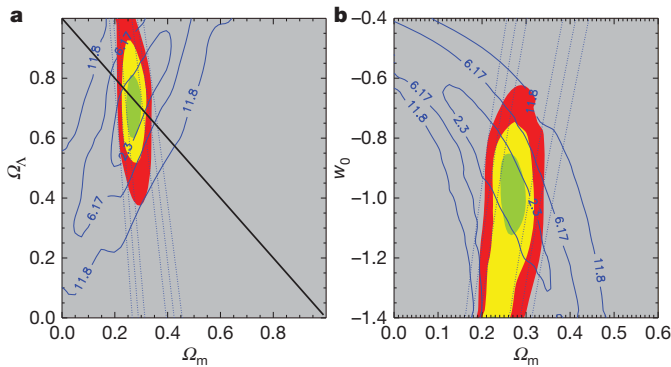


Figure 3 | Cosmological constraints on the abundance of dark energy Ω_Λ and on its nature w_Λ . Solid blue lines represent the isocontours of the logarithmic posterior $-\ln p$ (see Supplementary Information for definitions and details); they measure the level of credibility of a particular cosmological model given our AAP measurements. **a**, Constraints on the amplitude of the cosmological constant Λ obtained by projecting the posterior in the Ω_m – Ω_Λ plane and by assuming $w_\Lambda = w_0 = -1$ (that is, $\Omega_\Lambda \equiv \Omega_\Lambda$). Iso-levels are plotted for $-\ln p/p_{\text{best}} = 2.3, 6.17$ and 11.8 corresponding to 68.3%, 95.4% and 99.7% confidence intervals, respectively. The black solid line indicates cosmological models with a flat spatial geometry. **b**, Constraints on the null hypothesis that dark energy is effectively a cosmological constant. Contours are the same as before but the posterior is now projected in the Ω_m – w_0 parameter space. In both panels the dotted blue lines represent the confidence contours inferred from the analysis of baryon acoustic oscillations²⁸. Filled contours (red, yellow and green) show the constraints on cosmological parameters obtained from a joint analysis of the average anisotropy of pairs and the baryon acoustic oscillations geometrical probes. The acceleration of the Universe (a non-zero dark energy component) is detected with $>99.9\%$ confidence and there is strong evidence that it is induced by a cosmological constant ($w_0 = -1$).

allows us to translate the Λ detection into a geometric constraint for the curvature of the Universe. At the 68.3% confidence level we find $\Omega_k = 0.03 \pm 0.12$.

Within the framework of the dark energy scenario, we exclude at the 68.3% confidence level a constant dark energy parameter $w_0 > -0.85$ and $w_0 < -1.12$. Furthermore, if we compare constraints obtained from our test with those²⁹ inferred by a joint analysis of baryon acoustic oscillations (from SDSS Data Release 7) and supernovae (the union sample) we conclude that (1) for a flat Λ CDM model, the 68.3% confidence interval for Ω_Λ obtained with the AAP test alone has the same amplitude ($\Delta\Omega_\Lambda \approx 0.35$) as that inferred by combining supernovae type Ia and baryon acoustic oscillations; (2) if we relax the flatness condition but maintain $w_0 = -1$, then the 68.3% confidence interval for Ω_m and Ω_Λ obtained by combining AAP and baryon acoustic oscillations has the same amplitude as that obtained by combining baryon acoustic oscillations and supernovae type Ia (~ 0.05 and ~ 0.2 respectively). This is because the degeneracy axis of our results tends to be more aligned with the baryon acoustic oscillations direction than that of supernovae type Ia.

Given the observational economy of this ‘two-body’ technique, it will be possible to place even tighter limits when redshift surveys of the deep Universe soon become available.

Received 13 May; accepted 12 October 2010.

1. Riess, A. *et al.* Observational evidence from supernovae for an accelerating universe and a cosmological constant. *Astron. J.* **116**, 1009–1038 (1998).
2. Perlmutter, S. *et al.* Measurements of Ω_m and Ω_Λ from 42 high-redshift supernovae. *Astrophys. J.* **517**, 565–586 (1999).
3. Peebles, P. J. E. & Ratra, B. The cosmological constant and dark energy. *Rev. Mod. Phys.* **75**, 559–606 (2003).

4. Frieman, J. A., Turner, M. S. & Huterer, D. Dark energy and the accelerating universe. *Annu. Rev. Astron. Astrophys.* **46**, 385–432 (2008).
5. Alcock, C. & Paczynski, B. An evolution free test for non-zero cosmological constant. *Nature* **281**, 358–359 (1979).
6. Kim, Y.-R. & Croft, R. A. C. A potentially pure test of cosmic geometry: galaxy clusters and the real space Alcock-Paczynski test. *Mon. Not. R. Astron. Soc.* **374**, 535–546 (2007).
7. Ryden, B. S. Measuring q_0 from the distortions of voids in redshift space. *Astrophys. J.* **452**, 25–32 (1995).
8. Ryden, B. S. & Melott, A. Voids in real space and in redshift space. *Astrophys. J.* **470**, 160–171 (1996).
9. Phillips, S. A possible geometric measurement of the cosmological constant. *Mon. Not. R. Astron. Soc.* **269**, 1077–1081 (1994).
10. Matsubara, T. & Suto, Y. Cosmological redshift distortion of correlation functions as a probe of the density parameter and the cosmological constant. *Astrophys. J.* **470**, 1–5 (1996).
11. Ballinger, W. E., Peacock, J. & Heavens, A. F. Measuring the cosmological constant with redshift surveys. *Mon. Not. R. Astron. Soc.* **282**, 877–888 (1996).
12. Popowski, P. A., Weinberg, D. H., Rayden, B. S. & Osmer, P. Quasar clustering and spacetime geometry. *Astrophys. J.* **498**, 11–25 (1998).
13. Hui, L., Stebbins, A. & Burles, S. A geometrical test of the cosmological energy contents using the Ly- α forest. *Astrophys. J.* **511**, 5–8 (1999).
14. McDonald, P. Toward a measurement of the cosmological geometry at $z \sim 2$: Predicting Ly α forest correlation in three dimensions and the potential of future data. *Astrophys. J.* **585**, 34–51 (2003).
15. da Angela, J., Outram, P. J. & Shanks, T. Constraining $\beta(z)$ and Ω_m^0 from redshift-space distortions in $z \sim 3$ galaxy surveys. *Mon. Not. R. Astron. Soc.* **361**, 879–886 (2005).
16. Nusser, A. The Alcock-Paczynski test in redshifted 21-cm maps. *Mon. Not. R. Astron. Soc.* **364**, 743–750 (2005).
17. Barkana, R. Separating out the Alcock-Paczynski effect on 21-cm fluctuations. *Mon. Not. R. Astron. Soc.* **372**, 259–264 (2006).
18. McQuinn, M. *et al.* Cosmological parameter estimation using 21cm radiation from the epoch of reionisation. *Astrophys. J.* **653**, 815–834 (2006).
19. Abazajian, K. N. *et al.* The seventh data release of the Sloan Digital Sky Survey. *Astrophys. J. Suppl. Ser.* **182**, 543–558 (2009).
20. Davis, M. *et al.* The All-Wavelength Extended Groth Strip International Survey (AEGIS) data sets. *Astrophys. J.* **660**, 1–4 (2007).
21. Strauss, M. A. & Willick, J. A. The density and peculiar velocity fields of nearby galaxies. *Phys. Rep.* **261**, 271–431 (1995).
22. Marinoni, C. *et al.* Galaxy distances in the nearby Universe: corrections for peculiar motions. *Astrophys. J.* **505**, 484–505 (1998).
23. Marinoni, C., Bel, J. & Buzzi, A. The scale of cosmic isotropy. *Phys. Rev. Lett.* (submitted).
24. Coil, A. *et al.* The DEEP2 Galaxy Redshift Survey: clustering of galaxies in early data. *Astrophys. J.* **609**, 525–538 (2004).
25. Kessler, R. *et al.* First year SDSSII supernovae results: Hubble diagram and cosmological parameters. *Astrophys. J. Suppl. Ser.* **185**, 32–84 (2009).
26. Astier, P. *et al.* The Supernovae Legacy Survey: measurement of Ω_m , Ω_Λ and w from the first data set. *Astron. Astrophys.* **447**, 31–48 (2006).
27. Dunkley, J. *et al.* Five-year Wilkinson Microwave Anisotropy Probe observations: likelihoods and parameters from the WMAP data. *Astrophys. J. Suppl. Ser.* **180**, 306–329 (2009).
28. Eisenstein, D. J. *et al.* Detection of the baryon acoustic peak in the large-scale correlation function of SDSS luminous red galaxies. *Astrophys. J.* **633**, 560–574 (2005).
29. Percival, W. *et al.* Baryon acoustic oscillations in the Sloan Digital Sky Survey Data Release 7 galaxy sample. *Mon. Not. R. Astron. Soc.* **401**, 2148–2168 (2010).

Supplementary Information is linked to the online version of the paper at www.nature.com/nature.

Acknowledgements C.M. thanks J. Bel, P.-E. Crouzet, M. Davis, L. Guzzo, A. Blanchard, E. Branchini, P. S. Corasaniti, A. Ealet, A. Heavens, O. Le Fèvre, L. Moscardini, T. Schucker, P. Taxil and J. M. Virey for discussions. We thank R. Giovanelli, L. Lellouch and P. J. Morrison for reading versions of the manuscript. This paper has greatly benefited from the comments of M. Strauss. C.M. is grateful for support from the Projets Exploratoires Pluridisciplinaires: Physique Théorique et ses Interfaces of the CNRS and from specific project funding of the Institut Universitaire de France.

Author Contributions C.M. elaborated the testing formalism. C.M. and A.B. worked on the comparison of theoretical predictions with observations.

Author Information The posterior likelihood shown in Fig. 3 is available at www.cpt.univ-mrs.fr/~marinoni/Plik.tar.gz. Reprints and permissions information is available at www.nature.com/reprints. The authors declare no competing financial interests. Readers are welcome to comment on the online version of this article at www.nature.com/nature. Correspondence and requests for materials should be addressed to C.M. (marinoni@cpt.univ-mrs.fr).

The dynamical mass of a classical Cepheid variable star in an eclipsing binary system

G. Pietrzyński^{1,2}, I. B. Thompson³, W. Gieren¹, D. Graczyk¹, G. Bono^{4,5}, A. Udalski², I. Soszyński², D. Minniti⁶ & B. Pilecki^{1,2}

Stellar pulsation theory provides a means of determining the masses of pulsating classical Cepheid supergiants—it is the pulsation that causes their luminosity to vary. Such pulsational masses are found to be smaller than the masses derived from stellar evolution theory: this is the Cepheid mass discrepancy problem^{1,2}, for which a solution is missing^{3–5}. An independent, accurate dynamical mass determination for a classical Cepheid variable star (as opposed to type-II Cepheids, low-mass stars with a very different evolutionary history) in a binary system is needed in order to determine which is correct. The accuracy of previous efforts to establish a dynamical Cepheid mass from Galactic single-lined non-eclipsing binaries was typically about 15–30% (refs 6, 7), which is not good enough to resolve the mass discrepancy problem. In spite of many observational efforts^{8,9}, no firm detection of a classical Cepheid in an eclipsing double-lined binary has hitherto been reported. Here we report the discovery of a classical Cepheid in a well detached, double-lined eclipsing binary in the Large Magellanic Cloud. We determine the mass to a precision of 1% and show that it agrees with its pulsation mass, providing strong evidence that pulsation theory correctly and precisely predicts the masses of classical Cepheids.

We have detected several candidates for Cepheid variables in eclipsing binary systems in the Large Magellanic Cloud¹⁰ (LMC). Using high-resolution spectra, we confirmed the discovery of a classical fundamental-mode Cepheid pulsator OGLE-LMC-CEP0227 in a well detached, double-lined, eclipsing system with near-perfect properties for deriving the masses of its two components with very high accuracy. (We obtained the spectra with the MIKE spectrograph at the 6.5-m Magellan Clay telescope at the Las Campanas Observatory in Chile, and with the HARPS spectrograph attached to the 3.6-m telescope of the European Southern Observatory on La Silla.) A finding chart for the system can be found on the OGLE Project webpage¹⁰.

Our spectroscopic and photometric observations of the binary system are best fitted by assuming a mass ratio of 1.00 for the two components (Fig. 1). This value was used to disentangle the pulsational and orbital radial-velocity variations of the Cepheid component of the binary. The resulting orbital radial-velocity curves of the components, and the pulsational radial-velocity curve of the Cepheid, are shown in Fig. 2.

The spectroscopic and photometric observations were then analysed using the 2007 version of the standard Wilson–Devinney code^{11,12}. We accounted for the photometric variations of the Cepheid caused by the pulsations, as follows. First, we fitted a Fourier series of order 15 to the observations secured outside the eclipses. Second, we subtracted the corresponding variations in the eclipses in an iterative way, scaling the obtained fit according to the resulting Wilson–Devinney model. The *I*-band pulsational and orbital light curves, together with the best model obtained from the Wilson–Devinney code, are shown in Fig. 3. The corresponding astrophysical parameters of our system are presented in Table 1.

The mean radius of the primary (Cepheid) component that we obtained from our binary analysis shows excellent agreement with the radius predicted for its period from the Cepheid period–radius relation of ref. 13 ($32.3 R_{\odot}$, where R_{\odot} is the solar radius), strengthening our confidence in our results. In order to assign realistic errors to the derived parameters of our system, we performed Monte Carlo simulations. Our analysis of the very accurate existing data sets for OGLE-LMC-CEP0227 has resulted in a purely empirical determination of the dynamical mass of a classical Cepheid variable, with an unprecedented accuracy of 1%. We note that an end-to-end simultaneous solution for all parameters might reveal slightly different

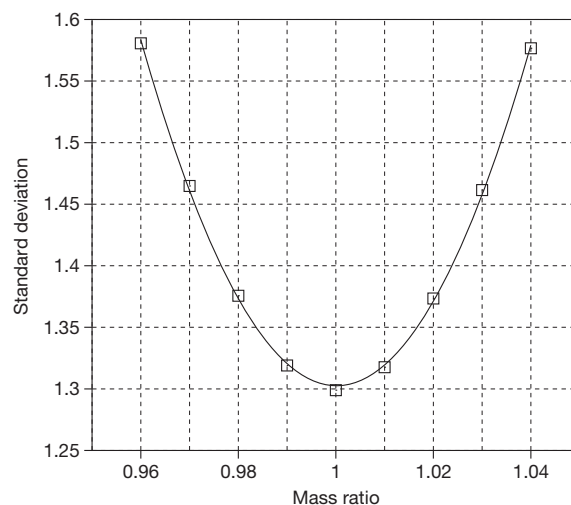


Figure 1 | The procedure adopted to separate pulsational and orbital motion of the Cepheid. The following final ephemeris for our system was derived from the OGLE photometric data: orbital period $P_{\text{orb}} = 309.673 \pm 0.030$ days, time of the minimum light of the binary system $T_{0,\text{orb}} = 2,454,895.91 \pm 0.05$ days; pulsational period $P_{\text{pul}} = 3.797086 \pm 0.000011$ days, time of the Cepheid maximum light $T_{0,\text{pul}} = 2,454,439.94 \pm 0.02$ days. Adopting the photometric ephemeris, and having radial velocities measured for the secondary, non-pulsating component, we can scale them with the mass ratio and subtract them from the observed radial velocities of the Cepheid component, producing the pulsation radial-velocity curve of the Cepheid. Since both photometric and spectroscopic data indicate that the mass ratio of our system must be very close to 1, a set of pulsational radial-velocity curves of the Cepheid were obtained in this way for a range of mass ratios around 1, and the dispersion on each of these curves was measured. The resulting function of dispersion (expressed as standard deviation) versus mass ratio displayed in the figure shows a very well defined minimum around a mass ratio of 1.00. Independently, a mass ratio of our system of 0.99 ± 0.01 was derived from a least squares fitting of the orbit (systemic velocity, velocity amplitudes, eccentricity, periastron passage, and mass ratio) plus a Fourier series of order eight fitted to the pulsational radial-velocity variations of the Cepheid. We therefore adopted a mass ratio of 1.00 to disentangle the pulsational and orbital radial-velocity variations of the Cepheid component in the binary system.

¹Universidad de Concepción, Departamento de Astronomía, Casilla 160-C, Concepción, Chile. ²Observatorium Astronomiczne Uniwersytetu Warszawskiego, Aleje Ujazdowskie 4, 00-478 Warszawa, Poland. ³Carnegie Observatories, 813 Santa Barbara Street, Pasadena, California 91101-1292, USA. ⁴Dipartimento di Fisica Università di Roma Tor Vergata, via della Ricerca Scientifica 1, 00133 Rome, Italy. ⁵INAF-Osservatorio Astronomico di Roma, Via Frascati 33, 00040 Monte Porzio Catone, Italy. ⁶Pontificia Universidad Católica de Chile, Departamento de Astronomía y Astrofísica, Casilla 306, Santiago 22, Chile.

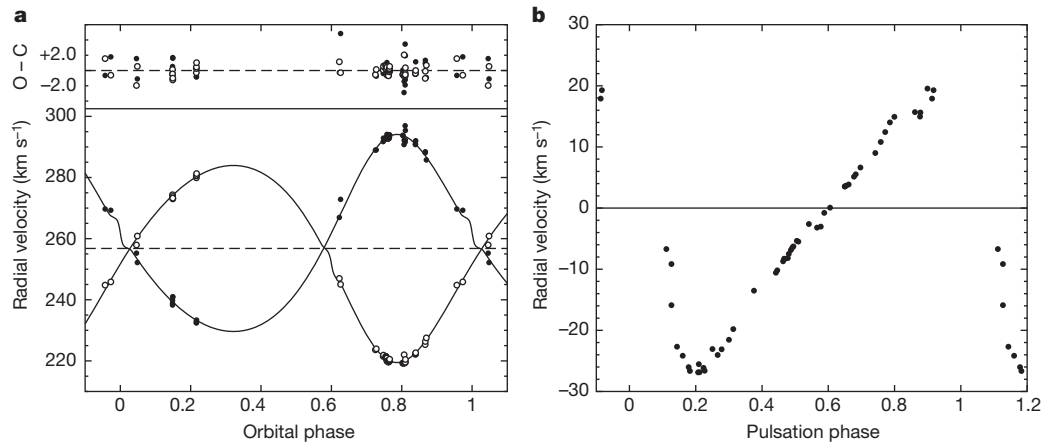


Figure 2 | Orbital motion of the two binary components, and the pulsational motion of the Cepheid variable in the binary system. **a**, Main panel: the computed orbital radial-velocity curves of the two components of the LMC-OGLE-CEP227 binary system, after accounting for the intrinsic variation of the Cepheid's radial velocity due to its pulsation, together with the observed data. Filled and open circles, primary and secondary component, respectively. Top, the residuals of the observed velocities (O) from the computed ones (C),

uncertainties, and would also illuminate the correlations in the uncertainties between the various derived quantities. From an evolutionary point of view, we have captured our system in a very short-lasting evolutionary phase, when both components are burning helium in their cores during their return from their first crossing of the Cepheid instability strip in the Hertzsprung–Russell diagram. The secondary component is slightly more evolved (it is larger and cooler), and is located just outside the Cepheid instability strip, so it is non-variable.

It is very important to note that OGLE-LMC-CEP0227 is a classical, high-mass Cepheid, and not a low-mass type-II Cepheid. This is clearly indicated by both its mass (Table 1) and its position on the period–luminosity diagram for OGLE Cepheids shown in Fig. 4 (which furthermore suggests that the star is a fundamental mode pulsator). Fundamental mode pulsation is also suggested by the strongly asymmetrical shapes and large amplitudes of the pulsation radial-velocity curve and of the I-band light curve (Figs 2 and 3). Of the three candidates for Cepheids in eclipsing binary systems detected earlier by the MACHO and OGLE projects^{8,9}, the objects MACHO-78.6338.24 and MACHO-6.6454.5 are type-II (low-mass) Cepheids^{8,10}; only the object

expressed in km s⁻¹. **b**, The pulsational radial-velocity curve of the Cepheid in the binary system from 54 individual observations. The radial-velocity amplitude of 47 km s⁻¹ is typical for a 4-day fundamental mode classical Cepheid. All individual radial velocities were determined by the cross-correlation method using appropriate template spectra and the HARPS and MIKE spectra, yielding in all cases velocity accuracies better than 150 m s⁻¹ (error bars are smaller than the circles in the figure).

OGLE-LMC_SC16-119952 (MACHO-81.8997.87) still appears to be a candidate for a classical Cepheid pulsating in the first overtone¹⁴. However, there are currently several problems with the correct interpretation of this last object^{9,14}, and clearly more photometric and spectroscopic data are needed in order to reveal the true nature of this interesting system and eventually use it for a mass determination for a first overtone classical Cepheid. We also note that the type-II Cepheid MACHO-6.6454.5 belongs to the class of peculiar W Virginis stars introduced in ref. 15.

To estimate the pulsation mass of the Cepheid in LMC-OGLE-CEP0227, we adopted a period–mass relation based on nonlinear, convective Cepheid models constructed for the typical chemical composition of LMC Cepheids (metallicity $Z = 0.008$, helium mass fraction $Y = 0.256$) (refs 5, 16, 17). This yields a pulsation mass of $M_p = 3.98 \pm 0.29 M_\odot$ (where M_\odot is the solar mass) for the star, which is independent of the assumed reddening and distance of the Cepheid and agrees within 1σ with its dynamical mass, providing strong evidence that the pulsation mass of a Cepheid variable is indeed correctly measuring its true, current mass. This result contributes significantly to settling the controversy about classical Cepheid masses.

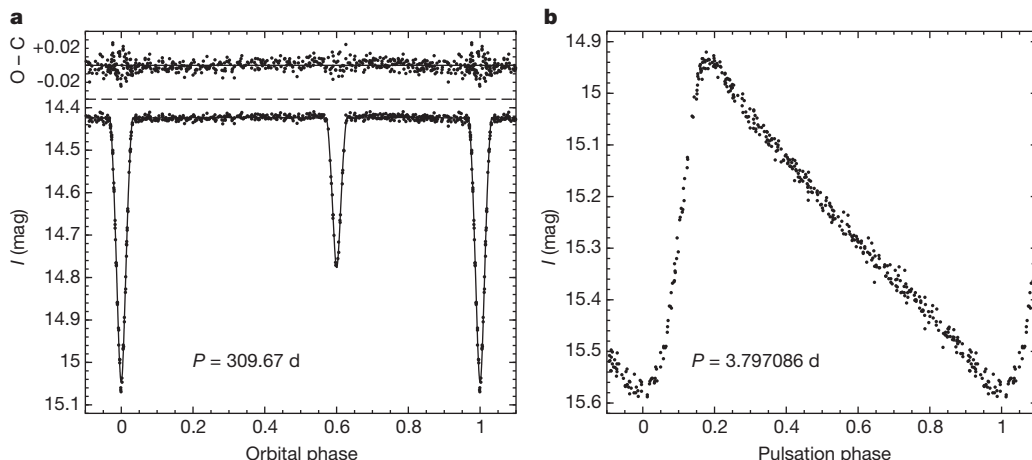


Figure 3 | Change of brightness of the binary system caused by the mutual eclipses, and the intrinsic change of the brightness of the Cepheid component caused by its pulsations. **a**, Main panel: the orbital I-band light curve (367 epochs collected over 6.5 years) of the Cepheid-containing binary system LMC-OGLE-CEP0227, after removal of the intrinsic brightness variation of the Cepheid component together with the solution, as obtained

with the Wilson–Devinney code. Top, the residuals of the observed magnitudes (O) from the computed orbital light curve (C). **b**, The pulsational I-band light curve of the Cepheid in the binary system, folded on a pulsation period of 3.797086 days. The asymmetric, large-amplitude light curve is characteristic of a classical fundamental mode Cepheid pulsator.

Table 1 | Astrophysical parameters of the OGLE-LMC-CEP0227 system

| Parameter | Primary | Secondary |
|---|------------------------------|-------------------|
| Mass (M/M_{\odot}) | 4.14 ± 0.05 | 4.14 ± 0.07 |
| Radius (R/R_{\odot}) | 32.4 ± 1.5 | 44.9 ± 1.5 |
| Effective temperature (T) | $5,900 \pm 250$ K | $5,080 \pm 270$ K |
| Eccentricity (e) | 0.1666 ± 0.0014 | |
| Periastron passage (ω) | 341.3 ± 1.1 degrees | |
| Systemic velocity (γ) | 256.7 ± 0.1 km s $^{-1}$ | |
| Period ($P_{\text{orb}}, P_{\text{pul}}$) | 309.673 ± 0.03 days | |
| | 3.797086 ± 0.000011 days | |
| Inclination (i) | 87.25 ± 0.25 degrees | |
| Orbit size (a/R_{\odot}) | 389.4 ± 1.2 | |
| Mass ratio (q) | 1.00 ± 0.01 | |

The parameters of the OGLE-LMC-0227 system, together with their uncertainties obtained from the modelling of the spectroscopic and photometric data.

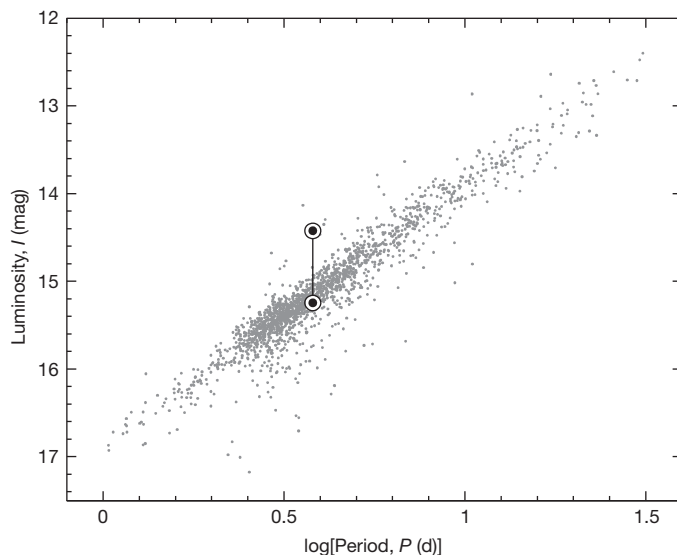


Figure 4 | The period and brightness of the Cepheid component of our system confirm that it is a classical Cepheid. The period–luminosity relation (period in days) defined by the OGLE Project for fundamental mode classical Cepheids in the LMC¹⁰ in the photometric I band together with the position of OGLE-LMC-CEP0227. The upper circle corresponds to the total mean out-of-eclipse brightness of the system which contains the contribution of the binary companion to the Cepheid, while the lower circle measures the mean intensity magnitude of the Cepheid freed from the companion contribution. The Cepheid in the binary system fits well on the fundamental mode sequence, and is beyond any doubt a classical (and not type-II) Cepheid.

The overestimation of Cepheid masses by stellar evolution theory may be the consequence of significant mass loss suffered by Cepheids during the pulsation phase of their lives—such loss could occur through radial motions and shocks in the atmosphere^{18,19}. The existence of mild internal core mixing in the main-sequence progenitor of the Cepheid, which would tend to decrease its evolutionary mass estimate, is another possible way to reconcile the evolutionary mass of Cepheids with their pulsation mass¹⁸.

Received 6 July; accepted 19 October 2010.

- Christy, R. F. The theory of Cepheid variability. *Q. J. R. Astron. Soc.* **9**, 13–39 (1968).
- Stobie, R. S. Cepheid pulsation—III. Models fitted to a new mass–luminosity relation. *Mon. Not. R. Astron. Soc.* **144**, 511–535 (1969).
- Cox, A. N. The masses of Cepheids. *Annu. Rev. Astron. Astrophys.* **18**, 15–41 (1980).
- Gieren, W. Towards a reconciliation of Cepheid masses. *Astron. Astrophys.* **225**, 381–390 (1989).
- Bono, G., Gieren, W., Marconi, M., Fouqué, P. & Caputo, F. Improving the mass determination of Galactic Cepheids. *Astrophys. J.* **563**, 319–324 (2001).
- Evans, N. R. *et al.* Direct detection of the close companion of Polaris with the Hubble Space Telescope. *Astron. J.* **136**, 1137–1146 (2008).
- Evans, N. R. in *Stellar Pulsation: Challenges for Theory and Observation* (eds Guzik, J. A. & Bradley, P. A.) 69–72 (AIP Conf. 1170, American Institute of Physics, 2009).
- Udalski, A. *et al.* The Optical Gravitational Lensing Experiment. Cepheids in the Magellanic Clouds. IV. Catalog of Cepheids from the Large Magellanic Cloud. *Acta Astron.* **49**, 223–317 (1999).
- Alcock, C. *et al.* The MACHO Project Large Magellanic Cloud variable star inventory. XII. Three Cepheid variables in eclipsing binaries. *Astrophys. J.* **573**, 338–350 (2002).
- Soszynski, I. *et al.* The Optical Gravitational Lensing Experiment. The OGLE-III catalog of variable stars. I. Classical Cepheids in the Large Magellanic Cloud. *Acta Astron.* **58**, 163–185 (2008).
- Wilson, R. E. & Devinney, E. J. Realization of accurate close-binary light curves: application to MR Cygni. *Astrophys. J.* **166**, 605–620 (1971).
- Van Hamme, W. & Wilson, R. E. Third-body parameters from whole light and velocity curves. *Astrophys. J.* **661**, 1129–1151 (2007).
- Gieren, W., Fouqué, P. & Gómez, M. Cepheid period–radius and period–luminosity relations and the distance to the Large Magellanic Cloud. *Astrophys. J.* **496**, 17–30 (1998).
- Lepischak, D., Welch, D. L. & van Kooten, P. B. M. The nature of the companion to the eclipsing overtone Cepheid MACHO 81.8997.87. *Astrophys. J.* **611**, 1100–1106 (2004).
- Soszynski, I. *et al.* The Optical Gravitational Lensing Experiment. The OGLE-III catalog of variable stars. II. Type II Cepheids and anomalous Cepheids in the Large Magellanic Cloud. *Acta Astron.* **58**, 293–312 (2008).
- Bono, G., Castellani, V. & Marconi, M. Classical Cepheid pulsation models. III. The predictable scenario. *Astrophys. J.* **529**, 293–317 (2000).
- Luck, R. E., Moffett, T. J., Barnes, T. G. & Gieren, W. P. Magellanic Cloud Cepheids—abundances. *Astron. J.* **115**, 605–634 (1998).
- Keller, S. C. Cepheid mass loss and the pulsation–evolutionary mass discrepancy. *Astrophys. J.* **677**, 483–487 (2008).
- Neilson, H. R. & Lester, J. B. On the enhancement of mass loss in Cepheids due to radial pulsation. *Astrophys. J.* **684**, 569–587 (2008).

Acknowledgements This work was supported by the Chilean Center for Astrophysics FONDAP, the BASAL Centro de Astrofísica y Tecnologías Afines (CATA), NSF, the Polish Ministry of Science, the Foundation for Polish Science (FOCUS, TEAM), and the GEMINI-CONICYT Fund. The OGLE project has received funding from the European Research Council (‘Advanced Grants’). We thank the staff astronomers at Las Campanas and ESO La Silla who provided support in the data acquisition. We also thank D. Queloz, S. Udry and C. Lovis for their help in reducing and analysing the radial-velocity data obtained with the HARPS instrument.

Author Contributions G.P., photometric and spectroscopic observations and reductions, data analysis; I.B.T., spectroscopic observations and reductions, radial-velocity measurements, data analysis; W.G., spectroscopic observations, data analysis; D.G., spectroscopic observations, modelling, data analysis; G.B., theoretical models; A.U., photometric observations and reductions, data analysis; I.S., photometric observations and reductions; D.M., spectroscopic observations; B.P., modelling. G.P. and W.G. worked jointly to draft the manuscript, with all authors reviewing and contributing to its final form.

Author Information Reprints and permissions information is available at www.nature.com/reprints. The authors declare no competing financial interests. Readers are welcome to comment on the online version of this article at www.nature.com/nature. Correspondence and requests for materials should be addressed to G.P. (pietrzyn@astrow.edu.pl).

Bose–Einstein condensation of photons in an optical microcavity

Jan Klaers, Julian Schmitt, Frank Vewinger & Martin Weitz

Bose–Einstein condensation (BEC)—the macroscopic ground-state accumulation of particles with integer spin (bosons) at low temperature and high density—has been observed in several physical systems^{1–9}, including cold atomic gases and solid-state quasiparticles. However, the most omnipresent Bose gas, blackbody radiation (radiation in thermal equilibrium with the cavity walls) does not show this phase transition. In such systems photons have a vanishing chemical potential, meaning that their number is not conserved when the temperature of the photon gas is varied¹⁰; at low temperatures, photons disappear in the cavity walls instead of occupying the cavity ground state. Theoretical works have considered thermalization processes that conserve photon number (a prerequisite for BEC), involving Compton scattering with a gas of thermal electrons¹¹ or photon–photon scattering in a nonlinear resonator configuration^{12,13}. Number-conserving thermalization was experimentally observed¹⁴ for a two-dimensional photon gas in a dye-filled optical microcavity, which acts as a ‘white-wall’ box. Here we report the observation of a Bose–Einstein condensate of photons in this system. The cavity mirrors provide both a confining potential and a non-vanishing effective photon mass, making the system formally equivalent to a two-dimensional gas of trapped, massive bosons. The photons thermalize to the temperature of the dye solution (room temperature) by multiple scattering with the dye molecules. Upon increasing the photon density, we observe the following BEC signatures: the photon energies have a Bose–Einstein distribution with a massively populated ground-state mode on top of a broad thermal wing; the phase transition occurs at the expected photon density and exhibits the predicted dependence on cavity geometry; and the ground-state mode emerges even for a spatially displaced pump spot. The prospects of the observed effects include studies of extremely weakly interacting low-dimensional Bose gases⁹ and new coherent ultraviolet sources¹⁵.

Fifty years ago, the invention of the laser provided us with a source of coherent light. In a laser, optical gain is achieved under conditions where both the state of the gain medium and the state of the light field are far removed from thermal equilibrium¹⁶. The realization of a light source with a macroscopically populated photon mode that is not the consequence of a laser-like gain, but is rather due to an equilibrium phase transition of photons has so far been prevented by the lack of a suitable number-conserving thermalization process¹⁷. For strongly coupled mixed states of photons and excitons (exciton polaritons), a thermalization process induced by interparticle interactions between excitons has been reported to lead to a (quasi-)equilibrium BEC of polaritons^{5–7}. In the present work, rapid decoherence due to frequent collisions of dye molecules with the solvent prevents coherent energy exchange between photons and dye molecules and therefore the condition of strong matter–field coupling is not met^{18,19}. We can therefore assume the relevant particles to be well described as photons instead of polaritons.

Our experiment confines photons in a curved-mirror optical microresonator filled with a dye solution, in which photons are repeatedly absorbed and re-emitted by the dye molecules. The small distance of 3.5 optical wavelengths between the mirrors causes a large frequency spacing between adjacent longitudinal modes (the free spectral range is 7×10^{13} Hz), comparable with the spectral width of the dye (see Fig. 1a), and modifies spontaneous emission such that the emission of photons with a given longitudinal mode number, $q = 7$ in our case, dominates over other emission processes. In this way, the longitudinal mode number is frozen out and the remaining transverse modal degrees of freedom make the photon gas effectively two-dimensional. Moreover, the dispersion relation becomes quadratic (that is, non-relativistic), as indicated in Fig. 1b, with the frequency of the $q = 7$ transverse ground mode (TEM₀₀) acting as a low-frequency cut-off with $\omega_{\text{cut-off}} \cong 2\pi \times 5.1 \times 10^{14}$ Hz. The curvature of the mirrors

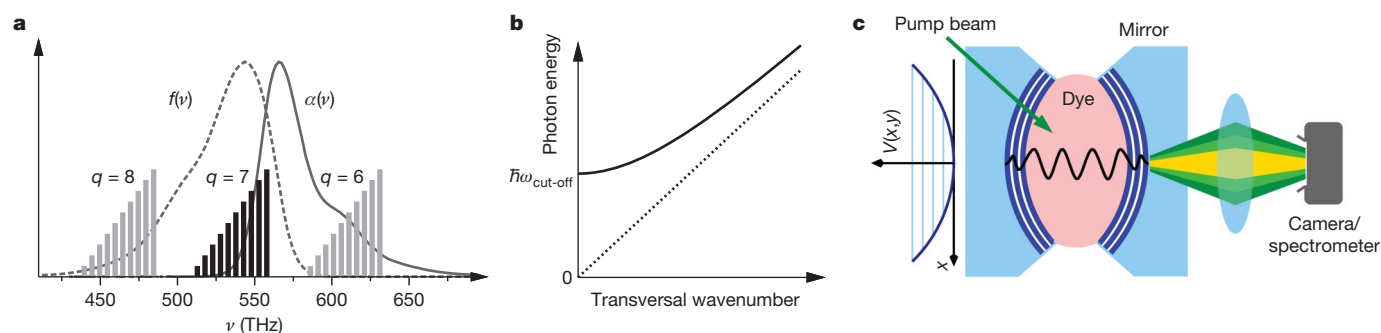


Figure 1 | Cavity mode spectrum and set-up. **a**, Schematic spectrum of cavity modes and (relative) absorption coefficient $\alpha(\nu)$ and fluorescence strength $f(\nu)$ of rhodamine 6G dye versus frequency ν . Transverse modes belonging to the manifold of longitudinal mode number $q = 7$ are shown by black lines, and those of other longitudinal mode numbers in grey. The degeneracy of a given transversal energy is indicated by the height of the bars. **b**, Dispersion relation of

photons in the cavity (solid line), with fixed longitudinal mode number ($q = 7$), and the free photon dispersion (dashed line). **c**, Scheme of the experimental set-up. The trapping potential $V(x,y)$ for the two-dimensional photon gas imposed by the curved mirrors—see the third term in equation (2) of the Methods—is indicated on the left hand side.

induces a harmonic trapping potential for the photons (see Methods). This is indicated in Fig. 1c, along with a scheme of the experimental set-up.

Thermal equilibrium of the photon gas is achieved by absorption and re-emission processes in the dye solution, which acts as heat bath and equilibrates the transverse modal degrees of freedom of the photon gas to the (rovibrational) temperature of the dye molecules (see Methods). The photon frequencies will accumulate within a range $k_B T/h$ ($\cong 2\pi \times 6.3 \times 10^{12}$ Hz at room temperature, where \hbar is the reduced Planck constant) above the low-frequency cut-off. In contrast to the case of a blackbody radiator, for which the photon number is determined by temperature (Stefan–Boltzmann law), the number of (optical) photons in our microresonator is not altered by the temperature of the dye solution, because purely thermal excitation is suppressed by a factor of the order of $\exp(\hbar\omega_{\text{cut-off}}/k_B T) \approx \exp(-80)$. The thermalization process thus conserves the average photon number.

Our system is formally equivalent to an ideal gas of massive bosons having an effective mass $m_{\text{ph}} = \hbar\omega_{\text{cut-off}}/c^2 \cong 6.7 \times 10^{-36}$ kg (where subscript ‘ph’ stands for ‘photon’) that are moving in the transverse resonator plane, harmonically confined with a trapping frequency $\Omega = c/\sqrt{D_0 R/2} \cong 2\pi \times 4.1 \times 10^{10}$ Hz (see Methods), with c as the speed of light in the medium, $D_0 \cong 1.46$ μm the mirror separation and $R \cong 1$ m the radius of curvature. A harmonically trapped two-dimensional ideal gas exhibits BEC at finite temperature^{20,21}, in contrast to the two-dimensional homogeneous case. We therefore expect a BEC when the photon wave packets spatially overlap at low temperatures or high densities, that is, the phase space density $n\lambda_{\text{th}}^2$ (where subscript ‘th’ stands for ‘thermal’) exceeds a value near unity. Here n denotes the number density in photons per area, and $\lambda_{\text{th}} = h/\sqrt{2\pi m_{\text{ph}} k_B T} \cong 1.58$ μm (defined in analogy to, for example, a gas of atoms¹⁷) is the de Broglie wavelength associated with the thermal motion in the resonator plane. We note that $\lambda_{\text{th}} = 2\sqrt{\pi}/k_{r, \text{r.m.s.}}$, where $k_{r, \text{r.m.s.}} = \sqrt{\langle k_r^2 \rangle_T}$ is the root mean square (r.m.s.) transverse component of the photon wavevector at temperature T . The precise onset of BEC in this two-dimensional, harmonically trapped system can be determined from a statistical description using a Bose–Einstein distributed occupation of trap levels^{14,20,21}, giving a critical particle number of:

$$N_c = \frac{\pi^2}{3} \left(\frac{k_B T}{\hbar \Omega} \right)^2 \quad (1)$$

At room temperature ($T = 300$ K), we arrive at $N_c \cong 77,000$. It is interesting to note that both the thermal energy $k_B T$ and the trap level spacing $\hbar\Omega$ are roughly a factor of 10^9 above the corresponding values in atomic physics BEC experiments^{2–4}, but that the ratio $k_B T/\hbar\Omega \cong 150$, corresponding to the mean excitation value per axis, is quite comparable.

By pumping the dye with an external laser we add to a reservoir of electronic excitations that exchanges particles with the photon gas, in the sense of a grand-canonical ensemble. The pumping is maintained throughout the measurement to compensate for losses due to coupling into unconfined optical modes, finite quantum efficiency and mirror losses. In a steady state, the average photon number will be $N_{\text{ph}} = N_{\text{exc}} \tau_{\text{ph}}/\tau_{\text{exc}}$, where N_{exc} is the number of molecular excitations, τ_{exc} is their electronic lifetime in the resonator (of the order of a nanosecond) and $\tau_{\text{ph}} \cong 20$ ps is the average time between emission and reabsorption of a photon. For a detailed description of the thermalization, it is important to realize that it originates from particle exchange with a reservoir that is in equilibrium. The reservoir is characterized by rovibrational molecular states that are highly equilibrated both in the lower and in the upper electronic levels owing to subpicosecond relaxation²² induced by frequent collisions with solvent molecules. This process efficiently decorrelates the states of absorbed and emitted photons, and leads to a temperature-dependent absorption and emission spectral profile that is responsible for the thermalization.

To relax both spatially and spectrally to an equilibrium distribution, a photon has to scatter several times off molecules before being lost. In previous work, we have shown that the photon gas in the dye-filled microcavity system can be well described by a thermal equilibrium distribution, showing that photon loss is sufficiently slow¹⁴. To avoid excessive population of dye molecule triplet states and heat deposition, the pump beam is acousto-optically chopped to 0.5- μs pulses, which is at least two orders of magnitude above the described timescales, with 8-ms repetition time.

Typical room-temperature spectra for increasing pumping power are given in Fig. 2a (recorded using rhodamine 6G dye solved in methanol, 1.5×10^{-3} M). At low pumping and correspondingly low intracavity power we observe a spectrally broad emission, which is in good agreement with a room-temperature Boltzmann distribution of photon energies above the cavity cut-off¹⁴. With increasing pump power the maximum of the spectral distribution shifts towards the cavity cut-off, that is, it more resembles a Bose–Einstein distribution function. For a pumping power above threshold, a spectrally sharp peak at the frequency of the cavity cut-off is observed, while the thermal wing shows saturation. The described signatures are in good agreement with theoretical spectra based on Bose–Einstein distributed transversal excitations (inset of Fig. 2a). At the phase transition the power inside the resonator is $P_{c, \text{exp}} = (1.55 \pm 0.60)$ W, corresponding to a critical photon number of $(6.3 \pm 2.4) \times 10^4$. This value still holds when rhodamine is replaced by perylene-diimide (PDI) solved in acetone (0.75 g l⁻¹); that is, for both dyes the measured critical number is in agreement with the value predicted for a BEC of photons (equation (1)).

Spatial images of the photon gas below and slightly above criticality are shown in Fig. 2b. In either case the lower energetic (yellow) photons are bound to the trap centre while the higher energetic (green) photons appear at the outer trap regions. Above the critical photon number a bright spot is visible in the trap centre with a full width at half-maximum (FWHM) diameter of (14 ± 3) μm , indicating a macroscopically populated TEM₀₀-mode (expected diameter 12.2 μm). Figure 2c shows normalized spatial intensity profiles along one axis for increasing pumping power near the critical value. Interestingly, we observe that the mode diameter enlarges with increasing condensate fraction, as shown in Fig. 2d. This effect is not expected for an ideal gas of photons. In principle, this could be due to a Kerr nonlinearity in the dye solution, but the most straightforward explanation is a weak repulsive optical self-interaction from thermal lensing in the dye (which can be modelled by a mean-field interaction; see Methods). From the increase of the mode diameter we can estimate the magnitude of this effective repulsive interaction, yielding a dimensionless interaction parameter of $\tilde{g} \approx (7 \pm 3) \times 10^{-4}$. This is much below the values $\tilde{g} = 10^{-2} \dots 10^{-1}$ reported for two-dimensional atomic physics quantum gas experiments and also below the value at which Kosterlitz–Thouless physics, involving ‘quasi-long-range’ order, is expected to become relevant²³. The latter is supported by an experiment directing the condensate peak through a shearing interferometer, in which we have not seen signatures of the phase blurring expected for a Kosterlitz–Thouless phase²⁴.

We have tested for a dependence of the BEC threshold on the resonator geometry. From equation (1) we expect a critical optical power $P_c = (\pi^2/12)(k_B T)^2(\omega_{\text{cut-off}}/\hbar c)R$, which grows linearly with the mirror radius of curvature R and is independent of the longitudinal mode number q . Figure 3a and the lower panel of Fig. 3b show corresponding measurements of the critical power, with results in good agreement with both the expected absolute values and the expected scaling. The upper panel of Fig. 3b gives the required optical pump power to achieve the phase transition versus the number of longitudinal modes, showing a decrease because of stronger pump power absorbance for larger mirror spacing. This is in strong contrast to results reported from ‘thresholdless’ optical microlasers, for which an increase of the threshold pumping power was observed^{25,26}. For a macroscopic laser a fixed value of the pump intensity is required to reach inversion.

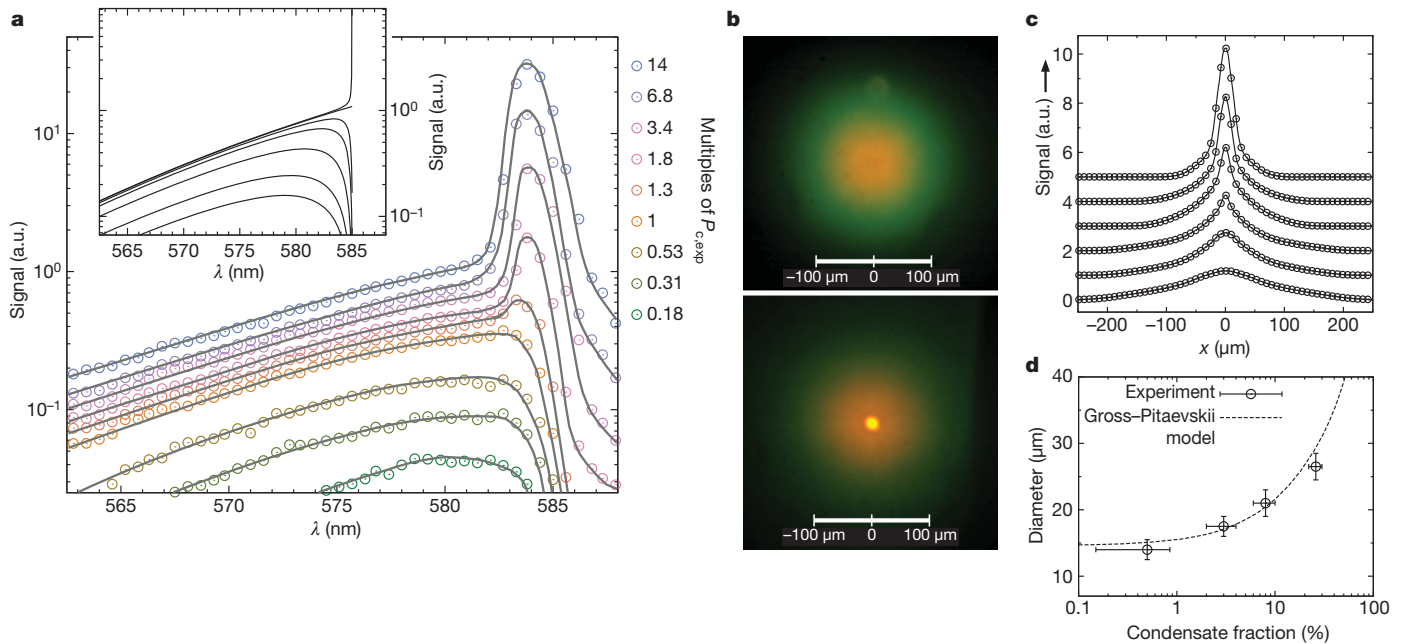


Figure 2 | Spectral and spatial intensity distribution. **a**, Spectral intensity distributions (connected circles) transmitted through one cavity mirror, as measured with a spectrometer, for different pump powers (see colour key). The intracavity power (in units of $P_{c, \text{exp}} = (1.55 \pm 0.60) \text{ W}$) is derived from the power transmitted through one cavity mirror. A spectrally sharp condensate peak at the cavity cut-off is observed above a critical power level, with a width limited by the spectrometer resolution. The inset gives theoretical spectra (solid lines) based on a Bose-Einstein distribution of photons for different particle numbers at room temperature¹⁴. a.u., arbitrary units. **b**, Images of the spatial

radiation distribution transmitted through one cavity mirror both below (upper panel) and above (lower panel) criticality, showing a macroscopically occupied TEM_{00} -mode for the latter case. **c**, **d**, Cut through the centre of the intensity distribution for increasing optical pump powers (**c**) and width of the condensate peak versus condensate fraction, along with a theoretical model based on the Gross-Pitaevskii equation with an interaction parameter $\bar{g} = 7 \times 10^{-4}$ (Methods) (**d**). Error bars are the systematic calibration uncertainties. $q = 11$ for **c** and **d**. All other measurements use $q = 7$.

Finally, we have investigated the condensation for a spatially mismatched pumping spot. Owing to the thermal redistribution of photons we expect that even a spatially displaced pump beam can provide a sufficiently high photon density at the trap centre to reach the phase transition. This effect is not known in lasers, but is observed in the framework of polariton condensation⁷. For our measurement, the pump beam (diameter about $35 \mu\text{m}$) was displaced at about $50 \mu\text{m}$ from the trap centre. Figure 4 shows a series of spatial intensity profiles recorded for a fixed pumping power and for different values of the cavity cut-off

wavelength $\lambda_{\text{cut-off}}$, which tunes the degree of thermalization¹⁴. The lower graph gives results recorded with $\lambda_{\text{cut-off}} \cong 610 \text{ nm}$, for which the maximum fluorescence is centred at the position of the pump spot (shown by a dashed line). The weak reabsorption in this wavelength range prevents efficient photon thermalization. When the cut-off is moved to shorter wavelengths, the stronger reabsorption in this wavelength range leads to increasingly symmetric photon distributions

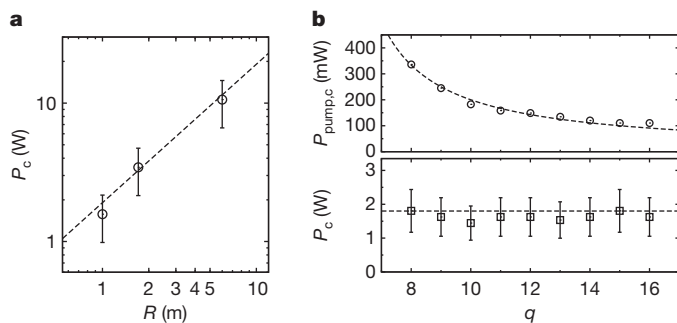


Figure 3 | Critical power. **a**, Intracavity power at criticality for different curvatures of the cavity mirrors. The dashed line shows the theoretical expectation based on equation (1). **b**, Intracavity power at criticality (lower panel) versus longitudinal mode number q . The upper panel shows the required optical pump power $P_{\text{pump}, c}$ (circles) along with a fit $P_{\text{pump}, c} \propto (q - q_0)^{-1}$ yielding $q_0 = 4.77 \pm 0.25$. For this we assume an inverse proportionality to the absorption length in the dye $q - q_0$, where q_0 incorporates an effective penetration depth into the cavity mirrors. The above value for q_0 is in good agreement with an independent measurement of the pump power transmission, yielding $q_0 = 4.77 \pm 0.17$. Error bars are systematic uncertainties.

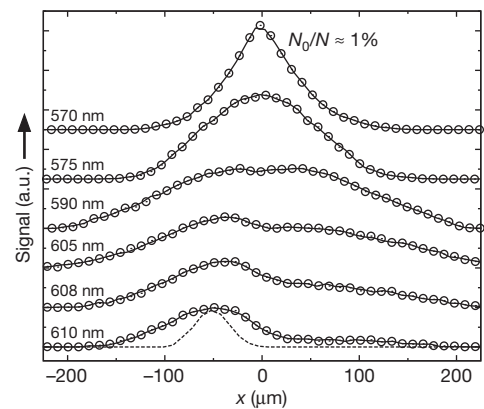


Figure 4 | Spatial redistribution of photons. Intensity profiles recorded with a pump beam spot (diameter about $35 \mu\text{m}$) spatially displaced by $50 \mu\text{m}$ from the trap centre, for different cut-off wavelengths. For a cut-off wavelength of 610 nm (bottom profile), where reabsorption is weak, the emitted radiation is centred at the position of the pump spot, whose profile is shown by the dashed line (measured by removing one of the cavity mirrors). When tuning the cavity cut-off to shorter wavelength values, where the reabsorption efficiency is increased, light is redistributed towards the trap centre. For data recorded with a 570 nm cut-off wavelength (top profile), a cusp appears, corresponding to a partly condensed state with a condensate fraction N_0/N of about 1%.

around the trap centre. For a cavity cut-off near 570 nm we observe a small bright spot at the position of the TEM₀₀-mode. The corresponding cusp in the intensity profile of Fig. 4 indicates a condensate fraction of roughly $N_0/N \approx 1\%$. These measurements show that owing to the photon thermalization, BEC can be achieved even when the pumping intensity at the position of the ground state mode is essentially zero.

To conclude, evidence for a BEC of photons was obtained from (1) the spectral distribution that shows Bose–Einstein distributed photon energies, including a macroscopically occupied ground state, (2) the observed onset of the phase transition, which occurs both at the predicted absolute value of the photon number and shows the expected scaling with resonator geometry, and (3) the condensation appearing at the trap centre even for a spatially disjunct pump spot. It is instructive to discuss the relation of a photon BEC to microlasers, which also use high finesse cavities to capture the emission of excited-state atoms and molecules in a small volume^{25–27}. The low lasing thresholds and potentially inversionless oscillation of microlasers, however, result from a high coupling efficiency of spontaneous photons into a single cavity mode—which is not the case here, as is evident from the observed highly multimodal emission below criticality. The main difference between a laser and BEC remains that the BEC (in contrast to the laser) is in thermal equilibrium, with the macroscopically populated mode being a consequence of equilibrium Bose statistics.

An interesting consequence of a grand-canonical particle exchange between photon gas and the reservoir of excited state dye molecules is that unusually large number fluctuations of the condensed phase could occur²⁸. We expect that the concept of photon condensation holds promise for the exploration of novel states of light, and for light sources in new wavelength regimes.

METHODS SUMMARY

Preparation of photon gas. Photons are confined in an optical microresonator consisting of two curved dielectric mirrors with >99.997% reflectivity, filled with dye solution. The dye is pumped with a laser beam near 532 nm wavelength (about 70 μm diameter except for Fig. 4) directed at an angle of 45° to the optical axis, exploiting a reflectivity minimum of the mirrors. The trapped photon gas thermalizes to the rovibrational temperature T of the dye solution by repeated absorption and emission processes, as follows from a detailed balance condition¹⁴ fulfilled in media obeying the Kennard–Stepanov relation²⁹ $f_T(\omega)/\alpha_T(\omega) \propto \omega^3 e^{-h\omega/k_B T}$, which describes a temperature-dependent frequency scaling of absorption coefficient $\alpha_T(\omega)$ versus emission strength $f_T(\omega)$. We note that this equilibrium between photons and the dye solution is reminiscent of Einstein's description of the heat contact between radiation and a Doppler-broadened gas³⁰.

Photon dispersion in cavity and optical self-interaction. The photon energy in the resonator as a function of transversal (k_r) and longitudinal (k_z) wavenumber reads $E = \hbar c \sqrt{k_z^2 + k_r^2}$, where c denotes the speed of light in the medium. The boundary conditions yield $k_z(r) = q\pi/D(r)$, where $D(r) = D_0 - 2(R - \sqrt{R^2 - r^2})$ gives the mirror separation at distance r from the optical axis. For fixed longitudinal mode number q and in paraxial approximation ($r \ll R$, $k_r \ll k_z$), one arrives at the dispersion of a particle with nonvanishing mass $m_{ph} = \hbar k_z(0)/c = \hbar \omega_{cut-off}/c^2$, with its motion restricted to the (two-dimensional) transverse resonator plane under harmonic confinement with trapping frequency $\Omega = c\sqrt{2}/D_0 R$; see ref. 14. A possible self-interaction of photons (Kerr lensing or thermal lensing in the limit of negligible transverse heat flow) can be incorporated by $n(r) = n_0 + n_2 I(r)$, where $I(r)$ is the optical intensity and n_0 (≈ 1.33 for methanol) and n_2 are the linear and nonlinear indices of refraction respectively, yielding:

$$E \approx m_{ph} c^2 + \frac{(\hbar k_r)^2}{2m_{ph}} + \frac{1}{2} m_{ph} \Omega^2 r^2 - m_{ph} c^2 \frac{n_2}{n_0} I(r) \quad (2)$$

The latter term resembles a mean-field interaction familiar from the Gross–Pitaevskii equation for atomic BECs, which, using a dimensionless interaction parameter²³ $\tilde{g} = -(m_{ph}^4 c^6 n_2)/(2\pi \hbar^3 n_0 q)$ and wavefunction $\psi(r)$ with $I(r) = (m_{ph} c^2)^2 (h q)^{-1} N_0 |\psi(r)|^2$, can be written in the more familiar form:

$$E_{int} = (\hbar^2/m_{ph}) \tilde{g} N_0 |\psi(r)|^2$$

Received 12 July; accepted 6 October 2010.

- Einstein, A. Quantentheorie des einatomigen idealen Gases. Zweite Abhandlung. *Sitz. ber. Preuss. Akad. Wiss.* **1**, 3–14 (1925).
- Anderson, M. H., Ensher, J. R., Matthews, M. R., Wieman, C. E. & Cornell, E. A. Observation of Bose–Einstein condensation in a dilute atomic vapor. *Science* **269**, 198–201 (1995).
- Davis, K. B. *et al.* Bose–Einstein condensation in a gas of sodium atoms. *Phys. Rev. Lett.* **75**, 3969–3973 (1995).
- Bradley, C. C., Sackett, C. A. & Hulet, R. G. Bose–Einstein condensation of lithium: observation of limited condensate number. *Phys. Rev. Lett.* **78**, 985–989 (1997).
- Deng, H., Weihs, G., Santori, C., Bloch, J. & Yamamoto, Y. Condensation of semiconductor microcavity exciton polaritons. *Science* **298**, 199–202 (2002).
- Kasprzak, J. *et al.* Bose–Einstein condensation of exciton polaritons. *Nature* **443**, 409–414 (2006).
- Balili, R., Hartwell, V., Snoke, D., Pfeiffer, L. & West, K. Bose–Einstein condensation of microcavity polaritons in a trap. *Science* **316**, 1007–1010 (2007).
- Demokritov, S. O. *et al.* Bose–Einstein condensation of quasi-equilibrium magnons at room temperature under pumping. *Nature* **443**, 430–433 (2006).
- Griffin, A., Snoke, D. W. & Stringari, S. (eds) *Bose–Einstein Condensation* (Cambridge University Press, 1995).
- Huang, K. *Statistical Mechanics* 2nd edn 293–294 (Wiley, 1987).
- Zel'dovich, Y. B. & Levich, E. V. Bose condensation and shock waves in photon spectra. *Sov. Phys. JETP* **28**, 1287–1290 (1969).
- Chiao, R. Y. Bogoliubov dispersion relation for a 'photon fluid': is this a superfluid? *Opt. Commun.* **179**, 157–166 (2000).
- Bolda, E. L., Chiao, R. Y. & Zurek, W. H. Dissipative optical flow in a nonlinear Fabry–Pérot cavity. *Phys. Rev. Lett.* **86**, 416–419 (2001).
- Klaers, J., Vewinger, F. & Weitz, M. Thermalization of a two-dimensional photonic gas in a 'white-wall' photon box. *Nature Phys.* **6**, 512–515 (2010).
- Jonkers, J. High power extreme ultra-violet (EUV) light sources for future lithography. *Plasma Sources Sci. Technol.* **15**, S8–S16 (2006).
- Siegman, A. E. *Lasers* (University Science Books, 1986).
- Ketterle, W., Durfee, D. S. & Stamper-Kurn, D. M. in *Bose–Einstein Condensation in Atomic Gases* (eds Inguscio, M., Stringari, S. & Wieman, C. E.) CXL, 67–176 (Proceedings of the International School of Physics 'Enrico Fermi', IOS Press, 1999).
- De Angelis, E., De Martini, F. & Mataloni, P. Microcavity superradiance. *J. Opt. B* **2**, 149–155 (2000).
- Yokoyama, H. & Brorson, S. D. Rate equation analysis of microcavity lasers. *J. Appl. Phys.* **66**, 4801–4805 (1989).
- Bagnato, V. & Kleppner, D. Bose–Einstein condensation in low-dimensional traps. *Phys. Rev. A* **44**, 7439–7441 (1991).
- Mullin, W. J. Bose–Einstein condensation in a harmonic potential. *J. Low-Temp. Phys.* **106**, 615–641 (1997).
- Lakowicz, J. R. *Principles of Fluorescence Spectroscopy* 2nd edn, 6 (Kluwer Academic/Plenum, 1999).
- Hadzibabic, Z. & Dalibard, J. Two-dimensional Bose fluids: an atomic physics perspective. Preprint at (<http://arxiv.org/abs/0912.1490>) (2009).
- Hadzibabic, Z., Krüger, P., Cheneau, M., Battelier, B. & Dalibard, J. Berezinskii–Kosterlitz–Thouless crossover in a trapped atomic gas. *Nature* **441**, 1118–1121 (2006).
- De Martini, F. & Jacobovitz, G. R. Anomalous spontaneous–stimulated-decay phase transition and zero-threshold laser action in a microscopic cavity. *Phys. Rev. Lett.* **60**, 1711–1714 (1988).
- Yokoyama, H. *et al.* Controlling spontaneous emission and threshold-less laser oscillation with optical microcavities. *Quantum Electron.* **24**, S245–S272 (1992).
- Yamamoto, Y., Machida, S. & Björk, G. Micro-cavity semiconductor lasers with controlled spontaneous emission. *Opt. Quantum Electron.* **24**, S215–S243 (1992).
- Kocharovskiy, V. V. *et al.* Fluctuations in ideal and interacting Bose–Einstein condensates: from the laser phase transition analogy to squeezed states and Bogoliubov quasiparticles. *Adv. At. Mol. Opt. Phys.* **53**, 291–411 (2006).
- McCumber, D. E. Einstein relations connecting broadband emission and absorption spectra. *Phys. Rev.* **136**, A954–A957 (1964).
- Einstein, A. Zur Quantentheorie der Strahlung. *Physik. Zeitschr.* **18**, 121–128 (1917).

Acknowledgements We thank J. Dalibard and Y. Castin for discussions. Financial support from the Deutsche Forschungsgemeinschaft within the focused research unit FOR557 is acknowledged. M.W. thanks the IFRAF for support of a guest stay at LKB Paris, where part of the discussion on interacting two-dimensional photon gases was developed.

Author Contributions J.K. and M.W. contributed to the experimental idea; J.K. carried out the experiments. J.S. contributed to the experimental set-up. All authors analysed the experimental data and discussed the results.

Author Information Reprints and permissions information is available at www.nature.com/reprints. The authors declare no competing financial interests. Readers are welcome to comment on the online version of this article at www.nature.com/nature. Correspondence and requests for materials should be addressed to M.W. (martin.weitz@uni-bonn.de).

Growth of graphene from solid carbon sources

Zhengzong Sun¹, Zheng Yan¹, Jun Yao², Elvira Beitler¹, Yu Zhu¹ & James M. Tour^{1,3}

Monolayer graphene was first obtained¹ as a transferable material in 2004 and has stimulated intense activity among physicists, chemists and material scientists^{1–4}. Much research has been focused on developing routes for obtaining large sheets of monolayer or bilayer graphene. This has been recently achieved by chemical vapour deposition (CVD) of CH₄ or C₂H₂ gases on copper or nickel substrates^{5–7}. But CVD is limited to the use of gaseous raw materials, making it difficult to apply the technology to a wider variety of potential feedstocks. Here we demonstrate that large area, high-quality graphene with controllable thickness can be grown from different solid carbon sources—such as polymer films or small molecules—deposited on a metal catalyst substrate at temperatures as low as 800 °C. Both pristine graphene and doped graphene were grown with this one-step process using the same experimental set-up.

With its extraordinary electronic and mechanical properties, graphene is showing promise in a plethora of applications^{7–13}. Graphene can now be obtained by several different approaches. The original mechanical peeling method from highly oriented pyrolytic graphite yields small amounts of high quality graphene¹. Liquid exfoliation and reduction of graphene oxide have been used to produce chemically converted graphene in large quantities^{14,15}. Annealing SiC, growth from amorphous carbon and CVD methods have been used to synthesize large-size graphene on wafers^{5–7,16,17}. By introducing Ni and Cu as the substrates for CVD growth, the size, thickness and quality of the produced graphene is approaching industrially useful specifications^{5–7}. However, intrinsic graphene is a zero bandgap material that shows a weak ambipolar behaviour; transistors based on such graphene show small 'on'/off current ratios, so they are too metallic for many designed electronics applications¹⁸. In order to modify the Fermi level of graphene and manipulate its electronic and optical properties, doping the graphene matrix with heteroatoms is a straightforward way to make an n-type, p-type or hybrid doped graphene^{19–23}.

In the present work, the growth of monolayer pristine graphene from solid carbon sources atop metal catalysts is demonstrated (Fig. 1a). The first solid carbon source used was a spin-coated poly(methyl methacrylate) (PMMA) thin film (~100 nm) and the metal catalyst substrate was a Cu film. At a temperature as low as 800 °C or as high as 1,000 °C (tested limit) for 10 min, with a reductive gas flow (H₂/Ar) and under low pressure conditions, a single uniform layer of graphene was formed on the substrate. The graphene material thus produced was successfully transferred to different substrates for further characterization (see Supplementary Materials and Supplementary Methods).

The Raman spectrum of this monolayer PMMA-derived graphene is shown in Fig. 1b and the spectrum is characteristic of >10 locations recorded over 1 cm² of the sample. The two most pronounced peaks in this spectrum are the G peak at 1,580 cm⁻¹ and the 2D peak at 2,690 cm⁻¹. The I_{2D}/I_G intensity ratio is about 4 and the full-width at half-maximum of the 2D peak is about 30 cm⁻¹, indicating that the graphene is a monolayer. The D peak (~1,350 cm⁻¹) is in the noise level, indicating the presence of few sp³ carbon atoms or defects²⁴.

The electrical properties of the PMMA-derived graphene were evaluated with back-gated graphene-based field-effect transistor (FET)

devices atop a 200-nm-thick SiO₂ dielectric. Typical data for the FET devices are shown in Fig. 1c. For this particular device, the estimated carrier (hole) mobility is ~410 cm² V⁻¹ s⁻¹ at room temperature and the 'on'/off current ratio is ~2, which is expected in graphene-based FET devices of this size²¹. Although the graphene was pristine without any doping atoms, it still shows weak p-type behaviour, with the neutrality point moved to positive gate voltage; this probably arises from the physisorption of small molecules, such as H₂O (ref. 10). Placing graphene FETs under high vacuum (10⁻⁵–10⁻⁶ torr) for several days moves the neutrality point to zero (Supplementary Fig. 1), confirming that the weak p-type behaviour was due to physisorption of volatile molecules¹⁰.

Transmission electron microscopy (TEM) images of the pristine PMMA-derived graphene and its diffraction pattern are shown in Fig. 1d–g. The selected area electron diffraction (SAED) pattern in Fig. 1d displays the typical hexagonal crystalline structure of graphene. The layer count on the edges of the images indicates the thickness of this PMMA-derived graphene. The edges in Fig. 1e–g were randomly imaged under TEM and most were monolayer or bilayer graphene, which corroborates the Raman data. Although most of the graphene surface was continuous and crystalline according to its diffraction pattern, there is adsorbed PMMA resulting from the transfer step. Metal atoms or ions were also found to be trapped on the graphene surface (black arrows in Fig. 1g) and became charge impurities, which should increase the charge density but decrease the mobility of the PMMA-derived graphene²⁵. Similar phenomena have been observed with CVD-generated graphene^{5–7}. Atomic force microscopy was used to characterize the surface profile of PMMA-derived graphene on a SiO₂/Si substrate. In Supplementary Fig. 2, the thickness of this graphene is about 0.7 nm, which confirms the monolayer nature of this material. However, limited by the wet-transfer technique, graphene's intrinsic corrugation is still obvious in the AFM image.

Graphene's electronic properties are strongly linked to its thickness²⁶. Therefore, it would be useful to be able to control the thickness when producing the graphene by tuning the growth parameters. We have found that the thickness of PMMA-derived graphene can be controlled—to give a monolayer, a bilayer, or a few layers—by changing the Ar and H₂ gas flow rate. Typical thicknesses were evaluated by Raman spectroscopy (Fig. 2a) and ultraviolet transmittance (Fig. 2b) of the graphene. At 1,000 °C, bilayer PMMA-derived graphene was obtained when the Ar flow rate was 500 cm³ STP min⁻¹ and the H₂ flow rate was 10 cm³ STP min⁻¹. When the Ar flow rate was 500 cm³ STP min⁻¹ and the H₂ flow rate was 3–5 cm³ STP min⁻¹, few-layer PMMA-derived graphene formed. When the H₂ flow rate was increased to 50 cm³ STP min⁻¹ or higher, only monolayer graphene was formed on the Cu substrate. Monolayer graphene showed a transmittance of 97.1% at 550 nm wavelength (Fig. 2b). It had a sheet resistance (R_s) of 1,200 Ω per square by the four-probe method, which makes it a transparent electrode material of interest. The bilayer graphene's transmittance at 550 nm wavelength is 94.3%, which shows linear enhancement in the ultraviolet absorption. The few-layer PMMA-derived graphene sheet in Fig. 2a has a transmittance of 83% at 550 nm, leading to an estimated six-layer thickness. Both the

¹Department of Chemistry, Rice University, 6100 Main Street, Houston, Texas 77005, USA. ²Applied Physics Program, Department of Bioengineering, Rice University, 6100 Main Street, Houston, Texas 77005, USA. ³Richard E. Smalley Institute for Nanoscale Science and Technology, Department of Mechanical Engineering and Materials Science, Rice University, 6100 Main Street, Houston, Texas 77005, USA.

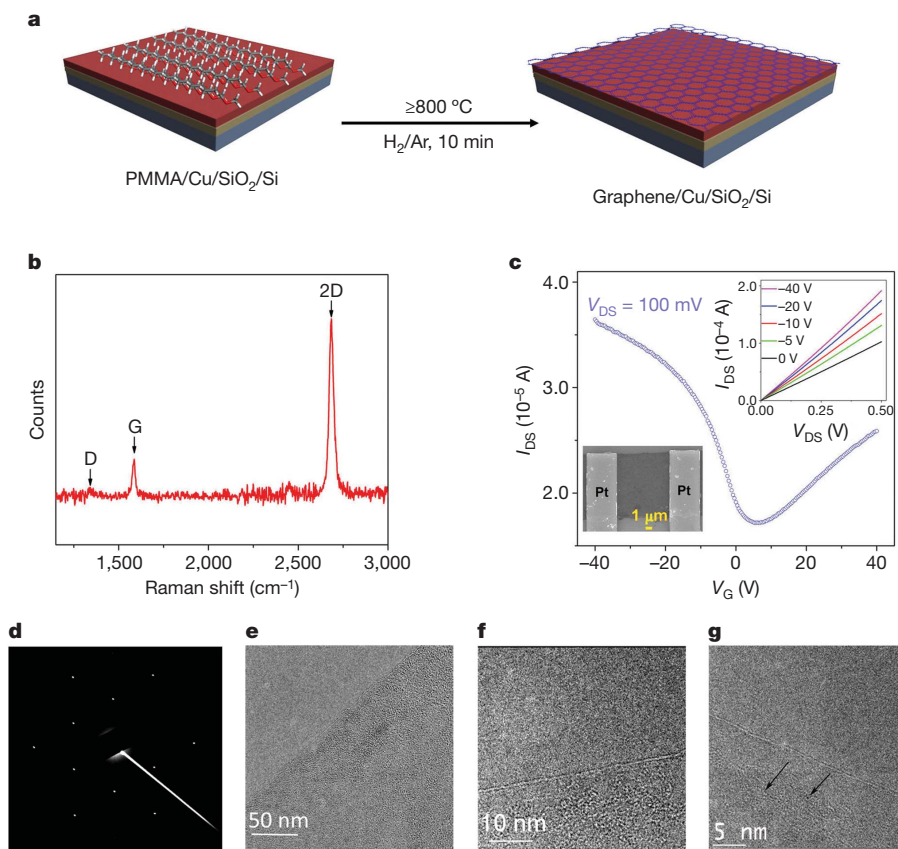


Figure 1 | Synthetic protocol, spectroscopic analysis and electrical properties of PMMA-derived graphene. **a**, Monolayer graphene is derived from solid PMMA films on Cu substrates by heating in an H₂/Ar atmosphere at 800 °C or higher (up to 1,000 °C). **b**, Raman spectrum (514 nm excitation) of monolayer PMMA-derived graphene obtained at 1,000 °C. See text for details. **c**, Room temperature $I_{\text{DS}}-V_{\text{G}}$ curve from a PMMA-derived graphene-based back-gated FET device. Top inset, $I_{\text{DS}}-V_{\text{DS}}$ characteristics as a function of V_{G} ;

shape and the positions of the 2D peak are significantly different from monolayer graphene to bilayer graphene and few-layer graphene (Supplementary Fig. 3). For monolayer graphene, the 2D peak can be fitted with a single sharp Lorentz peak. The observed 2D splitting in bilayer and few-layer PMMA-derived graphene can be assigned to the electronic band splitting caused by the interaction of the graphene planes²⁴. The Raman mapping of the G to 2D peak ratio illustrates the uniformity of the graphene films over the 70–75 μm^2 areas investigated (Supplementary Fig. 4). For monolayer graphene, more than 95% of the film has this signature, with $I_{\text{G}}/I_{\text{2D}} < 0.4$. The bilayer graphene has more than 85% coverage, with an $I_{\text{G}}/I_{\text{2D}} \approx 0.8$.

We interpret the effect of hydrogen as follows: hydrogen acts as both the reducing reagent and a carrier gas to remove C atoms that are extruded from the decomposing PMMA during growth. A slower H₂ flow leaves more C sources for the growth of multilayer graphene. Owing to the low concentration and solubility of the carbon source in Cu, traditional CVD-grown graphene on Cu usually terminates as a monolayer. In this experiment, highly concentrated and uniformly dispersed carbon sources favour multilayer graphene when the H₂ flow is low. The higher-order layers might form through graphitization directly atop the first layer, which blocks the contact of the carbon sources with the metal catalyst. Some metal catalysts, such as Ni, are known to reverse graphene growth by converting graphene to hydrocarbon products, therefore cutting graphene along specific directions²⁷. This reverse reaction does not appear to occur on the PMMA-derived graphene which is atop the Cu.

High quality monolayer PMMA-derived graphene was obtained at 800 °C by this method; this is lower than the CVD growth temperature

V_{G} changes from 0 V (bottom) to -40 V (top). Bottom inset, SEM (JEOL-6500 microscope) image of this device where the PMMA-derived graphene is perpendicular to the Pt leads. I_{DS} , drain-source current; V_{G} , gate voltage; V_{DS} , drain-source voltage. **d**, SAED pattern of PMMA-derived graphene. **e–g**, HRTEM images of PMMA-derived graphene films at increasing magnification. In **g**, black arrows indicate Cu atoms.

on Cu used in the original report⁶ (see Supplementary Fig. 5). For the semiconductor industry, the lower processing temperature is favourable because temperatures as high as 1,000 °C would be problematic in the fabrication of the multi-layer stacks of heterogeneous materials. Therefore, in addition to changing the Ar/H₂ flow rate, the graphene growth process was conducted at different temperatures. The quality of the graphene films was monitored by the D/G peak ratio from Raman spectroscopic analysis. The peak ratio for graphene sheets obtained at 800 °C was less than 0.1. At 750 °C, the peak ratio was ~ 0.35 ; hence 800 °C is the lower limit for obtaining high quality graphene from PMMA (Supplementary Fig. 5). We used other solid carbon sources—including fluorene (C₁₃H₁₀) and sucrose (table sugar, C₁₂H₂₂O₁₁)—to grow monolayer graphene on Cu catalyst under the same growth conditions as was used for the PMMA-derived graphene. Because these precursors are powders not films, 10 mg of each as a finely ground powder was placed directly on a 1 cm² Cu foil. After subjecting the powder-coated Cu films to the same reaction conditions as used for PMMA-derived graphene, Raman spectra indicated that all of the solid carbon sources were transformed into monolayer graphene with no D peak observed (Fig. 2c). Although these solid carbon precursors contain potential topological defect generators (the five-membered ring in fluorene) or high concentrations of heteroatoms (oxygen in sucrose), they produce high quality pristine graphene. It is possible that at elevated temperatures under vacuum, C has a higher affinity for the metal catalyst surface than the heteroatoms; atom rearrangement occurs and most of the topological defects are self-healed as the graphene is formed.

Other substrates—such as Ni, Si<100> with native oxide, and 200-nm-thick SiO₂ thermally grown—were also tested to determine if they

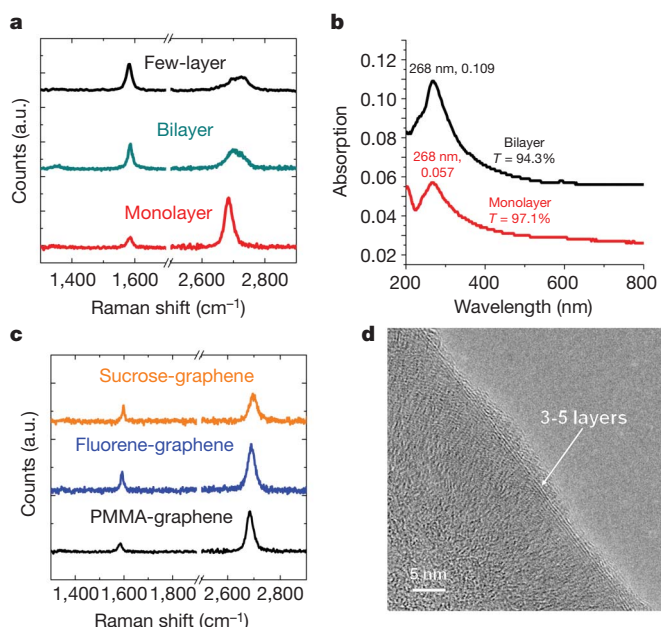


Figure 2 | Controllable growth of pristine PMMA-derived graphene films. **a**, Difference in Raman spectra from PMMA-derived graphene samples with controllable thicknesses derived from different flow rates of H_2 . **b**, The ultraviolet–visible absorption spectra of monolayer graphene and bilayer graphene; peaks are labelled with wavelength of maximum absorption, and value of maximum absorption. The UV transmittance (T in %) is measured at 550 nm. **c**, Raman spectra of graphene derived from sucrose, fluorene and PMMA. **d**, HRTEM picture of PMMA-derived graphene grown on a Ni film. The PMMA-derived graphene was 3–5 layers thick at the edges.

would grow graphene when coated with PMMA. Figure 2d is the high-resolution TEM image of PMMA-derived graphene grown on a Ni catalyst, which clearly illustrates the few-layer structure around the edges of PMMA-derived graphene. The Raman spectra (Supplementary Fig. 6) confirm that Ni is an efficient catalytic substrate that converts PMMA into highly crystalline graphene materials with no D peak around $1,350\text{ cm}^{-1}$. Under the same growth conditions, neither graphene nor amorphous carbon was obtained on Si or SiO_2 substrates, according to the Raman spectroscopic analysis of the surface after the reaction. This demonstrates the potential to grow patterned graphene from a thin film of shaped Ni or Cu deposited directly on SiO_2/Si wafers without post lithographic treatment, as PMMA-derived graphene will not grow on the Si or SiO_2 surfaces.

Pristine graphene can show weak p-type or n-type behaviour due to physisorption of small molecules, such as H_2O or NH_3 (ref. 8). However, this chemical doping effect induced by physisorption is labile, because the small molecules can be easily desorbed under heat or vacuum. Therefore, intrinsically nitrogen-doped (N-doped) graphene is more challenging to make than pristine graphene. Intrinsically N-doped graphene has been obtained by two methods: introducing a doping gas (NH_3) into the CVD systems during the graphene growth²¹ or treatment of synthesized graphene or graphene oxide with NH_3 by annealing or through plasma^{20,28,29}. Here, by using solid carbon sources and solid doping reagents, doped graphene can be grown in one step without any changes to the CVD system.

A doping reagent, melamine ($\text{C}_3\text{N}_6\text{H}_6$), was mixed with PMMA and spin-coated onto the Cu surface. In order to keep the nitrogen-atom concentration in the systems, we use conditions similar to those employed for the growth of PMMA-derived graphene, except that the growth was done at atmospheric pressure (Supplementary Information). The prepared polymer films were successfully converted into N-doped graphene, with an N content of 2–3.5%. The X-ray photoemission spectroscopy (XPS) data (Fig. 3a) show the difference in C 1s peaks between PMMA-derived graphene and N-doped

PMMA-derived graphene. The shoulder around 287 eV can be assigned to the C–N bonding. The N 1s peak of N-doped PMMA-derived graphene indicates that only one type of N is present, at 399.8 eV, corresponding to quaternary N in graphene²⁹. This new N 1s peak also has a 4 eV shift from that in melamine, which shows an N 1s peak at 395.8 eV (Supplementary Fig. 7). The new N 1s peak suggests that the N 1s signal does not come from the melamine, but that the N atoms are uniformly bound into the graphene structure. The D peak of this material is always present in the Raman spectra, because the heteroatoms break the graphene symmetry and thereby introduce defects that are detected by Raman analysis (Fig. 3c). The D' peak is also found in doped graphene materials obtained by the other doping methods^{22,28}. The $2\text{D}/I_{\text{G}}$ intensity ratio reveal that this N-doped PMMA-derived graphene is monolayer graphene. Compared to PMMA-derived graphene, the $I_{2\text{D}}/I_{\text{G}}$ ratio decreased from 4 to 2, implying a successful doping, according to the previously reported electrostatically gated Raman results³⁰.

Doping effects were also demonstrated by FETs based on N-doped PMMA-derived graphene. The n-type behaviour shown in Fig. 3d, with the neutrality point shifted to negative gate voltage, is consistently observed for devices on the same piece of N-doped PMMA-derived graphene. After keeping these FET devices under vacuum (10^{-5} – 10^{-6} torr) for 24 h, their neutrality point did not move to 0 V, indicative of the covalent bonding between carbon and nitrogen rather than just physisorption; the dopant N atoms donate free electrons to graphene. Meanwhile, the mobility of N-doped graphene calculated from the N-doped FETs was about two orders of magnitude lower than in PMMA-derived graphene²¹. Owing to the broken symmetry of the lattice structure of the N-doped graphene, the N atoms act as scattering centres that suppress its mobility²⁶. Patterned hydrogenation on graphene already shows its bandgap opening³¹. Similarly, if the doping atoms are periodically dispersed in graphene's matrix, they can not only

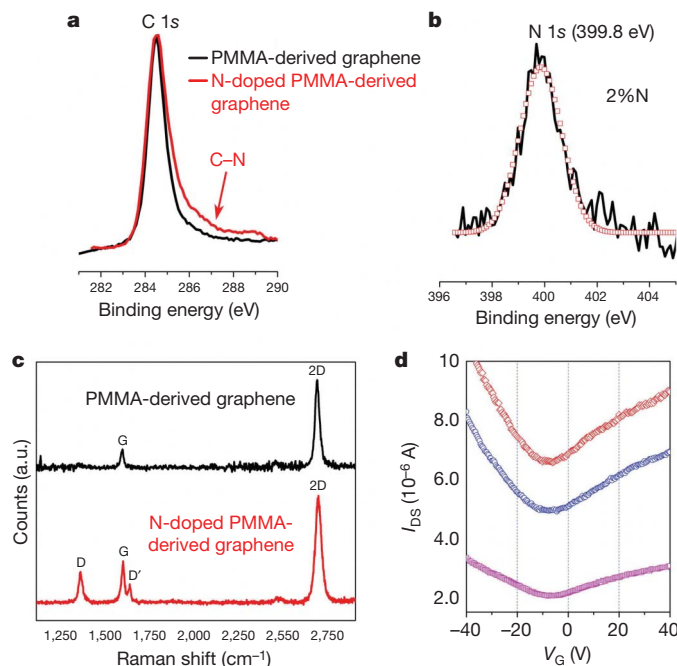


Figure 3 | Spectroscopic analysis and electrical properties of pristine and N-doped PMMA-derived graphene. **a**, XPS analysis from the C 1s peak of PMMA-derived graphene (black) and N-doped PMMA-derived graphene (red); the shoulder can be assigned to the C–N bond. **b**, XPS analysis, showing the N 1s peak (black line) and its fitting (squares), of N-doped PMMA-derived graphene. The atomic concentration of N for this sample is about 2% (C is 98%). No N 1s peak was observed for pristine PMMA-derived graphene. **c**, Raman spectra of pristine and N-doped PMMA-derived graphene. **d**, Room temperature $I_{\text{DS}}-V_{\text{G}}$ curves ($V_{\text{DS}} = 500\text{ mV}$) showing n-type behaviour obtained from three different N-doped graphene-based back-gated FET devices.

tune the Fermi level of graphene, but also tailor its bandgap. However, in the present N-doped graphene, the 'on'/off current ratio does not increase, which suggests that the N atoms are randomly incorporated into the graphenic matrix. In order to manipulate both the Fermi level and the bandgap of graphene, patterned doping has to be achieved³¹.

In conclusion, we have demonstrated a one-step method for the controllable growth of both pristine graphene and doped graphene using solid carbon sources. This stands as a complementary method to CVD growth while permitting growth at lower temperature.

METHODS SUMMARY

Raman spectroscopy was performed on transferred graphene films on 100 nm SiO₂/Si wafers with a Renishaw Raman microscope using 514-nm laser excitation at room temperature. The electrical properties were measured in a probe station (Desert Cryogenic TT-probe 6 system) under vacuum (10^{-5} – 10^{-6} torr). The *I*–*V* data were collected by an Agilent 4155C semiconductor parameter analyser. The high-resolution TEM images were taken using a 2100F field emission gun transmission electron microscope with graphene samples directly transferred onto a C-flat TEM grid (Protochips). XPS was performed on a PHI Quantera SXM scanning X-ray microprobe with 45° takeoff angle and 100 µm beam size.

Received 17 May; accepted 6 October 2010.

Published online 10 November 2010.

- Novoselov, K. S. *et al.* Electric field effect in atomically thin carbon films. *Science* **306**, 666–669 (2004).
- Geim, A. K. & Novoselov, K. S. The rise of graphene. *Nature Mater.* **6**, 183–191 (2007).
- Novoselov, K. S. *et al.* Two-dimensional gas of massless Dirac fermions in graphene. *Nature* **438**, 197–200 (2005).
- Ruoff, R. S. Graphene: Calling all chemists. *Nature Nanotechnol.* **3**, 10–11 (2008).
- Reina, A. *et al.* Large area, few-layer graphene films on arbitrary substrates by chemical vapor deposition. *Nano Lett.* **9**, 30–35 (2009).
- Li, X. *et al.* Large-area synthesis of high-quality and uniform graphene films on copper foils. *Science* **324**, 1312–1314 (2009).
- Kim, K. S. *et al.* Large-scale pattern growth of graphene films for stretchable transparent electrodes. *Nature* **457**, 706–710 (2009).
- Lin, Y. *et al.* Operation of graphene transistors at gigahertz frequencies. *Nano Lett.* **9**, 422–426 (2009).
- Lin, Y. *et al.* 100-GHz transistors from wafer-scale epitaxial graphene. *Science* **327**, 662 (2010).
- Schedin, F. *et al.* Detection of individual gas molecules adsorbed on graphene. *Nature Mater.* **6**, 652–655 (2007).
- Stankovich, S. *et al.* Graphene-based composite materials. *Nature* **442**, 282–286 (2006).
- Stoller, M. D. *et al.* Graphene-based ultracapacitors. *Nano Lett.* **8**, 3498–3502 (2008).
- Schlapbach, L. & Züttel, A. Hydrogen-storage materials for mobile applications. *Nature* **414**, 353–358 (2001).
- Hernandez, Y. *et al.* High-yield production of graphene by liquid-phase exfoliation of graphite. *Nature Nanotechnol.* **3**, 563–568 (2008).
- Stankovich, S. *et al.* Synthesis of graphene-based nanosheets via chemical reduction of exfoliated graphene oxide. *Carbon* **45**, 1558–1565 (2007).
- Berger, C. *et al.* Electronic confinement and coherence in patterned epitaxial graphene. *Science* **312**, 1191–1196 (2006).
- Zheng, M. *et al.* Metal-catalyzed crystallization of amorphous carbon to graphene. *Appl. Phys. Lett.* **96**, 063110 (2010).
- Li, X. *et al.* Chemically derived, ultrasmooth graphene nanoribbon semiconductors. *Science* **319**, 1229–1232 (2008).
- Panchakarla, L. S. *et al.* Synthesis, structure, and properties of boron- and nitrogen-doped graphene. *Adv. Mater.* **21**, 4726–4730 (2009).
- Wang, X. *et al.* N-doping of graphene through electrothermal reactions with ammonia. *Science* **324**, 768–771 (2009).
- Wei, D. *et al.* Synthesis of N-doped graphene by chemical vapor deposition and its electrical properties. *Nano Lett.* **9**, 1752–1758 (2009).
- Ci, L. *et al.* Atomic layer of hybridized boron nitride and graphene domains. *Nature Mater.* **9**, 430–435 (2010).
- Rao, C. N. R. *et al.* Some novel attributes of graphene. *J. Phys. Chem. Lett.* **1**, 572–580 (2010).
- Ferrari, A. C. *et al.* Raman spectrum of graphene and graphene layers. *Phys. Rev. Lett.* **97**, 187401–187404 (2006).
- Chen, J. H. *et al.* Charge-impurity scattering in graphene. *Nature Phys.* **4**, 377–381 (2008).
- Zhang, Y. *et al.* Direct observation of widely tunable bandgap in bilayer graphene. *Nature* **459**, 820–823 (2009).
- Ci, L. *et al.* Controlled nanocutting of graphene. *Nano Res.* **1**, 116–122 (2008).
- Lin, Y. *et al.* Controllable graphene N-doping with ammonia plasma. *Appl. Phys. Lett.* **96**, 133110 (2010).
- Li, X. *et al.* Simultaneous nitrogen doping and reduction of graphene oxide. *J. Am. Chem. Soc.* **131**, 15939–15944 (2009).
- Das, A. *et al.* Monitoring dopants by Raman scattering in an electrochemically top-gated graphene transistor. *Nature Nanotechnol.* **3**, 210–215 (2008).
- Balog, R. *et al.* Bandgap opening in graphene induced by patterned hydrogen adsorption. *Nature Mater.* **9**, 315–319 (2010).

Supplementary Information is linked to the online version of the paper at www.nature.com/nature.

Acknowledgements This work was funded by the AFOSR (FA9550-09-1-0581) and the ONR MURI graphene programme (00006766).

Author Contributions Z.S. designed the experiments, discovered the procedures for graphene growth, performed the spectroscopic characterizations and analysis and wrote the manuscript. Z.Y. optimized the growth conditions and contributed to the spectroscopic characterizations. J.Y. performed the electrical measurements and analysis. E.B. contributed to the electrical measurements and analysis. Y.Z. carried out the sheet resistance and transmittance measurements. J.M.T. oversaw all research phases and revised the manuscript. All authors discussed and commented on the manuscript.

Author Information Reprints and permissions information is available at www.nature.com/reprints. The authors declare no competing financial interests. Readers are welcome to comment on the online version of this article at www.nature.com/nature. Correspondence and requests for materials should be addressed to J.M.T. (tour@rice.edu).

Bottom-up effects of plant diversity on multitrophic interactions in a biodiversity experiment

Christoph Scherber^{1,2}, Nico Eisenhauer^{3,4}, Wolfgang W. Weisser², Bernhard Schmid⁵, Winfried Voigt², Markus Fischer^{6,7}, Ernst-Detlef Schulze⁸, Christiane Roscher^{2,9}, Alexandra Weigelt^{2,10}, Eric Allan², Holger Beßler¹¹, Michael Bonkowski¹², Nina Buchmann¹³, François Buscot¹⁴, Lars W. Clement², Anne Ebeling^{1,2}, Christof Engels¹¹, Stefan Halle², Ilona Kertscher², Alexandra-Maria Klein^{2,15}, Robert Koller¹², Stephan König¹⁴, Esther Kowalski², Volker Kummer⁷, Annely Kuu¹⁶, Markus Lange², Dirk Lauterbach², Cornelius Middelhoff⁸, Varvara D. Migunova¹⁷, Alexandru Milcu¹⁸, Ramona Müller², Stephan Partsch³, Jana S. Petermann^{5,19}, Carsten Renker^{14,20}, Tanja Rottstock⁷, Alexander Sabais³, Stefan Scheu³, Jens Schumacher^{8,21}, Vicky M. Temperton^{8,22} & Teja Tscharnkte¹

Biodiversity is rapidly declining¹, and this may negatively affect ecosystem processes², including economically important ecosystem services³. Previous studies have shown that biodiversity has positive effects on organisms and processes⁴ across trophic levels⁵. However, only a few studies have so far incorporated an explicit food-web perspective⁶. In an eight-year biodiversity experiment, we studied an unprecedented range of above- and below-ground organisms and multitrophic interactions. A multitrophic data set originating from a single long-term experiment allows mechanistic insights that would not be gained from meta-analysis of different experiments. Here we show that plant diversity effects dampen with increasing trophic level and degree of omnivory. This was true both for abundance and species richness of organisms. Furthermore, we present comprehensive above-ground/below-ground biodiversity food webs. Both above ground and below ground, herbivores responded more strongly to changes in plant diversity than did carnivores or omnivores. Density and richness of carnivorous taxa was independent of vegetation structure. Below-ground responses to plant diversity were consistently weaker than above-ground responses. Responses to increasing plant diversity were generally positive, but were negative for biological invasion, pathogen infestation and hyperparasitism. Our results suggest that plant diversity has strong bottom-up effects on multitrophic interaction networks, with particularly strong effects on lower trophic levels. Effects on higher trophic levels are indirectly mediated through bottom-up trophic cascades.

The loss of biodiversity from terrestrial ecosystems has been shown to affect ecosystem properties, such as primary productivity⁷, nutrient cycling⁸ and trophic interactions². In recent biodiversity experiments, focal organism groups (usually plants⁷) were used to establish gradients in species richness, and biodiversity effects were then measured at one or a few trophic levels^{5,9}. Traditionally, studies have focused on the effects of horizontal biodiversity loss, that is, loss of species within a single trophic level¹⁰. Biodiversity loss at a given trophic level has been predicted to affect the abundance, biomass and resource use of that trophic level⁵. However, horizontal species loss may also affect other

trophic levels, organism groups and processes, and, hence, vertical species loss and the associated multitrophic structure of ecosystems¹⁰. For example, declines in plant species richness may cause losses to herbivores, true predators, parasitoids, hyperparasitoids and omnivores, and may also alter mutualistic interactions such as pollination¹¹ or mycorrhizal association⁴. Overall, there is an increasing awareness that the network nature of ecological systems needs to be incorporated into studies of biodiversity–ecosystem functioning¹².

Recent meta-analyses^{4,5} and experiments at individual study sites^{13,14} have shown plant diversity effects on a wide range of different groups of organisms, including primary producers, first- and second-order consumers, detritivores, fungal diseases and mycorrhizae. Additional studies have addressed components of the below-ground subsystem and their linkages with above-ground biota¹⁵. However, interpretation and progress has been clouded by differences in study systems and by a general lack of an overarching theory incorporating both trophic and non-trophic interactions as well as direct and indirect interactions^{16,17}. So far, subcomponents of food webs have often been studied in isolation, for example primary producers, the decomposer subsystem¹⁸, soil nematodes¹⁹, soil microbes, plant pathogenic fungi²⁰, above-ground invertebrates¹³, pollinators²¹ and so on. Here we present data from one of the most comprehensive biodiversity experiments so far, and show that diversity effects on higher trophic levels are mostly indirect and mediated through bottom-up trophic cascades. We use structural equation modelling approaches to develop comprehensive above-ground/below-ground biodiversity food webs. Finally, we link our results to recent interaction web models and provide explicit parameter estimates that can be used in future modelling exercises.

We experimentally manipulated plant species and functional group richness in 82 sown grassland plots (Methods), and recorded abundances and species richness of all relevant organism groups and biotic interactions between 2002 and 2009 (Supplementary Table 1). All data were analysed on a standardized scale²² from zero to one and the relationship between plant species richness and the different response variables was modelled using a power function¹⁸ to allow comparisons and extrapolation to other systems (see Supplementary Table 1 and

¹Georg-August-University Göttingen, Department of Crop Sciences, Agroecology, Grisebachstrasse 6, 37077 Göttingen, Germany. ²Friedrich Schiller University of Jena, Institute of Ecology, Dornburger Strasse 159, 07743 Jena, Germany. ³Georg-August-University Göttingen, J. F. Blumenbach Institute of Zoology and Anthropology, Berliner Strasse 28, 37073 Göttingen, Germany. ⁴University of Minnesota, Department of Forest Resources, 115 Green Hall, 1530 Cleveland Avenue North, St Paul, Minnesota 55108, USA. ⁵Institute of Environmental Sciences, University of Zürich, Winterthurerstrasse 190, 8057 Zürich, Switzerland. ⁶University of Bern, Plant Sciences, Altenbergrain 21, 3013 Bern, Switzerland. ⁷University of Potsdam, Institute of Biochemistry and Biology, Maulbeerallee 1, 14469 Potsdam, Germany. ⁸Max-Planck-Institute for Biogeochemistry, Hans-Knöll-Strasse 10, 07745 Jena, Germany. ⁹UFZ Helmholtz Centre for Environmental Research, Department of Community Ecology, Theodor-Lieser-Strasse 4, 06120 Halle, Germany. ¹⁰University of Leipzig, Institut für Biologie I, Johannisallee 21–23, 04103 Leipzig, Germany. ¹¹Humboldt University, Department of Plant Nutrition, Albrecht-Thaer-Weg 4, 14195 Berlin, Germany. ¹²University of Cologne, Cologne Biocenter, Department of Terrestrial Ecology, Zulpicher Strasse 47b, 50674 Cologne, Germany. ¹³ETH Zurich, Institute of Plant, Animal and Agroecosystem Sciences, LFW C56, Universitätsstrasse 2, 8092 Zurich, Switzerland. ¹⁴UFZ Helmholtz Centre for Environmental Research, Department of Soil Ecology, Theodor-Lieser-Strasse 4, 06102 Halle, Germany. ¹⁵Leuphana University of Lüneburg, Institute of Ecology and Environmental Chemistry, Scharnhorststraße 1, 21335 Lüneburg, Germany. ¹⁶Tallinn University of Technology, Tartu College, Puistee 78, 51008 Tartu, Estonia. ¹⁷K. I. Skryabin All-Russian Institute of Helminthology, Bolschaya Tchernomuschinskaya Street 28, 117218 Moscow, Russia. ¹⁸NERC Centre for Population Biology, Division of Biology, Imperial College London, Silwood Park Campus, Ascot SL5 7PY, United Kingdom. ¹⁹University of British Columbia, Department of Zoology, 6270 University Boulevard, Vancouver, British Columbia V6T 1Z4, Canada. ²⁰Mainz Museum of Natural History, Reichklarastrasse 10, 55116 Mainz, Germany. ²¹Friedrich Schiller University of Jena, Institute of Stochastics, Ernst-Abbe-Platz 2, 07743 Jena, Germany. ²²Forschungszentrum Jülich GmbH, Phytosphere Institute (ICG-3), 52425 Jülich, Germany.

Supplementary Fig. 3 for untransformed data). Analyses consisted of three steps. First, every response variable was analysed separately using a common set of linear, saturating and exponential models with untransformed plant species richness as the main explanatory variable. The presence of legumes and grasses and the number of plant functional groups were fitted as additional covariates. Variance heterogeneity was modelled using variance functions. Model selection was based on the Akaike information criterion for small sample sizes (AICc). Then, for parsimony, models were refitted using a power function. This allowed comparisons between the abundance and species richness of herbivores, carnivores and all other functional groups. Finally, multivariate techniques (multivariate linear models and structural equation models) were used to account for non-independence of variables measured on the same field plots.

Plant species richness had highly significant overall effects on the abundances of other organisms ($T_{PB} = 0.56$ (Pillai–Bartlett trace), approximately F-distributed with $F_{10,37} = 4.741$, $P < 0.001$; Fig. 1a, c), the species richness of other organism groups ($T_{PB} = 0.788$, approx. $F_{9,38} = 15.69$, $P < 0.001$; Fig. 1b, d) and on trophic interactions ($T_{PB} = 0.733$, approx. $F_{10,22} = 6.04$, $P < 0.001$; Supplementary Fig. 1; see Supplementary Methods for definitions of interactions). The abundance and species richness of organisms and biotic interactions were affected in broadly similar ways by changes in plant species richness (Fig. 1 and Supplementary Fig. 1).

Model selection using the complete range of linear, saturating and exponential models (Supplementary Tables 2 and 3) showed that 90% of all relationships could be approximated by a power model of the form $y = a + bs^z$ (ref. 18), where the exponent z can take any real value (in particular zero and one as special cases). Only five out of 38 organism groups declined with plant species richness (abundances of hyperparasitoids, fungivorous nematodes and mites, and abundance and

species richness of plant invaders; Supplementary Table 4). Responses of the below-ground subsystem were consistently smaller (average power model exponent of 0.11) than above-ground responses (exponent of 0.14).

Although most responses were saturating, closer inspection (Supplementary Table 5a–c) revealed consistent differences between the responses of herbivores, carnivores, omnivores and other trophic groups that are likely to reflect a general pattern (Fig. 2): with increasing trophic distance and for omnivores, species richness effects dampened—as indicated by the magnitude of the exponent of the common power function (Supplementary Table 4). This effect was found both for organism abundances and organism species richness, both above and below ground, and it was further supported by structural equation models (Fig. 3 and Supplementary Tables 6–10). Together, these findings indicate that species richness effects are generally dampened along trophic cascades.

If plant species richness acts on other organisms along trophic cascades, and plant species richness is the only experimentally manipulated variable, then the simplest conceptual model in our case is a bottom-up model of plant species richness effects; that is, plant species richness effects are passed from one trophic level to the next. Several authors have suggested such a ‘bottom-up template’ perspective for terrestrial food webs²³. Both decomposers and predators have long

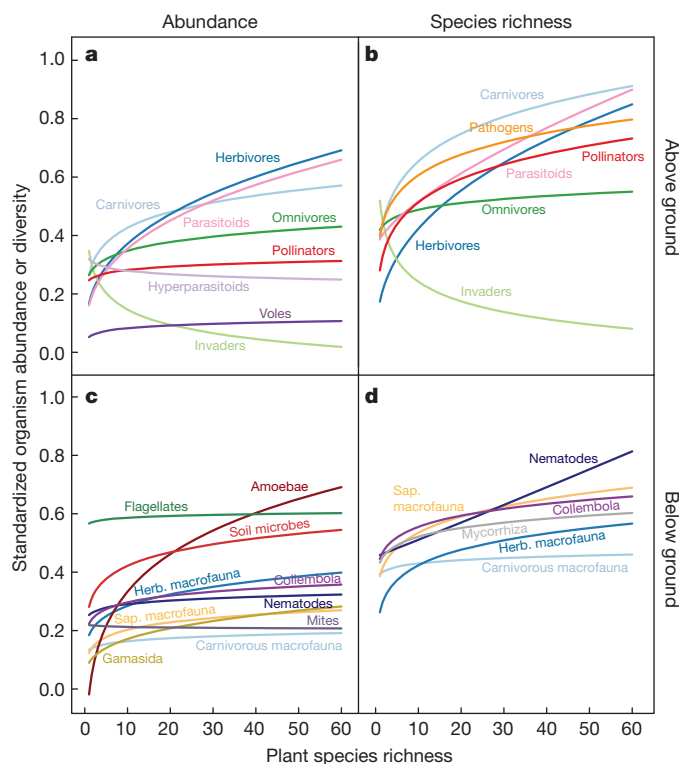


Figure 1 | Effects of plant species richness on above- and below-ground organisms in temperate grassland. a, b, Abundance (a) and species richness (b) of above-ground organisms. c, d, Abundance (c) and species richness (d) of below-ground organisms. All response variables scaled to [0, 1]. Every curve is fitted using a power function with covariates (Methods). Identical colours in each pair of panels indicate identical groups of organisms. For sample sizes, see Supplementary Table 1. Herb., herbivorous; Sap., saprophagous.

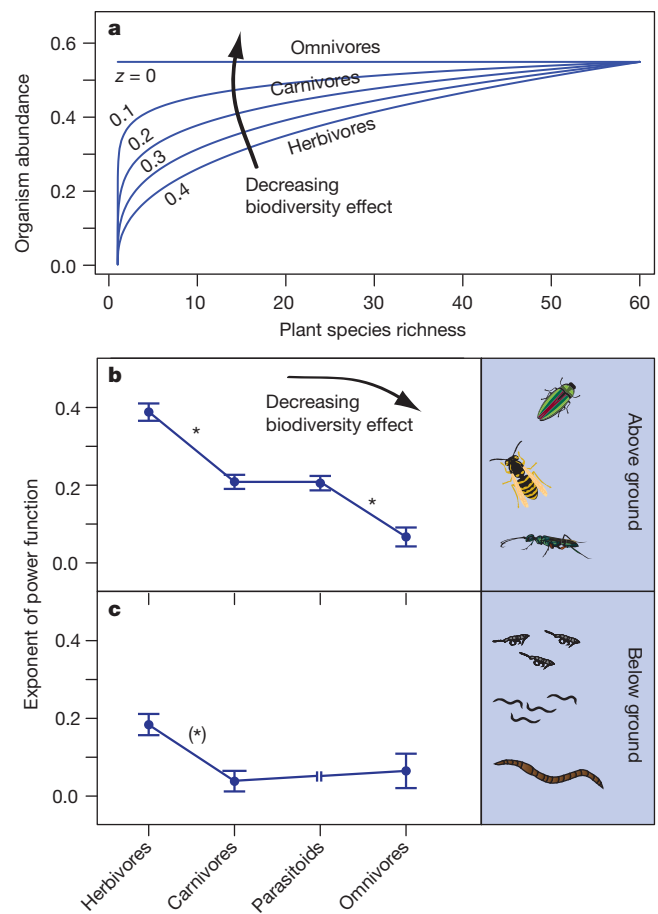


Figure 2 | Dampening of plant species richness effects with increasing trophic level. a, Conceptual figure showing how different values of z may influence biodiversity effects (x axis shows example range of 1–60 plant species). b, Estimates of z for above-ground herbivores, carnivores, parasitoids and omnivores. c, As in b, but for below-ground organisms. The y axes in b and c show estimated exponents of power functions fitted to data scaled to [0, 1]. Significant differences in z values are indicated by asterisks (* $P < 0.05$, $N = 50$ for above-ground organisms; (*) $P = 0.06$, $N = 82$ for below-ground organisms). Estimates are model predictions \pm s.e.

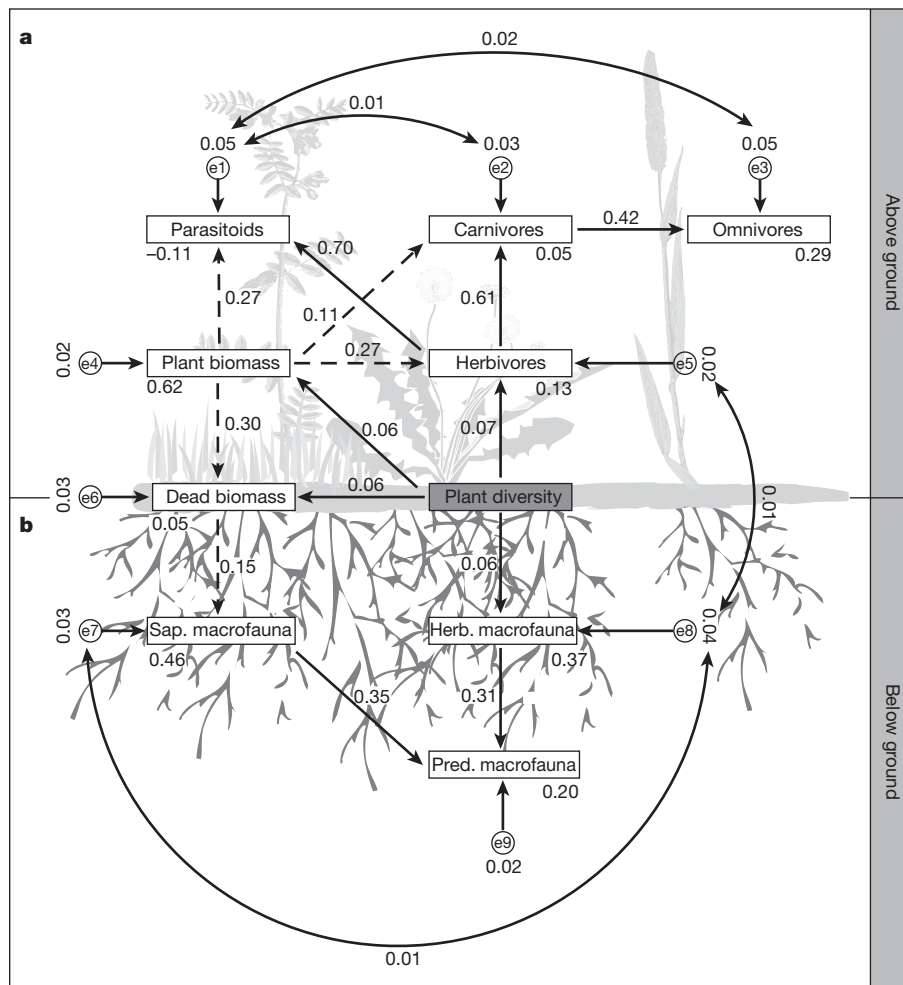


Figure 3 | Food web of above- and below-ground biodiversity. Results of a structural equation model with $N = 50$, $\chi^2 = 32.56$, $P = 0.212$, 27 degrees of freedom and a root mean squared error of approximation of 0.065 (90% confidence interval, [0, 0.135]). A model with top-down control of herbivores by carnivores had $\chi^2 = 32.07$, $P = 0.156$ and 25 degrees of freedom. **a**, Above-ground compartment; **b**, below-ground compartment. Unshaded rectangles represent observed variables (organism abundances). Circles indicate error

terms (e1–e9). Solid and dashed arrows connecting boxes show significant and non-significant effects, respectively. Numbers next to arrows and boxes are unstandardized slopes and intercepts, respectively. Double-headed arrows indicate correlations between error terms. Plant species richness was experimentally manipulated and has no error term. For details, see Supplementary Tables 6–10. Herb., herbivorous; Pred., predatory; Sap., saprophagous.

been proposed to be controlled essentially from the bottom up²⁴. However, top-down effects may also be expected, in particular if herbivores are not food limited²⁴.

Using structural equation models, we constructed a minimal adequate above-ground/below-ground biodiversity food web and found that plant species richness had almost exclusively bottom-up effects on higher trophic levels, both above and below ground (Fig. 3 and Supplementary Fig. 2). Three different theoretical constructs were used: a full model with bottom-up paths only; a full model with bottom-up and top-down paths; and all possible sets of reduced models, generated by single deletions of connections from full models (Supplementary Methods). These analyses showed that top-down control of herbivores by predators was not supported by the data. Other models (for example assuming direct effects of plant species richness on predators or omnivores) were rejected; that is, their implied covariance matrix differed significantly from the observed covariance matrix. In addition, we were able to reject hypotheses that assume positive responses only for specific trophic levels²⁵. Although plant biomass was indirectly linked to changes in predator or parasitoid abundance, these effects were not significant. This indicates that plant species richness effects are generally not mediated through vegetation density or biomass (Fig. 3a).

In a separate structural equation model for below-ground organisms, the amount of above-ground dead plant biomass entering the

below-ground system was generally less important than plant species richness per se (Supplementary Fig. 2). Hence, plant species richness had direct effects mainly on primary consumers, for example herbivorous macrofauna or herbivorous nematodes. In addition, there were strong direct effects of plant species richness on soil microbes and protozoans (Supplementary Fig. 2). It is likely that many of these below-ground responses are mediated either through changes in root production or through root exudates, but not through dead biomass or the amount of litter input (Supplementary Fig. 2). The direct plant species richness effects on microbes and protozoans could be mediated by changes in litter chemistry, litter diversity¹⁸ or root exudates²⁶.

Although structural equation models can be used to infer causality²⁷, strong inference requires experimental manipulation of trophic levels in addition to manipulations of plant diversity. We therefore exposed experimental nesting sites for prey (wild bees) and measured parasitism rates (Supplementary Fig. 1) as proxies for top-down control (Supplementary Methods). Parasitism increased with plant species richness, resulting in enhanced potential for biological control in species-rich systems.

One of the most fascinating developments in the theory of biodiversity and ecosystem processes is the inclusion of trophic and non-trophic interactions into generalized Lotka–Volterra models¹⁶. These models have theoretically predicted a bottom-up control of carnivores by plants,

with carnivore biomass indirectly controlled by plant and herbivore biomass, and top-down control of herbivores by carnivores. Structural equation models are a powerful tool for detecting such mutual dependencies, greatly enhancing our understanding of biodiversity effects in multitrophic systems. Overall, our results from a wide variety of organism groups provide strong support for a prominent role of plant species richness (rather than productivity or other covariates) in shaping multitrophic interactions.

Our results present the intriguing possibility that the effects of the species richness of one trophic level on others decrease with trophic distance. This hypothesis merits exploration by means of experimental manipulations of species numbers on other trophic levels. Because even an experiment as large as ours (82 plots) limits how many variables can reasonably be included in a multiple regression or structural equation model, future studies should be designed explicitly with a particular network of trophic interactions in mind. These studies could also be combinations of observational and experimental approaches.

We scaled all response variables to allow us to seek generalizations across different types of organism and trophic levels, but note that unscaled analyses might offer other types of insight. We also note that detailed collection of data at the level of each individual species, although prohibitively time consuming in a broad survey such as ours, is also likely to offer added insight. Our study should therefore be seen as a starting point rather than as an end point for further analyses of other data sets.

We have shown that the consequences of biodiversity loss are consistently negative for most organism groups and interactions, with particularly far-reaching feedback effects on basal trophic levels. Below-ground organisms will be less affected by biodiversity change (or will respond more slowly) than above-ground ones. Changes in plant species richness will affect neighbouring trophic levels and cascade up to higher trophic levels. Exponents of power functions ($y = bs^x$) will decline with trophic level. Our results highlight the importance of a diverse resource base²⁸ for trophic interactions in terrestrial ecosystems.

METHODS SUMMARY

Experimental design. In a 10-ha former arable field near Jena (Germany), we controlled the number of plant species, functional groups and plant functional identity in 82 plots, each 20 m × 20 m, in a randomized block design²⁹. Plots were seeded in May 2002 with 1, 2, 4, 8, 16 or 60 perennial grassland plant species, with 16, 16, 16, 16, 14 and 4 replicates, respectively. Plot compositions were randomly chosen from 60 plant species typical for local *Arrhenatherum* grasslands. Plots were maintained by mowing, weeding and herbicide applications.

Ecosystem variables. Sown and realized plant species richness were highly correlated (2006: Spearman's rank correlation coefficient, 0.995; $t = 91.94$; 80 degrees of freedom; $P < 2.2 \times 10^{-16}$); hence, sown richness was used for analysis. Above-ground invertebrates were collected on $N = 50$ plots using pitfall traps and suction sampling. Below-ground macro- and mesofauna were extracted from Kempson soil cores. Special sampling protocols were used for microorganisms (fungi, bacteria). Decomposition was measured using litter bags. Flower visitation was a count of pollinator visits. Parasitism was measured using a trap-nest technique. Hyperparasitism was measured from aphid mummy counts in 6.25-m² replicate plots. Pathogen damage above ground and herbivory were estimated visually. Plant invasion was a count of the numbers of an invader plant species per unit area. Microbial biomass was measured using glucose as an artificial substrate. A full description is available in the Supplementary Methods.

Statistics. Explanatory variables in linear models were block, plant species richness, plant functional group richness, and grass and legume presence. Nonlinear models contained plant species richness, with legume and grass presence and functional richness as covariates. Models were simplified and compared using AICc. To test for differences between slopes, multivariate linear models were constructed, and orthogonal contrasts were used to test linear hypotheses. Structural equation models were fitted to test specific hypotheses on causal relationships.

Received 3 August; accepted 9 September 2010.

Published online 27 October 2010.

1. Sala, O. E. *et al.* Global biodiversity scenarios for year 2100. *Science* **287**, 1770–1774 (2000).

2. Hooper, D. U. *et al.* Effects of biodiversity on ecosystem functioning: a consensus of current knowledge. *Ecol. Monogr.* **75**, 3–35 (2005).
3. Myers, N. Environmental services of biodiversity. *Proc. Natl Acad. Sci. USA* **93**, 2764–2769 (1996).
4. Balvanera, P. *et al.* Quantifying the evidence for biodiversity effects on ecosystem functioning and services. *Ecol. Lett.* **9**, 1146–1156 (2006).
5. Cardinale, B. J. *et al.* Effects of biodiversity on the functioning of trophic groups and ecosystems. *Nature* **443**, 989–992 (2006).
6. Cardinale, B. *et al.* in *Biodiversity, Ecosystem Functioning, and Human Wellbeing: an Ecological and Economic Perspective* (eds S. Naeem *et al.*) 105–120 (Oxford Univ. Press, 2009).
7. Hector, A. *et al.* Plant diversity and productivity experiments in European grasslands. *Science* **286**, 1123–1127 (1999).
8. Hooper, D. U. & Vitousek, P. M. Effects of plant composition and diversity on nutrient cycling. *Ecol. Monogr.* **68**, 121–149 (1998).
9. Petchey, O. L. *et al.* Species loss and the structure and functioning of multitrophic aquatic systems. *Oikos* **104**, 467–478 (2004).
10. Duffy, J. E. *et al.* The functional role of biodiversity in ecosystems: incorporating trophic complexity. *Ecol. Lett.* **10**, 522–538 (2007).
11. Biesmeijer, J. C. *et al.* Parallel declines in pollinators and insect-pollinated plants in Britain and the Netherlands. *Science* **313**, 351–354 (2006).
12. Tylianakis, J. M., Tscharntke, T. & Lewis, O. T. Habitat modification alters the structure of tropical host-parasitoid food webs. *Nature* **445**, 202–205 (2007).
13. Haddad, N. M. *et al.* Plant species loss decreases arthropod diversity and shifts trophic structure. *Ecol. Lett.* **12**, 1029–1039 (2009).
14. Koricheva, J., Mulder, C. P. H., Schmid, B., Joshi, J. & Huss-Danell, K. Numerical responses of different trophic groups of invertebrates to manipulations of plant diversity in grasslands. *Oecologia* **125**, 271–282 (2000).
15. Wardle, D. A. & Van der Putten, W. H. in *Biodiversity and Ecosystem Functioning* (eds Loreau, M., Naeem, S. & Inchausti, P.) 155–168 (Oxford Univ. Press, 2002).
16. Goudard, A. & Loreau, M. Nontrophic interactions, biodiversity, and ecosystem functioning: an interaction web model. *Am. Nat.* **171**, 91–106 (2008).
17. Ogushi, T., Craig, T. P. & Price, P. W. (eds) *Ecological Communities: Plant Mediation in Indirect Interaction Webs* (Cambridge Univ. Press, 2007).
18. Srivastava, D. S. *et al.* Diversity has stronger top-down than bottom-up effects on decomposition. *Ecology* **90**, 1073–1083 (2009).
19. De Deyn, G. B., Raaijmakers, C. E., van Ruijven, J., Berendse, F. & van der Putten, W. H. Plant species identity and diversity effects on different trophic levels of nematodes in the soil food web. *Oikos* **106**, 576–586 (2004).
20. Mitchell, C. E., Tilman, D. & Groth, J. V. Effects of grassland plant species diversity, abundance, and composition on foliar fungal disease. *Ecology* **83**, 1713–1726 (2002).
21. Ghazoul, J. Floral diversity and the facilitation of pollination. *J. Ecol.* **94**, 295–304 (2006).
22. Legendre, P. & Legendre, L. *Numerical Ecology* (Elsevier, 1998).
23. Hunter, M. D. & Price, P. W. Playing chutes and ladders: heterogeneity and the relative roles of bottom-up and top-down forces in natural communities. *Ecology* **73**, 724–732 (1992).
24. Hairston, N. G., Smith, F. E. & Slobodkin, L. B. Community structure, population control, and competition. *Am. Nat.* **94**, 421–425 (1960).
25. Schmid, B. *et al.* in *Biodiversity, Ecosystem Functioning & Human Wellbeing* (eds Naeem, S. *et al.*) Ch. 2, 14–29 (Oxford Univ. Press, 2010).
26. Eisenhauer, N. *et al.* Plant diversity effects on soil microorganisms support the singular hypothesis. *Ecology* **91**, 485–496 (2010).
27. Grace, J. B. *Structural Equation Modeling and Natural Systems* (Cambridge Univ. Press, 2006).
28. Price, P. W. The resource-based organization of communities. *Biotropica* **24**, 273–282 (1992).
29. Roscher, C. *et al.* The role of biodiversity for element cycling and trophic interactions: an experimental approach in a grassland community. *Basic Appl. Ecol.* **5**, 107–121 (2004).

Supplementary Information is linked to the online version of the paper at www.nature.com/nature.

Acknowledgements We thank J. M. Tylianakis, P. Batáry, Y. Clough, M. J. Crawley, J. Fox, J. Fründ, D. Gladbach and A. Hector for comments that improved this manuscript. The gardeners, technicians, student helpers and managers of the Jena Experiment are acknowledged for their assistance. This work was supported by the Deutsche Forschungsgemeinschaft (FOR 456).

Author Contributions C.S., C.M. and J.S. assembled all data. N.E. contributed data for the below-ground food webs. C.S. performed all analyses and wrote the manuscript. C.S. and T.T. are the principal authors, N.E. to A.W. are listed in descending order of the importance of their contributions, and the remaining authors contributed equally. All authors contributed their own data sets, discussed the analysis and results, and commented on the manuscript text.

Author Information Reprints and permissions information is available at www.nature.com/reprints. The authors declare no competing financial interests. Readers are welcome to comment on the online version of this article at www.nature.com/nature. Correspondence and requests for materials should be addressed to C.S. (christoph.scherber@agr.uni-goettingen.de).

Pericytes regulate the blood–brain barrier

Annika Armulik¹, Guillem Genové¹, Maarja Mäe¹, Maya H. Nisancioglu¹, Elisabet Wallgard^{1†}, Colin Niaudet¹, Liquan He^{1†}, Jenny Norlin¹, Per Lindblom², Karin Strittmatter^{1†}, Bengt R. Johansson³ & Christer Betsholtz¹

The blood–brain barrier (BBB) consists of specific physical barriers, enzymes and transporters, which together maintain the necessary extracellular environment of the central nervous system (CNS)¹. The main physical barrier is found in the CNS endothelial cell, and depends on continuous complexes of tight junctions combined with reduced vesicular transport². Other possible constituents of the BBB include extracellular matrix, astrocytes and pericytes³, but the relative contribution of these different components to the BBB remains largely unknown^{1,3}. Here we demonstrate a direct role of pericytes at the BBB *in vivo*. Using a set of adult viable pericyte-deficient mouse mutants we show that pericyte deficiency increases the permeability of the BBB to water and a range of low-molecular-mass and high-molecular-mass tracers. The increased permeability occurs by endothelial transcytosis, a process that is rapidly arrested by the drug imatinib. Furthermore, we show that pericytes function at the BBB in at least two ways: by regulating BBB-specific gene expression patterns in endothelial cells, and by inducing polarization of astrocyte end-feet surrounding CNS blood vessels. Our results indicate a novel and critical role for pericytes in the integration of endothelial and astrocyte functions at the neurovascular unit, and in the regulation of the BBB.

Platelet-derived growth factor (PDGF)-B/PDGF receptor- β (PDGFR- β) signalling is necessary for pericyte recruitment during angiogenesis^{4,5}. Perinatal lethality precludes analysis of postnatal processes in *Pdgfrb* or *Pdgfrb* null mice^{6,7}, but several other mouse mutants of this pathway are viable postnatally. Two such mutants were used here: PDGF-B retention motif knockouts (*Pdgfrb*^{ret/ret}) where PDGF-B binding to heparan sulphate proteoglycans was disrupted⁸; and mutants in which *Pdgfrb* null alleles were complemented by one or two copies of a conditionally silent human PDGF-B transgene targeted to the *Rosa26* locus and activated by endothelial Cre recombinase (hemizygous R26P^{+/-} or homozygous R26P^{+/+} mice; Supplementary Fig. 2a–d).

We quantified pericyte coverage in different regions of the CNS by CD13 or PDGFR- β staining (Fig. 1a, b, e and Supplementary Fig. 3). *Pdgfrb*^{ret/ret}, R26P^{+/-} and R26P^{+/+} mice displayed pericyte coverage corresponding to 26%, 40% and 72%, respectively, compared to controls (Fig. 1a, b). Quantification of absolute numbers of mural cells (pericytes and vascular smooth muscle cells) using the transgenic reporter XLacZ⁹ confirmed low mural cell densities in *Pdgfrb*^{ret/ret} and R26P^{+/-} mice, and close to normal levels in R26P^{+/+} mice (Supplementary Fig. 3b–p). We extended previous observations^{4,5,10,11} that reduced pericyte densities correlate with increased vessel diameter and reduced vessel density (Fig. 1c–e and Supplementary Fig. 4). Importantly, these phenotypes were almost completely normalized in R26P^{+/-} mice (Fig. 1d, e and Supplementary Fig. 4a–c).

Increased water content in brains of *Pdgfrb*^{ret/ret} mice (Fig. 1f) indicated impairment of the BBB. We tested the BBB integrity in the different mutants using a panel of tracers (Supplementary Table 1). The azo dye Evans blue¹² accumulated in mutant brain parenchyma in a time-dependent fashion (Fig. 1i) and in correlation with pericyte density: it was largest in *Pdgfrb*^{ret/ret} mice followed by R26P^{+/-} and R26P^{+/+}

(Fig. 1g, h, j and Supplementary Fig. 5a–c). Similarly, the fluorescent dye cadaverine Alexa Fluor-555 accumulated significantly in the brain parenchyma of *Pdgfrb*^{ret/ret} and R26P^{+/-} mice (Fig. 1j and Supplementary Fig. 5d, h, i). Additionally, fluorescently labelled albumin, 70 kDa dextran and IgG passed the BBB in *Pdgfrb*^{ret/ret} and R26P^{+/-} mice, but not in controls or in R26P^{+/+} mice (Fig. 1j and Supplementary Fig. 5e–g). These experiments establish a close correlation between pericyte density and permeability across the BBB for a range of tracers of different molecular masses (Supplementary Table 1).

Permeability in CNS vessels is impeded by continuous complexes of endothelial junctions^{13,14}. We studied such complexes in adult pericyte-deficient mutants using markers for adherens (VE-cadherin) and tight (ZO-1 and claudin 5) junctions. *Pdgfrb*^{ret/ret}, R26P^{+/-} and controls showed junctional marker expression at similar levels as judged by immunostaining and western blotting (Supplementary Fig. 6a–c and data not shown). The junctional markers were distributed in a pattern consistent with continuous junction complexes in both mutants and controls; however, mutants displayed focally increased junctional width and undulation. These patterns were confirmed by transmission electron microscopy, which failed to reveal any apparent abnormalities in the ultrastructure of endothelial junctions, with the exception that longer and irregular stretches of endothelial overlap were commonly found in pericyte-deficient mutants (Fig. 2c and Supplementary Fig. 6e).

Because continuity, ultrastructure and marker expression were consistent with retained integrity of endothelial junctions in the absence of pericytes, we took advantage of the fixable nature of the fluorescent tracers to explore the route of extravasation in *Pdgfrb*^{ret/ret} and R26P^{+/-} mice in more detail. Cadaverine Alexa Fluor-555 accumulated in endothelial cells and in the brain parenchyma in *Pdgfrb*^{ret/ret} and R26P^{+/-} mice, but not in controls or in R26P^{+/+} mice (Fig. 2a). Extravasated cadaverine Alexa Fluor-555 localized mainly to neurons (Figs 2a and 3d and Supplementary Fig. 7a). Similar patterns of distribution were observed for fluorescent albumin, IgG and 70 kDa dextran (Fig. 2b and Supplementary Fig. 7b). We also studied the distribution of horseradish peroxidase (HRP, 44 kDa) by transmission electron microscopy. We found increased uptake of HRP specifically in macrovesicular structures in the endothelium in *Pdgfrb*^{ret/ret} mice in comparison with controls (Fig. 2c, d and Supplementary Fig. 6d, e). *Pdgfrb*^{ret/ret} microvessels also showed marked accumulation of HRP reactivity at the vascular basement membrane, without apparent colocalization with endothelial junctions (Fig. 2c, d and Supplementary Fig. 6d, e). Together, these observations indicate that macromolecular permeability across the BBB in pericyte-deficient vessels occurs through a transcytosis route. Pericyte deficiency was not associated with changes in the polarization or with signs of fenestration in the endothelial cells (Supplementary Figs 4d, 6d, e and 7c), features that characterize the BBB defects observed as a result of impaired Wnt/ β -catenin signalling^{15,16}.

The BBB breaks open in conjunction with stroke, leading to life-threatening CNS oedema. A recent study demonstrated that the tyrosine kinase inhibitor imatinib counteracts oedema in experimental

¹Department of Medical Biochemistry and Biophysics, Division of Vascular Biology, Karolinska Institute, Scheeles väg 2, SE-171 77 Stockholm, Sweden. ²AstraZeneca AB, Clinical Development, SE-431 83 Mölndal, Sweden. ³The Electron Microscopy Unit, Institute for Biomedicine, The Sahlgrenska Academy, University of Gothenburg, PO Box 420, SE-405 30 Gothenburg, Sweden. [†]Present addresses: Department of Genetics and Pathology, Rudbeck Laboratory, Dag Hammarskjölds väg 20, Uppsala University, SE-751 85 Uppsala, Sweden (E.W.); Applied Biosystems Sweden, Lindhagensgatan 76, PO Box 12650, SE-112 92 Stockholm, Sweden (L.H.); German Cancer Research Center DKFZ, Im Neuenheimer Feld 280, 69120 Heidelberg, Germany (K.S.).

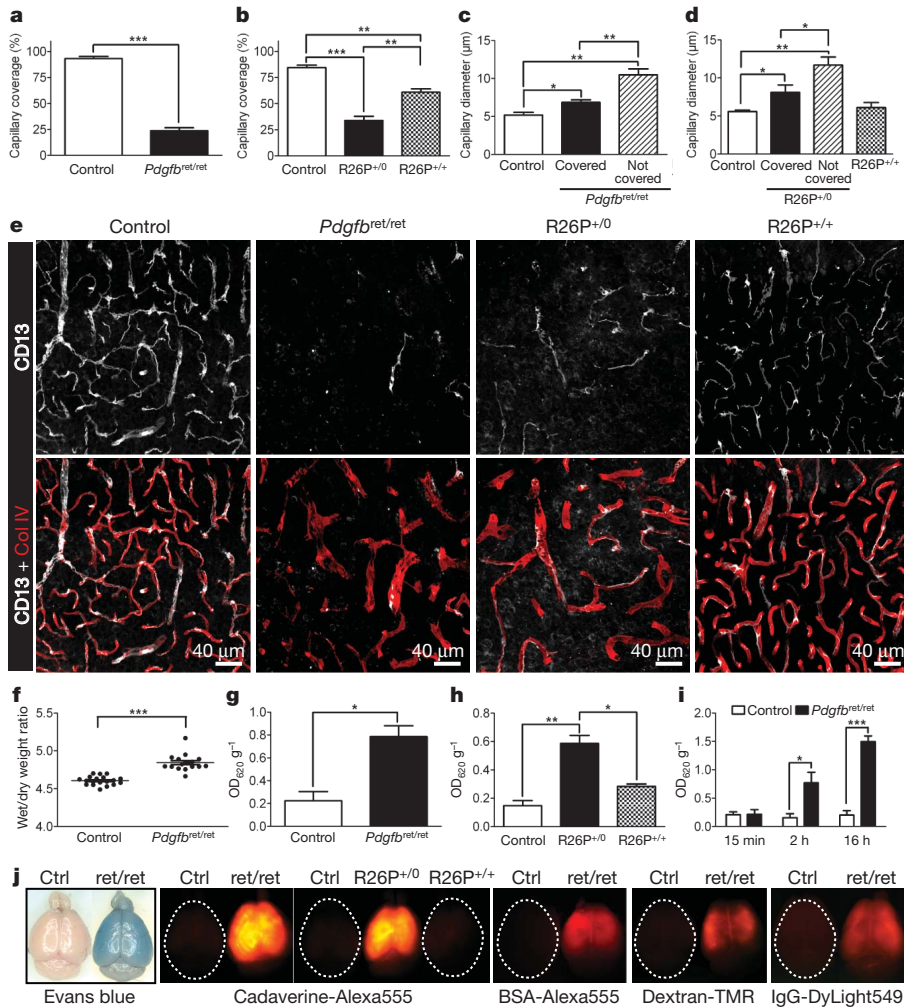


Figure 1 | Pericyte coverage correlates with BBB integrity. **a, b**, Quantification of pericyte coverage of capillaries in the cerebral neocortex of adult *Pdgfr^{ret/ret}* mice (**a**), and *R26P^{+/-}* and *R26P^{+/+}* mice (**b**). **c, d**, Capillary diameter in the cerebral neocortex of adult *Pdgfr^{ret/ret}* mice (**c**), and *R26P^{+/-}* and *R26P^{+/+}* mice (**d**), with or without pericyte coverage. **e**, Three-dimensional reconstructions of confocal image z-stacks of adult cerebral neocortex vasculature depicted by collagen IV (basement membrane) and CD13 (pericyte) staining in *Pdgfr^{ret/ret}*, *R26P^{+/-}* and *R26P^{+/+}* mice. **f**, Wet/dry weight ratios of control and *Pdgfr^{ret/ret}* mice. **g, h**, Quantification of Evans blue in *Pdgfr^{ret/ret}* mice (**g**) and *R26P^{+/-}* and *R26P^{+/+}* mice (**h**) in the cerebrum after 16 h of circulation. **i**, Time course of Evans blue accumulation in the cerebrum of *Pdgfr^{ret/ret}* animals. y-axis shows optical density (OD) at 620 nm per gram of tissue. **j**, Whole brains photographed after tracer circulation. Circulation time was 16 h for Evans blue, BSA-Alexa Fluor-555, dextran-TMR and IgG-DyLight 549, and 2 h for cadaverine Alexa Fluor-555. **P* < 0.03; ***P* < 0.007; ****P* < 0.0005. All error bars show mean ± s.e.m.

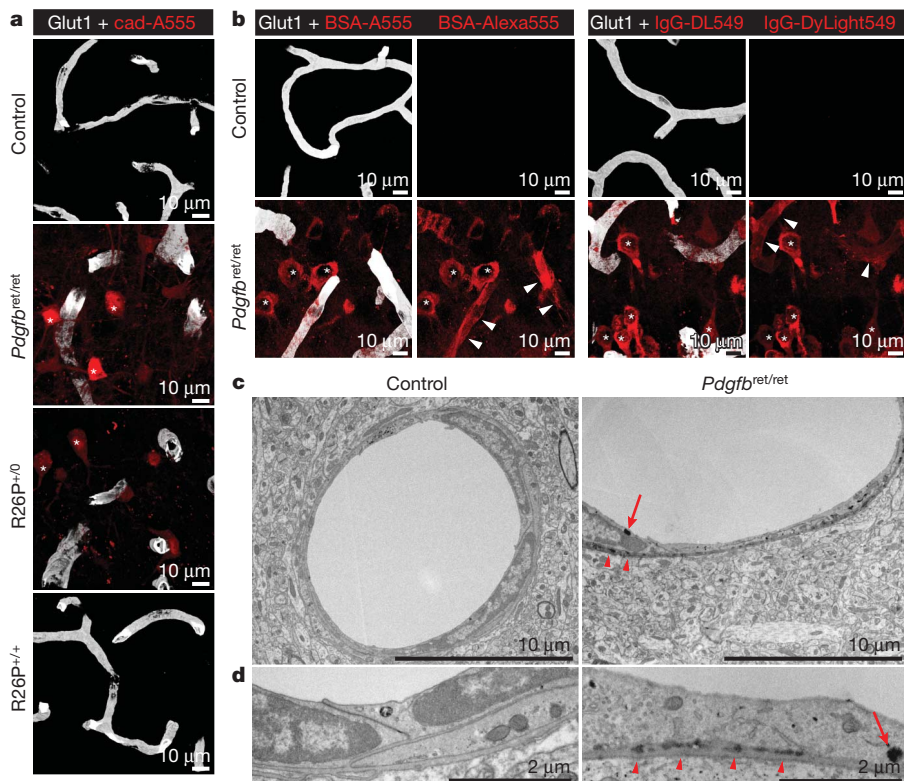


Figure 2 | Pericyte-deficient mice show accumulation of intravenously injected tracers in the brain parenchyma and in the endothelium. **a**, Accumulation of cadaverine Alexa Fluor-555 (red) in the cerebral neocortex in *Pdgfr^{ret/ret}* or *R26P^{+/-}* mice but not in control and *R26P^{+/+}* mice. **b**, Extravasation of BSA-Alexa Fluor-555 (red) and IgG-DyLight 549 (red) in *Pdgfr^{ret/ret}* mice but not in controls. Asterisks in **a** and **b** mark neuronal nuclei. Arrowheads in **b** point to tracer in endothelial cells. Endothelial cells in **a** and **b** are visualized by Glut1 immunostaining (white). **c, d**, Electron microscopy images show HRP in large vesicles (arrows) and at the basal lamina (arrowheads) in *Pdgfr^{ret/ret}* mice.

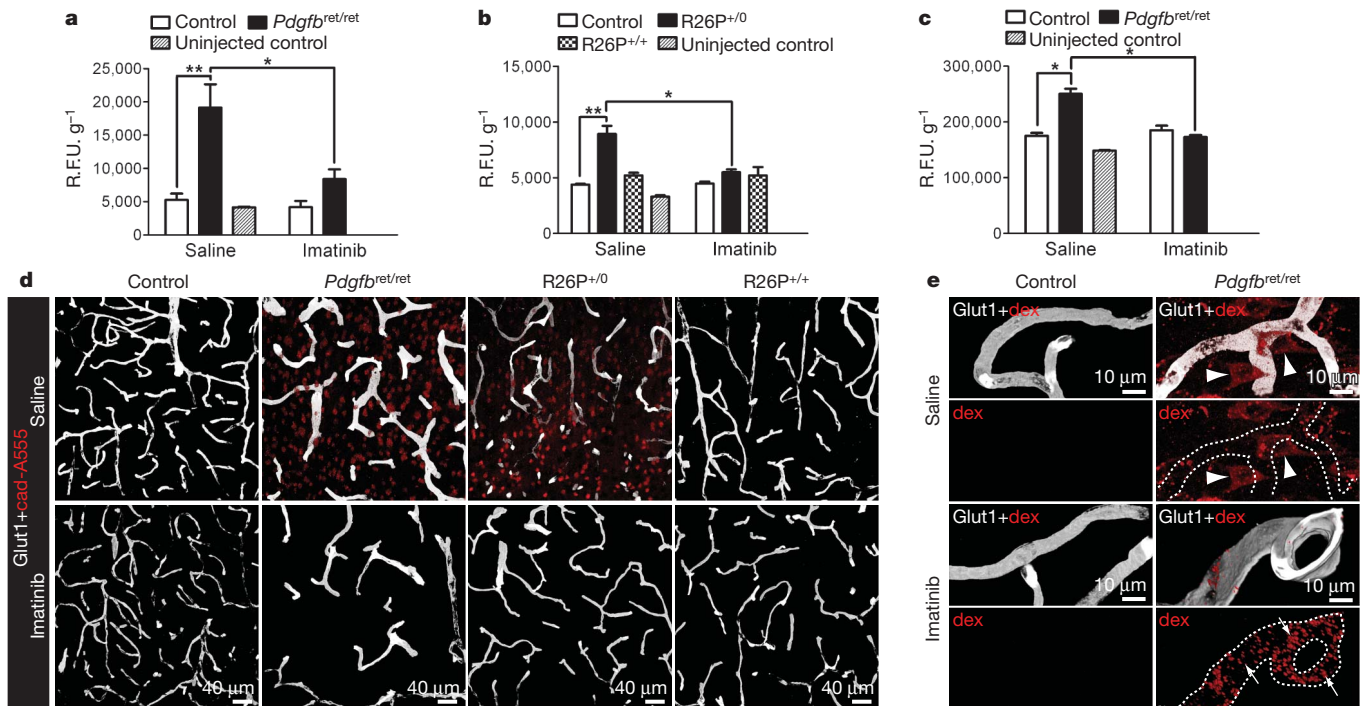


Figure 3 | Imatinib treatment abolishes accumulation of intravenously injected tracers in the brain parenchyma in pericyte-deficient mutants. **a–c**, Quantification of cadaverine Alexa Fluor-555 in *Pdgfrb*^{ret/ret} mice (**a**) and *R26P*^{+/0} and *R26P*^{+/+} mice (**b**) in the cerebrum after 2 h of circulation, and of IgG-DyLight 549 (**c**) in *Pdgfrb*^{ret/ret} mice in the cerebrum after 16 h of circulation, with and without previous imatinib treatment. *y* axis shows relative fluorescence units (R.F.U.) per gram of tissue. **d**, **e**, Three-dimensional

reconstructions of confocal image z-stacks of cerebral neocortex of mice injected intravenously with cadaverine Alexa Fluor-555 (**d**) or 70 kDa dextran-TMR (**e**). Whereas imatinib abolishes tracer accumulation in neurons in *Pdgfrb*^{ret/ret} and *R26P*^{+/0} mice (**d** and arrowheads in **e**), it increases punctuate accumulations in endothelial cells (arrows in **e**). **P* < 0.03; ***P* < 0.005. All error bars show mean ± s.e.m.

stroke induced in mice¹⁷. We found that imatinib treatment quickly and dose-dependently reversed brain parenchymal accumulation of all tested tracers in pericyte-deficient mice (Fig. 3 and Supplementary Fig. 8). In contrast, accumulation and punctuate distribution of fluorescent dextran and IgG in the endothelial cells was enhanced (Fig. 3e and Supplementary Fig. 8b, d, e). This indicates that imatinib inhibits the release of tracer from endothelial cells into the brain parenchyma, consistent with an effect on a late step in the endothelial transcytosis process. Notably, imatinib treatment did not normalize pericyte abundance, vessel diameter, density, or the convoluted appearance of endothelial junctions (Fig. 3d and Supplementary Fig. 9).

To address whether pericytes regulate brain-specific endothelial differentiation we used microarrays to assess the expression of known BBB markers³ in microvascular fragments isolated from adult pericyte-deficient mutants and controls. Such fragments mostly consist of endothelial cells¹⁸, but also include pericytes (when present) and astrocyte end-feet. We used previously obtained array data on embryonic brain microvascular fragments, isolated kidney glomeruli and whole brain for comparison^{18–20}. These analyses show that most BBB markers are unaffected by pericyte deficiency at the mRNA level (Fig. 4a, b and Supplementary Table 2). Two known BBB markers for which antibodies were available were assessed at the level of protein expression: Glut1 (predicted to be unaffected by pericyte deficiency) and transferrin receptor (CD71) (predicted to be downregulated in the pericyte-deficient state). In agreement with the gene expression data, we found that Glut1 protein was uniformly expressed in brain endothelial cells irrespective of the degree of pericyte coverage (Figs 2–4 and Supplementary Fig. 10), whereas CD71 expression was downregulated in the endothelium lacking pericyte contact (Supplementary Fig. 10). Together, these results indicate that pericytes exert a discrete influence on the endothelial BBB-specific gene and protein expression profile.

Astrocytes attach to blood vessels through cap-like cytoplasmic processes—end-feet—carrying specific channels and transporters,

for example, aquaporin 4 (Aqp4) and Kir4.1, which are targeted to astrocyte end-feet to control water and ion homeostasis at the vessel–neuron interface³. Little is known about how contacts between blood vessels and astrocyte end-feet are established and maintained²¹. Our gene array data indicated downregulation of several astrocyte markers in pericyte-deficient brain microvascular fragments (Supplementary Table 2 and data not shown). We therefore asked if pericytes, which are partially sandwiched between the endothelial cells and the astrocyte end-feet, might affect astrocytes, and, specifically, if pericyte deficiency leads to changes in astrocyte end-foot distribution or polarization. Three markers for the polarized astrocyte end-foot, Aqp4, α -syntrophin and laminin α 2 chain (Lama2), all provided uniform labelling of microvessel abluminal surfaces in control brains, consistent with a polarized expression of these markers (Fig. 4c–e and Supplementary Fig. 11). However, in pericyte-deficient mutants, the vascular staining for these markers was weaker than in controls, and the Aqp4 staining was also re-distributed to other regions of the astrocytes, indicating abnormal polarization of the astrocyte end-feet (Supplementary Fig. 11). Interestingly, we found that pericytes that were detached from the endothelial cells showed intense lining with Aqp4 and α -syntrophin immunostaining (Fig. 4d and data not shown). This indicates that pericytes express cues that mediate attachment of astrocyte end-feet. The strong reduction in deposition of the astrocyte-derived basement membrane component Lama2 (Fig. 4e) prompted us to study the expression of a range of other vascular basement membrane components. These analyses failed to show any significant changes in the deposition of endothelium-derived basement membrane proteins laminin α 4, laminin α 5, nidogen and perlecan in pericyte-deficient vessels (Supplementary Fig. 12).

BBB properties are not intrinsic to CNS endothelial cells, but are induced when the cells are in contact with astrocytes *in vitro* and *in vivo*^{22–24}. Recent evidence also suggests a role for neuronal precursors and Wnt signalling in BBB induction *in vivo*^{15,16,25}. A role for pericytes

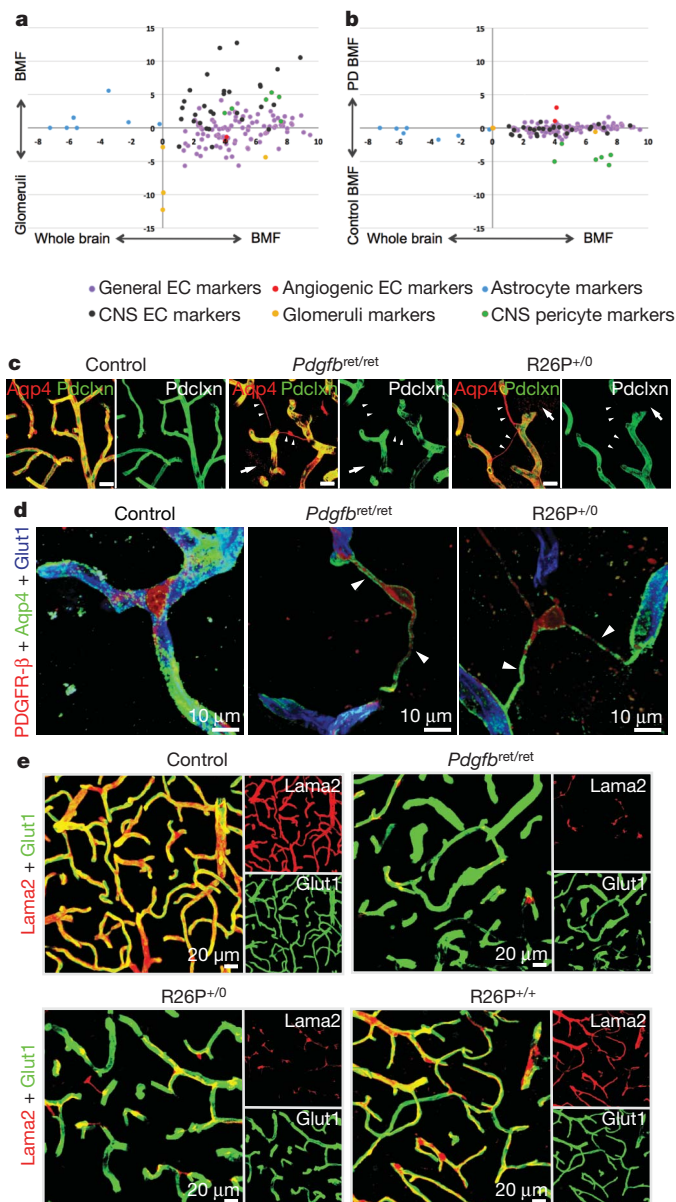


Figure 4 | Transcript profiling of brain microvasculature and characterization of the polarization defect of astrocyte end-feet in pericyte-deficient mutants. **a**, Relative expression (\log_2 fold difference) of known markers for the BBB, endothelial cells, astrocytes, pericytes and glomerular podocytes in adult brain microvascular fragments (BMF) versus whole brain (x axis) and brain microvascular fragments versus glomeruli (y axis). Note the higher expression of BBB markers in brain microvascular fragments compared to glomeruli. **b**, Relative expression of the same genes as in **a** for control and pericyte-deficient (PD) mutants (y axis; see Supplementary Tables 2 and 3 for gene identifiers and further information on methodology). **c**, **d**, Astrocyte end-feet (red) localize to microvessels (green) in controls but also to structures bridging adjacent vessels in *Pdgfrb^{ret/ret}* and *R26P^{+/-}* mice (arrowheads in **c**) that were identified as detached PDGFR- β positive pericytes (**d**, arrowheads). Arrows in **c** point to diffuse Aqp4 staining (red) in pericyte-deficient mice not associated with vessels (see also Supplementary Fig. 11a). **e**, *Pdgfrb^{ret/ret}* and *R26P^{+/-}* have reduced deposition of the astrocyte-derived basement membrane component laminin $\alpha 2$ -chain compared to control and *R26P^{+/-}* animals. Scale bars in **c**, 20 μ m.

in endothelial barrier formation has been suggested based on *in vitro* co-culture experiments^{26,27}, but evidence for any specific role of pericytes in BBB formation has so far been lacking. Here we provide evidence for an *in vivo* role of pericytes in regulating the mammalian BBB (schematically illustrated in Supplementary Fig. 1). The increased

endothelial transcytosis that occurs as a result of brain pericyte deficiency in the mouse mutants is compatible with a normal lifespan of the mouse mutants, in spite of the fact that this increase results in oedema and extravasation of plasma proteins in the brain. This is probably tolerated because leakage is slow, allowing the brain to adapt and compensate for any resulting changes in the interstitial environment. Viable pericyte-deficient animal models should therefore be useful in further studies of the putative functional consequences of BBB impairments for higher and integrated neuronal functions, learning and behaviour, and for the progression of brain diseases. Notably, we have demonstrated that the pericyte-deficient state makes the BBB permeable to immunoglobulins. Further elucidation of the molecular mechanisms that trigger opening and closure of this route across the BBB should therefore be of pharmaceutical significance.

METHODS SUMMARY

Animals. The following transgenic mouse lines were used for experiments: PDGF-B knockout⁶, PDGF-B retention motif knockout⁸, Tie2Cre (ref. 28), Rosa26 hPDGF-B (this study), XLacZ4 (ref. 9) and Z/EG (ref. 29). Animal experiments were approved by the Stockholm's North Ethical Committee for Animal Research. **Generation of Rosa26 hPDGF-B mice.** A full-length human PDGF-B cDNA sequence preceded by a splice acceptor site and a loxP-site-flanked transcription stop cassette was cloned into a vector designed for homologous recombination into the ubiquitously expressed ROSA26 locus³⁰ (Supplementary Fig. 2a). Gene-targeted mice were generated from the ES cells by standard methods. A detailed description is provided in Methods.

Intravenous injection of tracers and detection of injected tracers. The following tracers were used: Evans blue (Sigma Aldrich), lysine-fixable cadaverine conjugated to Alexa Fluor-555 (Invitrogen), bovine serum albumin conjugated to Alexa Fluor-555 (Invitrogen), lysine-fixable 70 kDa dextran conjugated to tetramethylrhodamine (TMR) (Invitrogen), and goat anti-human IgG conjugated to DyLight 549 (Jackson ImmunoResearch Laboratories). Evans blue in the brain was quantified by spectrophotometry as described¹⁷. Detailed information about the quantification of cadaverine-Alexa Fluor-555 and DyLight-549 conjugated goat anti-human IgG in the brain is given in Methods. When indicated, animals were treated with three or four doses of imatinib (150 mg kg⁻¹) twice per day before tracer injections.

Statistical analysis. Statistical significance was determined by using unpaired two-tailed or one-tailed Student's *t*-test (GraphPad Prism5). Differences were considered significant with a *P* value less than 0.05. Quantified data are presented as mean \pm s.e.m.

Full Methods and any associated references are available in the online version of the paper at www.nature.com/nature.

Received 29 April 2009; accepted 23 September 2010.

Published online 13 October 2010.

- Abbott, N. J., Rönnbäck, L. & Hansson, E. Astrocyte-endothelial interactions at the blood-brain barrier. *Nature Rev. Neurosci.* **7**, 41–53 (2006).
- Reese, T. S. & Karnovsky, M. J. Fine structural localization of a blood-brain barrier to exogenous peroxidase. *J. Cell Biol.* **34**, 207–217 (1967).
- Bernacki, J. *et al.* Physiology and pharmacological role of the blood-brain barrier. *Pharmacol. Rep.* **60**, 600–622 (2008).
- Enge, M. *et al.* Endothelium-specific platelet-derived growth factor-B ablation mimics diabetic retinopathy. *EMBO J.* **21**, 4307–4316 (2002).
- Bjarnegård, M. *et al.* Endothelium-specific ablation of PDGFB leads to pericyte loss and glomerular, cardiac and placental abnormalities. *Development* **131**, 1847–1857 (2004).
- Levéen, P. *et al.* Mice deficient for PDGF B show renal, cardiovascular, and hematological abnormalities. *Genes Dev.* **8**, 1875–1887 (1994).
- Soriano, P. Abnormal kidney development and hematological disorders in PDGF β -receptor mutant mice. *Genes Dev.* **8**, 1888–1896 (1994).
- Lindblom, P. *et al.* Endothelial PDGF-B retention is required for proper investment of pericytes in the microvessel wall. *Genes Dev.* **17**, 1835–1840 (2003).
- Tidhar, A. *et al.* A novel transgenic marker for migrating limb muscle precursors and for vascular smooth muscle cells. *Dev. Dyn.* **220**, 60–73 (2001).
- Lindahl, P. *et al.* Pericyte loss and microaneurysm formation in PDGF-B-deficient mice. *Science* **277**, 242–245 (1997).
- Hellström, M. *et al.* Lack of pericytes leads to endothelial hyperplasia and abnormal vascular morphogenesis. *J. Cell Biol.* **153**, 543–554 (2001).
- Moos, T. & Møllgård, K. Cerebrovascular permeability to azo dyes and plasma proteins in rodents of different ages. *Neuropathol. Appl. Neurobiol.* **19**, 120–127 (1993).
- Dejana, E., Tournier-Lasserre, E. & Weinstein, B. M. The control of vascular integrity by endothelial cell junctions: molecular basis and pathological implications. *Dev. Cell* **16**, 209–221 (2009).

14. Taddei, A. *et al.* Endothelial adherens junctions control tight junctions by VE-cadherin-mediated upregulation of claudin-5. *Nature Cell Biol.* **10**, 923–934 (2008).
15. Stenman, J. M. *et al.* Canonical Wnt signaling regulates organ-specific assembly and differentiation of CNS vasculature. *Science* **322**, 1247–1250 (2008).
16. Liebner, S. *et al.* Wnt/ β -catenin signaling controls development of the blood-brain barrier. *J. Cell Biol.* **183**, 409–417 (2008).
17. Su, E. J. *et al.* Activation of PDGF-CC by tissue plasminogen activator impairs blood-brain barrier integrity during ischemic stroke. *Nature Med.* **14**, 731–737 (2008).
18. Bondjers, C. *et al.* Microarray analysis of blood microvessels from PDGF-B and PDGF-R β mutant mice identifies novel markers for brain pericytes. *FASEB J.* **20**, 1703–1705 (2006).
19. Wallgard, E. *et al.* Identification of a core set of 58 gene transcripts with broad and specific expression in the microvasculature. *Arterioscler. Thromb. Vasc. Biol.* **28**, 1469–1476 (2008).
20. He, L. *et al.* The glomerular transcriptome and a predicted protein-protein interaction network. *J. Am. Soc. Nephrol.* **19**, 260–268 (2008).
21. Wolburg, H. *et al.* Agrin, aquaporin-4, and astrocyte polarity as an important feature of the blood-brain barrier. *Neuroscientist* **15**, 180–193 (2009).
22. Janzer, R. C. & Raff, M. C. Astrocytes induce blood-brain barrier properties in endothelial cells. *Nature* **325**, 253–257 (1987).
23. Hayashi, Y. *et al.* Induction of various blood-brain barrier properties in non-neural endothelial cells by close apposition to co-cultured astrocytes. *Glia* **19**, 13–26 (1997).
24. Sobue, K. *et al.* Induction of blood-brain barrier properties in immortalized bovine brain endothelial cells by astrocytic factors. *Neurosci. Res.* **35**, 155–164 (1999).
25. Daneman, R. *et al.* Wnt/ β -catenin signaling is required for CNS, but not non-CNS, angiogenesis. *Proc. Natl Acad. Sci. USA* **106**, 641–646 (2009).
26. Hori, S. *et al.* A pericyte-derived angiopoietin-1 multimeric complex induces occludin gene expression in brain capillary endothelial cells through Tie-2 activation *in vitro*. *J. Neurochem.* **89**, 503–513 (2004).
27. Dohgu, S. *et al.* Brain pericytes contribute to the induction and up-regulation of blood-brain barrier functions through transforming growth factor- β production. *Brain Res.* **1038**, 208–215 (2005).
28. Kisanuki, Y. Y. *et al.* Tie2-Cre transgenic mice: a new model for endothelial cell-lineage analysis *in vivo*. *Dev. Biol.* **230**, 230–242 (2001).
29. Novak, A. *et al.* Z/EG, a double reporter mouse line that expresses enhanced green fluorescent protein upon Cre-mediated excision. *Genesis* **28**, 147–155 (2000).
30. Zambrowicz, B. P. *et al.* Disruption of overlapping transcripts in the ROSA β geo 26 gene trap strain leads to widespread expression of β -galactosidase in mouse embryos and hematopoietic cells. *Proc. Natl Acad. Sci. USA* **94**, 3789–3794 (1997).

Supplementary Information is linked to the online version of the paper at www.nature.com/nature.

Acknowledgements We thank U. Eriksson and members of the Betsholtz laboratory for discussion, P. Soriano, L. Sorokin and R. Hallman for reagents, and S. Kamph and the Scheele animal house for technical assistance. This work was supported by the Leducq Foundation, the Swedish Governmental Agency for Innovation Systems (Vinnova), the EU Fp6 Program Lymphangiogenomics, the Swedish Cancer Society and Research Council, the Knut and Alice Wallenberg, Inga-Britt and Arne Lundberg, and Torsten and Ragnar Söderberg Foundations.

Author Contributions A.A. and C.B. conceived and designed the project. A.A., G.G., M.M., M.H.N., E.W., C.N., L.H., J.N., P.L., K.S. and B.R.J. performed experiments; C.B. and A.A. wrote the manuscript with significant input from M.M., G.G. and M.H.N. G.G. and M.M. contributed equally to the study.

Author Information Our microarray data have been deposited in NCBI's Gene Expression Omnibus (<http://www.ncbi.nlm.nih.gov/geo/>) and are accessible through GEO series accession number GSE15892. Reprints and permissions information is available at www.nature.com/reprints. The authors declare no competing financial interests. Readers are welcome to comment on the online version of this article at www.nature.com/nature. Correspondence and requests for materials should be addressed to C.B. (christer.betsholtz@ki.se) or A.A. (annika.armulik@ki.se).

METHODS

Animals. Progeny from the following transgenic mouse lines were used for experiments: PDGF-B knockout⁶, PDGF-B retention motif knockout⁸, Tie2Cre (ref. 28), Rosa26 hPDGF-B (this study), XLacZ4 (ref. 9), Z/EG (ref. 29). PDGF-B retention motif knockouts were analysed on a C57BL6/J genetic background and R26P^{+/-} and R26P^{+/+} animals on a mixed C57BL6/J and 129sv genetic background. Animal experiments were approved by the Stockholm's North Ethical Committee for Animal Research.

Generation of Rosa26 hPDGF-B mice. A DNA cassette consisting of a full-length human PDGF-B cDNA sequence preceded by a splice acceptor site and a loxP-site-flanked transcription stop cassette was cloned into a vector designed for homologous recombination into the ubiquitously expressed ROSA26 locus³⁰ (Supplementary Fig. 2a). The targeting vector was verified by sequencing and electroporated into endothelial cells. Positive clones were identified by PCR and confirmed by Southern blot hybridization as described³⁰. Gene-targeted mice were generated from the ES cells by standard methods. Animal genotyping was done by PCR. The following PCR primers were used: R26F2, 5'-AAAGTCGCT CTGAGTTGTTAT-3'; R26SR, 5'-CCCACTGGAAAGACCGGAAGAGT-3'; R523, 5'-GGAGCGGAGAAATGGATATG-3' generated a 250-bp PCR fragment from the mutant allele and a 500-bp fragment from the wild-type allele. Expression of hPDGF-B was activated in endothelial cells by crossing with Tie2Cre transgenes (Supplementary Fig. 2b).

Quantification of vessel diameter, density and pericyte coverage. Quantification of vessel pericyte coverage was performed on 50 µm vibratome brain sections. Four corresponding areas in three animals of each genotype were analysed at 3–5 months of age. Blood vessels were visualized by collagen IV and pericytes by CD13 or PDGFR-β immunostainings. 14–16-µm-thick z-stacks were captured using an LSM Meta 510 microscope (Carl Zeiss AG). Quantification of pericyte numbers, vessel length and diameter was performed using Volocity software (Improvision, a PerkinElmer Company).

Antibodies and immunohistochemistry. The following primary antibodies were used: rabbit anti-rat aquaporin 4 (AB3068, Chemicon); rat anti-mouse CD13 (558744, BD PharMingen); rabbit anti-mouse collagen IV (2150-1470, AbD Serotec); rabbit anti-Glut1 (07-1401, Millipore); rat anti-mouse PDGFR-β (14-1402, eBioscience); goat anti-mouse podocalyxin (AF1556, R&D Systems). Secondary antibodies (goat anti-rat, goat anti-rabbit, donkey anti-goat) conjugated with Alexa Fluor dyes were obtained from Invitrogen. For immunostainings in which two primary rabbit antibodies were used, one was directly labelled using the Zenon rabbit IgG labelling kit (Invitrogen). Immunohistochemistry was performed on 50 or 100 µm brain coronal vibratome sections. Specimens were analysed using an LSM 510 META (Carl Zeiss AG) microscope. Image processing was done using Volocity 64 (Improvision), Adobe Photoshop CS3, and Adobe Illustrator CS3 (Adobe Systems). All immunohistochemistry images presented are three-dimensional reconstructions of z-stacks.

Intravenous injection of tracers and detection of injected tracers. Tracers were injected intravenously into the tail vein in adult (2–8 months) mice. The following tracers were used: Evans blue (Sigma Aldrich), lysine-fixable cadaverine conjugated to Alexa Fluor-555 (Invitrogen), bovine serum albumin conjugated to Alexa Fluor-555 (Invitrogen), lysine-fixable 70 kDa dextran conjugated to tetramethylrhodamine (Invitrogen), and goat anti-human IgG conjugated to DyLight 549 (Jackson ImmunoResearch Laboratories). More detailed descriptions of the tracer experiments are given in the Supplementary Methods. Images of dissected brains were captured using a stereomicroscope (SterEO Lumar.V12, equipped with HBO 100 lamp and a Filter Set Lumar 43 HE; Carl Zeiss AG) equipped with an

AxioCam HRc (Carl Zeiss AG) camera. Evans blue in the brain was quantified by spectrophotometry as described¹⁷. For quantification of cadaverine-Alexa Fluor-555 and DyLight-549 conjugated goat anti-human IgG in the brain, anaesthetized animals were perfused for 5 min with Hanks' balanced salt solution (HBSS), brains and kidneys removed and homogenized in 1% Triton X-100 in PBS, pH 7.2. Brain and kidney lysates were centrifuged at 16,000 r.p.m. for 20 min and the relative fluorescence of the supernatant was measured on a fluorometer POLARstar Omega (BMG Labtech) (ex/em 544/590 nm). For *in situ* detection of fluorophore-conjugated tracers, anaesthetized animals were perfused for 1–2 min with HBSS, followed by 5 min perfusion with 4% PFA in PBS, pH 7.2. Brains were removed and the tissue was post-fixed in 4% PFA in PBS, pH 7.2 at 4 °C for 5–6 h. 50-µm-thick coronal brain sections were immunostained with anti-Glut1 antibody. Samples were analysed by confocal microscopy (LSM 510 META, Carl Zeiss AG). When indicated, animals were treated with three or four doses of imatinib (150 mg kg⁻¹) twice per day before tracer injections.

Transmission electron microscopy. Two-month-old mice were injected intravenously with horseradish peroxidase Type II (HRP) (100 mg ml⁻¹ in PBS, 10 mg per 20 g) (Sigma Aldrich). After 2 h, animals were anaesthetized and perfused with 2.5% glutaraldehyde in 0.1 M cacodylate buffer, pH 7.2. HRP-diaminobenzidine cytochemistry was performed on brain vibratome slices according to ref. 31 with minor modifications. After osmication and en bloc uranyl acetate treatment, tissue blocks were dehydrated and embedded in epoxy resin. Sections were cut with a diamond knife on a Leica EM UC7 ultramicrotome (Leica Microsystems) at 60 nm thickness setting and were examined without additional contrasting in a LEO 912AB energy-filtered transmission electron microscope (Carl Zeiss SMT AG). Digital images were captured with a MegaView III camera (Olympus SIS).

Brain water content determination. Animals were anaesthetized and perfused with HBSS for 5 min via the left ventricle of the heart. Brains were removed and weighed for wet weight. Tissue was dried at 62 °C for 6 days and weighed again for dry weight.

Purification of microvasculature and microarray analysis. Purification of microvasculature and RNA isolation was performed as described²⁰. Four RNA samples of each genotype were individually hybridized to Affymetrix GeneChip Mouse Genome 430 2.0 microarrays. Publicly available Affymetrix raw data files concerning wild-type adult whole brain³², isolated wild-type adult glomeruli²⁰, and wild-type embryonic and adult brain microvascular fragments¹⁹ were downloaded and treated in the same manner as data generated in this study. Array data was processed using the Affy and gcrma packages in the Bioconductor project (<http://www.bioconductor.org>). A Student's *t*-test was used to evaluate differential expression. The false discovery rate method was used to perform multiple test correction for *P* values³³. The log₂ change was calculated as the log₂ of the average expression difference between sample groups. A detailed description of the samples used in different comparisons is given in Supplementary Table 3.

Statistical analysis. Statistical significance was determined by using unpaired two-tailed or one-tailed Student's *t*-test (GraphPad Prism5). Differences were considered significant with a *P* value less than 0.05. Quantified data are presented as mean ± s.e.m.

1. Karnovsky, M. J. The ultrastructural basis of capillary permeability studied with peroxidase as a tracer. *J. Cell Biol.* **35**, 213–236 (1967).
2. Bender, A. *et al.* Creatine improves health and survival of mice. *Neurobiol. Aging* **29**, 1404–1411 (2008).
3. Benjamini, Y. & Hochberg, Y. Controlling the false discovery rate: a practical and powerful approach to multiple testing. *J. R. Stat. Soc. B* **57**, 289–300 (1995).

Pericytes are required for blood–brain barrier integrity during embryogenesis

Richard Daneman¹, Lu Zhou², Amanuel A. Kebede¹ & Ben A. Barres²

Vascular endothelial cells in the central nervous system (CNS) form a barrier that restricts the movement of molecules and ions between the blood and the brain. This blood–brain barrier (BBB) is crucial to ensure proper neuronal function and protect the CNS from injury and disease¹. Transplantation studies have demonstrated that the BBB is not intrinsic to the endothelial cells, but is induced by interactions with the neural cells². Owing to the close spatial relationship between astrocytes and endothelial cells, it has been hypothesized that astrocytes induce this critical barrier postnatally³, but the timing of BBB formation has been controversial^{4–9}. Here we demonstrate that the barrier is formed during embryogenesis as endothelial cells invade the CNS and pericytes are recruited to the nascent vessels, over a week before astrocyte generation. Analysing mice with null and hypomorphic alleles of *Pdgfrb*, which have defects in pericyte generation, we demonstrate that pericytes are necessary for the formation of the BBB, and that absolute pericyte coverage determines relative vascular permeability. We demonstrate that pericytes regulate functional aspects of the BBB, including the formation of tight junctions and vesicle trafficking in CNS endothelial cells. Pericytes do not induce BBB-specific gene expression in CNS endothelial cells, but inhibit the expression of molecules that increase vascular permeability and CNS immune cell infiltration. These data indicate that pericyte–endothelial cell interactions are critical to regulate the BBB during development, and disruption of these interactions may lead to BBB dysfunction and neuroinflammation during CNS injury and disease.

To understand the mechanisms of BBB formation, we investigated the sequence of cell generation and BBB formation in the developing CNS (Fig. 1 and Supplementary Figs 1–7). In the rat cerebral cortex, angiogenesis begins at embryonic day 12 (E12), as endothelial cells invade the neural tissue from the surrounding vascular plexus (Fig. 1a and Supplementary Fig. 1). Pericytes—platelet-derived growth factor receptor- β (PDGFR- β)⁺NG2⁺ vascular support cells—are found associated with endothelial tubes as nascent vessels are generated (Fig. 1b and Supplementary Fig. 1). Neural cells are produced from progenitors in a defined sequence, with neurons generated before glia. Oligodendroglia progenitor cells (OPCs), PDGFR- α ⁺NG2⁺ glial cells, are first observed at E19 and migrate throughout the cortex by birth (Fig. 1c). Astrocytes are first generated directly after birth and extend processes which contact vessels during the first postnatal week (Fig. 1d and Supplementary Fig. 2). If astrocytes induce the BBB, barrier properties should only be acquired after birth.

We next examined endothelial cell protein expression and barrier function during rat cortical development. BBB-forming endothelial cells are characterized by tight junctions, low rates of transcytosis, and the expression of specialized influx and efflux transporters. Tight junction molecules occludin, claudin 5 and ZO-1 were each expressed at endothelial junctions as early as E12 (Fig. 1e, Supplementary Fig. 4 and not shown). The same was observed with the BBB-specific influx transporter Glut1 (Fig. 1f and Supplementary Fig. 3). Notably, the BBB-specific efflux transporter Pgp is expressed at low

levels during embryogenesis, but increases during postnatal development (Fig. 1g), indicating a distinct regulation mechanism for efflux transport. Similar timing of cell generation and BBB gene expression was observed in the developing mouse, with vascularization of the cortex starting at E11 (Supplementary Fig. 6). The expression of genes that increase vascular permeability, including transcytosis (*Plvap*) and leukocyte infiltration (*Icam1*), decreased after initial high expression (Supplementary Fig. 7). The developmental timing of BBB function was examined by trans-cardiac perfusion with tracers. In adults, the small molecule tracer biotin stays within the lumen of CNS vessels and doesn't diffuse into the CNS parenchyma, whereas in non-neural tissue the tracer diffuses throughout the extracellular space (Fig. 1h–j). We used this method to examine BBB function in postnatal animals and dissected embryos. At each age tested (E15, E21, P1, P15 and P20) CNS vessels excluded the tracer from the CNS parenchyma (Fig. 1h–j and not shown). In embryonic time points, the tracer was excluded from most of the CNS; however, distinct regions of the CNS displayed leakiness, including regions close to the pia (Supplementary Fig. 5), indicating that serum contents may enter the CNS through pial coverings or choroid plexus. Thus, a functional BBB is present during embryogenesis before astrocyte generation.

Because pericyte recruitment to CNS vessels temporally correlates with the onset of barrier properties, we examined the role of these mural cells in regulating BBB function, structure and gene expression. Although pericytes are associated with the vasculature throughout the body, and thus are unlikely candidates to regulate brain-specific vascular properties, recent studies have demonstrated that CNS pericytes have a different developmental origin from other pericytes¹⁰, and several studies have suggested that pericytes are capable of regulating BBB properties *in vitro*^{11–13}. To determine if pericytes are necessary for BBB formation we compared the vascular permeability of *Pdgfrb*^{−/−} mice with littermate controls. PDGFBB signalling through PDGFR- β is essential for pericyte generation, and mice deficient for either the ligand or receptor completely lack CNS pericytes^{14,15}, exhibit endothelial cell hyperplasia, increased vessel diameter and morphological signs of increased vascular permeability¹⁶. These mice die at birth; therefore, we examined BBB function in dissected embryos. Indeed, *Pdgfrb*^{−/−} mice show an increased vascular permeability to biotin (0.5 kDa), as observed by an increase in tracer staining throughout the CNS parenchyma (Fig. 2a, b). Decreasing permeability was observed with increasing size of tracer (Fig. 2c).

CNS vessels have the highest pericyte coverage of any vessels, and the extent of pericyte coverage in vessels throughout the body inversely correlates with the relative permeability of these vessels¹⁷. To determine whether pericyte number, and not just presence or absence, is an important regulator of BBB permeability, we measured CNS vascular permeability in mice with different combinations of null, hypomorphic and wild-type *Pdgfrb* alleles. One study¹⁵ generated an allelic series of *Pdgfrb* hypomorphs, showing that varying the strength of PDGFR- β signalling leads to different pericyte:endothelial cell ratios. We compared the vascular permeability of *Pdgfrb*^{F7/−} and *Pdgfrb*^{F7/F7},

¹UCSF Department of Anatomy, 513 Parnassus Avenue, HSW1301, San Francisco, California 94143-0452, USA. ²Stanford University School of Medicine, Department of Neurobiology, Fairchild Science Building D200, Stanford, California 94305-5125, USA.

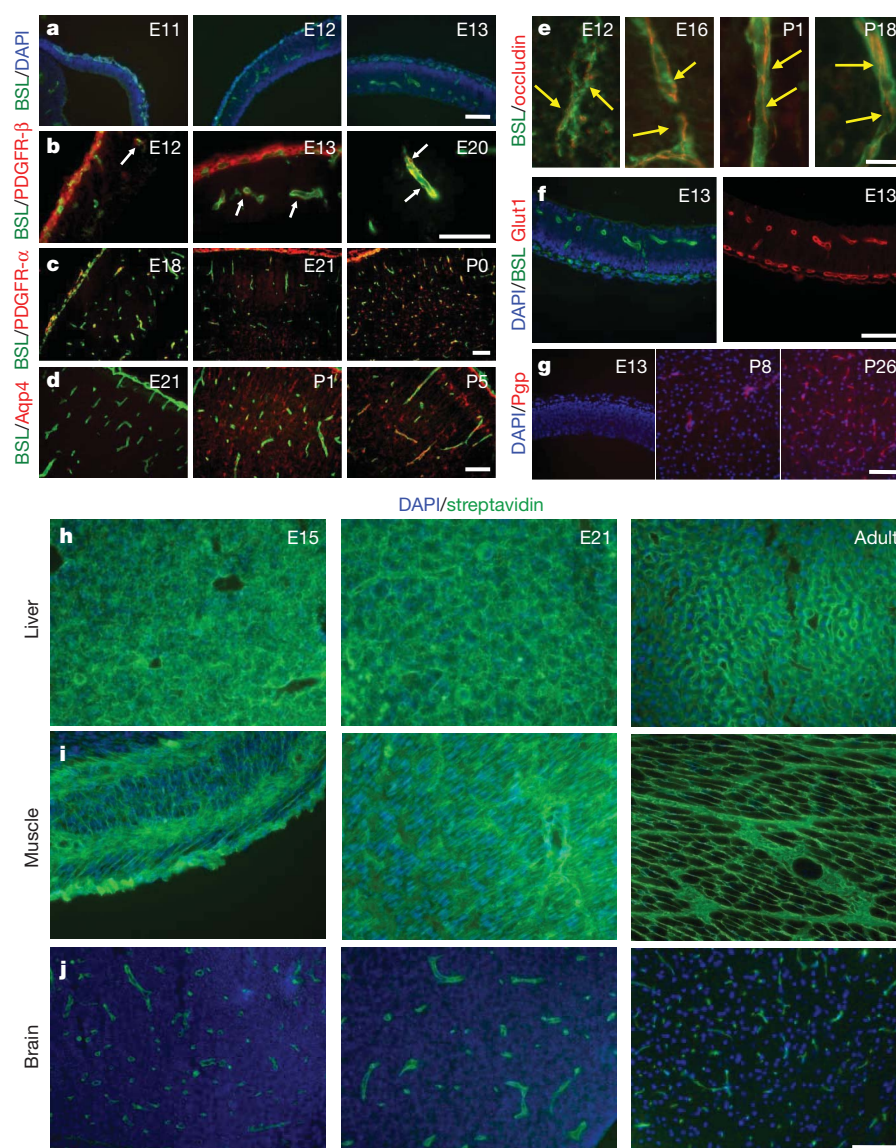


Figure 1 | Time course of cell generation and BBB development in the rat cerebral cortex. a–g, Sections of rat cerebral cortex at indicated ages were stained for endothelial cells with *Bandeiraea simplicifolia* lectin I (BSL) (green, a–f) and nuclei with DAPI (blue, a, f (left), g), pericytes with anti-PDGFR- β (red, b; white arrows point to pericytes), oligodendrocyte progenitors with anti-PDGFR- α (red, c), astrocytes with anti-aquaporin 4 (red, d), anti-occludin (red,

e; yellow arrows indicate tight-junction strands), anti-Glut1 (red, f (right)), and anti-Pgp (red, g). Scale bars represent 100 μ m (a–d, f, g) and 20 μ m (e). h–j, Rats aged E15 (left), E21 (middle) and adults (right) were given a transcardiac perfusion of biotin, and liver (h), muscle (i) and brain (j) tissue sections were stained with streptavidin (green) and DAPI (blue). Scale bar represents 100 μ m.

which respectively have approximately 40% and 50% of the pericyte coverage of littermate controls¹⁵ (Fig. 2d–g and Supplementary Fig. 8). Indeed, the permeability of the BBB in these neonatal mice, to both Evan's blue and biotin, inversely correlated with the pericyte coverage (Fig. 2h–k), demonstrating that pericyte number determines relative permeability of CNS vessels during development.

We next addressed the question of whether pericytes regulate endothelial transcytosis, tight-junction formation and/or transporter expression. Examination by electron microscopy revealed that CNS endothelial cells of *Pdgfrb*^{−/−} mice displayed an increase in membrane folding with membrane protrusions into the vessel lumen, as well as an increase in the number of cytoplasmic vesicles, indicating an increased rate of transcytosis (Fig. 3A–C). Indeed, examination of biotin leakage by electron microscopy, using streptavidin–horseradish peroxidase (HRP), revealed that the tracer was endocytosed into endothelial cell vesicles (Fig. 3A, d, e, and B, d, e), demonstrating transcellular passage is an important component of BBB leakiness in *Pdgfrb*^{−/−} mice. *Pdgfrb*^{−/−} mice and littermate controls expressed tight-junction proteins

occludin and claudin 5 at equal levels and these molecules were localized to cellular junctions (Figs 3E, F and 4a, b). Structural abnormalities in the tight junctions of the *Pdgfrb*^{−/−} mice were observed by electron microscopy (Fig. 3A, c and B, c). In control animals, the length of the junction was parallel to the plane of the vessel lumen; however, in *Pdgfrb*^{−/−} mice, the junctional alignment was random, being parallel, perpendicular, or at various angles to the lumen, with junctional membranes often dipping into the lumen or CNS parenchyma (Fig. 3A, c, B, c, and D). The polarized expression of Glut1 at the abluminal membrane was not affected (Supplementary Fig. 9).

To determine whether junctional abnormalities are due to a lack of pericytes, or other defects in *Pdgfrb*^{−/−} mice, we analysed the function, expression and localization of tight-junction proteins in purified brain endothelial cells cultured alone or with a feeding layer of purified brain pericytes. Purified CNS endothelial cells expressed the tight-junction proteins occludin and claudin 5, which were localized to cellular borders (Fig. 3G, H). Notably, endothelial cells cultured alone often contained large gaps between cell connections, whereas the endothelial

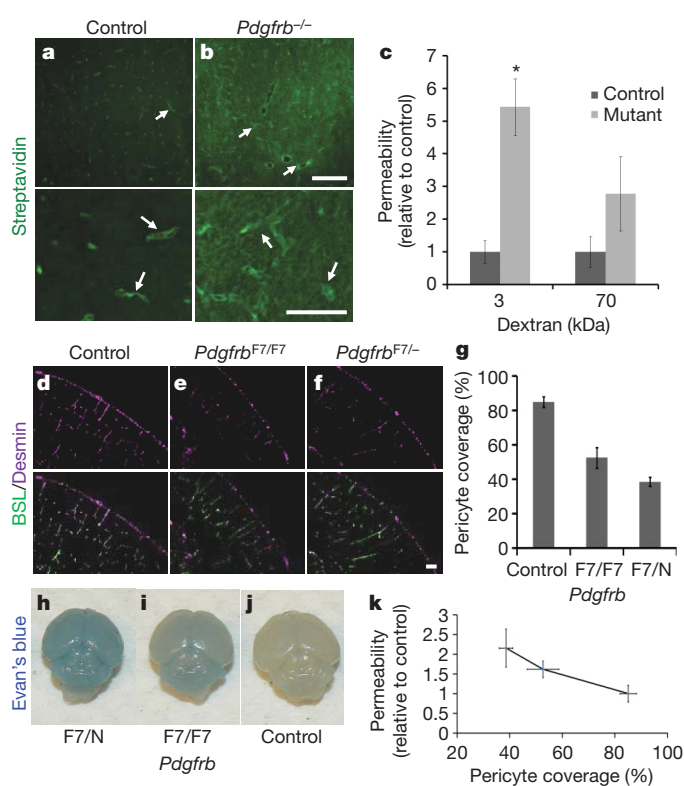


Figure 2 | Pericytes are required for BBB formation. **a, b**, E18 *Pdgfrb*^{-/-} mice (**b**) and littermate controls (**a**) were given a trans-cardiac perfusion of biotin, and tissue sections were stained with streptavidin (green; white arrows indicate tracer in vessels). Scale bars represent 200 μ m (upper panel) and 100 μ m (lower panel). **c**, E18 *Pdgfrb*^{-/-} mice and littermate controls were given a trans-cardiac perfusion of 3 kDa or 70 kDa biotinylated dextran, tissue sections stained with streptavidin-Alexa 488, fluorescence was quantified in ImageJ and permeability relative to control was graphed. * $P < 0.05$ by Student's *t*-test. **d–f**, Neonatal mouse cerebral cortex from *Pdgfrb*^{F7/-} (**f**), *Pdgfrb*^{F7/F7} (**e**) and littermate controls (**d**) were stained with BSL (green, **d–f** (bottom)) and for pericytes with anti-desmin (purple, **d–f** (top)). Scale bar represents 100 μ m. **g**, Pericyte coverage of CNS vessels in *Pdgfrb*^{F7/-}, *Pdgfrb*^{F7/F7} and littermate control mice was quantified by analysing per cent length of BSL⁺ vessels opposed to desmin⁺ pericytes. **h–j**, P5 *Pdgfrb*^{F7/-} mice (**h**), *Pdgfrb*^{F7/F7} mice (**i**) and littermate controls (**j**) were given an intraperitoneal injection of Evan's blue dye, and their brains were dissected the following day after PBS perfusion. **k**, Neonatal *Pdgfrb*^{F7/-}, *Pdgfrb*^{F7/F7} and littermate controls were given a trans-cardiac perfusion of biotin and leakage was quantified in tissue sections with streptavidin-Alexa-488 (y axis) and graphed versus pericyte coverage (x axis; values from panel **g**). All error bars represent s.e.m.

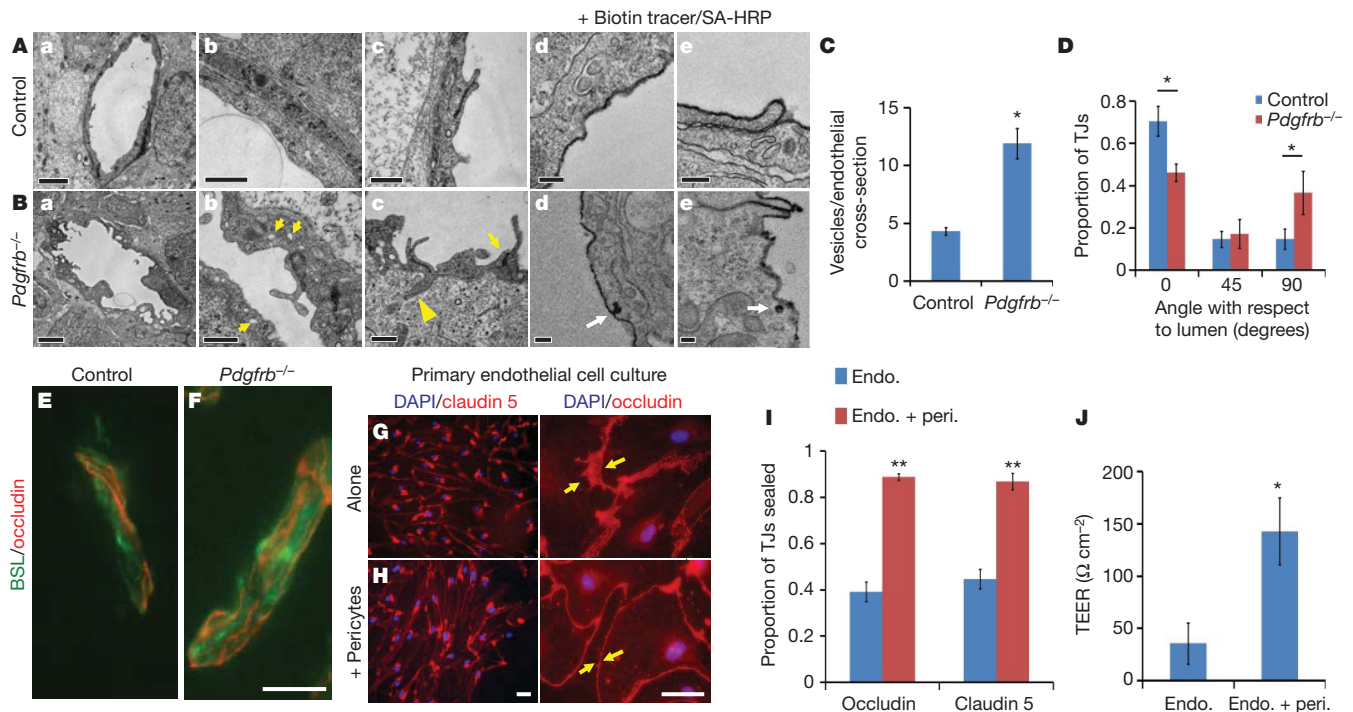


Figure 3 | Pericytes regulate structural aspects of the BBB. **A, B**, Electron microscopy images of CNS vessels from E18 *Pdgfrb*^{-/-} mice (**B**) and littermate controls (**A**) including whole endothelial cell cross-sections (**a**), cytoplasm (**b**; yellow arrows indicate cytoplasmic vessels), tight junctions (**c**; yellow arrows indicate altered junction alignment; yellow arrowheads indicate junctions dipping into parenchyma), and after perfusion with biotin followed by staining with streptavidin-HRP (**d, e**; white arrows indicate uptake of tracer). Scale bars represent 2 μ m (**a**), 0.5 μ m (**b, c**) and 0.2 μ m (**d, e**). **C**, Quantification of the number of vesicles per endothelial cross-section for *Pdgfrb*^{-/-} mice and littermates. **D**, Angles of tight junctions (TJs) for *Pdgfrb*^{-/-} mice and littermate controls were classified as parallel to the lumen (0°), perpendicular to the lumen (90°) or in between (45°). * $P < 0.05$ by Student's *t*-test. **E, F**, Cerebral cortex of

E18 *Pdgfrb*^{-/-} mice (**F**) and littermate controls (**E**) were stained with BSL (green) and anti-occludin (red). Scale bars represent 20 μ m. **G, H**, Purified murine brain endothelial cells were cultured alone (**G**) or with a feeding layer of purified brain pericytes (**H**) and stained with DAPI (blue) and anti-claudin 5 (left, red) or anti-occludin (right, red; yellow arrows indicate cell borders). Scale bars represent 100 μ m (left) and 50 μ m (right). **I**, Per cent length of sealed claudin 5 and occludin junctions in endothelial cells cultured alone or with pericyte feeder layers. ** $P < 0.01$ by Student's *t*-test. **J**, TEER measurements for purified murine brain endothelial cells cultured alone or with a feeding layer of purified brain pericytes. * $P < 0.05$ by Student's *t*-test. All error bars represent s.e.m.

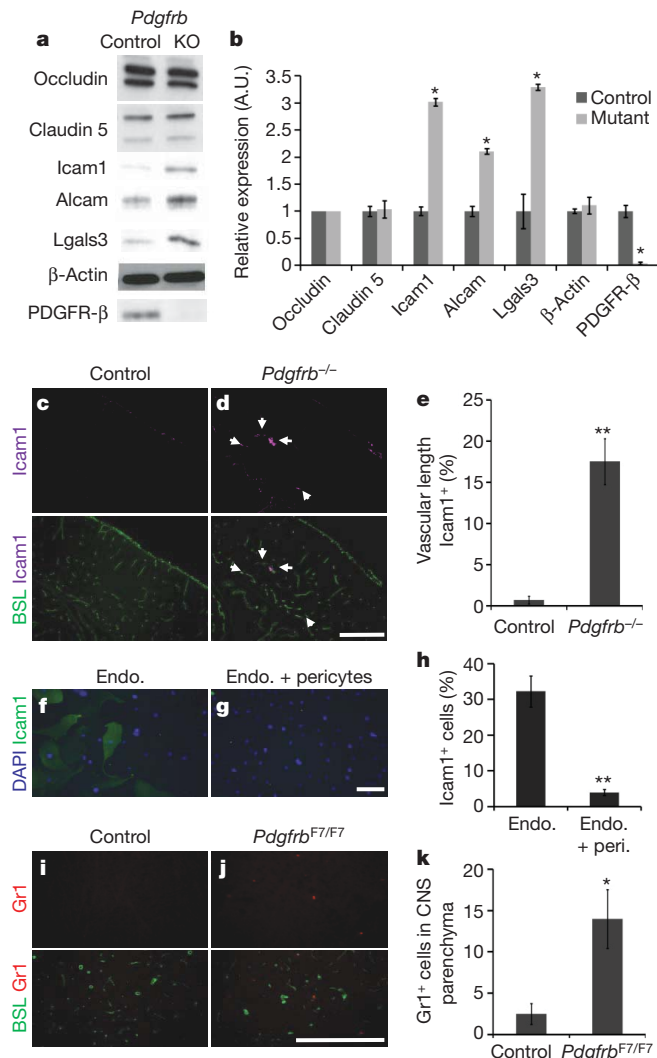


Figure 4 | Vascular expression of LAMs in *Pdgfrb*^{-/-} mice. **a, b**, Western blots of brain lysates from E18 *Pdgfrb*^{-/-} (KO) and littermate controls, probing occludin, claudin 5, Icam1, Alcam, Lgals3, β-actin and PDGFR-β. **a**, Representative blots; **b**, quantification; **P* < 0.05 by Student's *t*-test. **c-e**, Cerebral cortex of E18 *Pdgfrb*^{-/-} mice (d) and littermate controls (c) were stained with anti-Icam1 (purple) and BSL (green, bottom; white arrows indicate Icam1⁺ vessels), and per cent Icam1⁺ vascular length was quantified (e). Scale bar represents 250 μm. ***P* < 0.005 by Student *t*-test. **f-h**, Purified murine brain endothelial cells cultured alone (f) or with a feeding layer of purified brain pericytes (g) and stained for DAPI (blue) and anti-Icam1 (green), and proportion of Icam1⁺ cells was quantified (h). Scale bar represents 200 μm. ***P* < 0.005 by Student *t*-test. **i-k**, Five-week-old *Pdgfrb*^{F7/F7} mice (j) and littermate controls (i) were stained with anti-Gr1 (red) and BSL (green, bottom), and number of Gr1⁺ cells per sagittal section was counted (k). Scale bar represents 250 μm. **P* < 0.05 by Student's *t*-test. All error bars represent s.e.m.

junctions sealed and the intercellular space diminished when they were cultured with pericytes (Fig. 3G–I). This was accompanied by a four-fold increase in trans-endothelial cell electrical resistance (TEER), demonstrating that endothelial tight junctions are functionally tighter in the presence of pericytes (Fig. 3J).

To determine whether pericytes regulate endothelial gene expression, we used microarray analysis to compare the gene expression of CD31⁺ vascular cells purified from *Pdgfrb*^{-/-} mice and littermate controls. In *Pdgfrb*^{-/-} mice, no downregulation of BBB genes was observed, including tight-junction proteins and transporters (Supplementary Table 1 and Fig. 4a, b). Thus, pericytes are not necessary for induction of BBB-specific genes. In the absence of pericytes, however, expression of genes known to increase vascular permeability, including *Angpt2*,

Plvap and leukocyte adhesion molecules (LAMs), were upregulated. In *Pdgfrb*^{-/-} mice we observed a loss of vascular *Angpt1*, a Tie2 receptor ligand that decreases permeability, and a corresponding increase in *Angpt2*, a Tie2 ligand that increases vascular permeability^{18,19} (Supplementary Table 1), and co-culture of a feeder layer of pericytes with CNS endothelial cells was sufficient to decrease endothelial *Angpt2* expression (Supplementary Fig. 12). *Pdgfrb*^{-/-} mice also exhibited an increase in endothelial *Plvap* expression (Supplementary Table 1), which was verified by immunofluorescence (Supplementary Fig. 10). *Plvap* is involved in endothelial vesicle trafficking, and is highly expressed in permeable peripheral vessels and is upregulated in CNS endothelial cells during pathological breakdown of the BBB^{20,21}. Therefore, pericytes may limit transcytosis by suppressing *Plvap*.

We further examined the gene expression of acutely purified pericytes to identify pericyte-secreted signals (Supplementary Table 2). We identified that pericytes express molecules that regulate BBB properties including *Angpt1* and *Ace2* (refs 12, 22), as well as a number of other signalling molecules and matrix components. Furthermore, the extracellular matrix is altered in the *Pdgfrb*^{-/-} mouse, including a decrease in several collagen subunits and an upregulation of MMP9, a protease that increases the permeability of the BBB during disease (Supplementary Fig. 11)^{23,24}.

The transcription of several LAMs, including *Icam1*, *Alcam* and *Lgals3*, were significantly upregulated in the vasculature of *Pdgfrb*^{-/-} mice (Supplementary Table 1), and we confirmed a corresponding increase in protein expression (Fig. 4a, b). We found that *Icam1* was robustly upregulated in specific segments of the vasculature in *Pdgfrb*^{-/-} mice (Fig. 4c–e), and further demonstrated that co-culture of pericytes with endothelial cells is sufficient to decrease the number of Icam1⁺ endothelial cells (Fig. 4f–h). These data indicate that pericytes may provide signals that limit CNS immune surveillance, a critical feature of the BBB. Indeed, we observed an increase in the number of Gr1⁺ leukocytes in the CNS parenchyma of pericyte-deficient mice (Fig. 4i–k).

These findings demonstrate that pericytes are required for BBB formation during development, and absolute pericyte coverage controls relative BBB permeability. Although astrocytes are not required to initially induce the BBB, it remains likely that astrocytes act to regulate the maintenance of the BBB and its response to neural function and disease. In fact, reactive astrocytes are necessary for BBB repair after injury²⁵. Interestingly, even in the absence of pericytes, embryonic CNS endothelial cells express many BBB-specific molecules, indicating that neural progenitors may induce BBB gene expression. Indeed, neural-progenitor-derived Wnts are critical for CNS angiogenesis and the induction of BBB-specific transporter expression^{26–28}. We propose a new model for BBB formation: endothelial cells are induced to express BBB-specific genes by interactions with neural progenitors, and then the functional integrity of the BBB is regulated by pericytes during development and astrocytes in adulthood (Supplementary Fig. 13).

These findings have important implications for understanding BBB breakdown and repair, which is a common component of many neurodegenerative disorders, stroke, brain tumours, CNS trauma, multiple sclerosis and diabetic retinopathy¹. Notably, loss of pericytes occurs at early stages of diabetic retinopathy, and thus probably has a role in the vascular permeability defects observed during this disease²⁹. The finding that pericytes are necessary for limiting CNS immune surveillance has implications for controlling neuroinflammation. For instance, pericytes inhibit the expression of Alcam, which is upregulated in CNS vessels in multiple sclerosis (MS) patients and enhances leukocyte migration across endothelial cells³⁰. Identification of molecular mechanisms by which pericytes regulate BBB integrity may lead to new treatments for these diseases.

METHODS SUMMARY

Immunohistochemistry. Rodent tissues were fixed with 4% paraformaldehyde, 10% trichloroacetic acid or 95% ethanol followed by acetone. Tissue sections were blocked with 50% goat serum, permeabilized with 0.2% Triton X-100, and stained

with appropriate primary and secondary antibodies. Slides were mounted in vectashield with DAPI (Vector Labs) and visualized by fluorescence microscopy.

BBB permeability assays. Anaesthetized rodents were given a trans-cardiac perfusion, with a Dynamax peristaltic pump, of DPBS (Gibco) containing EZ-link sulfo NHS Biotin (Pierce) or biotinylated fixable dextrans (Invitrogen), followed by 4% paraformaldehyde. Tissue cryosections were stained with streptavidin Alexa-488 (Invitrogen) and analysed by fluorescence microscopy.

Cell culture. CNS endothelial cells were purified by anti-CD31 immunopanning and CNS pericytes were purified by anti-PDGFR- β immunopanning. For immunofluorescence analysis, CNS endothelial cells were grown on coverslips alone, or with a feeder layer of CNS pericytes grown on cell culture inserts. For TEER measurements, CNS endothelial cells were grown on cell culture inserts alone, or with a pericyte feeder layer grown in the culture well bottom beneath, and resistance measurements were recorded with an EVOM voltmeter.

Electron microscopy. E18 *Pdgfrb*^{-/-} and littermate controls were fixed in 2% glutaraldehyde/4% paraformaldehyde, and processed for electron microscopy. To image tracer permeability, E18 *Pdgfrb*^{-/-} and littermate controls were given a trans-cardiac perfusion of DPBS (Gibco) containing EZ-link sulfo NHS Biotin (Pierce) followed by 4% paraformaldehyde, and frozen tissue sections were fixed with 2% glutaraldehyde/4% paraformaldehyde then stained with a HRP-tagged streptavidin (Invitrogen) followed by DAB reaction.

Full Methods and any associated references are available in the online version of the paper at www.nature.com/nature.

Received 14 April 2009; accepted 23 September 2010.

Published online 13 October 2010.

- Zlokovic, B. V. The blood-brain barrier in health and chronic neurodegenerative disorders. *Neuron* **57**, 178–201 (2008).
- Stewart, P. A. & Wiley, M. J. Developing nervous tissue induces formation of blood-brain barrier characteristics in invading endothelial cells: a study using quail–chick transplantation chimeras. *Dev. Biol.* **84**, 183–192 (1981).
- Janzer, R. C. & Raff, M. C. Astrocytes induce blood-brain barrier properties in endothelial cells. *Nature* **325**, 253–257 (1987).
- Bauer, H. C. *et al.* Neovascularization and the appearance of morphological characteristics of the blood-brain barrier in the embryonic mouse central nervous system. *Brain Res. Dev. Brain Res.* **75**, 269–278 (1993).
- Bolz, S., Farrell, C. L., Dietz, K. & Wolburg, H. Subcellular distribution of glucose transporter (GLUT-1) during development of the blood-brain barrier in rats. *Cell Tissue Res.* **284**, 355–365 (1996).
- Butt, A. M., Jones, H. C. & Abbott, N. J. Electrical resistance across the blood-brain barrier in anaesthetized rats: a developmental study. *J. Physiol. (Lond.)* **429**, 47–62 (1990).
- Ek, C. J., Dziegielewska, K. M., Stolp, H. & Saunders, N. R. Functional effectiveness of the blood-brain barrier to small water-soluble molecules in developing and adult opossum (*Monodelphis domestica*). *J. Comp. Neurol.* **496**, 13–26 (2006).
- Hirase, T. *et al.* Occludin as a possible determinant of tight junction permeability in endothelial cells. *J. Cell Sci.* **110**, 1603–1613 (1997).
- Kniesel, U., Risau, W. & Wolburg, H. Development of blood-brain barrier tight junctions in the rat cortex. *Brain Res. Dev. Brain Res.* **96**, 229–240 (1996).
- Korn, J., Christ, B. & Kurz, H. Neuroectodermal origin of brain pericytes and vascular smooth muscle cells. *J. Comp. Neurol.* **442**, 78–88 (2002).
- Dohgu, S. *et al.* Brain pericytes contribute to the induction and up-regulation of blood-brain barrier functions through transforming growth factor- β production. *Brain Res.* **1038**, 208–215 (2005).
- Hori, S., Ohtsuki, S., Hosoya, K., Nakashima, E. & Terasaki, T. A pericyte-derived angiopoietin-1 multimeric complex induces occludin gene expression in brain capillary endothelial cells through Tie-2 activation *in vitro*. *J. Neurochem.* **89**, 503–513 (2004).
- Lai, C. H. & Kuo, K. H. The critical component to establish *in vitro* BBB model: Pericyte. *Brain Res. Brain Res. Rev.* **50**, 258–265 (2005).
- Lindahl, P., Johansson, B. R., Leveen, P. & Betsholtz, C. Pericyte loss and microaneurysm formation in PDGF-B-deficient mice. *Science* **277**, 242–245 (1997).
- Tallquist, M. D., French, W. J. & Soriano, P. Additive effects of PDGF receptor β signaling pathways in vascular smooth muscle cell development. *PLoS Biol.* **1**, e52 (2003).
- Hellstrom, M. *et al.* Lack of pericytes leads to endothelial hyperplasia and abnormal vascular morphogenesis. *J. Cell Biol.* **153**, 543–554 (2001).
- Shepro, D. & Morel, N. M. Pericyte physiology. *FASEB J.* **7**, 1031–1038 (1993).
- Lee, S. W., Kim, W. J., Jun, H. O., Choi, Y. K. & Kim, K. W. Angiopoietin-1 reduces vascular endothelial growth factor-induced brain endothelial permeability via upregulation of ZO-2. *Int. J. Mol. Med.* **23**, 279–284 (2009).
- Nag, S., Papneja, T., Venugopalan, R. & Stewart, D. J. Increased angiopoietin2 expression is associated with endothelial apoptosis and blood-brain barrier breakdown. *Lab. Invest.* **85**, 1189–1198 (2005).
- Shue, E. H. *et al.* Plasmalemmal vesicle associated protein-1 (PV-1) is a marker of blood-brain barrier disruption in rodent models. *BMC Neurosci.* **9**, 29 (2008).
- Ioannidou, S. *et al.* An *in vitro* assay reveals a role for the diaphragm protein PV-1 in endothelial fenestra morphogenesis. *Proc. Natl Acad. Sci. USA* **103**, 16770–16775 (2006).
- Wosik, K. *et al.* Angiotensin II controls occludin function and is required for blood brain barrier maintenance: relevance to multiple sclerosis. *J. Neurosci.* **27**, 9032–9042 (2007).
- Gidday, J. M. *et al.* Leukocyte-derived matrix metalloproteinase-9 mediates blood-brain barrier breakdown and is proinflammatory after transient focal cerebral ischemia. *Am. J. Physiol. Heart Circ. Physiol.* **289**, H558–H568 (2005).
- He, Z. J., Huang, Z. T., Chen, X. T. & Zou, Z. J. Effects of matrix metalloproteinase 9 inhibition on the blood brain barrier and inflammation in rats following cardiopulmonary resuscitation. *Chin. Med. J. (Engl.)* **122**, 2346–2351 (2009).
- Bush, T. G. *et al.* Leukocyte infiltration, neuronal degeneration, and neurite outgrowth after ablation of scar-forming, reactive astrocytes in adult transgenic mice. *Neuron* **23**, 297–308 (1999).
- Weidenfeller, C., Svendsen, C. N. & Shusta, E. V. Differentiating embryonic neural progenitor cells induce blood-brain barrier properties. *J. Neurochem.* **101**, 555–565 (2007).
- Daneman, R. *et al.* Wnt/ β -catenin signaling is required for CNS, but not non-CNS, angiogenesis. *Proc. Natl Acad. Sci. USA* **106**, 641–646 (2009).
- Stenman, J. M. *et al.* Canonical Wnt signaling regulates organ-specific assembly and differentiation of CNS vasculature. *Science* **322**, 1247–1250 (2008).
- Motiejunaite, R. & Kazlauskas, A. Pericytes and ocular diseases. *Exp. Eye Res.* **86**, 171–177 (2008).
- Cayrol, R. *et al.* Activated leukocyte cell adhesion molecule promotes leukocyte trafficking into the central nervous system. *Nature Immunol.* **9**, 137–145 (2008).

Supplementary Information is linked to the online version of the paper at www.nature.com/nature.

Acknowledgements We thank J. Perrino for electron microscopy preparations. Work was supported by grants from the NINDS (R01-NS045621; B.A.B.), Myelin Repair Foundation (B.A.B., R.D.), NMSS (Grant-RG3936A7; B.A.B.), UCSF Fellow's Program (R.D.) and AHA (R.D.).

Author Contributions R.D. and B.A.B. designed experiments and wrote the manuscript. R.D., L.Z. and A.A.K. performed and analysed experiments.

Author Information Reprints and permissions information is available at www.nature.com/reprints. The authors declare no competing financial interests. Readers are welcome to comment on the online version of this article at www.nature.com/nature. Correspondence and requests for materials should be addressed to R.D. (Richard.daneman@ucsf.edu).

METHODS

Animals. Sprague–Dawley rats and C57BL/6 mice were obtained from Charles River. Mice harbouring *Pdgfrb*^{−/−} and *Pdgfrb*^{F7} alleles were obtained from Phillippe Soriano (Fred Hutchinson Cancer Research Center), and lines were maintained by breeding with C57BL/6 mice.

Immunohistochemistry. For time course experiments, whole rat and mouse embryos before E15, and dissected brains of embryos between E15 and birth, were fixed overnight in 4% paraformaldehyde at 4 °C. Postnatal rats and mice were anaesthetized with a ketamine (100 mg kg^{−1})/xylazine (20 mg kg^{−1}) cocktail, and perfused with PBS followed by 4% paraformaldehyde with a dynamax peristaltic pump and then dissected brains were fixed overnight in 4% paraformaldehyde at 4 °C. Staining was performed as described previously²⁷, with antibodies directed against PDGFR-β (R&D systems, eBiosciences) and Ng2 (Chemicon) for pericytes, PDGFR-α for OPCs (Abcam), Aqp4 for astrocytes (sigma), Glut1 (Chemicon), Pgp (Sigma) and Icam1 (Abcam), and with appropriate Alexa-conjugated secondary antibodies and counter-stained with BSL-fluorescein (Vector Labs). For ZO-1 and Plvap immunofluorescence, embryos were fixed with 10% trichloroacetic acid for 1 h on ice, before cryopreservation and staining with anti-ZO-1 antibody (Invitrogen) or anti-Plvap antibody (AbD Serotec). Staining for occludin and claudin 5 was achieved by flash freezing dissected brains, or whole embryos for ages less than E15, in OCT. Tissue cryosections were obtained and fixed in cold 95% ethanol for 30 min, followed by 1 min in room temperature acetone. Sections were then rehydrated in PBS, blocked in 50% goat serum and stained with antibodies directed against occludin (Invitrogen), and claudin 5 (Invitrogen), followed by appropriate Alexa-fluorophore-conjugated secondary antibodies and counterstained with BSL-fluorescein (Vector Labs). Slides were mounted in vectashield with DAPI (Vector Labs) and visualized by fluorescence microscopy.

For pericyte-deficient mice, *Pdgfrb*^{−/−} and littermate control embryos were flash-frozen and stained using the ethanol/acetone fixation described above with antibodies directed against occludin (Invitrogen), claudin 5 (Invitrogen) and Plvap (AbD Serotec). For Icam1, Ng2 and Glut1 staining, brains of dissected *Pdgfrb*^{−/−} and littermate control embryos were fixed overnight in 4% paraformaldehyde at 4 °C and stained as described previously, with antibodies directed against Icam1 (Abcam), Ng2 (Chemicon) or Glut1 (Chemicon). For Gr1 staining, 5-week-old *Pdgfrb*^{F7/F7} and littermate controls were perfusion fixed, and dissected brains were further fixed overnight in 4% paraformaldehyde at 4 °C and stained as described previously, with antibodies directed against Gr1 (gift from I. Weissmann). For comparisons of *Pdgfrb*^{−/−} and littermate control brains, sections were analysed on a Nikon Eclipse E800 microscope and images were taken with a Diagnostics Instrument SPOT camera with set exposure to appropriately compare staining between genotypes. Percent length of vasculature with intense Icam1 staining was measured using ImageJ ($n \geq 4$ each for mutant and littermate controls for each stain). For pericyte staining comparing *Pdgfrb*^{+/+}, *Pdgfrb*^{+/-} and *Pdgfrb*^{-/-} mice, tissue sections were stained with anti-Zic1 (Novus) and anti-desmin antibody (Dako) after antigen retrieval by steaming in a 10 mM citrate buffer for 30 min, or anti-NG2 (Chemicon). For quantification of pericyte number in *Pdgfrb*^{+/+} and *Pdgfrb*^{+/-} mice the number of Zic1⁺ nuclei was counted and divided by vascular length quantified in ImageJ ($n \geq 7$ for each genotype). Pericyte coverage was quantified using ImageJ to measure the length of BSL⁺ vessels associated with desmin⁺ pericyte processes ($n \geq 5$ for each genotype). Total Gr1⁺ cells outside BSL⁺ vessels per medial sagittal brain section were counted ($n = 4$ each for *Pdgfrb*^{F7/F7} and littermate controls). For desmin staining, neonatal *Pdgfrb*^{F7/N}, *Pdgfrb*^{F7/F7} and littermate controls were perfusion-fixed and stained with anti-desmin antibody (Dako) after antigen retrieval by steaming in a 10 mM citrate buffer for 30 min. Pericyte coverage was quantified using ImageJ to measure the length of BSL⁺ vessels associated with desmin⁺ pericyte processes ($n \geq 3$ for each genotype). All quantification was performed blind to genotype.

BBB permeability assays. Animals were anaesthetized with a ketamine (100 mg kg^{−1})/xylazine (20 mg kg^{−1}) cocktail, and then the thoracic cavity was opened to reveal the heart. The right ventricle was severed and then a DPBS (Gibco) solution containing 1 mg ml^{−1} EZ-link sulfo NHS-biotin (Pierce) was perfused into the left ventricle using a Dynamax peristaltic pump for 3 min, followed by 5 min of perfusion with 4% paraformaldehyde. The flow rate of the pump was adjusted to match the cardiac output of the rats or mice. Tissues, including the brain, liver and muscle, were dissected and further submersion fixed in 4% paraformaldehyde overnight at 4 °C, before being submerged in 30% sucrose. Ten micrometre cryosections were generated after the tissue was frozen in a 2:1 30% sucrose: OCT mixture. For E15 time points, the entire embryo was submersion-fixed and processed. Tissue sections were treated with a 50% goat serum blocking solution, before staining with streptavidin-Alexa 488 (Invitrogen). Staining of streptavidin was analysed with a Nikon Eclipse E800 microscope and images were taken with a Diagnostics Instrument SPOT camera and analysed by SPOT software. For comparisons of *Pdgfrb*^{−/−} and littermate control brains, pregnant mice were anaesthetized with

ketamine/xylazine, and embryos were extracted and chosen blind to genotype for perfusions. Six embryos were chosen from each litter, one as a control perfused without tracer. The perfusion setup was standardized to minimize fluctuations for pH (7.09 ± 0.005 s.d.) and pO₂ (136.1 mm Hg ± 2.0 s.d.) and the perfusion pressure was maintained digitally with the dynamax pump. The heart beat was monitored and all embryos maintained heart beat throughout tracer perfusions. Perfusions were performed with EZ-link sulfo NHS-biotin (0.5 mg ml^{−1}, Pierce), 3 kDa biotinylated fixable dextran (0.15 mg ml^{−1}, Invitrogen) or 70 kDa biotinylated fixable dextran (3.5 mg ml^{−1} Invitrogen), and micrographs were taken with set exposure to appropriately compare the amount of biotin in the brain tissue. The concentrations of the dextrans were matched for molar concentrations ($n \geq 6$ for each sample group for each tracer). Fluorescence in tissue sections was compared by ImageJ software, using tissue sections of embryos perfused with DPBS without tracer as a background control. *Pdgfrb*^{+/+} and *Pdgfrb*^{+/-} mice were combined as littermate controls, as we did not observe any difference in leakage between the two genotypes. For Evan's blue extravasation assays, P5 *Pdgfrb*^{F7/-}, *Pdgfrb*^{F7/F7} and littermate controls were given an intraperitoneal injection of 10 μ l 2% Evan's blue. After 1 day, animals were perfused as described above with PBS followed by paraformaldehyde. Dissected brains were photographed. For quantification of biotin leakage in neonatal *Pdgfrb*^{+/+} and *Pdgfrb*^{+/-} mice, and in neonatal *Pdgfrb*^{F7/-}, *Pdgfrb*^{F7/F7} and littermate controls, trans-cardiac perfusion of biotin tracer was performed, followed by staining of tissue sections with streptavidin, and quantification of leakage with ImageJ. In each case, perfusions and analysis was done blind to genotype.

Electron microscopy. Cerebral cortex from E18 *Pdgfrb*^{−/−} and littermate controls was fixed in 2% glutaraldehyde/4% paraformaldehyde in sodium cacodylate buffer overnight at 4 °C and processed for electron microscopy as described previously³¹ ($n = 3$ for both mutant and littermate controls). To visualize tracer permeability by electron microscopy, E18 *Pdgfrb*^{−/−} and littermate controls were perfused with biotin followed by paraformaldehyde as described above. Frozen tissue sections were fixed with 2% glutaraldehyde/4% paraformaldehyde in sodium cacodylate buffer overnight and stained with a HRP-tagged streptavidin (Invitrogen) followed by DAB reaction before being processed for electron microscopy.

Endothelial cell culture. Endothelial cells from adult C57BL/6 mice brains were purified and cultured as previously described²⁷ and grown with puromycin for the first 3 days. For mouse and rat brain pericytes, brain tissue suspensions were prepared as described previously²⁷, and cell suspensions were incubated on two dishes coated with an anti-CD45 antibody to deplete microglia cells, followed by a dish coated with anti-PDGFR-β to select pericytes. The pericytes were recovered by trypsin treatment and plated on PDL-coated cell culture filter inserts in a DMEM-based medium (Invitrogen) containing SATO, insulin, pyruvate, penicillin, streptomycin, glutamine and 10% fetal calf serum (Invitrogen). After 2.5 weeks, pericyte growth media was exchanged for endothelial growth media, and pericyte inserts were added to endothelial cells for 3 days. Endothelial cells were fixed with 4% paraformaldehyde for 10 min, then blocked/permeabilized for 30 min in 50% goat serum and 0.2% Triton X-100, and stained with primary antibodies directed against occludin (Invitrogen), claudin 5 (Invitrogen), Icam1 (Abcam) or Angpt2 (Abcam) and appropriate Alexa-fluorophore-conjugated secondary antibodies, mounted in vectashield with DAPI and images were taken with a Diagnostics Instrument SPOT camera analysed using a Nikon Eclipse E800 microscope. Percent vascular length with closed tight junctions was analysed using ImageJ software. Specifically, total length of cell junctions between two cells was measured, and then the length of these junctions where a single band of occludin or claudin 5 (sealed-staining between arrows in Fig. 3H, right panel) or two bands with diffuse staining between (unsealed-staining between arrows in Fig. 3G, right panel) was measured ($n \geq 3$ paired cultures of endothelial cells alone and endothelial cells with pericyte feeder layer for each marker). For TEER measurements, endothelial cells were isolated as described and grown on the filter membrane of Costar HTS transwell plates, and cultured in puromycin for 3 days, before being transferred to a new dish with media containing hydrocortisone, without puromycin. In the new dish, half the filter membranes were placed in wells with pericytes cultured on the bottom well. Resistance measurements were taken between 10–19 days after co-culture with an EVOM voltmeter (World Precision Instruments) and subtracted from resistance of membrane without cellular culture. Unit resistance was calculated by multiplying the resistance by the area of the filter membrane, and averaged for each sample ($n = 6$ paired cultures of endothelial cells alone and endothelial cells with pericyte feeder layer).

GeneChIP. Vascular cells from E18 *Pdgfrb*^{−/−} and littermate controls were purified based on methods described previously²⁷. Acutely purified pericytes were purified from mouse brain by anti-PDGFR-β immunopanning as described. Purification of RNA from acutely isolated cells, generation of biotinylated cRNA, subsequent hybridization to Affymetrix Mouse Genome 430 2.0 Arrays

and raw image analysis with Affymetrix GCOS 1.3 software was performed as previously described³².

Western blots. Cerebral cortex from E18 *Pdgfra*^{-/-} and littermate controls were homogenized and re-suspended and lysed in RIPA buffer (50 mM Tris pH 7.4, 150 mM NaCl, 1 mM EDTA, 1% Triton X-100, 0.1% SDS), and protein concentration was quantified using BCA protein assay (Pierce). Samples were analysed by SDS-PAGE as previously described³³. Briefly, samples were resolved on SDS-PAGE and transferred to PVDF membranes. Membranes were blocked with 5% milk solution and then incubated with antibodies directed against occludin (Invitrogen), claudin 5 (Invitrogen), Icam1 (Abcam), Alcam (R & D Systems), Lgals3 (R & D Systems), Col I (Abcam), Col III (Abcam), vitronectin (Abcam), MMP9 (Abcam), PDGFR- β (eBiosciences) or β -actin (Sigma) followed by incubation with an appropriate

secondary conjugated to HRP (Jackson 1:10,000) and visualized using a chemiluminescent ECL substrate for HRP (GE), and either exposed on film and quantified with ImageJ or imaged with a Fuji-Film LAS 4000 and analysed with Multi Gauge V3.0 software ($n = 2-5$ for mutant and $n = 4-8$ for littermate controls).

31. Watkins, T. A., Emery, B., Mulinyawe, S. & Barres, B. A. Distinct stages of myelination regulated by γ -secretase and astrocytes in a rapidly myelinating CNS coculture system. *Neuron* **60**, 555–569 (2008).
32. Cahoy, J. D. *et al.* A transcriptome database for astrocytes, neurons, and oligodendrocytes: a new resource for understanding brain development and function. *J. Neurosci.* **28**, 264–278 (2008).
33. Chan, J. R. *et al.* NGF controls axonal receptivity to myelination by Schwann cells or oligodendrocytes. *Neuron* **43**, 183–191 (2004).

Selective activation of p53-mediated tumour suppression in high-grade tumours

Melissa R. Junttila^{1†}, Anthony N. Karnezis¹, Daniel Garcia¹, Francesc Madriles², Roderik M. Kortlever¹, Fanya Rostker¹, Lamorna Brown Swigart¹, David M. Pham³, Youngho Seo³, Gerard I. Evan^{1†} & Carla P. Martins^{1†}

Non-small cell lung carcinoma (NSCLC) is the leading cause of cancer-related death worldwide, with an overall 5-year survival rate of only 10–15%¹. Deregulation of the Ras pathway is a frequent hallmark of NSCLC, often through mutations that directly activate Kras². p53 is also frequently inactivated in NSCLC and, because oncogenic Ras can be a potent trigger of p53 (ref. 3), it seems likely that oncogenic Ras signalling has a major and persistent role in driving the selection against p53. Hence, pharmacological restoration of p53 is an appealing therapeutic strategy for treating this disease⁴. Here we model the probable therapeutic impact of p53 restoration in a spontaneously evolving mouse model of NSCLC initiated by sporadic oncogenic activation of endogenous Kras⁵. Surprisingly, p53 restoration failed to induce significant regression of established tumours, although it did result in a significant decrease in the relative proportion of high-grade tumours. This is due to selective activation of p53 only in the more aggressive tumour cells within each tumour. Such selective activation of p53 correlates with marked upregulation in Ras signal intensity and induction of the oncogenic signalling sensor p19^{ARF} (ref. 6). Our data indicate that p53-mediated tumour suppression is triggered only when oncogenic Ras signal flux exceeds a critical threshold. Importantly, the failure of low-level oncogenic Kras to engage p53 reveals inherent limits in the capacity of p53 to restrain early tumour evolution and in the efficacy of therapeutic p53 restoration to eradicate cancers.

Inactivation of the p53 (also known as Trp53) tumour suppressor pathway is a common feature of human cancers, fostering the attractive notion of restoring p53 function in established tumours as an effective and tumour-specific therapeutic strategy⁴. Indeed, p53 restoration was recently shown to trigger dramatic tumour regression *in vivo*^{7–9}. Although encouraging, these studies used tumour models (either transgene^{7,9} or radiation-induced⁸) driven by preternaturally high levels of oncogenes. Because high-level oncogene activity potently engages p53 via the p19^{ARF} tumour suppressor^{6,7,10}, p53 restoration has a marked impact in these models. Unlike high oncogenic activity, however, low-level expression of dominant oncogenes seems insufficient to engage intrinsic tumour suppression, even though it still suffices to drive tumorigenesis^{11,12}. This raises the spectre that many epithelial malignancies, initiated as they are by low-level oncogenic signals such as those arising from mutational activation of *ras* genes *in situ*, may be insensitive to p53 restoration—at least during certain phases of their evolution. To investigate this possibility we assessed the ability of p53 restoration to trigger tumour regression in the well-characterized *Lox-Stop-Lox-Kras*^{G12D} (*KR*) murine tumour model of NSCLC⁵ wherein tumorigenesis is driven by sporadic, low-level activation of mutant Kras. This model closely recapitulates its human disease counterpart¹³.

After inhalation of adenovirus-Cre, *KR* mice develop multiple, independently evolving lung tumours, permitting contemporaneous analysis of different disease stages within each animal. *KR* mice were

crossed into the p53^{KI/KI} switchable mouse model in which both alleles of the endogenous p53 gene are replaced by the conditional variant p53^{ER^{TAM}} (ref. 14). p53^{KI/KI} mice can be reversibly toggled *in vivo* between p53 wild-type and p53 null states by administration or withdrawal of tamoxifen (Tam). Importantly, once functionally restored in Tam-treated p53^{KI/KI} mice, p53-mediated tumour suppression is triggered only if p53-activating signals are present^{7,10}.

Kras^{G12D} was sporadically activated in *KR*;p53^{KI/+} and *KR*;p53^{KI/KI} lungs and tumours were allowed to develop for 16 weeks. In both genotypes, Kras^{G12D} activation induced a spectrum of lung tumour grades including hyperplasias, adenomas and adenocarcinomas. Like *KR*;p53-deficient animals¹⁵ (Supplementary Fig. 1), *KR*;p53^{KI/KI} mice show accelerated tumour progression and increased incidence of high-grade tumours relative to their *KR*;p53^{KI/+} counterparts. These data affirm that p53 restrains Kras-driven NSCLC yet indicate that, even when combined, Kras^{G12D} activation and p53 inactivation are insufficient to generate malignant tumours without additional, aleatory mutations.

To ascertain its therapeutic impact, p53 function was restored for 1 week in *KR*;p53^{KI/KI} lung tumours (Fig. 1a). Surprisingly, given the marked tumour regression induced by p53 restoration in other models^{7–9}, p53 restoration had no macroscopically evident impact on these tumours (Fig. 1b). Close inspection, however, indicated that p53 restoration did elicit a modest decrease in proliferating tumour cells (Fig. 1c; 14% Ki67 positive cells per Tam-treated tumours versus 21% in controls) and an increase in apoptosis (Supplementary Fig. 2 and Fig. 1d; 45% of p53-restored tumours contain apoptotic cells versus 13.5% of control tumours). Nevertheless, the distribution of apoptotic cells in tumours following p53 restoration was irregular and clustered (Fig. 1e). This high variability in the response to sustained p53 restoration was confirmed by micro-computed tomography imaging of individual tumours over 7 days. Whereas all control tumours grew during treatment, individual Tam-treated tumours showed all possible responses—some grew, others were unchanged, and many shrank (Fig. 2a and Supplementary Fig. 3). Such variability in tumour response to Tam might reflect heterogeneities among tumour cells in the efficiency of p53 restoration, in the presence of p53-activating signals, or in the engagement of downstream effectors following p53 restoration. To determine which, we first ascertained the efficiency with which Tam restored p53 function in tumours. Mice were treated for 7 days with Tam or vehicle and then exposed to a single dose of γ -radiation 2 h after the last treatment to activate p53 directly. p53 activity was then monitored in individual tumours by assaying induction of the prototypical p53-responsive gene, *CDKN1A* (p21^{cip1})^{16,17}. All tumours showed substantial *CDKN1A* induction (Fig. 2b), indicating that systemic Tam pervasively restores p53 function in all tumours. Hence, the heterogeneity of the therapeutic response to Tam is not a consequence of either variability in Tam-dependent p53 restoration or in the capacity of p53, once

¹University of California San Francisco, Department of Pathology and Helen Diller Family Comprehensive Cancer Center, San Francisco, California 94143-0502, USA. ²Cancer Research UK Cambridge Research Institute, Li Ka Shing Centre, Robinson Way, Cambridge CB2 0RE, UK. ³University of California San Francisco, Department of Radiology and Biomedical Imaging and Helen Diller Family Comprehensive Cancer Center San Francisco, California 94143, USA. [†]Present addresses: Cancer Research UK Cambridge Research Institute, Li Ka Shing Centre, Robinson Way, Cambridge CB2 0RE, UK (C.P.M.); Department of Biochemistry, Tennis Court Road, University of Cambridge, Cambridge CB2 1GA, UK (G.I.E.); Department of Molecular Biology, Genentech, Inc. South San Francisco, CA 94080, USA (M.R.J.).

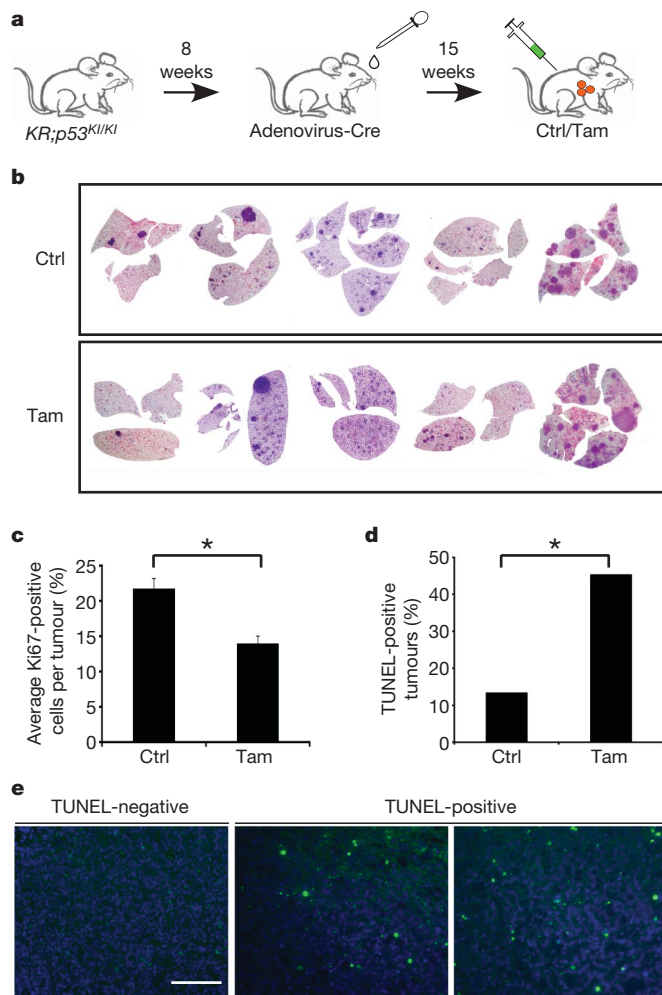


Figure 1 | Heterogeneous therapeutic impact of p53 restoration in *Kras*^{G12D}-driven lung tumours. **a**, Schematic representation of the experimental treatment regime. *Kras*^{G12D} was activated in the lung epithelium of 8-week-old *KR;p53*^{KI/KI} mice by adenoviral-Cre nasal inhalation and the resulting tumours treated with Tam or vehicle (Ctrl) 15 weeks after adenoviral infection. **b**, Haematoxylin and eosin staining of lung sections from *KR;p53*^{KI/KI} mice showing tumour load after 7-day control (Ctrl) or Tam treatments. **c**, Quantification of Ki67-positive cells per lung tumour from 7-day Tam/Ctrl-treated *KR;p53*^{KI/KI} mice. Error bars indicate standard error of mean (Ctrl: s.e.m = 1.20 *n* = 55; Tam: s.e.m = 1.31 *n* = 37). **P* = 0.0003, Student's *t*-test. **d**, Per cent of apoptotic (transferase dUTP nick-end labelling (TUNEL)-positive) tumours (scored as a minimum of one positive cell per tumour section) in 7-day Ctrl- and Tam-treated *KR;p53*^{KI/KI} lungs (*n* = 37 Ctrl; *n* = 22 Tam-treated tumours). **P* = 0.0064, Pearson Chi square. **e**, *KR;p53*^{KI/KI} lung tumours treated for 6 h with Tam, showing either no discernible TUNEL staining (negative) or significant levels of TUNEL staining (positive). Scale bar, 100 μm.

activated, to induce *CDKN1A*. By contrast, when p53 function was restored in the absence of concomitant DNA damage, *CDKN1A* was induced in only a minority of tumours (Fig. 2b). Hence, the variability in response to p53 restoration is because only a minority of tumours harbour endogenous p53-activating signals. Interestingly, whereas we see significant apoptosis in aggressive tumour cells following p53 restoration, other researchers do not, as described in the accompanying paper¹⁸, even though their mouse lung tumour model driven by spontaneous, sporadic *Kras* activation is ostensibly similar to ours. The reasons for this are unclear. However, the models differ in several ways. First, the mechanism of *Kras* activation is different, and may target distinct cell lineages with innately different sensitivities to p53-induced apoptosis. Second, they use *Cre-lox* recombination to restore p53 function, which is

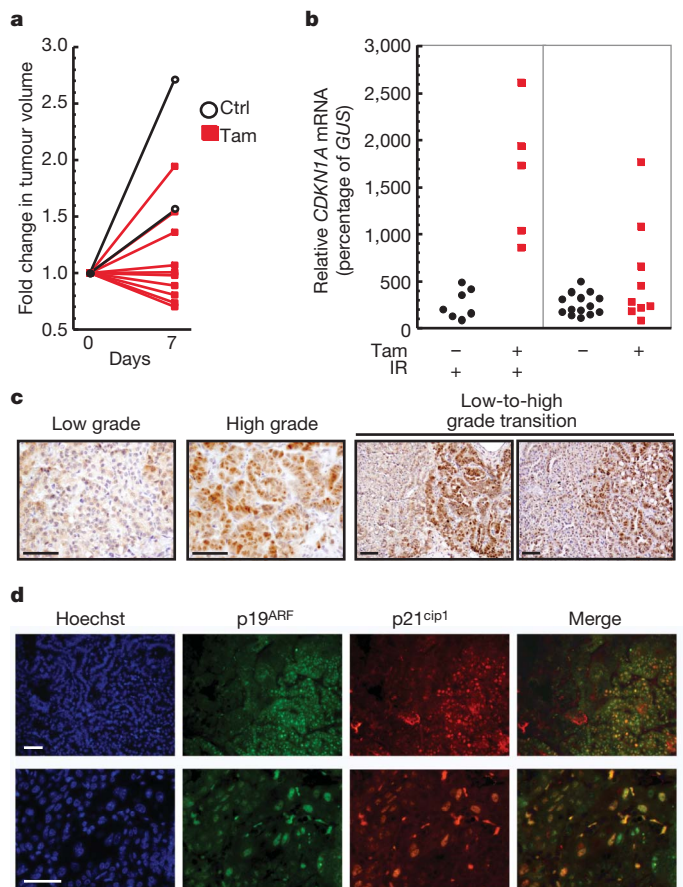


Figure 2 | Heterogeneous p53 activation and p19^{ARF} upregulation in *KR;p53*^{KI/KI} tumours. **a**, Micro-computer-tomography-derived plots depicting changes in tumour volume during a 7-day treatment. Ten independent tumours are shown before (day 0) and after (day 7) daily Tam (red lines, filled symbols) or sham (black lines, open symbols) treatments. **b**, TaqMan analysis of *CDKN1A* expression in individual laser microdissected lung tumours from *KR;p53*^{KI/KI} mice treated for 7 days with vehicle (black circles) or Tam (red squares). Tumours were collected 24 h after the final Ctrl/Tam treatment. Where indicated (IR +, left panel) mice were exposed to a single dose of γ -radiation 2 h after the last Tam/Ctrl treatment. Each circle/square represents a single tumour. **c**, IHC data comparing levels of p19^{ARF} expression in low- and high-grade tumours as well as in transitional lesions exhibiting both low- and high-grade features. Scale bars, 50 μm. **d**, Co-immunostaining for p19^{ARF} and p21^{cip1} in *KR;p53*^{KI/KI} lung tumours from mice treated for 6 h with Tam. Representative fields shown, one at low (upper panel) and one at high magnification (lower panel). Scale bar, 50 μm.

innately less synchronous than in our *p53ER*^{TAM} model and may make it difficult to see a transient wave of cell death. *Cre-lox* recombination may also introduce additional genotoxic stresses that further modify p53 output. In the end, however, whether apoptosis or arrest is the principal output of p53 restoration in aggressive tumour cells may not be so important because both p53-induced apoptosis⁷ and arrest⁹ are effective at eliciting tumour clearance.

Although p53 may be activated by a wide-range of stress signals, recent *in vivo* studies implicate induction of p19^{ARF} by oncogenic signalling as the critical p53-activating trigger in established tumours^{9,10}. Because oncogenic Ras can be a potent inducer of p19^{ARF} (ref. 19), we assayed for p19^{ARF} expression in *KR;p53*^{KI/KI} lung tumours. Immunohistochemical analysis (IHC) of *KR;p53*^{KI/KI} lungs revealed p19^{ARF} expression to be highly heterogeneous—generally limited to specific regions of certain tumours. Stratification of lung tumours into low- and high-grade, the latter comprising mostly adenocarcinomas (Supplementary Fig. 4)²⁰, revealed that p19^{ARF} was confined mostly to high-grade tumours. High p19^{ARF} cells were only rarely

observed in low-grade tumours and, when present, were restricted to small, sporadic foci. Close examination of transitional tumours comprising clearly defined high- and low-grade regions showed p19^{ARF} to be highly expressed only in high-grade/carcinoma areas (Fig. 2c).

Because p19^{ARF} is a potent activator of p53, we next ascertained whether the high-grade regions expressing elevated p19^{ARF} coincide with those that spontaneously activate p53 following restoration. p53 function was acutely restored in *KR;p53^{KI/KI}* mice and tumours analysed for expression of p19^{ARF} and p21^{cip1}. Upon p53 restoration, tumour areas positive for p19^{ARF} overlapped extensively with those positive for p21^{cip1} (Fig. 2d): ~70% of p19^{ARF}-positive cells from Tam-treated mice stained positive for p21^{cip1} compared with 2% of control. That p19^{ARF} has a causal role in engaging p53-mediated tumour suppression in high-grade tumours was corroborated by the rapid cessation of cell proliferation specific to p19^{ARF}-positive regions following

p53 restoration (Fig. 3a, Tam, two top rows). By contrast, proliferation remained high in p19^{ARF}-negative tumours after p53-restoration (Fig. 3a, Tam, two bottom rows). Of note, no γ -H2AX-staining DNA damage foci were detected in *KR;p53^{KI/KI}* lung tumours, although they were readily evident in tumours from γ -irradiated mice (Supplementary Fig. 5). This, together with the remarkable overlap between p53 activation and p19^{ARF} expression, strongly implicates p19^{ARF}, and not DNA damage, as the endogenous signal responsible for triggering p53 in high-grade lung tumours.

Although germ-line p53 deficiency significantly accelerates lung tumour progression and malignancy in *KR* mice¹⁵, our data indicate that p53 tumour suppression acts only at later stages of tumour evolution. Since p53 is specifically activated in the most atypical tumour cells, its restoration in a mixed tumour population should lead to a shift downwards in assigned tumour grade. Indeed, 7 days of p53 restoration

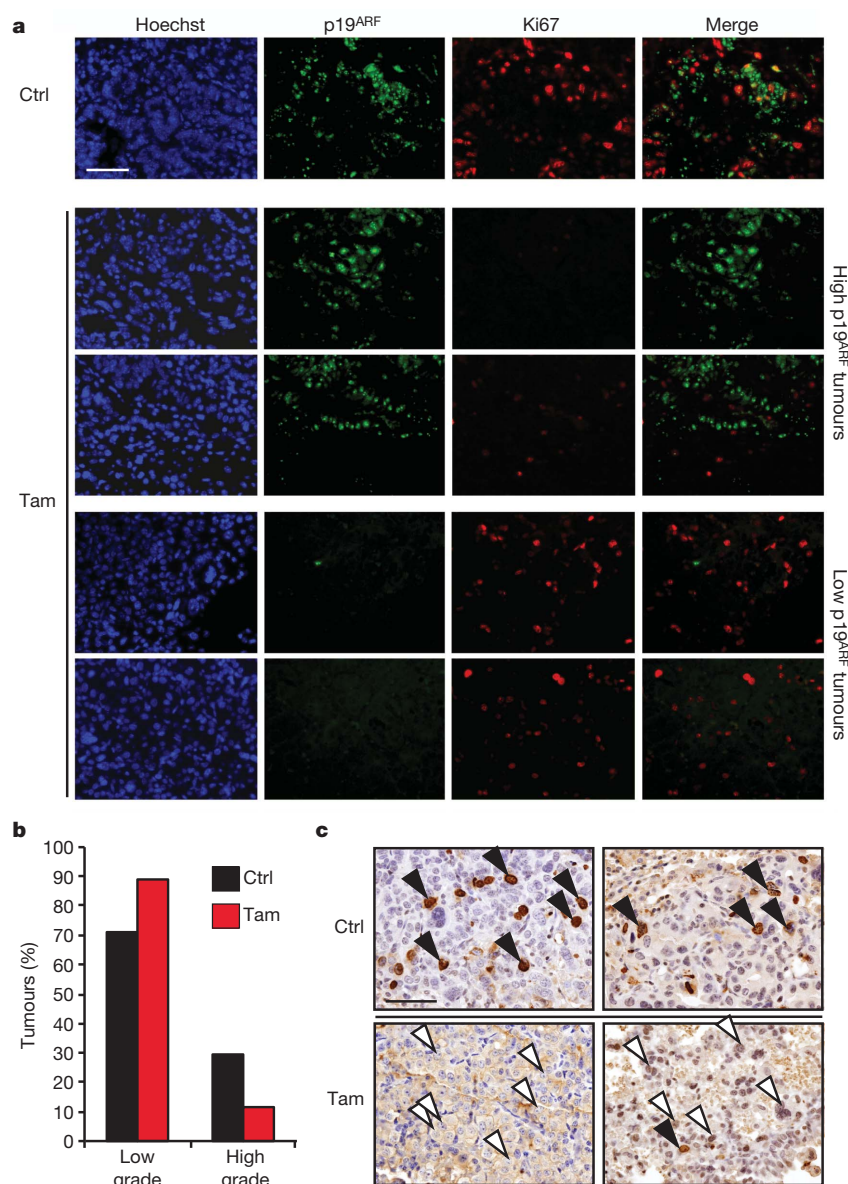


Figure 3 | p53 restoration targets high-grade, but not low-grade, lung tumour cells. **a**, Co-immunostaining for p19^{ARF} and the proliferation marker Ki67 in lung tumours from *KR;p53^{KI/KI}* mice treated for 24 h with vehicle (Ctrl, upper row) or Tam (four lower rows). Rows 2 and 3 illustrate the profound anti-proliferative impact (low Ki67) of p53 restoration in tumours with high p19^{ARF} levels. By contrast, the lower two rows show lack of growth inhibition following p53 restoration in tumours lacking detectable p19^{ARF}. Scale bar, 50 μ m.

b, Quantification of low- versus high-grade tumour frequencies in lungs of *KR;p53^{KI/KI}* mice treated for 7 days with either vehicle (Ctrl) or Tam ($n = 143$ Ctrl; $n = 163$ Tam). $P = 0.0001$, Pearson Chi square. **c**, Representative images show IHC for BrdU in high-grade tumours from 7-day treated Ctrl (upper panel) or Tam mice (lower panel). BrdU was administered 2 h before collection. Arrows highlight high-grade cells in each tumour (filled, BrdU-positive and open, BrdU-negative). Scale bars, 50 μ m.

in $KR;p53^{KI/KI}$ mice harbouring a mixture of low- and high-grade tumours elicited a downward shift in the frequency of high-grade tumours (from 29% to 11%) and a *pro rata* increase in the proportion of low-grade tumours (from 71% to 89%) (Fig. 3b and Supplementary Fig. 6). The percentage of bromodeoxyuridine (BrdU)-positive high-grade cells was also markedly reduced following treatment (Fig. 3c).

Our data show that the $p19^{ARF}/p53$ pathway is only engaged in high-grade $KR;p53^{KI/KI}$ cells, even though all tumour cells harbour oncogenic $Kras^{G12D}$. Hence, oncogenic activity of $Kras$ is not alone sufficient to induce $p19^{ARF}$ and engage p53-mediated tumour suppression. Interestingly, recent *in vivo* studies indicate that intrinsic tumour suppression is only engaged when oncogenic signals are prenatally elevated^{11,12}. Such observations echo *in vitro* data showing that expression of oncogenic $Kras^{G12D}$ from its endogenous promoter induces proliferation and immortalization, whereas $Kras^{G12D}$ overexpression engages p53-dependent replicative senescence^{21,22}. Because marked upregulation of the MAPK-pathway is a characteristic feature of advanced lung tumours in both mice¹⁵ and NSCLC in humans²³, we asked whether induction of $p19^{ARF}$ in high-grade tumours is a consequence of elevated flux through the Ras signalling network. Indeed, immunostaining showed a remarkably tight spatial concordance of tumour cells exhibiting elevated ERK phosphorylation (p-ERK), a signature of downstream Ras signalling, and those with high $p19^{ARF}$ (Fig. 4a and Supplementary Fig. 7); the cell-by-cell overlap between

upregulation of $p19^{ARF}$ and p-ERK was 91.2% ($n = 1312$; s.d. = 3.77). Hence, increased flux through oncogenic $Kras^{G12D}$ is the probable mechanism for both malignant progression and concomitant activation of (and eventual counter-selection against) the $p19^{ARF}/p53$ tumour suppressor pathway.

Many potential mechanisms might underlie the dramatic upregulation of p-ERK we observe in high-grade lung tumours, including changes in $Kras$ copy number (known to occur in human NSCLC), inactivation of $Kras$ negative feedback mechanisms and incidental activation of cooperating oncogenes^{24–27}. Initial analysis of whole low- versus high-grade tumours indicated downregulation of Sprouty 2 (also known as *Spry2*) or loss of the wild-type $Kras$ allele as possible mechanisms for $Kras$ signal upregulation in high p-ERK tumours (Supplementary Fig. 8). Because elevated Ras signalling is a property peculiar to high-grade tumour regions, we used p-ERK staining to demarcate high, low and mixed p-ERK areas of individual tumours (Fig. 4b, upper panel). These tumour regions were individually laser microdissected and their genomic DNA extracted and assessed for the relative copy representation of wild-type versus mutant $Kras$ alleles. We saw variable levels of wild-type $Kras$ retention in the low/mixed p-ERK tumour tissues, ranging from 100% in the low p-ERK tumour 14 to partial or total loss in the mixed grade tumours (for example, 21 and 18). Remarkably, the wild-type $Kras$ allele was lost in all high p-ERK tumours (Fig. 4b, lower panel) and the mutant $Kras$ allele often duplicated (Supplementary Fig. 9). Overall, across all tumour samples $Kras$ allelic imbalance, a known mechanism by which Ras signal strength is elevated²⁷, correlated tightly with high p-ERK.

Long-lived organisms must solve the problem of suppressing cancer without compromising the facility of normal cells to proliferate. This requires an accurate means of distinguishing between normal and oncogenic signals. However, emerging evidence hints at a ‘flaw’ in how our tumour suppressor pathways have evolved—rather than responding to the aberrant signal persistence that is actually responsible for oncogenesis, mammalian intrinsic tumour suppressor pathways have instead evolved to respond to the unusual elevation in signal intensity that often (but not invariably) accompanies oncogenic activation¹¹. Paradoxically, therefore, low-level oncogenic activities may be more efficient at initiating tumorigenesis than high-level oncogenic signals because they ‘fall beneath the radar’ of tumour surveillance²⁸; high-level oncogenic signals, which seem necessary to drive progression to malignancy, are tolerable only once p53 function has been quelled.

At first glance, our data showing limited therapeutic impact of restoring p53 in established lung tumours seem at odds with previous studies^{7–9}. However, such studies used advanced, relatively homogeneous tumours driven by high levels of oncogenic signalling that had already engaged the ARF pathway—hence the dramatic impact of re-instating p53. By contrast, the spontaneously evolving lung tumours that afflict KR mice are initiated by sporadic oncogenic activation of endogenous $Kras$ at a level insufficient to engage p53. Our data indicate that it is only relatively late in their evolution, at the point when sporadic elevation of Ras signalling precipitates tumours into aggressive, high-grade lesions, that the p53 pathway is triggered. Such considerations offer a compelling rationale for the long-baffling observation that selection for p53 pathway inactivation arises relatively late in the evolution of many solid human tumours.

The inability of low-level oncogenic signalling to engage p53 also casts a cautionary shadow over the potential efficacy of p53 restoration in treating cancer. Established tumours are typically comprised of heterogeneous clades of neoplastic clones that encompass all phases of oncogenic evolution. Although p53 restoration might cull the most malignant cells, less aggressive tumour cells driven by low-level oncogenic signals would presumably survive to evolve another day. At best, then, p53 restoration as a single therapy would be a means of temporary tumour containment rather than eradication.

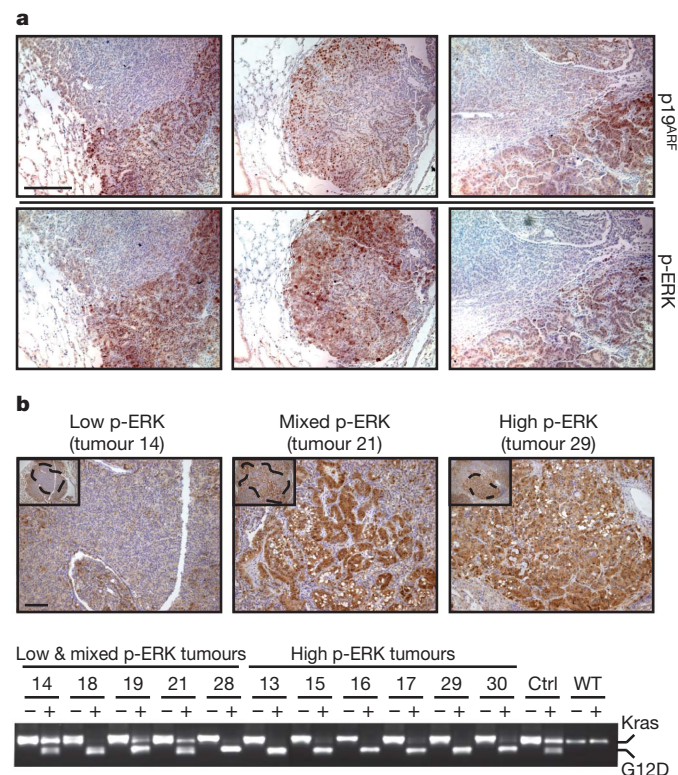


Figure 4 | High-grade lung tumours exhibit increased $Kras$ signalling.

a, IHC for $p19^{ARF}$ and p-ERK in consecutive sections of three independent low-to-high-grade transition tumours from $KR;p53^{KI/KI}$ mice. Scale bar, 200 μ m. **b**, $Kras$ allele analysis was performed on genomic DNA from $KR;p53^{KI/KI}$ lung tumours following laser microdissection. p-ERK IHC was used to define areas of low, mixed or high p-ERK (upper panel, scale bar, 50 μ m) and consecutive slides used for LCM of defined regions (see dotted areas). DNA was isolated from LCM material and the $Kras$ genomic region amplified by PCR and digested with HindIII (lower panel). For each tumour, the undigested (–) and digested (+) PCR fragments were run alongside and the wild-type ($Kras$, higher band) and mutant alleles (G12D, lower band) are indicated. Control lung tissue from heterozygous ($Kras^{G12D/+}$; Ctrl) and wild-type (WT) mice was also analysed.

METHODS SUMMARY

Tumour induction and treatment. Animals were maintained under UCSF IACUC-approved protocols. *KR*⁵ and *p53*^{K7} mice¹⁴ progeny were infected with adenovirus-CRE (5×10^7 plaque-forming units (p.f.u.) per mouse) by nasal inhalation at 8 weeks of age⁵. *p53* function was restored by intraperitoneal injection of tamoxifen (1 mg per mouse daily)^{7,10,14}. Where appropriate, mice were irradiated (4 Gy) 2 h after Ctrl/Tam treatment using a Mark 1-68 ¹³⁷Cs source (0.637 Gy min⁻¹). A minimum of five mice per cohort was used for each experiment.

Immunohistochemistry and immunofluorescence. Primary antibodies used were p19^{ARF} (gift from C. J. Sherr and M. F. Roussel²⁹); p21 (BD Pharmingen #556430); Ki67 (SP6 Neomarkers); P-ERK (Cell Signaling Technologies #4376) and phospho-histone H2AX (Upstate #05-636). They were detected with horseradish peroxidase-/Alexa-conjugated secondary antibodies. An ApopTag kit (Millipore) was used for terminal deoxynucleotidyl transferase dUTP nick-end labelling (TUNEL).

Laser capture microdissection, expression and copy number analysis. For *CDKN1A* TaqMan analysis⁷, laser capture microdissection of frozen samples³⁰ was followed by RNA preparation (Arcturus PicoPure RNA Isolation kit, Arcturus Engineering) and cDNA production (iScript cDNA Synthesis kit, Bio-Rad). For copy number analysis, laser microdissection (Zeiss P.A.L.M.) collection of paraffin samples was followed by DNA isolation (QIAamp DNA Micro kit #56304) and TaqMan (probes: β -actin: Mm00607939_s1; *Kras*: Mm03053281_s1, Applied Biosystems) or PCR (primers: *Kras*Hind3_F 5'-GCCATTAGCTGCTACAAAACAGTA-3' and *Kras*Hind3_R 5'-CCTCTATCGTAGGGTCGTACTCAT-3'). Following PCR the *Kras*^{G12D} and *Kras*^{wt} alleles were distinguished by the presence of a *Kras*^{G12D}-specific HindIII site in the amplified fragment (wild-type = 400 base pairs; *Kras*^{G12D} = 300 + 100 bp).

Micro-computed X-ray tomography. Pre- (day 0) and post-therapy (day 7) micro-computed tomography data was acquired using a FLEX X-O system (Gamma Medica-Ideas). Only clearly discrete tumours were measured.

Immunoblot analysis. Whole-cell lysates from dissected tumour halves were immunoblotted with anti-Spry2 (Abcam ab50317), anti-Dusp6 (Santa Cruz sc-28902) or anti- β -actin (Sigma A5441) antibodies.

Full Methods and any associated references are available in the online version of the paper at www.nature.com/nature.

Received 22 December; accepted 21 September 2010.

- Jemal, A. *et al.* Cancer statistics, 2006. *CA Cancer J. Clin.* **56**, 106–130 (2006).
- Meuwissen, R. & Berns, A. Mouse models for human lung cancer. *Genes Dev.* **19**, 643–664 (2005).
- Serrano, M., Lin, A., McCurrach, M., Beach, D. & Lowe, S. Oncogenic *ras* provokes premature cell senescence associated with accumulation of *p53* and *p16*^{INK4a}. *Cell* **88**, 593–602 (1997).
- Wang, W. & El-Deiry, W. S. Restoration of *p53* to limit tumor growth. *Curr. Opin. Oncol.* **20**, 90–96 (2008).
- Jackson, E. L. *et al.* Analysis of lung tumor initiation and progression using conditional expression of oncogenic *K-ras*. *Genes Dev.* **15**, 3243–3248 (2001).
- Kamijo, T. *et al.* Tumor suppression at the mouse *INK4a* locus mediated by the alternative reading frame product *p19*^{ARF}. *Cell* **91**, 649–659 (1997).
- Martins, C. P., Brown-Swigart, L. & Evan, G. I. Modeling the therapeutic efficacy of *p53* restoration in tumors. *Cell* **127**, 1323–1334 (2006).
- Ventura, A. *et al.* Restoration of *p53* function leads to tumour regression *in vivo*. *Nature* **445**, 661–665 (2007).
- Xue, W. *et al.* Senescence and tumour clearance is triggered by *p53* restoration in murine liver carcinomas. *Nature* **445**, 656–660 (2007).
- Christophorou, M. A., Ringshausen, I., Finch, A. J., Swigart, L. B. & Evan, G. I. The pathological response to DNA damage does not contribute to *p53*-mediated tumour suppression. *Nature* **443**, 214–217 (2006).
- Murphy, D. J. *et al.* Distinct thresholds govern Myc's biological output *in vivo*. *Cancer Cell* **14**, 447–457 (2008).

- Sarkisian, C. J. *et al.* Dose-dependent oncogene-induced senescence *in vivo* and its evasion during mammary tumorigenesis. *Nature Cell Biol.* **9**, 493–505 (2007).
- Sweet-Cordero, A. *et al.* An oncogenic *KRAS2* expression signature identified by cross-species gene-expression analysis. *Nature Genet.* **37**, 48–55 (2005).
- Christophorou, M. A. *et al.* Temporal dissection of *p53* function *in vitro* and *in vivo*. *Nature Genet.* **37**, 718–726 (2005).
- Jackson, E. L. *et al.* The differential effects of mutant *p53* alleles on advanced murine lung cancer. *Cancer Res.* **65**, 10280–10288 (2005).
- Dulić, V. *et al.* *p53*-dependent inhibition of cyclin-dependent kinase activities in human fibroblasts during radiation-induced G1 arrest. *Cell* **76**, 1013–1023 (1994).
- El Deiry, W. S. *et al.* *WAF1/CIP1* is induced in *p53*-mediated G1 arrest and apoptosis. *Cancer Res.* **54**, 1169–1174 (1994).
- Feldser, D. *et al.* Stage-specific sensitivity to *p53* restoration in lung cancer. *Nature* doi:10.1038/nature09535 (in the press).
- Palmero, I., Pantoja, C. & Serrano, M. *p19*^{ARF} links the tumour suppressor *p53* to Ras. *Nature* **395**, 125–126 (1998).
- Nikitin, A. Y. *et al.* Classification of proliferative pulmonary lesions of the mouse: recommendations of the mouse models of human cancers consortium. *Cancer Res.* **64**, 2307–2316 (2004).
- Guerra, C. *et al.* Tumor induction by an endogenous *K-ras* oncogene is highly dependent on cellular context. *Cancer Cell* **4**, 111–120 (2003).
- Tuveson, D. A. *et al.* Endogenous oncogenic *K-ras*(G12D) stimulates proliferation and widespread neoplastic and developmental defects. *Cancer Cell* **5**, 375–387 (2004).
- Vicent, S. *et al.* ERK1/2 is activated in non-small-cell lung cancer and associated with advanced tumours. *Br. J. Cancer* **90**, 1047–1052 (2004).
- Shaw, A. T. *et al.* Sprouty-2 regulates oncogenic *K-ras* in lung development and tumorigenesis. *Genes Dev.* **21**, 694–707 (2007).
- Wagner, P. L. *et al.* *In situ* evidence of *KRAS* amplification and association with increased *p21* levels in non-small cell lung carcinoma. *Am. J. Clin. Pathol.* **132**, 500–505 (2009).
- Zhang, Z. *et al.* Dual specificity phosphatase 6 (DUSP6) is an ETS-regulated negative feedback mediator of oncogenic ERK signaling in lung cancer cells. *Carcinogenesis* **31**, 577–586 (2010).
- Zhang, Z. *et al.* Wildtype *Kras2* can inhibit lung carcinogenesis in mice. *Nature Genet.* **29**, 25–33 (2001).
- Junttila, M. R. & Evan, G. I. *p53* – a Jack of all trades but master of none. *Nature Rev. Cancer* **9**, 821–829 (2009).
- Bertwistle, D., Zindy, F., Sherr, C. J. & Roussel, M. F. Monoclonal antibodies to the mouse *p19*^{ARF} tumor suppressor protein. *Hybrid. Hybridomics* **23**, 293–300 (2004).
- Lawlor, E. R. *et al.* Reversible kinetic analysis of Myc targets *in vivo* provides novel insights into Myc-mediated tumorigenesis. *Cancer Res.* **66**, 4591–4601 (2006).

Supplementary Information is linked to the online version of the paper at www.nature.com/nature.

Acknowledgements We are indebted to T. Jacks for the *KR* mice, C. Sherr and M. Roussel for the *p19*^{ARF} antibody, M. Dail and A.-T. Maia for advice on *Kras* copy number analysis and V. Weinberg for guidance on statistical analysis. We also thank D. Tuveson and all the members of the Evan laboratory for their comments. This work was supported by grants NCI CA98018, NCI CA100193, AICR 09-0649, the Ellison Medical Foundation and from the Samuel R. Waxman Cancer Research Foundation (all to G.I.E.). M.R.J. is the Enrique Cepero, PhD Fellow of the Damon Runyon Cancer Research Foundation.

Author Contributions C.P.M. and G.I.E. designed this study with help from M.R.J. C.P.M. and M.R.J. performed all experiments with assistance from D.G. and F.M. C.P.M., M.R.J. and G.I.E. analysed and interpreted the data. A.N.K. graded all tumours. L.B.S., F.R. and R.M.K. helped maintain the mouse colony. D.M.P. and Y.S. performed the micro-computed tomography analysis. C.P.M. and G.I.E. wrote the paper with help from M.R.J. and all authors contributed to editing.

Author Information Reprints and permissions information is available at www.nature.com/reprints. The authors declare no competing financial interests. Readers are welcome to comment on the online version of this article at www.nature.com/nature. Correspondence and requests for materials should be addressed to G.I.E. (gie20@cam.ac.uk).

METHODS

Mice, adenoviral infection and treatments. Animals were maintained in SPF conditions under UCSF IACUC-approved protocols. *KP*⁵ and *p53*^{KI} mice¹⁴ were crossed and *KP* and *KP;p53*^{KI/KI} animals were infected by nasal inhalation with adenovirus-CRE (5×10^7 plaque-forming units per mouse) at 8 weeks of age, as described⁵. *p53* function was restored by treating mice with tamoxifen (1 mg per mouse daily) delivered by intraperitoneal injection, as described^{7,10,14}. Where appropriate, mice were irradiated (4 Gy) 2 h after Ctrl/Tam treatment using a Mark 1-68 ¹³⁷Cs source (0.637 Gy min⁻¹). A minimum of five mice per cohort were used for each experiment.

Immunohistochemistry and immunofluorescence. IHC stainings were performed on z-fix fixed, 5-μm paraffin-embedded tissue sections. Sections were incubated overnight at 4 °C with the following primary antibodies: p19^{ARF} (gift from C. J. Sherr and M. F. Roussel²⁹); p21 (BD Pharmingen #556430); Ki67 (SP6, Neomarkers); P-ERK (Cell Signaling Technologies #4376), phospho-histone H2AX (Upstate #05-636). Antibodies were detected using Vectastain ABC detection (Vector Laboratories) or with specific biotinylated secondary antibodies (anti-rat biotinylated, Vector Laboratories BA-4001 and anti-rabbit biotinylated, Dako #E0432) followed with stable diaminobenzidine treatment (Invitrogen). Alternatively, Alexa-conjugated mouse, rat or rabbit IgG antibodies were used (Molecular Probes). TUNEL staining was performed using the ApopTag fluorescein labelled kit (Millipore) according to the manufacturer's directions.

Laser capture microdissection, expression and copy number analysis. For RNA analysis 30-μm sections from fresh frozen lung tissue were fixed, stained and laser microdissected, as described previously³⁰. Total RNA was isolated and DNase I

treated using the Arcturus PicoPure RNA Isolation kit (Arcturus Engineering). cDNA was produced using iScript cDNA Synthesis kit (Bio-Rad). Real-time quantitative PCR (qPCR) was performed as described previously⁷. For copy number analysis 5-μm sections were briefly de-paraffinized and laser microdissected using a Zeiss P.A.L.M. LCM microscope. Genomic DNA was isolated using the QIAamp DNA Micro Kit #56304 and analysed by TaqMan or PCR. Copy number TaqMan analysis was carried out using the following probes from Applied Biosystems: β-actin: Mm00607939_s1; Kras: Mm03053281_s1. PCR was performed using the following Kras-specific primers: KrasHind3_F 5'-GCCA TTAGCTGCTACAAAACAGTA-3' and KrasHind3_R 5'-CCTCTATCGTA GGGTCGTA CTACTCAT-3'. Due to the presence of a unique HindIII restriction site in the *Kras*^{G12D} allele, the mutant and wild-type alleles can be distinguished based on their HindIII restriction-digestion profile (wild type = 400 bp and *Kras*^{G12D} = 300 + 100 bp).

Micro-computed X-ray tomography. Computed tomography (CT) was performed using a micro CT system (FLEX X-O, Gamma Medica-Ideas) with an X-ray source with 75 kVp (kilovolts peak) and 0.315 mA. CT data were acquired as 512 projections over 120 s of continuous X-ray exposure. Pre-therapy CT data were acquired as the baseline time point and post-therapy CT performed after 7 days of sustained Tamoxifen administration. Only clearly discrete tumours were picked for volume measurements. Volumes of interest were drawn on axial slices, and the total tumour volumes were calculated planimetrically.

Immunoblot analysis. Whole-cell lysates from dissected tumour halves were prepared and immunoblotted with anti-Spry 2 (Abcam ab50317), Dusp6 (Santa Cruz sc-28902) or β-actin (Sigma A5441) antibodies.

Stage-specific sensitivity to p53 restoration during lung cancer progression

David M. Feldser¹, Kamena K. Kostova¹, Monte M. Winslow¹, Sarah E. Taylor¹, Chris Cashman¹, Charles A. Whittaker¹, Francisco J. Sanchez-Rivera¹, Rebecca Resnick¹, Roderick Bronson², Michael T. Hemann¹ & Tyler Jacks¹

Tumorigenesis is a multistep process that results from the sequential accumulation of mutations in key oncogene and tumour suppressor pathways. Personalized cancer therapy that is based on targeting these underlying genetic abnormalities presupposes that sustained inactivation of tumour suppressors and activation of oncogenes is essential in advanced cancers. Mutations in the p53 tumour-suppressor pathway are common in human cancer and significant efforts towards pharmaceutical reactivation of defective p53 pathways are underway^{1–3}. Here we show that restoration of p53 in established murine lung tumours leads to significant but incomplete tumour cell loss specifically in malignant adenocarcinomas, but not in adenomas. We define amplification of MAPK signalling as a critical determinant of malignant progression and also a stimulator of Arf tumour-suppressor expression. The response to p53 restoration in this context is critically dependent on the expression of Arf. We propose that p53 not only limits malignant progression by suppressing the acquisition of alterations that lead to tumour progression, but also, in the context of p53 restoration, responds to increased oncogenic signalling to mediate tumour regression. Our observations also underscore that the p53 pathway is not engaged by low levels of oncogene activity that are sufficient for early stages of lung tumour development. These data suggest that restoration of pathways important in tumour progression, as opposed to initiation, may lead to incomplete tumour regression due to the stage-heterogeneity of tumour cell populations.

Experimental restoration of p53 (also known as *Trp53*) tumour-suppressor function has highlighted the potential for therapeutic intervention of this pathway to treat cancer and has uncovered a diversity of anti-tumour responses in different tumour types^{4–6}. These studies imply that some types of cancer rely upon sustained inactivation of the p53 pathway as these tumours undergo rapid, and sometimes complete, regression once p53 is restored. To elucidate the role of p53 in lung cancer progression and to evaluate the therapeutic potential of p53 reactivation in this disease, we analysed the effect of *Trp53* restoration in a mouse model of *Kras*^{G12D}-driven lung cancer at different time points in tumour progression. *Trp53* restoration was achieved by delivering tamoxifen to 4-week-old *Kras*^{LA2/+}; *Trp53*^{LSL/LSL}; *Rosa26*^{CreERT2} mice (Supplementary Fig. 1). We measured tumour volumes with micro-computed tomography and tumour areas by histological analysis. Surprisingly, at this time point, *Trp53* restoration did not significantly change tumour size or number (Fig. 1a, b). Efficient deletion of the 'STOP' element from *Trp53*^{LSL} alleles was evident in all tumours analysed (Supplementary Fig. 2).

To establish the timing and stage of tumour progression when the effects of p53 mutation are evident, we compared *Kras*^{LA2/+}; *Trp53*^{LSL/LSL} tumours to tumours from age-matched *Kras*^{LA2/+}; *Trp53*^{+/+} mice. At four weeks, most tumours were adenomatous hyperplasias or alveolar adenomas with monomorphous epithelial cells and uniform nuclei (Supplementary Fig. 3). In *Kras*^{LA2/+}; *Trp53*^{LSL/LSL} mice at this age, a small fraction of tumours had mixed histological features with focal areas of

adenocarcinoma within lower grade lesions (Fig. 1c). Although most tumours in *Kras*^{LA2/+}; *Trp53*^{+/+} and *Kras*^{LA2/+}; *Trp53*^{LSL/LSL} mice were of similar grade, the presence of pleomorphic nuclei was a prominent feature of *Kras*^{LA2/+}; *Trp53*^{LSL/LSL} tumours compared to *Kras*^{LA2/+}; *Trp53*^{+/+} tumours (Fig. 1d). This observation may indicate

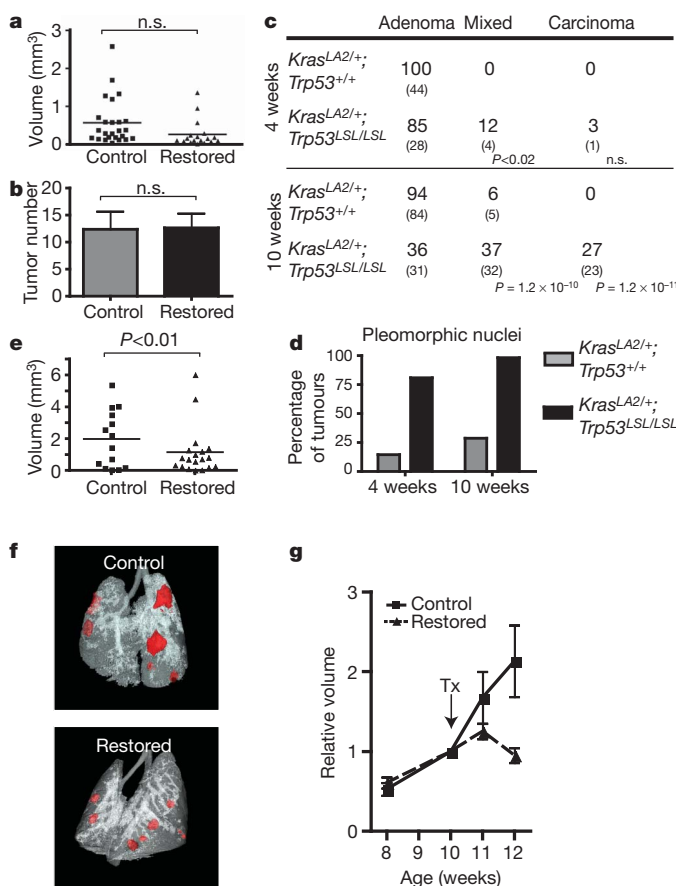


Figure 1 | Lung adenomas are apathetic to *Trp53* restoration, whereas adenocarcinomas are responsive. **a**, Individual tumour volumes were determined by micro-computed tomography 2 weeks after *Trp53*-restoration that began at 4 weeks of age. **b**, Histological sections were evaluated for tumour number in control ($n = 10$) and restored ($n = 12$) mice. **c**, Tumour number and grade at 4 and 10 weeks of age. Individual tumours from *Kras*^{LA2/+}; *Trp53*^{LSL/LSL} ($n = 5$) and *Kras*^{LA2/+}; *Trp53*^{+/+} ($n = 4$) mice. The percentage and number (in parentheses) of tumours is indicated. **d**, Pleomorphic nuclei in tumour samples from **c** (see also Supplementary Fig. 5). **e**, Restoration of *Trp53* in 10-week-old animals results in significantly diminished tumour size. Tumour volumes determined by micro-computed tomography 2 weeks after p53 restoration. **f**, Representative tomograms from micro-computed tomography analysis at 12 weeks. **g**, Serial micro-computed tomography analysis of individual tumours. Average relative size of tumours is plotted, error bars represent s.e.m. n.s., not significant; Tx, treatment.

¹Koch Institute for Integrative Cancer Research, Department of Biology, and Howard Hughes Medical Institute, Massachusetts Institute of Technology, 77 Massachusetts Avenue, Cambridge, Massachusetts 02139, USA. ²Tufts University, and Harvard Medical School, 77 Avenue Louis Pasteur, Boston, Massachusetts 02115, USA.

that $Kras^{LA2/+};Trp53^{LSL/LSL}$ tumour cells have a higher degree of genetic instability that may facilitate tumour progression at a later time point.

At 10 weeks of age, $Kras^{LA2/+};Trp53^{LSL/LSL}$ tumours were much more likely to exhibit nuclear pleomorphism and regions of advanced histopathology. Beyond these mixed grade tumours, frank adenocarcinomas were present exclusively in $Kras^{LA2/+};Trp53^{LSL/LSL}$ mice (Fig. 1c). Given that high-grade tumours were more prevalent in older mice, we restored $Trp53$ in 10-week-old $Kras^{LA2/+};Trp53^{LSL/LSL};Rosa26^{CreERT2}$ mice. Here, restoration of $Trp53$ resulted in significantly smaller tumours compared to controls after 2 weeks (Fig. 1e, f). To monitor the response of individual tumours, we performed serial micro-computed tomography before and after $Trp53$ restoration. Although control tumours continued to grow during the 2-week time course, we found that the average size of tumours after $Trp53$ restoration was static (Fig. 1g). However, the response of individual tumours was variable (Supplementary Fig. 4). Thus, we proposed that only a subset of tumours is sensitive to $Trp53$ restoration.

Upon $Trp53$ restoration, adenocarcinomas, but not adenomas, displayed multiple features of cellular senescence. Both p53 and the p53 target gene *Cdkn1a* (also known as p21) were detectable in tumours as early as 3 days after restoration, but were specifically confined to tumours with adenocarcinomatous features (Fig. 2b and Supplementary Fig. 5). In addition to observing p21 induction in the adenocarcinomas of 10-week-old mice (Fig. 2c), p21 was also induced in the few carcinomas found in the 4-week-old animals (data not shown). Moreover, $Trp53$ restoration caused reduced cellular proliferation (Fig. 2d). Of note, the percentage of tumours with adenocarcinomatous features was significantly diminished 2 weeks after $Trp53$ restoration with many tumours showing gaps between collections of low-grade tumour cells filled with foam macrophages (Fig. 2a, e). Despite this evidence of cell loss, we failed to find signs of apoptosis in lung tumours across an extensive time course after $Trp53$ restoration (Supplementary Fig. 6). Collectively, these data demonstrate that adenomas do not respond to p53 restoration, whereas adenocarcinomas are sensitive. Moreover, $Trp53$ mutation *per se* does not induce phenotypic changes in tumour grade but rather creates a permissive environment for the outgrowth of cells that have undergone additional steps in tumour progression. Finally, the alterations that drive tumour progression can also stimulate p53-dependent cellular responses.

To interrogate the mechanisms that drive tumour progression, we performed immunohistochemistry on tumours from $Kras^{LA2/+};Trp53^{+/+}$ and $Kras^{LA2/+};Trp53^{LSL/LSL}$ animals to assess the activity of multiple relevant pathways during the adenoma-adenocarcinoma transition. We found that phosphorylation levels of Mek1/2 (p-Mek, also known as Map2k1/2) and p42/p44 MAPK (p-Erk, also known as Mapk1) was markedly higher in adenocarcinomas compared to adenomas (Fig. 3a, b). This observation indicated that amplified MAPK signalling could drive progression of $Kras^{G12D}$ -initiated lung cancer. High levels of MAPK signalling downstream of oncogenic *Kras* induces cell cycle arrest/senescence mediated by Arf (a product of the *Cdkn2a* locus) and p53 in multiple cell types *in vitro*⁷⁻⁹. In contrast, physiological levels of oncogenic signalling elicited by a single oncogenic *Kras* allele do not activate the Arf/p53 tumour suppressor pathway and instead can drive proliferation and tumorigenesis in many cell types¹⁰⁻¹⁴. Some cancer models show that mutation of *Ras* family members can initiate tumorigenesis, while amplification of oncogenic *Ras* or loss of the wild-type *Ras* allele is associated with tumour progression¹⁵⁻¹⁷. Thus, we proposed that amplification of oncogenic signalling could simultaneously drive tumour progression and the outgrowth of cells that had inactivated the p53 pathway during the natural course of tumour evolution. Consistent with this hypothesis, fluorescent *in situ* hybridization (FISH) analysis showed that a subset of adenocarcinomas with high p-Erk had copy number gains of the *Kras* locus. Conversely, copy number alterations of *Kras* were never seen in adenomas (Fig. 3c). Together, these observations indicate that although the mechanisms that amplify oncogenic signalling are likely to be diverse, MAPK signal

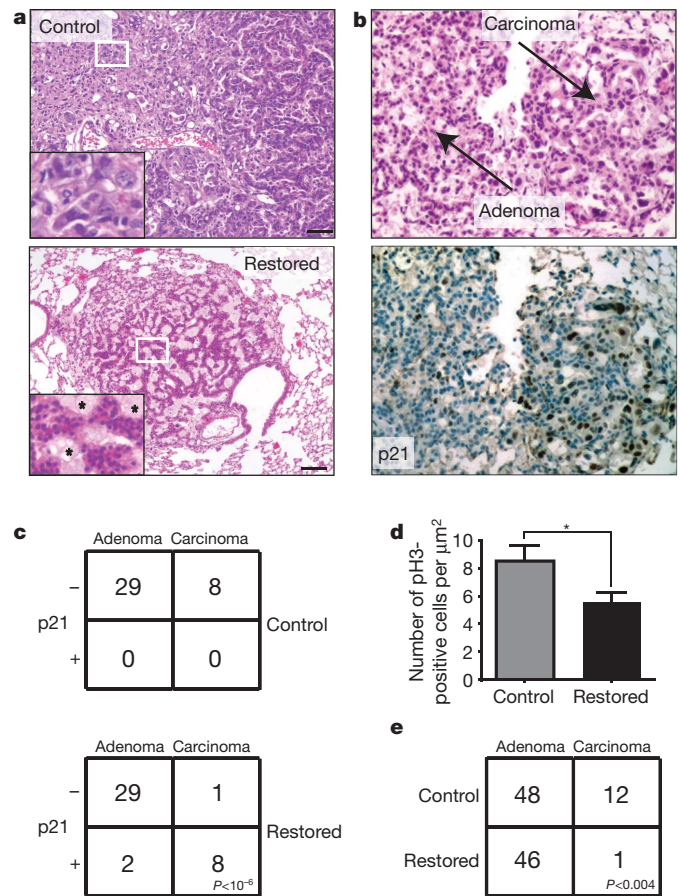


Figure 2 | Adenocarcinoma cells are sensitive to $Trp53$ restoration and are specifically eliminated from lung tumours. **a**, Histological sections from control and $Trp53$ -restored tumours stained with haematoxylin and eosin. Inset of $Trp53$ -restored tumours show monomorphic nuclei and tumour fissures filled with foam macrophages (asterisks). Scale bars, 50 μm . **b**, Tumour sections 3 days after $Trp53$ restoration. Haematoxylin and eosin-stained tumour section (top) with adenoma and carcinoma areas indicated. Serial section stained with p21 antibody (bottom). **c**, Contingency tables showing coincidence of p21 and adenocarcinoma 3 days after $Trp53$ restoration. **d**, Number of p3-positive cells per μm^2 for each tumour. Average and s.d. are shown. $Trp53$ restoration leads to significantly fewer mitoses. $*P < 0.05$. **e**, Tumour grades in control and $Trp53$ restored animals two weeks after initial treatment (vehicle-treated tumours, $n = 60$; tamoxifen-treated tumours, $n = 47$).

amplification typifies $Kras^{LA2}$ lung adenocarcinomas and may drive progression towards malignancy.

To test whether cells with amplified MAPK signalling persist after $Trp53$ restoration, we analysed $Kras^{LA2/+};Trp53^{LSL/LSL};Rosa26^{CreERT2}$ animals across a time course after tamoxifen administration. Loss of high p-Erk staining cells was evident 1 week after $Trp53$ restoration (Supplementary Fig. 7). Compared to controls, tumours with $Trp53$ restored showed significantly fewer p-Erk positive tumours after 2 weeks (Fig. 3d). This observation, in conjunction with the selective loss of histologically advanced tumour cells seen after $Trp53$ restoration, suggests that amplified MAPK signalling is incompatible with p53 expression.

Next, we micro-dissected tumours from $Kras^{LA2/+};Trp53^{LSL/LSL}$ mice and performed gene expression analysis to characterize better the molecular alterations that drive tumour progression. We developed an 'adenocarcinoma signature' by comparing the gene expression profiles of adenocarcinomas and adenomas (Fig. 4a). Gene set enrichment analysis showed that pathways associated with increased proliferation such as cell cycle processes, the Ras pathway and c-myc (also known as Myc) target genes were enriched in adenocarcinomas compared to adenomas (Fig. 4b). Other gene sets associated with adenocarcinomas were chemokine regulation, inflammation and immune responses, as

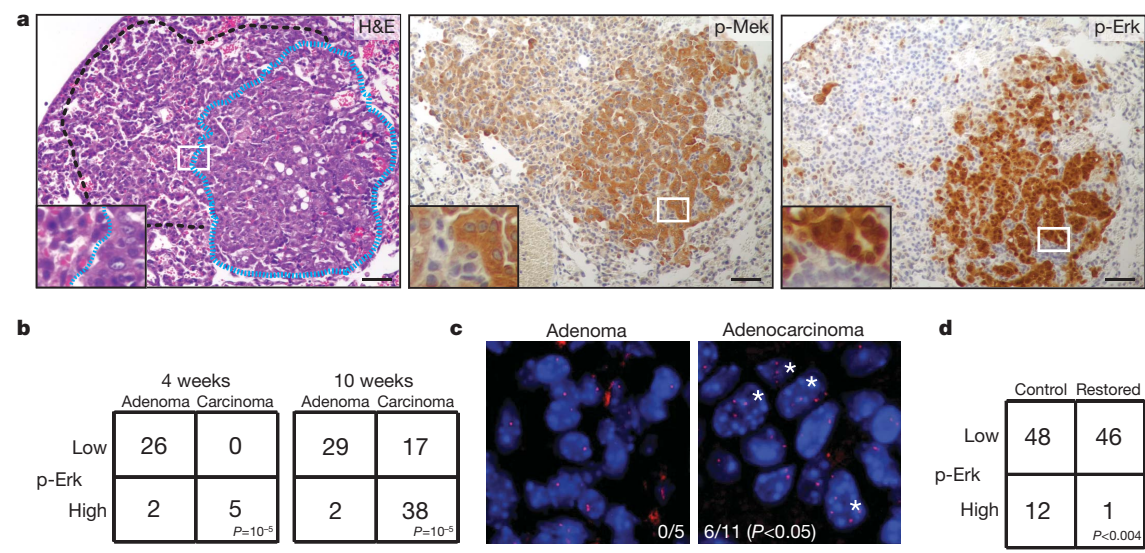


Figure 3 | Adenocarcinomas are typified by amplified MAPK signalling. **a**, Serial tumour sections of a mixed grade tumour stained with haematoxylin and eosin (H&E), anti-p-Mek or anti-p-Erk. Dashed lines outline high-grade (blue) and low-grade (black) areas. **b**, Contingency tables representing number of tumours with high or low MAPK signalling, and the corresponding tumour grades in *Kras*^{LA2/+}; *Trp53*^{LSL/LSL} at the 4- and 10-week time points. **c**, A subset of

well as *API* and *PEA3* (also known as *Jun* and *Etv4*, respectively) target genes. These data indicate that multiple pathways are enhanced upon progression to malignancy coincident with, or as a result of, amplified MAPK signalling.

To assess the response to p53 restoration in adenocarcinomas at the level of gene expression, we profiled micro-dissected tumours from *Kras*^{LA2/+}; *Trp53*^{LSL/LSL}; *Rosa26*^{CreERT2} mice seven days after *Trp53* restoration. Each tumour was histologically analysed for evidence consistent with a p53 response and the appearance of some adenocarcinoma features (Supplementary Fig. 7). We used the adenocarcinoma signature to perform hierarchical clustering on these p53-restored samples together with adenomas and adenocarcinomas. Interestingly,

tissue sections from **a** were stained with bacterial artificial chromosome probes surrounding the *Kras* locus on mouse chromosome 6. *Kras* signals (red) and DAPI/DNA (blue) counter stain are shown in an adenoma and a carcinoma. Asterisks indicate nuclei with greater than two *Kras* signals. **d**, Contingency plot of tumours with high p-Erk staining shows significantly fewer tumours with high p-Erk staining after *Trp53* restoration.

the p53-restored samples clustered with adenomas with high confidence. Additionally, adenocarcinoma specific gene sets were de-enriched in *Trp53*-restored tumours (Fig. 4a, b). These data are consistent with our observation that adenocarcinoma cells are specifically culled from these tumours leaving behind adenoma cells that are unresponsive to p53 restoration.

Hyperactive MAPK signalling has been shown to induce the transcription of *Cdkn2a*, leading to expression of Arf, an upstream activator of p53 (ref. 9). Consistent with this mechanism of triggering the p53 pathway, we found that *Cdkn2a* expression was higher in adenocarcinomas compared to adenomas (Supplementary Fig. 8a). Moreover, in tumours from *Kras*^{LA2/+}; *Trp53*^{LSL/LSL} mice, p-Erk co-localizes with Arf staining by immunofluorescence and immunohistochemistry specifically in adenocarcinomas and the higher-grade areas of mixed-grade tumours (Fig. 4c and Supplementary Fig. 8b, c). To test the functional requirement of Arf in the p53 response, we studied cell lines generated from *Kras*^{LA2/+}; *Trp53*^{LSL/LSL}; *Rosa26*^{CreERT2} lung adenocarcinomas. As we had observed *in vivo*, restoration of *Trp53* in cell culture led to prolonged cell cycle arrest without appreciable cell death. Further, the gene expression program elicited by *Trp53* restoration in these cell lines is similar to that observed *in vivo*, validating them as a relevant model with which to test Arf dependency for activation of p53 responses after *Trp53* restoration (Supplementary Fig. 9). We expressed shRNAs (short hairpin RNAs) targeted against either an Arf-specific

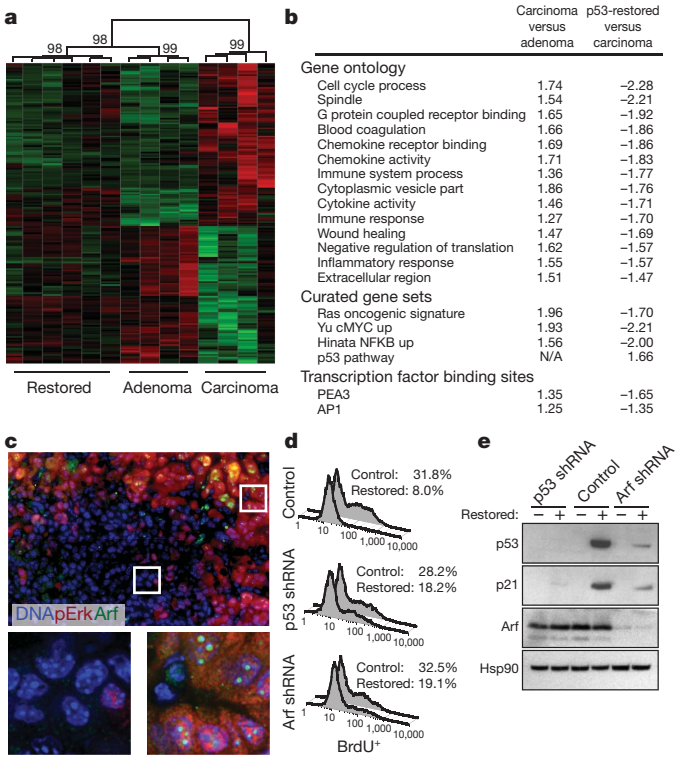


Figure 4 | Arf is specifically expressed in adenocarcinomas and sensitizes lung cancer cells to *Trp53* restoration. **a**, Hierarchical clustering of samples based on the adenocarcinoma signature. Confidence values (percent) are indicated at the top of major clades. **b**, GSEA (gene set enrichment analysis). Notable gene sets are listed with normalized enrichment scores indicate correlation and anti-correlation, respectively. **c**, Tissue sections from *Kras*^{LA2/+}; *Trp53*^{LSL/LSL} adenomas, mixed-grade tumours, and adenocarcinomas were co-labelled with antibodies to p-Erk (red) and Arf (green). Six adjacent fields of view of a mixed-grade tumour (top), and deconvoluted z-stack images (bottom) of dashed regions of an adenoma area (left) and adenocarcinoma area (right) are shown. **d**, Proliferation assay in adenocarcinoma-derived cell lines. Knockdown with retrovirally expressed shRNAs to *Trp53* or *Cdkn2a* (Arf-specific transcript), or control cells 48 h after *Trp53* restoration. Percentage of BrdU⁺ cells is indicated. **e**, Adenocarcinoma cell lysates from **d** were subjected to immunoblot analysis for p53, p21, Arf and Hsp90 (loading control).

transcript of *Cdkn2a* or *Trp53* in cell lines before *Trp53* restoration. As shown in Fig. 4d, inhibition of Arf or p53 allowed cells to continue to proliferate following addition of tamoxifen. Furthermore, Arf knock-down kept p53 levels low after *Trp53* restoration and limited the induction of the p53 target gene p21 (Fig. 4e and Supplementary Fig. 9c). These data indicate that Arf is required for p53 restoration-induced cell cycle arrest in this system.

Our failure to detect apoptosis following *Trp53* restoration stands in contrast to a report published together with ours in this issue¹⁸. The most likely explanation for this discrepancy is the different technologies used to control p53 function. Whereas our method restores a disrupted gene back to its wild-type state and allows otherwise normal p53 expression, our colleagues used a p53-ER fusion protein that might be expected to accumulate to high levels in advanced tumours that express Arf¹⁸. Thus, in that setting, p53-ER may induce more robust responses that include apoptosis when activated by tamoxifen.

Given our results on the requirement of Arf in the p53 response in this setting, one might imagine that Arf and p53 mutations would have equivalent effects in lung cancer progression. However, unlike in *Kras*^{LA2/+}; *Trp53*^{LSL/LSL} mice, carcinomas rarely develop in *Kras*^{LA2} mice carrying Arf mutations¹⁹. Thus, the clear effects of p53 mutation on tumour progression are likely to reflect additional functions of p53, including its role in responding to DNA damage and other forms of genomic instability²⁰.

The possibility that reactivation of defective p53 pathways will lead to variable and incomplete tumour regression is intriguing and may have important implications for anti-cancer therapies. As a tumour naturally progresses, multiple related, but genetically distinct clones co-evolve within the tumour. Conceptually akin to resistance mutations that are selected after targeted cancer therapies, pharmacological targeting of mutations that drive tumour progression, rather than initiation, may lead to significant pruning of some clones but leave behind others that still have significant potential to progress further in tumorigenesis. Although it is generally accepted that the elimination of the most advanced tumour cells within a cancer will be a significant benefit in cancer therapy, strategies to eliminate, or prevent progression of, the less advanced residual tumour cells may be important to allow durable therapeutic responses.

METHODS SUMMARY

Mice. Animal studies were approved by the Committee for Animal Care, and conducted in compliance with the Animal Welfare Act Regulations and other federal statutes relating to animals and experiments involving animals and adheres to the principles set forth in the Guide for the Care and Use of Laboratory Animals, National Research Council, 1996 (institutional animal welfare assurance no. A-3125-01). All animals were maintained on a mixed C57BL/6J x 129SvJ strain. Tamoxifen (Sigma) was administered intraperitoneally twice weekly at 200 µg per gram total body weight. Micro-computed tomography analysis was performed as described²¹.

Histology and immunohistochemistry. Formalin-fixed paraffin-embedded sections were stained with antibodies against p53 (Novocastra NCL-p53-CM5p), phosphorylated Mek1/2 (p-Mek), phosphorylated p42/p44 MAPK (p-Erk), cleaved caspase 3 (CC3), phosphorylated histone H3 (pH3) (Cell Signaling Technology), p19/Arf, or p21 (F5) (Santa Cruz Biotech). Immunofluorescence images were produced with a Delta Vision deconvolution microscope (Applied Precision) and SoftWorx software. Terminal deoxynucleotidyl transferase dUTP nick-end labelling (TUNEL) staining was performed following the manufacturer's instructions (*In situ* Cell Death Detection kit, Roche). FISH was performed with Texas Red-labelled bacterial artificial chromosome (BAC) clone RP23-188E5.

Gene expression analysis. RNA was extracted from micro-dissected tumours using TRIzol (Invitrogen). RNA was processed, labelled and hybridized to Affymetrix 430A_v2 chips. Gene expression data was deposited in Gene Expression Omnibus (GSE23875).

Cell lines. Cell lines were derived from *Kras*^{LA2/+}; *Trp53*^{LSL/LSL}; *Rosa26*^{CreERT2} adenocarcinomas. Retroviruses expressing shRNAs were designed and cloned as described previously²². Cell cycle analysis was performed according to the APC BrdU Flow Kit (BD Pharmingen).

Immunoblot analysis. p53 protein was detected using NCL-p53-505 (Novocastra), Hsp90 served as a loading control and was detected using a

monoclonal antibody (BD Transduction Laboratories). Other antibodies were as for immunohistochemistry.

Full Methods and any associated references are available in the online version of the paper at www.nature.com/nature.

Received 22 December 2009; accepted 27 September 2010.

1. Hanahan, D. & Weinberg, R. A. The hallmarks of cancer. *Cell* **100**, 57–70 (2000).
2. Selivanova, G. & Wiman, K. G. Reactivation of mutant p53: molecular mechanisms and therapeutic potential. *Oncogene* **26**, 2243–2254 (2007).
3. Wang, W. & El-Deiry, W. S. Restoration of p53 to limit tumor growth. *Curr. Opin. Oncol.* **20**, 90–96 (2008).
4. Xue, W. *et al.* Senescence and tumour clearance is triggered by p53 restoration in murine liver carcinomas. *Nature* **445**, 656–660 (2007).
5. Martins, C. P., Brown-Swigart, L. & Evan, G. I. Modeling the therapeutic efficacy of p53 restoration in tumors. *Cell* **127**, 1323–1334 (2006).
6. Ventura, A. *et al.* Restoration of p53 function leads to tumour regression *in vivo*. *Nature* **445**, 661–665 (2007).
7. Serrano, M., Lin, A. W., McCurrach, M. E., Beach, D. & Lowe, S. W. Oncogenic *ras* provokes premature cell senescence associated with accumulation of p53 and p16^{INK4a}. *Cell* **88**, 593–602 (1997).
8. Palmero, I., Pantoja, C. & Serrano, M. p19^{ARF} links the tumour suppressor p53 to Ras. *Nature* **395**, 125–126 (1998).
9. Lin, A. W. *et al.* Premature senescence involving p53 and p16 is activated in response to constitutive MEK/MAPK mitogenic signaling. *Genes Dev.* **12**, 3008–3019 (1998).
10. Tuveson, D. A. *et al.* Endogenous oncogenic *K-ras*^{G12D} stimulates proliferation and widespread neoplastic and developmental defects. *Cancer Cell* **5**, 375–387 (2004).
11. Haigis, K. M. *et al.* Differential effects of oncogenic K-Ras and N-Ras on proliferation, differentiation and tumor progression in the colon. *Nature Genet.* **40**, 600–608 (2008).
12. Sarkisian, C. J. *et al.* Dose-dependent oncogene-induced senescence *in vivo* and its evasion during mammary tumorigenesis. *Nature Cell Biol.* **9**, 493–505 (2007).
13. Jackson, E. L. *et al.* Analysis of lung tumor initiation and progression using conditional expression of oncogenic *K-ras*. *Genes Dev.* **15**, 3243–3248 (2001).
14. Johnson, L. *et al.* Somatic activation of the *K-ras* oncogene causes early onset lung cancer in mice. *Nature* **410**, 1111–1116 (2001).
15. Quintanilla, M., Brown, K., Ramsden, M. & Balmain, A. Carcinogen-specific mutation and amplification of Ha-*ras* during mouse skin carcinogenesis. *Nature* **322**, 78–80 (1986).
16. Bremner, R. & Balmain, A. Genetic changes in skin tumor progression: correlation between presence of a mutant *ras* gene and loss of heterozygosity on mouse chromosome 7. *Cell* **61**, 407–417 (1990).
17. Liu, M. L. *et al.* Amplification of Ki-*ras* and elevation of MAP kinase activity during mammary tumor progression in C3(1)/SV40 Tag transgenic mice. *Oncogene* **17**, 2403–2411 (1998).
18. Junttila, M. R. *et al.* Selective activation of p53-mediated tumour suppression in high-grade tumours. *Nature* doi:10.1038/nature09526 (this issue).
19. Young, N. P. & Jacks, T. Tissue-specific p19^{Arf} regulation dictates the response to oncogenic K-ras. *Proc. Natl Acad. Sci. USA* **107**, 10184–10189 (2010).
20. Lane, D. P. p53, guardian of the genome. *Nature* **358**, 15–16 (1992).
21. Meylan, E. *et al.* Requirement for NF-κB signalling in a mouse model of lung adenocarcinoma. *Nature* **462**, 104–107 (2009).
22. Dickens, R. A. *et al.* Probing tumor phenotypes using stable and regulated synthetic microRNA precursors. *Nature Genet.* **37**, 1289–1295 (2005).

Supplementary Information is linked to the online version of the paper at www.nature.com/nature.

Acknowledgements We would like to thank M. DuPage and C. Kim for critical reading of the manuscript. We are indebted to D. Crowley, E. Vasile and M. Griffin at the Koch Institute Core facilities (supported by Cancer Center Support (core) grant P30-CA14051 from the National Cancer Institute). We are grateful to M. Luo for microarray support. We thank M. Leversha at MSKCC for FISH. D.M.F. has been supported by the American Cancer Society (New England Area Fellow), and is a current Fellow of the Leukemia and Lymphoma Society. K.K.K. is supported by the John Reed Fund of the MIT undergraduate research program. M.M.W. was a Merck Fellow of the Damon Runyon Cancer Research Foundation and a Genentech postdoctoral fellow. T.J. is the David H. Koch Professor of Biology and a Daniel K. Ludwig Scholar. The Howard Hughes Medical Institute supported this work.

Author Contributions D.M.F. and T.J. conceived of the experiments and wrote the manuscript with comments from all authors; D.M.F., K.K.K., C.C., S.E.T. and R.R. performed the experiments and analysed the data; M.M.W. and F.J.S.-R. gave conceptual advice; R.B. performed histological evaluations; C.A.W. performed bioinformatics data analysis; and M.T.H. provided reagents and conceptual advice.

Author Information Gene expression data was deposited in Gene Expression Omnibus (GSE23875). Reprints and permissions information is available at www.nature.com/reprints. The authors declare no competing financial interests. Readers are welcome to comment on the online version of this article at www.nature.com/nature. Correspondence and requests for materials should be addressed to T.J. (tjacks@mit.edu).

METHODS

Mice. Animal studies were approved by the Committee for Animal Care, and conducted in compliance with the Animal Welfare Act Regulations and other federal statutes relating to animals and experiments involving animals and adheres to the principles set forth in the Guide for the Care and Use of Laboratory Animals, National Research Council, 1996 (institutional animal welfare assurance no. A-3125-01). All animals were maintained on a mixed C57BL/6J x 129SvJ strain. *Kras*^{LA2}, *Trp53*^{LSL} and *Rosa26*^{CreERT2} mice have been described^{6,14}. Tamoxifen (Sigma) was dissolved in corn oil (Sigma) and administered intraperitoneally twice weekly at 200 µg per gram total body weight. Lung tumour volumes were acquired from isoflurane-anesthetized mice using eXplore Locus MicroCT imager. Image acquisition was performed using eXplore Scan Control software, using a 45-µm voxel size program, and three-dimensional reconstruction was performed using eXplore Reconstruction Utility software. High-resolution tomograms were generated and individual tumour volumes were measured and calculated using MicroView software (all from GE Healthcare). For serial micro-computed tomography analysis, the relative size of each tumour was compared to the tumour volume at the 10-week time point.

Statistics. *P*-values indicated in contingency tables and FISH analysis were established by Fisher's exact test. Significance values from tumour volume studies and, proliferation (pH3) analyses were evaluated by Student's two-tailed *t*-test. Microarray statistics are described below.

Histology. All tissues were fixed in 10% formalin overnight, transferred to 70% ethanol, then embedded in paraffin. Four-micrometre sections were cut.

Tumour grading. All histological analyses were assisted by a board certified veterinary pathologist (R.B.). A tumour was scored positive for pleomorphic nuclei if it contained three or more such cells.

Immunohistochemistry. Slides were stained with haematoxylin and eosin or with antibodies to p53 (Novocastra NCL-p53-CM5p), phosphorylated Mek1/2 (p-Mek), phosphorylated p42/p44 MAPK (p-Erk), cleaved caspase 3 (CC3), phosphorylated histone H3 (pH3) (Cell Signaling Technology), p19/Arf, or p21 (F5) (Santa Cruz Biotech). Antigen retrieval was performed in 10 mM sodium citrate pH 6.0 by heating in a pressure cooker for 10 min.

Immunofluorescence. Images were captured with a 60×, 1.3 NA objective on a Delta Vision deconvolution microscope (Applied Precision). Image *z*-stacks were deconvoluted with SoftWorx software package, and maximum projections saved as tiff files. TUNEL staining was performed following the manufacturer's instructions (*In situ* Cell Death Kit, Roche).

FISH. BAC clone RP23-188E5 was labelled with Texas Red dye. Hybridizations and probe labelling was performed at the Memorial Sloan Kettering Cancer Center, cytogenetics core facility.

Cell line derivation, retrovirus production, and shRNA cloning. Tumours were isolated from *Kras*^{LA2/+}; *Trp53*^{LSL/LSL}; *Rosa26*^{CreERT2} animals, dissociated with collagenase and trypsin for one hour at 37 °C, and then grown in Dulbecco's modified Eagle media plus 10% fetal bovine serum. Retroviruses were produced by transfection of Phoenix cells (Lipofectamine 2000) and shRNAs were designed and cloned as previously described²². The 97-nucleotide oligomer used to generate the shRNA targeting the *Cdkn2a* locus was: 5'-TGCTGTTGACAGTGAGCGA CGCTCTGGCTTTCGTGAACATTAGTGAAGCCACAGATGTAATGTTTCAC GAAAGCCAGAGCGCTGCCTACTGCCTCGGA-3'. Cell cycle analysis was

performed according to the APC BrdU Flow Kit (BD Pharmingen). Data are representative of five cell lines derived from independent tumours. Cell lysates were prepared with RIPA buffer before separation on 4–12% BisTRIS NuPAGE gels (Invitrogen). Mouse p53 protein was detected using NCL-p53-505 (Novocastra). Hsp90 served as a loading control and was detected using a monoclonal antibody (BD Transduction Laboratories). Other antibodies were as for immunohistochemistry. Data are representative of two independent cell lines sorted by green fluorescent protein expression (expressed from within the shRNA retrovirus²²) for purity.

Gene expression analysis. Microarray analysis. RNA was extracted from micro-dissected adenocarcinomas, adenomas and *Trp53*-restored tumours from *Kras*^{LA2/+}; *Trp53*^{LSL/LSL} mice using TRIzol (Invitrogen). RNA was processed, labelled and hybridized to Affymetrix 430A_v2 chips according to the manufacturer's instructions. Affymetrix data analysis was done using statistical tools provided by the R and Bioconductor projects (<http://cran.r-project.org/>; <http://www.bioconductor.org/>). Data import and quality control assessment was done using the packages Affy and AffyPLM²³. Data was summarized and normalized using gcRMA²⁴. Differential expression analysis was carried out using limma²⁵. All the R commands, input data and environment-specific details required to duplicate these analyses are located here:

http://luria.mit.edu/caw_web/Feldser_supplemental/EtOH_TAM/

http://luria.mit.edu/caw_web/Feldser_supplemental/tumours/

Hierarchical clustering with *P*-values. The 'adenocarcinoma signature' consists of 71 genes up-regulated in adenocarcinomas and 57 genes up-regulated in adenomas (*P* < 0.05 and fold change > 1.75). Expression values were row-normalized using *z*-scores and the resulting data were subjected to hierarchical clustering (Ward's method) and a sample dendrogram was produced using the R package pvclust²⁶. The heat map was generated using Spotfire DecisionSite 9.1.1. The required R commands and the input data are located here:

http://luria.mit.edu/caw_web/Feldser_supplemental/pvclust/

Gene set enrichment analysis (GSEA). GSEA (<http://www.broad.mit.edu/gsea/>) was used to examine the distribution of the curated gene sets from the Broad Institute's MsigDB (<http://www.broadinstitute.org/gsea/msigdb/index.jsp>) in lists of genes ordered according to differential expression between various conditions. Positive and negative enrichment scores indicate correlation and anti-correlation respectively. The resulting data and the files required to duplicate these analyses are available here:

http://luria.mit.edu/caw_web/Feldser_supplemental/EtOH_TAM_GSEA/

http://luria.mit.edu/caw_web/Feldser_supplemental/tumours_GSEA/

23. Bolstad, B. M., Collin, F., Simpson, K. M., Irizarry, R. A. & Speed, T. P. Experimental design and low-level analysis of microarray data. *Int. Rev. Neurobiol.* **60**, 25–58 (2004).
24. Bolstad, B. M., Irizarry, R. A., Gautier, L. & Wu, Z. in *Bioinformatics and Computational Biology Solutions using R and Bioconductor* (eds Gentleman, R., Carey, V., Huber, W., Irizarry, R. & Dudoit, S.) Ch. 2, 13–32 (Springer, 2005).
25. Smyth, G. K., Michaud, J. & Scott, H. S. Use of within-array replicate spots for assessing differential expression in microarray experiments. *Bioinformatics* **21**, 2067–2075 (2005).
26. Suzuki, R. & Shimodaira, H. Pvclust: an R package for assessing the uncertainty in hierarchical clustering. *Bioinformatics* **22**, 1540–1542 (2006).

Tension directly stabilizes reconstituted kinetochore–microtubule attachments

Bungo Akiyoshi^{1,2*}, Krishna K. Sarangapani^{3*}, Andrew F. Powers^{3*}, Christian R. Nelson¹, Steve L. Reichow⁴, Hugo Arellano-Santoyo^{1,2,3}, Tamir Gonen^{4,5}, Jeffrey A. Ranish⁶, Charles L. Asbury³ & Sue Biggins¹

Kinetochore are macromolecular machines that couple chromosomes to dynamic microtubule tips during cell division, thereby generating force to segregate the chromosomes^{1,2}. Accurate segregation depends on selective stabilization of correct ‘bi-oriented’ kinetochore–microtubule attachments, which come under tension as the result of opposing forces exerted by microtubules³. Tension is thought to stabilize these bi-oriented attachments indirectly, by suppressing the destabilizing activity of a kinase, Aurora B^{4,5}. However, a complete mechanistic understanding of the role of tension requires reconstitution of kinetochore–microtubule attachments for biochemical and biophysical analyses *in vitro*. Here we show that native kinetochore particles retaining the majority of kinetochore proteins can be purified from budding yeast and used to reconstitute dynamic microtubule attachments. Individual kinetochore particles maintain load-bearing associations with assembling and disassembling ends of single microtubules for >30 min, providing a close match to the persistent coupling seen *in vivo* between budding yeast kinetochores and single microtubules⁶. Moreover, tension increases the lifetimes of the reconstituted attachments directly, through a catch bond-like mechanism that does not require Aurora B^{7–10}. On the basis of these findings, we propose that tension selectively stabilizes proper kinetochore–microtubule attachments *in vivo* through a combination of direct mechanical stabilization and tension-dependent phosphoregulation.

To isolate native yeast kinetochores, we modified a method that we previously developed to purify minichromosomes containing centromere-bound kinetochores¹¹. We affinity-purified the Dsn1–Flag epitope-tagged kinetochore protein under physiological concentrations of salt to maintain kinetochore structure¹¹. Although Dsn1 is a component of the four-member Mis12 kinetochore subcomplex (also called Mtw1/MIND complex¹²), silver-staining (Fig. 1a) and immunoblotting (Fig. 1b) of the detergent-eluate after SDS–polyacrylamide gel electrophoresis (SDS–PAGE) revealed co-purification of components from nearly all core subcomplexes. In contrast, purifications via tags on subcomplexes other than Mis12 did not isolate the majority of kinetochore subcomplexes (Supplementary Fig. 1 and refs 12, 13).

Kinetochore components were the most abundant proteins in the Dsn1–Flag-purified sample. Most bands on the silver-stained gels could be unambiguously assigned to core kinetochore proteins by gel shifts after epitope tagging (Supplementary Fig. 2), and their relative abundance was consistent between preparations (Figs 1a, 2a and Supplementary Figs 2, 4 and 6). Similarly, mass spectrometry indicated that core kinetochore proteins were the most abundant (Fig. 1c, Supplementary Table 1 and Supplementary Note 1). Spindle checkpoint and other kinetochore regulatory proteins also co-purified, although motor proteins and the Aurora B protein kinase were not detected (Supplementary Table 1 and Supplementary Note 2). To test whether the kinetochore proteins stably associate with Dsn1–Flag, we

performed gel filtration after Flag peptide elution. A peak fraction (~25 nm Stokes radius) containing DNA- and microtubule-binding kinetochore components was detected (Fig. 1d, Supplementary Fig. 3 and Supplementary Note 3). Taken together, these data show that stable, large assemblies spanning the entire kinetochore can be isolated from budding yeast.

To investigate whether the purified kinetochore particles are functional, we developed several bead- and fluorescence-based assays. First, we double-tagged Dsn1 so the particles could be coupled via anti-penta-His antibodies to polystyrene microbeads. Beads prepared with kinetochore particles from wild-type cells bound densely along taxol-stabilized microtubules (22 ± 1 beads per field; Fig. 2b). If instead the beads were prepared using particles from *ndc80-1* (*NDC80* is also known as *TID3*) or *spc105-15* mutant strains (Fig. 2a and Supplementary Fig. 4), binding was severely reduced (2 ± 1 or 4 ± 1 beads per field, respectively; Fig. 2b). Fluorescent kinetochore particles from strains containing the centromeric histone variant Cse4 fused to green fluorescent protein (Cse4–GFP) behaved similarly (Fig. 2c, Supplementary Figs 5 and 6). Previous work using recombinant Ndc80 and Spc105 has suggested that both subcomplexes contribute synergistically to microtubule binding¹⁴. The marked loss of binding in our assays with either *ndc80-1* or *spc105-15* is consistent with this hypothesis. Notably, kinetochore particles from *dad1-1* mutants (Dam1 complex) supported binding at near wild-type levels (18 ± 3 beads per field; Fig. 2b). This observation is consistent with previous analyses indicating that the initial attachment of kinetochores to the sides of microtubules does not require the Dam1 complex¹⁵.

During mitosis *in vivo*, kinetochores persistently attach to the assembling and disassembling ends of microtubules, and they withstand tensile forces ranging from about 0.4 to 8.0 pN^{3,16}. Time-lapse fluorescence imaging confirmed that the kinetochore particles track with disassembling ends *in vitro* (Fig. 2d, Supplementary Fig. 7, Supplementary Movies 1 and 2 and Supplementary Notes 4 and 5). Their disassembly-driven movement was highly processive, usually continuing until the filament depolymerized completely back to the seed. To test whether they also withstand physiological forces, we adapted a recently-developed bead motility assay^{16–19}. Beads prepared with kinetochore particles from wild-type and various mutant strains were attached near the growing ends of individual microtubules and constant tension was applied using a servo-controlled laser trap. Bead-bound wild-type particles remained associated with the microtubule end, supporting continuous loads up to 11 pN (Fig. 3a, Supplementary Fig. 8 and Supplementary Notes 4 and 5). These wild-type attachments were long lived, with a mean duration comparable to that of mitosis in yeast (Supplementary Fig. 9)⁶. They often persisted through multiple ‘catastrophe’ and ‘rescue’ events, where the filament switched from assembly to disassembly and vice versa (Fig. 3a, red trace, Supplementary Fig. 8 and Supplementary Movie 3), a behaviour exhibited by

¹Division of Basic Sciences, Fred Hutchinson Cancer Research Center, Seattle, Washington 98109, USA. ²Molecular and Cellular Biology Program, University of Washington, Seattle, Washington 98195, USA. ³Department of Physiology & Biophysics, University of Washington, Seattle, Washington 98195, USA. ⁴Department of Biochemistry, University of Washington, Seattle, Washington 98195, USA.

⁵Howard Hughes Medical Institute, University of Washington, Seattle, Washington 98195, USA. ⁶Institute for Systems Biology, Seattle, Washington 98103, USA.

*These authors contributed equally to this work.

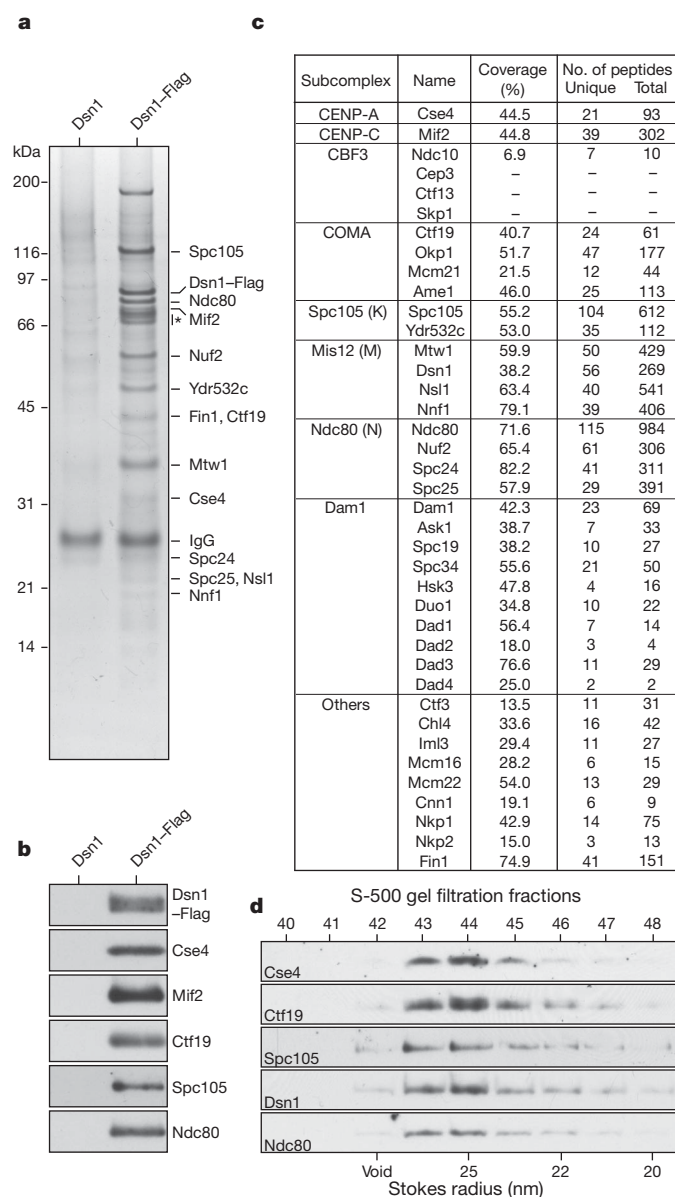


Figure 1 | Kinetochore particles can be isolated by affinity purification of Dsn1-Flag. **a**, Core kinetochore proteins co-purify with Dsn1-Flag as visualized by silver-stained SDS-PAGE. Asterisk indicates non-specific co-purifying proteins. **b**, Immunoblot confirms co-association of DNA- and microtubule-binding components with Dsn1-Flag. **c**, Mass spectrometry identifies all components of kinetochore subcomplexes except CBF3. Identities, percent sequence coverage, and number of identified peptides of core kinetochore proteins are shown. See Supplementary Table 1 for all proteins identified by mass spectrometry. Ndc10 and Ydr532c are also known as Cbf2 and Kre28, respectively. **d**, Eluted kinetochore particles were subjected to S-500 size exclusion chromatography and analysed by immunoblots. The kinetochore proteins analysed co-migrate as a complex (Stokes radius ~25 nm). Supplementary Fig. 3 shows additional fractions.

kinetochores *in vivo*. During disassembly, the attachments also moved in a direction opposite the trapping force, demonstrating that they can harness energy stored in the microtubule lattice to produce mechanical work. Notably, their coupling behaviour was more robust than simpler couplers based on recombinant Ndc80 and Dam1 complexes^{16–18} (Supplementary Fig. 9), and they formed strong attachments even when the Dsn1:bead ratio was reduced below 200:1 (Fig. 3b, c and Supplementary Fig. 10). Particles from the *dad1-1* mutant strain formed weaker attachments (Fig. 3b, c), whereas those from *ndc80-1* or *spc105-15* strains usually failed to interact detectably with the filaments (similar to the results with taxol-stabilized microtubules) (Fig. 3d).

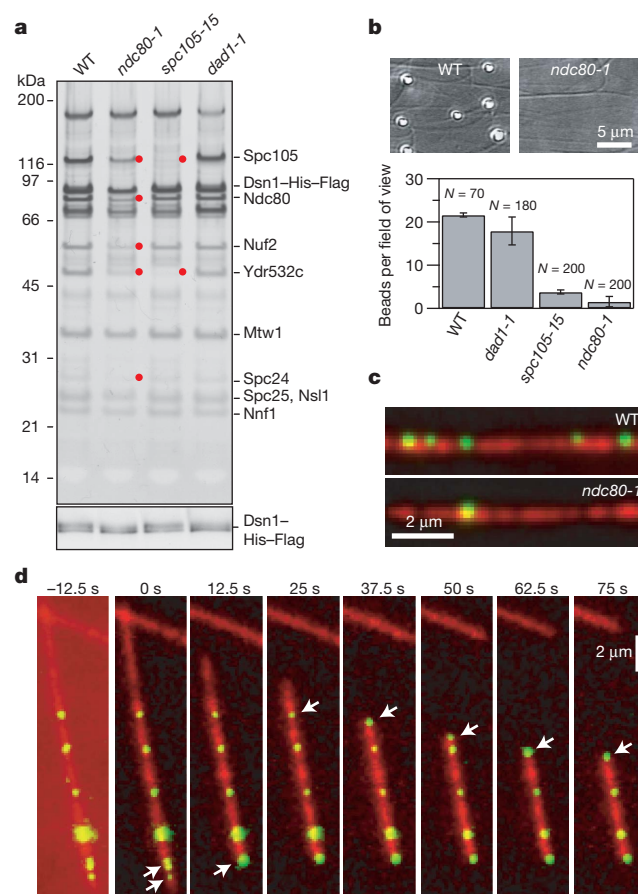


Figure 2 | Purified kinetochore particles bind microtubules *in vitro*.

a, Silver-stained SDS-PAGE of Dsn1-His-Flag kinetochore material from wild type (WT), *ndc80-1*, *spc105-15* and *dad1-1* mutants. Red dots indicate reduced proteins in the mutant preparations (see Supplementary Fig. 4). Bottom: anti-Flag immunoblot against Dsn1-His-Flag. **b**, Binding of beads prepared with material from indicated strains to taxol-stabilized microtubules (mean \pm s.d., from *N* fields, as indicated). **c**, Fluorescence images of Cse4-GFP kinetochore particles (green) from wild-type and *ndc80-1* strains bound to taxol-stabilized microtubules (red). **d**, Selected frames from Supplementary Movie 1 showing movement of Cse4-GFP particles (arrows) driven by the disassembling ends of a microtubule (red; see also Supplementary Fig. 7 and Supplementary Movie 2).

The robust behaviour of the wild-type kinetochore particles at low Dsn1:bead ratios indicates that few particles, perhaps just one, may be required to form a load-bearing coupler (Supplementary Note 6). If single particles suffice, then under conditions of limiting particle density the strength of the interaction should remain invariant as the density of particles on the beads is reduced. Consistent with this prediction, the force required to rupture attachments associated with growing microtubule ends was statistically indistinguishable, averaging 9.1 ± 0.2 pN, across a 100-fold range of Dsn1:bead ratios (Fig. 3b, c). A second prediction is that the fraction of active beads, $A(c)$, should vary according to the Poisson probability that a bead carries one or more active particles, $A(c) = 1 - e^{-\lambda c}$, where c is the relative Dsn1 concentration and λ is a fitting parameter. Indeed, this form of $A(c)$ matches closely the fraction of beads that formed attachments to growing ends (Fig. 3d). The observation that a measurable event becomes rarer upon dilution while its properties remain unchanged is the hallmark of a ‘single molecule’ experiment. Analogous observations first demonstrated that single motor enzymes such as kinesin and myosin V are processive, for example in refs 20–22. Here it indicates that robust coupling is an intrinsic and stable property of the purified kinetochore particles — artificial oligomerization on the bead surface is not required. It also demonstrates a close match to the physiological situation in budding yeast, where each individual kinetochore is coupled to the tip of a single microtubule²³.

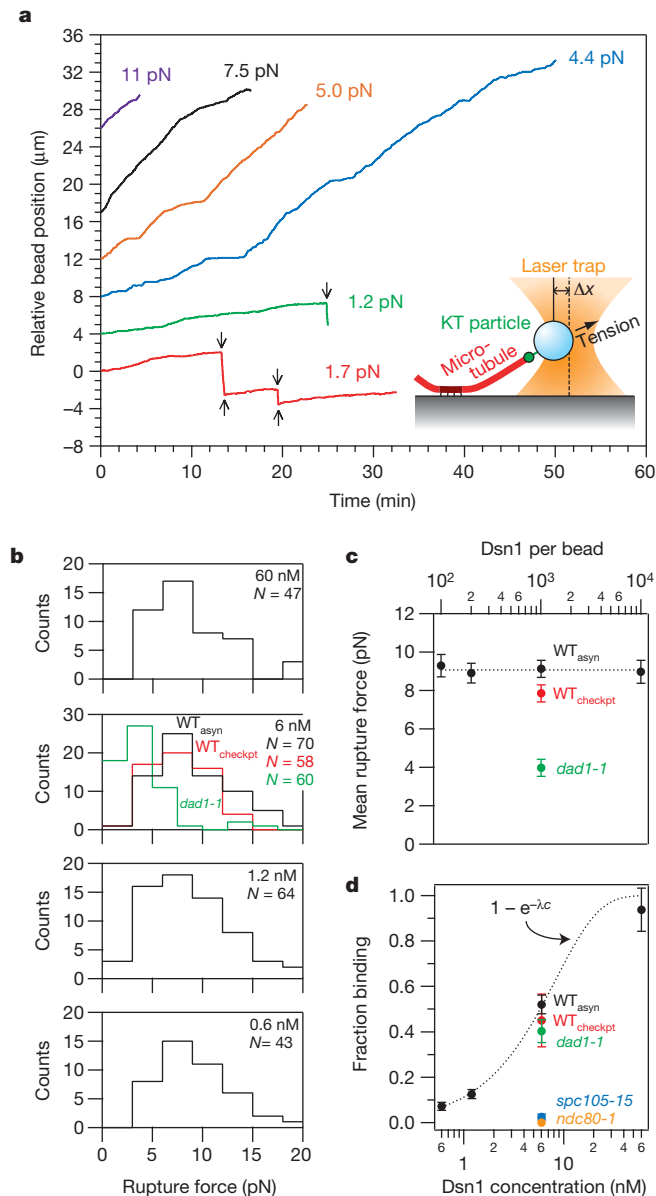


Figure 3 | Single kinetochore particles suffice for robust coupling.

The basis for accurate chromosome segregation is thought to be tension-dependent stabilization of bi-oriented kinetochore-microtubule attachments²⁴. This selective stabilization has been attributed to an indirect mechanism where tension inhibits phosphorylation of kinetochores by the Aurora B kinase^{4,5}. As a first step towards reconstituting this mechanism, we measured the effect of tension on attachment lifetimes for individual end-associated kinetochore particles. Considering that the particles lacked detectable Aurora B (Supplementary Table 1), that there was no ATP present to allow phosphorylation, and that protein-protein interactions are typically destabilized by force^{25,26}, we expected a monotonic decrease in lifetime with increasing tension. Surprisingly, increasing tension between 1 and 5 pN enhanced the

stability of the attachments (Fig. 4a), raising their mean lifetime from 21 ± 5 to 50 ± 17 min ($P = 0.0012$; based on $N = 15$ and 9 events observed for 5.2 and 7.5 h, respectively). This result shows that physiological levels of tension can stabilize kinetochore-microtubule attachments directly, by a mechanism that does not require Aurora B. The result is also reminiscent of 'catch bonds' between receptor-ligand pairs, which enhance cell adhesion in the presence of mechanical force⁷⁻¹⁰.

Catch bonds are often explained using two-state kinetic models in which the receptor-ligand pair can switch between a strongly and a weakly bound state, and tension promotes adoption of the strong state^{7,9}. Considering that microtubule tips also switch between two states, assembly and disassembly, we thought a similar model might apply to our reconstituted attachments (Fig. 4b). To test this, we measured independently how the rates of the following four events varied with tension: detachment during assembly, detachment during disassembly, catastrophe, and rescue. The detachment rate during assembly was low ($\sim 1 \text{ h}^{-1}$) and it increased gradually with tension (Fig. 4c, red). By comparison, detachment during disassembly was much faster (10- to 100-fold) but less sensitive to tension, decreasing with force (Fig. 4c, blue). We speculate that this suppression of detachment may arise from the force-dependent slowing of disassembly (Fig. 4e, blue). Together, the two detachment rates are consistent with a two-state catch bond-like

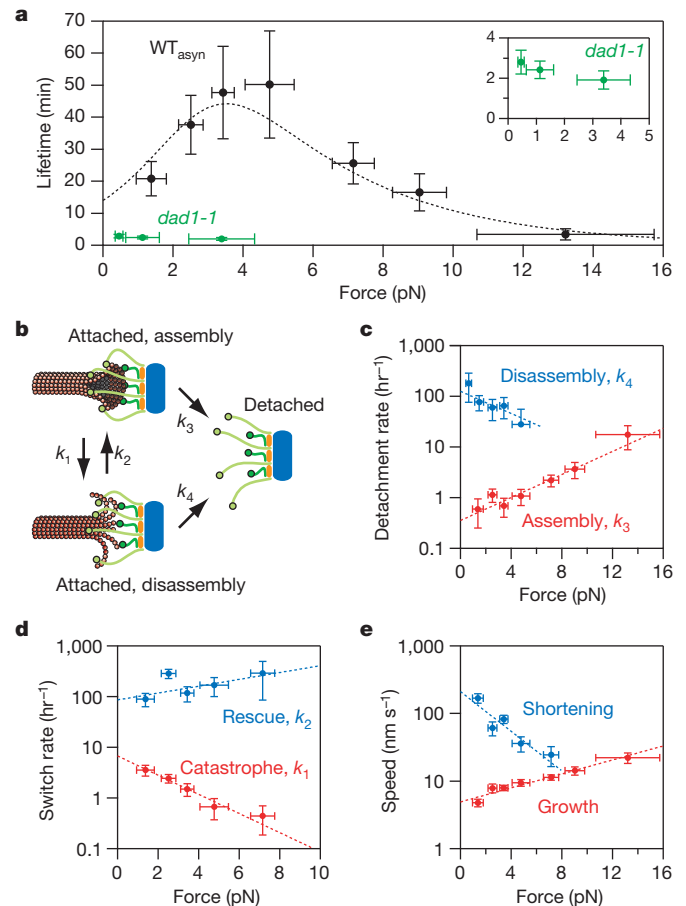


Figure 4 | Tension stabilizes attachments between kinetochore particles and dynamic microtubules. **a**, Measured attachment lifetimes for wild-type (WT_{asyt}) and $dad1-1$ particles. Tension initially prolongs and then shortens lifetimes for wild-type attachments. Dotted curve shows prediction of the two-state model (see text). **b**, Schematic of two-state model with detachment during assembly and disassembly (rates k_3 and k_4 , respectively), and interconversion between states (k_1 and k_2). **c-e**, Measured rates and exponential fits for detachment during assembly (c, red), detachment during disassembly (c, blue), catastrophe (d, red), rescue (d, blue), growth (e, red) and shortening (e, blue). Error bars represent (a-d) counting uncertainty ($N = 24-65$) and (e) s.e.m. ($N = 78-360$).

model in which the strongly- and weakly-bound states correspond to tip assembly and disassembly, respectively. Tension also inhibited catastrophes (Fig. 4d, red) and promoted rescues (Fig. 4d, blue), similar to our previous findings with Dam1-based attachments¹⁷. The lower catastrophe and higher rescue rates imply that filaments under tension spend less time in the disassembling state, when the kinetochore particles are most vulnerable to detachment. We fit the force-dependence of all four rates with exponential curves (Figs 4c, d and Supplementary Table 2) and, without further fitting, used these to predict the lifetime versus force relationship for the two-state catch bond-like model (Supplementary Note 7). The excellent quantitative agreement with measured lifetimes (see Fig. 4a) confirms that this model can explain the tension-dependent stabilization effect. If an analogous effect occurs at kinetochore-microtubule junctions *in vivo*, it could make an important contribution to the selective stabilization of bi-oriented attachments (see Supplementary Fig. 11).

In summary, our purification of active kinetochore particles has enabled the first direct measurements of the coupling strength between individual native kinetochore particles and dynamic microtubules. Robust coupling at the single particle level depends on the outer microtubule-binding subcomplexes from the budding yeast core kinetochore. Strikingly, tension enhances the stability of these attachments in a manner independent of Aurora B. On this basis we propose that selective stabilization of correct kinetochore-microtubule attachments occurs *in vivo* through a combination of at least two mechanisms, the canonical tension-dependent phosphoregulation, plus a more primitive mechanism based on tension-dependent modulation of tip dynamics.

METHODS SUMMARY

All yeast strains and plasmids used in this study are listed in Supplementary Tables 3 and 4. Media and genetic and microbial techniques were as described²⁷. Immunoblotting and SDS-PAGE were as described²⁸. Kinetochore particles were isolated by affinity-purifying Dsn1-Flag or Dsn1-His-Flag protein using a modified mini-chromosome purification protocol¹¹ (see Methods). A typical concentration of Dsn1-Flag or Dsn1-His-Flag was $\sim 4 \mu\text{g ml}^{-1}$ (60 nM). Size-exclusion chromatography was carried out on a Sephacryl S-500 HR column (Amersham). Estimation of Stokes radii was obtained using a high molecular weight calibration kit (Bio-Rad) and the void volume of the column was determined using 500 nm polystyrene beads (Polysciences). Mass spectrometry was performed as described¹¹. Total internal reflection fluorescence (TIRF) microscopy and flow cell preparation were performed as previously described^{16,18}. Purified Dsn1-His-Flag kinetochore particles were linked to polystyrene beads via biotinylated anti-penta-His antibody, essentially as described¹⁶. The laser trap has also been described previously¹⁶⁻¹⁹.

Full Methods and any associated references are available in the online version of the paper at www.nature.com/nature.

Received 13 April; accepted 19 October 2010.

1. Santaguida, S. & Musacchio, A. The life and miracles of kinetochores. *EMBO J.* **28**, 2511–2531 (2009).
2. Cheeseman, I. M. & Desai, A. Molecular architecture of the kinetochore-microtubule interface. *Nature Rev. Mol. Cell Biol.* **9**, 33–46 (2008).
3. Nicklas, R. B. The forces that move chromosomes in mitosis. *Annu. Rev. Biophys. Chem.* **17**, 431–449 (1988).
4. Maresca, T. J. & Salmon, E. D. Welcome to a new kind of tension: translating kinetochore mechanics into a wait-anaphase signal. *J. Cell Sci.* **123**, 825–835 (2010).
5. Liu, D., Vader, G., Vromans, M. J., Lampson, M. A. & Lens, S. M. Sensing chromosome bi-orientation by spatial separation of aurora B kinase from kinetochore substrates. *Science* **323**, 1350–1353 (2009).
6. Straight, A. F., Marshall, W. F., Sedat, J. W. & Murray, A. W. Mitosis in living budding yeast: anaphase A but no metaphase plate. *Science* **277**, 574–578 (1997).
7. McEver, R. P. & Zhu, C. Rolling cell adhesion. *Annu. Rev. Cell Dev. Biol.* **26**, 363–396 (2010).
8. Sarangapani, K. K. *et al.* Low force decelerates L-selectin dissociation from P-selectin glycoprotein ligand-1 and endoglycan. *J. Biol. Chem.* **279**, 2291–2298 (2004).

9. Thomas, W. E., Vogel, V. & Sokurenko, E. Biophysics of catch bonds. *Annu. Rev. Biophys.* **37**, 399–416 (2008).
10. Marshall, B. T. *et al.* Direct observation of catch bonds involving cell-adhesion molecules. *Nature* **423**, 190–193 (2003).
11. Akiyoshi, B., Nelson, C. R., Ranish, J. A. & Biggins, S. Quantitative proteomic analysis of purified yeast kinetochores identifies a PP1 regulatory subunit. *Genes Dev.* **23**, 2887–2899 (2009).
12. De Wulf, P., McAnish, A. D. & Sorger, P. K. Hierarchical assembly of the budding yeast kinetochore from multiple subcomplexes. *Genes Dev.* **17**, 2902–2921 (2003).
13. Nekrasov, V. S., Smith, M. A., Peak-Chew, S. & Kilmartin, J. V. Interactions between centromere complexes in *Saccharomyces cerevisiae*. *Mol. Biol. Cell* **14**, 4931–4946 (2003).
14. Cheeseman, I. M., Chappie, J. S., Wilson-Kubalek, E. M. & Desai, A. The conserved KMN network constitutes the core microtubule-binding site of the kinetochore. *Cell* **127**, 983–997 (2006).
15. Tanaka, K. *et al.* Molecular mechanisms of kinetochore capture by spindle microtubules. *Nature* **434**, 987–994 (2005).
16. Powers, A. F. *et al.* The Ndc80 kinetochore complex forms load-bearing attachments to dynamic microtubule tips via biased diffusion. *Cell* **136**, 865–875 (2009).
17. Franck, A. D. *et al.* Tension applied through the Dam1 complex promotes microtubule elongation providing a direct mechanism for length control in mitosis. *Nature Cell Biol.* **9**, 832–837 (2007).
18. Tien, J. F. *et al.* Cooperation of the Dam1 and Ndc80 kinetochore complexes enhances microtubule coupling and is regulated by aurora B. *J. Cell Biol.* **189**, 713–723 (2010).
19. Franck, A. D., Powers, A. F., Gestaut, D. R., Davis, T. N. & Asbury, C. L. Direct physical study of kinetochore-microtubule interactions by reconstitution and interrogation with an optical force clamp. *Methods* **51**, 242–250 (2010).
20. Howard, J., Hudspeth, A. J. & Vale, R. D. Movement of microtubules by single kinesin molecules. *Nature* **342**, 154–158 (1989).
21. Block, S. M., Goldstein, L. S. & Schnapp, B. J. Bead movement by single kinesin molecules studied with optical tweezers. *Nature* **348**, 348–352 (1990).
22. Mehta, A. D. *et al.* Myosin-V is a processive actin-based motor. *Nature* **400**, 590–593 (1999).
23. Winey, M. *et al.* Three-dimensional ultrastructural analysis of the *Saccharomyces cerevisiae* mitotic spindle. *J. Cell Biol.* **129**, 1601–1615 (1995).
24. Nicklas, R. B. & Ward, S. C. Elements of error correction in mitosis: microtubule capture, release, and tension. *J. Cell Biol.* **126**, 1241–1253 (1994).
25. Bell, G. I. Models for the specific adhesion of cells to cells. *Science* **200**, 618–627 (1978).
26. Merkel, R., Nassoy, P., Leung, A., Ritchie, K. & Evans, E. Energy landscapes of receptor-ligand bonds explored with dynamic force spectroscopy. *Nature* **397**, 50–53 (1999).
27. Rose, M. D., Winston, F. & Heiter, P. *Methods in yeast genetics*. (Cold Spring Harbor Laboratory Press, 1990).
28. Biggins, S. *et al.* The conserved protein kinase Ipl1 regulates microtubule binding to kinetochores in budding yeast. *Genes Dev.* **13**, 532–544 (1999).

Supplementary Information is linked to the online version of the paper at www.nature.com/nature.

Acknowledgements We thank A. Desai for antibodies, and J. Kilmartin, G. Barnes, D. Pellman, R. Tsien and the Yeast Resource Center for strains and plasmids. We also thank M. Press for constructing the Cse4-GFP strain, M. Yuan at the ISB for help, and the Seattle Mitosis Club for comments. We are grateful to T. Davis, W. Thomas, B. Zagotta, T. Tsukiyama, J. Stumpff, F. Rieke, S. Gordon and the Biggins lab for comments on the manuscript. This work was supported by an NSF IGERT fellowship (DGE-0504573) and NIH traineeships (T32GM07270) to A.F.P., an NIH Cardiovascular Pathology traineeship (T32HL007312) to K.K.S., a Beckman Young Investigator grant to S.B., NIH grants (GM078069 and GM064386) to S.B., an NCI Cancer Center Support grant (CA015704) and an NIGMS grant (PM50 GM076547/Center for Systems Biology) to J.A.R., a Searle Scholar Award (06-L-111) to C.L.A., a Packard Fellowship for Science and Engineering (2006-30521) to C.L.A. and an NIGMS grant (R01GM79373) to C.L.A. S.B. is a Scholar of the Leukemia and Lymphoma Society and T.G. is a Howard Hughes Medical Institute Early Career Scientist.

Author Contributions All authors designed various components of the research. B.A. and C.R.N. constructed plasmids and yeast strains and B.A. purified kinetochore particles and analysed composition. B.A. and J.A.R. performed mass spectrometry and data analysis. A.F.P., K.K.S., H.A.S. and C.L.A. performed microtubule experiments. S.L.R. performed gel filtration.

Author Information Reprints and permissions information is available at www.nature.com/reprints. The authors declare no competing financial interests. Readers are welcome to comment on the online version of this article at www.nature.com/nature. Correspondence should be addressed to S.B. (sbiggins@fhcrc.org) or C.L.A. (casbury@u.washington.edu) and requests for materials to S.B.

METHODS

Yeast strains, plasmids and microbial techniques. Media and genetic and microbial techniques were essentially as described²⁷. Mitotic cultures were prepared with benomyl as described¹¹. For temperature-sensitive mutants, cells were shifted to 37 °C for 3 h. Yeast strains and plasmids used in this study are listed in Supplementary Tables 3 and 4. The *ndc80-1* (ref. 29), *spc105-15* (ref. 13), *SPC105-GFP* (ref. 13), *YDR532c-GFP* (ref. 13), *dad1-1* (ref. 30) alleles were crossed to make strains for this study. Strains containing *NUF2-3GFP:His3* and *CSE4-GFP:URA3* were made by integrating plasmid pSB897 digested with XcmI at the *NUF2* locus and pSB1617 digested with StuI at the *URA3* locus, respectively. Deletions, as well as 3Flag, 13Myc and mCherry epitope tags were made using a PCR-based integration system and confirmed by PCR^{31–33}. The 6His–3Flag epitope tagging of the endogenous *DSN1* gene was performed using a PCR-based integration system using primers SB2434–SB2435 and plasmid pSB1590 as a template. All tagged strains we constructed are functional *in vivo* and do not cause any detectable growth defects or temperature sensitivity. Specific primer sequences are available on request.

Plasmid construction. pSB1590 (*DSN1-6His-3Flag, URA3*, integrating vector) was constructed in multiple steps as follows. First, pSB1110 (*DSN1-12Myc, URA3*, integrating vector) was made by amplification of *DSN1* from pSB624 (*DSN1, CEN, URA3*)³⁴ using primers SB1675 and SB1676. The PCR product was digested with XhoI and EcoRI and ligated into the same sites in pSB167 (*12Myc, URA3*, integrating vector)²⁸. Second, a DNA fragment encoding *3Flag* with 5' EcoRI and 3' XmaI sites engineered was made by annealing SB1698 and SB1699. The fragment was then integrated just before the *12myc* open reading frame of pSB1110 (*DSN1-12Myc, URA3*, integrating vector) that was digested with EcoRI and XmaI to make pSB1113 (*DSN1-3Flag, URA3*, integrating vector). Finally, to make pSB1590 (*DSN1-6His-3Flag, URA3*, integrating), a DNA fragment encoding the *6His* tag with EcoRI sites at both ends was made by annealing SB2432 and SB2433, which was then integrated just before *3Flag* of pSB1113 using EcoRI. The *Nuf2-3GFP* (pSB897) was made by PCR amplification of the carboxy-terminal 853 base pairs of *NUF2* using primers SB1124 and SB1125 that have EcoRI and BamHI restriction sites engineered, respectively. The resulting PCR product was digested with EcoRI–BamHI and ligated into the same sites of pSB623 (gift of D. Pellman). To make *Cse4-GFP* (pSB1617), *GFP* was amplified by PCR from pSB623 using primers SB2443 and SB2444, digested with XbaI, and integrated into the XbaI site of pSB241 (*CSE4, URA3*, integrating vector)³⁵. pSB1265 (*3Flag, TRP1*) was made by replacing *KAN* marker gene of pSB812 (*3Flag, KAN*) with *TRP1* marker gene from pSB450 (*TRP1*) using SpeI and SalI. pSB1643 (glutathione *S*-transferase fusion GST-N-Spc105 expression vector) was made by PCR amplification of the amino-terminal 798 bp of *SPC105* using primers SB2590 and SB2591 that have BamHI and EcoRI sites engineered, respectively. The resulting PCR product was digested with BamHI–EcoRI and ligated into the same sites of pGEX-2T (Amersham).

Isolation of kinetochore particles. Kinetochore particles were isolated by affinity-purifying Dsn1–Flag or Dsn1–His–Flag protein using a minichromosome purification protocol¹¹ with the following modifications. Briefly, cells were grown in complete YPD (yeast extract, peptone, dextrose) media and extract was prepared by breaking cells in a blender with dry ice, followed by ultracentrifugation. Beads conjugated with anti-Flag antibodies were incubated with extract for 3 h with constant rotation, followed by four washes with buffer H (BH)/0.15 (25 mM HEPES pH 8.0, 2 mM MgCl₂, 0.1 mM EDTA pH 8.0, 0.5 mM EGTA pH 8.0, 0.1% NP-40, 150 mM KCl, 15% glycerol) containing protease inhibitors, phosphatase inhibitors and 2 mM dithiothreitol (DTT). Beads were further washed twice with BH/0.15 with protease inhibitors. Associated proteins were eluted from the beads by gentle agitation of beads in elution buffer (0.5 mg ml^{−1} 3Flag peptide in BH/0.15 with protease inhibitors) for 25 min at room temperature. A typical concentration of Dsn1–Flag or Dsn1–His–Flag was ~4 µg ml^{−1} (60 nM) as determined by comparing the purified material with BSA standards on silver-stained SDS–PAGE gels. Similar results were obtained using SYPRO Ruby dye. Aliquots were made and stored at −80 °C. Typically, 2 l of asynchronously growing culture were used for microtubule-binding experiments, 24 l of mitotic culture for S-500 gel filtration experiments. Based on silver-stained SDS–PAGE, the composition of the kinetochore particles purified from mitotically arrested cells does not differ detectably from particles purified from asynchronous cultures. This finding is consistent with the observation that budding yeast kinetochores bind microtubules throughout most of the cell cycle³⁶. To identify co-purifying proteins, associated proteins were eluted with detergent and analysed by mass spectrometry as described¹¹.

Protein and immunological techniques. Immunoblotting was performed as described²⁸. Anti-Spc105 (1–266 amino acid) polyclonal antibodies were raised and affinity purified using pSB1643 (GST-N-Spc105) as previously described³⁴ and used at a 1:1,000 dilution. Anti-Flag antibodies (Sigma-Aldrich) were used at 1:3,000 and anti-Cse4 antibodies at 1:500 (ref. 34). Anti-Ndc80 (OD4, 1:10,000),

anti-Ndc10 (OD1, 1:5,000), anti-Mif2 (OD2, 1:6,000), and anti-Ctf19 (OD10, 1:15,000) antibodies were generous gifts from A. Desai¹¹. To compare microtubule binding activity between different kinetochore mutants, the concentration of Dsn1–Flag was normalized by quantifying its signal intensity using the Odyssey infrared imaging system (Li Cor Bioscience). Silver-staining was performed on 4–12% NuPAGE Novex Bis-Tris gels (Invitrogen) using a SilverQuest silver-staining kit according to instructions (Invitrogen). Size-exclusion chromatography was carried out on a Sephacryl S-500 HR column (Amersham) equilibrated in BH/0.15 at 4 °C. Estimation of Stokes radii was obtained using a high-molecular weight calibration kit (Bio-Rad) and the void volume of the column was determined using 500 nm polystyrene beads (Polysciences).

TIRF microscopy. We used a custom TIRF microscope and flow cell preparation that has been previously described^{6,18,37}. After an initial rinse with 0.3 ml double distilled H₂O, 'rigor' kinesin³⁸ diluted in BRB80 (80 mM PIPES, 1 mM MgCl₂, 1 mM EGTA at pH 6.9) containing 1 mg ml^{−1} κ-casein and 10 µM taxol (BCT) was introduced and allowed to bind for 5 min. Unbound kinesin was removed with 100 µl BCT, and Alexa 647-labelled taxol microtubules diluted in BCT plus oxygen scavengers (BCTscavs; 200 µg ml^{−1} glucose oxidase, 25 mM glucose, 35 µg ml^{−1} catalase and 5 mM DTT) were introduced and allowed to bind to the desired density. Flow cells were then washed with 50 µl BCTscavs, and fluorescent kinetochore particles (diluted in BCTscavs) were introduced and given 5 min to bind.

For experiments using dynamic microtubules, Alexa 647-labelled GMPCPP (guanylyl-(α,β)-methylene-diphosphonate) microtubules were bound to coverslip-adsorbed rigor kinesin, washed with 50 µl warm growth buffer (BRB80, 1 mg ml^{−1} κ-casein, 1 mM GTP, 200 µg ml^{−1} glucose oxidase, 25 mM glucose, 35 µg ml^{−1} catalase and 5 mM DTT) and then incubated with growth buffer supplemented with 2 mg ml^{−1} Alexa 647 tubulin (1% labelled) and fluorescent kinetochore particles. Dynamic extensions were grown for ~5 min at 30 °C, after which depolymerization was triggered by exchanging for tubulin-free buffer.

Assay for bead binding to taxol-stabilized microtubules. Purified Dsn1–His–Flag kinetochore particles were diluted in BRB80 plus 1 mg ml^{−1} κ-casein and linked to polystyrene beads via biotinylated anti-penta-His antibody, essentially as described in ref. 16. Flow cells (described in ref. 19) were treated with taxol-stabilized microtubules, which non-specifically adsorb to the coverslip surface, and then blocked with BCT for 10 min before the introduction of kinetochore particle-coated beads. After a 10 min incubation to allow for binding, the flow cells were imaged in DIC and the number of microtubule-bound beads per field of view was counted. Binding was negligible (2 beads in 150 fields) in negative controls using beads lacking the anti-penta-His antibody, prepared with wild-type kinetochore material at an equivalent Dsn1:bead ratio (100:1).

Constant-force laser trap assays. To determine if bead-bound kinetochore particles can couple physiologically relevant forces to dynamic microtubule tips, we used a laser trapping-based motility assay^{16–19,39}. Dynamic microtubule extensions were grown from coverslip-anchored GMPCPP-stabilized microtubule seeds in a buffer consisting of BRB80, 1 mg ml^{−1} κ-casein, 1 mM GTP, 250 µg ml^{−1} glucose oxidase, 25 mM glucose, 30 µg ml^{−1} catalase, 1 mM DTT and 1.5 mg ml^{−1} purified bovine brain tubulin. Assays were performed at 23 °C.

The laser trap has been described previously¹⁹. Position sensor response was mapped using the piezo stage to raster-scan a stuck bead through the beam, and trap stiffness was calibrated along the two principle axes using the drag force, equipartition and power spectrum methods. Force feedback was implemented with custom LabView software. During clamping of the force, bead-trap separation was sampled at 40 kHz while stage position was updated at 50 Hz to maintain the desired load. Bead and stage position data were decimated to 200 Hz before storing to disk.

All the wild-type kinetochore particle data shown in Figs 3a, 4 and Supplementary Fig. 9 were recorded using beads prepared at a Dsn1:bead ratio of 200:1 (1.2 nM Dsn1–His–Flag, 5.6 pM beads), well below the single particle limit. The statistics for kinetochore particles presented in Supplementary Fig. 9a, b were calculated from a set of 40 individual events, lasting a total of 11.5 h, during which the particles were subjected to a constant tensile force of 1.9 ± 0.4 pN (mean \pm s.d.). Event duration and travel distance were computed from the instant an attachment was fully loaded until the event ended, often due to bead detachment but sometimes for other reasons (for example, when another bead fell into the trap). All individual event durations and travel distances were averaged, irrespective of how the events ended.

The data for wild-type particles in Fig. 4a and 4c–e were calculated from a set of 170 individual events, lasting a total of 42.5 h, during which the kinetochore particles were subjected to constant tensile forces between 0.3 and 18 pN. This data set included all events used for Fig. 3a and Supplementary Fig. 9, plus an additional 130 events recorded to investigate microtubule dynamics and attachment lifetimes as functions of force. Lifetimes (Fig. 4a) were computed by summing the total time of all events in a given force range and dividing by the number of detachments in that range. Rates of detachment during assembly (Fig. 4c, red) and catastrophe (Fig. 4d, red) were computed by counting the numbers of these events

in a given force range and dividing by the total assembly time in that range. Likewise, rates of detachment during disassembly (Fig. 4c, blue) and rescue (Fig. 4d, blue) were computed by counting events and dividing by the total disassembly time in each force range.

Rupture force measurements. Beads were prepared with kinetochore material at molar ratios ranging from 100 to 10,000 Dsn1 molecules per bead. Individual beads were attached to the ends of growing microtubules and preloaded with a constant tension of 1.1 ± 0.1 pN for the *dad1-1* mutants, or 3.8 ± 0.2 pN for the wild-type kinetochore particles. The laser trap was programmed to subsequently ramp the force at a defined rate (0.25 pN s^{-1}) until the linkage ruptured or the load limit of the trap was reached (20 pN) and the bead escaped from the trap. At all but the highest densities of kinetochore material (that is, below 60 nM Dsn1–His–Flag), a small fraction ($\sim 14\%$) of the beads escaped the trap. Escape was \sim three-fold more likely at 60 nM Dsn1–His–Flag, suggesting that load might be shared by multiple particles at high densities. Note that for the Poisson probability curve in Fig. 4c, the fitting parameter λ accounts for both the number of Dsn1 molecules per particle and the proportion of particles that are geometrically inaccessible to the microtubule, or otherwise inactive.

29. Wigge, P. A. *et al.* Analysis of the *Saccharomyces* spindle pole by matrix-assisted laser desorption/ionization (MALDI) mass spectrometry. *J. Cell Biol.* **141**, 967–977 (1998).
30. Enquist-Newman, M. *et al.* Dad1p, third component of the Duo1p/Dam1p complex involved in kinetochore function and mitotic spindle integrity. *Mol. Biol. Cell* **12**, 2601–2613 (2001).
31. Longtine, M. S. *et al.* Additional modules for versatile and economical PCR-based gene deletion and modification in *Saccharomyces cerevisiae*. *Yeast* **14**, 953–961 (1998).
32. Gelbart, M. E., Rechsteiner, T., Richmond, T. J. & Tsukiyama, T. Interactions of Isw2 chromatin remodeling complex with nucleosomal arrays: analyses using recombinant yeast histones and immobilized templates. *Mol. Cell Biol.* **21**, 2098–2106 (2001).
33. Sikorski, R. S. & Hieter, P. A system of shuttle vectors and yeast host strains designed for efficient manipulation of DNA in *Saccharomyces cerevisiae*. *Genetics* **122**, 19–27 (1989).
34. Pinsky, B. A., Tatsutani, S. Y., Collins, K. A. & Biggins, S. An Mtw1 complex promotes kinetochore biorientation that is monitored by the Ipl1/Aurora protein kinase. *Dev. Cell* **5**, 735–745 (2003).
35. Buvelot, S., Tatsutani, S. Y., Vermaak, D. & Biggins, S. The budding yeast Ipl1/Aurora protein kinase regulates mitotic spindle disassembly. *J. Cell Biol.* **160**, 329–339 (2003).
36. Kitamura, E., Tanaka, K., Kitamura, Y. & Tanaka, T. U. Kinetochore microtubule interaction during S phase in *Saccharomyces cerevisiae*. *Genes Dev.* **21**, 3319–3330 (2007).
37. Gestaut, D. R., Cooper, J., Asbury, C. L., Davis, T. N. & Wordeman, L. Reconstitution and functional analysis of kinetochore subcomplexes. *Methods Cell Biol.* **95**, 641–656 (2010).
38. Rice, S. *et al.* A structural change in the kinesin motor protein that drives motility. *Nature* **402**, 778–784 (1999).
39. Asbury, C. L., Gestaut, D. R., Powers, A. F., Franck, A. D. & Davis, T. N. The Dam1 kinetochore complex harnesses microtubule dynamics to produce force and movement. *Proc. Natl Acad. Sci. USA* **103**, 9873–9878 (2006).

Nanoscale architecture of integrin-based cell adhesions

Pakorn Kanchanawong^{1*}, Gleb Shtengel^{2*}, Ana M. Pasapera¹, Ericka B. Ramko³, Michael W. Davidson^{3,4}, Harald F. Hess² & Clare M. Waterman¹

Cell adhesions to the extracellular matrix (ECM) are necessary for morphogenesis, immunity and wound healing^{1,2}. Focal adhesions are multifunctional organelles that mediate cell–ECM adhesion, force transmission, cytoskeletal regulation and signalling^{1–3}. Focal adhesions consist of a complex network⁴ of trans-plasma-membrane integrins and cytoplasmic proteins that form a <200-nm plaque^{5,6} linking the ECM to the actin cytoskeleton. The complexity of focal adhesion composition and dynamics implicate an intricate molecular machine^{7,8}. However, focal adhesion molecular architecture remains unknown. Here we used three-dimensional super-resolution fluorescence microscopy (interferometric photo-activated localization microscopy)⁹ to map nanoscale protein organization in focal adhesions. Our results reveal that integrins and actin are vertically separated by a ~40-nm focal adhesion core region consisting of multiple protein-specific strata: a membrane-apposed integrin signalling layer containing integrin cytoplasmic tails, focal adhesion kinase and paxillin; an intermediate force-transduction layer containing talin and vinculin; and an uppermost actin-regulatory layer containing zyxin, vasodilator-stimulated phosphoprotein and α -actinin. By localizing amino- and carboxy-terminally tagged talins, we reveal talin's polarized orientation, indicative of a role in organizing the focal adhesion strata. The composite multilaminar protein architecture provides a molecular blueprint for understanding focal adhesion functions.

Modern understanding of cellular function is founded on the revolution in the 1950s to 1970s in visualizing cellular ultrastructure by electron microscopy^{10,11}. Together with the identification of molecular components and their interactions, this has allowed biophysical mechanistic models for organelles such as the actin and microtubule cytoskeletons or the endomembrane transport machinery^{12–15}. In contrast, although there is a wealth of knowledge on the composition, interactions and dynamics of integrin-based focal adhesions, their ultrastructure remains poorly defined. No discernible protein organization pattern has been observed experimentally, either by immunoelectron microscopy⁶ or by two-dimensional super-resolution light microscopy¹⁶. Thus, it is unclear whether focal adhesions are structurally unorganized, or if the relevant structural organization is in the third dimension. Although many cartoon models of focal adhesion protein organization have been proposed based on *in vitro* protein–protein interaction data^{1,2}, true spatial architecture at the ultrastructural level has been impossible to infer. Thus, a mechanistic understanding of focal adhesion function has remained elusive.

To define focal adhesion molecular architecture, we sought to map the nanoscale organization of focal adhesion proteins. This capability has recently been enabled by advances in super-resolution light microscopy (reviewed in ref. 17). We used iPALM⁹, which combines photoactivated localization microscopy¹⁸ with simultaneous multi-phase interferometry of photons from each fluorescent molecule, to image a high density of specific fluorescence-tagged molecules with three-dimensional

nanoscale resolution (Supplementary Fig. 1). We constructed imaging probes with photoactivatable fluorescent proteins (PA-FP, tandem-dimer Eos¹⁹ or monomeric Eos²⁰) fused to focal adhesion proteins, and expressed them in human osteosarcoma (U2OS; Figs 1–3 and Supplementary Figs 1–8 and 11–19) or mouse embryonic fibroblast (MEF; Supplementary Fig. 10) cells plated on fibronectin-coated coverglasses. With iPALM, PA-FP brightness allows localization accuracy of typically 20 nm (full-width at half-maximum) or better in lateral (*xy*) dimensions¹⁸, and 10–15 nm in the vertical (*z*) axis⁹.

We first determined the vertical position of the ventral plasma membrane as a reference point for comparative localization with focal adhesion proteins, using PA-FP targeted to the cytoplasmic face of the plasma membrane via fusion with CAAX sequence. The localizations are represented by iPALM rendering (Fig. 1a) with colours indicating the vertical (*z*) coordinate relative to the coverglass surface (*z* = 0 nm). Focal adhesions near the cell edge appear as yellow regions where the membrane most closely approaches the substrate, with the ventral plasma membrane contour reflected by the colour gradient. Figure 1c shows the side-view (*xz*) projection of a focal adhesion area (red box, Fig. 1a), with the leading-edge plasma membrane also apparent. To quantify the localizations in the focal adhesion area (Fig. 1a, white box), vertical coordinate histograms (Fig. 1b) were fitted by a Gaussian with the centre (z_{centre}) and the width (σ_{vert} ; the standard deviation of the distribution) shown. The width parameter σ_{vert} of ~5 nm demonstrates the spatial resolution, with the positional uncertainty contributed by both the PA-FP brightness limitations¹⁸ and the probe size (~4–5 nm for the PA-FP plus a 25-amino-acid linker). The inner plasma membrane z_{centre} of ~32 nm from the coverglass surface is in good agreement with previous measurements by electron and interference reflection microscopy⁶.

We next used iPALM to determine the three-dimensional localization of integrin cytoplasmic tails which serve as recruiting sites for focal adhesion proteins. We co-expressed integrin α_v PA-FP fusion with untagged integrin β_3 to form integrin $\alpha_v\beta_3$, a fibronectin receptor (Fig. 1d). The vertical position histogram and side-view projection are shown in Fig. 1e. The z_{centre} and σ_{vert} for focal adhesion regions from several cells were quantified, yielding average z_{centre} = 36.8 \pm 4.5 nm and average σ_{vert} = 7.2 \pm 1.8 nm (Fig. 4a, b and Supplementary Table 1), indicating a tightly confined integrin α_v C-terminal position (Supplementary Fig. 6) close to the inner plasma membrane as expected^{1,2}.

To determine the vertical position of actin filaments which link to focal adhesions at stress fibre termini, we performed iPALM with an actin PA-FP probe and analysed focal adhesion regions near the cell edge. In contrast to the integrin localizations, this revealed a broader (average σ_{vert} = 31.0 \pm 8.7 nm) and significantly higher vertical distribution for actin, peaking at average z_{centre} of 96.9 \pm 15.2 nm (Figs 1f, g and 4a, b and Supplementary Table 1), and which was separated from the plasma membrane by a ~40-nm region containing low actin density.

¹National Heart Lung and Blood Institute, National Institutes of Health, Bethesda, Maryland 20892, USA. ²Howard Hughes Medical Institute, Janelia Farm Research Campus, Ashburn, Virginia 20147, USA.

³National High Magnetic Field Laboratory, The Florida State University, Tallahassee, Florida 32310, USA. ⁴Department of Biological Science, The Florida State University, Tallahassee, Florida 32306, USA.

*These authors contributed equally to this work.

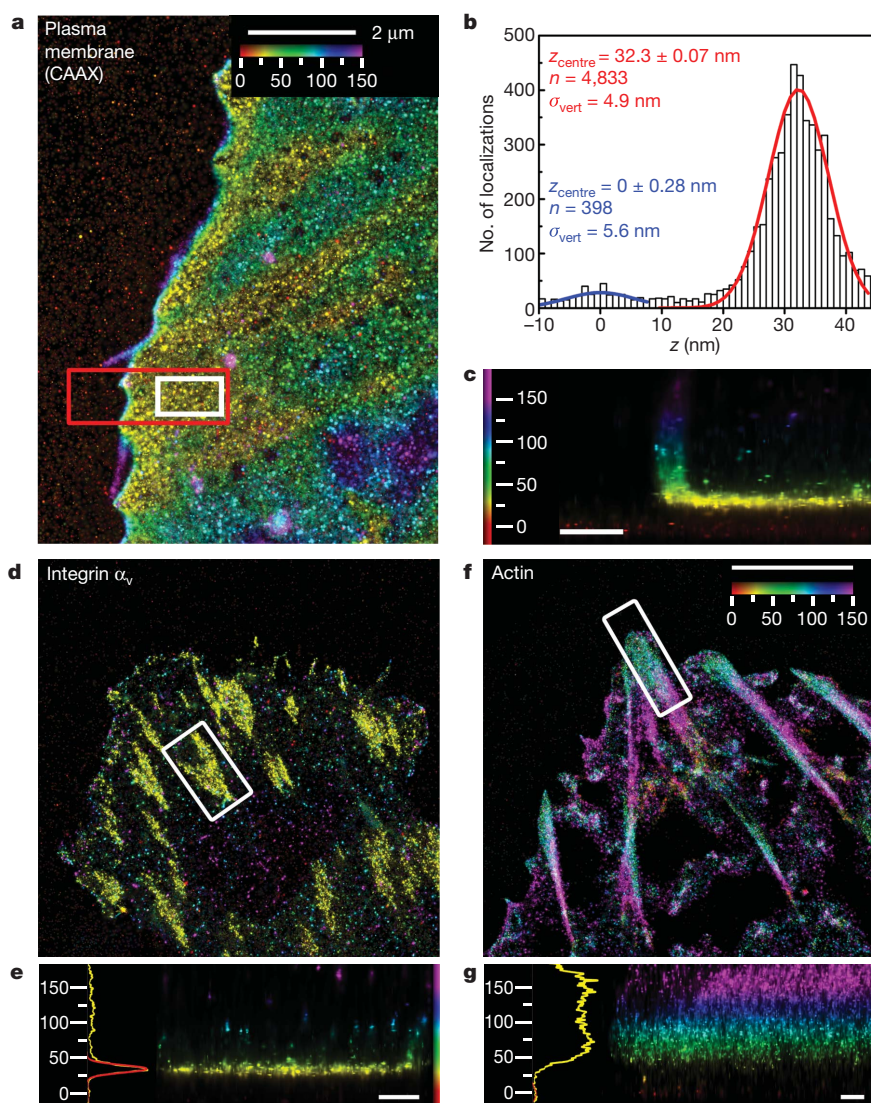


Figure 1 | iPALM imaging of a plasma membrane marker, integrin α_v and actin. **a–c**, Plasma membrane marker CAAX-tdEos. **a**, Top view; **b**, histogram and Gaussian fits for the z positions (white box in **a**) of PA-FP molecules (red) and nonspecific fluorescence adsorbed to substrate (blue); **c**, side view (red box in **a**). **d, e**, Integrin α_v -tdEos. **d**, Top view; **e**, side view (right), histogram and fits

(left). **f, g**, Actin-mEos2. **f**, Top view; **g**, side view (right), histograms and fits (left). The vertical distribution of actin is non-Gaussian, so the focal adhesion peak fit is not shown. Colours in **a, c–g** indicate the vertical (z) coordinate relative to the substrate ($z = 0 \text{ nm}$, red). Scale bars: 500 nm (**c, e, g**).

The observed lack of integrin–actin physical overlap in focal adhesions is consistent with the absence of their binding interactions *in vitro*^{1,2}, and stresses the importance of a ‘focal adhesion core’ domain bridging this gap.

We next sought to determine the nanoscale protein organization within the focal adhesion core domain. We imaged PA-FP fusions of key focal adhesion proteins representing three functional categories: integrin-mediated signalling (focal adhesion kinase (FAK), paxillin); cytoskeletal adaptors (vinculin, zyxin); and actin-regulatory proteins (vasodilator-stimulated phosphoprotein (VASP), α -actinin)^{1–4}. Remarkably, we observed that each protein occupied a distinct and characteristic vertical position within focal adhesions, apparent from their different colours in iPALM images (Fig. 2) and statistics of their vertical localizations (Fig. 4a, b and Supplementary Table 1).

We found that FAK and paxillin were both confined to a narrow plane at average z_{centre} of $36.0 \pm 4.7 \text{ nm}$ and $43.1 \pm 6.1 \text{ nm}$, with average σ_{vert} of $10.0 \pm 2.5 \text{ nm}$ and $8.6 \pm 2.8 \text{ nm}$, respectively (Figs 2a–d and 4a, b). In response to integrin engagement, FAK phosphorylates tyrosine residues on several focal adhesion proteins²¹ including paxillin, a key focal adhesion adaptor protein²². On the basis of their membrane proximity and signalling-related functions, these proteins may comprise

a signalling/adaptor subcompartment of the focal adhesion core, organized by clustered integrins.

In contrast to the membrane-apposed position of integrin signalling proteins, other proteins were localized to distinctly higher vertical positions. The peak of vinculin distribution (average $z_{\text{centre}} = 53.7 \pm 5.5 \text{ nm}$, $\sigma_{\text{vert}} = 13.1 \pm 3.9 \text{ nm}$) coincided with the lower boundary of actin density (Figs 1g and 2f and Supplementary Figs 7, 8 and 14). Vinculin is believed to have a role in reinforcing the connection between ECM and actin²³. Our results indicate that roughly half the vinculin molecules in focal adhesions may overlap with actin whereas the remainder reside lower in the focal adhesion core, positioning vinculin at a key site for regulating force transmission within focal adhesions. On the other hand, zyxin and VASP localized to higher vertical positions, overlapping to a greater degree with actin (zyxin: average $z_{\text{centre}} = 73.2 \pm 8.8 \text{ nm}$, $\sigma_{\text{vert}} = 17.5 \pm 3.5 \text{ nm}$; VASP: average $z_{\text{centre}} = 80.5 \pm 11.6 \text{ nm}$, $\sigma_{\text{vert}} = 23.4 \pm 4.5 \text{ nm}$). Their similar vertical localizations and overlaps with the lower actin boundary are consistent with their cooperative role in actin assembly regulation²⁴. Although α -actinin was present in lamellipodia (Fig. 2k and Supplementary Fig. 17), it was virtually excluded from the focal adhesion core (Fig. 2l; average $z_{\text{centre}} = 103.9 \pm 14.6 \text{ nm}$, $\sigma_{\text{vert}} = 22.8 \pm 5.1 \text{ nm}$) but overlapped fully with actin localizations,

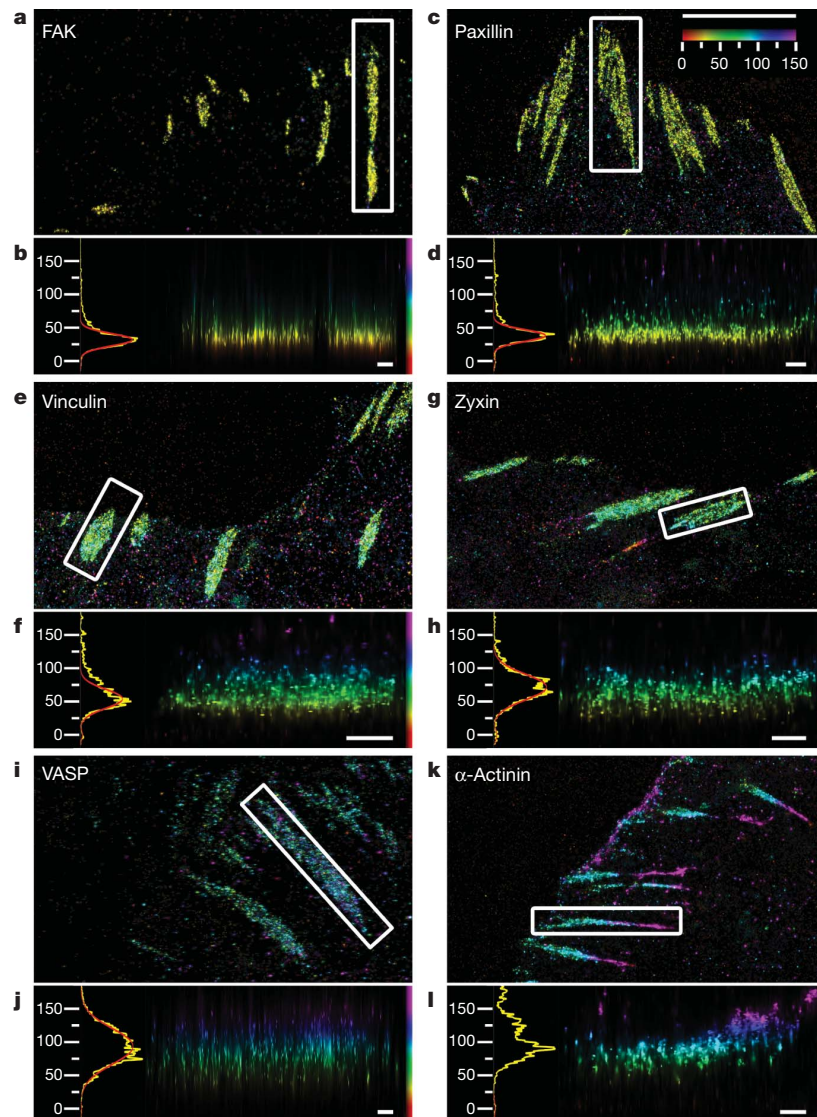


Figure 2 | Protein stratification of the focal adhesion core. Top view and side view iPALM images of focal adhesions (white boxes, top-view panels) and corresponding z histograms and fits. **a, b**, FAK–tdEos; **c, d**, paxillin–tdEos; **e, f**, vinculin–tdEos; **g, h**, zyxin–mEos2; **i, j**, VASP–mEos2; **k, l**, α -actinin–mEos2. The vertical distribution of α -actinin is non-Gaussian, so the focal

adhesion peak fit is not shown. Paxillin and α -actinin shown are C-terminal PA-FP-tagged (N-terminal fusions in Supplementary Figs 21 and 22). Colours: vertical (z) coordinate relative to the substrate ($z = 0$ nm, red). Scale bars: 5 μ m (**a, c, e, g, i, k**) and 500 nm (**b, d, f, h, j, l**).

exhibiting a tapered cross-section profile similar to that of actin stress fibres (Fig. 1 f, g and Supplementary Figs 7 and 8). This supports a role for α -actinin in actin organization at focal adhesions. The lack of overlap between α -actinin and integrin indicates that their interaction^{1,25} may only be transient or regulatory *in vivo*. Taken together, our results reveal the presence of protein-specific strata making up the focal adhesion core, bridging the ~ 40 -nm gap between the integrin cytoplasmic tails and the actin cytoskeleton.

Importantly, we found that the vertical distributions for each focal adhesion component were highly consistent across focal adhesions of diverse size and shape that arise from the continual and asynchronous focal adhesion assembly and maturation occurring in the cell population (Fig. 4a–c and Supplementary Fig. 9). The vertical positions for each focal adhesion component were uncorrelated with the area and morphology (aspect ratio) of focal adhesions, and were also similar between U2OS and MEF cells (Supplementary Figs 9 and 10). This suggests that the observed stratification of focal adhesion proteins represents a cell-type-independent organizing principle that persists throughout focal adhesion maturation stages.

To address the origin of the protein-specific stratified architecture of focal adhesions, we explored the localization and orientation of talin by iPALM. Talin is a large (270-kDa) protein implicated in the initiation of integrin-mediated adhesion and transmission of force between integrin and actin, and which possesses multiple binding sites for focal adhesion proteins including integrin, FAK, paxillin, vinculin and actin²⁶. We thus hypothesized that talin could form tethers that span the integrin–actin gap, thereby serving as a vertically oriented scaffold for the stratified focal adhesion core. To test this, we compared iPALM analyses of talin tagged with PA-FP probes at different sites (Fig. 3a). Both N- and C-terminally tagged talin PA-FP fusions dimerized with endogenous talin and localized to focal adhesions (Supplementary Figs 5 and 20). Imaging talin with the PA-FP probe at the N terminus (talin-N, Fig. 3a) revealed a narrow distribution close to the plasma membrane and similar in position to FAK, paxillin and integrin α_v (Fig. 3b, c; average $z_{\text{centre}} = 42.8 \pm 3.8$ nm; average $\sigma_{\text{vert}} = 9.8 \pm 2.4$ nm). We next probed talin tail position using a C-terminal PA-FP fusion, talin-C, and observed a distinctly different distribution from talin-N (average $z_{\text{centre}} = 76.7 \pm 10.6$ nm; average $\sigma_{\text{vert}} = 15.7 \pm 3.8$ nm;

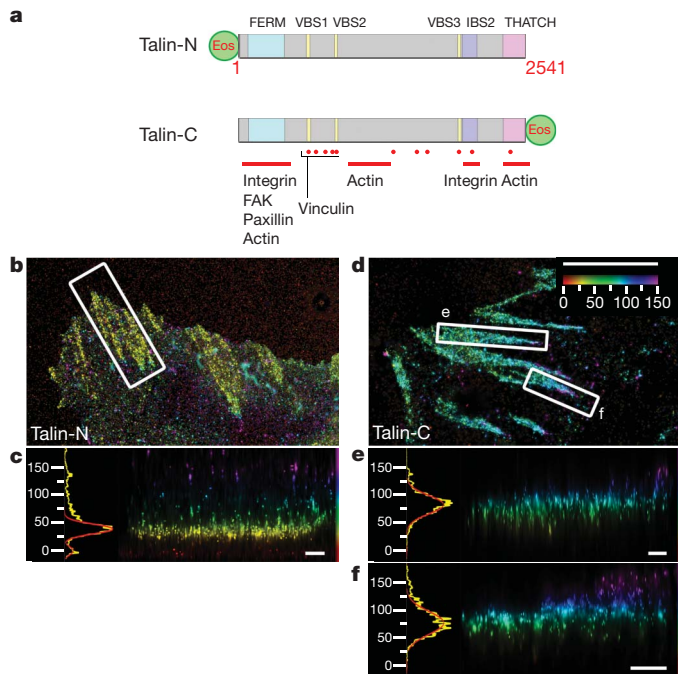


Figure 3 | Talin orientation in focal adhesions. **a**, Schematic diagram, with important domains and binding sites indicated for Talin PA-FP fusions (FERM, protein 4.1, ezrin, radixin, moesin domain; VBS, vinculin binding sequence; IBS, integrin binding site). Talin-N, N-terminal fusion; Talin-C, C-terminal fusion (Supplementary Table 3). **b–f**, Top view and side view iPALM images of focal adhesions (white boxes, top-view panels) and corresponding z histograms and fits for talin-N-tEos (**b**, **c**) and talin-C-tEos (**d**–**f**). Colours: vertical (z) coordinate relative to the substrate ($z = 0$ nm, red). Scale bars: 5 μ m (**b**, **d**) and 500 nm (**c**, **e**, **f**).

Fig. 3d–f), indicating a highly polarized orientation of talin, with the tail vertically displaced by at least 30 nm from the head. The talin tail position also substantially overlapped with those of zyxin, VASP, α -actinin and actin. Although integrin and actin binding sites have been identified throughout the length of talin²⁶, our results indicate that the integrin binding site in the N-terminal head and the C-terminal THATCH domain actin-binding site are the structurally relevant sites in focal adhesions. This is supported by iPALM analyses of talin fragments, which revealed membrane-proximal and upper localizations for the PA-FP-tagged head and THATCH domains, respectively (Supplementary Fig. 11). In contrast to the polarized talin orientation, we were unable to detect vertical polarizations for paxillin or α -actinin PA-FP tagged at either the N or C termini (Fig. 4c and Supplementary Figs 21 and 22). Together with the ~ 50 – 60 nm *in vitro* dimension of talin²⁶, our results indicate that talins are organized into arrays of elongated molecular tethers that diagonally span the stratified focal adhesion core.

Our results demonstrate that focal adhesions possess a surprisingly well-organized molecular architecture in which integrins and actin are separated by a ~ 40 -nm focal adhesion core region that contains multiple partially overlapping protein-specific strata. The stratification probably arises from spatial constraints in protein–protein interactions, but once formed may also impose spatial constraints on protein dynamics within focal adhesions. For example, distribution overlaps between given proteins in a focal adhesion should increase the frequency and duration of their interactions, whereas the lack of overlap indicates that the interactions may be transient or have no direct structural role. Partial overlaps between proteins as well as the width of the protein distributions in focal adhesions may also reflect heterogeneity in protein–protein binding interactions. The focal adhesion protein organization indicates a composite multilaminar architecture made up of at least three spatial and functional compartments that mediate

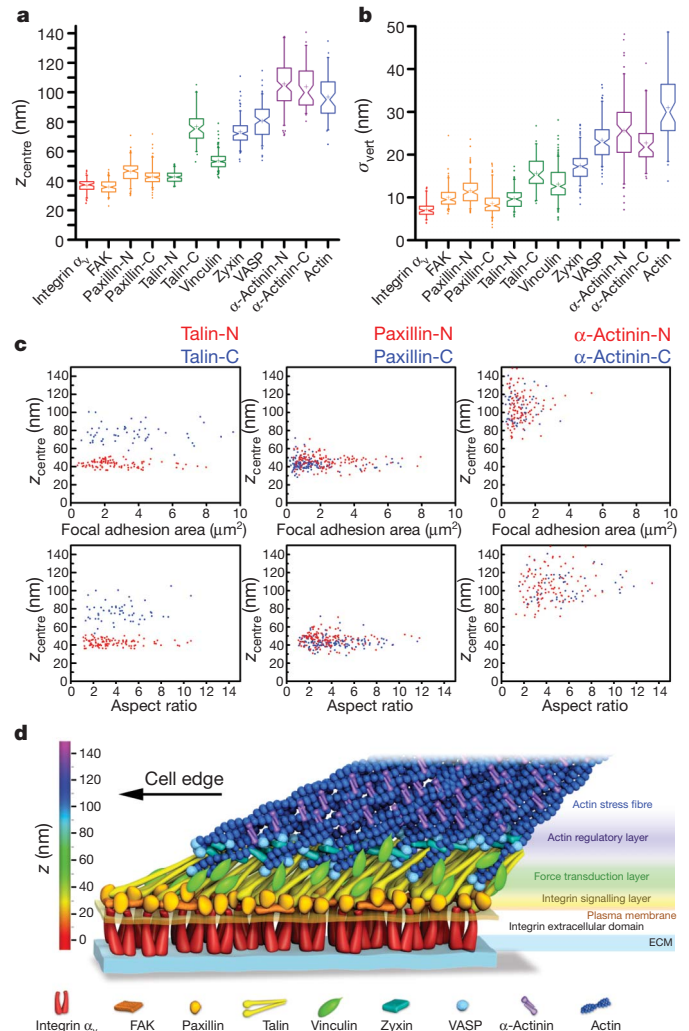


Figure 4 | Nanoscale architecture of focal adhesions. **a**, **b**, Peak position (z_{centre}) (**a**) and width parameter (σ_{vert}) (**b**) of PA-FP fusions in focal adhesions. Notched boxes, 1st and 3rd quartiles, median and confidence interval; whiskers, 5th and 95th percentiles; +, means, outliers also shown. (See also Supplementary Table 1.) **c**, z_{centre} protein positions (nm) versus focal adhesion area (μm^2) or aspect ratio for both N- (red) or C- (blue) terminal fusions of talin, paxillin and α -actinin. Each point corresponds to individual focal adhesion measurements. **d**, Schematic model of focal adhesion molecular architecture, depicting experimentally determined protein positions. Note that the model does not depict protein stoichiometry.

the interdependent functions of focal adhesions: an integrin signalling layer, a force transduction layer, and an actin regulatory layer (Fig. 4d). FAK and paxillin represent a membrane-proximal integrin signalling layer of the focal adhesion core that probably relays integrin–ECM engagement into signalling cascades that control adhesion dynamics and gene transcription^{21,22}. Talin and vinculin are observed in the broader central zone, with talin organized into arrays of diagonally oriented tethers that probably link integrin to actin directly. The distribution of vinculin is consistent with its binding to sites along talin rod domain and actin, which may serve to buttress the integrin–talin–actin linkages. Talin and vinculin have been implicated as regulatable force transmission links between actin and integrins^{23,27–29}. Their positions together thus define the force-transduction layer, signifying a structural basis for the ‘molecular clutch’^{17,27,28} machinery. Finally, the similar vertical localizations of VASP, zyxin and actin filament termini in the uppermost region indicate that a VASP–zyxin complex may comprise an actin regulatory layer involved in focal adhesion strengthening via

actin-barbed-end assembly and stress-fibre enlargement²⁴. α -Actinin appears to localize predominantly along the actin stress fibres where it may mediate their formation through actin filament cross-linking activity²⁵.

The observed molecular architecture also indicates how mechanical force may be essential for focal adhesion formation and maintenance^{1–3}. The diagonal talin orientation could arise from actomyosin pulling of the talin tails relative to the integrin-bound talin heads, with the resulting intramolecular tension straightening or stretching the talin. Subsequently, distinct sites along the length of talin may serve as spatial templates giving rise to the observed protein-specific stratification in focal adhesions. Further stretching of talin is also indicated in iPALM images of some focal adhesions (Fig. 3d, f), where a fraction of talin-C localizations extend significantly upward in the proximal end of focal adhesions, implying a head-to-tail length greater than the nominal talin length of 50–60 nm. Stretching of talin rod fragment has been shown to unmask cryptic vinculin binding sites³⁰, consistent with the observed talin and vinculin positions. Thus, via stretch-induced recruitment, talin may effectively serve as a molecular ruler that specifies focal adhesion molecular architecture.

METHODS SUMMARY

iPALM imaging. The principle and instrumentation for iPALM were described previously⁹ (see also Supplementary Fig. 1 and Supplementary Note 1). Gold nanoparticles (80–100 nm) immobilized to the coverglass were used as fiducials for calibration and drift correction. The vertical coordinate calibration was performed before each cell was imaged. For each cell, 25,000–75,000 image triplets were acquired, with 50 ms per frame exposure time, yielding $\sim 10^6$ localizations. Vertical coordinates relative to the coverglass surface are indicated by a colour scale from red to purple ($z = 0$ –150 nm). All side-view panels are shown with similar vertical scale and oriented with the nearest cell edge to the left.

Cell culture and fluorescent protein constructs. PA-FP protein fusions were constructed with green-to-red photoconvertible fluorescent protein, tandem-dimer Eos (tdEos)¹⁹ or monomeric Eos2 (mEos2)²⁰ fused to focal adhesion proteins via short linkers (Supplementary Table 3 and Supplementary Note 3). Fusion proteins were expressed in U2OS or MEF cells sparsely plated on fibronectin-coated, fiducial coverglasses, and fixed for imaging ~ 18 h after re-plating.

Analysis of protein positions. The histogram of vertical localization coordinates was calculated for each focal adhesion region. The local $z = 0$ nm level was defined by nonspecific fluorescence from the media that adsorbed to the coverglass, and was used to account for sample tilt. The centre positions (z_{centre}) and width parameter (σ_{vert}) were calculated from Gaussian fits or from the first and second moment of the distributions for non-Gaussian cases such as actin and α -actinin. For more detailed information see Methods and Supplementary Information.

Full Methods and any associated references are available in the online version of the paper at www.nature.com/nature.

Received 9 March; accepted 28 October 2010.

- Burridge, K. & Chrzanowska-Wodnicka, M. Focal adhesions, contractility, and signaling. *Annu. Rev. Cell Dev. Biol.* **12**, 463–518 (1996).
- Geiger, B., Bershadsky, A., Pankov, R. & Yamada, K. M. Transmembrane crosstalk between the extracellular matrix-cytoskeleton. *Nature Rev. Mol. Cell Biol.* **2**, 793–805 (2001).
- Bershadsky, A. D., Balaban, N. Q. & Geiger, B. Adhesion-dependent cell mechanosensitivity. *Annu. Rev. Cell Dev. Biol.* **19**, 677–695 (2003).
- Zaidel-Bar, R. *et al.* Functional atlas of the integrin adhesome. *Nature Cell Biol.* **9**, 858–867 (2007).
- Franz, C. M. & Muller, D. J. Analyzing focal adhesion structure by atomic force microscopy. *J. Cell Sci.* **118**, 5315–5323 (2005).
- Chen, W. T. & Singer, S. J. Immunoelectron microscopic studies of the sites of cell-substratum and cell-cell contacts in cultured fibroblasts. *J. Cell Biol.* **95**, 205–222 (1982).

- Wang, Y. L. Flux at focal adhesions: slippage clutch, mechanical gauge, or signal depot. *Sci. STKE* **2007**, pe10 (2007).
- Lauffenburger, D. A. & Horwitz, A. F. Cell migration: a physically integrated molecular process. *Cell* **84**, 359–369 (1996).
- Shtengel, G. *et al.* Interferometric fluorescent super-resolution microscopy resolves 3D cellular ultrastructure. *Proc. Natl Acad. Sci. USA* **106**, 3125–3130 (2009).
- Palade, G. E. & Porter, K. R. Studies on the endoplasmic reticulum. I. Its identification in cells *in situ*. *J. Exp. Med.* **100**, 641–656 (1954).
- Ledbetter, M. C. & Porter, K. R. A “microtubule” in plant cell fine structure. *J. Cell Biol.* **19**, 239–250 (1963).
- Patterson, G. H. *et al.* Transport through the Golgi apparatus by rapid partitioning within a two-phase membrane system. *Cell* **133**, 1055–1067 (2008).
- Liu, J., Kaksonen, M., Drubin, D. G. & Oster, G. Endocytic vesicle scission by lipid phase boundary forces. *Proc. Natl Acad. Sci. USA* **103**, 10277–10282 (2006).
- Keren, K. *et al.* Mechanism of shape determination in motile cells. *Nature* **453**, 475–480 (2008).
- Pollard, T. D. & Berro, J. Mathematical models and simulations of cellular processes based on actin filaments. *J. Biol. Chem.* **284**, 5433–5437 (2009).
- Shroff, H. *et al.* Dual-color superresolution imaging of genetically expressed probes within individual adhesion complexes. *Proc. Natl Acad. Sci. USA* **104**, 20308–20313 (2007).
- Hell, S. W., Schmidt, R. & Egner, A. Diffraction-unlimited three-dimensional optical nanoscopy with opposing lenses. *Nature Photon.* **3**, 381–387 (2009).
- Betzig, E. *et al.* Imaging intracellular fluorescent proteins at nanometer resolution. *Science* **313**, 1642–1645 (2006).
- Wiedenmann, J. *et al.* A fluorescent marker protein with UV-inducible green-to-red fluorescence conversion. *Proc. Natl Acad. Sci. USA* **101**, 15905–15910 (2004).
- McKinney, S. A. *et al.* A bright and photostable photoconvertible fluorescent protein. *Nature Methods* **6**, 131–133 (2009).
- Mitra, S. K., Hanson, D. A. & Schlaepfer, D. D. Focal adhesion kinase: in command and control of cell motility. *Nature Rev. Mol. Cell Biol.* **6**, 56–68 (2005).
- Brown, M. C. & Turner, C. E. Paxillin: adapting to change. *Physiol. Rev.* **84**, 1315–1339 (2004).
- Galbraith, C. G., Yamada, K. M. & Sheetz, M. P. The relationship between force and focal complex development. *J. Cell Biol.* **159**, 695–705 (2002).
- Yoshigi, M. *et al.* Mechanical force mobilizes zyxin from focal adhesions to actin filaments and regulates cytoskeletal reinforcement. *J. Cell Biol.* **171**, 209–215 (2005).
- Otey, C. A. & Carpen, O. Alpha-actinin revisited: a fresh look at an old player. *Cell Motil. Cytoskeleton* **58**, 104–111 (2004).
- Critchley, D. R. Biochemical and structural properties of the integrin-associated cytoskeletal protein talin. *Annu. Rev. Biophys.* **38**, 235–254 (2009).
- Hu, K. *et al.* Differential transmission of actin motion within focal adhesions. *Science* **315**, 111–115 (2007).
- Brown, C. M. *et al.* Probing the integrin-actin linkage using high-resolution protein velocity mapping. *J. Cell Sci.* **119**, 5204–5214 (2006).
- Jiang, G. *et al.* Two-piconewton slip bond between fibronectin and the cytoskeleton depends on talin. *Nature* **424**, 334–337 (2003).
- del Rio, A. *et al.* Stretching single talin rod molecules activates vinculin binding. *Science* **323**, 638–641 (2009).

Supplementary Information is linked to the online version of the paper at www.nature.com/nature.

Acknowledgements We thank J. Lippincott-Schwartz, G. Patterson and M. Parsons for sharing DNA; S. Xie for help with automation software; K. Jaqaman for MATLAB code; and HHMI Janelia Farm Scientific Computing and NIH Helix systems for computing resources. Funding: Division of Intramural Research, NHLBI (P.K., A.M.P. and C.M.W.); Howard Hughes Medical Institute (G.S. and H.F.H.).

Author Contributions P.K. and G.S. collected data and performed data analyses. G.S. and H.F.H. designed and built the instrument. A.M.P. performed immunoprecipitation and western blot experiments. E.B.R. and M.W.D. created expression constructs. P.K., C.M.W., G.S., H.F.H., M.W.D. and A.M.P. wrote the manuscript. P.K. and G.S. contributed equally to the study. All authors discussed the results and commented on the manuscript.

Author Information Reprints and permissions information is available at www.nature.com/reprints. The authors declare no competing financial interests. Readers are welcome to comment on the online version of this article at www.nature.com/nature. Correspondence and requests for materials should be addressed to C.M.W. (watermancm@nhlbi.nih.gov), H.F.H. (hessh@janelia.hhmi.org) or M.D.W. (davidson@magnet.fsu.edu).

METHODS

Preparation of fiducial coverglasses for cell culture. Fluorescent fiducials are critical for iPALM because they provide a constant internal reference for calibration, tracking and spatial drift correction. As described previously⁹, we use the plasmonic emission³¹ from 80 to 100 nm gold (Au) nanoparticles sparsely adsorbed ($\sim 2,000$ per mm^2) to the coverglass surface and immobilized by 30–50 nm of sputtered SiO_2 . Although gold nanoparticles can be added after cell attachment, their rigid immobilization is critical for high localization accuracy, and additionally allows optimization of proper fiducial density before cell culture. Fiducial coverglasses were ultraviolet-sterilized (15 min), rinsed with Dulbecco's phosphate buffered saline (DPBS, Invitrogen), incubated at 4 °C overnight with 10 $\mu\text{g ml}^{-1}$ (U2OS) or 1 $\mu\text{g ml}^{-1}$ (MEF) human plasma fibronectin (FC010-5MG, Chemicon International), and incubated with 1% heat-inactivated bovine serum albumin (A3059, Sigma) (1 h, 37 °C) before a final rinse with DPBS.

Cell culture and imaging sample preparation. U2OS (human osteosarcoma) cells were cultured in supplemented McCoy5A media (10% fetal bovine serum (FBS), 2 mM glutamine, and 100 units ml^{-1} of penicillin/streptomycin, Invitrogen). Mouse embryonic fibroblast (MEF) cells were cultured in supplemented DMEM media (10% FBS, 2 mM glutamine and 100 units ml^{-1} of penicillin/streptomycin). Cells were transfected by nucleofection with endotoxin-free expression vector DNA (U2OS, $\sim 0.2\text{--}1$ μg per $\sim 1 \times 10^6$ cells; MEF, 5–6 μg per $\sim 2\text{--}3 \times 10^6$ cells) per the manufacturer's protocol (Lonza). Transfected cells were cultured overnight, replated onto fiducial coverglasses, and incubated at 37 °C, 5% CO_2 . Cells were replated at a sparse density of $\sim 60\text{--}100$ cells mm^{-2} and fixed for imaging ~ 18 h after replating. At 18 h, most focal adhesions have not transformed into fibrillar adhesions, which are associated with fibronectin bundles that would affect the measurement of protein position relative to the substrate. Phenol-red free media was used to minimize background fluorescence. Cells were fixed with 2% paraformaldehyde and imaged in PHEM buffer (PIPES 60 mM, HEPES 25 mM, EGTA 10 mM, MgCl_2 2 mM, pH 6.9). Imaging chambers (thickness ~ 10 μm) were assembled from the 18-mm cell-containing fiducial coverglass and a 25-mm coverglass and sealed with 5-min epoxy (ITW Performance Polymers) and vaseline (Unilever). We imaged focal-adhesion-containing lamella areas, typically no greater than 15–20 μm from the cell edge, that also contained several fiducials for calibration and drift correction.

iPALM data acquisition and image processing. Imaging samples prepared as described above were mounted onto a piezo-electric-equipped sample holder. The optical configuration is described in Supplementary Note 1. Both top and bottom objectives were brought into focus and aligned using the images of the gold fiducials immobilized on the coverglass. The z -positions of the gold fiducials were determined and optimized for proper focus and interference modulation. This was carried out by piezo-based fine tuning of beamsplitter and mirror positions, while monitoring the z -calibration curve as described in detail below. Once the sample was in good initial alignment, the sample was translated laterally to find suitable cells for imaging. We imaged low-level expressing cells to avoid biological over-expression artefacts and to minimize background that can contribute to lower localization accuracy.

Once cells were located, the setup was fine-tuned until a z -calibration curve with an optimal modulation was attained and recorded. Key steps for the calibration are illustrated in Supplementary Fig. 1, with the fiducial positions shown in Supplementary Fig. 1c (inset: summed raw intensity data for calibration sets; main: iPALM image, note that fiducials are not prominent because the render program treats each fiducial as a single particle). The z -calibration data set was measured at 8-nm intervals as the sample was translated along the z -axis using piezo-electric translation stages (Physik Instrumente). This resulted in an intensity modulation between the three cameras due to interferometric effect⁹, as shown in Supplementary Fig. 1d for fiducial F1. To align the three-camera triplet of images for analysis, the coordinates of multiple fiducials were determined for each camera, using one camera image as reference. The similarity transformations for two other cameras with respect to the reference camera were determined using linear regression, and applied to the respective camera images to align them to the reference.

To extract calibration parameters, each of the molecule images in each frame of the triplet series was fit to a two-dimensional Gaussian, yielding Gaussian amplitudes $I_k(z)$, where $k = 1, 2, 3$, as plotted in Supplementary Fig. 1d for fiducial F1. Then a least square fit was used to determine the dependence of these amplitudes on z -coordinate according to the equation:

$$I_k = \frac{A_k \sin(\omega z + \phi_k) + B_k}{1 + (z/D)^2}, \quad k = 1, 2, 3 \quad (1)$$

This yielded a set of z -calibration coefficients: $\omega, D, A_k, \phi_k, B_k, k = 1, 2, 3$. The variable D in the denominator accounts for focal envelope function. A calibration curve and coefficients extracted for fiducial F1 are shown in Supplementary Fig. 1d, e.

Subsequently, we applied Newton's method³² to extract the z -coordinate of each fluorescent molecule or fiducial. This method finds a value of molecular z -coordinate by minimizing the difference between the intensities calculated by equation (1) using the calibration parameters (for example, Supplementary Fig. 1e) and the measured two-dimensional Gaussian amplitudes from the data triplet. Performing this procedure on the calibration set also provides a check for calibration quality and consistency, as shown in Supplementary Fig. 1f, where the extracted z position (diamonds) for fiducials F1–4 are compared to the actual sample z position (solid lines).

During the main acquisition sequences, each frame triplet contained images of a few individual fluorescent proteins that emitted during each frame imaging interval. The activation power (405 nm) was adjusted so that these individual fluorescent proteins were sparsely distributed and their images did not overlap. The localization procedure consisted of the following steps: (1) the individual camera images were aligned by applying the similarity transformations determined from previously recorded images of multiple fiducials in each camera, as described above; (2) these three aligned images of each fluorescent particle from a given frame triplet were added together to form a sum image; (3) the fluorescent particle in each sum image was fit to a two-dimensional Gaussian by nonlinear least-square fitting to obtain x and y coordinates; (4) each individual camera image in the triplet was also fit to a two-dimensional Gaussian, yielding amplitudes I_k , $k = 1, 2, 3$, which were used to extract the z -coordinate of each fluorescent molecule from equation (1) and the calibration parameters, using Newton's method as described above. The refractive index difference between the calibration data (when the sample was translated, the varying path-length difference between the two arms is in immersion oil, $n \sim 1.52$) and main acquisition (sample was stationary, $n \sim 1.40$ for cell) was accounted for by applying appropriate linear scaling. (5) Sample drift was corrected using the fiducial localizations. Lateral sample drift during all measurements was significantly lower than the lateral localization accuracy, which was typically ~ 20 nm full-width at half-maximum. The vertical (z -coordinate) sample drift in all measurements varied between 10 nm and 50 nm over the course of the measurements. The vertical drift was traced by determining in each frame the z -position of the same gold fiducials as were used for z -calibration. This drift was then subtracted from z -coordinates of all fluorescent particles. The residual z -coordinate uncertainty was typically less than 5 nm.

Typical measurements consisted of 25,000–75,000 image triplets (Supplementary Table 4) with the exposure time of 50 ms per frame; the 5–30-ms activation pulses were transmitted between the excitation pulses. Imaging parameters for iPALM data sets are summarized in Supplementary Table 4. Data acquisition was carried out using software written in LABVIEW (National Instruments). Data analysis and image processing was performed using software written in IDL (ITT Visual Information Solutions) and run on a Linux computational cluster at HHMI Janelia Farm Research Campus.

As described previously⁹, iPALM images were rendered from the processed list of three-dimensional molecular coordinates: the position and localization uncertainty of each localization is represented by a normalized two-dimensional Gaussian, whose width is proportional to localization uncertainty. Note that the lists of molecular coordinates were used for quantitative analysis, rather than the rendered images. For top-view (x, y) images, each molecule was represented by a normalized two-dimensional Gaussian. The width of the Gaussian is the positional uncertainties (σ_x, σ_y) of the calculated x, y position as described previously³³. The z -coordinate is encoded by colour. For side-view images, the molecule was also rendered by a normalized two-dimensional Gaussian, but with the vertical width corresponding to σ_z , the vertical uncertainty. Because the vertical (z) resolution is ~ 2 times better than xy , σ_z is also ~ 2 times smaller. A gamma of 0.5 (top view) and 0.75 (side view) was used to compress the tonal range of iPALM images to within the dynamic range of print and computer monitor.

A single colour scheme was used from red to purple, covering the range from $z = 0$ nm to $z = 150$ nm, where features within focal adhesions are seen. The same colour scheme was also used for side-view (xz) or (yz) image. Typically, the raw processed coordinates exhibited a minor tilt of $< 30\text{--}50$ nm over the image field of ~ 50 μm across, due to sample tilt or optical alignments. These were corrected by simple coordinate rotation to achieve a flat vertical substrate level, which was set to $z = 0$ nm for the z -colour-coded image rendering. For quantification of focal adhesion areas, local background level was used to control for long-range variations as described below.

Analysis of protein distributions in focal adhesions: z_{centre} and σ_{vert} calculation. iPALM localization data records both the fluorescent molecules localized within the focal adhesions as well as molecules in the cytoplasmic fraction and autofluorescent molecules inside and outside the cells. To quantify the spatial distribution of the proteins specifically residing within individual focal adhesion regions, we created binary region masks from top-view iPALM images, as depicted

in Supplementary Fig. 3. These areas covered the focal adhesion and immediately surrounding space, primarily for the quantification of the local substrate background level. A program written in Java as an ImageJ (NIH) plug-in was used to export the three-dimensional molecular coordinates for each region into separate files, which were subsequently analysed using a program written in LABVIEW. A histogram of vertical positions was calculated with 1-nm bins. The centre vertical positions (z_{centre}) and width parameter (standard deviation of the vertical coordinate distributions, σ_{vert}) which relates to full-width at half-maximum (FWHM) by: $\text{FWHM} = 2.35\sigma_{\text{vert}}$ were determined from a Gaussian fit to the focal adhesion molecule peak. In addition to the main peak, we also typically observed a smaller peak of substrate surface autofluorescent molecules. The observed background molecules probably originate from autofluorescence present in cell culture media, such as from fetal bovine serum and other trace contaminants³⁴ and were primarily localized to the coverglass surface because non-surface-adsorbed background molecules diffuse too rapidly to be visualized as single molecules. We defined the z_{centre} of the local substrate distribution as the $z = 0$ nm for each adhesion region. Because the substrate fluorescence density is low, typically the regional mask included the focal adhesion as well as a small surrounding region of a few square micrometres for good statistics. This local background provided an internal $z = 0$ nm reference that controls for long-range vertical variation due to sample tilt or optical field curvature. Gaussian fitting used the least-absolute-residuals minimizing algorithm in LABVIEW. Most focal adhesion proteins exhibited Gaussian-like peaks, except for actin and α -actinin which extend into the stress fibre, instead of localizing as well-defined layers. Thus, to quantify their positions for comparison with other proteins, we calculated the z_{centre} and the width parameter (σ_{vert}) as the first moment

$$z_{\text{centre}} = \frac{\sum_i f(z_i)z_i}{N} \quad \text{and second moment} \quad \sigma_{\text{vert}} = \sqrt{\frac{\sum_i f(z_i)(z_i - z_{\text{centre}})^2}{N}},$$
 respectively, where N denotes the total number of molecules, z_i denotes the z values for each histogram bin, i indexes the histogram z -bins, and $f(z_i)$ denotes the histogram of

z position. The statistics for the average z_{centre} and σ_{vert} are shown in Fig. 4a, b and Supplementary Table 1. Fit parameters to individual focal adhesion regions in Figs 1–3 are shown in Supplementary Table 2.

Analysis of z_{centre} and focal adhesion morphologies. To determine whether a relationship existed between focal adhesion protein vertical position and focal adhesion morphology, we quantified morphometric properties of focal adhesions. We first calculated image maps of the number-density and average z position from the molecule coordinates measured by iPALM, using a 33×33 nm² bin size. Programs written in MATLAB (Mathworks) were used to segment the areas corresponding to focal adhesions, calculate the areas, and measure the major and minor axes of the best-fit ellipse. The plots of protein position (z_{centre}) as a function of focal adhesion size (area in μm^2) or aspect ratio (major divided by minor axes), as well as correlation coefficients, are shown in Fig. 4c and Supplementary Figs 9, 21c and 22c. These plots also indicate the range of focal adhesion size and shape (aspect ratio of round focal adhesion = 1, and >1 for elongated focal adhesions) that were observed. As seen by the size distribution and as noted earlier, most regions analysed correspond to focal adhesion by previously defined morphometric criteria³⁵ (area $<8 \mu\text{m}^2$, aspect ratio <7). Note that small nascent adhesions were omitted if there was not sufficient background localization to allow accurate determination of local substratum level.

31. Dulkeith, E. *et al.* Plasmon emission in photoexcited gold nanoparticles. *Phys. Rev. B* **70**, 205424 (2004).
32. Press, W. H., Flannery, P. P., Teukolsky, S. A. & Vetterling, W. T. *Numerical Recipes* (Cambridge Univ. Press, 1986).
33. Thompson, R. E., Larson, D. R. & Webb, W. W. Precise nanometer localization analysis for individual fluorescent probes. *Biophys. J.* **82**, 2775–2783 (2002).
34. Aubin, J. E. Autofluorescence of viable cultured mammalian cells. *J. Histochem. Cytochem.* **27**, 36–43 (1979).
35. Zamir, E. *et al.* Molecular diversity of cell-matrix adhesions. *J. Cell Sci.* **112**, 1655–1669 (1999).

The amino-terminal disease hotspot of ryanodine receptors forms a cytoplasmic vestibule

Ching-Chieh Tung¹, Paolo A. Lobo¹, Lynn Kimlicka¹ & Filip Van Petegem¹

Many physiological events require transient increases in cytosolic Ca^{2+} concentrations. Ryanodine receptors (RyRs) are ion channels that govern the release of Ca^{2+} from the endoplasmic and sarcoplasmic reticulum¹. Mutations in RyRs can lead to severe genetic conditions that affect both cardiac and skeletal muscle, but locating the mutated residues in the full-length channel structure has been difficult^{2,3}. Here we show the 2.5 Å resolution crystal structure of a region spanning three domains of RyR type 1 (RyR1), encompassing amino acid residues 1–559. The domains interact with each other through a predominantly hydrophilic interface. Docking in RyR1 electron microscopy maps^{4,5} unambiguously places the domains in the cytoplasmic portion of the channel, forming a 240-kDa cytoplasmic vestibule around the four-fold symmetry axis. We pinpoint the exact locations of more than 50 disease-associated mutations in full-length RyR1 and RyR2. The mutations can be classified into three groups: those that destabilize the interfaces between the three amino-terminal domains, disturb the folding of individual domains or affect one of six interfaces with other parts of the receptor. We propose a model whereby the opening of a RyR coincides with allosterically coupled motions within the N-terminal domains. This process can be affected by mutations that target various interfaces within and across subunits. The crystal structure provides a framework to understand the many disease-associated mutations in RyRs that have been studied using functional methods, and will be useful for developing new strategies to modulate RyR function in disease states.

Ryanodine receptors are large (~2.2 MDa) tetrameric channels that control the release of Ca^{2+} from the endoplasmic and sarcoplasmic reticulum. Three isoforms (RyR1, RyR2 and RyR3) have been isolated in mammalian organisms. Excitation–contraction coupling primarily relies on RyR1 in skeletal muscle and RyR2 in cardiac muscle¹. Because Ca^{2+} is a potent messenger, the mishandling of Ca^{2+} release owing to point mutations in either isoform can lead to severe genetic diseases, including malignant hyperthermia, central core disease and multi-minicore disease for RyR1, and heart disorders such as catecholaminergic polymorphic ventricular tachycardia and arrhythmogenic right ventricular dysplasia for RyR2 (ref. 2). With a few exceptions, the point substitutions cluster in three distinct mutation ‘hotspots’³. RyRs are activated by Ca^{2+} , and most disease-associated mutations that have been analysed so far introduce a gain of function, either increasing the sensitivity of the RyR to activators or producing a leaky channel, or both⁶. Owing to the limited availability of high-resolution structures, a mechanistic description of the effect of the disease-associated mutations has been lacking.

To gain further insight into RyR function in physiological and disease states, we solved the 2.5 Å crystal structure of a 62-kDa region of rabbit RyR1 (amino acid residues 1–559) that covers most of the N-terminal hotspot (Fig. 1 and Supplementary Fig. 1). The structure was refined to a final R_{cryst} and R_{free} of 20.9% and 23.4%, respectively. The construct folds into three separate domains (A, B and C) that interact with each other through a mainly hydrophilic interface (Supplementary Table 1). Domain A (amino acid residues 1–205) forms a β -trefoil domain with

an additional α -helix, consistent with previous findings^{7,8}. Domain B (residues 206–394) forms another β -trefoil domain, whereas domain C (residues 395–532) forms a bundle of five α -helices. The carboxy-terminal 27 residues are not visible in the electron density and might be part of another domain. The domain interfaces cover a surface of 1,687 Å², of which 517 Å² is hydrophobic (Supplementary Table 1).

Cryo-electron microscopy (cryo-EM) studies have shown full-length RyR1 images at ~10 Å resolution^{4,5,9}. The availability of a crystal structure with more than 22,000 Å² of surface area enabled us to locate the 62-kDa N-terminal region unambiguously in the full-length RyR1 structure^{10,11}. The N-terminal domains are located in the cytoplasmic portion of the channel, forming a vestibule around the four-fold axis (Fig. 2, Supplementary Fig. 2 and Supplementary Movie 1).

To prove this result, we split the crystal structure into two parts (domain A and domain BC) and performed independent docking experiments with each part. Both parts dock to the same site and recapitulate the A–BC interface with near perfection (Fig. 2c). Given the vast number of possible orientations and locations of individual domains in a large cryo-EM map, the probability of reconstituting the crystal structure through chance is infinitesimally small (see Supplementary Discussion). In addition, the same position of the N-terminal domains is obtained with a very high docking contrast using three RyR1 maps of different resolution (9.6 Å, 10.3 Å and 14 Å)^{4,5,12}.

The apparent contradiction with other mapping studies^{13–15} probably results from the low resolution (~34 Å) in those experiments, combined with the use of long linkers and the size of the insertion proteins, which allow a difference density of >80 Å away from the insertion site. In this study, the docking was performed using a Laplacian filter^{11,16}, which was strictly required for the docking of individual parts of the structure. We suggest that this filtering approach be considered in future docking experiments of RyR domains and that a value for the docking contrast be reported. A complete validation of the docking and its relationship to previous attempts to locate the N-terminal region are available in the Supplementary Discussion. The docking shows that at least part of the intersubunit boundaries differs from those proposed previously¹⁷.

We mapped the positions of 33 disease-associated mutations in RyR1 and of 23 such mutations in RyR2 onto the RyR1 ABC structure (Fig. 3 and Supplementary Fig. 3). The positions can be grouped into three categories: those that are completely buried within a domain and thus probably cause local misfolding of the domain (6 mutations); those that lie at the interfaces between domains A, B and C within a subunit and thus probably destabilize the domain interactions (15 mutations); and those at interfaces with other RyR domains (35 mutations), including interfaces across subunits (Supplementary Table 2). Despite the presence of a large solvent-exposed surface area of the three domains within full-length RyR1, all mutations are either buried or at domain–domain interfaces. No mutations are simply exposed to solvent, where they would be less likely to cause a functional change, which further underlines the validity of the docking results (see also Supplementary Discussion).

Several mutations are concentrated at the boundary between domains A and C. This interface consists of a series of hydrogen-bonding and

¹Department of Biochemistry and Molecular Biology, University of British Columbia, Vancouver, British Columbia V6T 1Z3, Canada.

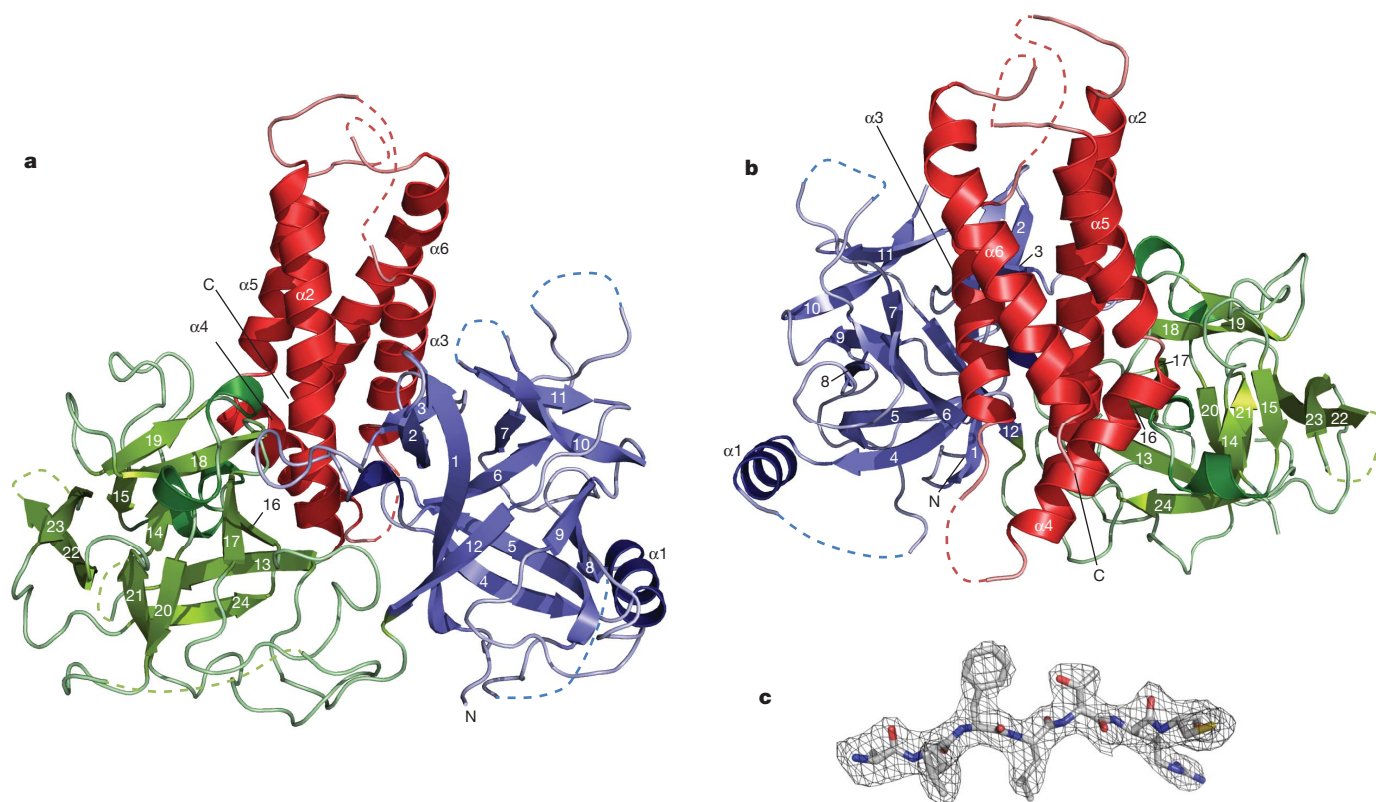


Figure 1 | Overall structure of the RyR1 A, B and C domains. **a**, Overall structure of rabbit RyR1 for amino acid residues 1–559. This portion of RyR1 consists of domain A (blue; 1–205), domain B (green; 206–394) and domain C (red; 395–532). The remaining 27 residues are not visible in the electron

charge-coupling interactions, including the amino acid R45 in domain A with D447 in domain C, and D61 and E40 in domain A with R402 in domain C (Fig. 3b). Both ionic pairs are the target of RyR1 mutations, through substitutions of R45, D61 and R402 (the residue numbering for rabbit RyR1 is used throughout for all disease-associated mutations) (Supplementary Table 2). Gel filtration and thermal melt experiments on the disease-associated RyR1 ABC mutant R402G (in which arginine has been substituted with glycine at position 402) show that this change does not cause overall misfolding but decreases the overall melting

density. Flexible loops are shown as dashed lines. For reference, α -helices ($\alpha 1$ – $\alpha 6$) and β -strands (1–24) are numbered. **b**, Different view of **a**. **c**, Typical omit difference density map in a randomly selected region, contoured at 3σ .

temperature by $>5^\circ\text{C}$ (Supplementary Fig. 4). It is therefore highly likely that this substitution simply destabilizes the A–C interface.

We have identified six individual interfaces between other parts of RyR1 and the A, B and C domains (Fig. 3c and Supplementary Fig. 3). One of these involves contacts with domains A and B across subunits (denoted interface 1). Depending on the cryo-EM map used, the domains are separated by a gap of ~ 5 – 11 Å, which can easily be bridged by two flexible loops in domain B (Fig. 3c). This variability in gap size may be due to differences in conformational purity of the

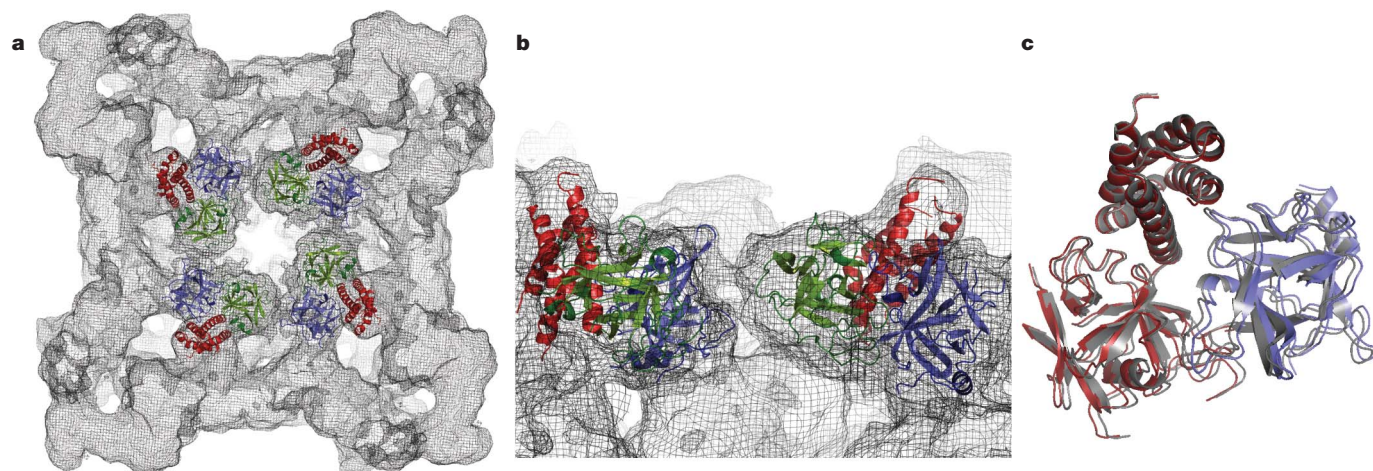


Figure 2 | Docking of RyR1 ABC in the 9.6 Å RyR1 cryo-EM map. **a**, View from the cytoplasmic side towards the endoplasmic reticulum, depicting domain A (blue), domain B (green) and domain C (red). **b**, Close-up lateral view from the four-fold symmetry axis. For clarity, only two monomers are

shown. **c**, Docking of domain A alone (blue) or domain BC alone (red) yields a near-perfect superposition on the docking position for ABC (grey). The probability of recapitulating the A–BC interface by chance is $<10^{-10}$ (see also Supplementary Discussion).

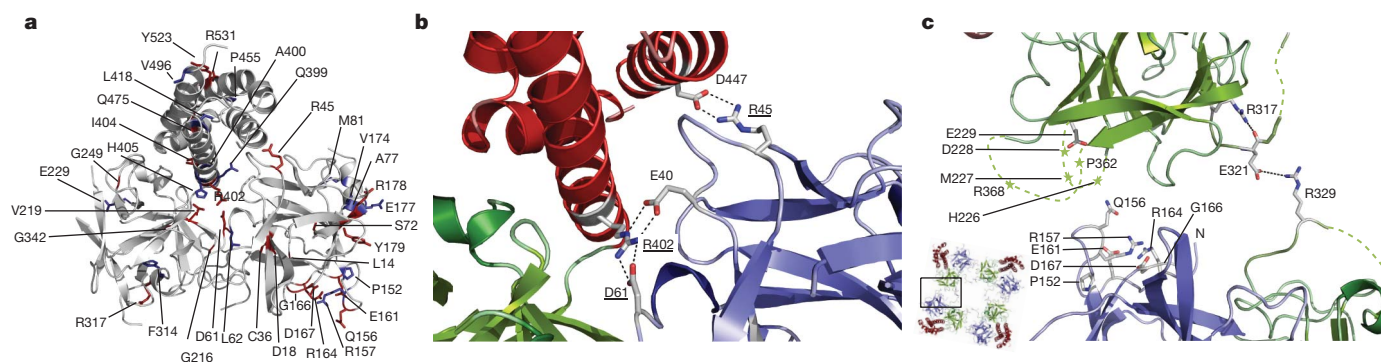


Figure 3 | Disease-associated mutations in RyR1 and RyR2. **a**, Position of disease-associated mutations in RyR1 (red) and additional such mutations in RyR2 (blue); regions not associated with disease (grey). For clarity, mutations in flexible loops are not shown. The view is similar to Fig. 1a. **b**, Salt bridges at the A–C interface. Domain A (blue), domain B (green) and domain C (red) are shown. Hydrogen bonds are represented by dashed lines. Underlined residues

RyR1 samples in the different studies⁹. Although most of the mutations on one side of this interface (domain B) are located in flexible loops, the docking shows the pairing of two oppositely charged residues (E321 and R329) on two adjacent B domains. The side chain of R329 is flexible in the crystal structure, but addition of the most common side-chain rotamer shows that the two residues can easily approach one another as close as 3.5 Å in the 10.3 Å map (Fig. 3c). Both residues are the target of disease-associated mutations, either directly (R329W in RyR1) or indirectly through mutation of a residue affecting the conformation of the main chain of E321 (R317L in RyR1, and R317W in RyR2) (Fig. 3c). Overall, 19 disease-associated mutations (in 16 positions) in RyR1 and RyR2 target this intersubunit interface, suggesting an important functional role for this contact area.

Other interfaces include areas lateral to domain A (interface 2) and domain C (interface 3) and areas 'below' domain A (interface 4), domain B (interface 5) and domain C (interface 6) (Supplementary Fig. 3). A large proportion of disease-associated mutations map to interface 4, connecting domain A to electron-dense columns extending towards the transmembrane domains (Supplementary Fig. 3a). This interface includes the single α -helix and the β 8– β 9 loop of domain A, two structural features that previously have been suggested to form important interactions with other RyR domains^{7,8}. The α -helix, which is the target of two disease-associated mutations and

are targets for disease-associated mutations. **c**, Interface 1 across ABC subunits, according to docking in the 10.3 Å RyR1 cryo-EM. Disease-associated mutation positions and E321 are labelled. Flexible loops are shown as coloured dashed lines. The R329 side chain is shown in its most common rotamer. R317 undergoes hydrogen bonding with the E321 main chain. The inset shows the relative view.

a deletion in RyR2 (refs 18,19), is also in contact with interface 2. Supplementary Table 2 gives a complete overview of the disease-associated mutations and their locations.

RyRs have been shown to be sensitive to redox modulation, a feature accomplished by several reactive cysteine residues that can be oxidized, nitrosylated or glutathionylated^{20–23}. In the context of full-length RyR1, C36 (rabbit RyR1 numbering) has been shown to be a target for glutathionylation²⁴. In domain A in isolation, C36 is highly flexible and accessible to solvent⁸; however, in the ABC crystal structure, it is completely buried by the β 16– β 17 loop of domain B (Fig. 4a and Supplementary Fig. 5). C36 is also the target for a disease-associated mutation (C36R) in RyR1. The A–B interface cannot accommodate an arginine residue or a glutathione moiety, both of which are bulkier than the cysteine residue. The fact that modification is possible in intact channels is strongly indicative that contacts between domains A and B are not static. In agreement with this idea, isothermal titration calorimetry experiments between domains A and BC that have been purified separately failed to show any interaction, suggesting that the contacts are inherently weak and can easily be broken (Supplementary Fig. 6).

Because docking of two individual parts of the crystal structure in the closed-state cryo-EM map recapitulates the same interface observed in the RyR1 ABC crystal structure (Fig. 2c), the ABC structure probably represents the relative domain orientation in the closed state of the

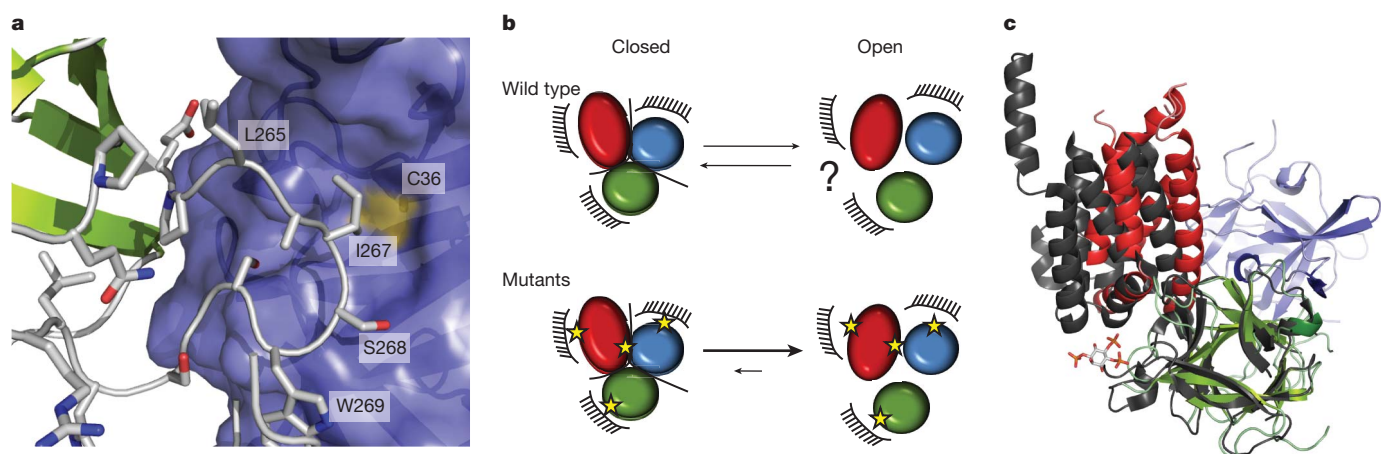


Figure 4 | The A–BC interface is labile. **a**, Surface of RyR1 domain A (blue) showing the C36 sulphhydryl (yellow), and representation of domain B (green). Selected residues from domain B are depicted as a grey stick structure, with oxygen atoms (red) and nitrogen atoms (blue) highlighted. C36 is inaccessible in the presence of domain B (Supplementary Fig. 5). **b**, Model showing the impact of disease-associated mutations (asterisks) on the motion of domains A, B and C (ovals). Interfaces with other RyR domains are indicated by black combs. The exact

nature and range of motion of these domains on opening of the channel are not known. Disease-associated mutations target multiple interfaces, thus facilitating motion of the domains. **c**, Superposition of the RyR1 ABC structure (coloured) with the InsP₃R BC structure (grey) bound to InsP₃ (stick representation; PDB ID: 1N4K), based on domain B of each structure. Treating the InsP₃R BC domain as a rigid unit shows a different relative orientation of domains B and C. This conformational difference might be induced by InsP₃ binding to InsP₃R.

channel. Although the existing cryo-EM maps of RyR1 in the open state are not publicly available for docking studies, they clearly show movements in the region where RyR1 ABC docks, including lateral movements away from the four-fold symmetry axis⁹. On the basis of the distribution of disease-associated mutations, we propose that the following occurs during the opening of RyR (Fig. 4b). Gating of the channel is allosterically coupled to movement of the A, B and C domains, either relative to one another or relative to other RyR domains. The distribution of disease-associated mutations at all observed interfaces suggests that all interfaces are prone to movement, including intersubunit contacts between domains A and B. Destabilization of any interface by disease-associated mutations facilitates the relative motion, resulting in a destabilized closed state and hence an increased probability of being open. This is compatible with previous functional studies showing that individual mutations either render the channels leaky or increase their sensitivity to activators⁶. The previously proposed 'zipper hypothesis' suggests that there is relative movement of the N-terminal and central disease hotspots²⁵. It is now clear, however, that the mutations do not target a single interface but instead affect multiple small zippers, both within and across the hotspots, as well as between the same hotspots on neighbouring subunits.

The N-terminal domains of another type of Ca²⁺-release channel, inositol-1,4,5-trisphosphate receptors (InsP₃Rs)^{26,27}, show clear structural homology with the corresponding RyR1 domains (Fig. 4c and Supplementary Fig. 7). In InsP₃Rs, domain A is known to decrease the affinity of domain BC for InsP₃ (ref. 27), but the mechanism for this is not fully understood because an intact InsP₃R ABC structure is not available. Previous NMR and small-angle X-ray scattering data for InsP₃R1 ABC have suggested that the binding of InsP₃ changes the relative orientation of domains B and C, resulting in a destabilized A–BC interface²⁸. In this respect, it is notable that the relative position of domains B and C differs between the RyR1 ABC and InsP₃-bound InsP₃R BC structures (Fig. 4c). Further experiments are needed to identify the exact domain movements that occur in both of these types of Ca²⁺-release channel.

METHODS SUMMARY

Rabbit RyR1 (residues 1–559) was expressed at 18 °C in *Escherichia coli* Rosetta (DE3) pLacI cells as a fusion protein containing a hexahistidine tag, maltose-binding protein and a cleavage site for tobacco etch virus protease. The protein was purified to homogeneity using standard fast protein liquid chromatography (FPLC) techniques, and the tag was removed before crystallization trials. The protein was crystallized in 1.2–1.5 M (NH₄)₂SO₄, 0–15% glycerol (vol/vol) and 0.1 M Tris–Cl buffer, pH 7–9. Crystals were flash frozen in the same condition supplemented with 30% glycerol (vol/vol), and used for diffraction experiments at the Canadian Light Source beamline 08ID-1 and the Stanford Synchrotron Radiation Lightsource beamline 9-2. Data at 2.5 Å were processed with the program XDS²⁹, and R32 was indicated as the space group. The phase problem was solved using the N-terminal domain of RyR1 (refs 7,8) as a search model for the program Phaser³⁰. Supplementary Table 3 shows the data collection and refinement statistics. Docking experiments were performed by exhaustive six-dimensional searches using the programs Situs¹¹ and ADP_EM¹⁰. ThermoFluor experiments, used to determine the melting temperatures of various constructs, were performed as described previously⁸.

Full Methods and any associated references are available in the online version of the paper at www.nature.com/nature.

Received 9 April; accepted 3 September 2010.

Published online 3 November 2010.

- Giannini, G., Conti, A., Mammarella, S., Scrobogna, M. & Sorrentino, V. The ryanodine receptor/calcium channel genes are widely and differentially expressed in murine brain and peripheral tissues. *J. Cell Biol.* **128**, 893–904 (1995).
- Betzenhauser, M. J. & Marks, A. R. Ryanodine receptor channelopathies. *Pflügers Arch.* **460**, 467–480 (2010).
- Robinson, R., Carpenter, D., Shaw, M. A., Halsall, J. & Hopkins, P. Mutations in *RyR1* in malignant hyperthermia and central core disease. *Hum. Mutat.* **27**, 977–989 (2006).
- Ludtke, S. J., Serysheva, I. I., Hamilton, S. L. & Chiu, W. The pore structure of the closed RyR1 channel. *Structure* **13**, 1203–1211 (2005).

- Samsó, M., Wagenknecht, T. & Allen, P. D. Internal structure and visualization of transmembrane domains of the RyR1 calcium release channel by cryo-EM. *Nature Struct. Mol. Biol.* **12**, 539–544 (2005).
- MacLennan, D. H. & Chen, S. R. Store overload-induced Ca²⁺ release as a triggering mechanism for CPVT and MH episodes caused by mutations in *RyR* and *CASQ* genes. *J. Physiol. (Lond.)* **587**, 3113–3115 (2009).
- Amador, F. J. et al. Crystal structure of type I ryanodine receptor amino-terminal β -trefoil domain reveals a disease-associated mutation 'hot spot' loop. *Proc. Natl Acad. Sci. USA* **106**, 11040–11044 (2009).
- Lobo, P. A. & Van Petegem, F. Crystal structures of the N-terminal domains of cardiac and skeletal muscle ryanodine receptors: insights into disease mutations. *Structure* **17**, 1505–1514 (2009).
- Samsó, M., Feng, W., Pessah, I. N. & Allen, P. D. Coordinated movement of cytoplasmic and transmembrane domains of RyR1 upon gating. *PLoS Biol.* **7**, e85 (2009).
- Garzon, J. I., Kovacs, J., Abagyan, R. & Chacon, P. ADP-EM: fast exhaustive multi-resolution docking for high-throughput coverage. *Bioinformatics* **23**, 427–433 (2007).
- Chacón, P. & Wriggers, W. Multi-resolution contour-based fitting of macromolecular structures. *J. Mol. Biol.* **317**, 375–384 (2002).
- Serysheva, I. I., Hamilton, S. L., Chiu, W. & Ludtke, S. J. Structure of Ca²⁺ release channel at 14 Å resolution. *J. Mol. Biol.* **345**, 427–431 (2005).
- Liu, Z. et al. Three-dimensional reconstruction of the recombinant type 3 ryanodine receptor and localization of its amino terminus. *Proc. Natl Acad. Sci. USA* **98**, 6104–6109 (2001).
- Wang, R. et al. Localization of an NH₂-terminal disease-causing mutation hot spot to the 'clamp' region in the three-dimensional structure of the cardiac ryanodine receptor. *J. Biol. Chem.* **282**, 17785–17793 (2007).
- Baker, M. L. et al. The skeletal muscle Ca²⁺ release channel has an oxidoreductase-like domain. *Proc. Natl Acad. Sci. USA* **99**, 12155–12160 (2002).
- Wriggers, W. & Chacón, P. Modeling tricks and fitting techniques for multiresolution structures. *Structure* **9**, 779–788 (2001).
- Serysheva, I. I. et al. Subnanometer-resolution electron cryomicroscopy-based domain models for the cytoplasmic region of skeletal muscle RyR channel. *Proc. Natl Acad. Sci. USA* **105**, 9610–9615 (2008).
- Bhuiyan, Z. A. et al. Expanding spectrum of human *RyR2*-related disease: new electrocardiographic, structural, and genetic features. *Circulation* **116**, 1569–1576 (2007).
- Marjamaa, A. et al. Search for cardiac calcium cycling gene mutations in familial ventricular arrhythmias resembling catecholaminergic polymorphic ventricular tachycardia. *BMC Med. Genet.* **10**, 12 (2009).
- Bellinger, A. M. et al. Hypernitrosylated ryanodine receptor calcium release channels are leaky in dystrophic muscle. *Nature Med.* **15**, 325–330 (2009).
- Durham, W. J. et al. RyR1 S-nitrosylation underlies environmental heat stroke and sudden death in Y522S RyR1 knockin mice. *Cell* **133**, 53–65 (2008).
- Eu, J. P., Sun, J., Xu, L., Stamler, J. S. & Meissner, G. The skeletal muscle calcium release channel: coupled O₂ sensor and NO signaling functions. *Cell* **102**, 499–509 (2000).
- Xu, L., Eu, J. P., Meissner, G. & Stamler, J. S. Activation of the cardiac calcium release channel (ryanodine receptor) by poly-S-nitrosylation. *Science* **279**, 234–237 (1998).
- Aracena-Parks, P. et al. Identification of cysteines involved in S-nitrosylation, S-glutathionylation, and oxidation to disulfides in ryanodine receptor type 1. *J. Biol. Chem.* **281**, 40354–40368 (2006).
- Ikemoto, N. & Yamamoto, T. Regulation of calcium release by interdomain interaction within ryanodine receptors. *Front. Biosci.* **7**, d671–d683 (2002).
- Bosanac, I. et al. Structure of the inositol 1,4,5-trisphosphate receptor binding core in complex with its ligand. *Nature* **420**, 696–700 (2002).
- Bosanac, I. et al. Crystal structure of the ligand binding suppressor domain of type 1 inositol 1,4,5-trisphosphate receptor. *Mol. Cell* **17**, 193–203 (2005).
- Chan, J. et al. Ligand-induced conformational changes via flexible linkers in the amino-terminal region of the inositol 1,4,5-trisphosphate receptor. *J. Mol. Biol.* **373**, 1269–1280 (2007).
- Kabsch, W. XDS. *Acta Crystallogr. D* **66**, 125–132 (2010).
- McCoy, A. J. et al. Phaser crystallographic software. *J. Appl. Cryst.* **40**, 658–674 (2007).

Supplementary Information is linked to the online version of the paper at www.nature.com/nature.

Acknowledgements We thank the staff at beamline 08ID-1 of the Canadian Light source, the Stanford Synchrotron Radiation Lightsource, K. Beam for the rabbit RyR1 clone, K. Lau for assistance with preparing the figures and the movie file, and C. Ahern, E. Moore and R. Pancaroglu for comments on the manuscript. F.V.P. is funded by the Canadian Institutes of Health Research (CIHR) and the Heart and Stroke Foundation of Canada, and is a CIHR new investigator and a Michael Smith Foundation for Health Research Scholar.

Author Contributions C.-C.T. expressed, purified and crystallized the protein, and collected diffraction data. P.A.L. cloned several initial constructs and assisted with the melting curve analysis. L.K. prepared the disease-associated mutation, purified the corresponding protein and measured the melting curves. F.V.P. designed and supervised the experiments, collected diffraction data, solved the structure, performed the docking experiments, and wrote the manuscript.

Author Information Atomic coordinates and structure factors for the RyR1 ABC structure have been deposited with the Protein Data Bank (<http://www.rcsb.org>) under accession code 2XOA. Reprints and permissions information is available at www.nature.com/reprints. The authors declare no competing financial interests. Readers are welcome to comment on the online version of this article at www.nature.com/nature. Correspondence and requests for materials should be addressed to F.V.P. (filip.vanpetegem@gmail.com).

METHODS

Cloning, expression and purification. Rabbit RyR1 (amino acid residues 1–559) was cloned into a modified pET28 vector containing, in tandem, a hexahistidine tag, maltose-binding protein and a cleavage site for tobacco etch virus (TEV) protease followed by the construct of interest³¹. The R402G mutation was produced by using the QuikChange protocol (Stratagene). The protein was expressed at 18 °C in *Escherichia coli* Rosetta (DE3) pLacI cells (Novagen), induced at an absorbance of ~0.6 at 600 nm by adding 0.2 mM isopropyl- β -D-thiogalactoside (IPTG) and grown for 20 more hours before collection. Cells were lysed by sonication in buffer A (250 mM KCl and 10 mM HEPES, pH 7.4) with 25 μ g ml⁻¹ DNase I, 25 μ g ml⁻¹ lysozyme, 14 mM β -mercaptoethanol and 1 mM phenylmethylsulphonyl fluoride. The lysate was applied to a 25 ml Poros MC column (Tosoh Bioscience), washed with five column volumes of buffer A and five column volumes of buffer A plus 2% (vol/vol) buffer B (250 mM KCl and 500 mM imidazole, pH 7.4) and eluted with 30% (vol/vol) buffer B. The protein was dialysed against buffer A plus 14 mM β -mercaptoethanol and then applied to a 25 ml amylose column (New England Biolabs). The protein was then washed with ten column volumes of buffer A plus 14 mM β -mercaptoethanol and eluted with buffer C (buffer A plus 10 mM maltose and 14 mM β -mercaptoethanol). The protein was dialysed overnight against buffer D (50 mM KCl, 10 mM HEPES, pH 7.4, and 14 mM β -mercaptoethanol) at 4 °C and was cleaved simultaneously with recombinant TEV protease. The sample was then applied to another 25 ml Poros MC column in buffer D, and the flow through was collected and applied to a 6 ml Resource Q column (GE Healthcare). The protein was eluted with a gradient of 0% to 40% buffer E (1.5 M KCl, 10 mM HEPES, pH 7.4, and 14 mM β -mercaptoethanol). The sample was run on a HiLoad 16/10 Phenyl Sepharose HP column (GE Healthcare) in buffer E and eluted with a gradient of 0% to 50% buffer D. Last, the sample was run on a HiLoad 16/60 Superdex 200 prep grade (GE Healthcare) gel filtration column using buffer A plus 14 mM β -mercaptoethanol. The protein sample was exchanged into 50 mM KCl, 10 mM HEPES, pH 7.4, and 5 mM dithiothreitol and was then concentrated to 10–20 mg ml⁻¹ using Amicon concentrators (30 kDa molecular mass cutoff; Millipore). The purified protein was stored at –80 °C.

Crystallization, data collection and structure solution. Crystals were obtained by hanging-drop vapour diffusion. Crystals appeared in a solution of 1.2–1.5 M (NH₄)₂SO₄, 0–15% glycerol (vol/vol) and 0.1 M Tris-Cl, pH 7–9. Crystals were transferred to the same condition supplemented with 30% glycerol (vol/vol), and flash frozen in liquid nitrogen before data collection. Data sets were collected at the Canadian Light Source (CLS) beamline 08ID-1 and the Stanford Synchrotron Radiation Lightsource beamline 9-2. The data set for final refinement was collected at the CLS at a wavelength of 0.9795 Å and a temperature of 100 K, and was processed using the XDS program²⁹. The structure of RyR1 domain A^{7,8} (PDB

ID: 3ILA) was used as a search model in molecular replacement with the Phaser program³⁰. The resultant electron-density maps were used for the initial placement of four α -helices and were then used for automated structure building implemented in the program ARP/wARP version 7.1 (ref. 32). The model was further completed and refined using alternating cycles of manual building in the programs Coot³³ and REFMAC version 5 (ref. 34). The geometry of the model was validated using the PROCHECK program³⁵, showing no residues in disallowed regions of the Ramachandran plots and with 87.5% in the core region. Residues with missing densities were not modelled. Supplementary Table 3 shows the data collection and refinement statistics.

Docking into cryo-EM maps. The resultant structure was docked into three RyR1 cryo-EM maps (Electron Microscopy Data Bank ID: 1275, 5014 and 1274), solved at a reported 9.6 Å (ref. 4), 10.3 Å (ref. 5) and 14 Å (ref. 12), respectively. We used extensive six-dimensional searches as implemented in the programs Situs¹¹ and ADP-EM¹⁰. Laplacian filtering was used to prevent a multitude of spurious solutions due to migration to regions with high electron density¹⁶. The search model was blurred to the same resolution as the cryo-EM map. No additional filtering was performed on the map. An angular step of 3° was used for the initial six-dimensional search, followed by Powell minimization. A confidence interval and docking precision estimate were obtained using methods described previously^{36,37}, making use of Fisher's *z* transform of the correlation coefficient and an estimated $\sigma(z)$ from the map volume and resolution.

Thermal melt analysis. Thermal melting curves for purified proteins were obtained from ThermoFluor experiments as described previously⁸. The midpoint of the transitions was used as an indicator of overall protein stability.

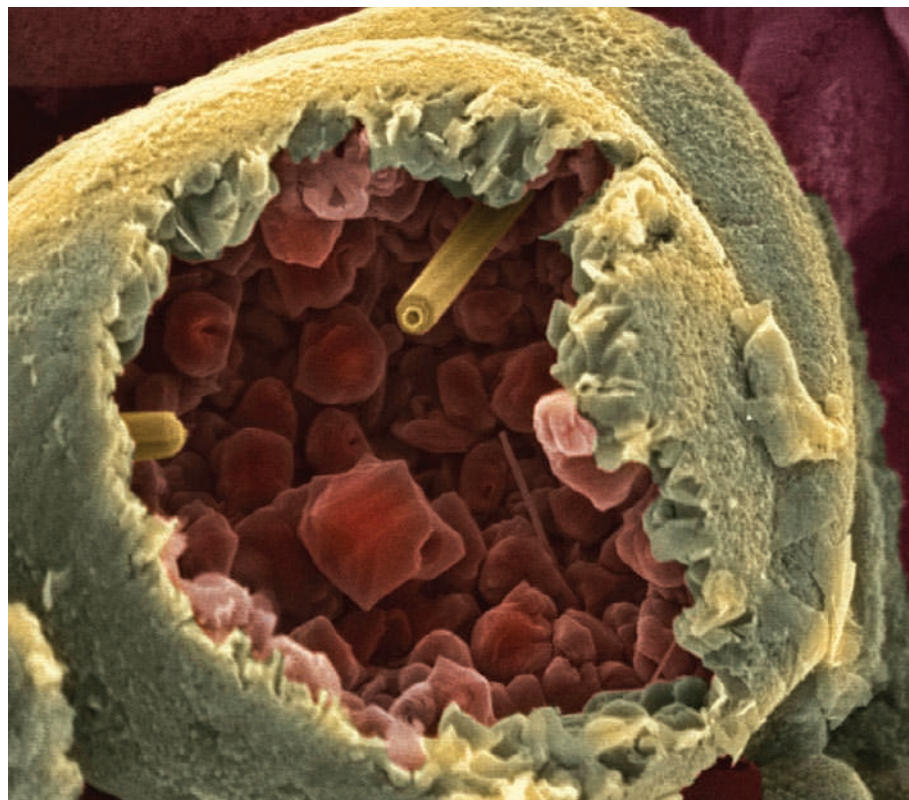
- Van Petegem, F., Clark, K. A., Chatelain, F. C. & Minor, D. L. Jr. Structure of a complex between a voltage-gated calcium channel β -subunit and an α -subunit domain. *Nature* **429**, 671–675 (2004).
- Langer, G., Cohen, S. X., Lamzin, V. S. & Perrakis, A. Automated macromolecular model building for X-ray crystallography using ARP/wARP version 7. *Nature Protocols* **3**, 1171–1179 (2008).
- Emsley, P. & Cowtan, K. Coot: model-building tools for molecular graphics. *Acta Crystallogr. D* **60**, 2126–2132 (2004).
- Murshudov, G. N., Vagin, A. A. & Dodson, E. J. Refinement of macromolecular structures by the maximum-likelihood method. *Acta Crystallogr. D* **53**, 240–255 (1997).
- Laskowski, R. A., MacArthur, M. W., Moss, D. S. & Thornton, J. M. PROCHECK: a program to check the stereochemical quality of protein structures. *J. Appl. Cryst.* **26**, 283–291 (1993).
- Volkman, N. Confidence intervals for fitting of atomic models into low-resolution densities. *Acta Crystallogr. D* **65**, 679–689 (2009).
- Volkman, N. & Hanein, D. Docking of atomic models into reconstructions from electron microscopy. *Methods Enzymol.* **374**, 204–225 (2003).

CAREERS

TURNING POINT Plant biologist seeks to thrive in a biomedical research environment **p.591**

UNITED STATES International student enrollment reaches record high **p.591**

NATUREJOBS For the latest career listings and advice www.naturejobs.com



Rod-shaped graphite nanocrystals are strong, stable electrical conductors with many potential uses.

NANOTECHNOLOGY

Small science yields big growth

Nanomaterials have evolved from innovation to application — and the career possibilities have blossomed.

BY CORINNA WU

Carbon-nanomaterial researchers had plenty to celebrate this autumn. In October, Rice University in Houston, Texas, threw a gala to commemorate the twenty-fifth anniversary of the discovery of the football-shaped carbon molecule buckminsterfullerene by Rice researchers. Physicist Andre Geim at the University of Manchester, UK, had planned to attend, but his plans got

derailed after he and his colleague Konstantin Novoselov won the Nobel Prize in Physics the week before the gala for their work on graphene, the one-atom-thick sheets of carbon that they produced in 2004 by peeling off layers of graphite with adhesive tape. It was a busy week for nanomaterials innovators.

It has been a busy 25 years. The discovery of buckminsterfullerene in 1985 sparked a revolution in materials science and nanotechnology. That excitement was soon extended to carbon

nanotubes, the mechanical and electrical properties of which suggested myriad uses. Now, these nanotubes are fulfilling their promise.

The maturation of the market for nanomaterials opens up job opportunities at all stages of commercialization — in academia, start-up companies, small businesses and large chemical manufacturers. Nanomaterials are finding their way into products such as photovoltaic cells, high-power batteries and advanced drug-delivery systems, and are creating opportunities for applications in industries from electronics and data storage to energy and biomedicine. Scientists with a strong interest and the right skills should find ample career possibilities.

INDUSTRIAL OPPORTUNITIES

Within the past two years, chemical suppliers such as Bayer in Leverkusen and BASF in Ludwigshafen, both in Germany, have begun manufacturing carbon nanotubes in bulk for industry. Most commonly, the tubes are mixed into polymers or metals to create strong, lightweight composites. Companies including Nanocyl in Sambreville, Belgium, and Nanocomp Technologies in Concord, New Hampshire, specialize in commercial nanotube production. The market is now estimated at US\$247 million worldwide, and is set to grow to \$2.7 billion by 2015, according to nanoposts.com, a nanotechnology consultancy in Stirling, UK. “A lot of nanotechnology applications have been in research space, but we’re now seeing a progression into the commercial space,” says Michael Strano, associate professor of chemical engineering at the Massachusetts Institute of Technology in Cambridge. This evolution and the projected future revenue and demand tell a promising story for job potential.

Companies all over the world are working on better ways to scale up production and chemically modify nanotubes for specific purposes. The tubes’ mechanical strength makes them an obvious ingredient for composites, and the earliest applications involved mixing them into polymers to create strong, lightweight materials used in the automotive and aerospace industries, and in sports equipment. By volume, such uses still command the largest demand for nanotubes, says Daniel Resasco, founder and chief scientist of SouthWest Nano Technologies in Norman, Oklahoma. Resasco’s company has been on a hiring spree over the past year, adding 14 people to its staff, including three PhD chemists, three chemical engineers with bachelor’s degrees, one technical chemist and a programme manager with an MBA. ►

Y. GOGOTSIS/SPL

RESEARCH OPPORTUNITIES

Nanotechnology and the environment

Mark Wiesner's nanotechnology talks used to include a slide with the Disney character Tinker Bell on one side and *Star Wars* villain Darth Vader on the other. The point, says Wiesner, a civil and environmental engineer at Duke University in Durham, North Carolina, is that the technology has its bright side and its dark side. Although many researchers are drawn to the field by the bright side (the applications), others are studying the toxic effects of nanomaterials on humans and the environment — phenomena as simple as the tendency for antimicrobial silver nanoparticles to kill useful bacteria.

Research into environmental, health and safety (EHS) effects of nanotechnology has proceeded alongside research into its applications, says Kristen Kulinowski, director of external affairs at the Center for Biological and Environmental Nanotechnology at Rice University in Houston, Texas. "It means not rushing into developing applications and then realizing they're not sustainable," she says. "Let's do risk-relevant research alongside the other stuff."

EHS research draws on disciplines including biology, toxicology, ecology, environmental engineering, chemistry, physics and maths. And materials scientists and chemical engineers seek to create nanoparticles with desirable physical properties but reduced toxicity — for example, by controlling their shapes and sizes or developing coatings to keep them from damaging cells.

Social scientists track policy and regulations involving nanotechnology. Because the field touches on so many scientific and societal issues, "one needs a multidisciplinary platform", says André Nel, director of the Center for Environmental

Implications of Nanotechnology (CEIN) at the University of California, Los Angeles. "A single scientific domain is not enough to address the completeness of the problem," he adds.

CEIN is one of two centres created in 2008 by the US National Science Foundation (NSF) and the Environmental Protection Agency (EPA) to study the environmental impact of nanotechnology. A collaboration between the Los Angeles and Santa Barbara campuses at the University of California, it has about 75 researchers, including 30 postdoctoral fellows and graduate students, says Nel.

Duke is headquarters for the second centre, CEINT, which includes five other universities. CEINT employs 36 faculty members and 76 undergraduate and graduate students, says Wiesner, who is the director of the centre. The NSF and the EPA granted the two centres US\$38 million over five years; the EPA's \$5-million contribution is the biggest it has ever given to the field.

"Looking at nanomaterials was a way of looking at human-induced disturbances to natural ecosystems," says Ben Colman, a postdoc at Duke who has been with CEINT since 2009. "That was attractive to me — asking what happens to these systems when you stress them with novel materials," he says. Colman has had to acquire skills in electron microscopy and X-ray spectroscopy to characterize nanoparticles, because the shape, size and number of particles makes a big difference to how they behave.

The centres are focusing first on the most widely used nanomaterials, including silver, titanium dioxide and carbon nanotubes. Even the most basic questions about what makes a nanoparticle toxic have not been answered, Kulinowski says; the discipline of nanotoxicology is rife with possibilities. **C.W.**

► Only a few universities offer interdisciplinary degrees in nanotechnology; they include the University of Washington in Seattle, the National University of Singapore and the University of Copenhagen (a list is available at go.nature.com/ciel5z). The field is still "highly disciplinary", says Strano, with researchers holding degrees in chemistry, physics, materials science and chemical or electrical engineering. But no matter what degree they pursue, all aspiring nanotube researchers would do well to take a course in solid-state physics — "the heart of nanotechnology", says Strano. "These materials are defined by the underlying physics," he adds.

That training will apply to all areas of nanotechnology, not just carbon nanotubes. "Graduates with a strong background in catalysis,

interfacial chemistry and nanotechnology will be sought by companies, universities and national labs," says Resasco. The ability to manipulate nanomaterials using electron microscopes and characterize them using spectroscopic techniques is essential for a growing suite of positions. "Working in nanomaterials," says Resasco, "you start developing a way of thinking that's more precise, more atomic-oriented than the typical microscopic research of two decades ago."

Many Rice graduates take postdoctoral positions, but "we have been sending more PhDs directly to industry than ever before", says Wade Adams, director of the Richard E. Smalley Institute for Nanoscale Science and Technology at the university. In the past few years, oil and gas service companies such as Baker Hughes,

Halliburton and Schlumberger, all based in Houston, have begun hiring nanotechnology graduates from Rice. The companies are "starting to see how nanotechnology is going to make a difference to them in the future" by developing better catalysts for oil refining, hardening drill bits and improving materials used in natural-gas recovery, says Adams. Graduates also find jobs in small businesses and start-ups that specialize in nanotechnology. In the Houston area alone, more than 20 such start-ups have opened their doors within the past two years, says Adams.

Although good jobs lure many graduates right out of university, postdoctoral research experience can benefit careers in both academia and industry. Many national laboratories do nanotechnology research and collaborate with university groups, says Resasco. "That is great, because they have tremendous infrastructure and facilities," he notes. A postdoc position, Resasco adds, allows a graduate to broaden his or her experience — important in a multi-disciplinary field. Resasco has hired PhD graduates with physical chemistry degrees who also had postdoctoral experience in chemical or electrical engineering. "We find this breadth of knowledge particularly useful. Many nanotechnology companies are relatively small, and people with flexibility and a broad set of skills are highly valued," he says.

Even as the commercial promise generates opportunities, basic research continues to interest universities (see 'Nanotechnology and the environment'). Graphene has become the new hot material; it is easily manufactured, flexible, strong and an excellent electrical conductor. It has been on the scene for only six years, and researchers are actively exploring its potential. According to a 2009 analysis by Lux Research in New York City, graphene is set to compete with nanotubes in price and performance in the coming years as a component of composites, coatings and energy-storage devices, and the market for it is projected to grow to \$59 million by 2015.

With plenty of scientific and technical challenges ahead, and so much money at stake, there should be lots of opportunities opening up. "The job market is awesome for nanotech researchers because we just don't have enough scientists — even at the master's and undergraduate levels," says Vincent Caprio, executive director of the NanoBusiness Alliance trade organization, based in Skokie, Illinois. "All these companies are hiring people." ■

Corinna Wu is a freelance writer based in Oakland, California.



"People with flexibility and a broad set of skills are highly valued."

Daniel Resasco

J. RESASCO

TURNING POINT

Mary Gehring

Plant biologist Mary Gehring joined the Whitehead Institute for Biomedical Research in Cambridge, Massachusetts, in September.

Why did plants attract you?

I went to Williams College in Williamstown, Massachusetts, planning to be a writer, but became interested in plant physiology after taking a course on plants and later working in the professor's lab. It is fascinating that much of the same molecular biology is going on in animals, but plants look like they're just sitting there. I saw a talk by Norman Borlaug, father of the green revolution, who exhorted young people to continue improving agriculture, and my interest was solidified.

How did your own plant research evolve?

In graduate school at the University of California, Berkeley, my interest in plant development evolved into a dissertation on epigenetics after a discovery that seed development was tied to the epigenome. I worked with Robert Fisher, a plant molecular biologist, to explore the genes that maintain the epigenome. We discovered how they are regulated.

How did you decide to pursue a postdoc at the Fred Hutchinson Cancer Research Center in Seattle, Washington?

I interviewed at three places for a postdoc — two were plant labs, the third was with Steven Henikoff, the only person at the Hutch studying plants. I was attracted to Steve's lab because it wasn't constrained by the organism — he really thought about the biological questions. For example, he investigated the different controls over genetic inheritance in both *Arabidopsis* and *Drosophila* — which allowed me to think about plant projects in a broader way.

What has been your best research decision?

I took the time to do a really tedious thing, dissecting seeds, that ultimately paid off scientifically. We wanted to know how epigenetics work between the embryo and endosperm. To do that, I had to collect embryo and endosperm DNA. *Arabidopsis* seeds are tiny, and I had to sit at a microscope with a needle and forceps and dissect them into three component parts. For just one experiment, I had to dissect roughly 1,500 seeds — which took 8 hours a day for a week. As a result of that task, we could document the changes to the epigenome that are necessary to make a viable seed. By monitoring



DNA methylation between endosperm and embryo, we identified many genes important for directing seed development.

Are you a plant biologist or an epigeneticist?

I have often been asked that in job interviews, and have found it hard to answer. I'm both. There is much more synergy between organisms than there are differences. As a scientist, I benefit from hearing about epigenetics in mice or fruitflies. When I think about my research, I'm thinking about what is most interesting to epigenetics rather than to plant biology, although one hopes those are the same. I work on endosperm, which is a plant-specific tissue. But the epigenetic processes going on there and in plant gametes are, potentially, similar to gametes in animals.

Why did you apply to the Whitehead, where there isn't a lot of plant research?

I knew that the Whitehead used to do plant biology, and still did some. It was a great place to work. But it was the 'follow the question' approach that I liked. The scientists here, like at the Hutch, weren't wedded to one organism, but to using the organisms to best answer a question. I felt that, because I had been at the Hutch, I could do well here, even without other plant biologists. One thing we discussed was how I'd be evaluated as the only person here in a plant field. I've been assured that I won't be asked to change focus, and that my work will be taken on its own merit. It is daunting because it's the Whitehead, but I'm excited.

What inspires you?

Wanting to help feed the world is what got me into plant biology. Day-to-day, my work may not seem to be too close to that aspiration, but it is still there. My work is interesting at a general biology level — and in the future could play a role in better manipulating plants to improve yield. ■

INTERVIEW BY VIRGINIA GEWIN

UNITED STATES

Overseas enrolment up

The number of international students at US institutions rose 3% to a record high of 690,923 in the 2009–10 academic year, with gains in engineering, maths and computer science, says a report from the Institute of International Education, a New York-based non-profit organization. The report, out on 15 November, found that the growth was driven by a 30% increase in the number of students from China, who now represent some 18% of international enrolment. The report found that 18% of overseas students are pursuing engineering, up 7%; 9% are in biological and physical sciences, down slightly; and 9% are studying maths and computer science, up almost 8%. Stronger recruiting efforts helped to promote the increases, but visa woes contributed to fewer students coming from some nations.

WORKFORCE

Changing order

China, Brazil and India have begun to challenge the traditional science leadership role of the United States, asserts a report from the United Nations Educational, Scientific and Cultural Organization (UNESCO). The *UNESCO Science Report 2010*, released on 10 November and last out in 2005, notes that the total number of researchers in China ballooned by 75% to 1.42 million in 2007, roughly the same number as in the United States and just below the European Union's 1.44 million. Lidia Brito, UNESCO's science policy director, says that this growth heralds new collaborative prospects for researchers in all nations. But success, she says, requires that young scientists develop multicultural teamwork talents.

GRANTS

Faculty seek support

US junior research faculty members want more grant-seeking support from their institutions, an annual survey has found. Results of the Tenure-Track Faculty Job Satisfaction Survey, administered by Harvard University's Collaborative on Academic Careers in Higher Education (COACHE) in Cambridge, Massachusetts, were released on 15 November. Todd Benson, COACHE assistant director, says that addressing key concerns such as grant management could help institutions recruit and retain junior faculty. COACHE shares survey results among participating universities to help them improve internal policies, he says.

HIGH ON THE HOG

Pig in the middle.

BY SEAN DAVIDSON

Someone told me the other day that there's 185 industrial uses for a pig. So I guess that makes me number 186. Which is kinda weird, 'cos until a few years ago, the closest I'd come to a real pig was riding my hog — my big, black, Harley Davidson '08 VRSCD Night Rod. Aww yeah! ... I was one with the machine, roaring down the highway, growling up the hills, grunting and snorting at the poncey Japanese bikes stopped at the lights. I practically lived on my hog. Couldn't separate us. Even after the crash. Not that I remember much about that. I remember the 'squeeeeeeeall ...' of the tyres as I took off from the lights, then the pigs behind me. The cops, I mean. And I remember a strange feeling of dislocation like I was somewhere floating, watching body and machine as we slammed into the road, scraping along making one hell of a racket ... once I would have said 'like a stuck pig' but I'm more considerate now. They said later it was like we'd been welded together, my leg fused with the chassis. Nothing they could do but cut us apart. Carve us up, like meat from the bone. I could use a few spare ribs, though, they said! Ha ha! They love their jokes, the paramedics. But gotta admit, they really saved my bacon.

I wasn't so familiar with the transplant scene back then. Of course I'd heard about human-to-human transplantation — that was old school, but it had run up against the predicted problem of supply and demand, then the real show-stopper: immune suppression. Without it, your new buddy-organ wouldn't stick around for long, but each new super-multi-extra-cross-resistant bug that appeared took out another swathe of the old 'planters. "Rejection by an organ is not a rejection of you as a person," the support groups said, but still, it felt like more than just a slap in the face.

Xenotransplantation — that was the Holy Grail. And finally the obstacles (there had been many) were overcome with fully humanized, cloned pigs. Why pigs? Well, turns out we don't have the heart of a lion, but one more like the

humble pig's! Not just our hearts but our kidneys, livers, lungs — nearly everything ... though they ran into some 'rejection at the patient level' when they tried it on with the trotters!

But I was too mashed up even for xeno. I knew it was bad when I woke, 'cos most of my body was missing. But I still wasn't ready for the shock of looking over, all dazed and confused, and there's Doug, mucking about

work: breathing, eating, digesting, filtering and pumping your blood, even ahem, urinating, et cetera."

"You've undergone 'holo-transplantation', he said. "That's transplantation of the whole animal," he added, as if I still hadn't got it.

Sometimes when we walk in the park it feels like I'm flying a kite in the shape of a pig. Other times it feels like he's flying me. We

go for walks quite a lot. I never used to when I had my own legs — hated nature and dirt — but these days I really enjoy it. Electricity's a bit steep now, so Doug literally does the leg-work, pulling my body along in our pig-chariot, but he's happy. I was worried, at first, that he'd resent working for the parasitic human grafted onto him, but he's become as attached to me as I am to him. I got us a great little bungalow flat to live in and ripped out all the floorboards so now it's full of the fresh smell of damp earth. We keep it clean though, I'd like to point out. A bit of mud is all right once in a while to cool down but that's not such an issue now he's got me, 'cos unlike pigs, of course, I can sweat. Just one of our many little shared benefits.

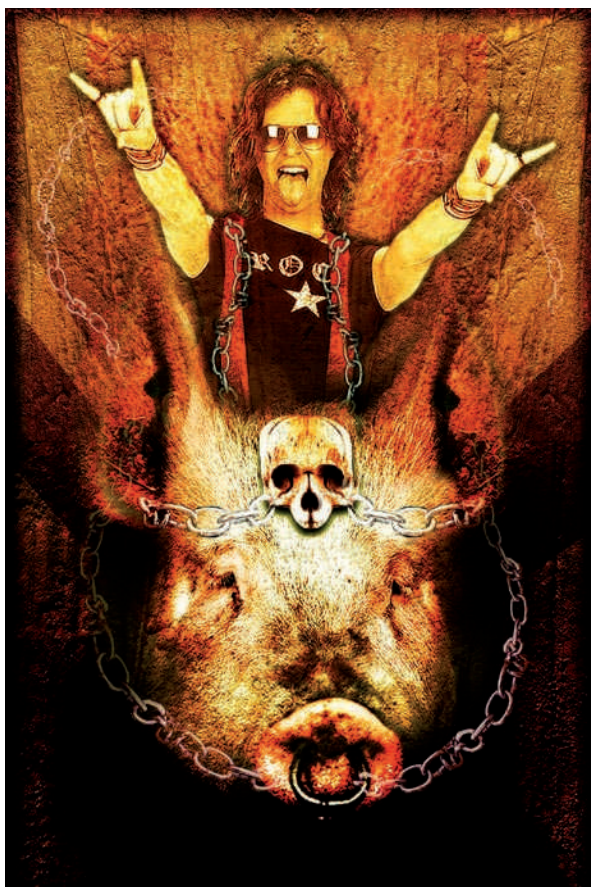
Turns out we like a lot of the same stuff. Corn, for instance. And rotten tomatoes. OK, that's probably a taste I've developed more recently but then I don't think I ever tried eating them back when I had my old stomach. Now Doug does the eating and when he eats rotten tomatoes we're in heaven! The doctors don't believe me, but you'd be amazed at how much you share in a blood relationship like this. I discovered that pretty quickly, the first time Doug and I left the hospital.

The flashbulbs of the press freaked him out and *the adrenaline!* It pumped straight from him into me and before I knew it we were both jumping about like crazies!

So you see, that's why the doctor won't be seeing us again. Oh, I'm sure he's correct and this new technique *will* do away with the need for the pig, but there'll be another test subject. In the meantime we're locking the door, and he's not coming in.

Not by the hair on my chinny chin chin! ■

Sean Davidson is a cardiovascular researcher working in London who enjoys taking things to their illogical conclusions.



in the sterilized mud in his pen next to me! Two long, thick, plastic tubes jumping between us: 'in' and 'out'. Not that I've got anything against pigs. In fact, you could say I've developed quite a connection. He must have sensed I was conscious then, because he suddenly looked around in surprise. I stared into his stunned-looking little blue eyes. That's all I remember of our first meeting.

Next time I woke, I was surrounded by white coats but I knew Doug was still there. "What's the bloody pig doing?" I yelled. "JR.16's sharing his blood with you," says the Doc. "From now on he'll do all the hard

➔ **NATURE.COM**
Discuss this story
online at:
go.nature.com/bd8b7r

Bold claims for optogenetics

ARISING FROM J. H. Lee *et al.* *Nature* **465**, 788–792 (2010)

In a recent Letter to *Nature*, Lee and colleagues¹ combined optogenetic stimulation with functional magnetic resonance imaging (ofMRI) to examine the relationship between pyramidal-cell spiking and the blood oxygenation level dependent (BOLD) signal. To do so, they injected an adeno-associated viral vector into the primary motor cortex (M1) of adult rats to drive the expression of channelrhodopsin (ChR2) in cortical projection neurons, thus making them sensitive to light¹. The authors then used combined light stimulation and functional magnetic resonance imaging (fMRI) to examine the effects of selective activation of the light-sensitive pyramidal cells on the BOLD signal, as well as to probe the value of this methodology for mapping brain connectivity. They found that excitation of these neurons induced positive BOLD signals both in the injected M1 region and in remote target thalamic nuclei receiving direct projections from that region, and concluded that ofMRI reliably links positive BOLD signals with increased local neuronal excitation. However, their analysis neglects the almost immediate activation of other circuits that could lead to the generation of BOLD signals through local perisynaptic rather than spiking activity. Their experiments therefore do not pin down the identity of the specific neuronal signals that give rise to the BOLD signal.

To be specific, the majority of axonal collaterals of neocortical pyramidal cells ascend back to and synapse in the superficial layers, while others distribute excitation on the horizontal plane, forming a strongly recurrent excitatory network². The strong input amplification caused by this kind of positive feedback loop is tightly controlled by a large variety of GABAergic interneurons³, which are interposed within this pyramidal network and target different neuronal subdomains⁴. In such recurrent networks, excitation and inhibition are electrically inseparable, and the final response of each cortical cell is actually determined by all feedforward, feedback and modulatory synapses⁵. Recurrent microcircuits are not specific to sensory cortices; they have been evident wherever they have been sought, including the primary motor and premotor cortices in all studied mammals. The primary motor cortex is known to have extensive interlaminar and horizontal connectivity⁶, underlying the strong interactions between excitation and inhibition.

The instant and unavoidable activation of local networks following stimulation of a single neuronal group is clearly evident also in other optogenetic studies. As the authors' laboratory previously showed, light-induced activation of inhibitory neurons in the prefrontal and barrel cortices of mice drives the spikes or postsynaptic potentials of these neurons while inhibiting the spiking of pyramidal cells^{7,8}. In a similar manner, stimulation of the excitatory neurons induces both increases and decreases in neural activity that are followed by a similar characteristic undershoot (dip) immediately after light cessation⁹, clearly suggesting that pyramidal cell activation, too, instantly engages a broader neural network of balanced excitation–inhibition, including recruitment of inhibitory neurons⁹.

Last but not least, Lee and colleagues observed robust BOLD responses in M1 following antidromic stimulation of M1 axons projecting to thalamus¹. But previous results demonstrate that antidromic stimulation itself does not induce significant metabolic changes at the site at which the cell bodies are located, in this case, M1; increases in glucose use are only observed at the presynaptic terminals during orthodromic stimulation, but not during antidromic stimulation¹⁰. Leaving aside the thalamocortical loops, the reported M1 BOLD response is most probably due to the activation of a large number of M1 excitatory or inhibitory neurons through the collaterals of the

CaMKIIa-expressing pyramidal cells, again demonstrating the inevitable activation of entire microcircuits that drive the haemodynamic responses. Indeed, antidromic stimulation of Betz cells has long been shown to activate recurrent collaterals and to induce the sequences of excitation–inhibition characterizing recurrent microcircuits¹¹, while antidromic stimulation of cells in layer VI of the primary visual cortex activates (through collaterals) neurons in layer IV, with a subsequent synaptic spread of activity to all layers¹².

To strengthen their claim that BOLD is driven by pyramidal cell spiking, the authors contrasted the BOLD maps obtained during pyramidal cell stimulation with those observed during stimulation of inhibitory parvalbumin-positive cells. Whereas pyramidal cell activation yielded exclusively positive BOLD responses, the activation of parvalbumin-positive cells gave rise to an additional zone of negative BOLD. Yet the activation maps in these two different cases were obtained by using coherence (positive quantity between 0 and 1) and coherence-thresholded phase (with opposite phases denoting positive and negative BOLD) for pyramidal and parvalbumin-positive cells respectively, making it difficult for the reader to compare activations. That aside, activation of pyramidal cells or parvalbumin-positive cells may lead to slightly different results even though they both activate local microcircuits owing to differences in the sequence of synaptic events. Normally, inhibitory inputs lag behind the excitatory ones¹³ and this reversal of the excitatory/inhibitory postsynaptic potential (EPSP/IPSP) order during parvalbumin-positive cell excitation may engage an unusually strong feedforward inhibition that results in slightly different BOLD responses. Such differences cannot be used to ascribe a special contribution of pyramidal cell activation to the generation of BOLD signal.

In conclusion, neural activity directly correlates with the BOLD signal¹⁴. The optogenetic methodology of the Lee *et al.* paper¹ cannot elucidate details of the relationship between stimulus- or task-selective neuronal activity and fMRI signals¹⁵ because the selectivity of the latter for subtypes of pyramidal cells is unknown, and indeed may not even exist.

Optogenetics is a promising methodology that is currently causing a great deal of justified enthusiasm in the field of neuroscience. Any new methodology, however, should be applied with extreme caution, and its limitations with respect to tested scientific hypotheses must be constantly evaluated to avoid drawing unjustified conclusions that could eventually harm both the field and specific methodology. A large number of fMRI studies made this very mistake and by ignoring the method's limitations, ultimately drew conclusions that went far beyond the capabilities of the technology. It must be our top priority to avoid making analogous mistakes in the field of optogenetics.

Nikos K. Logothetis^{1,2}

¹Max Planck Institute for Biological Cybernetics, Tuebingen, Germany.

²Imaging Science and Biomedical Engineering, University of Manchester, Manchester, UK.

e-mail: nikos.logothetis@tuebingen.mpg.de

Received 10 August 2010; accepted 9 September 2010.

1. Lee, J. H. *et al.* Global and local fMRI signals driven by neurons defined optogenetically by type and wiring. *Nature* **465**, 788–792 (2010).
2. Douglas, R. J. & Martin, K. A. C. Recurrent neuronal circuits in the neocortex. *Curr. Biol.* **17**, R496–R500 (2007).
3. Markram, H. *et al.* Interneurons of the neocortical inhibitory system. *Nature Rev. Neurosci.* **5**, 793–807 (2004).

4. Somogyi, P., Tamas, G., Lujan, R. & Buhl, E. H. Salient features of synaptic organisation in the cerebral cortex. *Brain Res. Brain Res. Rev.* **26**, 113–135 (1998).
5. Douglas, R. J., Martin, K. A. & Whitteridge, D. An intracellular analysis of the visual responses of neurones in cat visual cortex. *J. Physiol.* **440**, 659–696 (1991).
6. Keller, A. Intrinsic synaptic organization of the motor cortex. *Cereb. Cortex* **3**, 430–441 (1993).
7. Sohal, V. S., Zhang, F., Yizhar, O. & Deisseroth, K. Parvalbumin neurons and gamma rhythms enhance cortical circuit performance. *Nature* **459**, 698–702 (2009).
8. Cardin, J. A. *et al.* Driving fast-spiking cells induces gamma rhythm and controls sensory responses. *Nature* **459**, 663–667 (2009).
9. Han, X. *et al.* Millisecond-timescale optical control of neural dynamics in the nonhuman primate brain. *Neuron* **62**, 191–198 (2009).
10. Jueptner, M. & Weiller, C. Review: does measurement of regional cerebral blood flow reflect synaptic activity? Implications for PET and fMRI. *Neuroimage* **2**, 148–156 (1995).
11. Phillips, C. G. Actions of antidromic pyramidal volleys on single Betz cells in the cat. *Q. J. Exp. Physiol. Cogn. Med. Sci.* **44**, 1–25 (1959).
12. Ferster, D. & Lindstrom, S. Synaptic excitation of neurones in area 17 of the cat by intracortical axon collaterals of cortico-geniculate cells. *J. Physiol.* **367**, 233–252 (1985).
13. Okun, M. & Lampl, I. Instantaneous correlation of excitation and inhibition during ongoing and sensory-evoked activities. *Nature Neurosci.* **11**, 535–537 (2008).
14. Logothetis, N. K. & Wandell, B. A. Interpreting the BOLD signal. *Annu. Rev. Physiol.* **66**, 735–769 (2004).
15. Logothetis, N. K. What we can do and what we cannot do with fMRI. *Nature* **453**, 869–878 (2008).

Competing financial interests: declared none.

doi:10.1038/nature09532

Lee *et al.* reply

REPLYING TO N. K. Logothetis *Nature* **468**, doi:10.1038/nature09532 (2010)

This is a welcome opportunity to discuss ofMRI, a technology for testing the causal and global impact of defined cell populations *in vivo*¹. The accompanying Comment² reviews well-known neuroanatomy, but does seem, in its entirety, to be founded on a suggestion that, after experiments were conducted to drive a defined circuit element and measure resulting BOLD signals¹, we concluded that no other contributory circuit element was recruited by the driven population. This was not the case, however, as correctly understood by others in the fMRI community^{3–5} and as explained in the paper (for example, “contributions from additional cells and processes downstream of the defined optically triggered population are expected and indeed represent an important aspect of this approach”). Moreover, the complexity of the brain dictates that such possible contributory mechanisms are more numerous than listed in the Comment², including many other circuit and feedback mechanisms and classes of cells within neural circuitry^{6–10}. As was discussed¹, this is one of the most important and useful aspects of the ofMRI approach.

In genetics, when gain- or loss-of-function of a gene results in changes in the organism, it is not concluded that no other genes are involved in expression of phenotype; rather, it is essential that causal alteration of a gene trigger other events that give rise to phenotype. This principle does not diminish the value of genetics (for example, artificially overexpressing *Antennapedia*¹¹ is a paradigmatic, specific gain-of-function causal intervention that suffices to trigger antenna-to-leg transformation—a complex biological phenotype requiring a host of downstream effector genes). Optogenetics in this regard is no different from genetics. Controlling spikes in targeted neurons allows testing for causal impact of those defined events in target cells for triggering complex phenotypes—always (as with homeotic genes) through events in downstream effectors.

We found that directly exciting spatially and genetically defined local cortical excitatory neurons triggered BOLD responses that faithfully captured all of the phase- and timing-relationships of the complex dynamics of previously measured sensory-triggered BOLD¹. These results show that it is unnecessary to invoke processes not initiated by spiking of local, excitatory neurons to explain the complexity of BOLD signal dynamics, and provide a causal (rather than correlative) demonstration that coordinated spikes in genetically and spatially defined cells are sufficient to elicit all phases of the BOLD signal including delay, rise, decay, undershoot and recovery.

These results therefore illuminate the causal contributions of defined circuit elements and their activity patterns to fMRI BOLD signal generation, which the fMRI community has found to be of interest^{3–5}. But as we emphasized¹, this is only the first step; much work

remains, including testing for the necessity of various circuit elements in distinct phases of BOLD responses in many experimental settings. The diversity of events leading to haemodynamic responses will vary among systems^{6–10}, and systematically exploring this complexity with specific, causal and non-correlative interventions is now feasible with ofMRI. As we concluded, ofMRI provides “tools and approaches for further probing and defining the causal generation of BOLD signals”¹.

We also capitalized on axonal trafficking of microbial optogenetic proteins by illuminating photosensitive axons^{12,13} rather than cell bodies. To motivate this experiment, we noted that “ofMRI raises the current possibility of globally mapping the causal roles of these cells, accessing them by means of connection topology—that is, by the conformation of their functional projection patterns in the brain”¹. This experiment was therefore not conducted to prove that only antidromic drive could give rise to the resulting BOLD signal (as incorrectly suggested in the Comment²), but explicitly instead to develop an ofMRI technology for using axons to recruit their source cells both antidromically and orthodromically along with the resulting downstream targets, to map globally “the causal effects of specific cell types defined not only by genetic identity and cell body location, but also by axonal projection target”¹. We explained that “ChR2 readily triggers spikes in illuminated photosensitive axons that both drive local synaptic output and back-propagate throughout the axon to the soma of the stimulated cell”¹, reported that stimulation under ofMRI of ChR2-expressing axonal fibres (as the only photosensitive local circuit element) was “sufficient to elicit BOLD responses in remote areas”¹, and concluded in full that these results “illustrate the feasibility for *in vivo* mapping of the global impact of cells defined not only by anatomical location and genetic identity, but also by connection topology”¹.

Specificity may also be obtained by targeting cells in other ways for ofMRI—for example, light may be delivered to genetically and spatially defined somata¹, allowing for mapping of global impact in a manner not feasible with microelectrodes. Consider electrical stimulation of a neuromodulatory brain structure, with the goal of visualizing global neuromodulator-dependent effects⁵. Classical limitations confound this experiment, because electrodes will directly drive nontargeted fibres-of-passage and distant nontargeted cells that happen to have axonal projections or collaterals near the electrode (along with their distant axonal collaterals and resulting postsynaptic partners), and electrodes will also directly drive most local cell types (not just the neuromodulatory cells) in the stimulated region. This nonspecificity prevents global mapping of the causal influence of the cells under investigation; ofMRI now overcomes this problem^{1,5}.

As we demonstrated¹, specific local cells (or if desired, specific distant cells defined by axonal origin and trajectory¹) can now be directly activated for global, causal ofMRI mapping, and any additional activation of other circuit elements is appropriately dictated entirely by the functional output of the targeted components of the investigated circuit. Noted in the fMRI community^{3,5}, this “combination of optogenetics and fMRI permits, for the first time, investigation of genetically specified, large-scale networks in the brains of live animals”³.

Jin Hyung Lee^{1,2}, Remy Durand², Viviana Gradinaru², Feng Zhang², Inbal Goshen², Dae-Shik Kim^{3,4}, Lief E. Fenno², Charu Ramakrishnan² & Karl Deisseroth^{2,5,6,7}

¹Department of Electrical Engineering, Psychiatry and Biobehavioral Sciences, Bioengineering, and Radiology, University of California, Los Angeles, California 90095, USA.

²Department of Bioengineering, Stanford University, Stanford, California 94305, USA.

e-mail: deissero@stanford.edu

³Department of Electrical Engineering, Korea Advanced Institute of Science and Technology (KAIST), Daejeon 305-701, Korea.

⁴Department of Anatomy and Neurobiology, Boston University School of Medicine, Boston, Massachusetts 02118, USA.

⁵Howard Hughes Medical Institute, Stanford University, Stanford, California 94305, USA.

⁶CNC Program, Stanford University, Stanford, California 94305, USA.

⁷Department of Psychiatry and Behavioral Sciences, Stanford, California 94305, USA.

1. Lee, J. H. *et al.* Global and local fMRI signals driven by neurons defined optogenetically by type and wiring. *Nature* **465**, 788–792 (2010).
2. Logothetis, N. K. Bold claims for optogenetics. *Nature* **468**, doi:10.1038/nature09532 (2010).
3. Leopold, D. A. fMRI under the spotlight. *Nature* **465**, 700–701 (2010).
4. Palmer, H. S. Optogenetic fMRI sheds light on the neural basis of the BOLD signal. *J. Neurophysiol.* **104**, 1838–1840 (2010).
5. Vanzetta, I. & Sloviter, H. A. BOLD assumption. *Front. Neuroener.* **2**, 5 (2010).
6. Iadecola, C. & Nedergaard, M. Glial regulation of the cerebral microvasculature. *Nature Neurosci.* **10**, 1369–1376 (2007).
7. Hamel, E. Perivascular nerves and the regulation of cerebrovascular tone. *J. Appl. Physiol.* **100**, 1059–1064 (2006).
8. Cauli, B. *et al.* Cortical GABA interneurons in neurovascular coupling: relays for subcortical vasoactive pathways. *J. Neurosci.* **24**, 8940–8949 (2004).
9. Devor, A. *et al.* Stimulus-induced changes in blood flow and 2-deoxyglucose uptake dissociate in ipsilateral somatosensory cortex. *J. Neurosci.* **28**, 14347–14357 (2008).
10. Gordon, G. R. C., Choi, H. B., Rungta, R. L., Ellis-Davies, G. C. R. & MacVicar, B. A. Brain metabolism dictates the polarity of astrocyte control over arterioles. *Nature* **456**, 745–750 (2008).
11. Schneuwly, S., Klemenz, R. & Gehring, W. J. Redesigning the body plan of *Drosophila* by ectopic expression of the homoeotic gene *Antennapedia*. *Nature* **325**, 816–818 (1987).
12. Petreanu, L., Huber, D., Sobczyk, A. & Svoboda, K. Channelrhodopsin-2-assisted circuit mapping of long-range callosal projections. *Nature Neurosci.* **10**, 663–668 (2007).
13. Gradinaru, V. *et al.* Targeting and readout strategies for fast optical neural control *in vitro* and *in vivo*. *J. Neurosci.* **27**, 14231–14238 (2007).

doi:10.1038/nature09533

Snapshots of cooperative atomic motions in the optical suppression of charge density waves

Maximilian Eichberger^{1*}, Hanjo Schäfer^{1*}, Marina Krumova², Markus Beyer¹, Jure Demsar^{1,3}, Helmuth Berger⁴, Gustavo Moriena^{5,6}, Germán Sciaini^{5,6*} & R. J. Dwayne Miller^{5,6}

Macroscopic quantum phenomena such as high-temperature superconductivity, colossal magnetoresistance, ferrimagnetism and ferromagnetism arise from a delicate balance of different interactions among electrons, phonons and spins on the nano-scale¹. The study of the interplay among these various degrees of freedom in strongly coupled electron–lattice systems is thus crucial to their understanding and for optimizing their properties. Charge-density-wave (CDW) materials², with their inherent modulation of the electron density and associated periodic lattice distortion, represent ideal model systems for the study of such highly cooperative phenomena. With femtosecond time-resolved techniques, it is possible to observe these interactions directly by abruptly perturbing the electronic distribution while keeping track of energy relaxation pathways and coupling strengths among the different subsystems^{3–7}. Numerous time-resolved experiments have been performed on CDWs^{8–13}, probing the dynamics of the electronic subsystem. However, the dynamics of the periodic lattice distortion have been only indirectly inferred¹⁴. Here we provide direct atomic-level information on the structural dynamics by using femtosecond electron diffraction¹⁵ to study the quasi two-dimensional CDW system 1T-TaS₂. Effectively, we have directly observed the atomic motions that result from the optically induced change in the electronic spatial distribution. The periodic lattice distortion, which has an amplitude of ~ 0.1 Å, is suppressed by about 20% on a timescale (~ 250 femtoseconds) comparable to half the period of the corresponding collective mode. These highly cooperative, electronically driven atomic motions are accompanied by a rapid electron–phonon energy transfer (~ 350 femtoseconds) and are followed by fast recovery of the CDW (~ 4 picoseconds). The degree of cooperativity in the observed structural dynamics is remarkable and illustrates the importance of obtaining atomic-level perspectives of the processes directing the physics of strongly correlated systems.

1T-TaS₂ is one of the most-studied quasi-two-dimensional CDW systems^{16–19}. It has a simple crystalline structure, consisting of planes of hexagonally arranged tantalum (Ta) atoms, sandwiched by two sulphur (S) layers coordinating the central Ta atom in an octahedral arrangement^{16,17}. In the low-temperature CDW phase, the conduction electron density becomes modulated, modifying the forces among the ions and generating a periodic lattice distortion (PLD) with a periodicity of ~ 12 Å. This effect is illustrated in Fig. 1a, b together with the corresponding potential energy surfaces, $U(Q)$, where Q is the generalized coordinate of the atomic displacements. The corresponding changes in $U(Q)$ result in a shift of the equilibrium atomic positions to introduce a PLD. In 1T-TaS₂, the transition from its metallic, unmodulated, phase to an incommensurate CDW phase (ICP) happens at 550 K. At 350 K, a transition to a nearly commensurate CDW phase (NCCP) occurs, where the amplitude of the PLD increases abruptly

from 0.03 to 0.1 Å and the CDW wavevector undergoes a sudden angular rotation from $\phi = 0^\circ$ to $\sim 12.3^\circ$ with respect to the fundamental lattice vector of the host (unreconstructed) lattice. Finally, a transition to a commensurate CDW phase (CCP) takes place at 180 K, with $\phi = 13.9^\circ$ and a $\sqrt{13} \times \sqrt{13}$ periodicity¹⁷. This phase transition is characterized by the appearance of the gap throughout the Fermi surface, and is argued to be due to Mott localization²⁰. The appearance of the ICP can be described by the standard Peierls model². According to this, in low-dimensional systems the divergence in the static electronic susceptibility at the wavevector $2\mathbf{k}_F$, connecting parallel Fermi surfaces at \mathbf{k}_F and $-\mathbf{k}_F$ (where \mathbf{k}_F is the Fermi wavevector), gives rise to an instability of conduction electrons against the formation of the electron density modulation. Indeed, the comparison of the topology of the Fermi surface with parallel sections that can be connected by the modulation wavevector favours the standard Peierls model for the emergence of the ICP^{16–18}. The nature of the CCP and

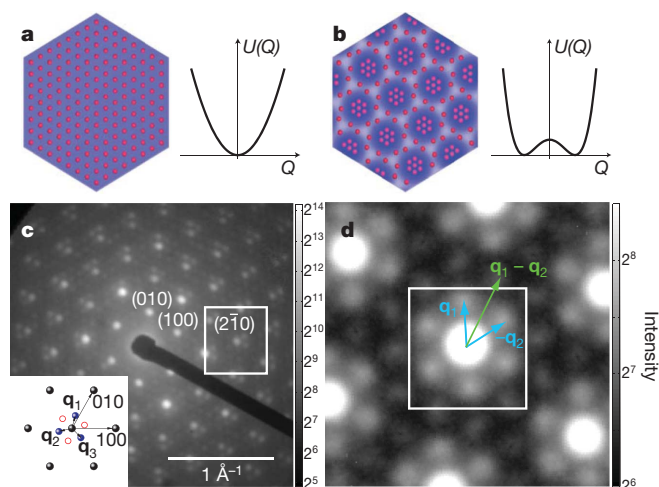


Figure 1 | FED data in the NCCP in 1T-TaS₂. **a**, **b**, Schematic real-space images of Ta atoms and the electron density in the metallic (**a**) and the CDW (**b**) states together with the corresponding potential energy, U , as a function of generalized coordinate, Q . **c**, The diffraction pattern of 1T-TaS₂ at 200 K (intensity is shown on a logarithmic scale in arbitrary units). Each Bragg reflection is surrounded by six first-order CDW reflections at the scattering wave-vectors \mathbf{q}_i , which each has an out-of-plane component of $\pm 1/3c^*$ (red and blue circles, respectively, in inset). The projections of the \mathbf{q}_i on the basal plane, with a modulus of $\sim 0.28a^*$, are tilted away from the closest fundamental lattice vector by an angle $\phi \approx 12.3^\circ$. **d**, Magnified view of the diffraction intensity (I) near the (210) Bragg peak (see box in **c**; for presentation purposes the diffraction image was symmetrized with respect to the six-fold axis). The secondary CDW reflections at the wavevector corresponding to the difference of the wavevectors of the first-order CDW peaks²⁰ are clearly resolved.

¹Physics Department and Center of Applied Photonics and Zukunftskolleg, University of Konstanz, D-78457 Konstanz, Germany. ²Department of Chemistry, University of Konstanz, D-78457 Konstanz, Germany. ³Complex Matter Department, Jozef Stefan Institute, SI-1000 Ljubljana, Slovenia. ⁴Physics Department, EPFL CH-1015 Lausanne, Switzerland. ⁵Institute for Optical Sciences and Departments of Chemistry and Physics, University of Toronto, Toronto, Ontario M5S 3H6, Canada. ⁶Max Planck Research Department for Structural Dynamics, Department of Physics, University of Hamburg, Centre for Free Electron Laser Science, DESY, D-22607 Hamburg, Germany.

*These authors contributed equally to this work.

the NCCP, as well as of the ICP–NCCP and NCCP–CCP transitions, is, however, still under debate¹⁸. Recently, 1T-TaS₂ received additional attention owing to the observation there of superconductivity below 5 K under high pressure¹⁹.

In this study, we investigated the structural dynamics of the PLD in 30-nm-thick, free-standing slices of 1T-TaS₂. We performed femto-second electron diffraction (FED) experiments in transmission geometry along the *c* axis, that is, perpendicular to the TaS₂ layers. The films were photoexcited with 140-fs optical pulses, and 50-keV electrons, in bursts of ≤ 250 fs, were used to monitor the structural changes by recording time-delayed diffraction patterns. The diffraction pattern of the NCCP (200 K) recorded in this set-up is shown in Fig. 1c together with the assignment of some of the scattering vectors. The intense peaks are the Bragg reflections of the host lattice. Each of the Bragg peaks is surrounded by six weak satellite peaks originating from the PLD, with modulation wavevectors \mathbf{q}_i (ref. 21), illustrated in Fig. 1c (inset) and Fig. 1d.

Figure 2a–e shows the time evolution of the relative change of the diffraction signal in the vicinity of a Bragg peak, following photoexcitation. The corresponding traces of the relative changes in the Bragg peaks ($\Delta I_{\text{Bragg}}/I_{\text{Bragg}}$), the inelastic background ($\Delta I_{\text{bckg}}/I_{\text{bckg}}$) and the CDW peaks ($\Delta I_{\text{CDW}}/I_{\text{CDW}}$) are shown in Fig. 2f (see also Supplementary Fig. 3). The intensity of the CDW peaks (the satellites of the Bragg peaks), I_{CDW} , is suppressed by $\sim 30\%$ on the timescale of hundreds of femtoseconds. The corresponding suppression of the PLD gives rise to more-efficient scattering into the Bragg reflections of the host lattice, manifested by an increase of the Bragg peak intensity, I_{Bragg} , by $\sim 15\%$. In the CDW state, the presence of the PLD suppresses I_{Bragg} similarly to the effect of thermally induced disorder; that is, the presence of PLD can be looked upon as an effective Debye–Waller effect. The decrease in I_{CDW} and the accompanying increase in I_{Bragg} thus illustrate a cooperative phenomenon in which the optically induced redistribution of electron density efficiently decreases the PLD amplitude. Because I_{CDW} is proportional to the square of the atomic displacements²², the resulting suppression of I_{CDW} , by $\sim 30\%$,

corresponds to $\sim 16\%$ change in atomic displacements (~ 0.02 Å). Following the initial increase, I_{Bragg} is found to partially recover on the 350-fs timescale. This recovery is accompanied by an increase in the inelastic background intensity, I_{bckg} —see the intensity changes in the area indicated by the circle in Fig. 2e for the frames between 300 (Fig. 2c) and 5,800 fs (Fig. 2e). This process can be attributed to the generation of phonons with non-zero momentum ($q \neq 0$); hence, I_{Bragg} is reduced owing to the conventional Debye–Waller effect, leading to an increase in the inelastic background.

A noteworthy feature of the data shown in Fig. 2f, and elaborated on in Fig. 3a, is the apparent difference between the dynamics of $\Delta I_{\text{Bragg}}/I_{\text{Bragg}}$ and $\Delta I_{\text{CDW}}/I_{\text{CDW}}$. Although the maximum in I_{Bragg} is reached at a time delay of ~ 300 fs (Fig. 3a, dashed vertical line), the minimum in I_{CDW} is reached at a time delay of ~ 500 fs (Fig. 3a, solid vertical line), at which point I_{Bragg} has decreased from its maximum. This difference can be naturally explained by considering the effects of both the suppression of the PLD and the increase in the $q \neq 0$ phonon population on the two diffraction intensities. For the case of I_{Bragg} , the first effect gives rise to its increase as the periodicity of the host lattice is enhanced, and the increase in the $q \neq 0$ phonon population (the Debye–Waller effect) has the opposite effect. Indeed, from the fast recovery of I_{Bragg} and the corresponding increase in I_{bckg} it follows that the energy transfer from electrons to $q \neq 0$ phonons in 1T-TaS₂ takes place on the timescale of a few hundred femtoseconds ($\tau_{\text{e-ph}} \approx 350$ fs). For I_{CDW} , both the displacive excitation of highly correlated atomic motions and phonon-induced disorder contribute to its suppression, explaining the longer timescale on which the minimum of I_{CDW} is reached.

It is instructive to compare the structural dynamics data with those of the electronic subsystem. We have performed all-optical pump–probe measurements, where the dynamics are mainly sensitive to the changes in the electronic properties. The photoinduced reflectivity change (Fig. 2g) shows a rapid onset on the 100-fs timescale, followed by a fast recovery with a decay time of 150 fs and subsequent slower decay with a relaxation time of ~ 4 ps, which is nearly identical to the

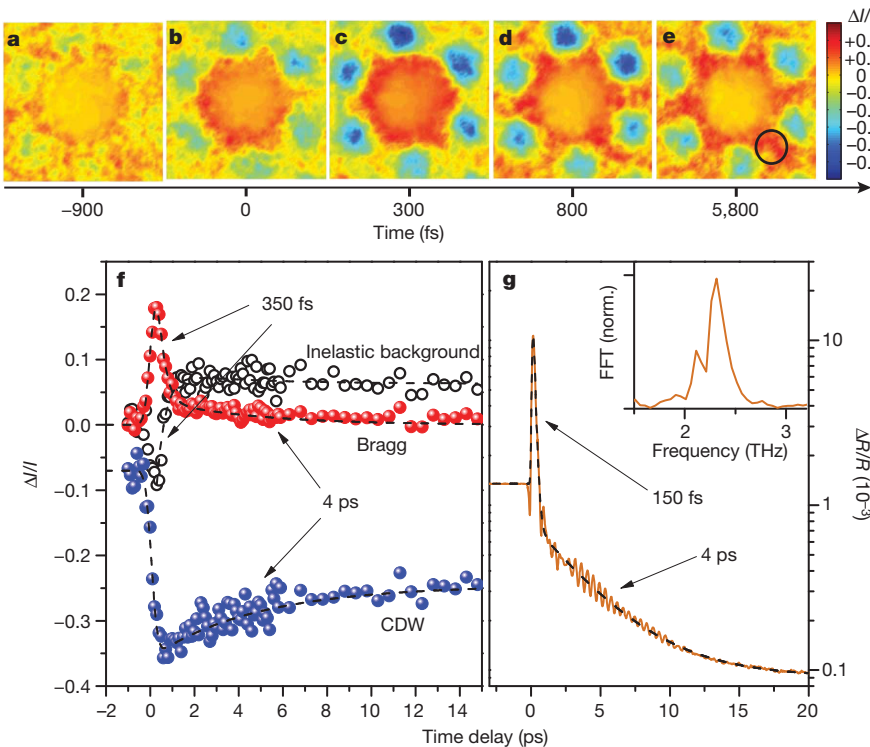


Figure 2 | Time evolution of the diffraction intensities following photoexcitation with a fluence of 2.4 mJ cm^{-2} . a–e, Evolution of Bragg, CDW and inelastic background intensities illustrated as relative change in the diffraction pattern at several time delays following photoexcitation with a fluence of 2.4 mJ cm^{-2} and a photon energy of 3.2 eV (see also Supplementary Fig. 4 and Supplementary Information). These images were obtained by averaging (area enclosed by the box in Fig. 1d) over all individual Bragg reflections to increase the signal-to-noise ratio. The circle in e represents the area over which the inelastic background intensity was monitored. f, Corresponding dynamics of $\Delta I_{\text{Bragg}}/I_{\text{Bragg}}$, $\Delta I_{\text{CDW}}/I_{\text{CDW}}$ and $\Delta I_{\text{bckg}}/I_{\text{bckg}}$ with fits to the data (dashed lines) and the extracted timescales. The suppression of the PLD, that is, the CDW peak intensity at negative time delays, is due to an increase in the sample temperature caused by the photoexcitation pulse train (accumulative heating). The initial drop in I_{bckg} is an artefact, a result of the decrease in the diffraction intensity of the nearby CDW peaks, whose tails extend well into the region where the inelastic background was evaluated (e). g, Dynamics of the differential reflectivity change, $\Delta R/R$, at 1.55 eV (800 nm), recorded at the same initial temperature and the same excitation energy density, together with the fit (dashed line). The signal has been offset vertically for presentation purposes. The oscillatory response corresponds to the coherently excited amplitude mode at 2.3 THz and phonon mode at 2.1 THz (refs 9, 11, 21). Inset, fast Fourier transform (FFT) of the oscillatory component.

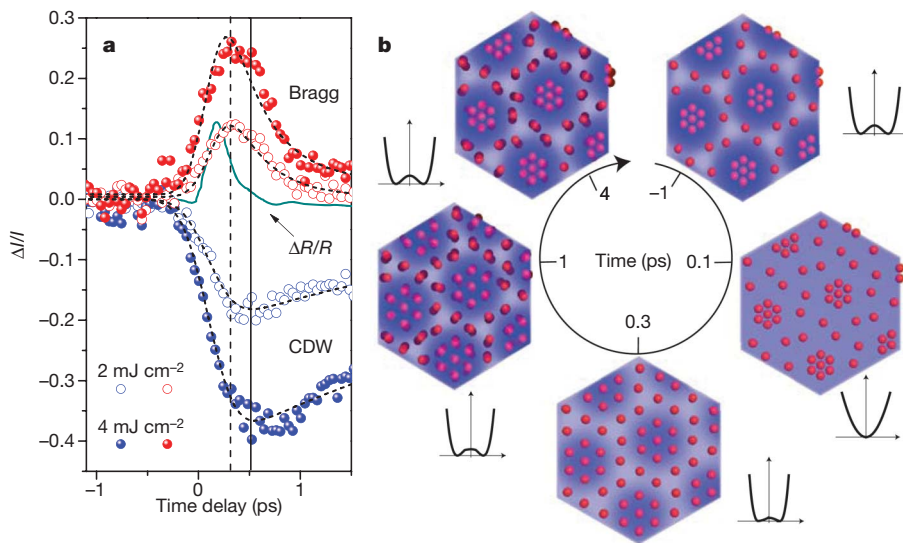


Figure 3 | Early time dynamics and emerging time evolution of the CDW state in 1T-TaS₂ on photoexcitation. **a**, Data were recorded with a 40-fs time step at two excitation fluences, and compared with the optical $\Delta R/R$ data. The maximum induced changes in the Bragg (dashed vertical line) and CDW (solid vertical line) peaks were achieved ~ 300 fs and, respectively, ~ 500 fs after photoexcitation. **b**, The evolution of the real-space structure of the Ta plane of 1T-TaS₂ following photoexcitation with an intense optical pulse (circles represent Ta atoms and blue shading represents the density of conduction electrons; the amplitudes are strongly exaggerated). Before photoexcitation ($t \approx -1$ ps), the Ta atoms are periodically displaced from their pure 1T structure, forming a nearly commensurate CDW. Intense perturbation of the electronic system gives rise to smearing of the electron density modulation ($t \approx 0.1$ ps), driving the lattice towards the undistorted state (at $t \approx 0.3$ ps, the hexagonal symmetry of the pure 1T phase is nearly recovered). In parallel, the energy is transferred from the electronic subsystem to phonons on the 300-fs timescale, resulting in recovery of the electron density modulation and thermal disordering of the lattice ($t \approx 1$ ps). The CDW order is recovered at $t \approx 4$ ps, after which time the sample is thermalized at a somewhat higher temperature.

CDW recovery time observed in the FED studies. The short decay timescale is identical to the one obtained in the NCCP by time- and angle-resolved photoemission spectroscopy¹¹ (tr-ARPES) and can be attributed to the electron–phonon energy transfer. Because the electron–phonon scattering rate is strongly momentum dependent ($\propto 1/q$), it is quite natural to observe shorter time constants in optics and tr-ARPES than in FED. In the former experiments the signal is dominated by the energy transfer to $q \approx 0$ phonons, whereas in the latter the behaviour of I_{Bragg} and I_{bckg} is governed by the population of large- q phonons. In the optical data, owing to their high signal-to-noise ratio, in addition to the electronic response a weak oscillatory signal is observed. The main mode observed at 2.3 THz is the totally symmetric amplitude mode^{9,11,23} of the CDW, whose amplitude is apparently smaller than the noise level in the FED data.

Despite the fact that a large amount of energy is transferred to phonons on the subpicosecond timescale, the system is not yet in thermal equilibrium 1 ps after photoexcitation. The recovery of the PLD amplitude is clearly observed in I_{Bragg} and I_{CDW} . This timescale is well decoupled from both subpicosecond timescales. By fitting the recovery of I_{CDW} with an exponential decay, we obtain a CDW recovery time of $\tau_{\text{rec}} \approx 4$ ps. As this timescale is much longer than the oscillation period of the amplitude mode, it is reasonable to assume that the electronic part of the order parameter follows the PLD on the aforementioned timescale. Here the process that governs the CDW recovery dynamics is the thermalization with the longer-wavelength acoustic phonons by means of anharmonic phonon decay. Indeed, the characteristic linewidths of the low-energy optical phonons²³ are about 10 cm^{-1} , corresponding to lifetimes of 3 ps. The two distinct relaxation timescales, one of the order of 100-fs and the other of several picoseconds, are commonly observed in optical experiments in CDWs^{8,10}. From the direct structural dynamics and optical data on 1T-TaS₂, we can conclude that the longer timescale describes the recovery of the coupled electron–lattice order parameter and that the shorter timescale corresponds to the partial recovery of the electronic part alone¹⁴.

To determine the time constant for the electronic suppression of the PLD, which leads to an increase in I_{Bragg} , we analysed its dynamics. By fitting (Supplementary Fig. 5 and Supplementary Information) the I_{Bragg} trace, taking into account the finite optical and electron pulse widths, we determined a timescale of $\tau_{\text{supp}} \approx 250 \pm 70$ fs for the PLD suppression.

Information complementary to the above findings comes from considering the energy flow following photoexcitation. In the experiments with fluences $F = 2\text{--}4 \text{ mJ cm}^{-2}$, no signature of the NCCP–ICP transition is observed. Only at $F = 4.8 \text{ mJ cm}^{-2}$ is the photoinduced NCCP–ICP transition realized (Supplementary Fig. 6 and Supplementary Information), as demonstrated by a strong suppression of the CDW peak intensity and a rotation of the primary CDW wavevectors, \mathbf{q}_i , by $\phi \approx 10^\circ$. Using the literature values of the optical constants and the overall specific heat (Supplementary Information), we obtained a temperature increase of $\sim 180 \text{ K}$ at $F = 4.8 \text{ mJ cm}^{-2}$. This implies that the energy needed to drive the phase transition is comparable to the energy required simply to heat the sample across the phase transition. The rapid energy transfer from the electronic system to phonons ($\tau_{\text{e-ph}} \approx 150\text{--}350$ fs), which is competing with the electronically driven PLD suppression process ($\tau_{\text{supp}} \approx 250$ fs), and the fact that the electronically excited symmetric amplitude mode does not map into the rotation of the CDW wavevector, suggest that the NCCP–ICP transition can be driven only thermally.

The direct structural information obtained with FED, supported by time-resolved optical and published tr-ARPES¹¹ data, enabled us to elucidate the dynamics of the coupled electron–lattice order parameter (Fig. 3b). Strong photoexcitation and subsequent electron–electron scattering creates a high density of electron–hole pairs within ≤ 100 fs, raising the effective electronic temperature to several thousand kelvin. The electronic modulation is thereby strongly suppressed, modifying the potential energy surface $U(Q)$. The collapse of the double-well potential brings about highly cooperative atomic motions towards a new quasi-equilibrium. This coherent process is, however, accompanied by the rapid recovery of the double-well potential due to cooling of the electronic subsystem through the electron–phonon scattering, which also takes place on the subpicosecond timescale^{8–13}. The resulting suppression of the PLD amplitude, by $\sim 20\%$ (0.02 \AA), happens within a time of $\tau_{\text{supp}} \approx 250 \pm 70$ fs, that is, about half the period of the amplitude mode, ~ 440 fs (refs 9, 11). After a time delay of $t \approx 300$ fs, the periodicity of the underlying lattice has increased and the amplitude of the PLD has decreased. By $t \approx 1$ ps, the electronic modulation has been largely recovered and the electrons have transferred the energy to $q \neq 0$ phonons, randomizing the atomic motions. Finally, the coupled electron–lattice order parameter recovers on the timescale of ~ 4 ps, when the excess energy is

redistributed by further thermalization with low-energy acoustic phonons.

These results demonstrate the extreme robustness of the PLD in 1T-TaS₂ against electronic excitation triggered by a femtosecond optical pulse. By contrast, in the insulating CCP the gap is fully suppressed¹¹ at only one-tenth of the absorbed energy density used in our study. The large difference in the two energy densities presents a strong argument that the NCCP–CCP transition is indeed Mott driven^{11,19}.

The present work illustrates the importance of directly observing atomic motions on timescales short enough to follow even the effect of non-equilibrium electronic distributions on strongly correlated lattice dynamics. In this respect, the introduction of table-top FED systems^{24–26} with sufficient brightness and time resolution^{24,26} is opening new pathways to the investigation of a myriad of cooperative systems in which electron–lattice correlations have an important role^{26–30}. In systems with reduced dimensionality, such as quasi-one-dimensional and quasi-two-dimensional systems, in which structural changes have a predominantly in-plane character, the use of FED may be particularly advantageous. Because information about structural dynamics over the entire two-dimensional Brillouin zone is obtained in a single experimental run by FED, it is easy to distinguish between different processes that give rise to changes in the diffraction intensities, as in the case of 1T-TaS₂. Moreover, with further instrumental improvements, for example an increase in the signal-to-noise ratio, FED could be used to find signatures of lattice modulations, which may be difficult to determine by means of static diffraction methods, much like modulation optical spectroscopy is used to determine the electronic band structure in solids.

METHODS SUMMARY

In the present study, we used electron bunches of ≤ 250 -fs duration containing 4,000 electrons, each of which had a kinetic energy of 50 keV. The electron beam (spot size, 150 μm) was collimated by a magnetic lens to scatter from the sample and generate a diffraction pattern downstream. The diffraction patterns formed on a phosphor screen after being intensified by a multichannel plate, and were recorded using a charge-coupled-device camera. The background pressures were 10^{-9} and 10^{-7} mbar in the electron gun and the sample chamber sections, respectively. We made the measurements in transmission mode at a repetition rate of 1 kHz. In this geometrical configuration, spatiotemporal mismatch and surface charging effects are negligible. The electron pulse duration was characterized using a recently developed electron/laser-pulse cross-correlation method based on ponderomotive scattering and *N*-body simulations. Photoinduced structural changes were initiated by 387-nm, 140-fs pump pulses focused to a spot with a full-width at half-maximum of 350 μm . The overall instrumental response time was 240–290 fs. The sample temperature, of 200 K, was achieved by using a cold finger attached to a well-conducting sample holder made of oxygen-free copper. We measured the temperature *in situ* using a calibrated temperature sensor. The 30-nm-thick, single-crystalline 1T-TaS₂ slices, $\sim 200 \mu\text{m} \times 200 \mu\text{m}$ in size (Supplementary Figs 2 and 3), were obtained by cleaving a thicker single crystal using an ultramicrotome. The slices were picked up from the water surface using a host copper mesh. All optical measurements were performed in reflection geometry using 60-fs optical pulses (carrier wavelength, 800 nm) at a repetition rate of 100 kHz. FED and all-optical experiments were carried out with the same excitation energy density and under the same sample temperature conditions.

Received 17 May; accepted 24 September 2010.

Published online 24 November 2010.

- Imada, M., Fujimori, A. & Tokura, Y. Metal-insulator transitions. *Rev. Mod. Phys.* **70**, 1039–1263 (1998).
- Grüner, G. *Density Waves in Solids* (Addison-Wesley, 1994).
- Kusar, P. *et al.* Controlled vaporization of the superconducting condensate in cuprate superconductors by femtosecond photoexcitation. *Phys. Rev. Lett.* **101**, 227001 (2008).
- Ogasawara, T. *et al.* General features of photoinduced spin dynamics in ferromagnetic and ferrimagnetic compounds. *Phys. Rev. Lett.* **94**, 087202 (2005).
- Averitt, R. D. *et al.* Ultrafast conductivity dynamics in colossal magnetoresistance manganites. *Phys. Rev. Lett.* **87**, 017401 (2001).

- Rini, M. *et al.* Control of the electronic phase of a manganite by mode-selective vibrational excitation. *Nature* **449**, 72–74 (2007).
- Kübler, C. *et al.* Coherent structural dynamics and electronic correlations during an ultrafast insulator-to-metal phase transition in VO₂. *Phys. Rev. Lett.* **99**, 116401 (2007).
- Demsar, J., Biljakovic, K. & Mihailovic, D. Single particle and collective excitations in the one-dimensional charge density wave solid K_{0.3}MoO₃ probed in real time by femtosecond spectroscopy. *Phys. Rev. Lett.* **83**, 800–803 (1999).
- Demsar, J. *et al.* Femtosecond snapshots of gap-forming charge-density-wave correlations in quasi-two-dimensional dichalcogenides 1T-TaS₂ and 2H-TaSe₂. *Phys. Rev. B* **66**, 041101 (2002).
- Yusupov, R. V. *et al.* Single-particle and collective mode couplings associated with 1- and 2-directional electronic ordering in metallic RTe₃ (R = Ho, Dy, Tb). *Phys. Rev. Lett.* **101**, 246402 (2008).
- Perfetti, L. *et al.* Time evolution of the electronic structure of 1T-TaS₂ through the insulator-metal transition. *Phys. Rev. Lett.* **97**, 067402 (2006).
- Schmitt, F. *et al.* Transient electronic structure and melting of a charge density wave in TbTe₃. *Science* **321**, 1649–1652 (2008).
- Tomeljak, A. *et al.* Dynamics of photoinduced charge-density-wave to metal phase transition in K_{0.3}MoO₃. *Phys. Rev. Lett.* **102**, 066404 (2009).
- Schäfer, H. *et al.* Disentanglement of the electronic and lattice parts of the order parameter in a 1D charge density wave system probed by femtosecond spectroscopy. *Phys. Rev. Lett.* **105**, 066402 (2010).
- Miller, R. J. D. *et al.* 'Making the molecular movie': first frames. *Acta Crystallogr. A* **66**, 137–156 (2010).
- Williams, P. M., Parry, G. S. & Scruby, C. B. Diffraction evidence for Kohn anomaly in 1T-TaS₂. *Phil. Mag.* **29**, 695–699 (1974).
- Wilson, J. A. Di Salvo, F. J. & Mahajan, S. Charge-density waves and superlattices in the metallic layered transition-metal dichalcogenides. *Adv. Phys.* **24**, 117–201 (1975).
- Clerc, F. *et al.* Lattice-distortion-enhanced electron-phonon coupling and Fermi surface nesting in 1T-TaS₂. *Phys. Rev. B* **74**, 155114 (2006).
- Sipos, B. *et al.* From Mott state to superconductivity in 1T-TaS₂. *Nature Mater.* **7**, 960–965 (2008).
- Fazekas, P. & Tosatti, E. Electrical, structural and magnetic-properties of pure and doped 1T-TaS₂. *Phil. Mag. B* **39**, 229–244 (1979).
- Scrubby, C. B., Williams, P. M. & Parry, G. S. The role of charge density waves in structural transformations of 1T-TaS₂. *Phil. Mag.* **31**, 255–274 (1975).
- Als-Nielsen, J. & McMorris, D. *Elements of Modern X-ray Physics* Ch. 4.4.5 (Wiley, 2001).
- Duffey, J. R., Kirby, R. D. & Coleman, R. V. Raman scattering from 1T-TaS₂. *Solid State Commun.* **20**, 617–621 (1976).
- Swick, B. J., Dwyer, J. R., Jordan, R. E. & Miller, R. J. D. An atomic-level view of melting using femtosecond electron diffraction. *Science* **302**, 1382–1385 (2003).
- Chergui, M. & Zewail, A. H. Electron and X-ray methods of ultrafast structural dynamics: advances and applications. *ChemPhysChem* **10**, 28–43 (2009).
- Scialini, G. *et al.* Electronic acceleration of atomic motions and disordering in bismuth. *Nature* **458**, 56–59 (2009).
- Sokolowski-Tinten, K. *et al.* Femtosecond X-ray measurement of coherent lattice vibrations near the Lindemann stability limit. *Nature* **422**, 287–289 (2003).
- Johnson, S. L. *et al.* Directly observing squeezed phonon states with femtosecond X-ray diffraction. *Phys. Rev. Lett.* **102**, 175503 (2009).
- Fritz, D. M. *et al.* Ultrafast bond softening in bismuth: mapping a solid's interatomic potential with X-rays. *Science* **315**, 633–636 (2007).
- Beaud, P. *et al.* Ultrafast structural phase transition driven by photoinduced melting of charge and orbital order. *Phys. Rev. Lett.* **103**, 155702 (2009).

Supplementary Information is linked to the online version of the paper at www.nature.com/nature.

Acknowledgements We would like to acknowledge discussions with V. V. Kabanov, T. Dekorsy, D. Mihailovic, U. Bovensiepen and M. Wolf, and thank A. Nagy for help in preparing the video in Supplementary Material. This research was supported by the Sofia Kovalevskaja Award of the Alexander von Humboldt Foundation, the Center for Applied Photonics and Zukunftskolleg at the University of Konstanz, the Natural Science and Engineering Research Council of Canada and the Canada Foundation for Innovation. M.E. acknowledges financial support through the Stiftung der Deutschen Wirtschaft. H.B. acknowledges financial support from the Swiss NSF and the NCCR MaNEP.

Author Contributions R.J.D.M. and J.D. directed this work. H.B. grew 1T-TaS₂ single crystals. M.E. and M.K. prepared thin films and performed transmission electron microscopy characterization. G.S., G.M., M.E. and H.S. performed the FED experiments at the University of Toronto. M.B., M.E. and H.S. performed the optical pump–probe experiments at the University of Konstanz. M.E., H.S. and J.D. performed the data analysis. J.D., G.S. and R.J.D.M. wrote the paper. All authors contributed to discussions.

Author Information Reprints and permissions information is available at www.nature.com/reprints. The authors declare no competing financial interests. Readers are welcome to comment on the online version of this article at www.nature.com/nature. Correspondence and requests for materials should be addressed to R.J.D.M. (dmiller@physics.utoronto.ca) or J.D. (jure.demsar@uni-konstanz.de).

Tumour vascularization via endothelial differentiation of glioblastoma stem-like cells

Lucia Ricci-Vitiani^{1*}, Roberto Pallini^{2*}, Mauro Biffoni¹, Matilde Todaro³, Gloria Invernici⁴, Tonia Cenci⁵, Giulio Maira², Eugenio Agostino Parati⁴, Giorgio Stassi^{3,6}, Luigi Maria Larocca⁵ & Ruggero De Maria^{1,7}

Glioblastoma is a highly angiogenetic malignancy, the neoformed vessels of which are thought to arise by sprouting of pre-existing brain capillaries. The recent demonstration that a population of glioblastoma stem-like cells (GSCs) maintains glioblastomas^{1,2} indicates that the progeny of these cells may not be confined to the neural lineage³. Normal neural stem cells are able to differentiate into functional endothelial cells⁴. The connection between neural stem cells and the endothelial compartment seems to be critical in glioblastoma, where cancer stem cells closely interact with the vascular niche and promote angiogenesis through the release of vascular endothelial growth factor (VEGF) and stromal-derived factor 1 (refs 5–9). Here we show that a variable number (range 20–90%, mean 60.7%) of endothelial cells in glioblastoma carry the same genomic alteration as tumour cells, indicating that a significant portion of the vascular endothelium has a neoplastic origin. The vascular endothelium contained a subset of tumorigenic cells that produced highly vascularized anaplastic tumours with areas of vasculogenic mimicry in immunocompromised mice. *In vitro* culture of GSCs in endothelial conditions generated progeny with phenotypic and functional features of endothelial cells. Likewise, orthotopic or subcutaneous injection of GSCs in immunocompromised mice produced tumour xenografts, the vessels of which were primarily composed of human endothelial cells. Selective targeting of endothelial cells generated by GSCs in mouse xenografts resulted in tumour reduction and degeneration, indicating the functional relevance of the GSC-derived endothelial vessels. These findings describe a new mechanism for tumour vasculogenesis and may explain the presence of cancer-derived endothelial-like cells in several malignancies.

From archival material, we selected a group of glioblastomas showing both remarkable angiogenesis and nuclear accumulation of mutant p53 in tumour cells (Supplementary Table 1). In 83.3% (20/24) of these tumours, we found cells with nuclear accumulation of mutant p53 that lined the lumens of capillaries and/or vascular glomeruli (Supplementary Fig. 1a and Supplementary Table 1). Double immunohistochemistry analysis of p53 and CD31 demonstrated the endothelial phenotype of the p53-positive cells facing the lumen of the vessels (Supplementary Fig. 1b). Mouse and human tumour-associated endothelial cells can harbour chromosomal alterations^{10–12}. To assess whether a subset of endothelial cells showed glioblastoma-specific chromosomal aberrations, we analysed the tumour vasculature in 15 glioblastomas by combined CD31 immunofluorescence and fluorescence *in situ* hybridization (FISH) using probes for the centromere of chromosome 10 (Cep10), for the telomere of chromosome 19 (Tel19q), and a locus-specific probe on chromosome 22 (breakpoint cluster region locus q11.2; LSI22). In all the tumours carrying aneuploidy for one or more of these chromosomes, we detected a substantial fraction of endothelial cells bearing the same

chromosomal aberrations (Supplementary Fig. 1c). Interestingly, double immunostaining of vascular glomeruli in glioblastoma revealed a significant number of GFAP⁺ microvascular cells showing an aberrant endothelial/glial phenotype (Supplementary Fig. 1d). Thus, a variable number of endothelial cells in glioblastoma seem to originate from the tumour. To quantify the contribution of tumour-derived endothelial cells to glioblastoma vasculature, we used FISH to analyse purified CD31⁺/CD144⁺ (VE-Cadherin⁺) endothelial cells from freshly dissociated glioblastoma specimens (Fig. 1a). Again, we detected CD31⁺/CD144⁺ endothelial cells that shared the same chromosomal alterations as the tumour cells in any given glioblastoma harbouring aberrations of chromosomes 10, 19 and 22 (Fig. 1b and Supplementary Table 2). The amount of endothelial cells with tumour-specific chromosomal changes ranged between 20 and 90% of the sorted cells (mean 60.7 ± 28.1 standard deviations (s.d.)).

We assessed further the phenotype of sorted CD31⁺/CD144⁺ glioblastoma cells by immunofluorescence, which showed that the vast majority of these cells (83.9 ± 4.2%; range 79–90%) expressed the mature endothelial cell marker von Willebrand factor (vWF), although a substantial proportion of them (30.9 ± 21.3%; range 10–76%) co-expressed vWF and GFAP (Fig. 1c, d). Thus, it seems that the CD31⁺/CD144⁺ cells harbouring chromosomal aberrations are glioblastoma-derived endothelial cells that either differentiated towards the canonical endothelial lineage (GFAP[−]) or showed a mixed endothelial/glial phenotype (GFAP⁺), whereas the euploid fraction is likely to represent endothelial cells derived from normal brain vessels. *In vitro* experiments using a microvascular culture of fresh CD31⁺ cells isolated by magnetic microbeads from glioblastoma samples confirmed the existence of endothelial cells with aberrant GFAP expression (Supplementary Fig. 2a–c), as well as the presence of a substantial number of aneuploid endothelial cells (Supplementary Fig. 2d, e). Grafting of freshly purified CD31⁺/CD144⁺ cells showed that three of five glioblastomas contained tumorigenic endothelial cells that produced highly vascularized anaplastic tumours (Supplementary Fig. 3a–c). These cells, however, lost their tumorigenic activity on *in vitro* culture with endothelial medium (Supplementary Fig. 3a).

Although there is no general agreement on the definition and markers identifying so-called cancer stem cells, there is good evidence that GSCs can be enriched by the use of anti-CD133 antibodies or through the generation of clusters of undifferentiated cells (neurospheres) in serum-free media containing epidermal growth factor (EGF) and basic fibroblast growth factor (FGF)^{1,5,7,13,14}. We demonstrated recently that GSCs can differentiate into mesenchymal cells, giving rise to osteoblastic and chondrocytic cells⁵. To determine the potential contribution to the angiogenic process of GSCs, we cultivated glioblastoma neurospheres and primary glioblastoma differentiated cells under endothelial conditions, or CD133⁺/CD31[−] and CD133[−]/CD31[−] cells derived from the

¹Department of Hematology, Oncology and Molecular Medicine, Istituto Superiore di Sanità, Viale Regina Elena 299, Rome 00161, Italy. ²Department of Neurosurgery, Catholic University of Rome, Largo Francesco Vito 1, Rome 00168, Italy. ³Department of Surgical and Oncological Sciences, University of Palermo, Via Liborio Guffrè 5, Palermo 90127, Italy. ⁴U. O. Cerebrovascular Disease Cellular Neurobiology Laboratory, Fondazione IRCCS, Neurological Institute “Carlo Besta”, Via Celoria 11, 20133 Milan, Italy. ⁵Institute of Pathology, Catholic University of Rome, Largo Francesco Vito 1, Rome 00168, Italy. ⁶Cellular and Molecular Oncology, Istituto di Ricovero e Cura a Carattere Scientifico Fondazione Salvatore Maugeri, Via S. Maugeri 6, Pavia 27100, Italy. ⁷Mediterranean Institute of Oncology, Via Penninazzo 7, 95029, Viagrande, Catania, Italy.

*These two authors contributed equally to the manuscript.

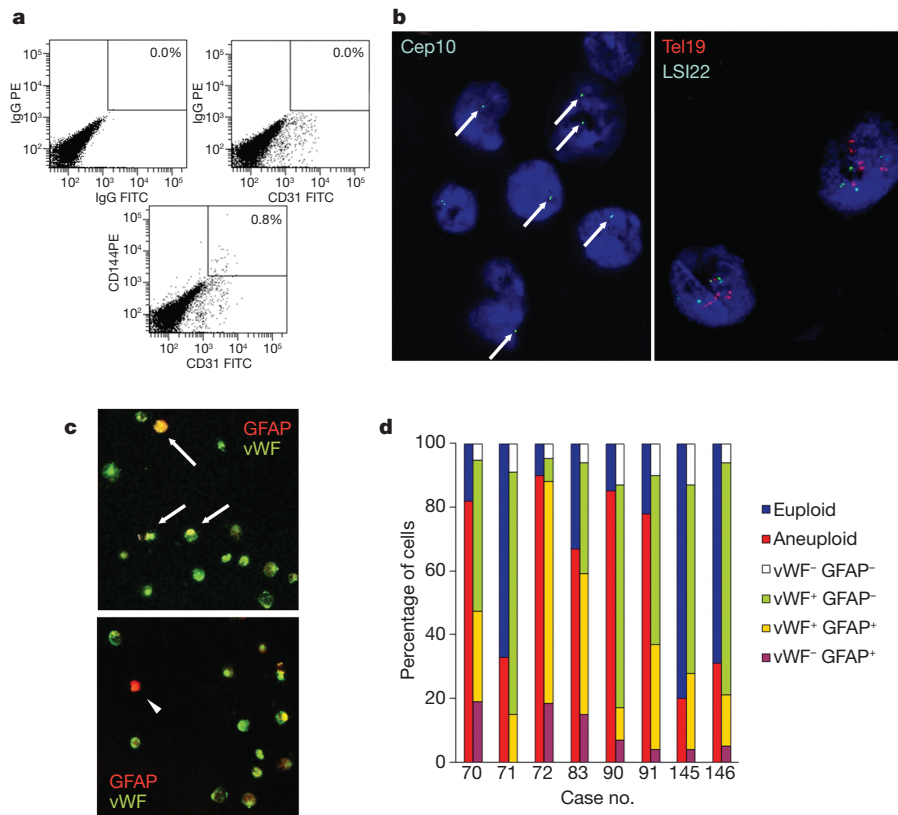


Figure 1 | Microvascular endothelial cells isolated from glioblastoma harbour tumour-specific chromosomal aberrations. **a**, CD31⁺/CD144⁺ cells were isolated from surgical glioblastoma specimens ($n = 15$). FITC, fluorescein isothiocyanate; PE, phycoerythrin. **b**, Sorted cells were analysed by interphase FISH assay for tumour-specific chromosomal changes, such as monosomy of Cep10 (left, arrows) or polysomy of Tel19 and LSI22 (right).

c, The phenotype of the CD31⁺/CD144⁺ sorted cells was further analysed by anti-GFAP and anti-vWF immunofluorescence. A fraction of the CD31⁺/CD144⁺ cells coexpressed GFAP and vWF (arrows), indicating an aberrant endothelial/glia phenotype. A minority of sorted cells were GFAP⁺/vWF⁻. **d**, Quantification of results from FISH and immunofluorescence analysis.

same tumours. Whereas cells enriched in GSCs generated microvascular cultures of CD31⁺ and Tie2⁺ cells, neither differentiated cells nor the U87MG cell line were able to produce endothelial-like cells (Fig. 2a). Such GSC-derived endothelial cells showed considerable tube-forming ability, together with low-density lipoprotein (LDL) uptake and endothelial nitric oxide synthase (eNOS) expression, which were completely absent in differentiated tumour cells and in the U87MG cell line (Fig. 2b–d and Supplementary Fig. 4). Unsupervised gene-expression analysis of glioblastoma and endothelial cells showed that neural-differentiated glioblastoma cells and normal endothelial cells constitute the two more distant groups in a dendrogram in which tumour endothelial cells cluster between normal endothelial cells and glioblastoma neurospheres (Supplementary Fig. 5).

To investigate the ability of GSCs to form endothelial vessels *in vivo*, we measured the relative amount of murine versus human endothelial cells within glioblastoma neurosphere xenografts (Fig. 3a). Flow cytometry analysis with human- and mouse-specific antibodies showed that about 70% of the CD31⁺ cells from the inner portion of the tumour were of human origin, whereas nearly all the CD31⁺ cells in the tumour capsule were murine (Fig. 3b). Likewise, human CD144⁺ cells were detected only in the core and not in the tumour capsule (Fig. 3b). Immunohistochemistry of subcutaneous and intracranial xenografts showed that glioblastoma neurosphere-derived tumours contained human vessels labelled by human-specific anti-CD31, whereas xenografts generated with U87MG or other glioma cell lines grown in serum did not (Fig. 3c, Supplementary Fig. 6a and data not shown). The presence of human-derived endothelial cells was confirmed by labelling sections of tumour xenografts obtained with GFP⁺ glioblastoma neurospheres with anti-GFP and anti-human

CD31 antibodies (Supplementary Fig. 6b). Moreover, immunofluorescence staining with validated human-specific endothelial antibodies showed that these cells expressed consistently CD34, CD144 and VEGFR2 (Fig. 3d) but not the stem-cell markers SSEA-1 and CD133 (Supplementary Fig. 6c). Such human-specific endothelial antigens identified microvascular structures containing circulating erythrocytes (Fig. 3d and Supplementary Fig. 6a), indicating the functional relevance of human angiogenesis in the tumour xenografts. Of note, a similar formation of human endothelial cells was observed in subcutaneous xenografts obtained with the injection of freshly purified CD133⁺/CD31⁻ cells, whereas CD133⁻/CD31⁻ cell xenografts contained only mouse endothelial vessels (Supplementary Fig. 7).

To trace *in vivo* angiogenesis, we injected RFP-labelled glioblastoma neurospheres into transgenic NOD/SCID mice expressing GFP under the Tie2 promoter. Examination of a thick-section plane by confocal microscopy showed that GFP⁺ mouse vessels were primarily outside the tumours (Supplementary Fig. 8a). To exclude the occurrence of fusion between tumour and mouse endothelial cells, we stained tumour xenograft sections with anti-human/mouse Tie2 and CD31 antibodies. Although CD31 staining showed the presence of vessels containing both mouse and human CD31⁺ cells at the periphery of the tumour, the majority of endothelial cells inside the tumour mass did not express mouse Tie2 and were of human origin in the absence of fusion (Supplementary Fig. 8b, c). Moreover, FISH analysis of nuclei extracted from microdissected vascular structures of GSC xenografts confirmed the absence of murine chromosomes in human cells (Supplementary Fig. 9). Together, these findings demonstrate that the tumour xenografts obtained by injection of human glioblastoma neurospheres develop an intrinsic vascular network composed by

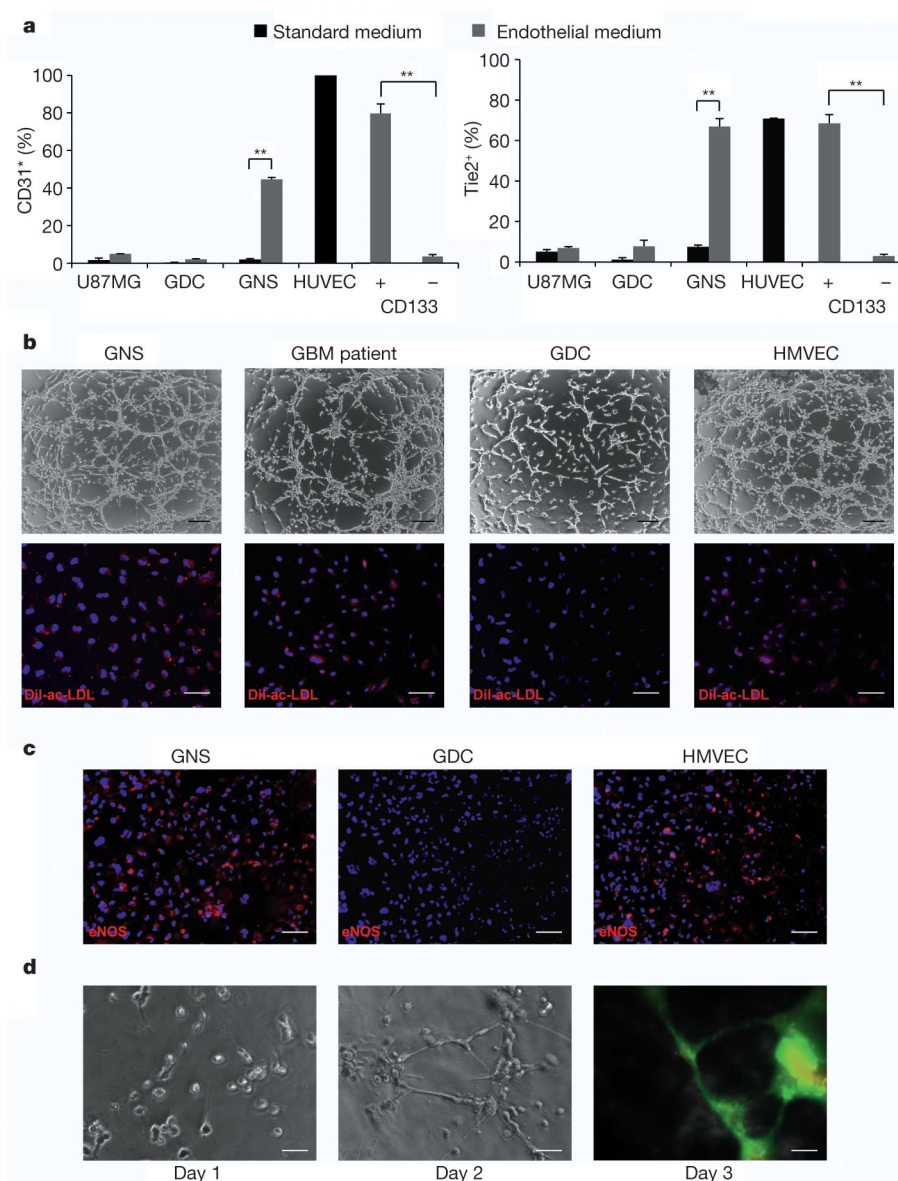


Figure 2 | GSCs cultured under endothelial differentiation conditions develop morphological, phenotypical and functional features of endothelial cells. **a**, Flow cytometry analysis of human umbilical vein endothelial cells (HUVEC), glioblastoma neurospheres (GNS), primary glioblastoma cells cultured in serum (GDC), U87MG, CD31[−]/CD133⁺ and CD31[−]/CD133[−] cells from freshly dissociated glioblastomas. Cells were cultured under standard (black) or endothelial (grey) condition. Error bars represent the mean \pm s.d. ($n = 4$). ** $P < 0.001$. **b**, Tube formation (top) and LDL-uptake (bottom) assay on cells under endothelial conditions as above (GNS and GDC), endothelial

cells isolated from glioblastoma patients (GBM patients) and human dermal microvascular endothelial cells (HMVEC). DiI-ac-LDL, 1,1'-dioctadecyl-3,3,3',3'-tetramethylindocarbocyanine-perchlorate-acetylated LDL. Scale bars, 200 μ m (top) and 50 μ m (bottom). **c**, Immunofluorescence for eNOS in HMVEC, GNS and GDCs treated as above. Scale bar, 100 μ m. **d**, *In vitro* perfusion assay on three-dimensional glioblastoma neurosphere-derived endothelial culture injected with fluorescein. Scale bar, 50 μ m. One representative of four independent experiments performed in blind is shown for b, c and d.

tumour cells with an aberrant endothelial phenotype. To determine whether the GSC-derived endothelial cells contribute to tumour growth, we transduced glioblastoma neurospheres with a lentiviral vector containing the herpes simplex virus thymidine kinase gene (*tk*) under the control of the transcription-regulatory elements of Tie2 (Tie2-*tk*; Supplementary Fig. 10a), so that the tumour-derived endothelial cells would be sensitive to ganciclovir^{15,16}. For this experiment, we selected glioblastoma neurospheres with no detectable expression of Tie2 (Supplementary Fig. 11). Control cells included glioblastoma neurospheres transduced with an empty viral vector and U87MG cells transduced either with Tie2-*tk* or with a vector conferring

constitutive expression of Tk (PGK-*tk*, Supplementary Fig. 10a). One week after ganciclovir administration, TdT-mediated dUTP nick end labelling (TUNEL) and double immunofluorescence labelling with anti-Tie2 antibodies in tumour subcutaneous xenografts showed selective apoptosis of the endothelial compartment only in animals injected with Tie2-*tk* neurospheres, whereas PGK-*tk* tumours contained a considerable number of apoptotic nuclei both in tumour and endothelial cells (Fig. 4a). Moreover, tumours generated by Tie2-*tk* neurospheres underwent a significant size reduction four weeks after ganciclovir administration, whereas control GSC xenografts increased their size over the same time interval (Fig. 4b).

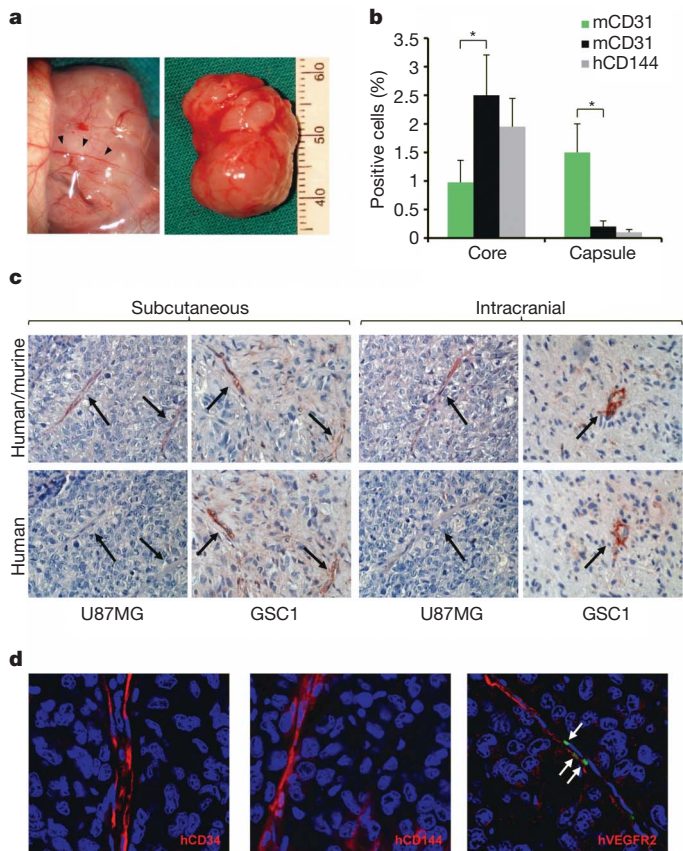


Figure 3 | Human origin of endothelial cells in glioblastoma neurosphere xenografts. **a**, Explanted subcutaneous xenograft obtained by injection of glioblastoma neurospheres. Detail of murine vessels on the surface of the xenograft (left, black arrowheads) and tumour after capsule removal (right). **b**, FACS evaluation of murine CD31⁺/CD45⁺ (mCD31), human CD31 (hCD31) and human CD144 (hCD144) in the capsule and core of the tumour (mean \pm s.d., $n = 4$, * $P < 0.05$). **c**, Immunohistochemistry of glioblastoma neurosphere (GSC1) and U87MG xenografts using either an anti-human CD31 or anti-human and murine CD31 (one out of four different glioblastoma neurosphere samples and serum-grown cell lines are shown). **d**, Immunofluorescence of tumour xenograft sections labelled with anti-human CD34 (left), anti-human CD144 (middle) or anti-human VEGFR2 (right). Arrows indicate circulating erythrocytes. Data represent one of four independent experiments obtained with different glioblastoma neurosphere samples.

Histological examination revealed massive degeneration in the tumour xenografts developed by injection of Tie2-*tk* neurospheres. Four weeks after ganciclovir treatment, these tumours were completely devoid of vascular glomeruli, tiny capillaries with ongoing phenomena of endothelial disruption being the only residual vascular structures (Supplementary Fig. 10b). Although all PGK-*tk* tumours degenerated massively, U87MG Tie2-*tk* xenografts were not affected by ganciclovir treatment (Supplementary Fig. 10c, d), confirming that this cell line was unable to generate endothelial cells. These findings indicate that GSC-derived angiogenesis is essential for tumour survival. Moreover, mouse models based on adherent cell lines grown in serum do not seem suitable for the study of glioblastoma angiogenesis.

Here we demonstrated that GSCs are able to differentiate in functional endothelial cells. Such angiogenic potential could be inherited from normal neural stem cells, which have been shown to differentiate in endothelial cells both *in vitro* and *in vivo*⁴. The formation of fluid-conducting networks by nonendothelial cells has been described for melanomas, sarcomas, breast, ovary, lung and prostate carcinomas^{17,18} as a result of vasculogenic mimicry, which is a feature associated with a pluripotent gene expression pattern in aggressive tumour cells¹⁹.

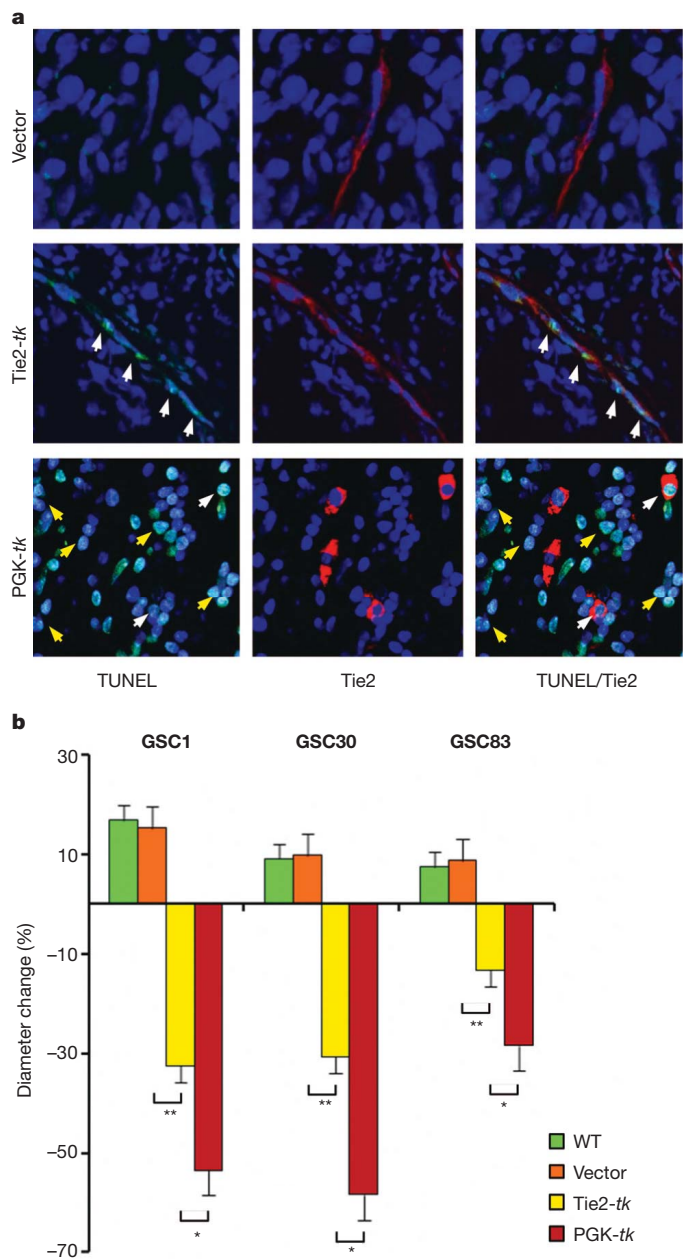


Figure 4 | Selective targeting of glioblastoma neurosphere-derived endothelial cells impairs the growth of subcutaneous tumour xenografts. **a**, Double immunofluorescence using anti-TUNEL and anti-Tie2 in xenografts from Tie2-*tk*, PGK-*tk* and vector glioblastoma neurosphere cells one week after ganciclovir administration. Arrows indicate apoptotic Tie2⁺ (white) and Tie2⁻ (yellow) cells. **b**, Tumour size measured four weeks after ganciclovir administration in xenograft obtained from three different glioblastoma neurosphere samples either untransduced (wild type (WT)) or transduced with vector, Tie2-*tk* or PGK-*tk*. Error bars are mean \pm s.d. of three different experiments. * $P < 0.005$, ** $P < 0.001$.

The ability of cancer stem-like cells to directly contribute to the tumour vasculature by endothelial cell differentiation represents a new mechanism of angiogenesis that might not be restricted to glioblastoma. A similar endothelial potential may be shared by CD44⁺ cells purified from ovarian cancer²⁰. However, the existence of tumour-derived endothelial cells in ovarian cancer has not been demonstrated yet. Endothelial-like cells with cancer-specific genomic alterations have been described in other tumour types, such as lymphoma and neuroblastoma^{11,12}. Although the angiogenic activity of cancer stem-like cells has not been investigated in other tumours, it is likely that the

endothelial cells bearing tumour-specific alterations derive from cancer cells endowed with stem-cell plasticity. Likewise, the vasculogenic mimicry might represent an incomplete differentiation of cancer stem-like cells towards the endothelial lineage, as indicated by the aberrant mixed phenotype of glioblastoma xenografts generated by the subset of CD31⁺/CD144⁺ cells that retain tumorigenic activity.

Our findings may have considerable therapeutic implications. On the one hand, endothelial cells bearing the same genomic alteration as cancer cells may show a different sensitivity to conventional anti-angiogenic treatments, such as VEGF/VEGFR targeting. On the other hand, our data indicate the possibility of targeting the process of GSC differentiation into endothelial cells, thus offering new therapeutic options for cancer treatment.

METHODS SUMMARY

Cell culture. Glioblastoma neurosphere cultures were established from freshly dissociated surgical specimens as described^{13,21,22}. Primary cultures of glioblastoma differentiated cells were obtained by plating cells from freshly dissociated samples in DMEM-F12 medium containing 10% FBS. For primary culture of glioblastoma microvascular endothelial cells, CD31⁺ cells were purified using Miltenyi Microbead Kit (Miltenyi Biotect) according to manufacturer's instructions and grown in endothelial basal medium (EBM Bullet kit; Biowhittaker Cambrex).

Immunohistochemistry, immunofluorescence and flow cytometry. Immunohistochemistry was performed as described²² on deparaffinized sections of glioblastoma tissue. For immunofluorescence, cells were fixed with 4% paraformaldehyde and permeabilized in 0.1% Triton X-100. Cytofluorimetric analysis was performed using a FACS Canto flow cytometer (Becton Dickinson). Cell sorting was performed with a FACS Aria cell sorter (Becton Dickinson).

Interphase FISH and combined immunohistochemistry and FISH (FICTION). Single- and dual-probe interphase FISH was performed as described³. Images were captured using a high-resolution black and white CCD microscope camera AxioCam MRm REV 2 (Karl Zeiss) and analysed using AxioVision 4 multichannel fluorescence basic workstation (Karl Zeiss).

Lentiviral infection. Selective targeting of the cells expressing endothelial phenotype was obtained by modifying the pRRLsin.Tie2p.TKiresGFP.spre lentiviral vector provided by L. Naldini^{15,16}. Viral particle production and GSC infection were performed as previously described²³.

In vivo experiments. Nude athymic and SCID mice (female, 4–5 weeks of age; Charles River) were used. Partially dissociated glioblastoma neurospheres were used for both orthotopic and subcutaneous injection, typically 10⁵ and 5 × 10⁵, respectively. For *in vivo* endothelial targeting, mice were injected with Tie2-*tk* glioblastoma neurospheres into the right flank and control vector glioblastoma neurospheres into the left flank. After having developed bilateral nodules mice received ganciclovir at 50 mg kg⁻¹ day⁻¹ intraperitoneally for 5 days. Ganciclovir-treated mice were killed at different time points to collect samples for histology and immunofluorescence.

Statistical analysis. Student's *t*-test was used to analyse data using Statistica (version 5.5; Statsoft) or Fig.P (version 2.7; Biosoft) softwares.

Full Methods and any associated references are available in the online version of the paper at www.nature.com/nature.

Received 22 October 2009; accepted 13 September 2010.

Published online 21 November 2010.

1. Singh, S. K. *et al.* Identification of human brain tumour initiating cells. *Nature* **432**, 396–401 (2004).
2. Vescovi, A. L., Galli, R. & Reynolds, B. A. Brain tumour stem cells. *Nature Rev. Cancer* **6**, 425–436 (2006).

3. Ricci-Vitiani, L. *et al.* Mesenchymal differentiation of glioblastoma stem cells. *Cell Death Differ.* **15**, 1491–1498 (2008).
4. Wurmser, A. E. *et al.* Cell fusion-independent differentiation of neural stem cells to the endothelial lineage. *Nature* **430**, 350–356 (2004).
5. Bao, S. *et al.* Stem cell-like glioma cells promote tumor angiogenesis through vascular endothelial growth factor. *Cancer Res.* **66**, 7843–7848 (2006).
6. Folkins, C. *et al.* Glioma tumor stem-like cells promote tumor angiogenesis and vasculogenesis via vascular endothelial growth factor and stromal-derived factor 1. *Cancer Res.* **69**, 7243–7251 (2009).
7. Calabrese, C. *et al.* A perivascular niche for brain tumor stem cells. *Cancer Cell* **11**, 69–82 (2007).
8. Gilbertson, R. J. & Rich, J. N. Making a tumour's bed: glioblastoma stem cells and the vascular niche. *Nature Rev. Cancer* **7**, 733–736 (2007).
9. Lathia, J. D. *et al.* Integrin $\alpha 6$ regulates glioblastoma stem cells. *Cell Stem Cell* **6**, 421–432 (2010).
10. Hida, K. *et al.* Tumor-associated endothelial cells with cytogenetic abnormalities. *Cancer Res.* **64**, 8249–8255 (2004).
11. Streubel, B. *et al.* Lymphoma-specific genetic aberrations in microvascular endothelial cells in B-cell lymphomas. *N. Engl. J. Med.* **351**, 250–259 (2004).
12. Pezzolo, A. *et al.* Tumor origin of endothelial cells in human neuroblastoma. *J. Clin. Oncol.* **25**, 376–383 (2007).
13. Singh, S. K. *et al.* Identification of a cancer stem cell in human brain tumors. *Cancer Res.* **63**, 5821–5828 (2003).
14. Galli, R. *et al.* Isolation and characterization of tumorigenic, stem-like neural precursors from human glioblastoma. *Cancer Res.* **64**, 7011–7021 (2004).
15. De Palma, M., Venneri, M. A. & Naldini, L. *In vivo* targeting of tumor endothelial cells by systemic delivery of lentiviral vectors. *Hum. Gene Ther.* **14**, 1193–1206 (2003).
16. De Palma, M., Venneri, M. A., Roca, C. & Naldini, L. Targeting exogenous genes to tumor angiogenesis by transplantation of genetically modified hematopoietic stem cells. *Nature Med.* **9**, 789–795 (2003).
17. Hendrix, M. J., Seftor, E. A., Hess, A. R. & Seftor, R. E. Vasculogenic mimicry and tumour-cell plasticity: lessons from melanoma. *Nature Rev. Cancer* **3**, 411–421 (2003).
18. Dome, B., Hendrix, M. J., Paku, S., Tovari, J. & Timar, J. Alternative vascularization mechanisms in cancer: pathology and therapeutic implications. *Am. J. Pathol.* **170**, 1–15 (2007).
19. Maniotis, A. J. *et al.* Vascular channel formation by human melanoma cells *in vivo* and *in vitro*: vasculogenic mimicry. *Am. J. Pathol.* **155**, 739–752 (1999).
20. Alvero, A. B. *et al.* Molecular phenotyping of human ovarian cancer stem cells unravels the mechanisms for repair and chemoresistance. *Cell Cycle* **8**, 158–166 (2009).
21. Eramo, A. *et al.* Chemotherapy resistance of glioblastoma stem cells. *Cell Death Differ.* **13**, 1238–1241 (2006).
22. Pallini, R. *et al.* Cancer stem cell analysis and clinical outcome in patients with glioblastoma multiforme. *Clin. Cancer Res.* **14**, 8205–8212 (2008).
23. Ricci-Vitiani, L. *et al.* Absence of caspase 8 and high expression of PED protect primitive neural cells from cell death. *J. Exp. Med.* **200**, 1257–1266 (2004).

Supplementary Information is linked to the online version of the paper at www.nature.com/nature.

Acknowledgements We thank L. Naldini for providing the lentiviral vectors and S. Forte for gene array data elaboration. This work was supported by grants from Associazione Italiana per la Ricerca sul Cancro.

Author Contributions L.R.-V. and R.P. performed most of the experiments and coordinated the project; M.B. performed cell sorting and flow cytometric analysis; M.T. and G.S. detected and characterized human endothelial cells in mouse xenografts; G.I. and E.A.P. developed the functional assays of the endothelial cell cultures; G.M. recruited the patients and performed surgery; T.C. and L.M.L. were involved in pathology assessment and detection of genomic aberration in endothelial cells; R.D.M. conceived the study and wrote the paper.

Author Information Data have been deposited at the European Bioinformatics Institute (<http://www.ebi.ac.uk/arrayexpress/>) under accession number E-MEXP-2891. Reprints and permissions information is available at www.nature.com/reprints. The authors declare no competing financial interests. Readers are welcome to comment on the online version of this article at www.nature.com/nature. Correspondence and requests for materials should be addressed to R.D.M. (demaria@iss.it) or R.P. (pallini@rm.unicatt.it).

METHODS

Glioblastoma neurosphere isolation and characterization. Glioblastoma tissue specimens were obtained from adult patients undergoing craniotomy at the Institute of Neurosurgery, Catholic University School of Medicine in Rome. Informed consent was obtained before surgery according to the protocols approved at the Catholic University. Cells were purified through mechanical dissociation of the tumour tissue and cultured at clonal density in a serum-free medium supplemented with EGF and basic FGF as described^{43,21,22}. Isolated cells were expanded and characterized both *in vitro* and *in vivo*. In these conditions, cells were able to grow *in vitro* in clusters called neurospheres and maintain an undifferentiated state, as indicated by morphology and expression of stem-cell markers such as CD133, SOX2, musashi and nestin. Such glioma neurosphere cells showed a clonal frequency higher than 10%, ability to coexpress astrocytic as well as neuronal phenotypic markers after serum-induced differentiation *in vitro*, and generation of glial tumours in immunodeficient mice.

Flow cytometry, immunohistochemistry and immunofluorescence. Cell suspension obtained by mechanical dissociation of the tumour tissue from glioblastoma patients from the Institute of Neurosurgery (Supplementary Table 2) was passed through a 100- μ m mesh to remove aggregates and stained with fluorochrome-conjugated antibodies to surface antigens. After 1 h of incubation on ice, cells were washed twice with PBS and finally resuspended in PBS or in PBS containing 7-aminoactinomycin D (7-AAD) 5 μ g ml⁻¹ to assess viability. Analysis was performed using a fluorescence-activated cell sorter (FACS) Canto flow cytometer (Becton Dickinson). Cell sorting was performed with a FACS Aria cell sorter (Becton Dickinson) equipped with an automatic cloning deposition unit. Cells were selected on the basis of physical parameters and fluorescence and were sorted on sterile tubes or on slides depending on their further utilization.

For immunocytochemistry, immunofluorescence and flow cytometry the following antibodies were used: mouse anti-human CD31 (Novocastra); mouse anti-CD31 (Dako); rat anti-mouse CD31 (BD, Pharmingen); rabbit anti-GFAP (Chemicon or Dako); mouse anti-vWF (Dako); goat anti-human Tie2 (R&D Systems); mouse anti-human VEGFR2 (R&D Systems); rabbit anti-Tie2 (Santa Cruz Biotechnology); mouse anti-human CD144 (R&D Systems); mouse anti-SSEA-1 (R&D Systems); mouse anti-human nuclei antigen (Chemicon); rabbit anti-GFP (Molecular Probes) and anti-eNOS (BD, Pharmingen). Validation of antibody specificity for human and mouse endothelial antigens is shown in Supplementary Fig. 12.

Interphase FISH and FICTION on glioblastoma sections. Single- and dual-probe interphase FISH was performed on histological sections of glioblastoma, on cell nuclei extracted from paraffin-embedded sections of glioblastoma, on cells sorted from glioblastoma samples, and on cultured microvascular endothelial cells of glioblastoma as described⁴. Aneuploidy was defined as loss or gain of one or more chromosome FISH signals. Briefly, locus-specific probes for Cep10, Tel19q and LSI22 were used (Vysis). Standard FISH protocols for pretreatment, hybridization and analyses were followed according to the manufacturer's instructions. Histological 4- μ m-thick paraffin sections were dewaxed with xylene and digested with proteinase K 1 μ g ml⁻¹ in 0.002 M Tris buffered saline (TBS) for 20 min at room temperature (20 °C). Samples were then dehydrated in a graded ethanol series and subjected to FISH analysis. After specimen/probe denaturation at 73 °C for 5 min, the probes (10 μ l per slide) were applied to the slides and subsequently incubated overnight at 42 °C for Cep10 and at 37 °C for 10–16 h for LSI22/Tel19q. Post-hybridization procedure included subsequent washing in 50% formamide/2 \times SSC (30 min at 46 °C) and 2 \times SSC 0.1% NP40 (5 min at room temperature). Nuclei were counterstained with 4',6-diamidino-2-phenylindole (DAPI; Vector Laboratories). The slides were studied with an Axioplan fluorescence microscope (Karl Zeiss) that was equipped with the appropriate filter sets (Vysis). Images were captured using a high-resolution black and white CCD microscope camera AxioCam MRm REV 2 (Karl Zeiss). The resulting images were reconstructed with green (FITC), orange and blue (DAPI) pseudocolour using AxioVision 4 multi-channel fluorescence basic workstation (Karl Zeiss) according to the manufacturer's instruction. Glioblastoma sorted cells were fixed in a solution of methanol and acetic acid (3:1) for 10 min and then processed for FISH as described.

Laser capture microdissection of vessels from GSC-derived xenografts. We isolated the vascular structures of tumour xenografts using the Laser Capture Microdissection (LCM) System (PixCell Iie, Arcturus; distributed by Euroclone). LCM was performed on CD31-immunostained (M-20, Santa Cruz Biotechnology) paraffin sections (10- μ m thick) of tumour xenografts. For each sample, laser power (50–70 mW) and laser duration (1–1.2 ms) were adjusted. The microdissected tissue was then transferred to an LCM cap and the cells were incubated in 100 ml digestion buffer (0.005% proteinase K in tris(hydroxymethyl)aminomethane (TRIS) 0.05M pH 7). Endothelial cell nuclei were isolated using the NE-PER Nuclear and Cytoplasmic Extraction Reagents (Thermo Scientific) following manufacturer recommendations. Successively, nuclei were washed with PBS and

fixed in a solution of methanol/acetic acid (3:1). Eight millilitres of nuclei suspension were placed on a positive charged slide and were dried in a 65 °C oven for 30 min.

FISH on cell nuclei extracted from tumour xenografts. To distinguish human endothelial cells from mice cells, we performed FISH analyses using locus-specific probes for Cep10 (Vysis) and a Cy3-conjugate mouse pan-centromeric chromosome (Cambio). FISH protocols for the Cep10 probe were performed as previously described, whereas for the mouse pan-centromeric probe we followed the manufacturer's instructions. Briefly, after enzymatic digestion with 4 mg ml⁻¹ pepsin in NaCl 0.9% pH 1.5 for 20 min at 37 °C, the nuclei were denatured in 70% formamide in 2 \times SSC for 2 min at 70 °C, and were subsequently immersed in ice-cold 70% ethanol and dehydrated through a series of alcohol washes at 79%, 90% and 100%. The probe was denatured for 10 min at 85 °C and immediately chilled on ice. After specimen/probe denaturation, probe was applied to the slide and subsequently incubated overnight at 37 °C. After washing, nuclei were then counterstained with DAPI (Vectashield mounting medium with DAPI; Vector Laboratories).

Isolation and culture of human glioblastoma microvascular endothelial cells.

Glioblastoma tissue specimens were stored in medium M199 (Gibco) containing penicillin 100 U ml⁻¹ at 4 °C for less than 24 h before processing. After several washes with PBS/antibiotics, tissue was finely minced using surgical scissors and then incubated for 2–3 h at 37 °C in Dulbecco's medium (Gibco) containing 0.2% bovine serum albumin (BSA), liberase blendzyme 2–2.5 mg ml⁻¹ (Roche Diagnostics). Cellular macroaggregates still present after enzymatic digestion were removed by filtration through a 10- μ m pore-size filter (Dako), thus obtaining a monocellular suspension. The filtrate was then washed twice with PBS and centrifuged, the pellet resuspended in 1 ml cold PBS/0.1% BSA pH 7.4. Selection of endothelial cells was performed by using CD31 Miltenyi Microbead Kit (Miltenyi Biotec) according to manufacturer's instructions directly on cell suspensions after enzymatic digestion. Purified cell clusters as well as the negative counterparts were separately resuspended in endothelial basal growth medium (EBM Bullet kit; Biowhitaker Cambrex). Cells were plated onto 25-cm² culture dishes, previously coated with 1 μ g cm⁻² collagen type I and 1 μ g cm⁻² fibronectin (Sigma), and maintained at 37 °C in an atmosphere of 5% CO₂. After 10–12 h, plated cells were washed three times with cold PBS to favour detachment of nonendothelial cells. The medium was changed every 3 days. Once at confluence, cells were detached by trypsinization with 0.25% Trypsin/EDTA (Gibco) and reseeded on collagen/fibronectin-coated culture dishes at a split ratio of 1:3. A second magnetic selection was performed on plated endothelial cells after 7–10 cell divisions in order to increase the purity of the cultures.

Endothelial function assays. For *in vitro* three-dimensional tube formation assay, twelve microlitres of tail collagen were dropped onto glass coverslips and allowed to polymerize for 1 h at 37 °C. Cells were then seeded on top of the gels at 50,000 cells per well and allowed to incubate. Then endothelial basal medium was added and cells were cultured for 7 days. To quantify the tube formation, image-analysis techniques were used that measure the length of the tubes and the number of the connections. Data were photographically recorded daily. The average total length and mean total number of junctions for different endothelial cords were further analysed using the two-sided Mann–Whitney U test. For microinjections, a Zeiss microscopy with a manipulator was used. Fluorescein (Monico) was prediluted 1:1,000 into medium and injected into three-dimensional culture with a Hamilton, and observed with a Zeiss Axiovision device camera.

To determine the uptake of acetylated LDLs, cells were incubated with 10 mg ml⁻¹ DiI-labelled (1,1'-dioctadecyl-3,3',3'-tetramethylindocarbocyanine perchlorate) acetylated LDL; Molecular Probes) at 37 °C for 4 h. The slides were analysed using a Nikon Eclipse TE300 inverted microscope equipped with a Zeiss Axiovision device camera.

Gene array. Total RNA was extracted from glioblastoma neurospheres, serum-differentiated glioblastoma neurospheres, glioblastoma neurospheres cultivated under endothelial condition and endothelial cells isolated from glioblastoma patients. Normal human umbilical vascular (HUVEC) or microvascular (HMVEC) endothelial cells were used as controls for endothelial gene expression patterns. RNA was labelled and hybridized to Affymetrix GeneChip 1.0ST arrays following the manufacturer's instructions. Hybridization values were normalized by the robust multiarray averaging (RMA) method and hierarchical clustering, with average linkage method, was performed according to samples' gene expression profile. Full data were submitted to ArrayExpress under the accession number E-MEXP-2891.

Lentiviral infection. Selective targeting of the cells expressing endothelial phenotype was obtained by modifying the pRRLsin.Tie2p.TKiresGFP.spre lentiviral vector provided by L. Naldini^{15,16}. Viral particle production and GSC infection were performed as previously described²³.

In vivo experiments. Studies involving animals were approved by the Ethical Committee of the Catholic University School of Medicine in Rome. Nude athymic

and SCID mice (female, 4–5 weeks of age; Charles River) were used. For subcutaneous xenografts, cells were resuspended 1×10^6 in 0.1 ml of cold PBS, mixed with an equal volume of cold Matrigel (BD Bioscience), and injected into the flanks of nude mice.

For intracranial xenografts, 2×10^5 cells in 5 μ l of PBS were injected stereotactically onto the striatum. Mice were killed by 16–20 weeks after grafting to collect tumour xenografts. On ganciclovir treatment, no major toxicity was observed in vital organs.

Single-molecule imaging reveals mechanisms of protein disruption by a DNA translocase

Ilya J. Finkelstein², Mari-Liis Visnapuu² & Eric C. Greene^{1,2}

In physiological settings, nucleic-acid translocases must act on substrates occupied by other proteins, and an increasingly appreciated role of translocases is to catalyse protein displacement from RNA and DNA^{1–4}. However, little is known regarding the inevitable collisions that must occur, and the fate of protein obstacles and the mechanisms by which they are evicted from DNA remain unexplored. Here we sought to establish the mechanistic basis for protein displacement from DNA using RecBCD as a model system. Using nanofabricated curtains of DNA and multicolour single-molecule microscopy, we visualized collisions between a model translocase and different DNA-bound proteins in real time. We show that the DNA translocase RecBCD can disrupt core RNA polymerase, holoenzymes, stalled elongation complexes and transcription RNA polymerases in either head-to-head or head-to-tail orientations, as well as EcoRI^{E111Q}, *lac* repressor and even nucleosomes. RecBCD did not pause during collisions and often pushed proteins thousands of base pairs before evicting them from DNA. We conclude that RecBCD overwhelms obstacles through direct transduction of chemomechanical force with no need for specific protein–protein interactions, and that proteins can be removed from DNA through active disruption mechanisms that act on a transition state intermediate as they are pushed from one non-specific site to the next.

RecBCD is a heterotrimeric translocase involved in initiating homologous recombination and processing stalled replication forks^{5,6}. RecB is a 3' → 5' SF1A helicase and contains a nuclease domain for DNA processing, RecD is a 5' → 3' SF1B helicase and RecC holds the complex together and coordinates the response to *cis*-acting Chi (crossover hot-spot instigator) sequences (5'-dGCTGGTGG-3'). RecD is the lead motor before Chi, RecB is the lead motor after Chi and Chi recognition is accompanied by a reduced rate of translocation corresponding to the slower velocity of RecB^{7,8}. Chi prompts RecBCD to process DNA, yielding 3' single-stranded DNA overhangs onto which RecA is loaded^{7,8}.

We monitored RecBCD activity using total-internal-reflection fluorescence microscopy and a DNA curtain assay that allows us to visualize hundreds of aligned molecules⁹ (Supplementary Fig. 1). When assayed on DNA curtains, RecBCD displayed rapid translocation ($1,484 \pm 167$ base pairs per second (bp s^{-1}), 37 °C, 1 mM ATP, $N = 100$; Supplementary Fig. 1b, c), high processivity ($36,000 \pm 12,500$ bp) and decreased velocity in response to Chi ($549 \pm 155 \text{ bp s}^{-1}$, 37 °C, 1 mM ATP, $N = 100$; Supplementary Fig. 1), in agreement with previous studies^{6,7}.

Escherichia coli contains ~2,000 molecules of RNA polymerase (RNAP), and $\geq 65\%$ of these are bound to the bacterial chromosome¹⁰, making RNAP one of the most commonly encountered obstacles in physiological settings. RNAP is of special interest because it is a high-affinity DNA-binding protein (dissociation constant, $K_d \approx 10$ pM for λP_R and 100 pM for λP_L) and a powerful translocase capable of moving under an applied load of ~14–25 pN (ref. 11). RNAP survives encounters with replication forks^{12–14} and stalls fork progression in head-on collisions^{15,16}, suggesting that RNAP is among the most formidable roadblocks encountered *in vivo*. During replication restart, RecBCD translocates towards *oriC*; therefore, most collisions with

RNAP will occur in a head-on orientation, suggesting that to survive these encounters RecBCD would need to exert more force than a replisome.

We used quantum dots (QDs) to fluorescently label RNAP (Supplementary Information). The binding distribution of QD–RNAP holoenzyme overlapped with known promoters (Fig. 1a), promoter targeting was σ^{70} dependent and promoter-bound holoenzymes were highly stable ($t_{1/2} = 23.2 \pm 1.42$ min (half-life), $N = 58$; Supplementary Fig. 3a, b, c). Core QD–RNAP dissociated when challenged with heparin ($t_{1/2} = 3.4 \pm 0.03$ s, $N = 150$), whereas promoter-bound

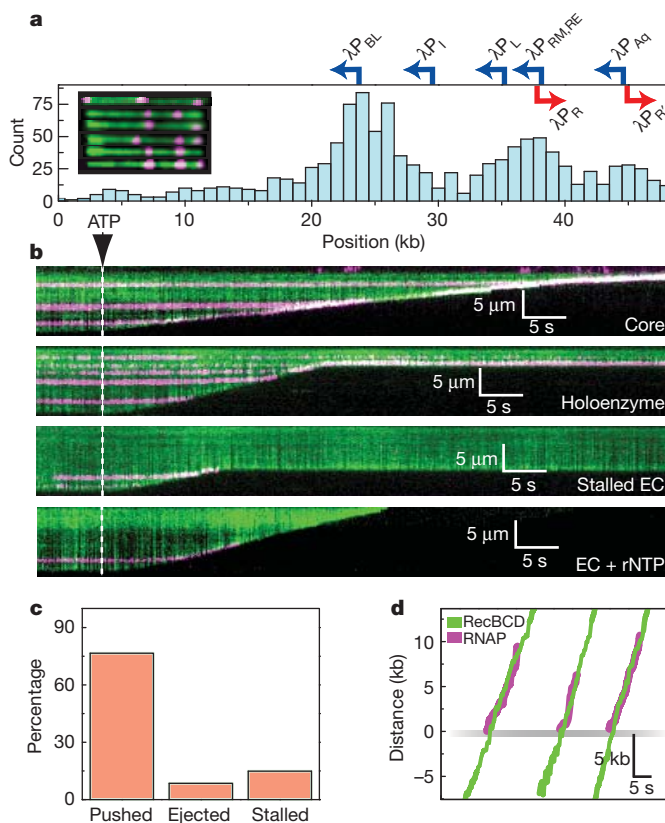


Figure 1 | RecBCD removes RNAP from DNA. **a**, Distribution of QD–RNAP bound to λ DNA. Locations of promoters are indicated; those facing left are shown in blue, those facing right are shown in red. The inset shows examples of YOYO-1-stained λ DNA (green) bound by RNAP (magenta). The tethered end of the DNA is on the left, and the free end of the DNA is on the right. kb, kilobase. **b**, Kymograms of RecBCD colliding with RNAP core, holoenzyme, stalled elongation complex (EC), and stalled elongation complex chased with ribonucleoside triphosphate (rNTP). Gaps in magenta traces correspond to quantum dot blinking. In these and all subsequent kymograms, the tethered end of the DNA is at the top, the free end is at the bottom, and buffer flow is from top to bottom. **c**, Distribution of event types. **d**, Tracking data for collisions, with traces aligned at the collisions.

¹Howard Hughes Medical Institute, Columbia University, New York, New York 10032, USA. ²Department of Biochemistry and Molecular Biophysics, Columbia University, New York, New York 10032, USA.

holoenzyme was heparin resistant ($t_{1/2} \gg 6.7$ min, $N = 58$), confirming open complex formation (Supplementary Fig. 3c, d). Bulk assays verified that QD–RNAP produced transcripts (Supplementary Fig. 3e), and single-molecule assays revealed a transcription velocity of 15.7 ± 8.6 bp s^{-1} ($N = 20$, $25^\circ C$, $250 \mu M$ of each ribonucleoside triphosphate; Supplementary Fig. 3f).

When RecBCD collided with RNAP, the polymerase was rapidly ejected from DNA ($t_{1/2} = 2.4 \pm 0.13$ s; Fig. 1b). Remarkably, RNAP could be pushed long distances ($10,460 \pm 7,690$ bp, $N = 44$; Fig. 1 and Supplementary Fig. 4) and RecBCD could disrupt core RNAP, holoenzymes, stalled elongation complexes and active elongation complexes (Fig. 1b and Supplementary Fig. 5). Out of 47 collisions with QD–RNAP holoenzyme, 15% (7 of 47) immediately stalled RecBCD, 8.5% (4 of 47) resulted in dissociation of RNAP with no sliding, 76.5% (36 of 47) of RNAP was pushed and 71% of pushed molecules were eventually ejected (Fig. 1c). The population of RNAP molecules that was directly ejected from the DNA increased ~ 5 -fold for stalled and active elongation complexes (Supplementary Fig. 5). RecBCD also pushed and evicted RNAP labelled with 40-nm fluorescent beads or Alexa Fluor 488, arguing against nonspecific interactions between RecBCD and the quantum dots (Supplementary Fig. 6a). RecBCD did not slow or pause on colliding with RNAP (Fig. 1d and Supplementary Fig. 4a), nor was there any reduction in processivity in comparison with naked DNA ($29,000 \pm 15,500$ bp). Similar outcomes were observed before and after Chi (not shown), indicating that RecBCD could dislodge RNAP regardless of whether RecB or RecD was the lead motor. We could unambiguously assign the orientation of RNAP at λP_{BL} (Fig. 1a and Supplementary Fig. 3f), and RecBCD dislodged RNAP bound at λP_{BL} during collisions in either direction (Fig. 1b and Supplementary Fig. 7a). RecBCD also pushed and ejected RNAP bound at all other locations regardless of DNA orientation (Fig. 1b). RecBCD even dislodged RNAP at lower velocities (446 ± 192 bp s^{-1} , 122 ± 128 bp s^{-1} and 78 ± 27 bp s^{-1} at $100 \mu M$, $25 \mu M$ and $15 \mu M$ ATP, respectively; see Supplementary Fig. 7 and below), indicating that proteins could be dislodged even under suboptimal translocation conditions. We conclude that RecBCD disrupts RNAP regardless of orientation, transcriptional status or translocation velocity.

We next asked whether RecBCD could dislodge other proteins. EcoRI^{E111Q} is a catalytically inactive version of EcoRI, which has high affinity ($K_d = 2.5$ fM) for cognate sites and even binds tightly to non-specific DNA¹⁷ ($K_d = 4.8$ pM). EcoRI^{E111Q} can halt *E. coli* RNA polymerase^{18,19}; T7 and SP6 RNA polymerases²⁰; SV40 large T antigen; *E. coli* UvrD, DnaB and T4 Dda helicases; SV40 replication forks²¹; and *E. coli* replication forks⁴. EcoRI withstands up to ~ 20 – 40 pN (ref. 22), and EcoRI^{E111Q} binds cognate sites ~ 3000 -fold stronger than wild-type EcoRI¹⁷ ($K_d = 6.7$ pM); thus, we infer that the catalytic mutant can resist at least as much force as the wild-type protein. *lac* repressor (LacI) is representative of a large family of bacterial transcription factors that has served as a model for transcriptional regulation and protein–DNA interactions. LacI binds tightly to specific sites²³ ($K_d = 10$ fM for a 21-bp symmetric operator) but binds weakly to nonspecific DNA²⁴ ($K_d \geq 1$ nM) and slides rapidly along nonspecific DNA rather than remaining at fixed locations^{25,26}. LacI also blocks RNAP and replication forks both *in vitro* and *in vivo*¹⁸, highlighting that it is a potent and physiologically relevant barrier to translocase progression.

We labelled EcoRI^{E111Q} and LacI with quantum dots (Supplementary Information), and QD–EcoRI^{E111Q} and QD–LacI bound to the correct locations on the DNA substrates, confirming that the tagged proteins retained normal DNA-binding activity (Fig. 2a and Supplementary Fig. 8). QD–LacI was rapidly released from DNA by isopropyl- β -D-thiogalactoside, as expected (Supplementary Fig. 9). When RecBCD collided with EcoRI^{E111Q}, it pushed the proteins $13,000 \pm 9,100$ bp ($N = 70$) before ejecting them from the DNA (Fig. 2b, c). In contrast, LacI was immediately ejected, and was not pushed within our resolution limits (Fig. 2b–d). There was no change

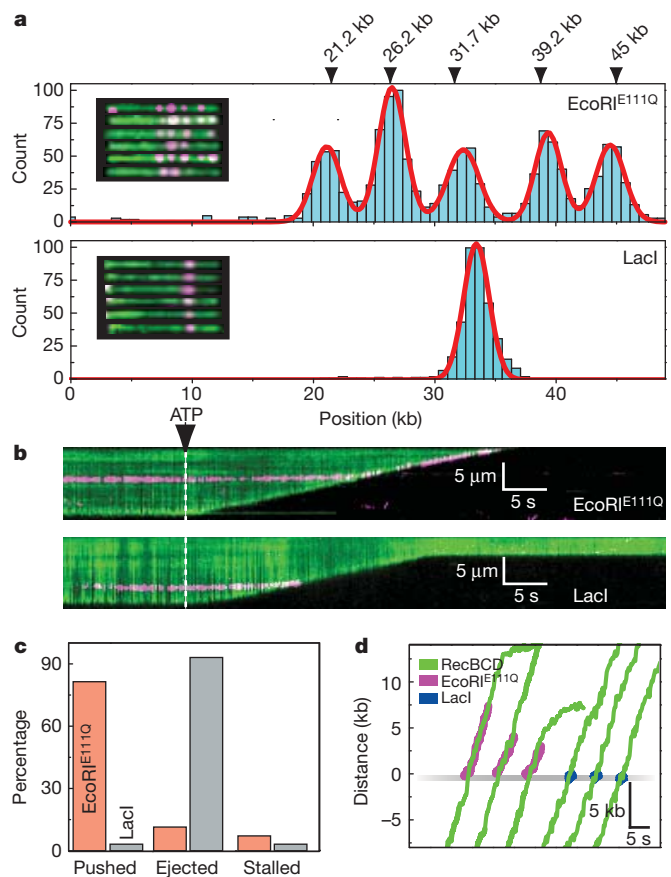


Figure 2 | Disruption of EcoRI^{E111Q} and *lac* repressor by RecBCD.

a, Histogram of EcoRI^{E111Q} (upper panel, $N = 1,481$) and LacI (lower panel, $N = 700$) bound to λ DNA. The locations of the five EcoRI sites found in λ DNA are indicated, along with examples of QD–EcoRI^{E111Q} bound to YOYO-1-stained λ DNA (inset, upper panel) and examples of QD–LacI bound to the DNA (inset, lower panel). **b**, Kymographs showing RecBCD colliding with EcoRI^{E111Q} and LacI (magenta), as indicated. **d**, Distribution of event types for EcoRI^{E111Q} and LacI. **e**, Tracking data for individual collisions.

in velocity or processivity upon colliding with either protein (Fig. 2b, d and Supplementary Fig. 4). Out of 70 collisions with QD–EcoRI^{E111Q}, 11.2% (5 of 70) stalled the translocase, 11.4% (8 of 70) resulted in immediate dissociation of EcoRI^{E111Q} with no detectable sliding, 81.4% (57 of 70) of EcoRI^{E111Q} was pushed along DNA and 92% of pushed molecules were eventually ejected (Fig. 2c). Out of 30 collisions with LacI, 3.3% (1 of 30) stalled the translocase, 93.3% (28 of 30) resulted in immediate dissociation of LacI with no detectable sliding and 3.3% (1 of 30) showed sliding before dissociation (Fig. 2c). A greater fraction of LacI might slide, but if so, the sliding events fall outside our resolution limits. Control experiments confirmed that RecBCD disrupted EcoRI^{E111Q} labelled with fluorescent beads or Alexa Fluor 488 (Supplementary Fig. 6b). As with RNAP, RecBCD could strip EcoRI^{E111Q} after Chi (not shown) and also disrupted EcoRI^{E111Q} and LacI during low-velocity collisions (see below). These findings confirm that RecBCD readily displaces tightly bound proteins from DNA.

In eukaryotes, nucleosomes are the most frequently encountered DNA-bound obstacles. Replisomes, transcription machinery and ATP-dependent chromatin remodellers all act through mechanisms requiring force generation, and the response of nucleosomes to these forces remains a long-standing question in chromatin biology. Heterologous systems have revealed fundamental principles underlying these processes^{27,28}: experiments with SP6 RNAP provided a theoretical framework for nucleosome repositioning²⁷, and studies with phage T4 proteins were among the first to address the fate of nucleosomes during

replication²⁸. Eukaryotic translocases exert forces in the same net direction as RecBCD, and RecBCD can unwind nucleosome-bound DNA²⁹, arguing that it can serve as a good protein-based force probe for studying the fate of nucleosomes when rammed by a translocase.

Recombinant nucleosomes were deposited on DNA curtains by salt dialysis, as described⁹. Remarkably, RecBCD could push nucleosomes ($7,311 \pm 5,373$ bp, $N = 75$; Fig. 3), and similar results were obtained with fluorescently labelled H2A–H2B dimer or H3–H4 tetramer (Fig. 3a). Control experiments demonstrated that RecBCD could also push nucleosomes labelled with either fluorescent beads or Alexa Fluor 488 (Supplementary Fig. 6c). Out of 357 collisions with nucleosomes, 24% (84 of 357) immediately stalled RecBCD, 11% (40 of 357) resulted in direct nucleosome ejection, 65% (233 of 357) led to sliding (Fig. 3b) and ~50% of these were eventually ejected ($t_{1/2} = 3.93 \pm 0.21$ s; Fig. 3b and Supplementary Fig. 4c). Nucleosomes reduced the processivity of RecBCD to $14,000 \pm 7,000$ bp, as anticipated²⁹, and the translocase stalled in a larger fraction of these collisions (24%) than in collisions with RNAP (15%), EcoRI^{E111Q} (7%) and LacI (3.3%). Relative to the other roadblock proteins, fewer of the pushed nucleosomes (50%) were subsequently ejected from the DNA, and there was a 10% reduction (t -test, $P = 0.0005$) in velocity while pushing nucleosomes (Fig. 3c and Supplementary Fig. 4c). These results demonstrate that intact nucleosomes can be pushed along DNA as theoretically predicted³⁰, but indicated that RecBCD had more difficulty pushing and evicting nucleosomes than it did the other protein roadblocks. The finding that RecBCD pushes and evicts nucleosomes also rules out mechanisms requiring species-specific protein–protein interactions.

Protein disruption mechanisms can be described by at least four models, which differ in the nature of the mobile intermediates and the stage of the chemomechanical cycle during which the proteins dissociate (Fig. 4a). In the first model, passive release, the proteins (S) are dislodged from a high-affinity specific site and then pushed from one sequential nonspecific site to the next. Subsequent dissociation occurs spontaneously simply because the proteins are bound to lower-affinity nonspecific DNA (N). This model assumes that the proteins have similar low affinities for all nonspecific sites sampled, and predicts that the observed rates of RecBCD-induced dissociation ($k_{\text{off,obs}}$) would be similar to that of spontaneous dissociation from nonspecific DNA in the absence of RecBCD ($k_{\text{off,obs}} \approx k_{\text{off,N}}$). This model also predicts that the distance (d) over which proteins are pushed will be dictated by their affinity for nonspecific DNA and will be proportional to velocity (V) such that faster translocation will lead to longer distances and slower

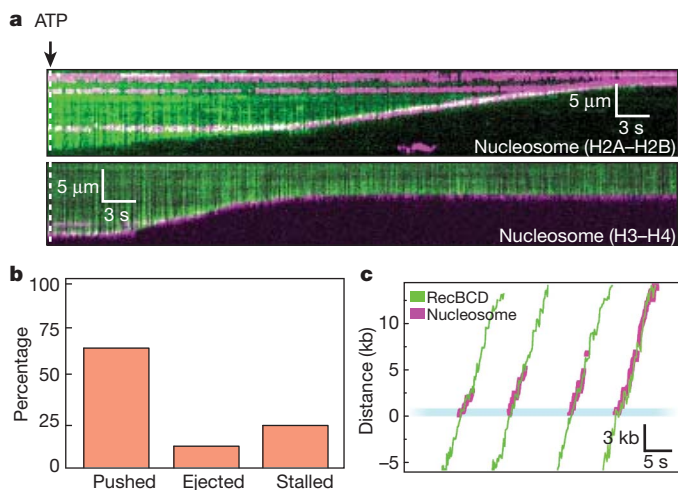


Figure 3 | Nucleosomes can be pushed along DNA. **a**, Kymograms showing RecBCD collisions with nucleosomes (magenta) that are labelled on either the H2A–H2B dimer or the H3–H4 tetramer, as indicated. **b**, Distribution of event types. **c**, Tracking data illustrating collisions between RecBCD and nucleosomes.

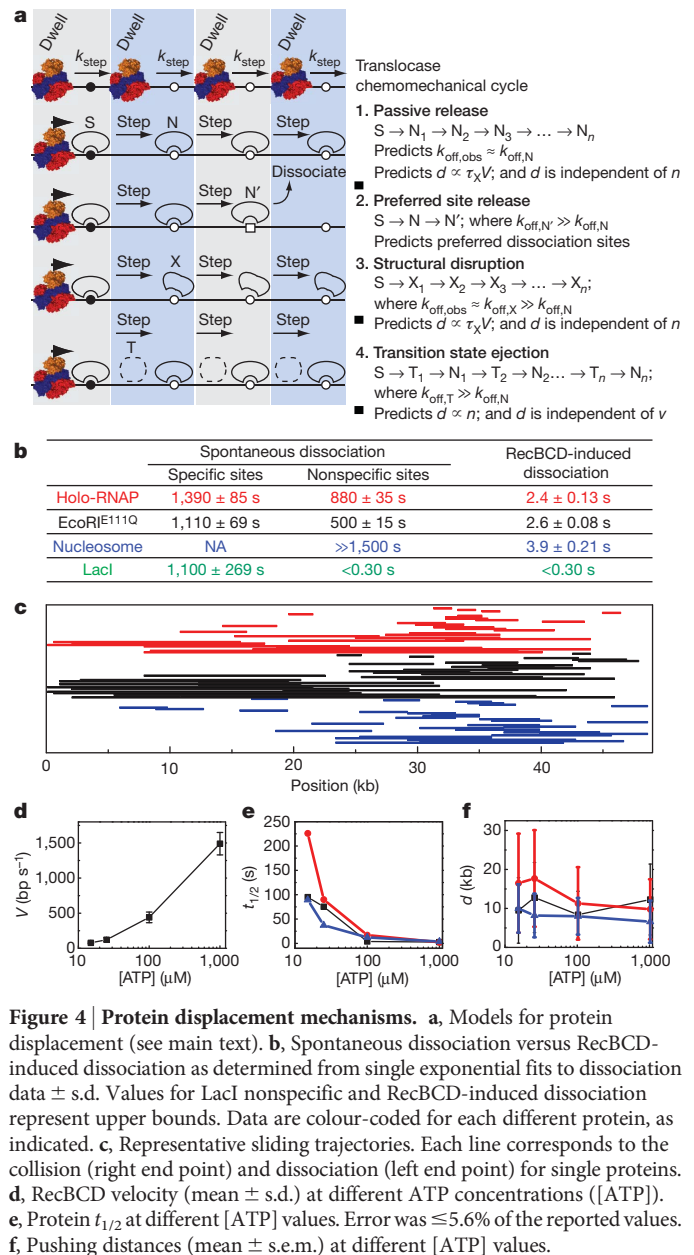


Figure 4 | Protein displacement mechanisms. **a**, Models for protein displacement (see main text). **b**, Spontaneous dissociation versus RecBCD-induced dissociation as determined from single exponential fits to dissociation data \pm s.d. Values for LacI nonspecific and RecBCD-induced dissociation represent upper bounds. Data are colour-coded for each different protein, as indicated. **c**, Representative sliding trajectories. Each line corresponds to the collision (right end point) and dissociation (left end point) for single proteins. **d**, RecBCD velocity (mean \pm s.d.) at different ATP concentrations ([ATP]). **e**, Protein $t_{1/2}$ at different [ATP] values. Error was $\leq 5.6\%$ of the reported values. **f**, Pushing distances (mean \pm s.e.m.) at different [ATP] values.

translocation will yield shorter distances. The second model, preferred site release, accounts for a situation in which proteins encounter rare sequences of exceptionally low affinity (N'), such that they preferentially dissociate from these sites ($k_{\text{off,N}'} \gg k_{\text{off,N}}$). In the third model, structural disruption, translocase collisions alter the conformation of the proteins (for example by permanently rupturing a subset of protein–DNA contacts) such that they persist as structurally perturbed complexes (X) after displacement from the high-affinity site. In this case, the mobile intermediates have a characteristic lifetime (τ_X) dictated by their weakened affinity for DNA, and this lifetime should be insensitive to translocation velocity. Therefore, the distance (d) over which proteins are pushed will be proportional to velocity (V), and faster translocation will lead to longer distances whereas slower translocation will yield shorter distances. The most important feature of this model, which distinguishes it from all of the other models, is that the structurally disrupted proteins are more weakly bound to DNA specifically as a consequence of the collision, such that the observed rate of RecBCD-induced dissociation ($k_{\text{off,obs}}$) would be greater than the rate of spontaneous dissociation from nonspecific DNA ($k_{\text{off,obs}} \approx k_{\text{off,X}} \gg k_{\text{off,N}}$). The fourth model, transition state ejection, is characterized by a series of

tightly bound nonspecific complexes (N) that must pass through a weakly bound transition state (T) as they are pushed from one position to the next. This model predicts that dissociation occurs predominantly during the transition state ($k_{\text{off},T} \gg k_{\text{off},N}$). The time required to pass through the transition state during one round of the chemomechanical cycle is equivalent to the time required for the translocase to take a single step (k_{step}), which is a fixed intrinsic value independent of ATP concentration. This relationship can be rationalized by considering that the velocity of RecBCD can be controlled by modulating ATP concentration (see below), with slower velocities resulting from longer dwell times between steps (while awaiting new ATP) rather than from changes in k_{step} . Therefore, the time it takes the roadblock to pass through the transition state during a single step will be independent of ATP concentration, whereas the cumulative time spent in the transition state will increase linearly with step number (n) irrespective of the overall observed translocation velocity. The probability of dissociation will then increase with step number, the observed lifetimes will be inversely proportional to velocity and the total distance the proteins are pushed before dissociation will be independent of velocity (that is, the roadblocks will be pushed similar distances regardless of how fast the translocase moves).

Each aforementioned model makes distinct predictions that can be experimentally evaluated. This evaluation is easier for RNAP, EcoRI^{E111Q} and nucleosomes because these proteins are pushed long distances (LacI is considered separately below). We first measured dissociation of these proteins from specific and nonspecific sites in the absence of RecBCD (Supplementary Information), and compared these results to RecBCD-induced rates of dissociation (Fig. 4b). RNAP, EcoRI^{E111Q} and nucleosomes all bind tightly to nonspecific DNA, and RecBCD-induced dissociation was ≥ 200 -fold faster than spontaneous dissociation from nonspecific sites, which is inconsistent with passive release. We next analysed pushing trajectories to determine whether there was any evidence supporting preferred site release. Comparison of these trajectories revealed that RecBCD-induced dissociation of all three roadblock proteins occurred at random locations (Fig. 4c), arguing against preferred site release. To distinguish between structural disruption and transition state eviction, we compared protein lifetimes and pushing distances at four different translocation velocities (Fig. 4d). Remarkably, a 3.3-fold decrease in RecBCD velocity ($446 \pm 192 \text{ bp s}^{-1}$ at $100 \mu\text{M}$ ATP) led to 1.5-, 7.0- and 3.4-fold increases in the post-collision half-lives of EcoRI^{E111Q}, RNAP and nucleosomes (Fig. 4e), respectively, although the distribution of distances over which the proteins were pushed remained largely unaltered (Fig. 4f and Supplementary Table 1). This effect was even more obvious at $15 \mu\text{M}$ ATP, where a 19-fold decrease in RecBCD velocity ($78 \pm 27 \text{ bp s}^{-1}$) led to 36-, 93- and 24-fold increases in the post-collision half-lives of EcoRI^{E111Q}, RNAP and nucleosomes, respectively, but pushing distances were either unaltered or increased in comparison with those corresponding to the faster velocities. These results indicated that dissociation was dictated by the number of steps the proteins were forced to take rather than the cumulative time it took to be pushed a given distance, which is most consistent with transition state ejection. Although our experiments did not reveal any evidence for a structural disruption eviction mechanism, this does not rule out the possibility that EcoRI^{E111Q}, RNAP and nucleosomes are structurally altered when acted upon by RecBCD. However, if they are structurally perturbed, this alone does not result in their eventual dissociation from DNA.

LacI differs from the other roadblocks in that it was immediately evicted from DNA, and the RecBCD-induced dissociation rate was comparable to the rate of spontaneous dissociation from nonspecific sites (Fig. 4b), which would seem consistent with a passive-release model. However, with current resolution limits we cannot completely rule out other mechanisms, and future studies will be necessary to fully address this issue. Importantly, RNAP, EcoRI^{E111Q} and nucleosomes all bind tightly to nonspecific DNA, whereas LacI binds much more weakly to nonspecific sequences (Fig. 4b), suggesting that LacI is released more

rapidly from DNA after the collisions due to its weaker affinity for nonspecific sites. This result demonstrates that the roadblock proteins and the nature of their interactions with nonspecific DNA are critical contributing factors to the outcome of the collisions.

This leaves the question of how much force RecBCD exerts, and how much is sufficient to disrupt obstacles. Although our experiments do not yield a direct read-out of force, we can safely conclude that the force exerted by RecBCD is sufficient to displace RNAP, EcoRI^{E111Q} LacI and nucleosomes from DNA. Our work has revealed unprecedented details of protein collisions on DNA and provides new insights into how translocases can disrupt nucleoprotein complexes. Given the flexibility of our experimental platform, we anticipate that these studies can be extended to other translocases and roadblock proteins, and it will be important to determine whether the mechanistic concepts developed here apply to different types of collision between proteins on DNA.

METHODS SUMMARY

We conducted total-internal-reflection fluorescence microscopy experiments on a home-built microscope using nanofabricated DNA curtains, as previously described⁹. For all initial experiments, and for all kymographs shown in the manuscript, we used YOYO-1 to stain the DNA. YOYO-1 does not affect the translocation rate or processivity of RecBCD⁶, and it did not affect the binding distributions of RNAP, EcoRI^{E111Q} or nucleosomes (not shown). In the presence of YOYO-1, the roadblock proteins showed the same general response to collisions with RecBCD, with identical distributions of ejection, stalling and pushing (and pushing velocities) seen with and without YOYO-1. However, the stain reduced the distance obstacles were pushed by 20–30%. Therefore, all sliding distances and half-lives reported here correspond to values measured in the absence of YOYO-1. Sliding distances are reported only for roadblock proteins that did not encounter any other quantum-dot-tagged proteins as they were pushed along the DNA. This ensures that each analysed collision/dissociation event involved only a single quantum-dot-tagged protein. Many reactions were observed in which multiple quantum-dot-tagged roadblock proteins were pushed into one another, but in these cases we could not determine the order in which each such protein was displaced from the DNA, and therefore could not measure sliding distances. To categorize the distributions of event type, we defined ‘sliding’ as the movement of any quantum-dot-tagged roadblock by more than $0.53 \mu\text{m}$ ($\sim 1,950 \text{ bp}$); anything less than this was scored as a direct dissociation event.

Received 8 August; accepted 6 October 2010.

Published online 24 November 2010.

1. Jankowsky, E., Gross, C., Shuman, S. & Pyle, A. Active disruption of an RNA-protein interaction by a DExH/D RNA helicase. *Science* **291**, 121–125 (2001).
2. Marquis, K. A. *et al.* SpoIIIE strips proteins off the DNA during chromosome translocation. *Genes Dev.* **22**, 1786–1795 (2008).
3. Krejci, L. *et al.* DNA helicase Srs2 disrupts the Rad51 presynaptic filament. *Nature* **423**, 305–309 (2003).
4. Guy, C. P. *et al.* Rep provides a second motor at the replisome to promote duplication of protein-bound DNA. *Mol. Cell* **36**, 654–666 (2009).
5. Singleton, M. R., Dillingham, M., Gaudier, M., Kowalczykowski, S. & Wigley, D. Crystal structure of RecBCD enzyme reveals a machine for processing DNA breaks. *Nature* **432**, 187–193 (2004).
6. Bianco, P. R. *et al.* Processive translocation and DNA unwinding by individual RecBCD enzyme molecules. *Nature* **409**, 374–378 (2001).
7. Spies, M., Amitani, I., Baskin, R. & Kowalczykowski, S. RecBCD enzyme switches lead motor subunits in response to chi recognition. *Cell* **131**, 694–705 (2007).
8. Taylor, A. F. & Smith, G. R. RecBCD enzyme is a DNA helicase with fast and slow motors of opposite polarity. *Nature* **423**, 889–893 (2003).
9. Visnapuu, M.-L. & Greene, E. Single-molecule imaging of DNA curtains reveals intrinsic energy landscapes for nucleosome deposition. *Nature Struct. Mol. Biol.* **16**, 1056–1062 (2009).
10. Ishihama, A. Functional modulation of *Escherichia coli* RNA polymerase. *Annu. Rev. Microbiol.* **54**, 499–518 (2000).
11. Herbert, K. M., Greenleaf, W. J. & Block, S. M. Single-molecule studies of RNA polymerase: motoring along. *Annu. Rev. Biochem.* **77**, 149–176 (2008).
12. Liu, B., Wong, M. & Alberts, B. A transcribing RNA polymerase molecule survives DNA replication without aborting its growing RNA chain. *Proc. Natl Acad. Sci. USA* **91**, 10660–10664 (1994).
13. Liu, B., Wong, M., Tinker, R., Geiduschek, E. & Alberts, B. The DNA replication fork can pass RNA polymerase without displacing the nascent transcript. *Nature* **366**, 33–39 (1993).
14. Liu, B. & Alberts, B. Head-on collision between a DNA replication apparatus and RNA polymerase transcription complex. *Science* **267**, 1131–1137 (1995).

15. Pomerantz, R. T. & O'Donnell, M. The replisome uses mRNA as a primer after colliding with RNA polymerase. *Nature* **456**, 762–766 (2008).
16. Pomerantz, R. T. & O'Donnell, M. Direct restart of a replication fork stalled by a head-on RNA polymerase. *Science* **327**, 590–592 (2010).
17. Wright, D. J., King, K. & Modrich, P. The negative charge of Glu-111 is required to activate the cleavage center of EcoRI endonuclease. *J. Biol. Chem.* **264**, 11816–11821 (1989).
18. Epshtein, V. & Toulm, E. F. Rahmouni, A. Borukhov, S. & Nudler, E. Transcription through the roadblocks: the role of RNA polymerase cooperation. *EMBO J.* **22**, 4719–4727 (2003).
19. Nudler, E., Kashlev, M., Nikiforov, V. & Goldfarb, A. Coupling between transcription termination and RNA polymerase inchworming. *Cell* **81**, 351–357 (1995).
20. Pavco, P. A. & Steege, D. A. Characterization of elongating T7 and SP6 RNA polymerases and their response to a roadblock generated by a site-specific DNA binding protein. *Nucleic Acids Res.* **19**, 4639–4646 (1991).
21. Byrd, A. K. & Raney, K. D. Displacement of a DNA binding protein by Dda helicase. *Nucleic Acids Res.* **34**, 3020–3029 (2006).
22. Noom, M. C., van den Broek, B., van Mameren, J. & Wuite, G. J. L. Visualizing single DNA-bound proteins using DNA as a scanning probe. *Nature Methods* **4**, 1031–1036 (2007).
23. Sadler, J. R., Sasmor, H. & Betz, J. L. A perfectly symmetric lac operator binds the lac repressor very tightly. *Proc. Natl Acad. Sci. USA* **80**, 6785–6789 (1983).
24. Lin, S.-Y. & Riggs, A. D. Lac repressor binding to DNA not containing the lac operator and to synthetic poly dAT. *Nature* **228**, 1184–1186 (1970).
25. Elf, J., Li, G.-W. & Xie, X. Probing transcription factor dynamics at the single-molecule level in a living cell. *Science* **316**, 1191–1194 (2007).
26. Wang, Y. M., Austin, R. H. & Cox, E. C. Single molecule measurements of repressor protein 1D diffusion on DNA. *Phys. Rev. Lett.* **97**, 048302 (2006).
27. Studitsky, V. M., Clark, D. J. & Felsenfeld, G. Overcoming a nucleosomal barrier to transcription. *Cell* **83**, 19–27 (1995).
28. Bonne-Andrea, C., Wong, M. & Alberts, B. *In vitro* replication through nucleosomes without histone displacement. *Nature* **343**, 719–726 (1990).
29. Eggleston, A. K., O'Neill, T. E., Bradbury, E. M. & Kowalczykowski, S. C. Unwinding of nucleosomal DNA by a DNA helicase. *J. Biol. Chem.* **270**, 2024–2031 (1995).
30. Mollazadeh-Beidokhti, L., Deseigne, J., Lacoste, D., Mohammad-Rafiee, F. & Schiessel, H. Stochastic model for nucleosome sliding under an external force. *Phys. Rev. E* **79**, 031922 (2009).

Supplementary Information is linked to the online version of the paper at www.nature.com/nature.

Acknowledgements We thank M. Gottesman, R. Gonzalez and members of the Greene laboratory for discussion and assistance throughout this work. We thank P. Modrich for providing an expression construct encoding EcoRI^{E111Q}, R. Landick and K. Adelman for providing RNAP constructs, and J. Gelles for providing plasmids encoding RecBCD. I.J.F. was supported by an NIH Fellowship (F32GM80864). Funding was provided by the National Institutes of Health (GM074739 and GM082848 to E.C.G.). This work was partially supported by the Initiatives in Science and Engineering program through Columbia University, the Nanoscale Science and Engineering Initiative of the National Science Foundation under NSF Award Number CHE-0641523, and by the New York State Office of Science, Technology, and Academic Research. E.C.G. is an Early Career Scientist with the Howard Hughes Medical Institute. We apologize to colleagues whose work we were unable to cite owing to length restrictions.

Author Contributions I.J.F. did all cloning and ensemble-level biochemical characterization, and conducted and analysed RecBCD collision experiments with RNAP, EcoRI^{E111Q} and LacI. M.-L.V. conducted and analysed RecBCD collision experiments with nucleosomes. I.J.F., M.-L.V. and E.C.G. discussed the data and co-wrote the paper.

Author Information Reprints and permissions information is available at www.nature.com/reprints. The authors declare no competing financial interests. Readers are welcome to comment on the online version of this article at www.nature.com/nature. Correspondence and requests for materials should be addressed to E.C.G. (ecg2108@columbia.edu).

Calcium-dependent phospholipid scrambling by TMEM16F

Jun Suzuki^{1,2}, Masato Umeda³, Peter J. Sims⁴ & Shigekazu Nagata^{1,2}

In all animal cells, phospholipids are asymmetrically distributed between the outer and inner leaflets of the plasma membrane¹. This asymmetrical phospholipid distribution is disrupted in various biological systems. For example, when blood platelets are activated, they expose phosphatidylserine (PtdSer) to trigger the clotting system^{2,3}. The PtdSer exposure is believed to be mediated by Ca^{2+} -dependent phospholipid scramblases that transport phospholipids bidirectionally^{1,4}, but its molecular mechanism is still unknown. Here we show that TMEM16F (transmembrane protein 16F) is an essential component for the Ca^{2+} -dependent exposure of PtdSer on the cell surface. When a mouse B-cell line, Ba/F3, was treated with a Ca^{2+} ionophore under low- Ca^{2+} conditions, it reversibly exposed PtdSer. Using this property, we established a Ba/F3 subline that strongly exposed PtdSer by repetitive fluorescence-activated cell sorting. A complementary DNA library was constructed from the subline, and a cDNA that caused Ba/F3 to expose PtdSer spontaneously was identified by expression cloning. The cDNA encoded a constitutively active mutant of TMEM16F, a protein with eight transmembrane segments⁵. Wild-type TMEM16F was localized on the plasma membrane and conferred Ca^{2+} -dependent scrambling of phospholipids. A patient with Scott syndrome^{6,7}, which results from a defect in phospholipid scrambling activity^{8,9}, was found to carry a mutation at a splice-acceptor site of the gene encoding TMEM16F, causing the premature termination of the protein.

When mouse Ba/F3 cells were treated with 1.0 μM A23187 for 15 min in the presence of 0.5 mM CaCl_2 , the cells underwent necrosis or became propidium iodide (PI)-positive. However, when the same treatment was performed in Ca^{2+} -free conditions, most of the cells exposed PtdSer and the PI-positive population was low (Fig. 1a). Chelating intracellular Ca^{2+} with bis-(*o*-aminophenoxy)ethane-*N,N,N',N'*-tetra-acetic acid acetoxymethyl ester (BAPTA-AM) blocked the PtdSer exposure (Fig. 1b), indicating that the process required the mobilization of intracellular calcium. This PtdSer exposure was reversible: treatment of the PtdSer-exposing cells with BAPTA-AM at 37 °C for 5 min (Fig. 1c) or culturing them in Ca^{2+} -free medium at 37 °C for 12 h (data not shown) eliminated the PtdSer from the cell surface. These results suggest that under low- Ca^{2+} conditions, A23187 mobilized the intracellular Ca^{2+} , which activated a phospholipid scramblase to expose PtdSer. When the intracellular Ca^{2+} concentration was lowered, the phospholipid scramblase lost activity, and flippases returned the PtdSer to the inner leaflet.

To characterize the PtdSer-exposure process, we used its reversible nature under low- Ca^{2+} conditions to establish a cell line that overexposed PtdSer. Ba/F3 cells were treated with 1.0 μM A23187 in the absence of calcium, and subjected to fluorescence-activated cell sorting (FACS) based on PtdSer exposure. A population (0.5–5%) that showed intense staining with Annexin V was collected, cultured for 15 h in Ca^{2+} -free medium, returned to normal medium, and subjected to the next sorting. After this cycle of sorting and expansion had been repeated 12 times, the cells (Ba/F3-PS12) showed roughly 100-fold

higher staining with Annexin V than the original Ba/F3 cells (Ba/F3-PS0) on treatment with 125 nM A23187 (Fig. 1d). The sorting and expansion were repeated another seven times, and the resulting cell line (Ba/F3-PS19) was used for further studies.

There were two possible causes of the strong PtdSer exposure in Ba/F3-PS19 cells. One was the overexpression or overactivation of phospholipid scramblase, and the other was the inactivation of flippase¹⁰ that transports PtdSer from the outer to the inner leaflet of the plasma membrane. To examine which possibility was correct, DsRed-expressing Ba/F3-PS19 cells were fused with green fluorescent protein (GFP)-labelled parental Ba/F3 (Ba/F3-PS0) cells. The PtdSer-exposure response of the hybrid cells to 1.0 μM A23187 was similar to, or slightly weaker than, that of Ba/F3-PS19 cells (Fig. 1e), suggesting that the phenotype of Ba/F3-PS19 cells was dominant to that of Ba/F3-PS0 cells, and that the phospholipid scramblase was overactivated in Ba/F3-PS19 cells. To identify the gene responsible for the enhanced phospholipid scramblase activity, a cDNA library (9.3×10^5 clones) was prepared from Ba/F3-PS19 cells, and introduced into the parental Ba/F3 cell line. The stably transformed cells were treated with 125 nM A23187, and a population that stained strongly with Annexin V was sorted (Fig. 1f). At the third cycle of sorting and expansion (Library-Derived (LD)-PS3), about 35% of the cells exposed PtdSer without A23187 treatment, and this cell population (LD-PS4) was characterized.

LD-PS4 cells carried two or three different cDNAs, but the *Tmem16f* cDNA (GenBank accession number NM_175344) was present in two independent experiments, suggesting that TMEM16F caused the PtdSer exposure. The two *Tmem16f* cDNAs identified in the different experiments contained an A-to-G mutation at nucleotide 1226, which caused an aspartic residue to be replaced by glycine at codon 409 (Fig. 2a). TMEM16A, another member of the TMEM16 family, was recently shown to be a Ca^{2+} -dependent Cl^- channel^{11–13}. However, the Cl^- -channel activity of TMEM16F was lower than that of TMEM16A¹⁴. To examine the function of TMEM16F, the wild-type and mutant (D409G) forms of TMEM16F were tagged with Flag or monomeric red fluorescent protein (mRFP) at the carboxy terminus, and expressed in Ba/F3 or human 293T cells. Western blotting of the cell lysates with anti-Flag showed broad bands at 125 and 500 kDa on SDS-PAGE (Fig. 2b), suggesting that mouse TMEM16F (calculated molecular mass 106 kDa) is glycosylated and/or aggregated. Observation of the 293T cells expressing TMEM16F-mRFP indicated that TMEM16F is located at the plasma membrane (Fig. 2c).

Annexin V was able to bind to the Ba/F3 cells expressing the D409G mutant, but not the wild-type, TMEM16F (Fig. 2d), suggesting that the mutant TMEM16F-expressing cells constitutively expose PtdSer. This was confirmed by binding of MFG-E8, which specifically binds to PtdSer^{15,16} (Supplementary Fig. 1). Chelating the intracellular Ca^{2+} with BAPTA-AM decreased the exposed PtdSer level in the mutant TMEM16F-expressing cells (Fig. 2d). When cells expressing wild-type TMEM16F were treated with A23187, PtdSer was exposed without a lag time, reaching saturation more quickly than the vector-transformed

¹Department of Medical Chemistry, Graduate School of Medicine, Kyoto University, Yoshida, Sakyo-ku, Kyoto 606-8501, Japan. ²Core Research for Evolutional Science and Technology, Japan Science and Technology Corporation, Kyoto 606-8501, Japan. ³Department of Synthetic Chemistry and Biological Chemistry, Graduate School of Engineering, Kyoto University, Katsura, Nishikyo-ku, Kyoto 615-8510, Japan. ⁴Department of Pathology and Laboratory Medicine, University of Rochester Medical Center, 601 Elmwood Avenue, Rochester, New York 14642, USA.

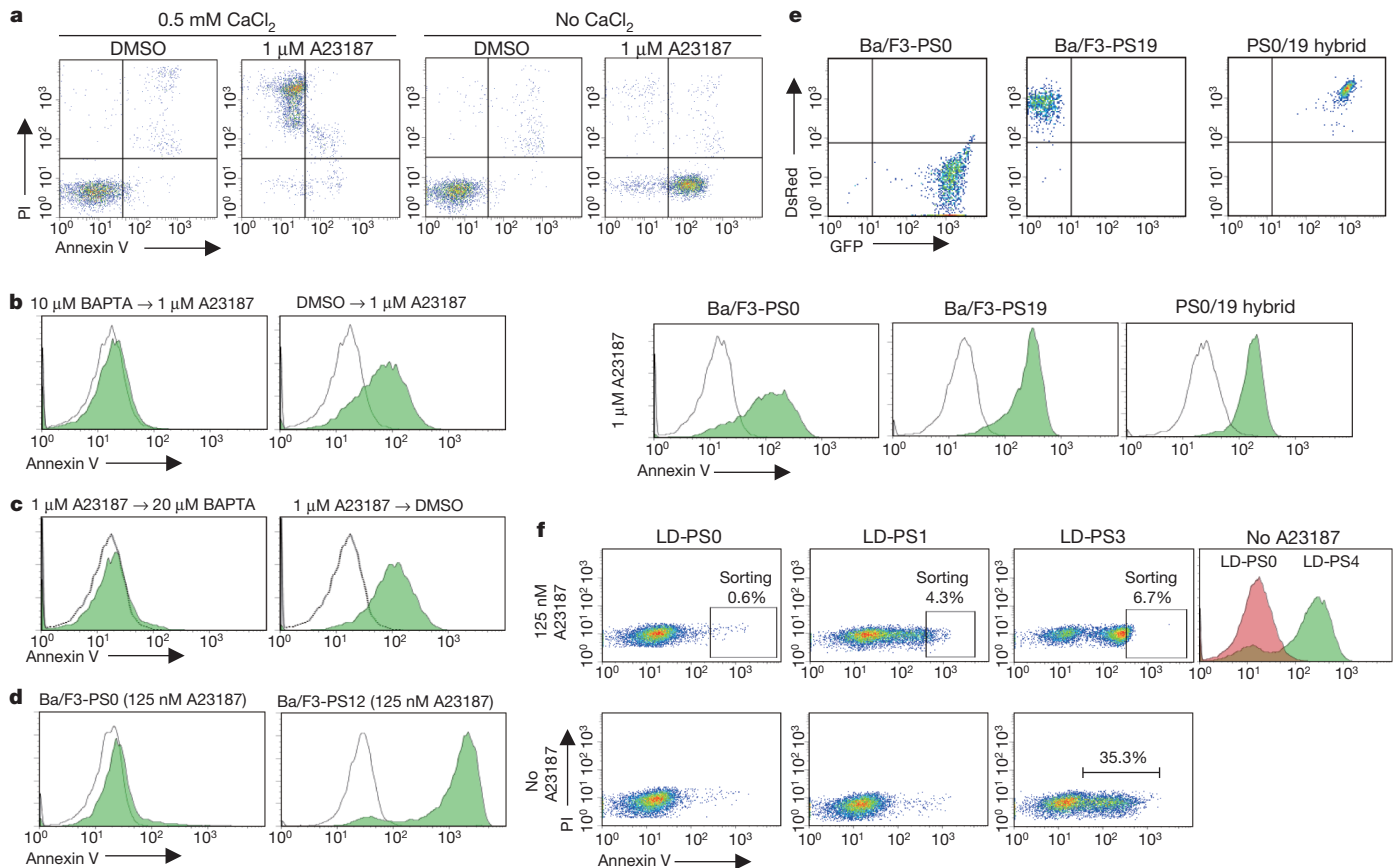


Figure 1 | Molecular cloning of TMEM16F. **a**, Ba/F3 cells were treated with A23187 with or without CaCl_2 , and stained with Annexin V and PI. DMSO, dimethylsulphoxide. **b**, Ba/F3 cells were incubated with BAPTA-AM and treated with A23187. An Annexin V profile in a PI-negative population is shown. Open curve, profile of resting cells. **c**, Ba/F3 cells were treated with A23187 and then with BAPTA-AM for 5 min, and stained with Annexin V. **d**, Ba/F3 cells and cells after sorting for 12 cycles (PS12) were treated with

A23187 and stained with Annexin V. **e**, GFP and DsRed profiles of PS0, PS19 and PS0/19 hybrid cells are shown. Bottom: the same cells were treated with A23187 and stained with Annexin V. **f**, Ba/F3 cells transformed with PS19 cDNA library were treated with A23187, stained with Annexin V and sorted (LD-PS0). Annexin V and PI profiles of cells after first (LD-PS1) and third (LD-PS3) sorting are shown. Right: Annexin V profile of original cells (LD-PS0) and after fourth sorting (LD-PS4) without A23187.

Ba/F3 cells (Fig. 2e). The intracellular Ca^{2+} concentration and the kinetics of the Ca^{2+} influx after treatment with A23187 was similar among the vector-transformed cells and those expressing wild-type and D409G mutant TMEM16F (Supplementary Fig. 2). These results indicated that TMEM16F mediates a Ca^{2+} -dependent scramblase activity for PtdSer, and that its D409G mutant is sensitized to respond to the normal intracellular concentration of Ca^{2+} to expose PtdSer.

Phospholipid scramblase mediates the bidirectional transfer between plasma membrane leaflets of all phospholipids. Cells expressing the D409G mutant TMEM16F were stained with Ro09-0198 (Supplementary Fig. 3a), a tetracyclic polypeptide that specifically binds phosphatidylethanolamine (PtdEtn)¹⁷, indicating that they constitutively exposed PtdEtn, a phospholipid that, like PtdSer, is normally sequestered to the inner leaflet. Treatment of Ba/F3 cells with A23187 caused exposure of PtdEtn. This process was accelerated by overexpressing wild-type TMEM16F (Supplementary Fig. 3b). When 1-oleoyl-2-[6-[(7-nitro-2-1,3-benzoxadiazol-4-yl)amino]hexanoyl]-sn-glycero-3-phosphocholine (NBD-PtdCho) was added to the culture, it was quickly internalized by the D409G-mutant-expressing cells (Fig. 2f): of the cell-associated NBD-PtdCho, more than 40% became resistant to extraction with BSA within 6 min. When the cells expressing wild-type TMEM16F were treated with A23187, they incorporated NBD-PtdCho faster than the parental cells, and about 40% of the cell-associated NBD-PtdCho was inside the cells within 4 min (Fig. 2g). Similar results—that is, constitutive internalization by cells expressing the mutant TMEM16F, and enhanced A23187-induced incorporation by cells expressing wild-type

TMEM16F—were obtained with *N*-[6-[(7-nitro-2-1,3-benzoxadiazol-4-yl)amino]hexanoyl]-sphingosine-1-phosphocholine (NBD-SM) (Supplementary Fig. 4). The internalized NBD-PtdCho and NBD-SM were intact (Supplementary Fig. 5). Dynasore, which inhibits dynamin-mediated endocytosis¹⁸ inhibited the internalization of these phospholipids only slightly or not at all (Supplementary Fig. 6), suggesting that the contribution of endocytosis to TMEM16F-mediated phospholipid internalization may not be great.

Expression of endogenous TMEM16F in Ba/F3 cells was then knocked down by expressing *Tmem16f* short hairpin RNA (shRNA). As shown in Fig. 3a and Supplementary Fig. 7, the expression level of *Tmem16f* messenger RNA in five transformants was decreased to 20–35% of that in the cells expressing the control shRNA. The rate of A23187-induced exposure of PtdSer and PtdEtn was decreased in these transformants (Fig. 3b, c). Similarly, the uptake of NBD-PtdCho and NBD-SM was slower in *Tmem16f* shRNA-transformed cells (Fig. 3d, e).

Platelets and other blood cells from patients with Scott syndrome show a defect in their ability to expose PtdSer in response to a Ca^{2+} ionophore^{7,19}. B-cell lines have been established from a patient with Scott syndrome and from the patient's parents²⁰. In agreement with previous reports^{8,20}, the patient-derived cells did not expose PtdSer in response to a Ca^{2+} ionophore (Fig. 4a). In contrast, A23187 elicited PtdSer exposure in cell lines derived from the patient's parents at the same levels as in cell lines from healthy volunteers. An RT-PCR analysis of the *TMEM16F* mRNA (GenBank accession number NM_001025356) showed that the 5' part (1,320 base pairs (bp)), corresponding to exons

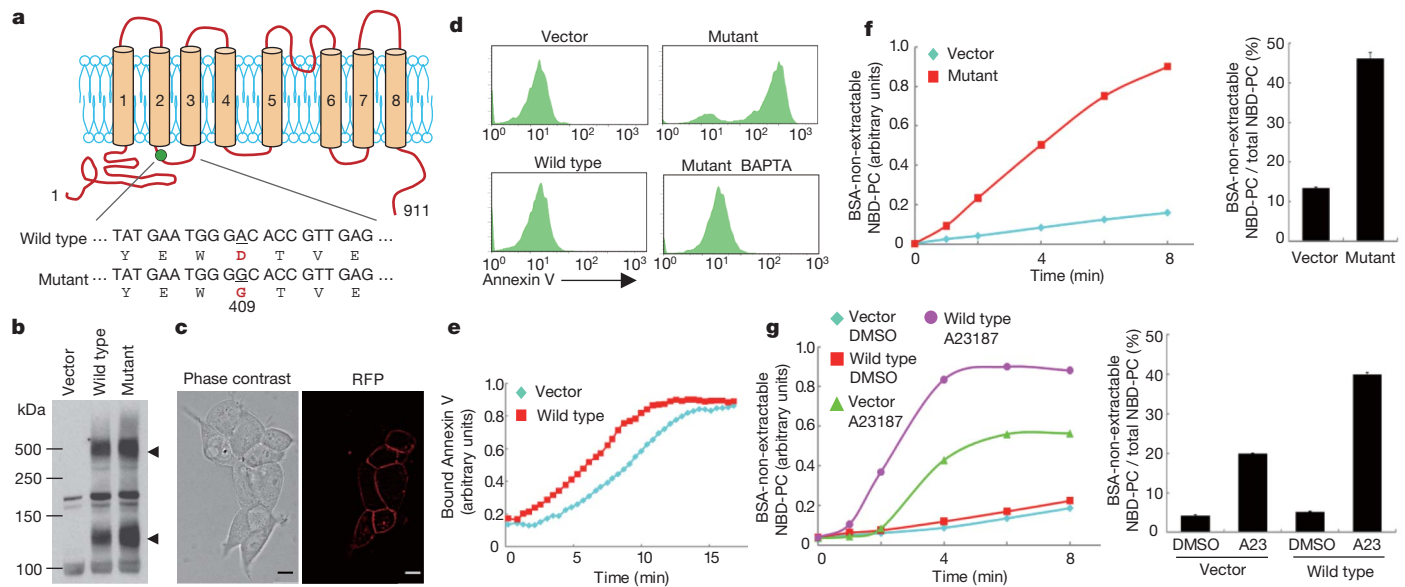


Figure 2 | Phospholipid scrambling in TMEM16F-expressing cells. **a**, Schematic representation of mouse TMEM16F and D409G mutant. **b**, Western blotting of Ba/F3 cells expressing Flag-tagged wild-type and mutant TMEM16F with anti-Flag. Arrowheads, monomer and multimer of TMEM16F. **c**, 293T cells expressing TMEM16F-mRFP were observed under a fluorescent microscope. Scale bars, 10 μ m. **d**, Vector-transformed Ba/F3 cells, or cells expressing wild-type or mutant TMEM16F, were stained with Annexin V with or without pretreatment with BAPTA-AM. **e**, Vector-transformed or wild-type TMEM16F-Ba/F3 cells were preincubated with Annexin V. After addition of A23187, the fluorescence was monitored. The y axis shows fluorescence intensity on FACS. **f**, Vector-transformed or mutant

TMEM16F-expressing Ba/F3 cells were incubated for 8 min at room temperature (26–27 °C) with 0.5 μ M NBD-PtdCho in Hanks balanced salt solution containing Ca^{2+} . After dilution with fatty-acid-free BSA buffer, the fluorescence intensity was determined by FACS. **g**, Vector-transformed or wild-type TMEM16F-expressing Ba/F3 cells were preincubated at 4 °C with 0.1 μ M NBD-PtdCho. A23187 (A23) was added and incubated for 8 min at room temperature, and internalized NBD-PtdCho was determined as above. In **f** and **g** the percentage of BSA-non-extractable NBD-PtdCho was determined in triplicate at 4 min (**f**) or 6 min (**g**) after the addition of NBD-PtdCho and is plotted as mean and s.d. All experiments were performed at least three times.

1–12, was identical in the patient and the parents, whereas its 3' half, corresponding to exons 11–20, was shorter in the patient than in the parents (Fig. 4b). A sequence analysis indicated that the cDNA of the patient lacked the 226-bp sequence corresponding to exon 13. Direct

sequencing of the chromosomal DNA indicated that the *TMEM16F* gene of the patient carried a G-to-T homozygous mutation at the splice-acceptor site in intron 12, whereas both parents were heterozygous for the mutation at this position (Fig. 4c). PCR analysis of the *TMEM16F* mRNA with primers at exons 12 and 16 showed a 608-bp band from the control and a 382-bp band from the cell line from the patient with Scott syndrome (Fig. 4d), indicating that a mutation in the splice acceptor site caused exon 13 to be skipped. This skipping caused a frame shift resulting in the premature termination of the protein in exon 14 (Fig. 4e) at the third transmembrane segment of human TMEM16F (Fig. 4f). The nonsense-mediated mRNA decay²¹ may explain the decreased concentration of the exon-13-deleted form of *TMEM16F* mRNA in the patient's parents (Fig. 4d).

Repeated FACS analysis has been used previously to establish cell lines that overexpress a particular cell-surface protein^{22,23}. Here, this method yielded TMEM16F carrying a point mutation that rendered the process extremely sensitive to Ca^{2+} , such that in the cells expressing the mutated TMEM16F the phospholipid scramblase functioned even in resting cells, in which the cytosolic Ca^{2+} concentration was below 100 nM (ref. 24). The TMEM16 family, to which TMEM16F belongs, consists of ten members in humans and mice⁵. The founding member of the family, human TMEM16A, is a Ca^{2+} -dependent Cl^- channel^{11–13}. Although the direct binding of Ca^{2+} to TMEM16 members has yet to be demonstrated, the amino-terminal region of TMEM16A seems to have a regulatory role²⁵. Similarly, the increased sensitivity of the D409G mutant to Ca^{2+} suggests that either Ca^{2+} or a Ca^{2+} -sensing molecule binds to this N-terminal region of TMEM16F. The overexpression of TMEM16A in Ba/F3 cells had no effect on the ionophore-induced exposure of PtdSer (data not shown), suggesting that different members of this family have distinct functions. The PtdSer exposure or scrambling of phospholipids occurs in other biological processes^{1,4,26–29}, such as apoptotic cell death, the fusion of muscle, bone or trophoblast cells, and the release of neurotransmitters and microvesicles. It will be

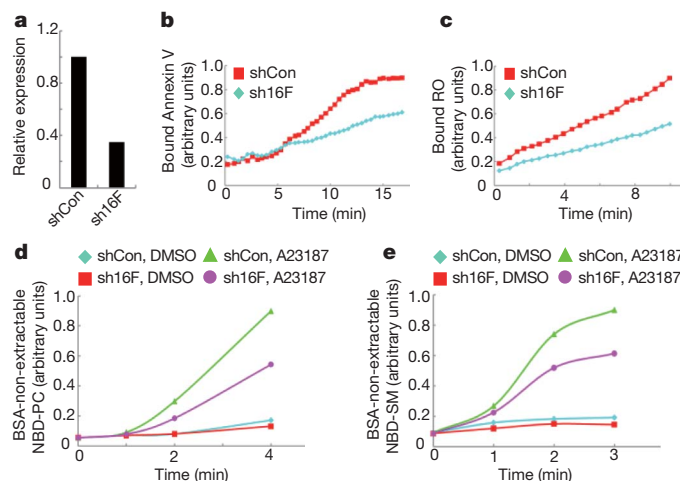


Figure 3 | Requirement of TMEM16F for phospholipid scrambling. **a**, Ba/F3 transformants expressing shRNA for *Tmem16f* (sh16F) or scrambled shRNA (shCon). *Tmem16f* mRNA level was normalized to β -actin mRNA and is shown as relative expression. **b**, **c**, Ba/F3 cells expressing sh16F or shCon were preincubated with Cy5-Annexin V (**b**) or biotin-Ro09-0198 (RO) and allophycocyanin (APC)-labelled streptavidin (**c**). A23187 was added and fluorescence was monitored. **d**, **e**, Ba/F3 cells expressing sh16F or shCon were preincubated with 0.5 μ M NBD-PtdCho (**d**) or NBD-SM (**e**) in Hanks balanced salt solution containing Ca^{2+} . A23187 was added, incubated and diluted with fatty-acid-free BSA buffer, and fluorescence was determined. Experiments in **b–e** were performed at least three times.

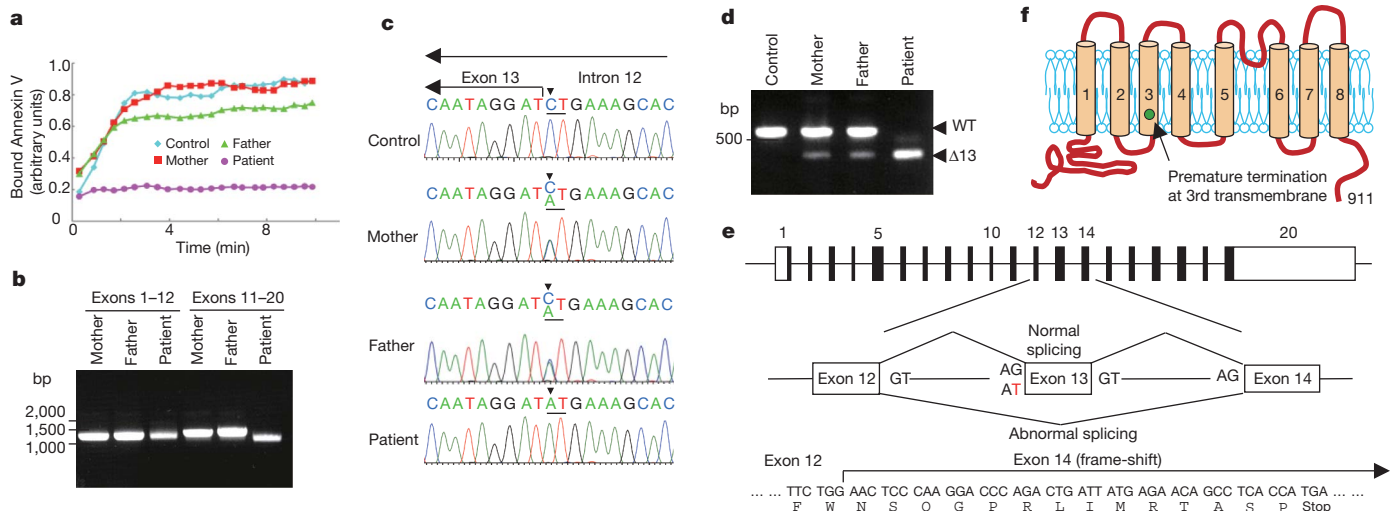


Figure 4 | A splice mutation of *TMEM16F* in a patient with Scott syndrome. **a**, Cells from control, from a patient with Scott syndrome and from the patient's parents, were preincubated with Annexin V. A23187 was added and fluorescence was monitored. **b**, RT-PCR for *TMEM16F* mRNA for exons 1–12 and 11–20 with RNA from the patient and parents. **c**, The junction between exon 13 and intron 12 of the *TMEM16F* gene sequenced from the 3' end. The CT complementary to the splice acceptor site AG is underlined. Arrowheads

indicate the mutation. **d**, RT-PCR for exons 12–16. Arrowheads indicate fragments for the wild-type (WT) and exon-13-deleted forms. **e**, Splicing in the patient's *TMEM16F* gene. The mutation causes the skipping of exon 13, resulting in a frame-shift mutation in exon 14. **f**, Schematic representation of the frame-shift mutation in the Scott patient that causes premature termination in the third transmembrane region of *TMEM16F*.

METHODS SUMMARY

To expose PtdSer reversibly on the cell surface, Ba/F3 cells were treated at 37 °C with A23187 under Ca^{2+} -free conditions. The exposed PtdSer was detected by binding of Annexin V at 4 °C in Ca^{2+} -containing Annexin V-binding buffer. A subline (Ba/F3-PS19) of Ba/F3 cells that was extremely sensitive to Ca^{2+} -ionophore-elicited PtdSer exposure was selected by repeating the sorting 19 times with FACSaria (BD Bioscience). A cDNA library was established with mRNA from Ba/F3-PS19 cells in retrovirus vector, and the cDNA (*Tmem16f*) that caused Ba/F3 cells to expose PtdSer constitutively was identified by expression cloning. The Epstein-Barr virus (EBV)-transformed cell lines from a patient with Scott syndrome and from the patient's parents were described previously²⁰. The *TMEM16F* mRNA in these cell lines was analysed by RT-PCR. The *TMEM16F* chromosomal gene was amplified by PCR from the genomic DNA of the cell lines, and was directly sequenced by cycle sequencing with an ABI 3100 genetic analyser (Applied Biosystems). Exposure of PtdSer and PtdEtn on the cell surface was analysed by the binding of Cy5-labelled Annexin V and biotin-labelled Ro09-0198 (ref. 17), respectively. The internalization of NBD-PtdCho and NBD-SM was analysed by the BSA-extraction method essentially as described³⁰. For the knock-down experiment, shRNA-retrovirus vectors for *Tmem16f* and control scrambled sequence were obtained from OriGene, and the resultant retrovirus was used to infect Ba/F3 cells.

Full Methods and any associated references are available in the online version of the paper at www.nature.com/nature.

Received 19 April; accepted 13 October 2010.

Published online 24 November 2010.

- Leventis, P. A. & Grinstein, S. The distribution and function of phosphatidylserine in cellular membranes. *Annu. Rev. Biophys.* **39**, 407–427 (2010).
- Zwaal, R. F., Comfurius, P. & Bevers, E. M. Lipid-protein interactions in blood coagulation. *Biochim. Biophys. Acta* **1376**, 433–453 (1998).
- Lentz, B. Exposure of platelet membrane phosphatidylserine regulates blood coagulation. *Prog. Lipid Res.* **42**, 423–438 (2003).
- Balasubramanian, K. & Schroit, A. Aminophospholipid asymmetry: a matter of life and death. *Annu. Rev. Physiol.* **65**, 701–734 (2003).
- Galletta, L. The TMEM16 protein family: a new class of chloride channels? *Biophys. J.* **97**, 3047–3053 (2009).
- Weiss, H. & Lages, B. Family studies in Scott syndrome. *Blood* **90**, 475–476 (1997).
- Zwaal, R., Comfurius, P. & Bevers, E. Scott syndrome, a bleeding disorder caused by defective scrambling of membrane phospholipids. *Biochim. Biophys. Acta* **1636**, 119–128 (2004).
- Williamson, P. *et al.* Phospholipid scrambling activation pathways in lymphocytes. *Biochemistry* **40**, 8065–8072 (2001).

- Wielders, S. J. *et al.* Absence of platelet-dependent fibrin formation in a patient with Scott syndrome. *Thromb. Haemost.* **102**, 76–82 (2009).
- Daleke, D. Phospholipid flippases. *J. Biol. Chem.* **282**, 821–825 (2007).
- Caputo, A. *et al.* TMEM16A, a membrane protein associated with calcium-dependent chloride channel activity. *Science* **322**, 590–594 (2008).
- Schroeder, B., Cheng, T., Jan, Y. & Jan, L. Expression cloning of TMEM16A as a calcium-activated chloride channel subunit. *Cell* **134**, 1019–1029 (2008).
- Yang, Y. *et al.* TMEM16A confers receptor-activated calcium-dependent chloride conductance. *Nature* **455**, 1210–1215 (2008).
- Schreiber, R. *et al.* Expression and function of epithelial anoctamins. *J. Biol. Chem.* **285**, 7838–7845 (2010).
- Shi, J. & Gilbert, G. Lactadherin inhibits enzyme complexes of blood coagulation by competing for phospholipid-binding sites. *Blood* **101**, 2628–2636 (2003).
- Hanayama, R., Tanaka, M., Miwa, K. & Nagata, S. Expression of developmental endothelial locus-1 in a subset of macrophages for engulfment of apoptotic cells. *J. Immunol.* **172**, 3876–3882 (2004).
- Emoto, K., Toyama-Sorimachi, N., Karasuyama, H., Inoue, K. & Umeda, M. Exposure of phosphatidylethanolamine on the surface of apoptotic cells. *Exp. Cell Res.* **232**, 430–434 (1997).
- Macia, E. *et al.* Dynasore, a cell-permeable inhibitor of dynamin. *Dev. Cell* **10**, 839–850 (2006).
- Toti, F., Satta, N., Fressinaud, E., Meyer, D. & Freyssinet, J. Scott syndrome, characterized by impaired transmembrane migration of procoagulant phosphatidylserine and hemorrhagic complications, is an inherited disorder. *Blood* **87**, 1409–1415 (1996).
- Kojima, H. *et al.* Production and characterization of transformed B-lymphocytes expressing the membrane defect of Scott syndrome. *J. Clin. Invest.* **94**, 2237–2244 (1994).
- Shyu, A., Wilkinson, M. & van Hoof, A. Messenger RNA regulation: to translate or to degrade. *EMBO J.* **27**, 471–481 (2008).
- Kavathas, P. & Herzenberg, L. A. Amplification of a gene coding for human T-cell differentiation antigen. *Nature* **306**, 385–387 (1983).
- Suda, T., Takahashi, T., Golstein, P. & Nagata, S. Molecular cloning and expression of the Fas ligand: a novel member of the tumor necrosis factor family. *Cell* **75**, 1169–1178 (1993).
- Berridge, M., Bootman, M. & Roderick, H. Calcium signalling: dynamics, homeostasis and remodelling. *Nature Rev. Mol. Cell. Biol.* **4**, 517–529 (2003).
- Ferrera, L. *et al.* Regulation of TMEM16A chloride channel properties by alternative splicing. *J. Biol. Chem.* **284**, 33360–33368 (2009).
- Nagata, S., Hanayama, R. & Kawane, K. Autoimmunity and the clearance of dead cells. *Cell* **140**, 619–630 (2010).
- Huppertz, B., Bartz, C. & Kokozidou, M. Trophoblast fusion: fusogenic proteins, syncytins and ADAMs, and other prerequisites for syncytial fusion. *Micron* **37**, 509–517 (2006).
- Helming, L. & Gordon, S. Molecular mediators of macrophage fusion. *Trends Cell Biol.* **19**, 514–522 (2009).
- van den Eijnde, S. *et al.* Transient expression of phosphatidylserine at cell-cell contact areas is required for myotube formation. *J. Cell Sci.* **114**, 3631–3642 (2001).
- Williamson, P. *et al.* Transbilayer phospholipid movements in ABCA1-deficient cells. *PLoS ONE* **2**, e729 (2007).

Supplementary Information is linked to the online version of the paper at www.nature.com/nature.

Acknowledgements We thank T. Wiedmer for critical reading of our manuscript, and M. Fujii and M. Harayama for secretarial assistance. This work was supported in part by Grants-in-Aid for Specially Promoted Research (to S.N.) and for Young Scientists Start-up (to J.S.) from the Japan Society for the Promotion of Science. J.S. is supported by a research fellowship from the Japan Society for the Promotion of Science. P.J.S. was supported by grants from the National Institutes of Health, USA.

Author Contributions J.S. designed and performed the experiments, and wrote the manuscript. M.U. provided biotin-labelled Ro09-0198 peptide. P.J.S. provided

EBV-transformed cell lines from a patient and the patient's parents, and commented on the manuscript. S.N. was responsible for the overall study design and for writing the manuscript.

Author Information Reprints and permissions information is available at www.nature.com/reprints. The authors declare no competing financial interests. Readers are welcome to comment on the online version of this article at www.nature.com/nature. Correspondence and requests for materials should be addressed to S.N. (snagata@mfour.med.kyoto-u.ac.jp).

METHODS

Cell lines, recombinant proteins, antibodies, serum and reagents. Mouse interleukin (IL-3)-dependent Ba/F3 cells were maintained in RPMI medium containing 10% fetal calf serum (FCS; Gibco), 45 U ml⁻¹ recombinant mouse IL-3 and 50 µM 2-mercaptoethanol. The EBV-transformed human cell lines²⁰ from a patient with Scott syndrome and the patient's parents were grown in RPMI1640 medium containing 10% FCS and 50 µM 2-mercaptoethanol. Human 293T cells and Plat-E packaging cells³¹ were cultured in DMEM medium containing 10% FCS. Recombinant mouse IL-3 was produced by mouse C1271 cells transformed with a bovine papillomavirus expression vector bearing mouse *Il-3* cDNA as described³². Biotin-labelled Ro09-0198 was prepared as described previously³³. Flag-tagged mouse MFG-E8 was produced in human 293T cells as described³⁴, and the secreted MFG-E8 was purified with anti-Flag M2 beads (Sigma-Aldrich).

Ca²⁺/Mg²⁺-free RPMI1640 medium was purchased from Cell Science & Technology Institute. Ca²⁺-free RPMI medium contained 0.5 mM MgSO₄. Ca²⁺-free FCS was prepared by dialysing FCS for 2 days against PBS, with four changes of buffer. Dynasore was purchased from Calbiochem.

BAPTA-AM was from Dojindo. NBD-PtdCho and NBD-SM were purchased from Avanti Polar Lipids.

Treatment with Ca²⁺ ionophore, flow cytometry, and cell sorting. To expose PtdSer on the cell surface, 2 × 10⁵ cells in a 96-well microtitre plate were washed with PBS, resuspended in 200 µl of HBSS (Gibco) and treated with A23187 (Sigma-Aldrich) at 37 °C for 15 min. The cells were stained on ice for 15 min with 2,500–5,000-fold diluted Cy5-labelled Annexin V (Biovision) in staining buffer (10 mM Hepes-NaOH pH 7.4 containing 140 mM NaCl and 2.5 mM CaCl₂) in the presence of 5 µg ml⁻¹ PI. Flow cytometry was performed on a FACSaria (BD Bioscience) or FACSCalibur (BD Bioscience) and the data were analysed with FlowJo Software (True Star).

A subline of Ba/F3 cells that was sensitive to Ca²⁺-ionophore-elicited PtdSer exposure was selected by repetitive sorting with a FACSaria. In brief, after 2 × 10⁷ Ba/F3 cells in HBSS had been treated at 37 °C for 15 min with A23187, they were suspended in 1 ml of Annexin V staining buffer that had been prechilled to 4 °C. The cells were stained with Cy5-Annexin V on ice as described above, and sorted with a FACSaria whose injection chamber was kept at 4 °C. Cells providing the highest level of Cy5 fluorescence signal (the top 0.5–5.0%) were collected and resuspended at a density of more than 10⁵ cells ml⁻¹ in Ca²⁺-free RPMI containing 5% dialysed FCS, 45 U ml⁻¹ IL-3 and 50 µM 2-mercaptoethanol. After 24 h the cells were resuspended in normal Ca²⁺-containing RPMI medium and expanded for the next sorting.

Construction of the cDNA library. Total RNA was prepared from Ba/F3 PS19 cells with an RNeasy Mini Kit (Qiagen), and poly(A)⁺ RNA was purified with an mRNA Purification Kit (GE Healthcare) with two cycles of oligo(dT)-cellulose column chromatography. Double-stranded cDNA was synthesized with random hexamers as primers, using a cDNA synthesis kit (SuperScript Choice System for cDNA Synthesis; Invitrogen). A BstXI adaptor was attached, and the fragments were size-fractionated by electrophoresis through a 1% agarose gel (Seakem GTG agarose; Lonza). DNA fragments longer than 2.5 kb were recovered from the gel with a DNA extraction kit (Wizard SV Gel and PCR Clean-up System; Promega) and ligated into a BstXI-digested pMXs vector³⁵. *Escherichia coli* DH10B cells (ElectroMax DH10B; Invitrogen) were transformed by electroporation with a Gene Pulser (Bio-Rad). About 9.3 × 10⁵ clones were produced, and plasmid DNA was prepared with a QIAfilter Plasmid Maxi Kit (Qiagen).

Cell fusion. Ba/F3-PS0 and Ba/F3-PS19 cells were transduced with pMXs-puro EGFP and pMXs-neo DsRed, respectively, and cultured in the presence of 1 µg ml⁻¹ puromycin or 1 mg ml⁻¹ G418. Ba/F3-PS0 EGFP cells and Ba/F3-PS19 DsRed cells were fused in the presence of PEG1500 and cultured in the presence of 1 µg ml⁻¹ puromycin and 1 mg ml⁻¹ G418. The EGFP/DsRed double-positive cells were sorted with a FACSaria.

Screening of cDNA library. Plasmid DNA (108 µg) from the cDNA library was introduced by lipofection with FuGENE6 (Roche Diagnostics) into 7.2 × 10⁷ PLAT-E packaging cells³¹ grown in eighteen 10-cm dishes. Two days after the transfection, the viruses in the culture supernatant were centrifuged at 4 °C and 6,000g for 16 h, resuspended in RPMI1640 medium containing 10% FCS and 45 U ml⁻¹ IL-3, and used to infect 7.2 × 10⁶ Ba/F3 cells in the presence of 8 µg ml⁻¹ Polybrene (Sigma-Aldrich). After a 24-h culture, the medium was replaced with fresh medium, and the cells were further cultured for 2 days. The sorting of cells that were sensitive to ionophore-induced PtdSer exposure was performed as described above.

Isolation of cDNA fragments from Annexin V-positive Ba/F3 cells. To isolate the cDNA integrated into the retroviral vector, the genomic DNA was extracted from Ba/F3 cell transformants with the Wizard Genomic DNA Purification System (Promega) and subjected to PCR with the Expand Long Template PCR System (Roche Diagnostics). The PCR primers (5'-CCCGGGGGTGGACCATCTCT-3'

and 5'-CCCCTTTTCTGGAGACTAAAT-3') carried sequences from the pMXs vector, and the conditions for PCR were 10 s at 96 °C, 30 s at 58 °C and 4 min at 68 °C for 35 cycles. The PCR fragments were cloned into the pGEM-T Easy vector (Promega) and subjected to DNA sequencing analysis with an ABI PRISM 3100 Genetic Analyser (Applied Biosystems).

Expression vector for TMEM16F and its mutants. The Flag-tag sequence was integrated into the *EcoRI* and *XhoI* sites of the retroviral vector pMXs-puro, resulting in pMXs-puro c-Flag. The full-length coding sequence for mouse TMEM16F (GenBank accession number NM_175344) was prepared by RT-PCR with the mRNA from Ba/F3 cells. The primers used were as follows (in each primer the *EcoRI* recognition sequence is underlined): 5'-ATATGAATTCGACATGCAGATGATGACTAGGAA-3' and 5'-ATATGAATTCGAGTTTGGCCGCACGCTGT-3'.

The PCR fragments were inserted into the *EcoRI* site of pMXs-puro c-Flag, and the authenticity of the cDNAs was verified by DNA sequencing.

For the expression plasmid of TMEM16F-mRFP, the coding sequence for mRFP in pcDNA-mRFP (Invitrogen) was joined in-frame to the C terminus of mouse TMEM16F and introduced into pMXs vector.

Expression in mouse Ba/F3 and human 293T cells. The expression vector for Flag-tagged TMEM16F in pMXs-puro was introduced into Plat-E cells. The retrovirus produced was concentrated as described above and used to infect Ba/F3 cells to establish stable transformants. The transformants were selected by culturing the cells in medium containing puromycin (1.0 µg ml⁻¹). To express TMEM16F-mRFP, human 293T cells were transfected by lipofection with FuGENE6 with the pMXs vector carrying the TMEM16F-mRFP sequence. One day later, the transfected cells were observed by fluorescence microscopy (BioRevo BZ-9000; Keyence).

Western blotting. Cells were lysed in RIPA buffer (50 mM Hepes-NaOH pH 8.0 containing 1% Nonidet P40, 0.1% SDS, 0.5% sodium deoxycholate, 150 mM NaCl and 10% protease inhibitor cocktail (Complete Mini; Roche Diagnostics)). The lysate was mixed with 5 × SDS sample buffer (200 mM Tris-HCl pH 6.8, 10% SDS, 25% glycerol, 5% 2-mercaptoethanol, 0.05% bromophenol blue), boiled for 5 min and separated by electrophoresis on a 10% polyacrylamide gel (Bio Craft). After the proteins had been transferred to a poly(vinylidene difluoride) membrane (Millipore), the membranes were probed with horseradish peroxidase-conjugated mouse anti-Flag M2 (Sigma), and peroxidase activity was detected with a Western Lightning enhanced chemiluminescence system (PerkinElmer).

RT-PCR of TMEM16F cDNA and sequencing of its chromosomal gene in a patient with Scott syndrome. Total RNA was prepared from EBV-transformed cell lines from a patient with Scott syndrome and from the patient's parents, and from a healthy control. The RNA was reverse-transcribed with Superscript III (Invitrogen), in accordance with the manufacturer's protocol, and the TMEM16F cDNA was analysed by PCR with the following sets of primers (in each primer the additional sequence is underlined): Ex1-FW (5'-ATATGAATTCGACATGAAAAAGATGAGCAGGAA-3'), Ex11/12-RV (5'-GCGTCTCTCTCTCTGAGTAA-3'), Ex11/12-FW (5'-TTACTCAGGAAGAAGAACGC-3'), Ex20-RV (5'-ATATGAATTCCTCTGATTTTGGCCGTAAT-3'), Ex12-FW (5'-CTGTGTCAGTGTCTGTCTTT-3') and Ex16-RV (5'-CTGCAGATGGTAGTCTCTGTT-3').

For the sequence analysis of the human TMEM16F chromosomal gene, genomic DNA was prepared from human cell lines and a 965-bp DNA fragment carrying the 226-bp exon 13 and its 5'-flanking and 3'-flanking regions (about 370 bp each) was amplified by PCR with the following primers: 5'-CCA GAGTATGCTACTAGTTG-3' and 5'-TCTCAGCAACCGAGGAACAT-3'. The PCR products were purified with a Wizard SV PCR and Gel Clean-up System. Cycle sequencing was performed with a BigDye Terminator v3.1 Cycle Sequencing kit with a primer of 5'-GGACCTTACCGAAGTTAGTA-3', and analysed with an ABI PRISM 3100 Genetic Analyser.

Analysis of exposure of PtdSer and PtdEtn. To analyse the exposure of PtdSer and PtdEtn, 10⁵ cells at early exponential phase were washed with PBS, suspended in 1.0 ml of cold Annexin V staining buffer with 2,500–5,000-fold diluted Cy5-labelled Annexin V or 800-fold diluted biotin-Ro09-0198 (ref. 33) followed by 1.0 µg ml⁻¹ APC-labelled streptavidin and 5 µg ml⁻¹ PI. The samples were incubated on ice for 15 min, and flow cytometry was performed on a FACSaria or FACSCalibur as described above. For binding of MFG-E8, the cells were suspended in RPMI1640 containing 10% FCS and then incubated on ice for 20 min with Flag-tagged D89E mutant of MFG-E8 (0.4 µg ml⁻¹)³⁴. The cells were washed with the above medium and incubated on ice for 20 min with 1.0 µg ml⁻¹ hamster monoclonal antibody against mouse MFG-E8 (clone 2422). This was followed by incubation with phycoerythrin-labelled mouse anti-hamster IgG (BD Bioscience) and analysis by flow cytometry with a FACSaria.

To study the requirement for intracellular Ca²⁺, 10⁵ cells were incubated with 10 µM BAPTA-AM in RPMI1640 medium containing 10% FCS at 37 °C for 5 min for the PtdSer exposure, or for 60 min for the PtdEtn exposure. The cells were

washed with Annexin V staining buffer, and stained with Cy5-Annexin V or biotin-Ro09-0198 as described above.

For the kinetic study of the Ca^{2+} -induced PtdSer and PtdEtn exposure, 10^6 cells were washed with PBS, suspended in 1.0 ml of cold Annexin V staining buffer with Cy5-labelled Annexin V or a mixture of biotin-Ro09-0198 and APC-labelled streptavidin, and $5 \mu\text{g ml}^{-1}$ PI. Cells were mixed on ice with A23187 at a final concentration of 0.25 or $0.5 \mu\text{M}$, and applied to the injection chamber of a FACSARIA that was set at 20°C (for Ba/F3 cells) or 37°C (for human cell lines) to induce the A23187 reaction. Data were recorded for the indicated periods, and the PI-positive cells were excluded from the analysis.

Internalization of NBD-PtdCho and NBD-SM. The internalization of NBD-lipid analogues was analysed by flow cytometry essentially as described in refs 8 and 30. In brief, 10^6 cells were washed with HBSS and resuspended in 0.5 ml of HBSS containing 2 mM CaCl_2 (HBSS-Ca). An equal volume of HBSS-Ca containing $1 \mu\text{M}$ NBD-PtdCho or NBD-SM was added to the cell suspension and incubated at room temperature. At each time point, 150 μl of cell suspension was collected, mixed with 150 μl of the prechilled (4°C) HBSS-Ca containing 5 mg ml^{-1} fatty-acid-free BSA (Sigma-Aldrich), to extract the unincorporated fluorescent lipids, and 500 nM Sytoxblue (Molecular Probes). To measure the total fluorescence, samples were mixed with HBSS-Ca in the absence of BSA. After incubation for 10 min at 4°C to extract the lipid, the cells were analysed with a FACSARIA for forward scatter, side scatter, logarithmic green fluorescence (NBD), and Sytoxblue fluorescence. The Sytoxblue-positive dead cells were excluded from the analysis. The fluorescence of NBD-phospholipids that were resistant to the BSA extraction was regarded as representing phospholipids that had been incorporated into cells.

To examine the effect of the Ca^{2+} ionophore, 5×10^5 cells were washed with HBSS-Ca, resuspended in 0.5 ml of cold HBSS-Ca, and incubated on ice for 7 min. Cold HBSS (0.5 ml) containing $0.2 \mu\text{M}$ NBD-PtdCho or NBD-SM was added to the cell suspension and incubated further on ice for 3 min. The cells were then mixed with A23187 and incubated at room temperature to induce lipid incorporation. A 150- μl aliquot was used to determine the incorporated lipid quantity as described above.

Thin-layer chromatography. After incubation of cells with NBD-PtdCho or NBD-SM, the phospholipids were extracted from the cells by incubation at room temperature for 30 min with a mixture of chloroform, methanol and water (5:10:4,

by volume). The phospholipids were separated by thin-layer chromatography on a silica gel 60 plate (Merck) with chloroform/acetone/methanol/acetic acid/water (5:2:1:1:0.5 by volume) as a solvent. The fluorescence on the plate was detected with a LAS4000 image analyser (Fuji Film).

Intracellular Ca^{2+} and Ca^{2+} influx. To determine the intracellular Ca^{2+} concentration, 10^6 cells were suspended in HBSS, incubated at 37°C for 10 min with $0.4 \mu\text{M}$ Fluo-4-AM (Molecular Probes), washed with HBSS, and analysed with a FACSARIA.

The Ca^{2+} influx was measured as described³⁶. In brief, 10^6 cells were labelled for 30 min at 37°C with $1 \mu\text{M}$ Fluo-4-AM in RPMI containing 10% FCS. After being washed with the Annexin V staining buffer, the cells were kept at 4°C in Annexin V staining buffer. The Ca^{2+} ionophore A23187 was added to the mixture at a final concentration of $0.5 \mu\text{M}$, and the change in mean fluorescence intensity was directly recorded with a FACSCalibur system. The data was analysed with FlowJo Software. **shRNA.** shRNA expression plasmids for mouse *Tmem16f* in a pRS shRNA vector carrying the puromycin-resistance gene were purchased from OriGene. The target sequence of the shRNA for *Tmem16f* was 5'-CATCTACTCTGTGAAGTTC TTCATTTCCT-3'. The scrambled non-effective shRNA (5'-GCACTACCAGA GCTAACTCAGATAGTACT-3') in pRS was from OriGene. Ba/F3 cells were infected with retrovirus containing the shRNA, and cultured in the presence of $1.0 \mu\text{g ml}^{-1}$ puromycin. Puromycin-resistant cells were subjected to cloning by limited dilution. The *Tmem16f* mRNA was quantified by real-time PCR, and the clones that showed the decreased expression were used for further study.

31. Morita, S., Kojima, T. & Kitamura, T. Plat-E: an efficient and stable system for transient packaging of retroviruses. *Gene Ther.* **7**, 1063–1066 (2000).
32. Fukunaga, R., Ishizaka-Ikeda, E. & Nagata, S. Purification and characterization of the receptor for murine granulocyte colony-stimulating factor. *J. Biol. Chem.* **265**, 14008–14015 (1990).
33. Aoki, Y., Uenaka, T., Aoki, J., Umeda, M. & Inoue, K. A novel peptide probe for studying the transbilayer movement of phosphatidylethanolamine. *J. Biochem.* **116**, 291–297 (1994).
34. Hanayama, R. *et al.* Identification of a factor that links apoptotic cells to phagocytes. *Nature* **417**, 182–187 (2002).
35. Kitamura, T. *et al.* Retrovirus-mediated gene transfer and expression cloning: powerful tools in functional genomics. *Exp. Hematol.* **31**, 1007–1014 (2003).
36. Bernhagen, J. *et al.* MIF is a noncognate ligand of CXC chemokine receptors in inflammatory and atherogenic cell recruitment. *Nature Med.* **13**, 587–596 (2007).

Glioblastoma stem-like cells give rise to tumour endothelium

Rong Wang^{1,2,3}, Kalyani Chadalavada⁴, Jennifer Wilshire⁵, Urszula Kowalik¹, Koos E. Hovinga^{1,6}, Adam Geber¹, Boris Fligelman¹, Margaret Leversha⁴, Cameron Brennan^{1,3,7} & Viviane Tabar^{1,2,3}

Glioblastoma (GBM) is among the most aggressive of human cancers¹. A key feature of GBMs is the extensive network of abnormal vasculature characterized by glomeruloid structures and endothelial hyperplasia². Yet the mechanisms of angiogenesis and the origin of tumour endothelial cells remain poorly defined^{3–5}. Here we demonstrate that a subpopulation of endothelial cells within glioblastomas harbour the same somatic mutations identified within tumour cells, such as amplification of *EGFR* and chromosome 7. We additionally demonstrate that the stem-cell-like CD133⁺ fraction includes a subset of vascular endothelial-cadherin (CD144)-expressing cells that show characteristics of endothelial progenitors capable of maturation into endothelial cells. Extensive *in vitro* and *in vivo* lineage analyses, including single cell clonal studies, further show that a subpopulation of the CD133⁺ stem-like cell fraction is multipotent and capable of differentiation along tumour and endothelial lineages, possibly via an intermediate CD133⁺/CD144⁺ progenitor cell. The findings are supported by genetic studies of specific exons selected from The Cancer Genome Atlas⁶, quantitative FISH and comparative genomic hybridization data that demonstrate identical genomic profiles in the CD133⁺ tumour cells, their endothelial progenitor derivatives and mature endothelium. Exposure to the clinical anti-angiogenesis agent bevacizumab⁷ or to a γ -secretase inhibitor⁸ as well as knockdown shRNA studies demonstrate that blocking VEGF or silencing *VEGFR2* inhibits the maturation of tumour endothelial progenitors into endothelium but not the differentiation of CD133⁺ cells into endothelial progenitors, whereas γ -secretase inhibition or *NOTCH1* silencing blocks the transition into endothelial progenitors. These data may provide new perspectives on the mechanisms of failure of anti-angiogenesis inhibitors currently in use. The lineage plasticity and capacity to generate tumour vasculature of the putative cancer stem cells within glioblastoma are novel findings that provide new insight into the biology of gliomas and the definition of cancer stemness, as well as the mechanisms of tumour neo-angiogenesis.

Blood vessels within GBM express a variety of markers, including CD31 and CD105 (also known as PECAM1 and ENG, respectively); CD105 is a proliferation-associated molecule expressed in angiogenic endothelium⁹. Quantitative analysis of 16 GBM specimens by fluorescence-activated cell sorting (FACS) and immunohistochemistry showed that more than 70% of CD105⁺ cells co-express CD31 (Fig. 1a, b), VEGFR2 (also known as KDR) and von Willebrand factor (also known as VWF), exhibit endothelial morphology, and labelling by DiI-AcLDL (1,1'-dioctadecyl-3,3,3',3'-tetramethyl-indocarbocyanine perchlorate, ref. 10), suggesting an endothelial phenotype (Supplementary Fig. 1a). On average, ~5% of the total cell population expressed CD31 in normal brain and GBM specimens ($n = 7$), whereas CD105⁺ cells were essentially absent in normal brain (Supplementary Fig. 1b). CD105⁺ cells were also isolated by FACS from fresh GBM

specimens and injected with a collagen matrix¹¹ into the flank of NOD-SCID mice. The resulting implants were composed of a network of vascular channels of human origin, expressed CD105 and CD31 and showed evidence of uptake of systemically injected lectin (Fig. 1c).

Whereas endothelial cells in GBMs are often classified as “hyperplastic”², the abnormal blood vessel architecture, the distinct gene expression profiles¹² and the selective emergence of abnormal vessels in GBMs versus lower grade gliomas² suggest a more complex ontogeny of GBM endothelium. We performed quantitative fluorescence *in situ* hybridization (FISH) analyses for *EGFR* and chromosome 7 (ref. 13) on CD105⁺ cells isolated by FACS and on sections of the corresponding GBM parent tumour (Fig. 1d, e and Supplementary Fig. 2). The proportion of CD105⁺ cells harbouring ≥ 3 copies of the *EGFR* amplicon or the centromeric portion of chromosome 7 was comparable to the proportion of tumour cells with the same aberrations (Supplementary Table 1a). We also performed quantitative PCR (qPCR) for three segments of the *EGFR* amplicon (exons 4, 9 and 11), known to be mutated at high frequency according to data from The Cancer Genome Atlas⁶. The data demonstrate a similar copy number in the CD105⁺ cells and the corresponding parent tumour (Supplementary Table 1b) and indicate that a proportion of tumour endothelial cells within GBM is in fact neoplastic.

CD133 is a cell surface glycoprotein used extensively as a marker of putative cancer stem cells (CSCs) but also expressed in haematopoietic stem cells^{14–18}. Although the specific identity and definition of CSCs remains a matter of debate, we proposed that the CD133⁺ fraction may be related to the endothelial differentiation potential observed. Acutely dissociated cells from a series of 14 GBMs were fractionated into four groups: (1) CD144⁺/CD133[–], (2) CD144⁺/CD133⁺ (double positive, DP), (3) CD133⁺/CD144[–] and (4) CD133[–]/CD144[–] (double negative, DN) (Fig. 2a). All samples contained the four fractions, with the DN being the largest population (Supplementary Table 4). Quantitative PCR with reverse transcription (qRT-PCR) analysis for endothelial markers (Supplementary Fig. 3a) demonstrated marked enrichment of *VEGFR2* and the endothelial progenitor marker *CD34* in the CD144⁺/CD133[–] and in the DP populations. CD105 was consistently absent in the CD133⁺ and CD144⁺ fractions. To define lineage potential further, DP cells were cultured for 5 days in endothelial cell medium which resulted in the downregulation of CD144, the upregulation of CD105 and CD31 as well co-expression of VEGFR2 and CD34 and labelling with DiI-AcLDL (Fig. 2b and Supplementary Fig. 3b). When grown in three-dimensional (3D) gel cultures, the *in vitro* DP-derived endothelial cells form vascular networks reminiscent of normal endothelium, but also thickened channel walls and areas of confluence more suggestive of abnormal tumour vessels (Fig. 2c, d). The primary CD105⁺ cells also form glomeruloid-like structures in 3D gel, with high lectin uptake (Supplementary Fig. 1c). DP-derived CD105⁺ cells were sorted and injected subcutaneously in NOD/SCID mice, giving rise to

¹Department of Neurosurgery, Memorial Sloan Kettering Cancer Center, New York, New York 10065, USA. ²Center for Stem Cell Biology, Memorial Sloan Kettering Cancer Center, New York, New York 10065, USA. ³Brain Tumor Center, Memorial Sloan Kettering Cancer Center, New York, New York 10065, USA. ⁴Molecular Cytogenetics, Memorial Sloan Kettering Cancer Center, New York, New York 10065, USA. ⁵Flow Cytometry Core, Memorial Sloan Kettering Cancer Center, New York, New York 10065, USA. ⁶Neurosurgical Center Amsterdam, Academic Medical Center, Amsterdam 1105 AZ, The Netherlands. ⁷Human Oncology and Pathogenesis Program, Memorial Sloan Kettering Cancer Center, New York, New York 10065, USA.

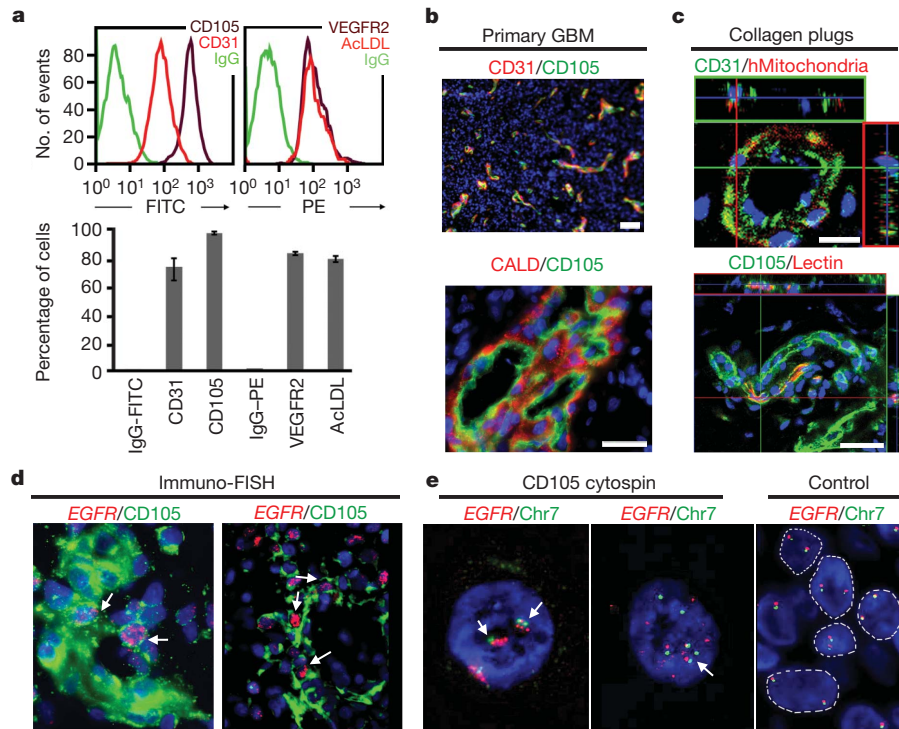


Figure 1 | CD105⁺ endothelial cells in GBM harbour genomic aberrations. **a**, FACS analysis and quantification of GBM-derived CD105⁺ cells shows co-expression of other endothelial cell markers (CD31, VEGFR2) and uptake of DiI-AcLDL ($n = 3$). FITC, fluorescein isothiocyanate; PE, phycoerythrin. **b**, CD105 immunostaining in GBMs delineates microvessels co-labelling with CD31 and glomeruloid vessels surrounded by caldesmon (CALD)-expressing pericytes. **c**, Functional neovessel formation by GBM-derived CD105⁺ cells in the flank of NOD-SCID mice. Confocal immunofluorescence demonstrates

co-localization of a human mitochondria marker with CD31 and uptake of lectin by the CD105⁺ vessels in the implants. **d**, Immuno-FISH of CD105⁺ vessels in GBM specimens (case 76, 78) shows multiple copies of the *EGFR* amplicon (arrows). **e**, FISH on CD105⁺ cells sorted from GBMs confirms amplification of *EGFR* (red) and chromosome 7 centromere (Chr7, green) (arrows). Control nuclei, individually contoured, are from normal human fibroblasts. Scale bars, 50 μ m. Error bars, s.d.

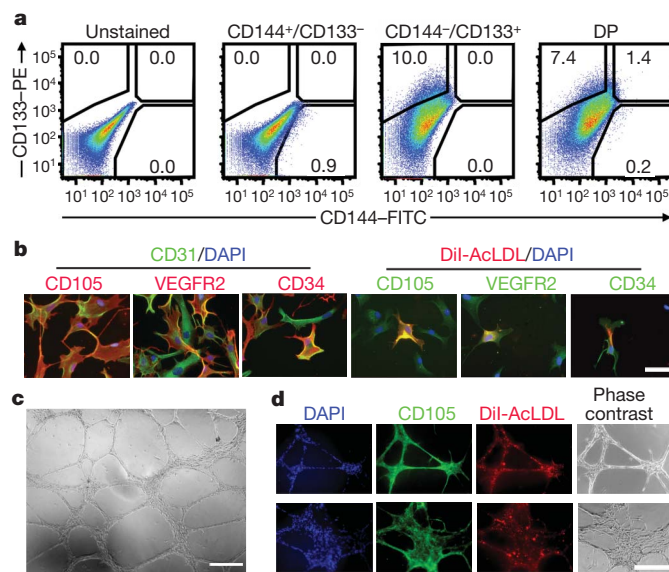


Figure 2 | GBM-derived CD133⁺ cells include a fraction of endothelial progenitors **a**, Representative FACS analysis of a GBM specimen with fractionation into four cell subpopulations based on the expression of CD133 and vascular E-cadherin (CD144). **b**, Immunofluorescence analysis of DP (CD133⁺/CD144⁺) cells upon differentiation demonstrates co-expression of endothelial markers and DiI-AcLDL uptake. **c**, **d**, In Matrigel, DP cells will exhibit DiI-AcLDL uptake and form tubular networks comparable to those shown by normal endothelial cells, as well as areas of thickened walls where cells are more proliferative. Scale bars, 100 μ m in **b** and **d**; 300 μ m in **c**.

vascularized plugs identical to those obtained from primary CD105⁺ cells (Supplementary Fig. 1d).

The CD144⁺/CD133⁻ cell fraction was often very small but showed a restricted differentiation and immunohistochemical profile (Supplementary Fig. 3c, d). When grown in Matrigel, the CD144⁺/CD133⁻ cells develop tubular, capillary-like structures¹⁹ and no glomeruli (Supplementary Fig. 3e). CD144⁺/CD133⁻ cells do not express neural markers or form neurospheres, thus indicating a more restricted endothelial precursor cell identity (Supplementary Fig. 3f). Unsupervised clustering of transcriptome data was performed on several data sets including independent samples of the four sorted tumour subpopulations, as well as CD144⁺ human embryonic stem-cell-derived endothelial precursors and bone-marrow-derived CD34⁺ endothelial progenitors (Supplementary Fig. 3g). Taken together, these results indicate that GBMs comprise cell fractions capable of endothelial cell differentiation.

The identification of genomic aberrations in tumour endothelium and the presence of endothelial progenitors within the CD133⁺ putative CSC fraction in GBMs, led us to postulate that DP cells may represent the neoplastic origin of tumour endothelium and could derive from the CD133⁺ CSC fraction. CD133⁺/CD144⁻ cells were then labelled with *EF α -1::GFP* (elongation factor α 1-green fluorescent protein) lentiviral vectors, triple sorted, and GFP⁺/CD133⁺/CD144⁻ cells were co-cultured in the presence of tumour cells. On day 5, FACS analysis demonstrated the emergence of a GFP⁺-DP population (Fig. 3a, b). When placed in collagen cultures, the GFP⁺-DP cells had intracellular vacuoles suggestive of early lumen formation by endothelial tubes²⁰ (Fig. 3c), and differentiation into cells that express CD105 and CD31 and exhibit DiI-AcLDL uptake (Fig. 3d and Supplementary Fig. 4a). Importantly, co-culture with tumour cells is essential for the emergence of DP cells (Fig. 3a, b). Our data confirm that the DP endothelial

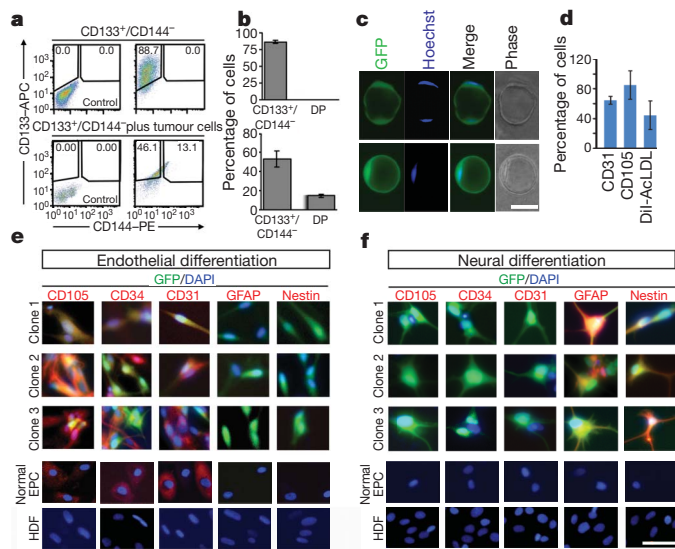


Figure 3 | CD133⁺/CD144⁻ cells are multipotential and give rise to endothelial cells via an endothelial progenitor intermediate. **a, b,** Co-cultures of CD133⁺/CD144⁻ cells with tumour cells give rise to endothelial progenitors that co-express CD133 and CD144 (DP) as shown and quantified by FACS analysis ($n = 3$). APC, allophycocyanin. **c,** GFP⁺-derived DP cells form intracellular vacuolar structures in collagen gel, characteristic of endothelial cells. **d,** Immunohistochemistry of CD133⁺/CD144⁻-derived endothelial cells ($n = 3$). **e, f,** Single cell clonal analysis of GFP-labelled CD133⁺/CD144⁻ cells. GFP⁺ clones derived from single cells are seeded under neural or endothelial conditions. Normal endothelial precursor cultures (EPC) and human dermal fibroblasts (HDF) were used as controls. Under endothelial conditions, all cells except HDF express endothelial but not neural markers. Under neural conditions, cells from the same GFP/CD133⁺ clone are positive for GFAP and nestin but not endothelial markers, while controls are negative for all markers. Scale bar, 50 μ m. Errors are s.d.

progenitors within GBM can arise from the CD133⁺ cell population and are capable of differentiating into endothelial cells of tumour origin. Of note, the tumour cells used in these co-culture experiments originate from tumours with different genetic backgrounds and transcriptomal subclasses (Supplementary Tables 2 and 3).

Recent data support a close interaction²¹ or a lineage relationship²² between endothelial cells and neural stem cells. We next explored whether endothelial differentiation of CD133⁺/CD144⁻ can be further promoted by extrinsic signals. To this end, CD133⁺/CD144⁻ cells were isolated from GBM samples, stably transduced with *EF α -1::GFP* lentiviral vectors, sorted for GFP⁺/CD133⁺/CD144⁻ and co-cultured with tumour-derived endothelial cells. GFP-expressing endothelial cells were identified at 7–10 days *in vitro* as demonstrated by co-labelling of GFP with CD105 and CD31, and also incorporation of DiI-AcLDL. Control experiments using GFP-labelled CD133⁻ cells did not yield any endothelial cells (Supplementary Fig. 4b). The CD133⁺/CD144⁻ population formed neurospheres and readily differentiated along the three main CNS lineages (Supplementary Fig. 4c). Whereas these data are suggestive of the multipotent nature of the CD133⁺/CD144⁻ cells, they do not rule out the presence of heterogeneous populations within the CD133⁺/CD144⁻ fraction with distinct differentiation potentials. We thus performed single-cell clonal studies of CD133⁺/CD144⁻ cells as well as normal endothelial cells and fibroblasts as controls (Supplementary Fig. 4d). The data demonstrate both endothelial and neural differentiation potential within a single-cell derived clone confirming that CD133⁺/CD144⁻ cells are capable of generating tumour cells and tumour-derived endothelium (Fig. 3e, f). FISH for *EGFR* and chromosome 7 in the clones confirmed the presence of genomic amplifications identical to those exhibited by the parent tumour tissue (Supplementary Fig. 4e).

We next tested the fate of the various tumour cell fractions upon transplantation *in vivo*. CD133⁺/CD144⁻, DP, CD144⁺/CD133⁻ and DN cells were injected into the striatum of immunodeficient mice. All grafted animals developed tumours with the exception of those that received cells from the DN and CD144⁺/CD133⁻ fraction. DP and CD133⁺/CD144⁻ gave rise to large, highly infiltrative and hyperproliferative tumours showing strong expression of nestin (Fig. 4a). Whereas all xenograft tumours had a comparable volume and proliferation rate, the DP-derived tumours showed significantly increased levels of vascularization as demonstrated quantitatively (Supplementary Fig. 5a).

Some of the animals were grafted with stably GFP-marked CD133⁺/CD144⁻ cells allowing us to serially passage GFP-labelled CD133⁺/CD144⁻ cells from the primary xenograft in NOD-SCID mice. Secondary tumours formed at similar efficiency and showed comparable cell composition to the first passage cells. FACS analysis of GFP labelled xenograft cells demonstrates expression of endothelial markers, including CD105 and CD34 (Fig. 4b). After a second passage *in vivo*, tumours were sorted again for GFP⁺/CD133⁺/CD144⁻ cells, which upon culture gave rise to GFP-labelled CD31⁺ and CD105⁺ cells, thus demonstrating maintenance of the multipotential phenotype (Fig. 4c). Immunohistochemical analysis, including confocal microscopy, demonstrated tumour vessels with typical morphology that express human markers. Tumour-bearing animals were also injected systemically with lectin, resulting in vessel-specific uptake and co-labelling with human markers (Fig. 4d, e and Supplementary Fig. 6). Thus, multipotency—including differentiation capacity along endothelial lineages—is maintained within the CD133⁺/CD144⁻ population *in vivo* and upon passaging. However, in the absence of clonal studies *in vivo*, true multipotency of tumour stem-like cells cannot be definitively confirmed.

A more comprehensive and quantitative analysis of genomic aberrations was conducted in order to verify the lineage relationship among the different tumour subpopulations. qPCR for the *EGFR* exons as described above⁶ demonstrates the highest copy number within the CD133⁺/CD144⁻ population followed by the endothelial progenitors (DP) and the CD105⁺ cells (Supplementary Fig. 5b). Interestingly, the CD31⁺ cells and the CD144⁺/CD133⁻ progenitors showed lower levels of amplification, indicating that they may include a significant proportion of genotypically normal cells. We propose that these cells largely represent normal endothelium and circulating endothelial progenitors, respectively. This is compatible with the more restricted endothelial fate demonstrated by the CD144⁺/CD133⁻ cells as shown above (Supplementary Fig. 3c, e, f). Quantitative FISH studies for copy number of *EGFR* and chromosome 7 per cell were performed on CD133⁺/CD144⁻, DP and CD105⁺ cells and revealed a substantial proportion of cells bearing the neoplastic aberrations in each population, ranging from 47.3% to 71.7% (Supplementary Fig. 5c). To address genomic alterations in tumour cells in a more unbiased manner we performed array comparative genomic hybridization (CGH) on the fractionated populations (Supplementary Fig. 7). The CGH data showed similar patterns of genomic aberrations in tumour cells as well as the endothelium and its progenitors, at variable amplitudes and across different regions, thus demonstrating a similar paradigm even in tumours that do not exhibit *EGFR* gain. We performed transcriptome analyses on a set of 18 tumours used in this study and found a random distribution of commonly described genotypes as well as representation of all TCGA-defined transcriptomal classes (Supplementary Table 3). Finally, we performed metaphase spreads on purified cell fractions of CD133⁺/CD144⁻, DP and CD105⁺ following short-term culture. The majority of the cells had a highly abnormal but near-diploid karyotype, indicating that nuclear fusion is a very unlikely explanation for the lineage transition from cancer cell to endothelial progenitor or mature cell (Supplementary Fig. 5d). Vascular mimicry has been described in melanoma²³ and other tumours²⁴; aneuploidy was also shown in renal cell cancer endothelium, but not matched to parent tumour cells²⁵.

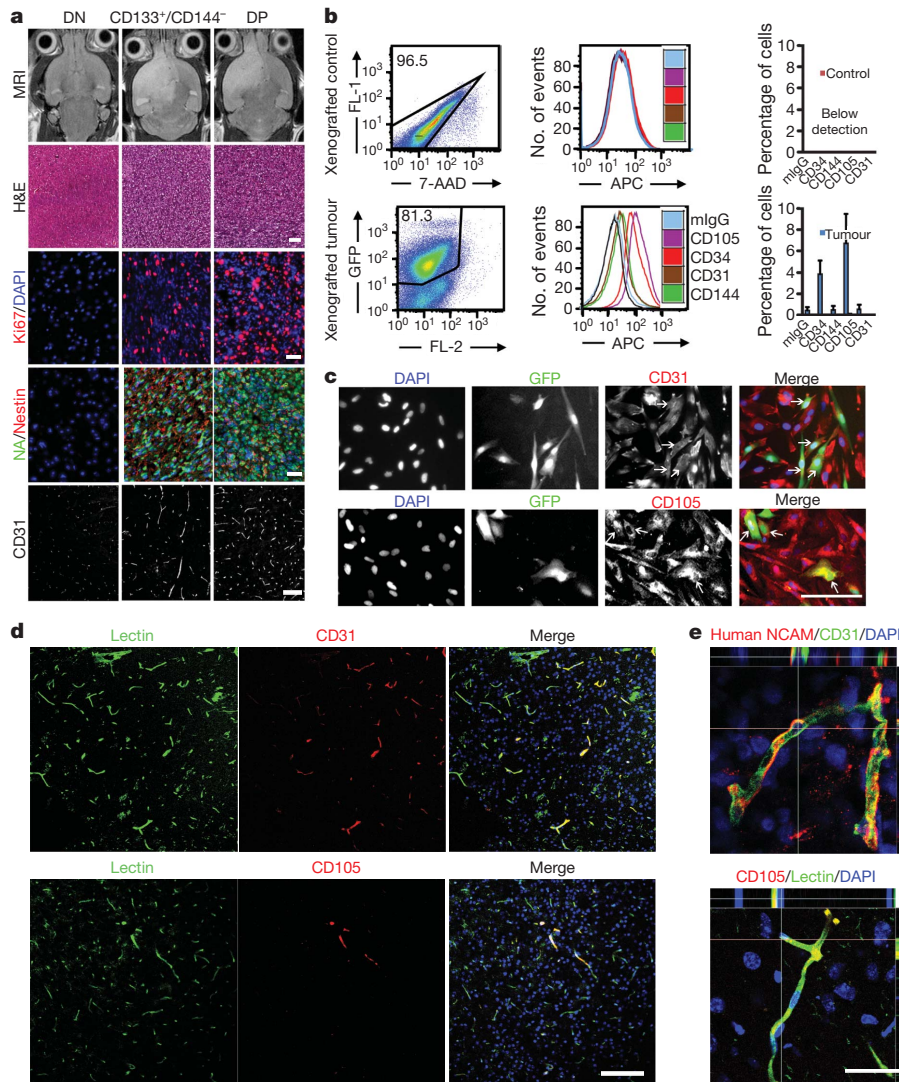


Figure 4 | Cancer stem-like cells and endothelial progenitors give rise to tumour and endothelial cells *in vivo*. **a**, Representative magnetic resonance imaging (MRI) images from mice that received injection of DN, CD133⁺/CD144⁻ or DP cells from primary GBM specimens. T2 sequences demonstrate infiltrative tumours except in the DN group. Tumours were hypercellular on haematoxylin and eosin (H&E), showed high proliferation rates (Ki67) and nestin expression. Immunostaining for human-specific CD31 demonstrates the presence of vessels of human origin within the tumours. NA, human nuclear antigen. **b**, FACS plots (left) and quantitative analysis (right) for

endothelial marker expression in xenograft tumours (GFP⁺/CD133⁺/CD144⁻ cells) and controls (DN). ($n = 3$, s.d.). 7-AAD, 7-aminoactinomycin. FL-1 and 2, fluorescent channels 1 and 2; mIgG, mouse immunoglobulin G. **c**, Xenograft derived GFP⁺/CD133⁺/CD144⁻ cells express endothelial markers upon *in vitro* differentiation (arrows). **d**, Uptake of systemic lectin in tumour xenografts demonstrates blood vessels that co-label with human endothelial markers (CD31 and CD105). **e**, Confocal microscopy of xenograft microvasculature. Scale bars, 100 μ m in **a**; 50 μ m in **c**; 140 μ m in **d**; 10 μ m in **e**.

We investigated the impact of DAPT (N-[N-(3,5-difluorophenacetyl)-L-alanyl]-S-phenylglycine *t*-butyl ester), a γ -secretase inhibitor that effectively inhibits Notch signalling⁸, and bevacizumab, a VEGFA-binding antibody⁷ currently in clinical use, on the differentiation of CD133⁺/CD144⁻ to DP and then to CD105⁺ cells. Exposure to bevacizumab did not have an impact on the ability of CD133⁺/CD144⁻ cells to differentiate into endothelial progenitors, yet it blocked further maturation from DP into CD105⁺ endothelial cells. In contrast, γ -secretase inhibition resulted in significant suppression of the transition from CD133⁺/CD144⁻ to DP, but did not affect maturation to CD105⁺ cells. To demonstrate the specific roles of the Notch and VEGF pathways, we performed knockdown studies targeting the *NOTCH1* and *VEGFR2* receptors. The gene silencing data further supported the results of the inhibitor studies (Supplementary Figs 8b and 9). Gene expression analysis shows significant upregulation of *NOTCH1/2* and *VEGFR1/2* in the CD133⁺/CD144⁻ and DP groups, respectively (Supplementary Fig. 8). These preliminary studies offer a

novel perspective of the roles of the VEGF and Notch pathways in glioma biology, although the functional consequences of VEGF or Notch blockade remain to be determined.

Despite some promise, bevacizumab therapy is often interrupted by GBM progression characterized by a decrease in abnormal vascularity and significant invasive tumour behaviour²⁶. Based on the paradigm presented here (Supplementary Fig. 9a), bevacizumab failure could be conceivably due to the disruption of the dynamic relationships between the tumour fractions.

In summary, our data demonstrate that a subpopulation of cells within GBM can give rise to endothelial cells via a bipotential progenitor intermediate, and that the CD133⁺ cancer stem-cell-like fraction includes a population of endothelial progenitors. An in-depth understanding of the lineage relationship between tumour cells and endothelial progeny should provide new insights into CSC biology and tumour self-renewal. Given the strong correlation of tumour grade and neoplastic vasculature in human gliomas, agents that could block endothelial

transition of tumour cells may provide a novel therapeutic strategy for this currently intractable disease.

METHODS SUMMARY

All experiments were conducted on freshly obtained surgical specimens of glioblastoma tumour; a neuropathologist confirmed the diagnosis on frozen section before tissue acquisition. Tumours were newly diagnosed or recurrent. A total of 78 tumours were used in the study. Cell fractions were sorted using standard methods at our FACS facility; *in vitro* experiments were conducted on short-passage cultures (maximum of five passages) if needed. A total of 34 xenografts were obtained in immunodeficient mice following intrastriatal implantation of cell populations as indicated in the Methods. A lentiviral vector expressing GFP under a PGK promoter (gift from M. Sadelain) was used for cell labelling and sorting. Cytogenetic analyses were conducted using standard methods at the Cytogenetics Core facility at Sloan Kettering Cancer Center. Knockdown experiments were performed using lentiviral vectors expressing shRNA for *NOTCH1* or *VEGFR2* (Santa Cruz). All experiments were carried out in triplicates or greater. Data are expressed as mean \pm s.d. *P* values were determined following two-tailed student's *t*-test. A *P* value of <0.05 was considered significant. Tissues were obtained after patients' written consent under a protocol approved by the institution's Institutional Review Board.

Full Methods and any associated references are available in the online version of the paper at www.nature.com/nature.

Received 10 May; accepted 1 November 2010.

Published online 21 November 2010.

- Stupp, R. *et al.* Radiotherapy plus concomitant and adjuvant temozolomide for glioblastoma. *N. Engl. J. Med.* **352**, 987–996 (2005).
- Kleihues, P. *et al.* The WHO classification of tumors of the nervous system. *J. Neuropathol. Exp. Neurol.* **61**, 215–225 (2002).
- Kioi, M. *et al.* Inhibition of vasculogenesis, but not angiogenesis, prevents the recurrence of glioblastoma after irradiation in mice. *J. Clin. Invest.* **120**, 694–705 (2010).
- Lyden, D. *et al.* Impaired recruitment of bone-marrow-derived endothelial and hematopoietic precursor cells blocks tumor angiogenesis and growth. *Nature Med.* **7**, 1194–1201 (2001).
- Du, R. *et al.* HIF1 α induces the recruitment of bone marrow-derived vascular modulatory cells to regulate tumor angiogenesis and invasion. *Cancer Cell* **13**, 206–220 (2008).
- The Cancer Genome Atlas Research Network. Comprehensive genomic characterization defines human glioblastoma genes and core pathways. *Nature* **455**, 1061–1068 (2008).
- Kreisl, T. N. *et al.* Phase II trial of single-agent bevacizumab followed by bevacizumab plus irinotecan at tumor progression in recurrent glioblastoma. *J. Clin. Oncol.* **27**, 740–745 (2009).
- Hovinga, K. E. *et al.* Inhibition of Notch Signaling in Glioblastoma Targets Cancer Stem Cells Via an Endothelial Cell Intermediate. *Stem Cells* **28**, 1019–1029 (2010).
- Dallas, N. A. *et al.* Endoglin (CD105): a marker of tumor vasculature and potential target for therapy. *Clin. Cancer Res.* **14**, 1931–1937 (2008).
- Voyta, J. C., Via, D. P., Butterfield, C. E. & Zetter, B. R. Identification and isolation of endothelial cells based on their increased uptake of acetylated-low density lipoprotein. *J. Cell Biol.* **99**, 2034–2040 (1984).
- Laib, A. M. *et al.* Spheroid-based human endothelial cell microvessel formation *in vivo*. *Nature Protocols* **4**, 1202–1215 (2009).
- Beatty, R. M. *et al.* *PLXDC1* (*TEM7*) is identified in a genome-wide expression screen of glioblastoma endothelium. *J. Neurooncol.* **81**, 241–248 (2007).
- Verhaak, R. G. *et al.* Integrated genomic analysis identifies clinically relevant subtypes of glioblastoma characterized by abnormalities in *PDGFRA*, *IDH1*, *EGFR*, and *NF1*. *Cancer Cell* **17**, 98–110 (2010).
- Singh, S. K. *et al.* Identification of human brain tumour initiating cells. *Nature* **432**, 396–401 (2004).
- Richardson, G. D. *et al.* CD133, a novel marker for human prostatic epithelial stem cells. *J. Cell Sci.* **117**, 3539–3545 (2004).
- Al-Hajj, M., Wicha, M. S., Benito-Hernandez, A., Morrison, S. J. & Clarke, M. F. Prospective identification of tumorigenic breast cancer cells. *Proc. Natl Acad. Sci. USA* **100**, 3983–3988 (2003).
- Shmelkov, S. V., St, C. R., Lyden, D. & Rafii, S. AC133/CD133/Prominin-1. *Int. J. Biochem. Cell Biol.* **37**, 715–719 (2005).
- Uchida, N. *et al.* Direct isolation of human central nervous system stem cells. *Proc. Natl Acad. Sci. USA* **97**, 14720–14725 (2000).
- Koh, W., Mahan, R. D. & Davis, G. E. Cdc42- and Rac1-mediated endothelial lumen formation requires Pak2, Pak4 and Par3, and PKC-dependent signaling. *J. Cell Sci.* **121**, 989–1001 (2008).
- Kamei, M. *et al.* Endothelial tubes assemble from intracellular vacuoles *in vivo*. *Nature* **442**, 453–456 (2006).
- Shen, Q. *et al.* Endothelial cells stimulate self-renewal and expand neurogenesis of neural stem cells. *Science* **304**, 1338–1340 (2004).
- Wurmser, A. E. *et al.* Cell fusion-independent differentiation of neural stem cells to the endothelial lineage. *Nature* **430**, 350–356 (2004).
- Hendrix, M. J. *et al.* Transendothelial function of human metastatic melanoma cells: role of the microenvironment in cell-fate determination. *Cancer Res.* **62**, 665–668 (2002).
- El Hallani, S. *et al.* A new alternative mechanism in glioblastoma vascularization: tubular vasculogenic mimicry. *Brain* **133**, 973–982 (2010).
- Akino, T. *et al.* Cytogenetic abnormalities of tumor-associated endothelial cells in human malignant tumors. *Am. J. Pathol.* **175**, 2657–2667 (2009).
- Iwamoto, F. M. *et al.* Patterns of relapse and prognosis after bevacizumab failure in recurrent glioblastoma. *Neurology* **73**, 1200–1206 (2009).

Supplementary Information is linked to the online version of the paper at www.nature.com/nature.

Acknowledgements We would like to thank J. Imai, H. Xu, G. Lee, M. Tomishima and L. Studer for critical reading of the manuscript, P. Gutin for assistance with tissue acquisition and discussions, B. Weksler for the brain endothelial cell line (hCMEC), S. Jhanwar for the clinical cytogenetics data and M. Sadelain and E. Papapetrou for the lentiviral vectors. Funding was provided in part through a grant from the New York State Stem Cell Science Fund (NYSTEM).

Author Contributions R.W. and V.T. conceived the project, analysed the data and wrote the manuscript. R.W. and remaining authors performed experiments and analysed data.

Author Information Microarray and CGH data are deposited in NCBI's Gene Expression Omnibus (GSE24244, GSE24446, GSE24452, GSE24557 and GSE24558). Reprints and permissions information is available at www.nature.com/reprints. The authors declare no competing financial interests. Readers are welcome to comment on the online version of this article at www.nature.com/nature. Correspondence and requests for materials should be addressed to V.T. (tabarv@mskcc.org).

METHODS

Tissue processing. Surgical specimens were collected from the surgical suite at Memorial Sloan Kettering Cancer Center, following diagnostic confirmation by a neuropathologist. Tissues were obtained after patients' written consent under a protocol approved by the institution's Institutional Review Board. Tumours were cut mechanically first (McIlwain Tissue Chopper) then dissociated into single cells with Liberase Blendzyme 1 (Roche) as described previously²⁷.

Single cells were blocked with human FcR (1:20, Miltenyi Biotec) at 4 °C for 20 min before incubation with primary antibodies for 30 min. Cells from xenografts were further blocked with 2,4-G2 (1:100; Santa Cruz Biotechnology) before incubation with antibodies. Cells were incubated with primary antibodies, washed and reincubated with appropriate secondary antibodies and resuspended in FACS buffer²⁷ (containing $1 \times \text{Ca}^{2+}/\text{Mg}^{2+}$ -free HBSS (Invitrogen), 10 mM of HEPES, 0.156% of glucose and 0.5% of low endotoxin BSA fraction V, all from Sigma (Sigma-Aldrich), at a pH of 7.2) with $1 \mu\text{g ml}^{-1}$ 7-aminoactinomycin D (7-AAD, BD Pharmingen) before analysis. Mouse IgG1 or secondary antibody alone served as control for unspecific binding. Samples were analysed on a FACS Aria flow cytometer with CellQuest software (BD Biosciences) and data were analysed using FlowJo software (Tree star). A minimum of 10,000 events were counted and cell surface expression was analysed in 7-AAD-negative live cells. Antibodies used include: phycoerythrin- or allophycocyanin-conjugated anti-CD133 (1:20, Miltenyi Biotec); FITC-conjugated anti-CD144 (1:20, Abcam), anti-CD105 (1:20, BD Biosciences) and anti-CD31 (1:20, BD Biosciences); mouse anti-human CD31 (1:40; BD Biosciences), mouse anti-human CD105 (1:40; Dako), mouse anti-human VEGFR2 (1:40; Abcam), mouse anti-human CD34 (1:20; Abcam), mouse anti-human CD144 (1:20; Abcam); mouse anti-human CD133 antibodies (AC141 and AC133 epitopes (1:20 each), Miltenyi). FITC-conjugated lectin and tetramethyl rhodamine isothiocyanate (TRITC)-conjugated lectins were purchased from Vector and Sigma separately.

DNA and RNA preparation. FACS-sorted cell populations from 21 glioblastoma patients were used to extract total RNA using an Absolutely RNA Nanoprep kit (Stratagene) or an RNeasy Kit (Qiagen). All RNA samples were pre-treated with DNase. Sorted cell populations from eight glioblastoma patients were used to isolate genomic DNA using the Picopure DNA extraction kit (Molecular Devices), followed by phenol (Invitrogen) extraction.

In vivo studies. Adult female NOD/SCID or male NOD/SCID gamma (NSG) mouse (Jackson Laboratory) were anaesthetized with ketamine/xylazine (Hospira) and placed in a stereotaxic frame (Stoelting Company). Freshly sorted cells were injected into the right striatum immediately after sorting at the following coordinates (relative to bregma): AP = +0.5, ML = -2, and DV = -2.7. Animals received 10,000 cells each of CD133⁺/CD144⁻, CD133⁻/CD144⁺ or DP. NSG mice received 500 cells each of CD133⁺/CD144⁻ or DP. DN cells were used in three separate doses (10,000, 50,000 and 100,000 cells). Animals were killed upon exhibiting symptoms. Some animals received FITC-conjugated lectin by retro-orbital injection before killing. Total animals grafted $n = 40$.

The gel implantation assay was modified from ref. 11. Briefly, GBM- or DP-derived CD105⁺ (10^6 or 2×10^6 per ml) were resuspended in Collagen IV (Chemicon). GBM- or DP-derived cell-gel suspension (500 μl) was injected subcutaneously below the xiphoid in four or three mice separately. Some animals received TRITC-conjugated lectin by tail vein injection before killing. After transplantation (21 days) the implants were retrieved, fixed overnight in 4% (v/v) buffered formalin at 4 °C, embedded in Optimal Cutting Temperature Compound (O.C.T. compound, Sakura Finetek) and sectioned on a freezing cryostat (Leica) for histological examination. Animals were housed and cared for in accordance with the National Institutes of Health (NIH) guidelines for animal welfare and all animal experiments were performed in accordance with protocols approved by our Institutional Animal Care and Use Committee (IACUC).

Animal imaging. *In vivo* magnetic resonance imaging was performed on a Bruker Biospec 4.7-Tesla 40-cm horizontal bore magnet. The system is equipped with a 200 mT m⁻¹ gradient system. Examinations were conducted using a 72-mm birdcage resonator for excitation, and detection was achieved using a 3 cm surface coil. T2-weighted spin echo images were acquired consecutively using a rapid-acquisition relaxation enhanced sequence (RARE). Animals were anesthetized with 2% isoflurane in N₂/O₂ mixture.

Immunofluorescence. Primary antibodies were chicken anti-GFP (1:1,000; Chemicon), mouse anti-human CD31 (1:400; Abcam); mouse anti-human CD34 (1:400; Abcam), mouse anti-human CD105 (1:400; Dako); mouse anti-human vWF (1:100; Dako); mouse anti-human VEGFR2 (1:200; Abcam); mouse anti-human Ki67 (1:400; Dako); mouse anti-human NCAM (1:150; Santa Cruz Biotechnology), mouse anti-human mitochondria (1:200; Chemicon), mouse anti-human nestin (1:400; Millipore), mouse anti-human nuclear antigen (1:500; Chemicon), rabbit anti-human GFAP (1:1,000; Chemicon), mouse anti-human Tuj1 (1:500; Covance), mouse anti-O4 (1:200; Chemicon), rabbit anti-human caldesmon (1:400; Novus

Biology). The following secondary antibodies were used: Alexa Fluor 488-conjugated goat anti-chicken or mouse or rabbit (1:1,000), Alexa Fluor 555-conjugated goat anti-mouse or rabbit (1:1,000), Alexa Fluor 555-conjugated goat anti-mouse IgM (1:500), all from Molecular Probes (Invitrogen).

Cell culture and clonal assays. GFP labelling was obtained by incubation with a PGK-GFP lentiviral vector (gift from M. Sadelain). For sphere cultures, freshly sorted CD133⁺/CD144⁻, DP and CD133⁻/CD144⁺ cells were cultured under clonal conditions (1,000 cells per cm² or 5 cells per μl) in low-adherence plates (Corning) and maintained in serum free-Neurobasal medium supplemented with N2 (Invitrogen), 2 mM L-glutamine, 20 ng ml⁻¹ recombinant human epidermal growth factor, and 10 ng ml⁻¹ recombinant human fibroblast growth factor 2 (all from Invitrogen). Neurospheres were reseeded every 5 days after dissociation with Accutase (Innovative Cell Technologies). For neural differentiation, CD133⁺/CD144⁻ cells were cultured in laminin coated plates (BD Biosciences) using NeuroCult NS-A Differentiation Kit (human) (Stem Cell Technologies).

For endothelial progenitor cells, freshly sorted DP or CD144⁺/CD133⁻ cells were seeded on human fibronectin-coated plates (BD Biosciences) at a density of 10^5 ml^{-1} with endo-cult liquid medium Kit (Stem Cell Technologies) for propagation. DP, CD144⁺/CD133⁻ or CD133⁺/CD144⁻-derived DP cells were grown to 75% confluence and switched to M199 medium (Invitrogen) for quantification of endothelial differentiation as described previously¹⁹. GBM-derived CD105⁺ cells were grown in M199 medium¹⁹ for 2 days before FACS analysis. The functional assay for endothelial cells was performed by incubation of cells with $10 \mu\text{g ml}^{-1}$ of DiI-labelled acetylated low density lipoproteins (DiI-AcLDL) (Molecular Probes, Invitrogen) for 4 h.

For DP induction culture, GFP-labelled CD133⁺/CD144⁻ were co-cultured with tumour cells at a 20:1 ratio in N2 medium. The CD133⁺/CD144⁻-derived DP cells were sorted by FACS after 5 days for further characterization. A minimum of 100 cells were counted in triplicate assays. They were cultured in three-dimensional collagen gel²⁰. For differentiation of CD133⁺/CD144⁻ to endothelial cells, tumour endothelial cells and GFP labelled CD133⁺/CD144⁻ cells or control cells were resuspended in endo-cult medium and grown on fibronectin coated plates for 7 days at a ratio of 100:1. Single cell clonal assays were performed by seeding freshly sorted single GFP-labelled cells on multi-well plates. Wells containing single green cells were identified and monitored until clone formation is established. Single-cell-derived clones were further sub-cloned and propagated twice, dissociated and seeded under neural and endothelial differentiation conditions as described above. Human umbilical cord-derived CD133⁺ endothelial precursor cells (Biochain) or human dermal fibroblasts (Cell Applications) were maintained as per manufacturer instructions and used as control in clonal analysis.

Inhibitor studies. For drug treatment assays, cells were cultured in DP induction medium or endothelial differentiation medium containing 5 μM of the γ -secretase inhibitor DAPT (N-[N-(3,5-difluorophenacetyl)-L-alanyl]-S-phenylglycine *t*-butyl ester, Sigma-Aldrich) or 1 $\mu\text{g ml}^{-1}$ of bevacizumab (Genentech). Treated cells were analysed by FACS analysis after 48 h incubation. VEGF was measured in the culture medium with a human VEGF ELISA Kit (Invitrogen) following the manufacturer directions.

Knockdown studies. GBM-derived fresh DP and GFP-CD133sp cells were infected with shRNA virus targeting VEGFR2 or NOTCH1 or a control virus (all from Santa Cruz Biotechnology). NOTCH1 shRNA lentiviral vector mix contains three target-specific constructs: CACCAGTTTGATGTCATTCACAGAGATTGACCATTCAACTGGTGTGTTTTT; CCCATGGTACCAATCATGATTCAGAGATCATGATTGGTACCATGGTGTGTTTTT; CCATGGTACCAATCATGATTCAGAGATTCATGATTGGTACCATGGTGTGTTTTT. VEGFR2 shRNA lentiviral vector mix contains three target-specific constructs: ACTGTGGTGATTCCATGTCTTCAAGAGAGACATGGAATCACCACAGTGTGTTTTT; ACTGTGTAACCCGAGACCTATTCAAGAGATAGGTCTCGGTTTACAAGTGTGTTTTT; CACC GTTTTGCAAGAACTTTTCAAGAGAAAGTTCTTGCACCAAGGTGTGTTTTT. The infected cells were selected with 2–4 $\mu\text{g ml}^{-1}$ puromycin (Santa Cruz Biotechnology) and used for FACS analysis and/or collected for RT-PCR as described above after 5 days in selection.

In vitro angiogenesis assay. Intracellular vacuole formation was evaluated by culturing CD133⁺/CD144⁻-derived DP cells in three-dimensional collagen gel as described in ref. 20. Tubular network formation was assessed by culture in growth factor reduced Matrigel assay Kit (BD Biosciences) following the protocol from ref. 19.

Cytogenetic analyses and genomic PCR. Fluorescence *in situ* hybridization was performed using BAC clone RP11-339F13 and PAC clone RP5-1091E12 spanning the EGFR locus in 7p11, both labelled with Red-dUTP, together with a chromosome 7 centromere repeat DNA probe labelled with Green-dUTP targeted at the centromeric region of chromosome 7 (7p11.1–7q11.1 D7Z1 alpha satellite region). FISH was performed on sorted cells post cytospin on glass slides. A minimum of 100 cells in interphase were analysed. Human dermal fibroblasts

(HDF) served as normal control. The false positive rates for FISH probes was determined as 1% (s.d. = 1.3) and the cut-off level for the diagnosis of amplification was set at 5% ($>3s.d.$) ($n = 3$, total counted 2,000 control cells).

FISH on tumour sections, as reported in Supplementary Tables 1b and 2, was performed independently by the Clinical Cytogenetics Facility at Memorial Sloan Kettering Cancer Center, as part of a now routine molecular diagnostic test. The probe used is the 7p12 LSI EGFR and the 7p11.1–7q11.1 CEP (D7Z1 alpha satellite) dual colour probe, purchased from Abbott Molecular.

Fluorescence immunophenotyping and interphase cytogenetics, a technique combining immunohistochemistry for CD105 and FISH for *EGFR*, was carried out on 10- μ m thick tissue sections. Normal human brain cerebral-cortex sections (Biochain) were used as controls.

In a copy number quantification reaction by real-time PCR, *EGFR* primers were designed based on published data^{6,28,29,30}. Genomic DNA (10 ng) from sorted cells or normal human brain was used as template to examine the copy number of exons 4, 9, 11 in the *EGFR* gene; *GAPDH* was used as reference gene. Each replicate was normalized to *GAPDH* to obtain a ΔC_t , and then an average ΔC_t value for each sample (from the three replicates) was calculated. All samples were then normalized to the calibrator sample (normal human brain) to determine $\Delta\Delta C_t$. Relative quantity (RQ) is $2^{\Delta\Delta C_t}$, and copy number is $2 \times RQ$. The *EGFR* copy number in each population was defined by the average of copy number from three exons. Error bars indicate the range of the data from the three exons in each of the three samples.

Karyotype analysis was performed on metaphase spread of FACS-purified cell subpopulations that were in culture for 3 days. The cultures were treated with Colcemid ($0.1 \mu\text{g ml}^{-1}$) for 1.5 h before *in situ* metaphase preparation according to standard cytogenetics procedures.

CGH studies. Comparative genomic hybridization (CGH) assay was performed by hybridizing genomic DNA from sorted cells with 44K human genome CGH arrays, and frozen banked whole tumour on 244K and 1M human genome CGH arrays (all commercial arrays from Agilent). DNA from sorted cells was prepared as described above. DNA extraction, purification, labelling and hybridization were performed at Sloan Kettering Cancer Center's Genomics Core Facility according to the manufacturer's instructions. \log_2 ratios were normalized by Lowess against probe intensity and mean %GC of the genomic region mapped to by the probe. Segmentation of normalized \log_2 ratios was by Circular Binary Segmentation (CBS, R package DNAcopy).

A separate method was used to investigate whether an amplicon identified by CBS in one cell fraction might be present in a minor subpopulation in other cell fraction at a level not detected by CBS. A region of interest (ROI) is defined by the boundaries of the amplicon detected by CBS. Then this region is investigated in the CGH profiles of the other cell fractions as follows: the \log_2 ratios of the N probes under the ROI (within amplicon boundaries) are compared to \log_2 ratios of all the other probes in the entire chromosome by Student's t -test (one-tailed). The observed t -score is then compared to the distribution of t -scores obtained by equivalently testing all other sets of N neighbouring probes in the chromosome. The ROI is considered to be significantly gained if the observed t -score is seen or exceeded in less than 0.1% of all other chromosomal regions.

Expression microarray studies of whole tumours. Gene expression profiling was performed for a subset of 16 tumours for which additional frozen material was available using exon expression arrays (Human Exon 1.0, Affymetrix). RNA was extracted, labelled and hybridized at Sloan Kettering Cancer Center's Genomics Core Facility according to the manufacturer's instructions. Data was normalized in a cohort of 80 gliomas using Aroma.affymetrix (R package aroma.affymetrix). Expression was derived for RefSeq transcripts, and multiple transcripts for the same gene were distilled to a single gene expression value by median.

Transcriptomal class assignment was based on the nearest centroid of the four transcriptomal classes reported in ref. 13, using the subset of 840 signature genes described by this study (Supplementary Table 6; http://tcga-data.nci.nih.gov/docs/publications/gbm_exp/). Distances to centroids were defined using Pearson correlation and class assignments made by the largest correlation value. If the largest correlation was <0.2 , the sample was labelled 'indeterminate'. Correlations and class assignments are given in Supplementary Table 6.

Microscopic analysis. Sections were examined with confocal laser scanning microscopy (Leica Microsystems; Carl Zeiss MicroImaging). The data was analysed with Velocity or LSM5 (Carl Zeiss MicroImaging) software.

Tumour microvessel density (MVD) was assessed by quantification of the numbers of CD31⁺ tumour vessels in pixels using MetaMorph (Molecular Devices) image analysis software using unbiased sampling.

Gene expression analysis and quantitative real-time PCR for sorted cell populations. Total RNA of four subpopulations from two specimens were hybridized with human U133-plus2 array at Sloan Kettering Cancer Center's Genomics Core Facility and according to the manufacturer's instructions. Reference databases, including one set of CD34⁺ human haematopoietic progenitor cells (GSM476781) and two independent sets of human embryonic stem cell-derived endothelial progenitors (GSM492830 and GSM492828) were downloaded from Gene Expression Omnibus database. The array data are analysed by Partek software. The data from 11 samples were normalized by RMA algorithms and the tumour samples then assigned in four groups based on the expression of membrane markers CD133 and CD144. The gene list is created by ANOVA with unadjusted P value less than 0.05 and then used as input for unsupervised hierarchical clustering by using Euclidian similarity metric.

For RT-PCR, total RNA (100–300 ng) was reverse-transcribed using random-primer and superscript III (Invitrogen) according to the manufacturer's instructions. Quantitative real-time PCR was performed with an Applied Biosystems Prism 7900HT sequence Detection System using SYBR Green PCR Master Mix (Applied Biosystems).

Primers: *CD34* (F: TCTGATCTCCATGGCTTCCT; R: ACTGAGGCAACAGCTCAACC), *CD144* (F: TCGTCATGGACCGAGGTT; R: TCTACAATCCCTTGACGTGTGA), *VEGFR2* (F: GCAGGGGACAGAGGGACTTG; R: GAGGCCATCGCTGCACTCA), *CD31* (F: TTCCTGACAGTGTCTTGAGTGG; R: GCTAGGCGTGGTCTCATCT), *CD133* (F: TCTGGGTCTACAAGGACTTTCC; R: GCGCGCTGAGTCACTAC), *ACTIN* (F: GCGCGCTGAGTCACTAC; R: GGAATCCTTCTGACCCATGC), *VEGFR1* (F: TCTCACATCGACAAACCAATACA; R: GGTAGCAGTACAATTGAGGACAAGA), *VEGF* (F: CTACCTCCACCATGCCAAGT; R: CCACTTCGTGATGATTCTGC).

Human angiogenesis PCR arrays (SABiosciences) were used to examine the expression profiles of angiogenic genes in sorted cell populations. Heat Map construction and analysis of qPCR data was conducted according to ref. 31.

27. Panchision, D. M. *et al.* Optimized flow cytometric analysis of central nervous system tissue reveals novel functional relationships among cells expressing CD133, CD15, and CD24. *Stem Cells* **25**, 1560–1570 (2007).
28. Franco-Hernandez, C. *et al.* Gene dosage and mutational analyses of EGFR in oligodendrogliomas. *Int. J. Oncol.* **30**, 209–215 (2007).
29. Mellingerhoff, I. K. *et al.* Molecular Determinants of the response of glioblastomas to EGFR kinase inhibitors. *N. Engl. J. Med.* **353**, 2012–2024 (2005).
30. Brennan, C. *et al.* Glioblastoma subclasses can be defined by activity among signal transduction pathways and associated genomic alterations. *PLoS ONE* **4**, e7752 (2009).
31. Guo, P. *et al.* Dual nature of the adaptive immune system in lampreys. *Nature* **459**, 796–801 (2009).

Structures of APC/C^{Cdh1} with substrates identify Cdh1 and Apc10 as the D-box co-receptor

Paula C. A. da Fonseca^{1*}, Eric H. Kong^{1*}, Ziguo Zhang¹, Anne Schreiber¹, Mark. A. Williams², Edward P. Morris¹ & David Barford¹

The ubiquitylation of cell-cycle regulatory proteins by the large multimeric anaphase-promoting complex (APC/C) controls sister chromatid segregation and the exit from mitosis^{1,2}. Selection of APC/C targets is achieved through recognition of destruction motifs, predominantly the destruction (D)-box³ and KEN (Lys-Glu-Asn)-box⁴. Although this process is known to involve a co-activator protein (either Cdc20 or Cdh1) together with core APC/C subunits^{1,2}, the structural basis for substrate recognition and ubiquitylation is not understood. Here we investigate budding yeast APC/C using single-particle electron microscopy and determine a cryo-electron microscopy map of APC/C in complex with the Cdh1 co-activator protein (APC/C^{Cdh1}) bound to a D-box peptide at ~10 Å resolution. We find that a combined catalytic and substrate-recognition module is located within the central cavity of the APC/C assembled from Cdh1, Apc10—a core APC/C subunit previously implicated in substrate recognition^{5–7}—and the cullin domain of Apc2. Cdh1 and Apc10, identified from difference maps, create a co-receptor for the D-box following repositioning of Cdh1 towards Apc10. Using NMR spectroscopy we demonstrate specific D-box–Apc10 interactions, consistent with a role for Apc10 in directly contributing towards D-box recognition by the APC/C^{Cdh1} complex. Our results rationalize the contribution of both co-activator and core APC/C subunits to D-box recognition^{8,9} and provide a structural framework for understanding mechanisms of substrate recognition and catalysis by the APC/C.

The APC/C is a multimeric E3 ubiquitin ligase assembled from 13 individual subunits^{1,2}. Many of the core proteins of the APC/C are comprised of multiple repeat motifs whose principle function is to provide a molecular scaffold, but whose exact biological role is not well understood. The best-characterized APC/C subunits are the cullin and RING proteins Apc2 and Apc11, which are responsible for catalytic activity, and the tetratricopeptide repeat (TPR) subunit Apc3/Cdc27, which interacts with a co-activator (either Cdc20 or Cdh1)^{10–12} and the APC/C subunit Apc10 (also known as Doc1)¹³. Both co-activator^{9,11,14–17} and core APC/C subunits^{5–9} have been implicated in substrate recognition, but the structural basis for this process is unknown. To address this question, we used single-particle electron microscopy (EM) to determine structures of budding yeast APC/C^{Cdh1} and substrates. The resultant EM maps are of excellent quality and detail. The maps show the characteristic triangular shape of the APC/C^{18–21} (Supplementary Fig. 1), but at higher resolution we visualize a lattice-like scaffold assembled from individual APC/C subunits defining a central cavity.

The APC/C co-activator Cdh1 was identified in negative-stain EM reconstructions as a prominent and discrete density feature present within the central cavity of APC/C^{Cdh1} and absent from APC/C (Fig. 1a, b). Its disc-shaped density, characteristic of an exposed WD40 β-propeller domain, is connected to the APC/C via an edge-on interface. Overall, with the exception of the Cdh1 density, APC/C and APC/C^{Cdh1} are similar, and the large conformational changes that

accompany co-activator binding to vertebrate APC/C^{19,21} are not evident. An ellipsoid-shaped density feature, resembling the β sandwich of Apc10 (refs 13, 22), situated adjacent to but not in contact with Cdh1, is more prominent in the presence of Cdh1 (Fig. 1a, b). Its close proximity to Cdh1 was intriguing in view of the role of Apc10 in contributing towards substrate recognition⁶, and the D-box-dependent processivity of the ubiquitylation reaction^{5,7}. To unequivocally identify Apc10 we generated APC/C^{ΔApc10} in complex with Cdh1 (APC/C^{ΔApc10–Cdh1}). The resultant APC/C^{ΔApc10–Cdh1} map showed complete loss of this ellipsoid density (Fig. 1c), confirming its identity as Apc10. Deletion of Apc10 also resulted in a depletion of Cdh1 density around the circumference of the β-propeller most distant from its contact to APC/C (Fig. 1c). Because deletion of Apc10 does not affect the APC/C subunit composition⁶ or abrogate Cdh1 binding (Supplementary Fig. 2), the partial loss of Cdh1 density is indicative of an increased flexibility of the WD40 domain of Cdh1. This finding and the reduced density of Apc10 in APC/C imply conformational interdependence of Apc10 and Cdh1.

To identify substrate-binding sites on APC/C^{Cdh1}, we used a fragment of Hsl1, a D-box (RxxLxxI/VxN)³ and KEN-box⁴-containing substrate with high affinity for APC/C^{Cdh1} (refs 14, 23). The ternary APC/C^{Cdh1–Hsl1} complex was catalytically competent, as judged by its ability to ubiquitylate Hsl1 (Supplementary Fig. 3a). Engagement of Hsl1 with APC/C^{Cdh1} is accompanied by a pronounced structural change involving Cdh1 and Apc10 (Fig. 1d). Specifically, the β-propeller domain of Cdh1 is bulkier, shifts ~7 Å towards Apc10, and new, well-defined density bridges Cdh1 to Apc10. Thus, Hsl1 promotes the formation of new connections between Cdh1 and Apc10, a result consistent with direct co-activator–substrate interactions^{9,11,14–17} and a role for Apc10 in mediating optimal substrate binding^{5–7,23}.

To define the specific roles of the D- and KEN-boxes in contributing to these conformational changes, we determined structures of APC/C^{Cdh1} in complex with synthetic peptides containing either a D-box or a KEN-box. Similar to previous results with D-box peptides^{11,24}, an 18-residue D-box peptide modelled on cyclin B (*Schizosaccharomyces pombe* Cdc13) completely inhibited APC/C^{Cdh1} activity towards Clb2 (a mitotic cyclin with D- and KEN-boxes) at 0.1 mM (Supplementary Fig. 4a). Figure 1e shows that D-box peptide generated similar structural changes to Hsl1; specifically, the WD40 domain of Cdh1 is shifted and new density connects it with Apc10 (Supplementary Movie 1). However, in contrast to the APC/C^{Cdh1–Hsl1} map, the extent of new density associated with Cdh1 is markedly reduced, indicating that the additional density in APC/C^{Cdh1–Hsl1} represents the larger Hsl1 substrate. Control experiments show that a mutant D-box peptide, which fails to bind APC/C^{Cdh1} (Supplementary Fig. 4c), induces no conformational changes (Supplementary Fig. 5). Binding of the KEN-box peptide to APC/C^{Cdh1} also promotes a repositioning of Cdh1 towards Apc10, but notably without the connecting density (Fig. 1f). This indicates that only D-box substrates promote a physical interconnection between Cdh1 and Apc10.

¹Section of Structural Biology, Institute of Cancer Research, Chester Beatty Laboratories, 237 Fulham Road, London SW3 6JB, UK. ²Institute of Structural and Molecular Biology, Department of Biological Sciences, Birkbeck, University of London, Malet Street, London WC1E 7HX, UK.

*These authors contributed equally to this work.

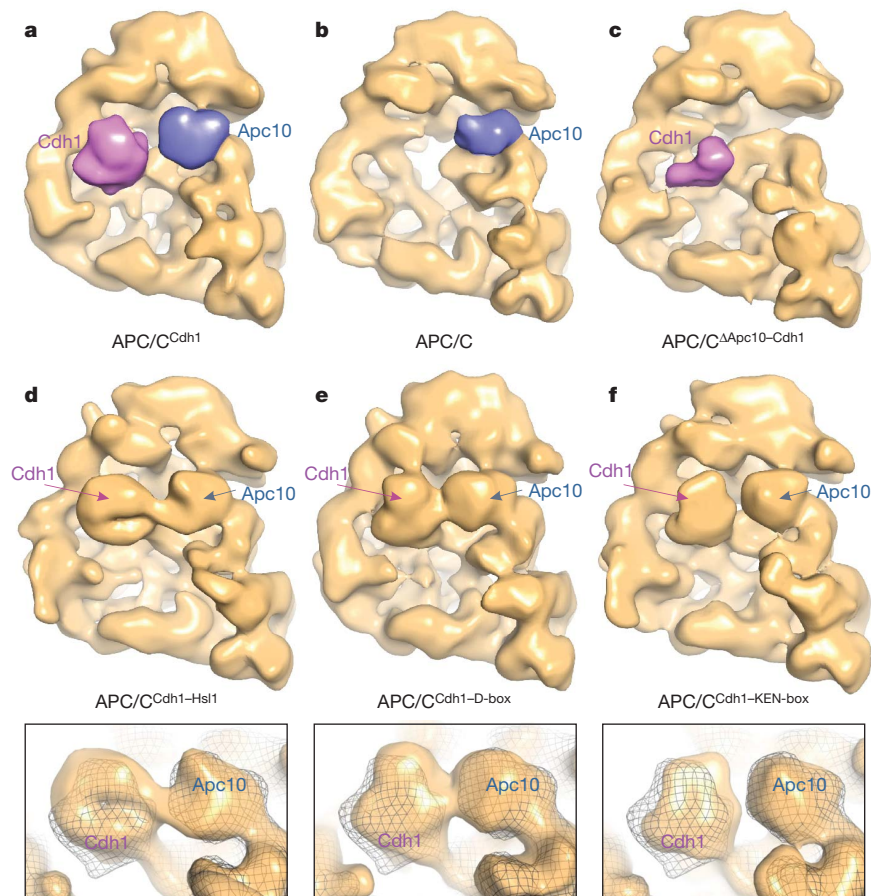


Figure 1 | Negative-stain EM reconstructions of budding yeast APC/C show that substrate binding to APC/C^{Cdh1} involves Cdh1 and Apc10. a–c, Molecular envelopes of APC/C^{Cdh1} (a), APC/C (b) and APC/C^{ΔApc10-Cdh1} (c). Density assigned to Cdh1 and Apc10 is shown in magenta and blue, respectively. The resolution of the APC/C^{Cdh1} binary complex is ~18–20 Å (Supplementary Fig. 10d). d–f, Negative-stain EM reconstructions of APC/C^{Cdh1}-Hsl1 complex (d), APC/C^{Cdh1}-D-box (e) and APC/C^{Cdh1}-KEN-box (f). Lower panels in d, e and f show details of the structural changes associated with Cdh1 and Apc10 in the presence of substrate compared with the superimposed binary APC/C^{Cdh1} map represented in mesh. Hsl1 and D-box and KEN-box peptides were used at saturating concentrations to promote stoichiometric APC/C^{Cdh1}-substrate ternary complexes.

To explore the structure of APC/C^{Cdh1}-D-box in more detail, we collected cryo-EM images of the complex and determined its structure at ~10 Å resolution. The cryo-EM map reproduces the overall features of the APC/C^{Cdh1}-D-box map generated from negatively stained particles, but with greatly enhanced detail and resolution (Fig. 2 and Supplementary Figs 6 and 7). Similar to the APC/C^{Cdh1}-D-box ternary complex obtained from negative-stain EM, the cryo-EM reconstruction shows density connecting Cdh1 and Apc10 (Figs 2 and 3). Docking the crystal structure of Apc10 (refs 13, 22) and the modelled

Cdh1 WD40 domain into their respective densities indicates further unassigned density linking Cdh1 to Apc10 (Fig. 3a, c). Notably, the best fit of Apc10 into the cryo-EM map positions a highly conserved loop required for D-box recognition⁷ adjacent to the density linking Apc10 with Cdh1. In contrast, residues on the opposite surface of Apc10 that contribute to APC/C interactions⁷ are oriented towards Apc2 (Fig. 3c).

These structural data revealing that Cdh1 and Apc10 become interconnected by bridging density in the presence of D-box substrates

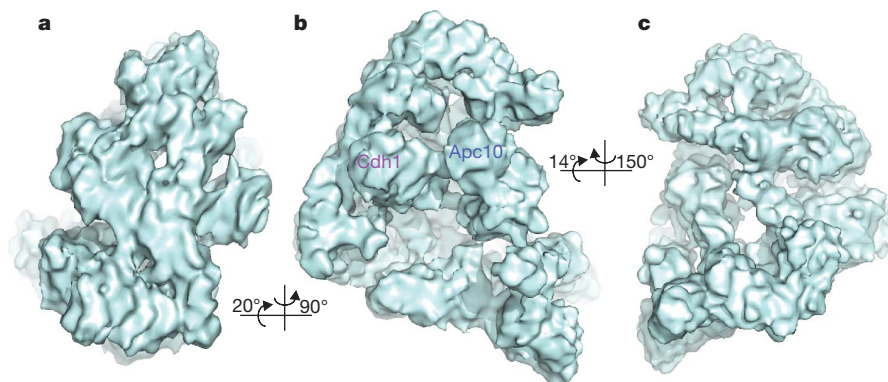


Figure 2 | Cryo-EM reconstruction of budding yeast APC/C^{Cdh1}-D-box reveals the lattice-like architecture of the complex. a–c, Three views of the complex with b similar to views shown in Fig. 1. Resolution is ~10 Å (Supplementary Fig. 12c).

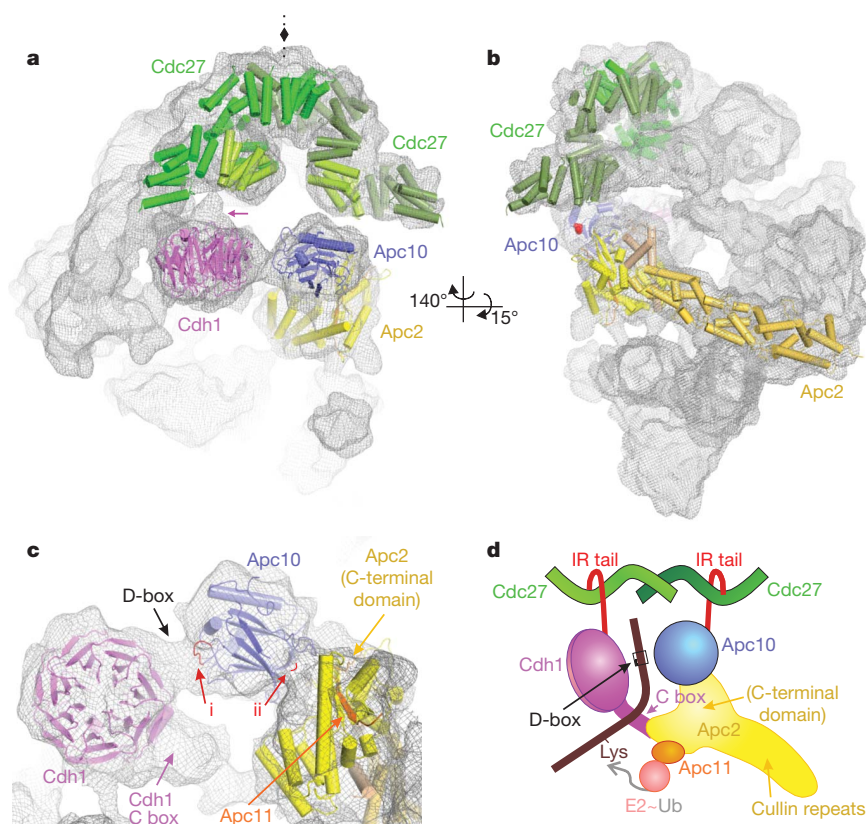


Figure 3 | Cdh1, Apc10, Apc2 and Apc11 form a substrate-recognition catalytic module. **a, b**, Two views of the cryo-EM APC/C^{Cdh1-D-box} complex. Protein density is represented by a mesh with fitted atomic coordinates of the Cdh1 β -propeller (modelled), Apc10 (ref. 22), Apc2–Apc11 (modelled on Cul4a–Rbx1 of SCF) and Cdc27 (ref. 26). Only the N-terminal β strand of Apc11 bound to the Apc2 C-terminal domain is modelled (orange). The two subunits of Cdc27 are shown in light and dark green. The view in **a** shows the two-fold symmetry axis of Cdc27. Density connecting Cdh1 to a TPR superhelix of the Cdc27 dimer is indicated by an arrow. TPR motifs 8 to 10 of Cdc27, implicated in IR-tail recognition²³, are shown in lighter colours. In **b**, the final residue of Apc10 observed in the crystal structure (Ser 256), 25 residues

rationalizes biochemical studies demonstrating that both co-activator and core APC/C subunits^{8,9,11,14–17}, specifically Apc10 (refs 5–7, 23), contribute to D-box-dependent recognition and processive ubiquitylation. The unassigned density bridging Apc10 and Cdh1 in the APC/C^{Cdh1-D-box} complex can be modelled as a D-box peptide, indicating that the binding site for the D-box is shared between the WD40 domain of Cdh1 and the β sandwich of Apc10. Cdh1 and Apc10 therefore generate a D-box co-receptor (Supplementary Fig. 8). Although biochemical data show that the D-box interacts with the conserved surface of the WD40 domain of the co-activator^{11,15}, direct interactions between D-box and Apc10 alone have not been previously demonstrated (unpublished data and ref. 7), possibly owing to the weak affinity of isolated Apc10 for D-box.

We used ¹H-¹⁵N-heteronuclear single quantum coherence (HSQC) NMR, a technique suitable for detecting weak protein–ligand interactions, to investigate potential Apc10–D-box interactions. The ¹H-¹⁵N-HSQC NMR spectrum of *Saccharomyces cerevisiae* Apc10, shown in Fig. 4, has a substantial number of well-dispersed peaks consistent with the Apc10 β -sandwich architecture²². However, the number of visible peaks is approximately half that expected for a 221-residue protein, and the visible peaks have a wide range of intensities. Reduced peak number and intensity variation are characteristic of proteins undergoing exchange between different conformational or oligomeric states. Spectra recorded with a twofold difference in protein concentration showed no change in position or shape of any dispersed peak, indicating that there is no sensitivity to any possible oligomerization equi-

N-terminal to the IR motif, is indicated by red spheres. **c**, Details of the Cdh1 and Apc10 co-receptor for D-box. Both Cdh1 and Apc10 connect to Apc2. The N terminus of Cdh1, including the C box linking the WD40 domain to Apc2, is not modelled. The first red arrow (i) denotes the conserved loop (residues His 239 to Asp 244) of Apc10 implicated in D-box recognition⁷, and the second red arrow (ii) denotes the Lys 162 and Arg 163 of Apc10 responsible for APC/C affinity⁷. Two models for a possible fit of D-box to the density interconnecting Cdh1 and Apc10 are shown in Supplementary Fig. 8. **d**, Schematic of combined catalytic and substrate-recognition module responsible for D-box binding and substrate ubiquitylation. D-box is represented as binding to an interface between Cdh1 and Apc10.

librium. Consequently, the features of the ¹H-¹⁵N-HSQC spectrum are best explained as a result of Apc10 adopting multiple conformations in intermediate to slow exchange (submillisecond to second timescales) in solution. Addition of a stoichiometric excess (~40-fold) of the D-box peptide used to generate the APC/C^{Cdh1-D-box} ternary complex resulted in more than 20 changes in amide peak position or relative intensity (Fig. 4). NMR-based measurement of the translational diffusion coefficient showed that the NMR-observed species is an Apc10 monomer of ~26 kDa. Thus, the changes in specific peaks on addition of peptide demonstrate that the D-box peptide interacts with monomeric Apc10, altering the chemical environment and/or the conformational equilibrium of a subset of its residues. However, the low intensity and proportion of visible amide peaks made sequential assignment and full characterization of the D-box binding site on Apc10 impracticable.

To establish whether the peptide-induced changes of the Apc10 NMR spectrum are specifically D-box dependent, we performed a series of control experiments. First, a different D-box peptide (a 19-residue peptide modelled on *S. cerevisiae* Clb2 whose sequence identity with Cdc13 is confined to the D-box) produced very similar NMR spectral changes to the Cdc13 D-box (Fig. 4). Second, a mutant D-box Cdc13 peptide resulted in only minor changes in the Apc10 NMR spectrum, consistent with greatly reduced binding. Finally, the Hsl1 KEN-box peptide that, from the APC/C^{Cdh1-KEN-box} EM analysis, does not bridge Cdh1 and Apc10, resulted in an essentially identical spectrum to that of the apoprotein, with none of the changes seen for

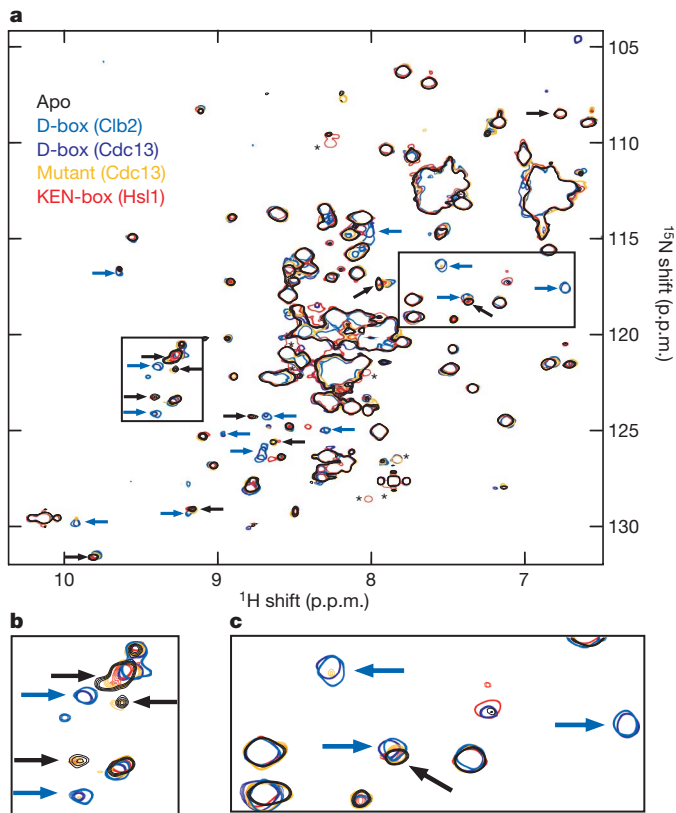


Figure 4 | ^1H - ^{15}N HSQC spectra of Apc10. **a–c**, Overlaid are spectra of the apoprotein and protein in the presence of stoichiometric excess of each of four peptides. The complete amide region (**a**) and, for clarity, expanded views of two boxed sub-regions (**b**, **c**) are shown. Spectra in the presence of either of the two D-box-containing peptides show common changes with respect to the apoprotein spectrum, namely absence of the peaks seen in the apoprotein (black arrows) and new or shifted peaks not seen in the apospectrum (blue arrows). In contrast, spectra in the presence of either the Cdc13-derived peptide in which four residues of the D-box motif are mutated to alanine or a peptide containing a KEN-box motif are very similar to the apospectrum, retaining all of the peaks marked by black arrows. The spectrum with the mutant Cdc13 peptide does in some cases show low-intensity peaks at the positions indicated by blue arrows (see expanded views in **b** and **c**), indicating a very weak residual interaction. These spectra are consistent with a D-box-dependent interaction with Apc10. Peaks arising from natural abundance ^{15}N amides in the unbound peptide that are protected from solvent exchange are indicated by an asterisk.

the two D-box-containing peptides. These NMR data therefore provide strong evidence for a direct interaction between Apc10 and D box, supporting the notion that Apc10 participates in D-box recognition.

To gain further insight into the mechanisms of substrate recognition and ubiquitylation, we modelled atomic structures of Apc2 and Cdc27 into the molecular envelope of the APC/C^{Cdh1-D-box} map. We fitted a homology model of Apc2, based on Cul4a-Rbx1, allowing for small adjustments of the carboxy-terminal domain relative to the cullin repeats (Fig. 3 and Supplementary Figs 7 and 9). Continuous density attaches the globular C-terminal domain to that of the cullin repeats, which are seen as a long stalk-like density that transverses one side of the complex (Fig. 3 and Supplementary Fig. 7). The APC/C^{Cdh1-D-box} cryo-map reveals that Cdh1 and Apc10 are both connected to the Apc2 C-terminal domain (Fig. 3c and Supplementary Fig. 7). Notably, the interaction of the C-terminal domain of Apc2 with substrate adaptor subunits contrasts with the Skp1-cullin-F-box (SCF) complex in which the amino-terminal cullin repeat of Cul1 interacts with substrate adaptors²⁵.

Cdc27 is a dimer and we docked its N-terminal dimerization domain²⁶ into the globular structure at the head of the TPR sub-complex, and independently positioned the modelled C-terminal

TPR superhelices of the Cdc27 subunits into the curved tubular densities extending from the globular domain (Fig. 3a, b and Supplementary Fig. 7), consistent with the mapping of Cdc27 (unpublished data). Although not imposed in the fitting, these docked TPR superhelices are related by the same dyad symmetry as the Cdc27 dimerization domain, therefore preserving the overall two-fold symmetry of Cdc27 (Fig. 3a). The organization of Apc2 and Cdc27 in close proximity to Cdh1 and Apc10 visualized in our APC/C^{Cdh1-D-box} structure unifies previous models of APC/C subunit topologies^{10,12,13,23} (Fig. 3d). Cdh1 is known to interact through its C-terminal Ile-Arg (IR) tail with Cdc27^{10–12}, and in *S. cerevisiae*, Cdh1 also requires Apc2 for optimal binding¹². The structures fitted to the EM map show that with the C terminus of Cdh1 in contact with Cdc27, its N-terminal C box is positioned to contact Apc2 (Fig. 3 and Supplementary Fig. 7)^{12,17}. Pull-down experiments on recombinant human proteins have shown that Apc10 interacts with Cdc27 through its C-terminal region, which also contains an IR motif¹³, whereas in *S. cerevisiae*, Apc10 associates preferentially with a sub-complex of Apc1, Apc2 and Apc11 (ref. 12). Our EM data position Apc10 close to the second Cdc27 subunit. Consequently, the human and yeast biochemical data are explained by the extensive interface between Apc10 and Apc2, and the flexible C-terminal IR tail of Apc10 binding to the Cdc27 TPR superhelix.

This study identifies Cdh1 and Apc10 as a co-receptor for D-box. Individually, co-activator and APC/C possess low affinity and specificity for substrate⁹ and therefore cooperatively enhance substrate affinity through multivalency. Definition of the subunit organization and generation of a pseudo-atomic structure of the APC/C (unpublished data), together with characterization of the D-box co-receptor presented here, provide the conceptual framework for a mechanistic understanding of the APC/C.

METHODS SUMMARY

Generation of APC/C and complexes with Cdh1 and substrates. APC/C and APC/C^{Apc10} were isolated from *S. cerevisiae* and ubiquitylation assays were performed essentially as described⁶. *S. cerevisiae* His₆-Cdh1 was expressed in *Spodoptera frugiperda* (Sf9) cells and purified using nickel-nitrilotriacetic acid (Ni-NTA). APC/C^{Cdh1} was prepared by loading excess Cdh1 onto APC/C immobilized on calmodulin resin, and eluted as for APC/C. APC/C^{Cdh1}-substrate complexes were generated as described in Methods.

EM and image analysis. Purified APC/C (~0.2 mg ml⁻¹) from peak elution fractions was applied to Quantifoil 1.2- or 2-μm aperture grids coated with continuous thin carbon and either negatively stained for EM at room temperature (20 °C) or flash frozen using a Vitrobot for cryo-EM. Images were recorded in an FEI TF20 electron microscope under low-dose conditions using a Tietz F415 CCD camera. Three-dimensional maps were calculated from molecular images using programs from Imagic²⁷, Spider²⁸ and EMAN²⁹.

NMR analysis. ^1H - ^{15}N HSQC spectra were recorded at 25 °C over 5.5 or 11 h for samples of Apc10 alone and in the presence of the four peptide samples using a (^1H , ^{15}N , ^{13}C) triple resonance cryoprobe on a 700 MHz Bruker Avance III spectrometer. Spectra were processed identically and displayed to compensate for concentration and/or recording time differences.

Full Methods and any associated references are available in the online version of the paper at www.nature.com/nature.

Received 30 November 2009; accepted 1 November 2010.

Published online 24 November 2010.

- Peters, J. M. The anaphase promoting complex/cyclosome: a machine designed to destroy. *Nature Rev. Mol. Cell Biol.* **7**, 644–656 (2006).
- Thornton, B. R. & Toczyński, D. P. Precise destruction: an emerging picture of the APC. *Genes Dev.* **20**, 3069–3078 (2006).
- Glotzer, M., Murray, A. W. & Kirschner, M. W. Cyclin is degraded by the ubiquitin pathway. *Nature* **349**, 132–138 (1991).
- Pfleger, C. M. & Kirschner, M. W. The KEN box: an APC recognition signal distinct from the D box targeted by Cdh1. *Genes Dev.* **14**, 655–665 (2000).
- Carroll, C. W. & Morgan, D. O. The Doc1 subunit is a processivity factor for the anaphase-promoting complex. *Nature Cell Biol.* **4**, 880–887 (2002).
- Passmore, L. A. *et al.* Doc1 mediates the activity of the anaphase-promoting complex by contributing to substrate recognition. *EMBO J.* **22**, 786–796 (2003).
- Carroll, C. W., Enquist-Newman, M. & Morgan, D. O. The APC subunit Doc1 promotes recognition of the substrate destruction box. *Curr. Biol.* **15**, 11–18 (2005).

8. Yamano, H., Gannon, J., Mahbubani, H. & Hunt, T. Cell cycle-regulated recognition of the destruction box of cyclin B by the APC/C in *Xenopus* egg extracts. *Mol. Cell* **13**, 137–147 (2004).
9. Eytan, E., Moshe, Y., Braunstein, I. & Herskho, A. Roles of the anaphase-promoting complex/cyclosome and of its activator Cdc20 in functional substrate binding. *Proc. Natl Acad. Sci. USA* **103**, 2081–2086 (2006).
10. Vodermaier, H. C., Gieffers, C., Maurer-Stroh, S., Eisenhaber, F. & Peters, J. M. TPR subunits of the anaphase-promoting complex mediate binding to the activator protein CDH1. *Curr. Biol.* **13**, 1459–1468 (2003).
11. Kraft, C., Vodermaier, H. C., Maurer-Stroh, S., Eisenhaber, F. & Peters, J. M. The WD40 propeller domain of Cdh1 functions as a destruction box receptor for APC/C substrates. *Mol. Cell* **18**, 543–553 (2005).
12. Thornton, B. R. *et al.* An architectural map of the anaphase-promoting complex. *Genes Dev.* **20**, 449–460 (2006).
13. Wendt, K. S. *et al.* Crystal structure of the APC10/DOC1 subunit of the human anaphase-promoting complex. *Nature Struct. Biol.* **8**, 784–788 (2001).
14. Burton, J. L. & Solomon, M. J. D box and KEN box motifs in budding yeast Hsl1p are required for APC-mediated degradation and direct binding to Cdc20p and Cdh1p. *Genes Dev.* **15**, 2381–2395 (2001).
15. Hilioti, Z., Chung, Y. S., Mochizuki, Y., Hardy, C. F. & Cohen-Fix, O. The anaphase inhibitor Pds1 binds to the APC/C-associated protein Cdc20 in a destruction box-dependent manner. *Curr. Biol.* **11**, 1347–1352 (2001).
16. Pfeleger, C. M., Lee, E. & Kirschner, M. W. Substrate recognition by the Cdc20 and Cdh1 components of the anaphase-promoting complex. *Genes Dev.* **15**, 2396–2407 (2001).
17. Schwab, M., Neutzner, M., Mockler, D. & Seufert, W. Yeast Hct1 recognizes the mitotic cyclin Clb2 and other substrates of the ubiquitin ligase APC. *EMBO J.* **20**, 5165–5175 (2001).
18. Passmore, L. A. *et al.* Structural analysis of the anaphase-promoting complex reveals multiple active sites and insights into polyubiquitylation. *Mol. Cell* **20**, 855–866 (2005).
19. Dube, P. *et al.* Localization of the coactivator Cdh1 and the cullin subunit Apc2 in a cryo-electron microscopy model of vertebrate APC/C. *Mol. Cell* **20**, 867–879 (2005).
20. Ohi, M. D. *et al.* Structural organization of the anaphase-promoting complex bound to the mitotic activator Slp1. *Mol. Cell* **28**, 871–885 (2007).
21. Herzog, F. *et al.* Structure of the anaphase-promoting complex/cyclosome interacting with a mitotic checkpoint complex. *Science* **323**, 1477–1481 (2009).
22. Au, S. W., Leng, X., Harper, J. W. & Barford, D. Implications for the ubiquitination reaction of the anaphase-promoting complex from the crystal structure of the Doc1/Apc10 subunit. *J. Mol. Biol.* **316**, 955–968 (2002).
23. Matyskiela, M. E. & Morgan, D. O. Analysis of activator-binding sites on the APC/C supports a cooperative substrate-binding mechanism. *Mol. Cell* **34**, 68–80 (2009).
24. Yamano, H., Tsurumi, C., Gannon, J. & Hunt, T. The role of the destruction box and its neighbouring lysine residues in cyclin B for anaphase ubiquitin-dependent proteolysis in fission yeast: defining the D-box receptor. *EMBO J.* **17**, 5670–5678 (1998).
25. Zheng, N. *et al.* Structure of the Cul1–Rbx1–Skp1–F box^{Skp2} SCF ubiquitin ligase complex. *Nature* **416**, 703–709 (2002).
26. Zhang, Z. *et al.* Molecular structure of the N-terminal domain of the APC/C subunit Cdc27 reveals a homo-dimeric tetratricopeptide repeat architecture. *J. Mol. Biol.* **397**, 1316–1328 (2010).
27. van Heel, M. *et al.* Single-particle electron cryo-microscopy: towards atomic resolution. *Q. Rev. Biophys.* **33**, 307–369 (2000).
28. Frank, J. *et al.* SPIDER and WEB: processing and visualization of images in 3D electron microscopy and related fields. *J. Struct. Biol.* **116**, 190–199 (1996).
29. Ludtke, S. J., Baldwin, P. R. & Chiu, W. EMAN: semiautomated software for high-resolution single-particle reconstructions. *J. Struct. Biol.* **128**, 82–97 (1999).

Supplementary Information is linked to the online version of the paper at www.nature.com/nature.

Acknowledgements This work was funded by a Cancer Research UK grant to D.B. We thank F. Beuron for help with the early stages of this project and for EM support. We are grateful to J. Kirkpatrick for the use of the facilities of the UCL/Birkbeck Institute of Structural Molecular Biology (ISMB) Biomolecular NMR Centre.

Author Contributions All authors contributed to experimental design, data analysis and manuscript preparation. P.C.A.d.F. and E.H.K. collected and analysed EM data, E.H.K. prepared APC/C samples and performed ubiquitylation assays. P.C.A.d.F. determined the three-dimensional EM reconstructions and fitted coordinates. M.A.W. performed NMR experiments and analysed NMR data. E.P.M. helped collect and analyse EM data.

Author Information EM maps have been deposited in the Electron Microscopy Data Bank (EMDB) under accession numbers EMD-1815 (cryo-EM APC/C^{Cdh1-D-box}), EMD-1816 (apo APC/C), EMD-1817 (APC/C^{Cdh1}), EMD-1818 (APC/C^{Cdh1-KEN-box}) and EMD-1819 (APC/C^{Cdh1-Hsl1}). Reprints and permissions information is available at www.nature.com/reprints. The authors declare no competing financial interests. Readers are welcome to comment on the online version of this article at www.nature.com/nature. Correspondence and requests for materials should be addressed to D.B. (david.barford@icr.ac.uk).

METHODS

Generation of APC/C and complexes with Cdh1 and substrates. APC/C and APC/C^{ΔApc10} were isolated from *S. cerevisiae* and ubiquitylation assays were performed as described^{6,30} except that the calmodulin resin elution buffer was 25 mM HEPES (pH 8.0), 150 mM NaCl, 1 mM MgCl₂, 2 mM EGTA, 3 mM tris(2-carboxyethyl)phosphine (TCEP), and 0.03% (v/v) n-dodecyl-β-D-maltoside (DDM). Peak elution fractions were used for EM analysis. *S. cerevisiae* His₆-Cdh1 was expressed in Sf9 cells and purified using Ni-NTA. APC/C^{Cdh1} was prepared by loading excess Cdh1 onto APC/C immobilized on calmodulin resin, thereby ensuring formation of a stoichiometric APC/C^{Cdh1} complex, and eluted as for APC/C. Association of Cdh1 to APC/C was confirmed by SDS-PAGE and western blotting analyses (Supplementary Fig. 2), and by E3 ligase assays showing that APC/C^{Cdh1} ubiquitylated Hsl1 and Clb2 (Supplementary Figs 3 and 4). Hsl1^{667–872} was expressed in BL21(DE3) RIL cells and purified by Ni-NTA and gel-filtration chromatography and added to APC/C^{Cdh1} to a final concentration of 1.5 μM for EM data collection, greatly in excess of the APC/C^{Cdh1} concentration (Supplementary Fig. 3a). Previous work had shown that Hsl1 forms a stable 1:1 complex with APC/C^{Cdh1} at ~0.05 μM (ref. 23). APC/C^{Cdh1} was completely inhibited towards Clb2 (Supplementary Fig. 3b). D-box peptide inhibited APC/C^{Cdh1} ubiquitylation of Clb2 at 0.1 mM (Supplementary Fig. 4a), similar to previous findings^{11,24}. APC/C^{Cdh1-D-box} and APC/C^{Cdh1-AD-box} were prepared by adding peptide to APC/C^{Cdh1} to a final concentration of 0.3 mM. KEN-box peptide inhibited APC/C^{Cdh1} ubiquitylation of Clb2 at 1 mM (Supplementary Fig. 4b) and was therefore used at 10 mM for the APC/C^{Cdh1-KEN-box} structure. Peptides used in the EM structural analysis and ubiquitylation assays were as follows. D-box, NVPKKRHALDDVSNFHNK; AD-box, NVPKKAHAADDVSAFHNK; KEN-box, GVSTNKENEGPEYPTKIK KEHQK (D-box, mutant D-box and KEN-box underlined). D-box and KEN-box peptides were modelled on *S. pombe* Cdc13 and *S. cerevisiae* Hsl1, respectively. Stock solutions were dissolved at 10–20 mM in 100 mM Tris HCl (pH 8.0). For competitions assays, peptides were used at the final stated concentrations.

EM of negative-stained samples. Purified APC/C and its Cdh1 and substrate complexes at ~0.2 mg ml⁻¹ were applied to Quantifoil 2/2 EM grids coated with a second layer of thin carbon. The grids were negatively stained with 2% (w/v) uranyl acetate. The samples were imaged at room temperature (20 °C) in an FEI Tecnai TF20 electron microscope at an accelerating voltage of 200 kV, in low-dose mode with an exposure of ~100 e⁻ Å⁻², a nominal magnification of ×50,000 and an underfocus of ~1.2 μm, giving rise to a first minimum in the contrast transfer function at ~17 Å. Images were recorded using a Tietz F415 (4k × 4k) CCD camera and adjacent boxes of 2 × 2 pixels were averaged, resulting in a calibrated sampling of 3.47 Å pixel⁻¹. The images recorded for all negatively stained samples were consistent with that of APC/C^{Cdh1} shown in Supplementary Fig. 10a, including those of samples of APC/C^{ΔApc10-Cdh1} (Supplementary Fig. 11).

Cryo-EM. Samples of purified APC/C^{Cdh1-D-box} were applied to Quantifoil 1.2/1.3 EM grids coated with a second layer of thin carbon, blotted and plunged into liquid ethane using an FEI Vitrobot. The grids were transferred into a Tecnai TF20 and maintained at approximately -178 °C using a Gatan 626 cryo-holder. Images were recorded in a similar way to that described for negatively stained samples, except that focal pairs were recorded at an underfocus of ~2.5 μm and ~4 μm, using an electron dose of ~20 e⁻ Å⁻² (for each exposure) and a nominal magnification of ×63,000, resulting in a sampling of 2.82 Å pixel⁻¹. The first recorded CCD images of each focal pair (closer to focus) were carefully screened and only those with a power spectrum showing Thon rings extending isotropically beyond 10 Å were selected for further analysis.

Image analysis of negatively stained samples. Image processing was performed using Imagic²⁷, Spider²⁸ and EMAN²⁹ programs. Image processing was initiated with the analysis of the APC/C^{Cdh1} complex. Molecular images were manually selected (Supplementary Fig. 10a) using the EMAN boxer software in order to assemble a data set ultimately formed of 12,529 images. A preliminary evaluation of the resulting data set was carried out by calculating reference-free image-class averages using the refine2d routine from EMAN. Three classes, which were judged to be approximately mutually orthogonal, were selected from the preliminary set for angular assignment using the Imagic C1 start-up procedure. These were used to assign angles, by angular reconstitution, to a further selection of 112 classes, which were subsequently back-projected in order to create an *ab initio* three-dimensional map. This map was used as the first reference for refinement using a combination of Imagic and Spider software. The refinement consisted of multiple rounds of multi-reference alignment, classification, angular assignment (to selected image-class averages) by projection matching and three-dimensional reconstruction by back-projection. In the last round of refinement a total of 4,000 class averages were calculated, of which 1,433 were selected to calculate the final three-dimensional map. Examples of class averages used in the reconstruction and their respective reprojections are shown in Supplementary Fig. 10b. The angular distribution of the classes used in the final reconstruction is shown in

Supplementary Fig. 10c. The resolution of the final map of APC/C^{Cdh1} was estimated by Fourier shell correlation as 18–20 Å, depending on the resolution criteria (Supplementary Fig. 10d). Negatively stained APC/C^{ΔApc10-Cdh1} appear indistinguishable from APC/C^{Cdh1} (Supplementary Fig. 11).

The final map calculated for APC/C^{Cdh1} was used as a starting reference for the analysis of all other negatively stained APC/C complexes, followed by the same refinement procedures. The total number of molecular images used in the image analysis of each sample is summarized in Supplementary Table 1. Representations of the maps were generated using PyMOL (<http://www.pymol.org>).

Image analysis of data from cryo-EM. The contrast transfer function (CTF) was measured for each CCD image selected for analysis and corrected by phase reversal. A data set of 9,474 molecular images of the APC/C^{Cdh1-D-box} complex was assembled manually using the EMAN boxer software, from the first recorded CCD image of each focal pair (closer to focus, Supplementary Fig. 12a), using the higher contrast second image as an aid for the selection. The subsequent analysis was performed using Imagic and Spider software. The map of the APC/C^{Cdh1-D-box} complex determined by the analysis of negatively stained samples was used as a starting reference for the analysis. The molecular images were aligned and their angular assignment performed by projection matching against the initial reference map. A first three-dimensional reconstruction was calculated by back-projection and this was further refined by multiple rounds of alignment, angular assignment by projection matching and back-projection. The angular distribution of the images for the calculation of the final map is shown in Supplementary Fig. 12b. The resolution of the final map, estimated by Fourier shell correlation, is 9–10 Å, depending on the resolution criteria (Supplementary Fig. 12c). For the representation of the final reconstruction a reverse B factor of -300 was applied, in order to optimize the agreement between the resulting reconstruction and the fitted coordinates, followed by a Fourier low-pass filtration to 9.5 Å. PyMOL (<http://www.pymol.org>) was used to generate the representations of the map.

Fitting atomic coordinates to cryo-EM map of APC/C^{Cdh1-D-box}. Apc10 is based on *S. cerevisiae* Apc10/Doc1 (PDB code 1GQP)²², the N-terminal dimerization domain of Cdc27 is based on *E. coli* Cdc27 (PDB code 3KAE)²⁶ and the C-terminal TPR superhelix is based on the model in ref. 26 (overall sequence identity of 16%). *S. cerevisiae* Cdh1 and Apc2 were modelled using the PHYRE server³¹ based on coordinates (PDB codes 2GNQ (WDR5)³² and 2HYE (Cul4a-Rbx1)³³, respectively, with overall sequence identities of 17% and 11%).

Atomic coordinates of Apc10 (PDB code 1GQP) and the N-terminal homodimerization domain of Cdc27 (PDB code 3KAE) and the molecular models of Cdh1, Apc2 (cullin domain and cullin repeats independently) and two copies of the model of the C-terminal TPR repeats of Cdc27 were docked into the cryo-EM map of the APC/C^{Cdh1-D-box} complex using URO software³⁴ (correlation coefficient of 0.82). The fitted coordinates were converted to densities, Fourier low-pass filtered to 9.5 Å and rendered to yield a volume corresponding to their calculated molecular mass of 243 kDa, assuming a protein density of 0.844 Da Å⁻³. The filtered coordinates were used to guide the rendering of the APC/C^{Cdh1-D-box} map, resulting in a volume corresponding to ~1.13 MDa. Furthermore, the comparison of the level of detail shown by the docked coordinates and that in our three-dimensional map of APC/C^{Cdh1-D-box} determined from cryo-EM data, is supportive of a resolution estimate of ~10 Å (Supplementary Fig. 7).

The protocol by which the *ab initio* APC/C^{Cdh1} map was calculated, which was the initial reference for the analysis of all complexes presented here, results in three-dimensional maps with ambiguity with respect to their hand. However, the hand of the APC/C complex as presented here has been previously determined by random conical tilt methods^{19,21}. In the present work the hand shown is supported by the agreement between the docked coordinates and their respective densities.

NMR analysis. Uniformly ¹⁵N-labelled Apc10 was purified from *E. coli* grown in a defined minimal medium supplemented with ¹⁵N-ammonium sulphate using constructs and protocols previously described²². Peptides (Supplementary Table 2) were dissolved in 100 mM Tris/MOPS to the lower limit of either their maximum solubility or a 100 mM concentration, and their pH was adjusted to ~8 with NaOH. Peptide was added to protein stock to a final concentration of 5 mM. Protein solubility and propensity to aggregation determined the optimal solution conditions for NMR data collection. All NMR samples were in 90% H₂O:10% D₂O, 77–85 mM NaCl, 4.5 mM DTT, 90 mM Tris/MOPS buffer pH 8.0. For the spectra shown, with the exception of the Clb2 sample, final protein concentration was 130–160 μM. Addition of the Clb2 D-box-containing peptide caused substantial precipitation of the protein (also seen to a lesser degree with the Cdc13 D-box peptide), leading to a final protein concentration in this sample of 64 μM. The pH of final protein-peptide mixtures was confirmed by NMR chemical shift of Tris methylene peaks³⁵ to be 8.0 ± 0.1. The Hsl1 KEN-box peptide used for NMR studies inhibited APC/C^{Cdh1}-catalysed ubiquitylation of Clb2 at a concentration of 2 mM (data not shown).

¹H-¹⁵N HSQC spectra of 1,024 × 128 complex points were recorded for each sample using a (¹H, ¹⁵N, ¹³C) triple resonance cryoprobe on a 700 MHz Bruker

Avance III spectrometer with identical spectral widths. Data were recorded at 25 °C for 5.5 or 11 h. The same spectral processing was applied to each spectrum (Gaussian apodization in ^1H and sine-bell apodization in ^{15}N dimensions and zero filling to $2,048 \times 512$ points before Fourier transformation and polynomial baseline correction) using NMRPipe³⁶. Spectra were overlaid in CCPNmr Analysis³⁷ and contour levels matched for concentration and recording time differences using the intense peaks common to all five spectra.

The field-gradient dependence of the signal intensity of the central region of the ^{15}N -edited spectrum (containing the strongest signals) of the APC10 with the Cdc13 D-box peptide was used to measure the extent of translational diffusion during a fixed time interval³⁸. The data fit a model corresponding to a single species of molecular mass ~ 26 kDa, that is, that of the monomer, with no indication of a significant NMR-observable population of dimer or higher-order oligomers.

30. Passmore, L. A., Barford, D. & Harper, J. W. Purification and assay of the budding yeast anaphase-promoting complex. *Methods Enzymol.* **398**, 195–219 (2005).

31. Kelley, L. A. & Sternberg, M. J. Protein structure prediction on the web: a case study using the Phyre server. *Nature Protocols* **4**, 363–371 (2009).
32. Schuetz, A. *et al.* Structural basis for molecular recognition and presentation of histone H3 by WDR5. *EMBO J.* **25**, 4245–4252 (2006).
33. Angers, S. *et al.* Molecular architecture and assembly of the DDB1–CUL4A ubiquitin ligase machinery. *Nature* **443**, 590–593 (2006).
34. Navaza, J., Lepault, J., Rey, F. A., Alvarez-Rua, C. & Borge, J. On the fitting of model electron densities into EM reconstructions: a reciprocal-space formulation. *Acta Crystallogr. D Biol. Crystallogr.* **58**, 1820–1825 (2002).
35. Baryshnikova, O. K., Williams, T. C. & Sykes, B. D. Internal pH indicators for biomolecular NMR. *J. Biomol. NMR* **41**, 5–7 (2008).
36. Delaglio, F. *et al.* NMRPipe: a multidimensional spectral processing system based on UNIX pipes. *J. Biomol. NMR* **6**, 277–293 (1995).
37. Vranken, W. F. *et al.* The CCPN data model for NMR spectroscopy: development of a software pipeline. *Proteins* **59**, 687–696 (2005).
38. Wu, D., Chen, A. & Johnson, C. S. Jr. An improved diffusion-ordered spectroscopy experiment incorporating bipolar-gradient pulses. *J. Magn. Reson. A* **115**, 260–264 (1995).

Melanomas acquire resistance to B-RAF(V600E) inhibition by RTK or N-RAS upregulation

Ramin Nazarian^{1,2*}, Hubing Shi^{1,2*}, Qi Wang^{1,2}, Xiangju Kong^{1,2}, Richard C. Koya^{2,3}, Hane Lee^{2,4}, Zugen Chen^{2,4}, Mi-Kyung Lee^{1,2}, Narsis Attar^{2,5}, Hooman Sazegar^{2,5}, Thinnie Chodon^{2,5}, Stanley F. Nelson^{2,4,6}, Grant McArthur⁷, Jeffrey A. Sosman⁸, Antoni Ribas^{2,3,5} & Roger S. Lo^{1,2}

Activating B-RAF(V600E) (also known as BRAF) kinase mutations occur in ~7% of human malignancies and ~60% of melanomas¹. Early clinical experience with a novel class I RAF-selective inhibitor, PLX4032, demonstrated an unprecedented 80% anti-tumour response rate among patients with B-RAF(V600E)-positive melanomas, but acquired drug resistance frequently develops after initial responses². Hypotheses for mechanisms of acquired resistance to B-RAF inhibition include secondary mutations in *B-RAF(V600E)*, MAPK reactivation, and activation of alternative survival pathways^{3–5}. Here we show that acquired resistance to PLX4032 develops by mutually exclusive PDGFR β (also known as PDGFRB) upregulation or *N-RAS* (also known as *NRAS*) mutations but not through secondary mutations in *B-RAF(V600E)*. We used PLX4032-resistant sub-lines artificially derived from *B-RAF(V600E)*-positive melanoma cell lines and validated key findings in PLX4032-resistant tumours and tumour-matched, short-term cultures from clinical trial patients. Induction of PDGFR β RNA, protein and tyrosine phosphorylation emerged as a dominant feature of acquired PLX4032 resistance in a subset of melanoma sub-lines, patient-derived biopsies and short-term cultures. PDGFR β -upregulated tumour cells have low activated RAS levels and, when treated with PLX4032, do not reactivate the MAPK pathway significantly. In another subset, high levels of activated N-RAS resulting from mutations lead to significant MAPK pathway reactivation upon PLX4032 treatment. Knockdown of *PDGFR β* or *N-RAS* reduced growth of the respective PLX4032-resistant subsets. Overexpression of PDGFR β or N-RAS(Q61K) conferred PLX4032 resistance to PLX4032-sensitive parental cell lines. Importantly, MAPK reactivation predicts MEK inhibitor sensitivity. Thus, melanomas escape B-RAF(V600E) targeting not through secondary B-RAF(V600E) mutations but via receptor tyrosine kinase (RTK)-mediated activation of alternative survival pathway(s) or activated RAS-mediated reactivation of the MAPK pathway, suggesting additional therapeutic strategies.

We selected three *B-RAF(V600E)*-positive parental (P) cell lines, M229, M238 and M249, exquisitely sensitive to PLX4032-mediated growth inhibition *in vitro* and *in vivo*⁶, and derived PLX4032-resistant (R) sub-lines by chronic PLX4032 exposure. In cell survival assays, M229 R, M238 R and M249 R sub-lines displayed strong resistance to PLX4032 (GI₅₀, the concentration of drug that inhibits growth of cells by 50%, not reached up to 10 μ M) and paradoxically enhanced growth at low PLX4032 concentrations, in contrast to parental cells (Supplementary Fig. 1a). Morphologically, both M229 R and M238 R sub-lines appear flatter and more fibroblast-like compared to their parental counterparts, but this morphologic switch was not seen in the M249 P versus M249 R4 pair (Supplementary Fig. 2a).

There were no secondary mutations in the drug target *B-RAF(V600E)* observed on bi-directional Sanger sequencing of all 18 *B-RAF* exons in 15 M229 R (R1–R15), two M238 R (R1 and R2), and one M249 R (R4) acquired resistant sub-lines (Supplementary Table 1 and Supplementary Fig. 3a, left column). Based on Sanger sequencing, this lack of secondary *B-RAF(V600E)* mutation along with retention of the original *B-RAF(V600E)* mutation was confirmed in 16/16 melanoma tumour biopsies (from 12 patients) with clinically acquired resistance to PLX4032 (that is, initial >30% tumour size decrease or partial response, as defined by RECIST (response evaluation criteria in solid tumours) and subsequent progression on PLX4032 dosing; see examples in Supplementary Fig. 4) and 5/5 short-term melanoma cultures established from 5 resistant tumours obtained from 4 patients (Supplementary Table 2). Given recent reports of B-RAF-selective inhibitors having a growth-promoting effect on *B-RAF* wild-type tumour cells^{7–9}, retention of the original *B-RAF* alleles in PLX4032-resistant sub-lines, tissues and cultures indicates that PLX4032 chronic treatment did not select for the outgrowth of a pre-existing, minor *B-RAF* wild-type sub-population. Furthermore, immunoprecipitated B-RAF kinase activities from resistant sub-lines and short-term cultures were similarly sensitive to PLX4032 as B-RAF kinase activities immunoprecipitated from parental cell lines (Supplementary Fig. 3b; Pt48 R and Pt55 R resistance to PLX4032 (ref. 10) and the pre-clinical analogue PLX4720 (ref. 11) shown in Supplementary Fig. 5a and b, respectively; Pt, patient). These results demonstrate that, in all tested acquired resistant cell lines and cultures, the mutated B-RAF(V600E) kinase lacks secondary mutations and hence retains its ability to respond to PLX4032.

Given that minority PLX4032-resistant sub-populations in tissues may acquire B-RAF(V600E) secondary mutations not detectable by Sanger sequencing, we analysed “ultra-deep” (Supplementary Fig. 6) and deep (Supplementary Fig. 7) sequences of *B-RAF* (exons 2–18) using the Illumina platform for 9/11 acquired resistant tumour samples without tumour-matched short-term cultures (one sample, Pt111-010 DP2, intentionally analysed by both methods; DP, disease progression). Ultradeep *B-RAF* sequencing of five PLX4032-resistant melanoma tissues resulted in every base of exons 2–18 being sequenced at a median coverage of 127 \times (27 \times –128 \times) (Supplementary Fig. 6a and b). The known variant, V600E, was detected in all five samples with significantly high non-reference allele frequencies (NAF) (Supplementary Fig. 6c). In all five tissues, exon 13, where the T529 gatekeeper residue¹² is located, was independently amplified and uniquely bar-coded twice. Rare variants (none at the T529 codon; Supplementary Fig. 6d) detected in these independent exon 13 analyses do not overlap and helped define the true, signal NAF at >4.81% (Supplementary

¹Division of Dermatology/Department of Medicine, UCLA's Jonsson Comprehensive Cancer Center, 52-121 CHS, Los Angeles, California 90095-1750, USA. ²David Geffen School of Medicine, University of California, Los Angeles, California 90095-1750, USA. ³Division of Surgical Oncology/Department of Surgery, UCLA's Jonsson Comprehensive Cancer Center, 54-140 CHS, Los Angeles, California 90095-1782, USA. ⁴Department of Human Genetics, UCLA's Jonsson Comprehensive Cancer Center, 5506A Gonda Center, Los Angeles, California 90095-7088, USA. ⁵Division of Hematology & Oncology/Department of Medicine, UCLA's Jonsson Comprehensive Cancer Center, 9-954 Factor Building, Los Angeles, California 90095-1678, USA. ⁶Department of Pediatrics, UCLA's Jonsson Comprehensive Cancer Center, 5506A Gonda Center, Los Angeles, California 90095-7088, USA. ⁷Peter MacCallum Cancer Center, St Andrews Place, East Melbourne 3002, Australia. ⁸Department of Medicine, Vanderbilt-Ingram Cancer Center, 777 Preston Research Building, Nashville, Tennessee 37232-6838, USA.

*These authors contributed equally to this work.

Methods). Furthermore, deep *B-RAF* (exons 2–18) sequence analysis of PLX4032-resistant melanoma tissues from a whole exome sequencing project resulted in 2,396 base pairs of *B-RAF* coding regions having coverage $\geq 10\times$ (average coverage per exon in each tissue shown in Supplementary Fig. 7a). After filtering, no position harboured a variant with a NAF $>4.81\%$, except for the known V600E mutation in all five resistant samples. Together, these data strongly corroborate the lack of *B-RAF*(V600E) secondary mutations during the evolution of PLX4032 acquired resistance in the majority of patients and their tumours.

To begin to understand PLX4032-resistance *in vitro*, we used phospho-specific antibodies to probe the activation status of the RAF downstream effectors, MEK1/2 and ERK1/2 (also known as MAP2K1/2 and MAPK3/1, respectively), in parental versus resistant sub-lines, with and without PLX4032 (Fig. 1a). As expected, PLX4032 induced dose-dependent decreases in p-MEK1/2 and p-ERK1/2 in all parental cells. However, the pattern of MEK-ERK sensitivity to PLX4032 varied among resistant sub-lines, suggesting distinct mechanisms. In contrast to M249 R4, which showed strong resistance to PLX4032-induced MEK/ERK inhibition (suggesting MAPK reactivation), M229 R5 and M238 R1 were both similarly sensitive to PLX4032-induced decreases in the levels of p-MEK1/2 and p-ERK1/2. Gene expression profiling (Fig. 1b) further supported distinct PLX4032 acquired resistant mechanisms represented by M229 R5/M238 R1 versus M249 R4. We first used the gene expression alterations responsive to PLX4032 in parental cells to define a *B-RAF*(V600E)-responsive gene signature, which is similar to gene sets defined by a MEK1 inhibitor (PD325901)¹³ and by PLX4720 (ref. 14; Supplementary Fig. 8). Concordant with the western blot results (Fig. 1a), M249 R4 demonstrated striking resistance to PLX4032 treatment with a gene signature of persistent MEK-ERK activation, whereas both M229 R5 and M238 R1 retained a PLX4032-sensitive gene signature (Fig. 1b). These data confirm that M229 R5 and M238 R1 share key characteristics of resistance, which are in line with unsupervised clustering of these two resistant sub-lines in genome-wide, differential expression patterns (Supplementary Fig. 9).

Gene set enrichment analysis demonstrated an enrichment of RTK-controlled signalling in M229 R5 and M238 R1 but exclusive of M249 R4 (Supplementary Table 3). Unsupervised clustering of the receptor tyrosine kinase gene expression profiles showed that M229 R5 and M238 R1 clustered away from M229 and M238 parental cell lines largely based on higher expression levels of *KIT*, *MET*, *EGFR* and *PDGFR β* (Supplementary Fig. 10a, yellow highlight). RNA upregulation of these four RTKs was consistently not associated with genomic DNA (gDNA) copy number gain (Supplementary Fig. 10b). Of these four candidate RTKs, EGFR and PDGFR β protein levels were overexpressed (Fig. 2a, left; Fig. 3b; Supplementary Fig. 10c), but only PDGFR β displayed elevated activation-associated tyrosine phosphorylation in a phospho-RTK array (Fig. 2a, right). PDGFR β RNA upregulation was a common feature among additional M229 R and M238 R sub-lines (Supplementary Fig. 11a) but could not be observed in any of ten randomly selected parental melanoma cell lines (Supplementary Fig. 11b). Interestingly, tyrosine phosphorylation of PDGFR β correlated with an upregulation of a gene signature unique to PDGFR β (ref. 15; Supplementary Fig. 12) but is not due to mutational activation, as PDGFR β cDNAs derived from M229 R5, M238 R1 and Pt48 R are wild type (Supplementary Table 1).

We then validated our *in vitro* finding *in vivo* by studying clinical trial patient-derived samples (Supplementary Table 2; Fig. 2b) and tumour-matched short-term cultures (Fig. 2c and d). In 4/11 available, paired biopsy specimens, the resistant tumours showed a tumour-associated overexpression of PDGFR β compared to the baseline tumour in the same patients (Fig. 2b; Supplementary Table 2 and Supplementary Fig. 13). PDGFR β -positive areas of tissue sections were consistently strongly positive for S100 or MART1 (melanoma markers; MART1 is also known as MLANA) but lacked CD31 (an endothelial, platelet, macrophage marker, also known as PECAM1) staining (data not shown). We were able to validate this finding further in an available short-term culture (Pt48 R) derived from a PLX4032-resistant, PDGFR β -positive tumour. Pt48 R was established from an intracardiac mass progressing 6 months after initiating treatment with PLX4032.

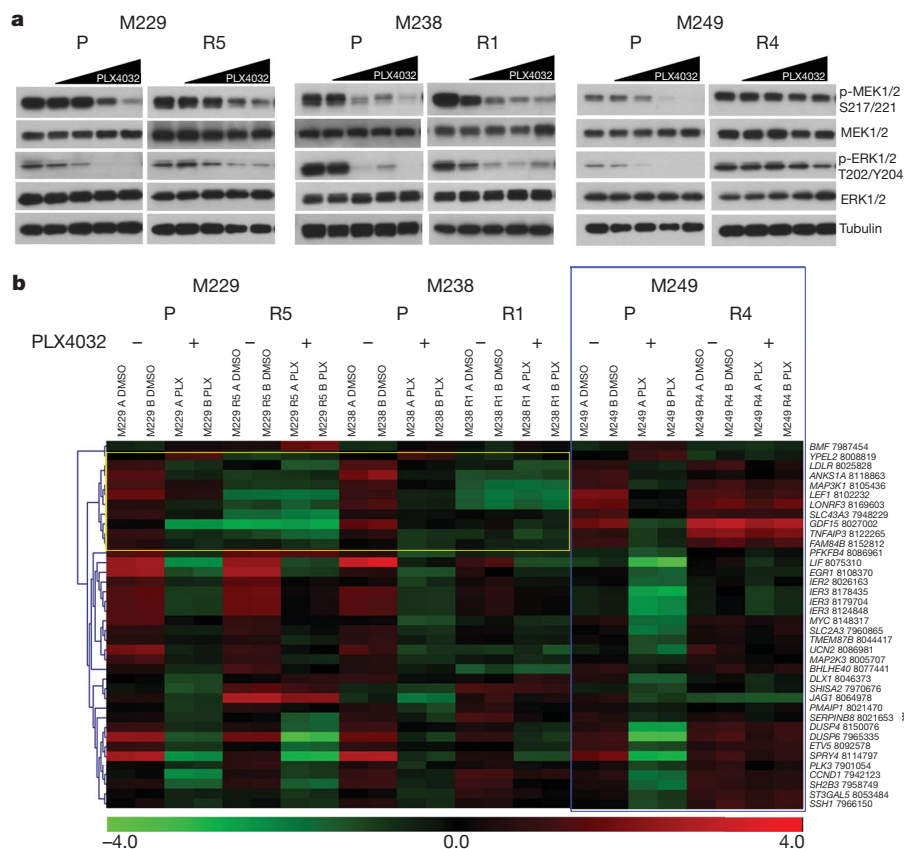
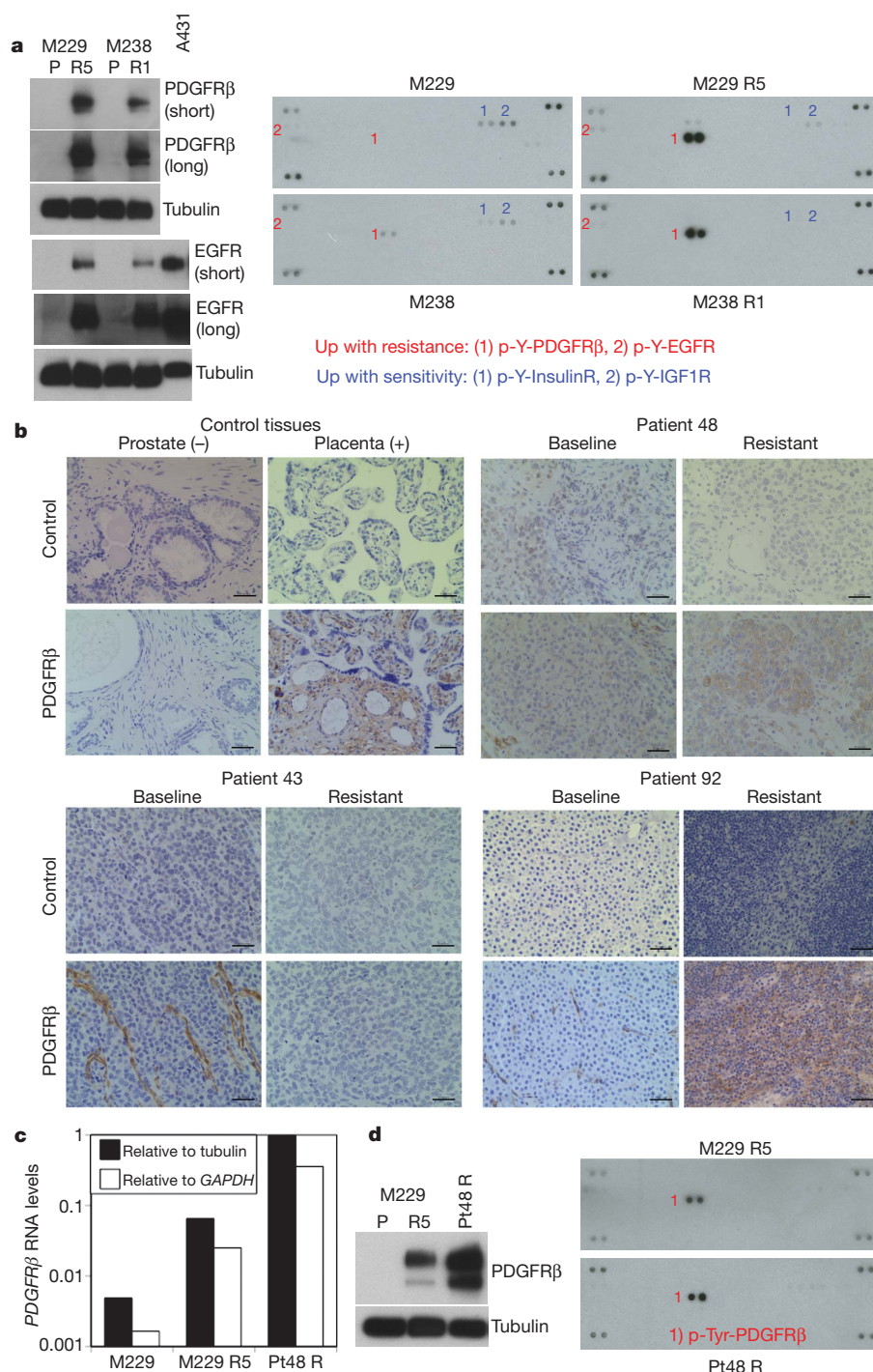


Figure 1 | *In vitro* models of PLX4032 acquired resistance display differential MAPK reactivation. **a**, Parental and PLX4032-resistant sub-lines were treated with increasing PLX4032 concentration (0, 0.01, 0.1, 1 and 10 μ M), and the effects on MAPK signalling were determined by immunoblotting for p-MEK1/2 and p-ERK1/2 levels. Total MEK1/2, ERK1/2 and tubulin levels, loading controls. **b**, Heat map for B-RAF(V600E) signature genes in each of the cell lines treated with DMSO or PLX4032. Colour scale, log₂-transformed expression (red, high; green, low) for each gene (row) normalized by the mean of all samples. Blue box showing M249 R4 MAPK reactivation. Yellow box showing diminished, baseline expression of B-RAF(V600E) signature genes in M229 and M238 resistant sub-lines (FDR < 0.05). The probeset number is shown after each gene.

Figure 2 | PDGFR β upregulation is strongly correlated with PLX4032 acquired resistance.

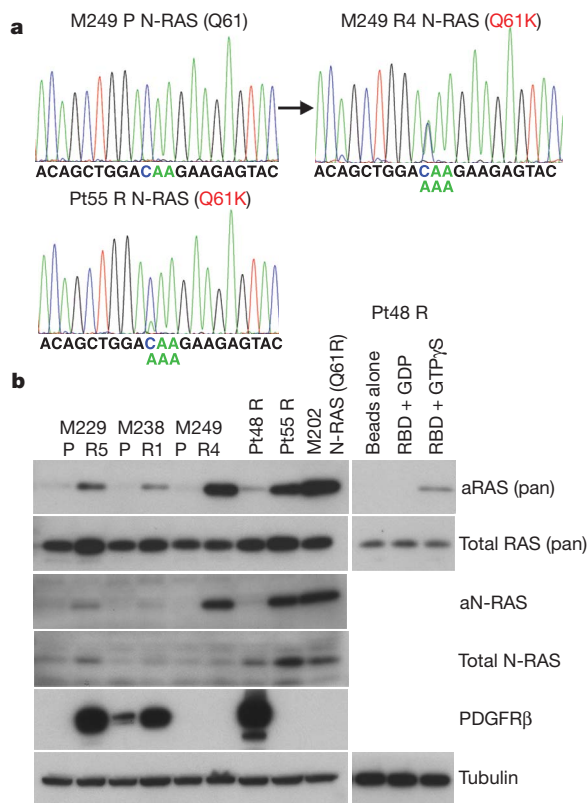
a, Left, total levels of PDGFR β and EGFR. A431, an EGFR-amplified cell line. Tubulin levels, loading control. Right, whole-cell extracts were incubated on the RTK antibody arrays, and phosphorylation status was determined by subsequent incubation with anti-phosphotyrosine horseradish peroxidase (each RTK spotted in duplicate, positive controls in corners, gene identity below). **b**, Anti-PDGFR β immunohistochemistry of formalin-fixed, paraffin-embedded tissues. Prostate, negative control; placenta, positive control. Black bar, 50 μ m. **c**, Relative RNA levels of PDGFR β in M229 P/R5 and Pt48 R as determined by real-time, quantitative PCR (average of duplicates). **d**, Total PDGFR β (left) and p-RTK (right) levels in Pt48 R versus M229 R5.



The Pt48 R short-term culture demonstrated clear overexpression of PDGFR β RNA (Fig. 2c), protein and p-Tyr levels (Fig. 2d).

In M249 R4, we sequenced all exons of *N-RAS*, *K-RAS* (also known as *KRAS*) or *H-RAS* (also known as *HRAS*) (to include codons 12, 13, and 61 as well as mutational hotspots of emerging significance¹⁶) and *MEK1* (ref. 17; Supplementary Table 1 and data not shown) because we proposed a resistance mechanism reactivating MAPK despite not having a secondary *B-RAF* mutation. Interestingly, M249 R4 harbours a *N-RAS*(Q61K) activating mutation not present in the parental M249 cell line (Fig. 3a). We found *N-RAS* mutations in 2/16 acquired resistant biopsy samples (note that both came from Pt55; Supplementary Table 2 and Supplementary Fig. 14). A *N-RAS*(Q61K) mutated sample, Pt55 DP1 (for disease progression 1) was obtained from a biopsy taken from an isolated, nodal metastasis that partially regressed on PLX4032 but increased in size 10 months after starting on therapy with PLX4032

(Supplementary Fig. 4a). This patient continued on therapy with PLX4032 until 6 months later, when several other nodal metastases developed (Supplementary Fig. 14a, b). Analysis of a biopsy taken at a second progression site (Pt55 DP2) demonstrated a different mutation in *N-RAS*, *N-RAS*(Q61R) (Supplementary Fig. 14b). Both Pt55 DP1 and DP2 tissue *N-RAS* mutations were confirmed in their respective short-term cultures, Pt55 R and Pt55 R2 (Fig. 3a and Supplementary Fig. 14b). Also, both DP1 and DP2 (and their respective cultures) harboured increased *N-RAS* gDNA copy numbers (Supplementary Fig. 14c and d). Both Pt55 R and Pt55 R2 also showed increased *N-RAS* RNA (Supplementary Fig. 14e) and protein levels (Fig. 3b). In addition, *N-RAS*(Q61K) mutation in M249 R4 and Pt55 R correlated with a marked increase in activated *N-RAS* levels (Fig. 3b). Of note, the *N-RAS* mutations were mutually exclusive with PDGFR β overexpression in all samples (Supplementary Table 2).



Knockdown of *PDGFRβ* or *N-RAS* using small interfering RNA (siRNA) pools preferentially growth-inhibited melanoma cells with upregulated *PDGFRβ* or *N-RAS*, respectively (Supplementary Fig. 15a, b and Supplementary Table 4). We then selected two resistant sub-lines

Figure 3 | N-RAS upregulation correlates with a distinct subset of PLX4032 acquired resistance. **a**, Detection of a *N-RAS*(Q61K) allele in M249 R4 and Pt55 R. **b**, The levels of activated RAS (aRAS) and N-RAS (aN-RAS) eluted after pull-down using the RAS-binding domain (RBD) of RAF-1. The total levels of RAS, N-RAS, *PDGFRβ* and tubulin (loading control) from the whole-cell lysates are shown by immunoblotting. Effects of GDP and GTPγS pre-incubation on RBD pull-down and beads without RBD pull-down from Pt48 R lysates are shown as controls.

or cultures to test the effects of individual *PDGFRβ* and *N-RAS* short hairpin RNAs (shRNAs; Fig. 4a and b, respectively). Stable knockdown of *PDGFRβ* caused an admixture of G0/G1 cell cycle arrest (in a MEK inhibitor-dependent manner due to compensatory signalling; Supplementary Fig. 16a and data not shown) and apoptosis in M229 R5 and a G0/G1 cell cycle arrest in M238 R1. This effect was specific, as stable *PDGFRβ* knockdown in M249 R4 and Pt55 R did not result in G0/G1 cell cycle arrest (Supplementary Fig. 17a). In contrast, stable *N-RAS* knockdown resulted in a predominantly apoptotic response in M249 R4 and Pt55 R (Fig. 4b) but not in M229 R5, M238 R1 or Pt48 R (Supplementary Fig. 17b). Moreover, stable *N-RAS* knockdown markedly conferred PLX4032 sensitivity to M249 R4 and Pt55 R but had no effect on M229 R5 PLX4032 resistance (Supplementary Fig. 18a). Flag-*N-RAS*(Q61K) stable overexpression conferred PLX4032 resistance in the M249 parental cell line (Supplementary Fig. 18b), whereas stable *PDGFRβ*-MYC overexpression conferred reduced PLX4032 sensitivity in both M229 and M238 parental cell lines (Supplementary Fig. 19).

We then asked whether *N-RAS*-dependent growth and reactivation of the MAPK pathway (Fig. 1a and Supplementary Fig. 20) would selectively sensitize M249 R4 and Pt55 R to MEK inhibition. Indeed, whereas the growth of M229 R5, M238 R1 and Pt48 R was uniformly highly resistant to the MEK inhibitor AZD6244 (and U0126, Supplementary Fig. 21), the growth of M249 R4 and Pt55 R was sensitive to MEK inhibition in the presence of PLX4032 (Fig. 4c) or absence of PLX4032 (Supplementary Fig. 22). It is known that activated *N-RAS* in melanoma cells uses C-RAF (also known as RAF1) over B-RAF to

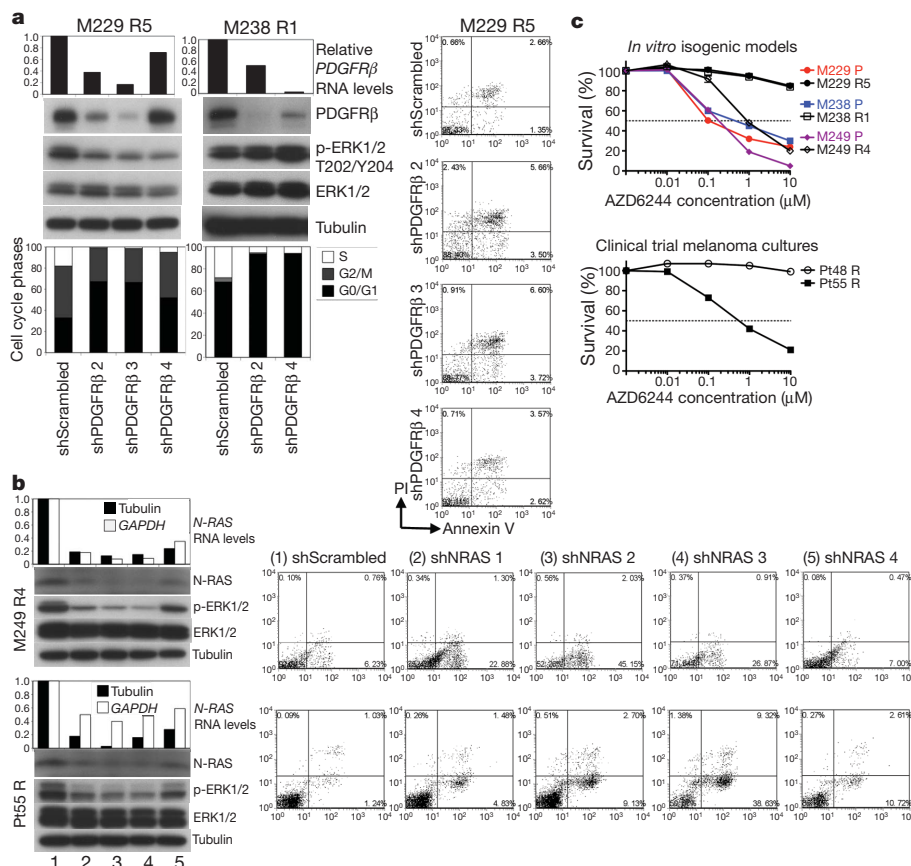


Figure 4 | *PDGFRβ*- and *N-RAS*-mediated growth and survival pathways differentially predict MEK inhibitor sensitivity.

a, Transduction of *PDGFRβ* shRNAs in M229 R5 and M238 R1 (1 μM PLX4032), RNA (relative to *GAPDH*) and protein knockdown, effects on p-ERK levels, cell cycle distribution, and apoptosis (when applicable). M229 R5 was also treated with 0.5 μM AZD6244. PI, propidium iodide. **b**, Transduction of *N-RAS* shRNAs in M249 R4 and Pt55 R (1 μM PLX4032), RNA and protein knockdown, effects on p-ERK levels and apoptosis. **c**, Survival curves for isogenic cell line pairs and melanoma cultures treated with the indicated AZD6244 concentration for 72 h (relative to DMSO-treated controls; mean ± s.e.m., *n* = 5). PLX4032-resistant cells were grown with PLX4032. Dashed line, 50% cell killing.

signal to MEK-ERK¹⁸. Thus, N-RAS activation would be capable of bypassing PLX4032-inhibited B-RAF, reactivating the MAPK pathway. It is worth noting that PDGFR β -upregulated, PLX4032-resistant melanoma sub-lines (M229 R5 and M238 R1) and culture (Pt48 R) are resistant not only to AZD6244 but also to imatinib, which is at least partially due to rebound, compensatory survival signalling (Supplementary Fig. 23 and unpublished observations, H.S. and R.S.L.).

We propose (Supplementary Fig. 1b) that *B-RAF(V600E)*-positive melanomas, instead of accumulating *B-RAF(V600E)* secondary mutations, can acquire PLX4032 resistance by (1) activating an RTK (PDGFR β)-dependent survival pathway in addition to MAPK, or (2) reactivating the MAPK pathway via N-RAS upregulation. These two mechanisms account for acquired PLX4032 resistance in 5/12 patients in our study cohort, and additional mechanisms await future discovery. Some patients who relapse on PLX4032 are already being enrolled in a phase II MEK inhibitor trial (ClinicalTrials.gov identifier NCT01037127) based on the assumption of MAPK reactivation. Our findings directly imply a strategy to stratify patients who relapse on PLX4032 and should prompt a search for rational combinations of targeting agents most optimal for distinct mechanisms of acquired resistance to PLX4032 as well as other B-RAF inhibitors (for example, GSK2118436) in clinical development.

METHODS SUMMARY

Cell culture, infections and compounds. Cells were maintained in Dulbecco's modified Eagle medium (DMEM) with 10 or 20% fetal bovine serum and glutamine. shRNAs were sub-cloned into the lentiviral vector pLL3.7 and infections carried out with protamine sulphate. Stocks of PLX4032 (Plexxikon) and AZD6244 (commercially available) were made in DMSO. Cells were quantified using CellTiter-GLO Luminescence (Promega).

Protein detection. Western blots were probed with antibodies against p-MEK1/2 (S217/221), MEK1/2, p-ERK1/2 (T202/Y204), ERK1/2, PDGFR β , and EGFR (Cell Signaling Technologies), and N-RAS (Santa Cruz Biotechnology), pan-RAS (Thermo Scientific) and tubulin (Sigma). p-RTK arrays were performed according to the manufacturer's recommendations (Human Phospho-RTK Array Kit, R&D Systems). For PDGFR β immunohistochemistry, paraffin-embedded formalin-fixed tissue sections were antigen-retrieved, incubated with a PDGFR β antibody followed by horseradish peroxidase-conjugated secondary antibody (Envision System, DakoCytomation). Immunocomplexes were visualized using the DAB (3,3'-diaminobenzidine) peroxidase method and nuclei haematoxylin-counterstained. For activated RAS pull-down, lysates were incubated with beads coupled to glutathione-S-transferase (GST)-RAF-1-RAS-binding domain of RAF1 (RBD) (Thermo) for 1 h at 4 °C.

RNA quantifications. For real-time quantitative PCR, total RNA was extracted and cDNA quantified. Data were normalized to tubulin and *GAPDH* levels. Relative expression is calculated using the delta-Ct method. For RNA expression profiling, total RNAs were extracted, and generated cDNAs were fragmented, labelled and hybridized to the GeneChip Human Gene 1.0 ST Arrays (Affymetrix). Expression data were normalized, background-corrected, and log₂-transformed for parametric analysis. Differentially expressed genes were identified using significance analysis of microarrays (SAM) with the R package 'samr' (false discovery rate (FDR) < 0.05; fold change > 2).

Cell cycle and apoptosis. For cell cycle analysis, cells were fixed, permeabilized and stained with propidium iodide (BD Pharmingen). Cell cycle distribution was analysed by Cell Quest Pro and Modifit software. For apoptosis, cells were co-stained with Annexin V-V450 and propidium iodide (BD Pharmingen). Data were analysed with the FACS Express V2 software.

Full Methods and any associated references are available in the online version of the paper at www.nature.com/nature.

Received 27 July; accepted 2 November 2010.

Published online 24 November 2010.

1. Davies, H. *et al.* Mutations of the *BRAF* gene in human cancer. *Nature* **417**, 949–954 (2002).

2. Flaherty, K. T. *et al.* Inhibition of mutated, activated BRAF in metastatic melanoma. *N. Engl. J. Med.* **363**, 809–819 (2010).
3. Jänne, P. A., Gray, N. & Settleman, J. Factors underlying sensitivity of cancers to small-molecule kinase inhibitors. *Nature Rev. Drug Discov.* **8**, 709–723 (2009).
4. Montagut, C. *et al.* Elevated CRAF as a potential mechanism of acquired resistance to BRAF inhibition in melanoma. *Cancer Res.* **68**, 4853–4861 (2008).
5. Poulikakos, P. I., Zhang, C., Bollag, G., Shokat, K. M. & Rosen, N. RAF inhibitors transactivate RAF dimers and ERK signalling in cells with wild-type BRAF. *Nature* **464**, 427–430 (2010).
6. Søndergaard, J. N. *et al.* Differential sensitivity of melanoma cell lines with *BRAF*^{V600E} mutation to the specific Raf inhibitor PLX4032. *J. Transl. Med.* **8**, 39–50 (2010).
7. Halaban, R. *et al.* PLX4032, a selective *BRAF*^{V600E} kinase inhibitor, activates the ERK pathway and enhances cell migration and proliferation of *BRAF*^{WT} melanoma cells. *Pigment Cell Melanoma Res.* **23**, 190–200 (2010).
8. Hatzivassiliou, G. *et al.* RAF inhibitors prime wild-type RAF to activate the MAPK pathway and enhance growth. *Nature* **464**, 431–435 (2010).
9. Heidorn, S. J. *et al.* Kinase-dead BRAF and oncogenic RAS cooperate to drive tumor progression through CRAF. *Cell* **140**, 209–221 (2010).
10. Bollag, G. *et al.* Clinical efficacy of a RAF inhibitor needs broad target blockade in *BRAF*-mutant melanoma. *Nature* **467**, 596–599 (2010).
11. Tsai, J. *et al.* Discovery of a selective inhibitor of oncogenic B-Raf kinase with potent antimelanoma activity. *Proc. Natl Acad. Sci. USA* **105**, 3041–3046 (2008).
12. Whittaker, S. *et al.* Gatekeeper mutations mediate resistance to BRAF-targeted therapies. *Sci. Transl. Med.* **2**, 35ra41 (2010).
13. Pratilas, C. A. *et al.* *BRAF*^{V600E} is associated with disabled feedback inhibition of RAF-MEK signaling and elevated transcriptional output of the pathway. *Proc. Natl Acad. Sci. USA* **106**, 4519–4524 (2009).
14. Packer, L. M., East, P., Reis-Filho, J. S. & Marais, R. Identification of direct transcriptional targets of BRAF/MEK signalling in melanoma. *Pigment Cell Melanoma Res.* **22**, 785–798 (2009).
15. Wu, E. *et al.* Comprehensive dissection of PDGF-PDGFR signaling pathways in PDGFR genetically defined cells. *PLoS ONE* **3**, e3794 (2008).
16. Smith, G. *et al.* Activating K-Ras mutations without 'hotspot' codons in sporadic colorectal tumours - implications for personalised cancer medicine. *Br. J. Cancer* **102**, 693–703 (2010).
17. Emery, C. M. *et al.* MEK1 mutations confer resistance to MEK and B-RAF inhibition. *Proc. Natl Acad. Sci. USA* **106**, 20411–20416 (2009).
18. Dumaz, N. *et al.* In melanoma, RAS mutations are accompanied by switching signaling from BRAF to CRAF and disrupted cyclic AMP signaling. *Cancer Res.* **66**, 9483–9491 (2006).

Supplementary Information is linked to the online version of the paper at www.nature.com/nature. A figure summarizing the main result of this paper is also included as SI.

Acknowledgements We are grateful to G. Bollag and P. Lin (Plexxikon) for providing PLX4032, J. S. Economou for biopsies, B. Comin-Anduix for FACS assistance, S. Mok for assistance with virus production, C. Ng for tissue acquisition and culture establishment, R. Huang for patient tissue processing, N. Doan for immunohistochemistry, P. Mischel for discussion, B. Chmielowski for coordinated patient care, T.L. Toy for technical help with library generation for deep sequencing, and B. Harry for help with analysis of deep sequence data. R.S.L. acknowledges funding from the following: Dermatology Foundation, Burroughs Wellcome Fund, STOP CANCER Foundation, Margaret E. Early Medical Trust, Ian Copeland Memorial Melanoma Fund, V Foundation for Cancer Research, Melanoma Research Foundation, American Skin Association, Caltech-UCLA Joint Center for Translational Medicine, Wesley Coyle Memorial Fund, and Melanoma Research Alliance. R.N. is supported by a post-doctoral fellowship from the T32 Tumor Immunology Training Grant (S. Dubinett). A.R. is supported by the California Institute for Regenerative Medicine (CIRM), the Jonsson Cancer Center Foundation (JCCF), and Caltech-UCLA Joint Center for Translational Medicine. Array and sequence work were performed within the Jonsson Comprehensive Cancer Center Gene Expression Shared Resource. Patient-informed consent was obtained for the research performed in this study. We would like to thank all the patients that participated in this study.

Author Contributions R.N., H.S., Q.W., X.K., H.L., Z.C. designed and performed experiments and analysed data. M.L. helped analyse data. R.C.K., N.A., H.S., T.C., G.M., J.A.S., and A.R. provided reagents. S.F.N. helped design experiments and interpreted data. A.R. and R.S.L. designed research aims. H.L., S.F.N., G.M., J.A.S. and A.R. helped write the paper. R.S.L. designed and performed experiments, analysed data, provided reagents, and wrote the paper.

Author Information Gene expression and copy number data are deposited at Gene Expression Omnibus under accession numbers GSE24862 and GSE24890, respectively. Reprints and permissions information is available at www.nature.com/reprints. The authors declare competing financial interests: details accompany the full-text HTML version of the paper at www.nature.com/nature. Readers are welcome to comment on the online version of this article at www.nature.com/nature. Correspondence and requests for materials should be addressed to R.S.L. (rio@mednet.ucla.edu).

METHODS

Cell culture, lentiviral constructs and infections. All cell lines were maintained in DMEM with 10% or 20% (short-term cultures) heat-inactivated FBS (Omega Scientific) and 2 mmol l^{-1} glutamine in humidified, 5% CO_2 incubator. To derive PLX4032-resistant sub-lines, M229 and M238 were seeded at low cell density and treated with PLX4032 at $1\text{ }\mu\text{M}$ every 3 days for 4–6 weeks and clonal colonies were then isolated by cylinders. M249 R was derived by successive titration of PLX4032 up to $10\text{ }\mu\text{M}$. PLX4032-resistant sub-lines and short-term cultures were replenished with $1\text{ }\mu\text{M}$ PLX4032 every 2 to 3 days. shRNAs were sub-cloned into the lentiviral vector pLL3.7. N-RAS(Q61K) mutant overexpression construct was made by PCR-amplifying from M249 R4 cDNA and sub-cloning into the lentiviral vector (UCLA Vector Core), creating pRRLsin.cPPT.CMV.hTERT.IRES.GFP-Flag-Q61K-NRAS. Wild-type PDGFR β overexpression construct was PCR-amplified from cDNA and sub-cloned into a lentiviral vector (Clontech), creating pLVX-Tight-Puro-PDGFR β -Myc. Lentiviral constructs were co-transfected with three packaging plasmids into HEK293T cells. Infections were carried out with protamine sulphate.

Cellular proliferation, drug treatments and siRNA transfections. Cell proliferation experiments were performed in a 96-well format (five replicates), and baseline quantification performed at 24 h after cell seeding along with initiation of drug treatments (72 h). Stocks and dilutions of PLX4032 (Plexxikon), AZD6244 (Selleck Chemicals) and U0126 (Promega) were made in DMSO. siRNA pool (Dharmacon) transfections were carried out in 384-well format. TransIT transfection reagent (Mirus) was added to each well and incubated at $37\text{ }^{\circ}\text{C}$ for 20 min. Subsequently, cells were reverse transfected, and the mixture was incubated for 51–61 h at $37\text{ }^{\circ}\text{C}$. Cells were quantified using CellTiter 96 Aqueous One Solution (Promega) or CellTiter-GLO Luminescence (Promega) following the manufacturer's recommendations.

Protein detection. Cell lysates for western blotting were made in RIPA (Sigma) with protease inhibitor cocktail (Roche) and phosphatase inhibitor cocktails I and II (Santa Cruz Biotechnology). Western blots were probed with antibodies against p-MEK1/2 (S217/221), total MEK1/2, p-ERK1/2 (T202/Y204), total ERK1/2, PDGFR β , and EGFR (all from Cell Signaling Technologies), B-RAF and N-RAS (Santa Cruz Biotechnology), pan-RAS (Thermo Scientific) and tubulin (Sigma). p-RTK arrays were performed according to the manufacturer's recommendations (Human Phospho-RTK Array Kit, R&D Systems). For PDGFR β immunohistochemistry, paraffin-embedded formalin fixed tissue sections were subjected to antigen retrieval and incubated with a rabbit monoclonal anti-PDGFR β antibody (Cell Signaling Technology) followed by labelled anti-rabbit polymer horseradish peroxidase (Envision System, Dako Cytomation). Immunocomplexes were visualized using the DAB (3,3'-diaminobenzidine) peroxidase method and nuclei haematoxylin-counterstained.

In vitro kinase assay. Cells were harvested and protein lysates prepared in a NP40-based buffer before subjected to immunoprecipitation (IP). IP beads were then resuspended in ADBI buffer (with Mg/ATP cocktail) and incubated with an inactive, recombinant MEK1 or a truncated RAF-1 (positive control) (Millipore), and with DMSO or $1\text{ }\mu\text{M}$ PLX4032 for 30 min at $30\text{ }^{\circ}\text{C}$. The beads were subsequently pelleted and the supernatant resuspended in sample buffer for western blotting to detect p-MEK and total MEK.

Activated RAS pull-down assay. Melanoma lysates were incubated with glutathione agarose beads coupled to $80\text{ }\mu\text{g}$ GST-RAF-1-RBD (Thermo) for 1 h at $4\text{ }^{\circ}\text{C}$. As controls, Pt48 R lysate was pre-incubated with either 0.1 mM GTP γS (positive control) or 1 mM GDP (negative control) in the presence of 10 mM EDTA (pH 8.0) at $30\text{ }^{\circ}\text{C}$ for 15 min. Reactions were terminated by adding 60 mM MgCl_2 . After washing with Wash Buffer (Thermo), proteins bound to beads were eluted by protein sample buffer. RAS or NRAS levels were detected by immunoblotting.

Quantitative real-time PCR for relative RNA levels. Total RNA was extracted using the RiboPure Kit (Ambion), and reverse transcription reactions were performed using the SuperScript First-Strand Synthesis System (Invitrogen). Real-time PCR analyses were performed using the iCycler iQ Real Time PCR Detection System (BioRad) (Supplementary Table 5). To discriminate specific from non-specific cDNA products, a melting curve was obtained at the end of each run. Data were normalized to tubulin and/or *GAPDH* levels in the samples in duplicates. Relative expression is calculated using the delta-Ct method using the following equations: $\Delta\text{Ct}(\text{Sample}) = \text{Ct}(\text{Target}) - \text{Ct}(\text{Reference})$; relative quantity = $2^{-\Delta\text{Ct}}$.

Quantitative real-time PCR for relative DNA copy numbers. gDNAs were extracted using the FlexiGene DNA Kit (Qiagen) (Human Genomic DNA-Female, Promega). NRAS relative copy number was determined by quantitative PCR (cycle conditions available upon request) using the MyiQ single colour Real-Time PCR Detection System (Bio-Rad). Total DNA content was estimated by assaying β -globin for each sample (Supplementary Table 5), and 20 ng of gDNA was mixed with the SYBR Green QPCR Master Mix (Bio-Rad) and 2 pmol l^{-1} of each primer.

Sequencing. gDNAs were isolated using the Flexi Gene DNA Kit (QIAGEN) or the QIAamp DNA FFPE Tissue Kit. B-RAF and RAS genes were amplified from genomic DNA by PCR. PCR products were purified using QIAquick PCR Purification Kit (QIAGEN) followed by bi-directional sequencing using BigDye v1.1 (Applied Biosystems) in combination with a 3730 DNA Analyzer (Applied Biosystems). PDGFR β was amplified from cDNA by PCR and sequenced (primers listed in Supplementary Table 1).

B-RAF ultra-deep sequencing. Exon-based amplicons were generated using Platinum high-fidelity Taq polymerase, and libraries were prepared following the Illumina library generation protocol version 2.3. For each sample, one library was generated with 18 exons pooled at equal molarity and another library was generated for exon 13 only for validation purpose. Each library was indexed with an unique four base long barcode within the custom made Illumina adaptor. All 10 indexed samples were pooled and sequenced on one lane of Illumina GAIIx flow-cell for single-end 76 base pairs. For error rate estimation, phiX174 genome was spiked in. Base-calling was performed by Illumina RTA version 1.8.70. Alignment was performed using the Novocraft Short Read Alignment Package version 2.06 (<http://www.novocraft.com/index.html>). First, all reads were aligned to the phiX174 reference genome downloaded from the NCBI. The mismatch rates at each position of the reads were calculated to estimate the error rate of the sequencer (set at 1.67% or five standard deviations, SD) based on the phiX genome data (mean error rate = 0.57%, s.d. = 0.22%). Then, the .qseq.txt files were converted into .fastq file using a custom script (available on request) and during this process, the first 5 bases (unique 4-base barcode and the T at the fifth position) were stripped off from the reads and concatenated to the read name. The .fastq file was parsed into 10 .fastq files for each barcode and only the reads with the first 5 bases perfectly matching any of the 10 barcodes were included. Each .fastq file was aligned to chromosome 7 fasta file, generated from the Human Genome reference sequence (hg18, March 2006, build 36.1) downloaded from the Broad Institute (ftp://ftp.broadinstitute.org/pub/gsa/gatk_resources.tgz) using the Novoalign program. Base calibration option was used, and the output format was set to SAM. Using SAMtools (<http://samtools.sourceforge.net/>), the .sam files of each lane were converted to .bam files and sorted, followed by removal of potential PCR duplicates using Picard (<http://picard.sourceforge.net/>). The true background rate was inferred from analysis of independent exon 13 amplicons. None of the 14 positions within exon 13 that had non-reference allele frequency (NAF) > 1.67% in all-exon-samples were validated in the exon13-only samples and vice versa for the one position in the exon 13-only sample, inferring that the true background error rate could be higher at 4.81% (5s.d., mean error rate = 2.72%, s.d. = 0.4%). In total, 12 positions had NAF > 4.81%, and none of them occurred at the same position. We note that the four sample gDNAs extracted from formalin-fixed paraffin-embedded (FFPE) blocks had 5–6 times more variants with NAF above background than the sample extracted from frozen tissue, and the 12 positions with NAF > 4.81% were scattered only across the FFPE samples. The numbers of variants within and outside the kinase domain were not significantly different.

B-RAF deep sequence from whole exome sequence analysis. Genomic libraries were generated following the Agilent SureSelect Human All Exon Kit Illumina Paired-End Sequencing Library Prep Version 1.0.1 protocol at the UCLA Genome Center. Agilent SureSelect All Exon ICGC version was used for capturing ~50 megabase (Mb) exome. The Genome Analyzer IIX (GAIIx) was run using standard manufacturer's recommended protocols. Base-calling was done by Illumina RTA version 1.6.47. Two lanes of Illumina single end (SE) run were generated for each of Pt111-001 normal, baseline and DP2 samples, and one lane of Illumina paired end (PE) run was generated for each of Pt111-001 DP1, DP3 as well as Pt111-010 normal, baseline, DP1 and DP2 samples. Alignment was performed using the Novocraft Short Read Alignment Package version 2.06. Human Genome reference sequence (hg18, March 2006, build 36.1), downloaded from the UCSC genome database located at <http://genome.ucsc.edu> and mirrored locally, was indexed using novoindex program (-k 14 -s 3). Novoalign program was used to align each lane's qseq.txt file to the reference genome. Base calibration option and adaptor stripping option for paired-end run were used and the output format was set to SAM. Using SAMtools (<http://samtools.sourceforge.net/>), the .sam files of each lane were converted to .bam files, sorted and merged for each sample and potential PCR duplicates were removed using Picard (<http://picard.sourceforge.net/>). The .bam files were filtered for SNV calling and small INDEL calling to reduce the likelihood of using spuriously mis-mapped reads to call the variants. For the .bam file to call SNVs, the last 5 bases were trimmed and only the reads lacking indels were retained. For the .bam file to call small INDELs, only the reads containing one contiguous INDEL but not positioned at the beginning or the end of the read were retained. SOAP consensus-calling model implemented in SAMtools was used to call the variants, both SNVs and indels, and generate the .pileup files for each .bam file. Coding regions $\pm 2\text{ bp}$ of B-RAF gene were extracted

from the .pileup files and the reads were manually examined for rare variants (non reference alleles).

Microarray data generation and analysis. Total RNAs were extracted using the RiboPure Kit (Ambion) from cells (DMSO or PLX4032, 1 μ M, 6 h). cDNAs were generated, fragmented, biotinylated, and hybridized to the GeneChip Human Gene 1.0 ST Arrays (Affymetrix). The arrays were washed and stained on a GeneChip Fluidics Station 450 (Affymetrix); scanning was carried out with the GeneChip Scanner 3000 7G; and image analysis with the Affymetrix GeneChip Command Console Scan Control. Expression data were normalized, background-corrected, and summarized using the RMA algorithm implemented in the Affymetrix Expression ConsoleTM version 1.1. Data were log-transformed (base 2) for parametric analysis. Clustering was performed with MeV 4.4, using unsupervised hierarchical clustering analysis on the basis of Pearson correlation and complete/average linkage clustering. Differentially expressed genes were identified using significance analysis of microarrays (SAM) with the R package 'samr' (R 2.9.0; FDR < 0.05; fold change greater than 2). To identify and rank pathways enriched among differentially expressed genes, *P*-values (Fisher's exact test) were calculated for gene sets with at least 20% differentially expressed genes. Curated gene sets of canonical pathways in the Molecular Signatures Database (MSigDB) were used.

Copy number variation analysis. Illumina HumanExon510S-DUO bead arrays (Illumina) were performed following the manufacturer's protocol. Scanned array data were imported into BeadStudio software (Illumina), where signal intensities for samples were normalized against those for reference genotypes. Log₂ ratios were calculated, and data smoothed using the median with window size of 10 and step size of five probes.

Cell cycle and apoptosis analysis. All infected cells were replenished with PLX4032 24 h after infections (M229 R5 treated with AZD6244 to inhibit rebound p-ERK on PDGFR β KD), fixed, permeabilized, and treated with RNase (Qiagen). Cells were stained with 50 mg ml⁻¹ propidium iodide (BD Pharmingen) and the distribution of cell cycle phases was determined by Cell Quest Pro and ModFit software. For apoptosis, post-infection cells were stained with Annexin V-V450 (BD Pharmingen) and propidium iodide for 15 min at room temperature. Flow cytometry data were analysed by the FACS Express V2 software.

Image acquisition and data processing. Statistical analyses were performed using InStat 3 Version 3.0b (GraphPad Software), and graphical representations using DeltaGraph or Prism (Red Rock Software). An Optronics camera system was used in conjunction with Image-Pro Plus software (MediaCybernetics) and Adobe Photoshop 7.0.

COT drives resistance to RAF inhibition through MAP kinase pathway reactivation

Cory M. Johannessen^{1,2*}, Jesse S. Boehm^{1*}, So Young Kim^{1,2,3,†}, Sapana R. Thomas^{1,2}, Leslie Wardwell², Laura A. Johnson^{1,2}, Caroline M. Emery², Nicolas Stransky¹, Alexandria P. Cogdill⁴, Jordi Barretina^{1,2,5}, Giordano Caponigro⁶, Haley Hieronymus^{1,7,8}, Ryan R. Murray^{3,9,10}, Kourosh Salehi-Ashtiani^{3,9,10}, David E. Hill^{3,9,10}, Marc Vidal^{3,9,10}, Jean J. Zhao^{9,11}, Xiaoping Yang¹, Ozan Alkan¹, Sungjoon Kim¹², Jennifer L. Harris¹², Christopher J. Wilson⁶, Vic E. Myer⁶, Peter M. Finan⁶, David E. Root¹, Thomas M. Roberts⁹, Todd Golub^{1,5,8}, Keith T. Flaherty⁴, Reinhard Dummer¹³, Barbara L. Weber⁶, William R. Sellers⁶, Robert Schlegel⁶, Jennifer A. Wargo⁴, William C. Hahn^{1,2,3,5} & Levi A. Garraway^{1,2,5}

Oncogenic mutations in the serine/threonine kinase B-RAF (also known as BRAF) are found in 50–70% of malignant melanomas¹. Pre-clinical studies have demonstrated that the B-RAF(V600E) mutation predicts a dependency on the mitogen-activated protein kinase (MAPK) signalling cascade in melanoma^{2–6}—an observation that has been validated by the success of RAF and MEK inhibitors in clinical trials^{7–9}. However, clinical responses to targeted anticancer therapeutics are frequently confounded by *de novo* or acquired resistance^{10–12}. Identification of resistance mechanisms in a manner that elucidates alternative ‘druggable’ targets may inform effective long-term treatment strategies¹³. Here we expressed ~600 kinase and kinase-related open reading frames (ORFs) in parallel to interrogate resistance to a selective RAF kinase inhibitor. We identified *MAP3K8* (the gene encoding COT/Tpl2) as a MAPK pathway agonist that drives resistance to RAF inhibition in B-RAF(V600E) cell lines. COT activates ERK primarily through MEK-dependent mechanisms that do not require RAF signalling. Moreover, COT expression is associated with *de novo* resistance in B-RAF(V600E) cultured cell lines and acquired resistance in melanoma cells and tissue obtained from relapsing patients following treatment with MEK or RAF inhibitors. We further identify combinatorial MAPK pathway inhibition or targeting of COT kinase activity as possible therapeutic strategies for reducing MAPK pathway activation in this setting. Together, these results provide new insights into resistance mechanisms involving the MAPK pathway and articulate an integrative approach through which high-throughput functional screens may inform the development of novel therapeutic strategies.

To identify kinases capable of circumventing RAF inhibition, we assembled and stably expressed 597 sequence-validated kinase ORF clones representing ~75% of annotated kinases (Center for Cancer Systems Biology (CCSB)/Broad Institute Kinase ORF Collection) in A375, a B-RAF(V600E) malignant melanoma cell line that is sensitive to the RAF kinase inhibitor PLX4720¹⁴ (Fig. 1a, b, Supplementary Table 1 and Supplementary Fig. 2). ORF-expressing cells treated with 1 μ M PLX4720 were screened for viability relative to untreated cells and normalized to an assay-specific positive control, MEK1(S218/222D) (MEK1^{DD})¹⁵ (Supplementary Table 2 and summarized in Supplementary Fig. 1). Nine ORFs conferred resistance at levels exceeding two standard deviations from the mean (Fig. 1b and Supplementary

Table 2) and were selected for follow-up analysis (Supplementary Fig. 3). Three of the nine candidate ORFs were receptor tyrosine kinases, underscoring the potential of this class of kinases to engage resistance pathways. Resistance effects were validated and prioritized across a multi-point PLX4720 drug concentration scale in the B-RAF(V600E) cell lines A375 and SKMEL28. The Ser/Thr MAP kinase kinase kinases (MAP3Ks) *MAP3K8* (COT/Tpl2) and *RAF1* (C-RAF) emerged as top candidates from both cell lines; these ORFs shifted the PLX4720 half-maximal growth inhibitory concentration (GI₅₀) by 10–600-fold without affecting viability (Supplementary Table 3 and Supplementary Figs 4 and 5). Both COT and C-RAF reduced sensitivity to PLX4720 in multiple B-RAF(V600E) cell lines (Fig. 1c) confirming the ability of these kinases to mediate resistance to RAF inhibition.

Next, we tested whether overexpression of these genes was sufficient to activate the MAPK pathway. At baseline, COT expression increased ERK phosphorylation in a manner comparable to MEK1^{DD}, consistent with MAP kinase pathway activation (Fig. 2a and Supplementary Fig. 6). Overexpression of wild-type COT or C-RAF resulted in constitutive phosphorylation of ERK and MEK in the presence of PLX4720, whereas kinase-dead derivatives had no effect (Fig. 2a and Supplementary Fig. 7). Based on these results, we proposed that COT and C-RAF drive resistance to RAF inhibition predominantly through re-activation of MAPK signalling. Notably, of the nine candidate ORFs from our initial screen, a subset (three) did not show persistent ERK/MEK phosphorylation following RAF inhibition, suggesting MAPK pathway-independent alteration of drug sensitivity (Supplementary Fig. 8).

Several groups have shown that C-RAF activation and heterodimerization with B-RAF constitute critical components of the cellular response to B-RAF inhibition^{16–19}. In A375 cells, endogenous C-RAF–B-RAF heterodimers were measurable and inducible following treatment with PLX4720 (Supplementary Fig. 9). However, endogenous C-RAF phosphorylation at S338—an event required for C-RAF activation—remained low (Supplementary Fig. 9). In contrast, ectopically expressed C-RAF was phosphorylated on S338 (Supplementary Fig. 9) and its PLX4720 resistance phenotype was associated with sustained MEK/ERK activation (Fig. 2a, Supplementary Fig. 9). Moreover, ectopic expression of a high-activity C-RAF truncation mutant (C-RAF(W22)) was more effective than wild-type C-RAF in mediating PLX4720 resistance and ERK activation (Supplementary Fig. 10), further indicating that

¹Broad Institute of Harvard and Massachusetts Institute of Technology, 7 Cambridge Center, Cambridge, Massachusetts 02142, USA. ²Department of Medical Oncology, Dana-Farber Cancer Institute, Harvard Medical School, 44 Binney Street, Boston, Massachusetts 02115, USA. ³Center for Cancer Systems Biology (CCSB), Dana-Farber Cancer Institute, Boston, Massachusetts 02115, USA. ⁴Division of Surgical Oncology, Medical Oncology and Dermatology, Massachusetts General Hospital, 55 Fruit Street, Boston, Massachusetts 02114, USA. ⁵Center for Cancer Genome Discovery, Dana-Farber Cancer Institute, Harvard Medical School, 44 Binney Street, Boston, Massachusetts 02115, USA. ⁶Novartis Institutes for Biomedical Research, 250 Massachusetts Avenue, Cambridge, Massachusetts 02139, USA. ⁷Current address: Human Oncology and Pathogenesis Program, Memorial Sloan-Kettering Cancer Center, New York, New York 10065, USA. ⁸Department of Pediatric Oncology, Dana-Farber Cancer Institute, Harvard Medical School, 44 Binney Street, Boston, Massachusetts 02115, USA. ⁹Department of Cancer Biology, Dana-Farber Cancer Institute, Boston, Massachusetts 02115, USA. ¹⁰Department of Genetics, Harvard Medical School, Boston, Massachusetts 02115, USA. ¹¹Department of Pathology, Harvard Medical School, Boston, Massachusetts 02115, USA. ¹²Genomics Institute of the Novartis Research Foundation, San Diego, California 92121, USA. ¹³Department of Dermatology, University Hospital of Zurich, Zurich CH-8091, Switzerland. [†]Present address: Duke Institute for Genome Sciences and Policy, Duke University Medical Center, Durham, North Carolina 27710, USA (S.Y.K.).

*These authors contributed equally to this work.

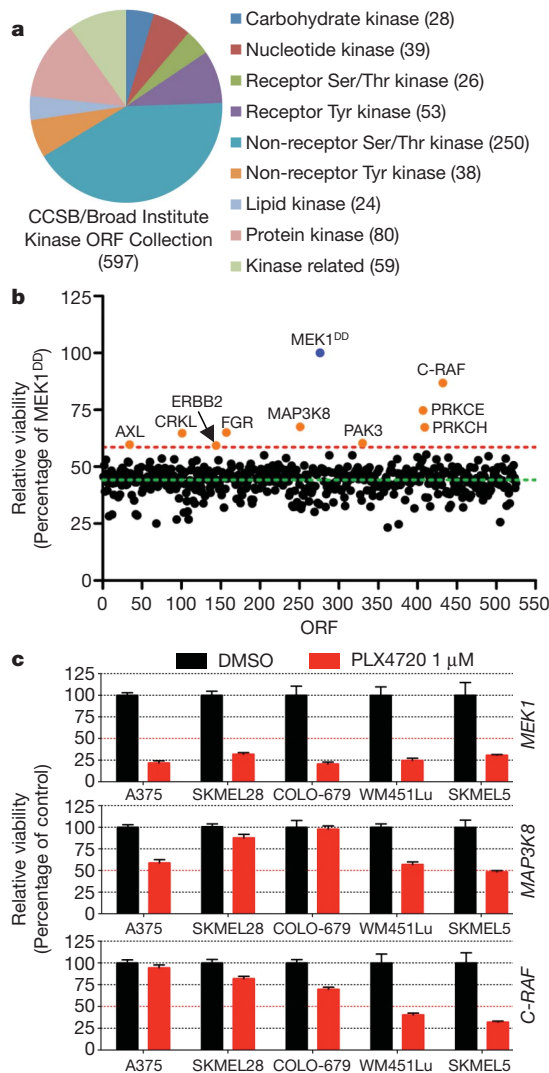


Figure 1 | An ORF-based functional screen identifies COT and C-RAF kinases as drivers of resistance to B-RAF inhibition **a**, Overview of the CCSB/Broad Institute Kinase ORF collection. Kinase classification and number of kinases per classification are noted. **b**, A375 cells expressing the CCSB/Broad Institute Kinase ORF collection were assayed for relative viability in 1 μM PLX4720 and normalized to constitutively active MEK1 (MEK1^{DD}). Nine ORFs (orange disks) scored 2 standard deviations (red dashed line, 58.64%) from the mean of all ORFs (green dashed line, 44.26%). **c**, Indicated ORFs were expressed in five B-RAF(V600E) cell lines and treated with DMSO or 1 μM PLX4720. Viability (relative to DMSO) was quantified after 4 days. Error bars represent standard deviation between replicates ($n = 6$).

elevated C-RAF activity may direct resistance to this agent. Consistent with this model, oncogenic alleles of *NRAS* and *KRAS* conferred PLX4720 resistance in A375 cells (Fig. 2b) and yielded sustained C-RAF(S338) and ERK phosphorylation in the context of drug treatment (Fig. 2c). Thus, although genetic alterations that engender C-RAF activation (for example, oncogenic RAS mutations) tend to show mutual exclusivity with B-RAF(V600E) mutation, such co-occurring events^{20,21} might be favoured in the context of acquired resistance to B-RAF inhibition.

To investigate the role of COT in melanoma, we first determined its expression in human melanocytes. We found that primary immortalized melanocytes (B-RAF wild-type) expressed COT (Fig. 2d), although ectopic B-RAF(V600E) expression reduced *MAP3K8* mRNA levels (Supplementary Fig. 11) and rendered COT protein undetectable (Fig. 2d). Conversely, whereas ectopically expressed COT was only weakly detectable in A375 cells (Fig. 2a, e), short hairpin RNA (shRNA)-mediated depletion of endogenous B-RAF(V600E) caused an increase in COT

protein levels that correlated with the extent of B-RAF knockdown (Fig. 2e). Moreover, treatment of COT-expressing A375 cells with PLX4720 led to a dose-dependent increase in COT protein (Fig. 2a) without affecting ectopic *MAP3K8* mRNA levels (Supplementary Fig. 11). Thus, oncogenic B-RAF may antagonize COT expression largely through altered protein stability (Fig. 2a, d, e and Supplementary Fig. 11), and B-RAF inhibition may potentiate the outgrowth of COT-expressing cells during the course of treatment. Notably, neither C-RAF nor B-RAF alone or in combination was required for ERK phosphorylation in the context of COT expression, even in the presence of PLX4720 (Fig. 2e, f and Supplementary Fig. 12), suggesting that COT expression is sufficient to induce MAP kinase pathway activation in a RAF-independent manner.

We predicted that cell lines expressing elevated COT in a B-RAF(V600E) background should show *de novo* resistance to PLX4720 treatment. To identify such instances, we screened a panel of cell lines for evidence of *MAP3K8* copy number gains coincident with the B-RAF(V600E) mutation. Of 534 cell lines that had undergone copy number analysis and mutation profiling, 38 cell lines (7.1%) contained the B-RAF(V600E) mutation. Within this subgroup, two cell lines—OUMS-23 (colon cancer) and RPMI-7951 (melanoma)—also showed evidence of chromosomal copy gains spanning the *MAP3K8* locus (Fig. 3a and Supplementary Fig. 13) and robust COT protein expression (Fig. 3b and Supplementary Fig. 14). We also screened a panel of melanoma short-term cultures for COT protein expression. Only one of these lines expressed COT: M307, a short-term culture derived from a B-RAF(V600E) tumour that developed resistance to allosteric MEK inhibition following initial disease stabilization¹⁵ (Fig. 3c). All three cell lines were refractory to PLX4720 treatment, with GI₅₀ values in the range of 8–10 μM (Fig. 3d), and showed sustained ERK phosphorylation in the context of B-RAF inhibition (Fig. 3e, f). OUMS-23 and RPMI-7951 are MAPK pathway inhibitor-naïve cell lines, implying that COT may confer *de novo* resistance to RAF inhibition (a phenomenon observed in ~10% of B-RAF(V600E) melanomas⁷).

Next, we examined COT expression in the context of resistance to the clinical RAF inhibitor PLX4032 by obtaining biopsy material from three patients with metastatic, B-RAF(V600E) melanoma. Each case consisted of frozen, lesion-matched biopsy material obtained before and during treatment ('pre-treatment' and 'on-treatment'; Fig. 3g and Supplementary Table 4); additionally, one sample contained two independent biopsy specimens from the same relapsing tumour site ('post-relapse'; Fig. 3g). Consistent with the experimental models presented above, quantitative real-time PCR with reverse transcription (qRT-PCR) analysis revealed increased *MAP3K8* mRNA expression concurrent with PLX4032 treatment in two of three cases. *MAP3K8* mRNA levels were further increased in a relapsing specimen relative to its pre-treatment and on-treatment counterparts (Fig. 3g, Patient 1). An additional, unmatched relapsed malignant melanoma biopsy showed elevated *MAP3K8* mRNA expression comparable to levels observed in RAF inhibitor-resistant, *MAP3K8*-amplified cell lines (Supplementary Fig. 15). This specimen also exhibited robust MAPK pathway activation and elevated expression of B-RAF, C-RAF and COT relative to matched normal skin or B-RAF(V600E) cell lines (Supplementary Fig. 15). Sequencing studies of this tumour revealed no additional mutations in *B-RAF*, *NRAS* or *KRAS* (data not shown). These analyses provided clinical evidence that COT-dependent mechanisms may be operant in at least some PLX4032-resistant malignant melanomas.

To determine if COT might actively regulate MEK/ERK phosphorylation in B-RAF(V600E) cells that harbour naturally elevated COT expression, we introduced shRNA constructs targeting *MAP3K8*/COT into RPMI-7951 cells. Depletion of COT suppressed RPMI-7951 viability (Supplementary Fig. 16) and decreased ERK phosphorylation (Fig. 3h), implying that targeting COT kinase activity might suppress MEK/ERK phosphorylation in cancer cells with COT overexpression or amplification. Treatment of RPMI-7951 cells with a small molecule COT kinase inhibitor^{22–24} resulted in dose-dependent suppression of

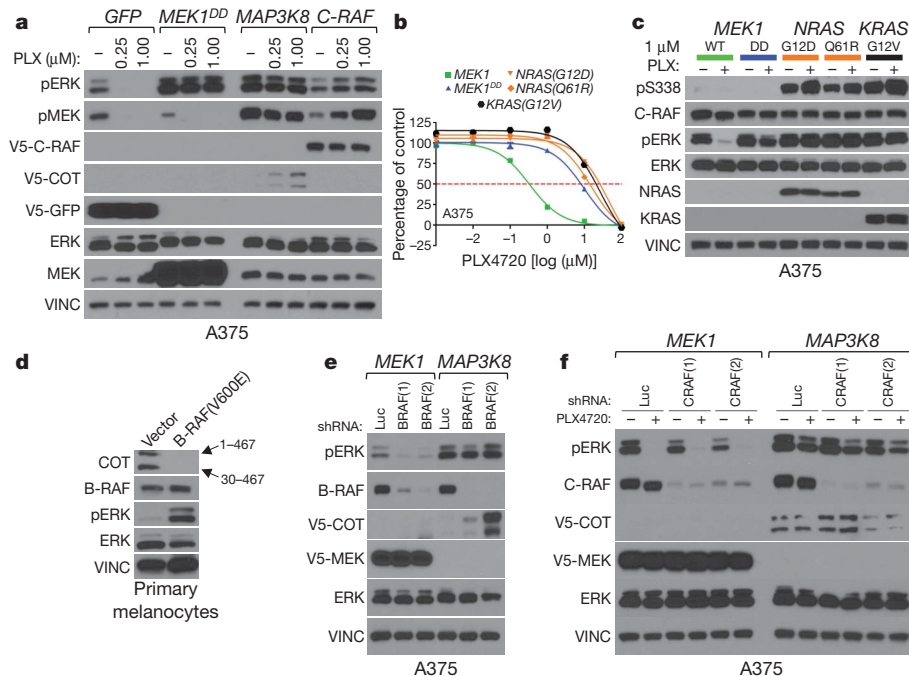


Figure 2 | Resistance to B-RAF inhibition via MAPK pathway activation

a, Indicated ORFs were expressed in A375. Levels of phosphorylated MEK and ERK were assayed after 18 h treatment with DMSO (–) or PLX4720 (concentration noted). GFP, green fluorescent protein; V5-C-RAF, V5-COT, V5-GFP, V5 epitope-tagged C-RAF, COT and GFP, respectively; PLX, PLX4720. **b**, Proliferation of A375 expressing indicated ORFs. Error bars represent standard deviation between replicates ($n = 6$). **c**, C-RAF (S338) and ERK phosphorylation in lysates from A375 expressing indicated ORFs. VINC, vinculin; WT, wild type; pS338, C-RAF phosphorylated on Ser338. **d**, COT

expression in lysates from immortalized primary melanocytes expressing BRAF(V600E) or empty vector. MAP3K8 mRNA has an internal start codon (30^M) resulting in two protein products of different lengths; amino acids 1–467 or 30–467, noted with arrows. **e**, COT expression and ERK phosphorylation in lysates from A375 expressing indicated ORFs following shRNA-mediated B-RAF depletion (shBRAF) relative to control shRNA (shLuc). **f**, ERK phosphorylation in lysates from A375 expressing indicated ORFs following shRNA-mediated C-RAF depletion (shCRAF) or control shRNA (shLuc), after 18 h treatment with DMSO (–) or 1 μM PLX4720 (+).

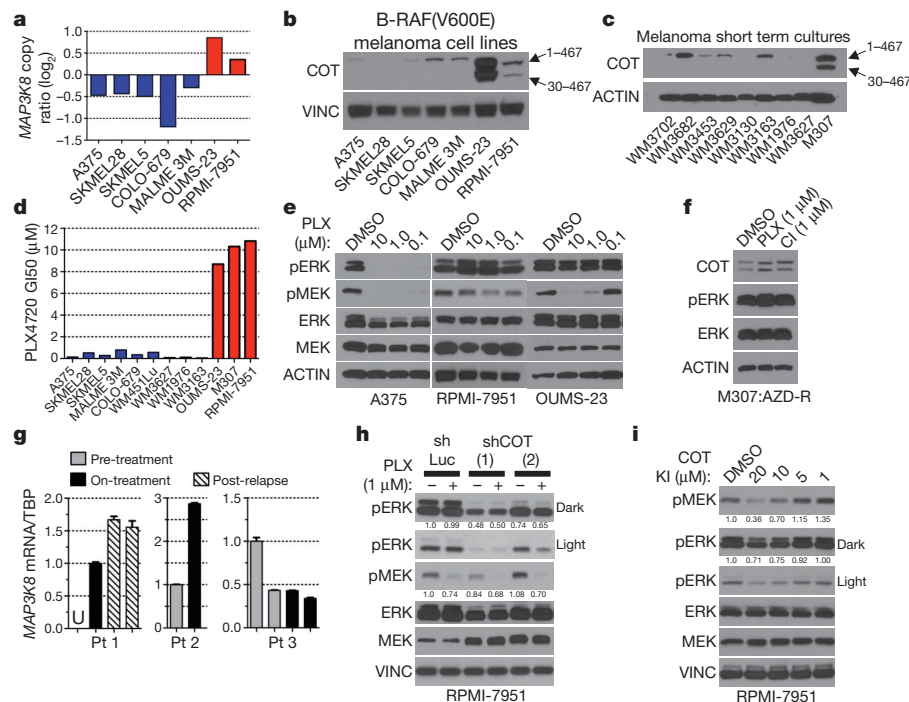


Figure 3 | COT expression predicts resistance to B-RAF inhibition in cancer cell lines **a**, MAP3K8 copy numbers. Red bars, MAP3K8 amplification; blue bars, non-amplified COT. **b**, COT expression in B-RAF(V600E) cell lines and **c**, short-term cultures. **d**, PLX4720 GI₅₀ in B-RAF(V600E) cell lines. Colours as in **a**. **e**, MEK and ERK phosphorylation after treatment with DMSO or PLX4720 (concentration indicated). **f**, ERK phosphorylation in M307 lysates (AZD-R; AZD6244-resistant) treated with DMSO or 1 μM PLX4720 (PLX) or CI-1040 (CI). **g**, MAP3K8 mRNA expression (qRT-PCR) in patient/lesion-matched

PLX4032-treated metastatic melanoma tissue samples. Patients 1 and 3 had multiple biopsies from the same lesion. Error bars represent s.e.m. ($n = 3$). Pt, patient; U, undetermined/undetectable; TBP, TATA binding protein. **h**, ERK and MEK phosphorylation in RPMI-7951 following shRNA-mediated COT depletion (shCOT) versus control (shLuc) and treatment with DMSO (–) or 1 μM PLX4720 (+). ERK and MEK phosphorylation are quantified. **i**, ERK and MEK phosphorylation in RPMI-7951 after 1 h treatment with a small molecule COT kinase inhibitor. ERK and MEK phosphorylation are quantified.

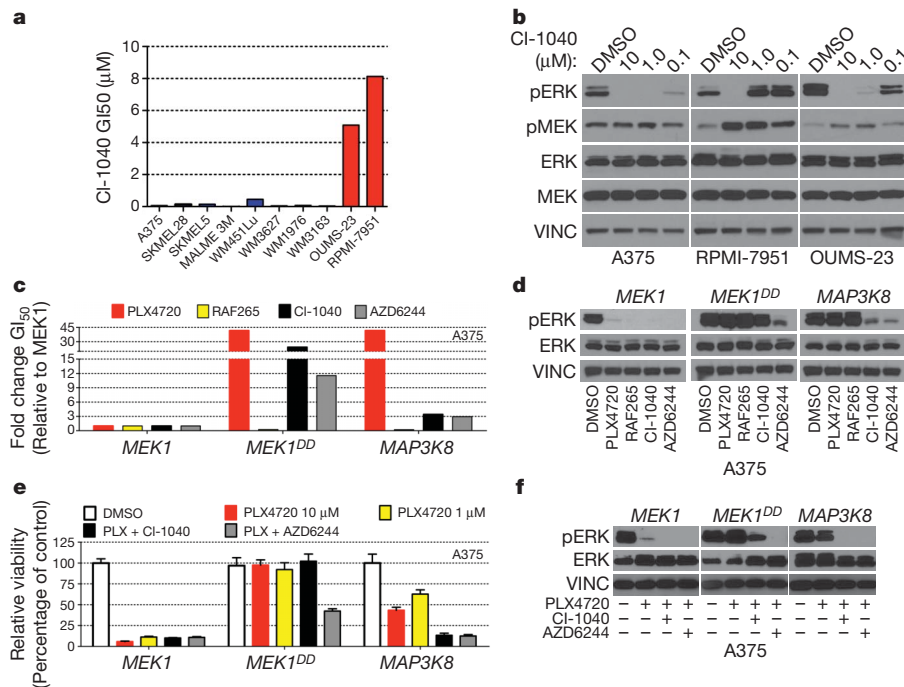


Figure 4 | COT-expressing B-RAF(V600E) cell lines exhibit resistance to allosteric MEK inhibitors **a**, CI-1040 GI₅₀ in a panel of B-RAF(V600E) cell lines. Red bars, COT expression/amplification; blue bars, undetectable/non-amplified COT. **b**, MEK and ERK phosphorylation in lysates from indicated cell lines treated with DMSO or CI-1040 (concentration noted). **c**, Fold change (relative to MEK1) GI₅₀ of A375 ectopically expressing the indicated ORFs for PLX4720, RAF265, CI-1040 and AZD6244. **d**, ERK phosphorylation in A375

MEK and ERK phosphorylation, providing additional evidence that COT contributes to MEK/ERK activation in these cells (Fig. 3i).

We then considered whether COT-expressing cancer cells remain sensitive to MAPK pathway inhibition at a target downstream of COT or RAF. Here, we queried the OUMS-23 and RPMI-7951 cell lines for sensitivity to the MEK1/2 inhibitor CI-1040. Interestingly, both cell lines were refractory to MEK inhibition (Fig. 4a) and displayed sustained ERK phosphorylation even at 1 μM CI-1040 (Fig. 4b). Ectopic COT expression in A375 and SKMEL28 cells also conferred decreased sensitivity to the MEK inhibitors CI-1040 and AZD6244, suggesting that COT expression alone was sufficient to induce this phenotype (Fig. 4c, d and Supplementary Fig. 17). Similar to results observed with pharmacological MEK inhibitors, MEK1/2 knockdown only modestly suppressed COT-mediated ERK phosphorylation in A375 cells (Supplementary Fig. 18). In accordance with prior observations²⁵, these data raised the possibility that COT may activate ERK through MEK-independent as well as MEK-dependent mechanisms. To test this hypothesis directly, we performed an *in vitro* kinase assay using recombinant COT and ERK1. Indeed, recombinant COT induced pThr 202/Tyr 204 phosphorylation of ERK1 *in vitro* (Supplementary Fig. 18), indicating that in certain contexts COT expression may potentiate ERK activation in a MEK-independent manner.

In experimental models, the use of RAF and MEK inhibitors in combination can override resistance to single agents¹⁵. We therefore reasoned that combined RAF/MEK inhibition might circumvent COT-driven resistance. In the setting of ectopic COT expression, exposure to AZD6244 or CI-1040 in combination with PLX470 (1 μM each) reduced cell growth and pERK expression more effectively than did single-agent PLX4720, even at concentrations of 10 μM (Fig. 4e, f and Supplementary Fig. 19). These data underscore the importance of this pathway in B-RAF(V600E) tumour cells and support earlier findings¹⁵ that dual B-RAF/MEK inhibition may help circumvent resistance to RAF inhibitors.

B-RAF mutations are found in ~8% of all cancers and at high frequencies in malignant melanoma, colon and thyroid cancers¹.

expressing indicated ORFs following treatment with DMSO or 1 μM of PLX4720, RAF265, CI-1040 or AZD6244. **e**, Viability of A375 expressing the indicated ORFs and treated with DMSO, PLX4720 (concentration indicated) and PLX4720 in combination with CI-1040 or AZD6244 (all 1 μM). Error bars represent the standard deviation ($n = 6$). **f**, ERK phosphorylation in A375 expressing indicated ORFs following treatment with DMSO, PLX4720 (1 μM) or PLX4720 in combination with CI-1040 or AZD6244 (all 1 μM).

The clinical promise of selective RAF inhibitors has widespread ramifications for patient treatment, yet single-agent targeted therapy is almost invariably followed by relapse due to acquired drug resistance. Our results suggest that ORF-based, systematic functional screening may offer a powerful means to identify clinically relevant resistance mechanisms that also specify novel treatment strategies. In particular, resistance to RAF inhibition can be achieved by multiple MAP3K-dependent mechanisms of MEK/ERK reactivation but might be intercepted through combined therapeutic modalities for MAPK pathway inhibition (for example, RAF/MEK or RAF/COT combinations). Future systematic drug resistance studies may be expanded to a genome scale that encompasses many compounds, thereby enabling comprehensive identification of both therapy-specific resistance genes and drug targets of novel therapeutics.

METHODS SUMMARY

The arrayed, lentiviral ORF screen was performed as described previously²⁶. Effects of individual ORFs on drug resistance were determined by measuring differential viability (ratio of raw viability in 1 μM PLX4720 over control) and subsequent normalization to an assay-specific positive control, MEK1^{DD}. Secondary screens were performed with the top nine candidate ORFs in 96-well format in A375 and SKMEL28 cells. Prioritization was accomplished via generation of a GI₅₀ for each ORF across a multi-point PLX4720 concentration range in both cell lines. The effects of identified resistance ORFs on MAPK pathway activation were demonstrated using both biochemical and cell biological approaches. Cell line copy number data was obtained as previously described²⁷. Detailed descriptions of all procedures are included in Methods.

Full Methods and any associated references are available in the online version of the paper at www.nature.com/nature.

Received 4 March; accepted 25 October 2010.

Published online 24 November 2010.

1. Davies, H. *et al.* Mutations of the *BRAF* gene in human cancer. *Nature* **417**, 949–954 (2002).

2. Hoefflich, K. P. *et al.* Antitumor efficacy of the novel RAF inhibitor GDC-0879 is predicted by BRAF^{V600E} mutational status and sustained extracellular signal-regulated kinase/mitogen-activated protein kinase pathway suppression. *Cancer Res.* **69**, 3042–3051 (2009)
3. McDermott, U. *et al.* Identification of genotype-correlated sensitivity to selective kinase inhibitors by using high-throughput tumor cell line profiling. *Proc. Natl Acad. Sci. USA* **104**, 19936–19941 (2007).
4. Solit, D. B. *et al.* BRAF mutation predicts sensitivity to MEK inhibition. *Nature* **439**, 358–362 (2006).
5. Wan, P. T. *et al.* Mechanism of activation of the RAF-ERK signaling pathway by oncogenic mutations of B-RAF. *Cell* **116**, 855–867 (2004).
6. Wellbrock, C. *et al.* ^{V599E}B-RAF is an oncogene in melanocytes. *Cancer Res.* **64**, 2338–2342 (2004).
7. Flaherty, K. T. *et al.* Inhibition of mutated, activated BRAF in metastatic melanoma. *N. Engl. J. Med.* **363**, 809–819 (2010).
8. Infante, J. R. *et al.* Safety and efficacy results from the first-in-human study of the oral MEK 1/2 inhibitor GSK1120212. *J. Clin. Oncol.* **28** (suppl.), 2503 (2010).
9. Schwartz, G. K. *et al.* A phase I study of XL281, a selective oral RAF kinase inhibitor, in patients (Pts) with advanced solid tumors. *J. Clin. Oncol.* **27** (suppl.), 3513 (2009).
10. Engelman, J. A. *et al.* MET amplification leads to gefitinib resistance in lung cancer by activating ERBB3 signaling. *Science* **316**, 1039–1043 (2007).
11. Gorre, M. E. *et al.* Clinical resistance to STI-571 cancer therapy caused by BCR-ABL gene mutation or amplification. *Science* **293**, 876–880 (2001).
12. Heinrich, M. C. *et al.* Molecular correlates of imatinib resistance in gastrointestinal stromal tumors. *J. Clin. Oncol.* **24**, 4764–4774 (2006).
13. Daub, H., Specht, K. & Ullrich, A. Strategies to overcome resistance to targeted protein kinase inhibitors. *Nature Rev. Drug Discov.* **3**, 1001–1010 (2004).
14. Tsai, J. *et al.* Discovery of a selective inhibitor of oncogenic B-Raf kinase with potent antimelanoma activity. *Proc. Natl Acad. Sci. USA* **105**, 3041–3046 (2008).
15. Emery, C. M. *et al.* MEK1 mutations confer resistance to MEK and B-RAF inhibition. *Proc. Natl Acad. Sci. USA* **106**, 20411–20416 (2009).
16. Hatzivassiliou, G. *et al.* RAF inhibitors prime wild-type RAF to activate the MAPK pathway and enhance growth. *Nature* **464**, 431–435 (2010).
17. Heidorn, S. J. *et al.* Kinase-dead BRAF and oncogenic RAS cooperate to drive tumor progression through CRAF. *Cell* **140**, 209–221 (2010).
18. Karreth, F. A., DeNicola, G. M., Winter, S. P. & Tuveson, D. A. C-Raf inhibits MAPK activation and transformation by B-Raf^{V600E}. *Mol. Cell* **36**, 477–486 (2009).
19. Poulikakos, P. I., Zhang, C., Bollag, G., Shokat, K. M. & Rosen, N. RAF inhibitors transactivate RAF dimers and ERK signalling in cells with wild-type BRAF. *Nature* **464**, 427–430 (2010).
20. Edlundh-Rose, E. *et al.* NRAS and BRAF mutations in melanoma tumours in relation to clinical characteristics: a study based on mutation screening by pyrosequencing. *Melanoma Res.* **16**, 471–478 (2006).
21. Seth, R. *et al.* Concomitant mutations and splice variants in KRAS and BRAF demonstrate complex perturbation of the Ras/Raf signalling pathway in advanced colorectal cancer. *Gut* **58**, 1234–1241 (2009).
22. George, D. *et al.* Discovery of thieno[2,3-*c*]pyridines as potent COT inhibitors. *Bioorg. Med. Chem. Lett.* **18**, 4952–4955 (2008).
23. Hirata, K. *et al.* Inhibition of tumor progression locus 2 protein kinase suppresses receptor activator of nuclear factor- κ B ligand-induced osteoclastogenesis through down-regulation of the c-Fos and nuclear factor of activated T cells c1 genes. *Biol. Pharm. Bull.* **33**, 133–137 (2010).
24. Lee, K. M., Lee, K. W., Bode, A. M., Lee, H. J. & Dong, Z. Tpl2 is a key mediator of arsenite-induced signal transduction. *Cancer Res.* **69**, 8043–8049 (2009).
25. Tsatsanis, C., Patriotic, C. & Tsichlis, P. N. Tpl-2 induces IL-2 expression in T-cell lines by triggering multiple signaling pathways that activate NFAT and NF- κ B. *Oncogene* **17**, 2609–2618 (1998).
26. Barbie, D. A. *et al.* Systematic RNA interference reveals that oncogenic KRAS-driven cancers require TBK1. *Nature* **462**, 108–112 (2009).
27. Beroukhi, R. *et al.* The landscape of somatic copy-number alteration across human cancers. *Nature* **463**, 899–905 (2010).

Supplementary Information is linked to the online version of the paper at www.nature.com/nature.

Acknowledgements We thank members of the Broad Institute/Novartis Cancer Cell Line Encyclopedia (CCLE) for contributing cell line genomic data, expression data and pharmacological cell line sensitivity data; J. Thibault and A. Shipway for CCLE related tissue culture; R. Depinho, G. Dunn, S. Ethier, H. Greulich, A. Henderson, D. Kaplan, R. Levine, C. Miller, H. Piwnicka-Worms, H. Suzuki, M. Vigny, D. Vollrath and the Harvard Institute of Proteomics for contributing templates for the kinase collection; J. Du and D. B. Wheeler for assistance with functional testing of kinases; D. A. Barbie for helpful discussions, S. E. Moody and H. W. Cheung for technical assistance, and J. K. Grenier and S. J. Silver for compiling and annotating the list of kinases. This work was supported by the NIH Director's New Innovator Award (L.A.G.), grants from the Novartis Institutes for Biomedical Research (L.A.G.), Melanoma Research Alliance (L.A.G.), Starr Cancer Consortium (L.A.G.) the US National Cancer Institute (R33 CA128625, RC2 CA148268) (W.C.H.), NIH (CA134502) (J.J.Z.) the Swiss National Foundation (310040-103671) (R.D.), the Gottfried and Julia Bangerter Rhyner Stiftung (R.D.) the Ellison Foundation (M.V. and CCSB) and institute sponsored research funds from the DFCI Strategic Initiative (M.V. and CCSB).

Author Contributions C.M.J., J.S.B. and L.A.G. designed the experiments, with help from C.M.E. C.M.J., S.Y.K. and L.W. performed the primary screen, supervised by W.C.H. L.A.J. helped perform drug sensitivity profiling. J.S.B. designed and created the CCSB/Broad Institute Kinase ORF Collection in collaboration with S.R.T., H.H., R.R.M., K.S.-A., J.J.Z., M.V., T.M.R., T.G., D.E.H. and W.C.H. Additional help with ORF experiments was provided by X.Y., D.E.R. and O.A. Clinical samples were collected or experiments performed by C.M.J., A.P.C., K.T.F., R.D. and J.A.W. Large scale cell genomic and expression profiling along with pharmacological screening efforts were designed and data analysed by N.S., J.B., G.C., S.K., J.H., C.J.W., V.E.M., P.M.F., B.L.W., W.R.S., R.S. and L.A.G. C.M.J. and L.A.G. wrote the manuscript. All authors discussed results and edited the manuscript.

Author Information Reprints and permissions information is available at www.nature.com/reprints. The authors declare competing financial interests: details accompanying the full-text HTML version of the paper at www.nature.com/nature. Readers are welcome to comment on the online version of this article at www.nature.com/nature. Correspondence and requests for materials should be addressed to L.A.G. (Levi_Garraway@dfci.harvard.edu).

METHODS

Center for Cancer Systems Biology (CCSB)/Broad Institute Kinase Open Reading Frame Collection. We assembled a library of 597 kinase ORFs in pDONR-223 Entry vectors (Invitrogen). Individual clones were end-sequenced using vector-specific primers in both directions. Clones with substantial deviations from reported sequences were discarded. Entry clones and sequences are available via Addgene (http://www.addgene.org/human_kinases). Kinase ORFs were assembled from multiple sources; 337 kinases were isolated as single clones from the ORFeome 5.1 collection (<http://horfdb.dfci.harvard.edu>), 183 kinases were cloned from normal human tissue RNA (Ambion) by reverse transcription and subsequent PCR amplification to add Gateway sequences (Invitrogen), 64 kinases were cloned from templates provided by the Harvard Institute of Proteomics (HIP), and 13 kinases were cloned into the Gateway system from templates obtained from collaborating laboratories. The Gateway-compatible lentiviral vector pLX-Blast-V5 was created from the pLKO.1 backbone. LR Clonase enzymatic recombination reactions were performed to introduce the 597 kinases into pLX-Blast-V5 according to the manufacturer's protocol (Invitrogen).

High throughput ORF screening. A375 melanoma cells were plated in 384-well microtitre plates (500 cells per well). The following day, cells were spin-infected with the lentivirally-packaged kinase ORF library in the presence of $8 \mu\text{g ml}^{-1}$ polybrene. At 48 h post-infection, media were replaced with standard growth media (two replicates), media containing $1 \mu\text{M}$ PLX4720 (two replicates, two time points) or media containing $10 \mu\text{g ml}^{-1}$ blasticidin (two replicates). After 4 and 6 days, cell growth was assayed using Cell Titer-Glo (Promega) according to manufacturer instructions. The entire experiment was performed twice.

Identification of candidate resistance ORFs. Raw luminescence values were imported into Microsoft Excel. Infection efficiency was determined by the percentage of duplicate-averaged raw luminescence in blasticidin-selected cells relative to non-selected cells. ORFs with an infection efficiency of less than 0.70 were excluded from further analysis along with any ORF having a standard deviation of $>15,000$ raw luminescence units between duplicates. To identify ORFs whose expression affects proliferation, we compared the duplicate-averaged raw luminescence of individual ORFs against the average and standard deviation of all control-treated cells via the z -score, or standard score, below,

$$z = \frac{x - \mu}{\sigma}$$

where x is the average raw luminescence of a given ORF, μ is the mean raw luminescence of all ORFs and σ is the standard deviation of the raw luminescence of all wells. Any individual ORF with a z -score $> +2$ or < -2 was annotated as affecting proliferation and removed from final analysis. Differential proliferation was determined by the percentage of duplicate-averaged raw luminescence values in PLX4720 ($1 \mu\text{M}$)-treated cells relative to untreated cells. Subsequently, differential proliferation was normalized to the positive control for PLX4720 resistance, MEK1(S218/222D) (MEK1^{DD}), with MEK1^{DD} differential proliferation = 1.0. MEK1^{DD}-normalized differential proliferation for each individual ORF was averaged across two duplicate experiments, with two time points for each experiment (day 4 and day 6). A z -score was then generated, as described above, for average MEK1^{DD}-normalized differential proliferation. ORFs with a z -score of >2 were considered hits and were followed up in the secondary screen.

ORF and shRNA expression. ORFs were expressed from pLX-Blast-V5 (lentiviral) or pWZL-Blast, pBABE-Puro or pBABE-zeocin (retroviral) expression plasmids. For lentiviral transduction, 293T cells were transfected with $1 \mu\text{g}$ of pLX-Blast-V5-ORF or pLKO.1-shRNA, 900 ng $\Delta 8.9$ (*gag*, *pol*) and 100 ng VSV-G using 6 μl Eugene6 transfection reagent (Roche). Viral supernatant was harvested 72 h post-transfection. Mammalian cells were infected at a 1:10–1:20 dilution of virus in 6-well plates in the presence of $5 \mu\text{g ml}^{-1}$ polybrene and centrifuged at 2,250 r.p.m. (1,178g) for 1 h at 37°C . Twenty-four hours after infection blasticidin (pLX-Blast-V5, $10 \mu\text{g ml}^{-1}$) or puromycin (pLKO.1, $0.75 \mu\text{g ml}^{-1}$) was added and cells were selected for 48 h. For retrovirus production, 293T cells were transfected with $1 \mu\text{g}$ of retroviral plasmid-ORF, $1 \mu\text{g}$ pCL-AMPHO and 100 ng VSV-G, as described above. Cells were infected with retrovirus containing supernatant at a 1:2 dilution in $5 \mu\text{g ml}^{-1}$ polybrene overnight, followed by media change to growth media. Infection was repeated once more (twice total), followed by selection, above.

Secondary screen. A375 (1.5×10^3) and SKMEL28 cells (3×10^3) were seeded in 96-well plates for 18 h. ORF-expressing lentivirus was added at a 1:10 dilution in the presence of $8 \mu\text{g ml}^{-1}$ polybrene, and centrifuged at 2,250 r.p.m. (1,178g) and 37°C for 1 h. Following centrifugation, virus-containing media were changed to normal growth media and allowed to incubate for 18 h. Twenty-four hours after infection, DMSO (1:1,000) or $10\times$ PLX4720 (in DMSO) was added to a final concentration of 100, 10, 1, 0.1, 0.01, 0.001, 0.0001 or 0.00001 μM . Cell viability was assayed using WST-1 (Roche), per manufacturer recommendation, 4 days after the addition of PLX4720.

Cell lines and reagents. A375, SKMEL28, SKMEL30, COLO-679, WM451lu, SKMEL5, Malme 3M, SKMEL30, WM3627, WM1976, WM3163, WM3130, WM3629, WM3453, WM3682 and WM3702 were all grown in RPMI (Cellgro), 10% FBS and 1% penicillin/streptomycin. M307 was grown in RPMI (Cellgro), 10% FBS and 1% penicillin/streptomycin supplemented with 1 mM sodium pyruvate. 293T, OUMS-23 and RPMI-7951 cells (ATCC) were grown in MEM (Cellgro), 10% FBS and 1% penicillin/streptomycin. Wild-type primary melanocytes were grown in HAM's F10 (Cellgro), 10% FBS and 1% penicillin/streptomycin. B-RAF(V600E)-expressing primary melanocytes were grown in TIVA media (Ham's F-10 (Cellgro), 7% FBS, 1% penicillin/streptomycin, 2 mM glutamine (Cellgro), $100 \mu\text{M}$ IBMX, 50 ng ml^{-1} TPA (12-*O*-tetradecanoyl-phorbol-13-acetate), 1 mM 3',5'-cyclic AMP dibutyrate (dbcAMP; Sigma) and $1 \mu\text{M}$ sodium vanadate). CI-1040 (PubChem ID: 6918454) was purchased from Shanghai Lechen International Trading Co., AZD6244 (PubChem ID: 10127622) from Selleck Chemicals, and PLX4720 (PubChem ID: 24180719) from Symansis. RAF265 (PubChem ID: 11656518) was a generous gift from Novartis Pharma AG. Unless otherwise indicated, all drug treatments were for 16 h. Activated alleles of NRAS and KRAS have been described previously^{28,29}.

Pharmacologic growth inhibition assays. Cultured cells were seeded into 96-well plates (3,000 cells per well) for all melanoma cell lines; 1,500 cells were seeded for A375. Twenty-four hours after seeding, serial dilutions of the relevant compound were prepared in DMSO added to cells, yielding final drug concentrations ranging from $100 \mu\text{M}$ to $1 \times 10^5 \mu\text{M}$, with the final volume of DMSO not exceeding 1%. Cells were incubated for 96 h following addition of drug. Cell viability was measured using the WST1 viability assay (Roche). Viability was calculated as a percentage of control (untreated cells) after background subtraction. A minimum of six replicates were performed for each cell line and drug combination. Data from growth-inhibition assays were modelled using a nonlinear regression curve fit with a sigmoid dose-response. These curves were displayed and GI_{50} generated using GraphPad Prism 5 for Windows (GraphPad). Sigmoid-response curves that crossed the 50% inhibition point at or above $10 \mu\text{M}$ have GI_{50} values annotated as $>10 \mu\text{M}$. For single-dose studies, the identical protocol was followed, using a single dose of indicated drug ($1 \mu\text{M}$ unless otherwise noted).

Immunoblots and immunoprecipitations. Cells were washed twice with ice-cold PBS and lysed with 1% NP-40 buffer (150 mM NaCl, 50 mM Tris pH 7.5, 2 mM EDTA pH 8, 25 mM NaF and 1% NP-40) containing $2\times$ protease inhibitors (Roche) and $1\times$ Phosphatase Inhibitor Cocktails I and II (CalBioChem). Lysates were quantified (Bradford assay), normalized, reduced, denatured (95°C) and resolved by SDS gel electrophoresis on 10% Tris/Glycine gels (Invitrogen). Protein was transferred to PVDF membranes and probed with primary antibodies recognizing pERK1/2 (T202/Y204), pMEK1/2 (S217/221), MEK1/2, MEK1, MEK2, C-RAF (rabbit host), pC-RAF (pS338) (Cell Signaling Technology; 1:1,000), V5-HRP (HRP, horseradish peroxidase; Invitrogen; 1:5,000), COT (1:500), B-RAF (1:2,000), Actin (1:1,000), Actin-HRP (1:1,000; Santa Cruz), C-RAF (mouse host; 1:1,000; BD Transduction Labs), Vinculin (Sigma; 1:20,000), AXL (1:500; R&D Systems). After incubation with the appropriate secondary antibody (anti-rabbit, anti-mouse IgG, HRP-linked; 1:1,000 dilution, Cell Signaling Technology or anti-goat IgG, HRP-linked; 1:1,000 dilution; Santa Cruz), proteins were detected using chemiluminescence (Pierce). Immunoprecipitations were performed overnight at 4°C in 1% NP-40 lysis buffer, as described above, at a concentration of $1 \mu\text{g ml}^{-1}$ total protein using an antibody recognizing C-RAF (1:50; Cell Signaling Technology). Antibody: antigen complexes were bound to Protein A agarose (25 μl , 50% slurry; Pierce) for 2 h at 4°C . Beads were centrifuged and washed three times in lysis buffer and eluted and denatured (95°C) in $2\times$ reduced sample buffer (Invitrogen). Immunoblots were performed as above. Phospho-protein quantification was performed using NIH ImageJ.

Lysates from tumour and matched normal skin were generated by mechanical homogenization of tissue in RIPA (50 mM Tris (pH 7.4), 150 mM NaCl, 1 mM EDTA, 0.1% SDS, 1.0% NaDOC (sodium deoxycholate), 1.0% Triton X-100, 25 mM NaF, 1 mM Na_3VO_4) containing protease and phosphatase inhibitors, as above. Subsequent normalization and immunoblots were performed as above.

Biopsied melanoma tumour material. Biopsied tumour material consisted of discarded and de-identified tissue that was obtained with informed consent and characterized under protocol 02-017 (paired samples, Massachusetts General Hospital) and 07-087 (unpaired sample, Dana-Farber Cancer Institute). For paired specimens, 'on-treatment' samples were collected 10–14 days after initiation of PLX4032 treatment (Supplementary Table 4).

Inhibition of COT kinase activity. Adherent RPMI-7951 cells were washed twice with $1\times$ PBS and incubated overnight in serum-free growth media. Subsequently, 4-(3-chloro-4-fluorophenylamino)-6-(pyridin-3-yl-methylamino)-3-cyano-[1,7]-naphthyridine (EMD; TPL2 inhibitor I; catalogue number 616373, PubChem ID:

9549300), suspended in DMSO at the indicated concentration, was added to cells for 1 h, after which protein extracts were made as described above.

Quantitative RT-PCR. mRNA was extracted from cell lines and fresh-frozen tumours using the RNeasy kit (Qiagen). Total mRNA was used for subsequent reverse transcription using the SuperScript III First-Strand Synthesis SuperMix (Invitrogen) for cell lines and unpaired tumour samples, and the SuperScript VILO cDNA synthesis kit (Invitrogen) for paired frozen tumour samples. The reverse transcription reaction (5 µl) was used for quantitative PCR using SYBR Green PCR Master Mix and gene-specific primers, in triplicate, using an ABI 7300 Real Time PCR System. Primers used for detection are as follows; *COT* forward: 5'-CAAGTGAAGAGCCAGCAGTTT-3'; *COT* reverse: 5'-GCAAGCAAATCC TCCACAGTTC-3'; *TBP* forward: 5'-CCCGAAACGCCGAATATAATCC-3'; *TBP* reverse: 5'-GACTGTTCTTCACTCTTGGCTC-3'; *GAPDH* forward: 5'-CATCATCTCTGCCCCCTCT-3'; *GAPDH* reverse: 5'-GGTGCTAAGCAG TTGGTGGT-3'.

In vitro kinase assay. *In vitro* kinase assays were performed as described previously¹⁵ using 1 µg each of COT (amino acids 30–397, R&D Systems) and inactive ERK1 (Millipore).

Cellular viability assays. Adherent RPMI-7951 cells were infected with virus expressing shRNAs against *COT* or *Luciferase* as described above. Following selection, cells were plated (1.5×10^5 cells per well) onto a 24-well plate in quadruplicate. Viable cells were counted via trypan blue exclusion using a VI-CELL Cell Viability Analyser, following manufacturer's specifications. Quadruplicate cell counts were averaged and normalized relative to that of the control shRNA.

The Cancer Cell Line Encyclopedia (CCLE). The Cancer Cell Line Encyclopedia (CCLE) project is a collaboration between the Broad Institute, the Novartis Institutes for Biomedical Research (NIBR) and the Genomics Institute of the Novartis Research Foundation (GNF) to conduct a detailed genetic and pharmacologic characterization of a large panel of human cancer models, to develop

integrated computational analyses that link distinct pharmacologic vulnerabilities to genomic patterns and to translate cell line integrative genomics into cancer patient stratification. Chromosomal copy number and gene expression data used for this study are available online at <http://www.broadinstitute.org/cgi-bin/cancer/datasets.cgi>.

Expression profiling of cancer cell lines. We carried out oligonucleotide microarray analysis using the GeneChip Human Genome U133 Plus 2.0 Affymetrix expression array (Affymetrix). Samples were converted to labelled, fragmented, cRNA following the Affymetrix protocol for use on the expression microarray.

shRNA constructs used (pLKO.1). The shRNA constructs used were shLuc (TRCN0000072243, 5'-CTTCGAAATGTCCGTTCCGGTT-3'), shBRAF(1) (TRCN0000006289, NM_004333.2-1106s1c1, 5'-CTTCGAAATGTCCGTTCCGTT-3'), shBRAF(2) (TRCN0000006291, NM_004333.2-2267s1c1, 5'-GCTGG TTTCCAAACAGAGGAT-3'), shCRAF(1) (TRCN0000001066, NM_002880.x-1236s1c1, 5'-CGGAGATGTTGCAGTAAAGAT-3'), shCRAF(2) (TRCN0000001068, NM_002880.x-1529s1c1, 5'-GAGACATGAAATCCAACAATA-3'), shMEK1(1) (TRCN0000002332, NM_002755.x-1015s1c1, 5'-GATTACATAGTCAACGAG CCT-3'), shMEK1(2) (TRCN0000002329, NM_002755.x-455s1c1, 5'-GCTTC TATGGTGCCTTCTACA-3'), shMEK2(1) (TRCN0000007007, NM_030662.2-1219s1c1, 5'-TGGACTATATTGTGAACGAGC-3'), shMEK2(2) (TRCN0000007005, NM_030662.2-847s1c1, 5'-CCAACATCCTCGTGAACCTCTA-3'), shCOT(1) (TRCN0000010013, NM_005204.x-1826s1c1, 5'-CAAGAGCCGCAGACCTAC TAA-3') and shCOT(2) (TRCN0000196518, NM_005204.2-2809s1c1, 5'-GAT GAGAATGTGACCTTTAAG-3').

28. Boehm, J. S. *et al.* Integrative genomic approaches identify *IKBKE* as a breast cancer oncogene. *Cell* **129**, 1065–1079 (2007).
29. Lundberg, A. S. *et al.* Immortalization and transformation of primary human airway epithelial cells by gene transfer. *Oncogene* **21**, 4577–4586 (2002).